INFORMATION TO USERS

This manuscript has been reproduced from the microfilm master. UMI films the text directly from the original or copy submitted. Thus, some thesis and dissertation copies are in typewriter face, while others may be from any type of computer printer.

The quality of this reproduction is dependent upon the quality of the copy submitted. Broken or indistinct print, colored or poor quality illustrations and photographs, print bleedthrough, substandard margins, and improper alignment can adversely affect reproduction.

In the unlikely event that the author did not send UMI a complete manuscript and there are missing pages, these will be noted. Also, if unauthorized copyright material had to be removed, a note will indicate the deletion.

Oversize materials (e.g., maps, drawings, charts) are reproduced by sectioning the original, beginning at the upper left-hand corner and continuing from left to right in equal sections with small overlaps.

Photographs included in the original manuscript have been reproduced xerographically in this copy. Higher quality 6" x 9" black and white photographic prints are available for any photographs or illustrations appearing in this copy for an additional charge. Contact UMI directly to order.

ProQuest Information and Learning
300 North Zeeb Road, Ann Arbor, MI 48106-1346 USA
800-521-0600

THE UNIVERSITY OF OKLAHOMA

GRADUATE COLLEGE

TITANIUM DIOXIDE AEROGELS AS PHOTOCATALYSTS FOR INDOOR AIR DECONTAMINATION

A DISSERTATION

SUBMITTED TO THE GRADUATE FACULTY

in partial fulfillment of the requirements for the

degree of

Doctor of Philosophy

By

MARTINA DREYER
Norman, Oklahoma
2002

ProQuest Information and Learning Company
300 North Zeeb Road
P.O. Box 1346
Ann Arbor, MI 48106-1346

TITANIUM DIOXIDE AEROGELS AS PHOTOCATALYST
FOR INDOOR AIR DECONTAMINATION

A DISSERTATION APPROVED FOR THE
SCHOOL OF CHEMICAL ENGINEERING AND MATERIALS SCIENCE

BY

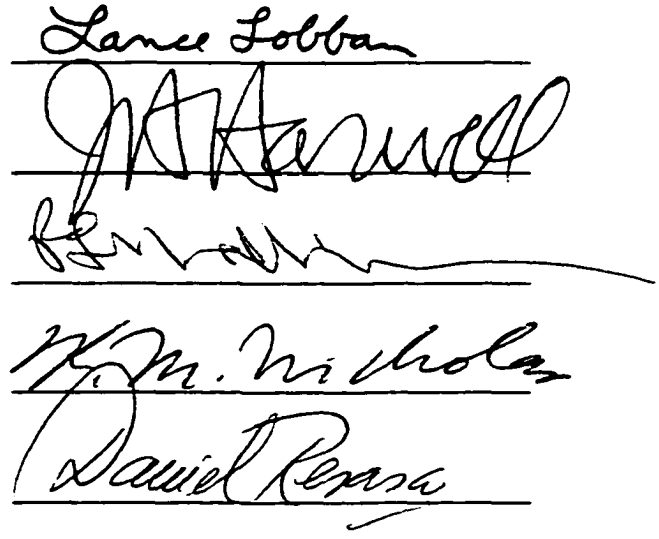

In appreciation to
Gerard K. Newman

ACKNOWLEDGMENTS

First comes first: Dr. Lance Lobban. One of my first classes I took at OU was taught by Dr. Lobban. Thanks to his excellent teaching skills in class and the extra mile he goes to help "lost" students (such as myself at times) outside of class, I learned how to approach solving problems, how to think in broader dimensions, and how to apply previously gained knowledge – simply, how to close the gap between "not knowing" and knowledge. But, it did not end there. Dr. Lobban became my research advisor (how lucky I am!). Simply saying "thank you" would not be enough for the impact this high-spirited facilitator of independent critical thinking has had on my way of thinking and analytical approaching problems. I am ever grateful for his teaching, his flexibility, his understanding, and his encouragement in situations of procrastination.

Special thanks go equally to Dr. Jeffrey Harwell, Dr. Daniel Resasco, Dr. Richard Mallinson, and Dr. Kenneth Nicholas for serving on my advisory committee and for their valuable criticism.

Most of all, I want to thank Jerry Newman for his guidance and caring support he provided over the past ten years. I can only vaguely describe how fortunate I was for being able to have worked under the supervision and guidance of such a creative and never resting researcher. I am very grateful for his direction and friendship. ***What I am today is, in big part, because of him.*** At the same time, I wish to express my appreciation to Penny Newman for her advice and moral support, which helped me in many ways.

David Elliott from the Technical Center of Kerr-McGee in Oklahoma City deserves recognition. He graciously helped me out with pore size distribution measurements of the aerogel samples and when otherwise some emergency measurements had to be performed. I am also grateful for Ron Conlon's XRD measurements and the valuable discussions with him. Greg Stroud and Bill Chissoe from the Microbiology Department had an incredible amount of patience and endurance with never-ending requests for TEM and SEM sessions. Thanks for their contributions.

I would not have been able to run my experiments so smoothly without Larry Isley's contribution. The amazing quality with Larry is that he did never simply work on requests for repair or help with modifications on the experimental setup. Moreover, his experience and creative mind always toped off any ideas brought to him that were related to requests for special devices or other impossible utensils. I want to thank him for having been more than a technician, for having been someone who showed interest and cared about the student's research projects.

I could barely imagine how I would have finished any papers, reports, calculations, or presentations in a timely manner without Rick Wheeler's advice and his ever often actively putting hands on with computer related problems. I wish to express my gratitude to him, who prevented me from several nervous breakdowns after hours of struggling with PC or laptop problems. I also thank the staff, the secretaries, and assistants in the office of the Chemical Engineering Department for solving so many bureaucratic matters. I would like to specially thank Sherry Childress, Donna King, Suzan Cates, and all the helpful personnel in the office. I extend my appreciation to all the Chemical Engineering and OU professors for teaching and providing me with a valuable education. I am also thankful for

the good-fellowship and lab assistance of several graduate students such as Walter Alvarez, Garry Jacobs, and Zoran Juric. I equally appreciate all the help with experimental work of several undergraduate students such as Scott Kersey, April Smith, Bee Wooi Soo, Rui Wang, and Yann Buzar.

Unforgettable is the time I spent at the chemistry department of the University Blaise Pascal in Clermont-Ferrand. My special thanks go to Rachid Mahiou and Daniel Zambon from Les Laboratoires des Materiaux Inorganic who invited me to come to France and generously offered their facilities for my catalyst characterization studies. I also appreciate the scientific input as well as the friendship of Kristine , Diallo, Miloud, and Damien.

I surely do not want to forget acknowledging my roommate and friend Kwo Ue Ngai who always brightened my day with her smile when coming back home after a long day of work. I especially want to thank her for her endless patience with me and for her help. I always could rely on her when I was under time pressure or in the need for a helping hand.

Thanks to Carolyn Lauren for having helped and struggled with me since the Masters program and for continuously giving much advice, moral support during hour-long cheering conversations, which continued even after she had left OU and Norman in 1996. Some of her advising wisdom still keeps me driving forwards when the going gets tough.

Since there can't be an inspired mind without a 100% functioning body, I want to acknowledge all those who were always available fixing some twisted bones and muscles or keeping me otherwise healthy and fit, such as Dr. Steven Smith and Eric Runnels from

the Goddard Health Center, Dr. Joel Holloway, Bill Graves, and Ronald Tripp from Sooner Judo, and Lyn Cramer from the OU Dance Department.

Most importantly, my deepest appreciation goes to my Mom who raised my brother and me always encouraging pursuing a good education. Danke, Mami, fuer Deine Liebe, Deine unendliche Geduld, Deine mit mir geteilte Zeit, Deine Aufopferungen, Deine Weisheit, Deine Ratschläge (die nie Belehrungen waren), Deine stete Unterstützung (selbst wenn ich auch manchmal nicht Deiner Meinung war), und Danke für Deine erstaunlichen Gabe meißtens zu wissen, was für mich richtig oder besser war und ist. I wish to express my gratefulness for her moral support along the path of my live. At the same time, I do not want to forget acknowledging my stepfather who patiently guided me since my youngest years towards the path of science. I am especially grateful for the numerous opportunities he provided to develop my basic technical skills, which helped me so often when assembling any apparatus or while trouble shooting equipment. I want to express my thanks to my parents and my brother for their love and encouragement.

Thankful recognition goes to the Center for Indoor Air Research, the Oklahoma Center for the Advancement of Science and Technology, and the International Environmental Corporation for their financial support

Table of Content

List of Tables

List of Figures

Abstract

Reducing air pollution, specifically volatile organic compounds, has become an increasing concern for the public, environmental protection organizations, and governmental agencies. One method for destroying air contaminants that can meet desired characteristics such as working at ambient conditions (e.g. room temperature, atmospheric pressure, and use of oxygen from air as oxidizing agent) is photocatalytic oxidation. Anatase titanium dioxide has shown to be the most promising active photocatalyst for decomposition of air contaminants such as carbohydrates, volatile organic compounds, and odorants to harmless products like water and carbon dioxide. This work presents some new forms of photocatalysts that could significantly improve the available technology for photocatalytic degradation of air contaminants.

Pure low density as well as ultra-low density titanium dioxide aerogels have been synthesized in our labs and several tests of photocatalytic activity of the TiO_2 aerogel catalysts have been carried out using methane, ethane, ethylene, and acetone as air contaminants. The same tests have been carried out on Degussa P25, a TiO_2 containing 70 % anatase and 30 % rutile. The effectiveness of the aerogels in removing the here-applied contaminants is compared to the commercially available P25 on several different bases (mass, illuminated cell window area, and UV accessible catalyst volume and catalyst surface area). The superiority of the aerogel was attributed to a larger fraction of interior surface, to the high porosity resulting in a higher accessibility of reaction sites, as

well as to a higher UV light penetration into the catalyst bulk. UV transmittance measurements of dispersed catalyst powders in a UV-transparent agar gel showed that all aerogel samples demonstrated a higher UV light transmittance compared to the nonporous Degussa P25, thus allowing for UV light to penetrate five times deeper through an aerogel material compared to Degussa P25.

The aerogels' activity was further enhanced by thermal treatment and by the deposition of platinum. A platinum content of 1.2wt% increased the ethylene oxidation reaction rate constant by 35% for the Degussa P25 and by 11% for the aerogel T36.

Ethylene photooxidation under humid conditions showed a decrease in photocatalytic activity of all tested catalysts. But even at a relative humidity close to 50%, the aerogel photocatalyst retained good photocatalytic activity.

The adsorption equilibrium constants and the reaction rate constants for methane, ethane, ethylene, and acetone were determined from initial rate data using a Langmuir-Hinshelwood model. The obtained models provided satisfactory fits to the experimental data.

1 Introduction

Pollution and pollution control has attracted a lot of attention over the past three to four decades. Pollution can be described as the contamination of air, water, or soil with one or several compounds that distract from the nature's ability to support the original ecosystem or to provide some human need or use[1]. Progressively more waste from industrial and human sources has been carelessly discharged into the environment especially since the industrial revolution. But many pollutants are bio-accumulative. Simply dilution to concentrations below certain threshold levels does not make them disappear. A constant exposure to even small amounts of toxicants can lead to chronic illnesses by humans and to destruction of vegetation and wildlife. Only after transformation of toxic wastes to nontoxic compounds can they be tolerated and assimilated by Nature. Several techniques have been developed and applied for pollution control and remediation. However, most of these processes are designed to separate and concentrate the hazardous wastes instead of eliminating them. Research has therefore focused on developing new techniques that can handle both the removal and destruction of toxic pollutants. One of the new promising processes for waste control and remediation is photocatalysis. A major concern is to find suitable photocatalysts that make this process efficient enough for commercial applications. The present work will discuss characterization and investigation of the activity of aerogel photocatalysts and compare the aerogels efficiency to that of the best commercially available photocatalyst.

2 Literature Review and Theoretical Background

2.1 History of Pollution and Pollution Control

Reducing pollution of soil, water, and air has increasingly become a concern for environmental protection agencies and governmental organizations. However, pollution has not just been a recent problem. As early as 1285, the smoke from burning of "sea-coale" in limekilns in London was reported as a discomfort and health hazard[2]. Recognizing that improving the air quality situation was not possible without active intervention, King Edward I released an order banning the burning of sea coal. In the US, the first smoke control ordinances were passed in Chicago and Cincinnati in 1881 and many larger cities had followed by 1912. Between 1930 and 1950, smoke pollution reached its peak in larger industrial cities. The switch from burning coal to cleaner-burning oil and gas, as well as the use of better control devices provided for some relief. But the more complex problems of air pollution, such as photochemical smog, had not been recognized yet. Even though some researchers indicated that photochemical reaction, rather than direct emission, was responsible for the harmful pollutants in the smog of Los Angeles, these findings were attacked and dismissed by several groups, but later proved to be true. For example, in 1948, a four-day smog in Donora (Pennsylvania) was responsible for illness in 7000 people, resulting even in 20 deaths. And in 1952, about 4000 deaths had occurred due to an air pollution episode. State and local governments in the US began to exert more and more control over air pollution emission. The Air Pollution Control Act of 1955 provided funds for federal research and technical assistance. The Clean Air Act of 1963 provided funds not only for federal research but

also for grants outside of research agencies. Another piece of legislation was the Motor Vehicle Act of 1965, recognizing the need to control emissions from new motor vehicles and other new technologies. The Air Quality Act of 1967 went one step further by extending the duty of federal government to enforce the use of control equipment. After that, several amendments to the Clean Air Act were passed by federal legislation. As a result of the Clean Air Act Amendments (CAAA) of 1970, along with the National Environmental Policy Act, the Environmental Protection Agency (EPA) was created to put some enforcement behind air pollution control. The EPA established National Ambient Air Quality Standards (NAAQS)that were designed to protect public health and welfare. These standards ranged from regulations of automobile emissions to certain requirements for new industrial plants. The CAAA of 1997 retained the basic philosophy of federal management and state implementation, reviewing and updating air quality data, if necessary. Significant changes were introduced to the Clean Air Act with the CAAA of 1990, when for the first time global air pollution problems were taken into consideration. Some of the key issues that were addressed were urban air pollution (e.g. ozone and CO), mobile sources, air toxics, and stratospheric ozone protection (e.g. CFCs, halons).

Today, most of the air pollution is a result of fuel combustion for industrial production, petroleum refining, organic chemicals and synthetic industries, milling and coal conversion, textile processing and production of energy. But not only industry, also consumers play an important role in polluting the environment by utilization of fuel for transportation and heating, the use of pesticides, fertilizers, aerosol sprays and more[3]. Six criteria air pollutants have been established by National Ambient Air Quality Standards

of which five are classified as primary pollutants and one as secondary. Particulate matter less than 10 šm in diameter, sulfur dioxide, nitrogen dioxide, carbon monoxide, and particulate lead are the five primary pollutants and are directly emitted into the atmosphere. Secondary pollutants, such as ozone, relate to pollutants formed in the lower atmosphere caused by reactions involving sunlight and primary pollutants like hydrocarbons and nitrogen oxides. Another major class of hazardous air contaminants is the class of volatile organic compounds (VOC) with appreciable vapor pressures, such as hydrocarbons (aldehydes, organic acids, ketones) as well as hydrocarbons containing chlorine (halogens), sulfur, nitrogen, and fluorine. Under the Clean Air Act Amendments of 1990, it was estimated that the control of VOCs costs the industry about $1.2 billion. In 1995, 14 maximum achievable control technology (MACT) standards had been completed describing the types of emission controls and/or practices required to limit the emission of 189 listed hazardous air pollutant. These standards describe techniques or technologies to establish a level of emission control that must be achieved.

2.2 Available Remediation Technology

Many conventional technologies are available, as summarized by McInnes, ranging from incinerators (thermal or catalytic oxidation) to separation methods such as filter systems, compression, condensation, adsorption (e.g. on carbon), and liquid absorption[4]. One disadvantage of using incinerators is the high operating costs involved. Some new emission control techniques, however, show promise for providing more cost-effective hazardous air pollutant control, especially due to the latest enhancements made to already existing conventional technologies improving performance and thus making them more

cost-effective and more versatile concerning the types of compounds to be controlled. Biofiltration, already successfully applied in Germany and Sweden to control odors from a wide range of sources, uses compost, peat, or soil as filter material to treat a substantial variety of hazardous air pollutants (HAP) and appears to be most applicable to high-volume/low-concentration (flow of 10,000 ft^3/min at 1000 to 5000 ppm) gas streams. A new biofiltration system, activated carbon biofilters, can handle spike loads of VOCs and has lower overall maintenance requirements due to shorter residence times and longer filter bed activity than the previous method using soil. On the other hand, the cost of activated carbon filters is still five times higher than compost or peat filters. Membrane separation is a viable pollutant control approach for gas streams containing relatively high concentrations of 10,000 ppm VOCs. This system consists mainly of a compression/condensation step, recovering a large portion of the organics, followed by a membrane separation step through membranes with 10 to 100 times higher permeability to organics than to air. Depending on the system design, air streams of 200 ft^3/min containing more than 1% VOC can be treated with resulting hazardous pollutant control efficiencies greater than 90%. Another VOC/HAP control technology is adsorption on adsorbents such as granulated activated carbon, carbon filters, zeolites, and polymeric adsorbents. Carbon filters are an alternative to granulated activated carbon. Carbon filters have more surface micropores available therefore reducing the adsorption/desorption time by about six fold compared to granulated carbon. In addition, carbon filters contain 50 – 90% fewer transition metals promoting hydrolysis. The lower reaction rates, the frequent (but short) regeneration cycles, and the thoroughness of regeneration allow only a small amount of solvents to remain on the bed, thus limiting

heat generation and heat build-up in the bed. In addition, the generated exothermic reaction heat from the carbon bed is quickly removed due to the small fiber diameter and a low density of the carbon fibers. Zeolites are hydrated alkali-aluminosilicates with approximately 70 known different structures (composition and crystallinity). They were seen as a new adsorbent compound to replace granulated activated carbon since carbon shows limitations in performance for control of hot (100°F) and humidity saturated air streams. Zeolites find applications as dehumidifying agents, as ion-exchange resins, and as catalysts in the petroleum refining industry. New hydrophobic zeolites can attract and hold organic molecules and can, depending on pore size, trap molecules up to 8 Å in diameter. An advantage of zeolites is their ability to not to adsorb water in air streams of up to 90% relative humidity (compared to carbon which reduces its organic adsorptive capacity after exceeding humidity levels of 60 %). Although the adsorption capacity of zeolites is generally lower than that for carbon, they have demonstrated higher removal efficiencies for certain compounds during the first minutes of the adsorption process, especially for process streams of 100 ppm or less. This suggests the utilization of zeolites preferably for short adsorption cycles. A way to get around the limitations of adsorption and humidity is to use polymeric adsorbents, a group of products based on styrene/divinylbenzene polymers having an excellent mechanical stability. The ability to tailor their surface properties allows for optimizing this product to control the most common VOCs even under high humidity conditions while retaining a relatively high adsorptive capacity.

One of the drawbacks of the previously mentioned separation techniques is that these methods merely remove the contaminant from one stream to another instead of

eliminating them, therefore producing waste streams of the separated contaminants in higher concentrations. Regeneration of adsorbed organics and their destruction becomes necessary. As a result, more energy is required and additional waste is created throughout the cleaning process of filters or separation devices. Although, there are existent methods that can deal with contaminants in high concentrations, such as catalyst based incinerators or catalyst beds as described by McInnes in[4], it is still desired to find economical sound methods for handling toxic compounds that are widely spread in air, as well as collect and destroy contaminants in diluted air streams[5]. This is especially of importance for air purification and decontamination of completely or partially enclosed atmospheres such as office buildings, hospitals, schools, homes, factories, spacecrafts, and airplanes.

A new method for gas phase destruction of pollutants, which has been studied under laboratory conditions for several years already, is ultraviolet oxidation. Terr-Aqua Enviro Systems has already commercialized one of these technologies and evaluated it for spray paint emission control, as reviewed by McInnes[4]. Organics are destroyed by the combination of a tuned-frequency UV light and an added oxidant (e.g., oxygen), a process similar to that occurring in nature where naturally occurring oxidants reduce and/or oxidize organics under the influence of UV light from the sun. The efficiency of this new process, however, depends largely on the organic compounds involved, the relative composition, and the total organic load. Since generally not all organics will be oxidized during the first stage of the process (photolytic stage), water scrubbers and/or carbon adsorbers need still to be employed to remove partially oxidized organics, new intermediate compounds and reaction byproducts. The efficiency of the overall process

is optimized by adjusting residence time, light frequency, and the amount of oxidants. Full-scale UV systems have been installed controlling up to 90,000 ft^3/m of process streams from e.g. spray-painting operations and a furniture manufacturing plant. The main advantage of UV technology is that it is an energy efficient process as only the organic compounds are affected (and not the surrounding air mass) and that the only energy required for operation are UV light sources and cooling fans. In addition, the process operates at ambient conditions while achieving high removal rates of 90-95% with insignificant amounts of byproducts. However, one draw back is that water treatment from scrubbers might be necessary, requiring different cleanup techniques. Another limitation derives from the fact that the light absorption maximum for different organics lies at different wavelengths and not all VOCs are responsive to photolysis and that the range of treatable hazardous air pollutants has not yet been fully investigated. Moreover, in many cases, this form of photodegradation leads to the formation of partially oxidized products, therefore creating additional and sometimes even more hazardous wastes. Nonetheless, the advantages of environmental clean-up techniques utilizing the effect of UV illumination are apparent, thus showing a potential for future applications in industrial waste management and air pollution control.

Throughout research and development of new technologies, heterogeneous photocatalysis has been shown to be an attractive alternative or addition to existing degradation processes. Photocatalytic processes are especially attractive as they can be applied to organic contaminants at concentrations down to the ppm level. An example for a successful application of photocatalysis is an experimental plant in Livingstone

(Tennessee). There, methylene blue is used as photosensitizing agent to disinfect water processing up to 144,000 gallons of wastewater per day[6].

2.3 Heterogeneous Photocatalysis

2.3.1 Introduction

Heterogeneous catalytic oxidation of gas phase pollutants has already found application in practice, for example in automotive exhausts and, as mentioned earlier, in catalytic incineration. A downside of these types of catalysts is that they only function at elevated temperatures. This is on one hand rather cost intensive and on the other hand not very suitable for indoor air applications. Therefore, it is important to develop a catalytic method that is capable of destroying air contaminants at room temperature, atmospheric pressure, and use of oxygen from air. One promising method that can meet the required characteristics is the photocatalytic oxidation on metal oxide semiconductors. In contrast to metals, which have a continuum of electronic states, photocatalytic semiconductors are characteristic for possessing a moderate band gap between their valence and conduction band. Activation of the photocatalyst is achieved by illumination with light in the UV-range below 380 nm[3]. When a photon (hv) with energy larger or equal to the band gap, commonly ranging from 1 to 3.7 eV, is absorbed by the catalyst an electron from the valence band is photo-excited into the conduction band leaving an electron hole in the valence band. The created electron/holepairs may then migrate to the surface of the catalyst where they serve as powerful oxidation and reduction reagents. The availability for either oxidation or reduction makes this a useful tool for detoxification of both, organic and inorganic pollutants.

2.3.2 Historical Review

2.3.2.1 Heterogeneous Photocatalysis in Aqueous Media

One of the most intensively investigated photocatalysts over the past 20 to 30 years is anatase titanium dioxide (TiO_2). It was found that it has in its anatase form the highest catalytic activity compared to other available photocatalysts, e.g. ZnO, WO_3, and CdS[3,6,7,8,9]. The cost of titanium dioxide is low, it works at ambient conditions (room temperature, atmospheric pressure), and it completely destroys a large variety of compounds to nontoxic carbon dioxide and water leaving no or an insignificant amount of side products. Most of the investigations have been performed for aqueous decontamination applications. It has been demonstrated that different kinds of organics can be oxidized including alkanes (the most unreactive of organic compounds), alkenes, aromatics, and ketones, as well as compounds containing phosphorus, sulfur, halogen heteroatoms, and nitrogen. Other compounds often found in contaminated waste streams are halocarbons, pesticides, and surfactants; studies have shown that all those can be photoctalytic degraded using TiO_2[10]. Pelizzetti et al.[3] reported the complete destruction of hexadecane and dodecane while detecting only CO_2 as reaction product in the gas phase. The occurrence of intermediate oxidation products such as 1-dodecanol and dodecanoic acid were assumed to likely happen, however, only traces of these intermediates were measured as they oxidized faster than dodecane. One kind of pollutants most investigated by means of photoctalysis is the group of chloroaromatics and chlorocarbons. Several studies from the early 1980s are summarized by Pelizzetti et al.[3] reporting complete mineralization of 2,3-dichlorophenol, 2,4,5-trichlorophenoxy-acetic acid, and 2,4,5-trichlorophenol of 1 ppm solutions with 100% recovery of initial

chlorine as free chloride ion. Reaction intermediates such as 2,3-dichlorobenzoquinone and 2,3-dichlorohydroquinone were observed but disappeared simultaneously with the 2,3-dichlorophenol. Other reported compounds proven to be completely converted to CO_2, along with complete recovery of nitrogen, sulfur, and chlorine as free sulfate, nitrate, and chloride ions, included the herbicides bentazone (3-isopropyl-2, 1, 3-benzo-thiadiazin-4-one-2.2-dioxide) and s-triazine (atrazine, simazine, trietazine, prometone, and prometryne). A paper published by Tanguay et al. in 1989[11] described the photocatalytic destruction of dichloromethane over different forms of titanium dioxide they had prepared in their labs. Their results indicated that from the investigated pure anatase, pure rutile, anatase as a film on carbon felt, and amorphous TiO_2 on different pillared clays the synthetic rutile was the most active catalyst followed by pure anatase. A different observation was made by Reeves et al.[12], who studied the photocatalytic activity of several commercial available titanium dioxide catalysts having different crystallinity. These researchers observed a complete mineralization of dyes in wastewater (malachite green, crystal violet, methyl orange, congo red, methylene blue, sodium alizarinsulfonate, and fluorescein) to CO_2 and inorganic sulfur and nitrate ions and found that Degussa P25, a TiO_2 powder of 70% anatase and the remainder rutile, was the most active. The photocatalytic degradation of monuron, a widely used weed controlling herbicide carrying the risk of leaching into groundwater, was investigated in aqueous solutions containing a slurry of TiO_2, ZnO, WO_3, or SnO_2[13]. Photocatalytic conversion was successfully tested to show complete degradation of this contaminant to CO_2 and nitrate ions at herbicide concentrations of up to 10,000 ppm. Similar to the findings from other researchers mentioned earlier, TiO_2 was found to be the most active

of all tested catalysts. In contrast to the findings of Tanguay et al., however, rutile was practically inactive. Similar observations were made by other researchers[14, 15, 16]. A review of engineering developments of solar photocatalytic detoxification and disinfection processes in aqueous phase by Goswami[17] summarized a few of the successful engineering scale demonstrations for groundwater treatment. A nonconcentrating solar reactor was tested at Tyndal Airforce Base in 1992. Groundwater contaminated with fuel, oil, lubricants and other organics like benzene, toluene, ethylbenzene, and xylene (BTEX) coming from leaking tanks was effectively treated. Although, the reaction rates were lower than the rates obtained in laboratory tests using city water spiked with the same contaminants, but the technology has proved to be practicable. Another engineering field scale demonstration for groundwater treatment includes a project conducted by the National Renewable Energy Laboratory at the Lawrence Livermore National Laboratory treating groundwater contaminated with trichloroethylene (TCE) in 1993. A 0.1%-titanium dioxide slurry reduced TEC concentrations of 200 ppm down to 5 ppm in a system with a capacity of 1700 ft^3. In 1994, Blanco and Malato conducted an engineering field demonstration of industrial wastewater treatment from a resins factory. They achieved 100 percent degradation of 600 ppm of TOC from phenols, phthalic acid, fumeric acid, maleic acid, glycols, xylene, toluene, methanol, butanol, and phenylethylene in a slurry using 100 mg/ml Degussa P25 TiO_2 as photocatalyst. Zaidi and his collaborators demonstrated the potential of solar photocatalytic technology by a similar project including pretreatment of distillery water by anaerobic microbiological methods to reduce COD and color in 1995. The same year, Anheden and his coworkers[18] had shown the promise of solar photocatalytic oxidation for

decolorization and reduction of chemical oxygen demand (COD) in wastewater of a 5-fluorouracil (a cancer drug) manufacturing plant. They demonstrated a 80 percent color reduction of the wastewater within one hour and a 70 to 80 percent decrease of COD in 16 hours by using 0.1 percent TiO_2 in combination with 2400 ppm peroxide as an oxidizing additive. A newly developed anatase TiO_2 catalyst powder, Hombikat UV 100 from Sachtleben Chemie, was found to be up to four times more efficient for complete dichloracetate than the presently best performing commercially available catalyst Degussa P25. This new novel material has been successfully employed under real solar conditions at the Plataforma Solar de Almeria in Spain to treat wastewater of the local industrial company[19]. These projects demonstrated that processes utilizing photocatalysis for organic waste control and remediation carry a large potential to be successfully applied in industry.

2.3.2.2 Gas-Phase Heterogeneous Photocatalysis

The majority of research in heterogeneous photocatalytic oxidation of organics has been performed for aqueous solutions [15]. However, a growing interest to find new suitable processes for decontamination of air, especially with respect to indoor air applications, contributed to focus research on the investigation of heterogeneous photocatalysis in the gas phase. Heterogeneous oxidation catalysts function at elevated temperatures, but the photocatalytic processes operates under ambient temperature and pressure. The attractiveness of this process is obvious since near all of the inhabited environments of concern to humans exist at or near 20-25°C where molecular oxygen, a needed oxidant for the photoreaction, is available in large excess. Different types of

studies of gas phase heterogeneous catalysis include oxygen adsorption phenomena, isotopic exchange onto the catalyst surface, oxidation of alkanes, alcohols and ketones, of aromatics, heteroatom organic compounds, trichlorethylene, as well as organic acid decarboxylation and ammonia oxidation. Teichner and his colleagues carried out the first systematic studies of gas phase heterogeneous photocatalysis of organics in the early 1970s[20]. They developed a first differential photoreactor used for kinetic studies primarily on alkanes. They found that small alkanes, such as methane and ethane, easily oxidize completely to CO_2 and H_2O. Alkanes with more than three carbons formed ketones and other alkanes but were eventually also converted to CO_2 and water. In studies on the conversion of isobutene to acetone Gravelle et al.[21] concluded that polycrystalline anatase titanium dioxide is a very efficient photocatalyst in partial oxidation at room temperature. A complete oxidation was observed for ethane, propene, 1-butene, and 2-butene. Their objective was to point out what species are responsible for the photocatalytic conversion. They established the fact that the presence of only adsorbed $O_{2(ads)}^-$, (created throughout illumination of wavelengths up to 520 nm) is not sufficient for catalytic oxidation to occur. Furthermore, irradiation of wavelengths in the near UV range (below 350 nm) is necessary to produce so called excitons or electron-hole pairs. Only when holes are present an activated complex is formed required for the interaction between paraffin and oxygen. In a follow-up study it was established that there exists a "critical thickness" of the catalyst bed for which the catalyst is irradiated[22] and that the yield of the reaction depends only on the surface of the catalyst, and not on its total mass[23]. More studies were performed on the photoadsorption of oxygen[24] and on the partial photo-oxidation of isobutene[25] and 2-methylbutane[26] to determine which

species would be responsible for the break-up of the organic compound. However, at this point it was still disputed whether the holes react with the negatively charged OH-groups or with various types of oxygen species, like adsorbed oxygen or oxygen from surface lattice. Sabate et al.[27] studied the degradation of 3-chlorosalicylic acid over TiO_2 membranes supported on glass. They observed a complete dechlorination of this acid with more than 98% converted to chloride ions. Substantive concentrations of intermediates were not present. A dependency of the photocatalytic activity on temperature was not noticed. In an investigation of photocatalytic oxidation of atmospheric trace contaminants, Peral and Ollis [28] examined the oxidation of acetone and n-butanol in a flow-through reactor. Acetone was completely mineralized to carbon dioxide and water with no other organic species detected while 1-butanol reacted mainly to butyraldehyde at conversions of 20-30%. They also investigated the effect of water on the reaction rate since the relative humidity of room atmosphere under ambient conditions can vary between 10-80%. From relative humidity studies they found that, depending on the organic to be oxidized, water could act as an inhibitor (e.g., for trichlorethylene, acetone), a promoter (e.g., for toluene) or had no effect on the reaction (e.g., for n-butanol)[29]. More studies followed on the effect of humidity on the oxidation of toluene and trichloretylene, confirming the results of Ollis and Peral[30,31,32]. Other humidity studies on the oxidation of toluene, formaldehyde, and 1,3-butadiene, gases that are commonly found in buildings and transportation vehicles established that the reaction rate depends critically on the concentration of the contaminant. At sub-ppm levels the oxidation rate increased with decreasing humidity levels[33],[34]. Several research groups investigated the photocatalytic oxidation of TCE in wastewater and air due to the

remarkable high photocatalytic quantum yield[33, 35]. During these studies no notable amounts of side products were observed. In contrast to their findings, however, Nimlos and co-workers revealed in a study that a significant amount of byproducts was produced in the gas-phase[36]. An interesting study performed by Hennezel and Ollis[37] illustrated that the addition of TCE can enhance the photocatalytic oxidation over TiO_2 of several organic compounds. For example, all photocatalyzed degradation rates of branched aromatics and oxygenates were enhanced by the addition of TCE, e.g. toluene, ethylbenzene, m-xylene, methyl ethyl ketone, acetaldehyde, butyraldehyde, methylacrylate, and hexane. It was suggested that the rate enhancement was due to the added radicals from the TCE. Their experimental results indicated that a chlorine radical attack is involved in the slow step of organic conversion. No conclusion was made why the benzene and methanol oxidation remained unaffected and the acetone, methylene chloride, and chloroform oxidations were inhibited by the presence of TCE. Besides destroying organics, photocatalysis might also serve as a potential candidate for disinfection. TiO_2 is non-toxic to animals but under UV illumination highly toxic to microorganisms and effective in killing bacteria[38]. Goswami et al. reported one hundred percent destruction of bacteria and a complete inactivation of microorganisms in a study of the antibacterial effect of photocatalytic oxidation in indoor air using titanium dioxide[39].

One of the disadvantages of gas-phase photocatalysis is that the catalytic efficiency of the photoxidation process does not depend on the mass of catalyst employed, as is the case for liquid environments. UV light can penetrate the catalyst only up to 4.5 μm into the bulk[29]. Photoreactors, therefore, need to be designed such that either the catalytic

material is kept in constant motion in order to utilize all of the available catalyst, like in a fluidized bed reactor, or the catalyst needs to be prepared in thin layers that the UV light is still able to penetrate. This requires a more complicated reactor design for deposition and immobilization of the catalytic material as well as to account for space limitations, for example in air conditioning units. Formenti et al., who first reported about the existence of a critical bed thickness, deposited titanium dioxide on a Millipore film[22]. Other deposition techniques include TiO_2 ceramic membranes supported on a glass tube for an annular reactor[27], a thin layer of TiO_2 on a flat porous glass frit [28, 29, 37], a titanium dioxide particles coated ceramic honeycomb monolith[40], TiO_2 wash-coated on an alumina reticulate[33, 36] or a microscope glass slide[34], TiO_2 coated inside of pyrex tubes[41], and dip coating on fiberglass air conditioning filter[39]. An advantage of the aforementioned powder layer reactor configurations is that the mass transfer resistances are negligible due to very small interstitial distances between particles[7]. Other reactor types that employ the use of mobilized catalysts are summarized in a review by Peral and co-workers[20]. An annular down-flow transport reactor was used to investigate the effect of particle size, flow rate and catalyst concentration in the reactor. The researchers observed a yield dependency on the amount of catalyst in the gas stream. The existence of an optimum concentration was explained by two opposing trends. At concentrations below the optimum the rate decreased because of an insufficient amount of catalyst present to capture all the light. At much higher concentrations above the optimum , however, the flowing catalyst bed became too opaque for the light to illuminate all of the catalytic material. This result confirmed the observations from Formenti and colleagues[22] about a critical catalyst bed thickness where the reaction rate does not increase anymore with

increasing amount of catalyst. An apparent quantum efficiency (number of molecules formed per number of incident photons) of up to 10% was measured with this reactor. Another reactor configuration employed in laboratory scale gas-phase heterogeneous photocatalysis is the fluidized bed. Quantum efficiencies of above 10% had been observed for ammonia oxidation and trichlorethylene destruction in humidified air[20].

Another hurdle for gas-phase photocatalysis is byproduct formation. In many cases the byproducts are strongly adsorbed on the catalyst and thus contribute to the deactivation of the catalytic material. In addition, the photo-efficiency of the available catalytic material is not quite sufficient to make photocatalysis a feasible process for practical industrial applications. Much research is being performed to find ways to improve the catalysts' performance. Approaches include new different methods of synthesizing the catalyst and modifying the surface and structure of the catalytic material to reduce or eliminate the factors inhibiting the photoactivity. Cao et al.[42], for example, discussed the oxidation of 1-butane over a nanoscale TiO_2 photocatalysts prepared via a sol-gel synthesis. They assumed that quantum size effects are responsible for the higher photoactivity achieved compared to that of Degussa P25. Similar findings were reported by Kormann et al. and Chhabra and co-workers [16, 43]. The sol-gel technology has drawn a lot of attention in regards to catalyst preparation. Not only can quantum-size particles be synthesized, in addition one obtains catalysts with a higher surface area and better adsorption properties, both important characteristics for an effective catalyst. Binary silica-titanium catalysts prepared by sol-gel synthesis were found to have an enhanced mechanical strength in addition to possessing a photoreactivity similar[44] and even up to three times higher[45] than Degussa. This enhancement was attributed to the added SiO_2

having a positive effect on the porosity, surface area, and translucency in the aerogel produced. Photocatalytic activities may also be influenced by the addition of an inert support. The remarkable enhancement of the decomposition rate of propizamide over TiO_2 supported on activated carbon and that of pyridine over a TiO_2-loaded zeolite was attributed to providing a high-concentration environment around the catalyst[46]. The advantage of a TiO_2 loaded supports lies in that the intermediates are retained on the catalyst/adsorbent and can be subsequently decomposed, reducing therefore the concentration of toxic intermediates. [47] Vast research was and is performed in the area of metal doping and deposition in order to achieve an improved photoreactivity. Doped metal ions promote inhibition of electron-hole recombination by trapping holes and the electrons[48] or serve as better electron traps than the titanium dioxide[49]. Photocatalytic activity is also positively affected due to enhanced light absorption as the metal ions respond to a larger fraction of the light spectrum[5]. Other studies rationalized the reaction rate enhancement as a result of the enhanced rate of interfacial electron-transfer from the semiconductor to the adsorbed species[50].

2.3.3 Characterization of Photocatalysis

2.3.3.1 Definition of Photocatalysis

Oswald, the founder of modern catalysis, described the importance of photocatalytic processes (in conjunction with the processes of photosynthesis) in a rather poetic way: "Life is like a water mill. The effect produced by the falling water is achieved by the rays of sun. Without the sun the wheel of life cannot be kept going. But we have to

investigate more closely which circumstances and laws of nature bring about this remarkable transformation of the sunrays into food and warmth."[51]

First attempts to define photocatalysis were undertaken by Plotkinow in the early 1920's who considered all those reactions photocatalytic that are accelerated by the influence of light. However, this definition was not satisfactory, as it would apply to any photochemical reaction. Over the past three decades, a number of authors tried to find clear definitions and classifications to describe the characteristics of photocatalyis. Terms like photoenhancement, photoacceleration, photosensitization, light-stimulated reactions, or true photocatalysis had been proposed. But these terms led rather to more misunderstandings than to a clarification. It was in 1983 with a discussion initiated by Kisch and Henning on the topic "What means photocatalysis?", who separated all kinds of photocatalytic reactions into two categories using the quantum yield, the ratio of moles of photons to number of moles of product generated, as distinguishing criteria[51]. One category, photocatalytic reactions, included all those reactions that do not require further irradiation after the initial photogeneration of a catalyst. These reactions were portrayed as catalytic in the number of incident photons with quantum yields of product formation larger than unity. The other category, photoassisted reactions, comprised reactions that require continuous irradiations to observe product formation and display quantum yields of product formation not exceeding "one". Reactions of this type were characterized as catalytic in the concentration of the photocatalyst. However, discussions from other scientist followed arguing that using only the quantum yield as identification criterion could lead to wrong conclusions. For example, some initial photoreactions forming the active catalyst are very slow compared to the continuing reactions. This could lead to an

overall quantum yield less than unity, even though the catalyst is able to enter many cycles of substrate conversion and would thus belong to the class with a quantum yield larger than "one". Other critics pointed out that the above definitions did not satisfy the conceptual requirements of catalytic processes, e.g., the rate of a chemical reaction is changed without changing the position of the reaction equilibrium. Today, it is widely accepted to use the term of photocatalysis in its broadest sense when both light and a catalyst are necessary to bring about an appropriate reaction. In order to clarify the term of catalysis further an additional distinction of different reaction groups was applied. Accordingly, all interactions of a catalyst with a substrate forming a product under the influence of light are divided into two basic groups[52]. One group represents reactions that are once initiated by light and continue to go on without any further illumination. Only one photon is needed to start a sequence of reactions. The other group includes those reactions that stop immediately after the light source has been switched off. For this type of photocatalytic reaction at least one photon is needed for one or more of the following steps in the photocatalytic cycle. The latter category of reactions may be further divided into three groups: photoassisted reactions, sensitized photoreactions, and catalyzed photo-reactions as outlined in Figure 2-1.

1) Photoinduced catalytic reaction: one absorbed photon by the catalyst is sufficient for the conversion of substrate, no further illumination is necessary.

$$N \xrightarrow{h\nu} N^* \xrightarrow{S} C \xrightarrow{S} C + P \rightarrow \ldots$$

2) Photoassisted reaction: one photon absorbed by the catalyst is necessary for each substrate molecule to be transformed.

$$N \xrightarrow{h\nu} N^* \xrightarrow{S} N + P \xrightarrow{h\nu} N^* \xrightarrow{S} N + P \rightarrow \ldots$$

3) Sensitized photo-reaction: excited catalyst transfers its excitation energy to a ground state substrate which reacts from its excited state to a product),

$$N \xrightarrow{h\nu} N^* \xrightarrow{S} N + S^* \xrightarrow{h\nu} N + P \xrightarrow{S} N^* \rightarrow \ldots$$

4) Catalyzed photo-reaction: the photon is absorbed by the substrate, the excited substrate is transformed to a product on a ground state catalyst.

$$S \xrightarrow{h\nu} S^* \xrightarrow{C} C + P \xrightarrow{h\nu, S} S^* \xrightarrow{C} C + P \rightarrow \ldots$$

* denotes excited state, N = nominal catalyst, S = substrate, C = active catalyst, P = product[51]

Figure 2-1 Simplified representation of photocatalytic pathways

2.3.3.2 Mechanism of Photocatalysis

What is it that makes the photocatalytic reactions possible? What is so special about semiconductor catalysts compared to metal catalysts? The difference between a metal and a semiconductor is best described using the molecular orbital model and the distribution of electronic energy levels[53]. Metals can be seen as supermolecules held together by delocalized bonds that are formed from the atomic orbitals of all the atoms forming the metal crystal. Due to the large number of atoms comprising the metal, a large number of atomic orbitals is formed in the molecule. As a result, the energy spacing between the

levels of all the orbitals is so small that one can consider this as a "band" of orbitals over a range of energies. This band is composed of as many levels as there are contributing atomic orbitals and it can be filled from the lowest level up to an energy called the Fermi level. In the ground state, the levels higher than the Fermi level are empty and are available to accept electrons upon absorption of either thermal energy or light. Due to the continuum of electronic states metals can absorb light of almost any energy promoting an electron to a higher level. This is followed by a rapid relaxation in form of dissipation of small increments of heat or reemission of light, thus returning the material to its ground state. This continuum of states is disadvantageous to induce photochemical charge separation. Since there is no mechanism preventing or hindering the electrons from returning to their original state, energetically favored relaxation occurs virtually instantaneously. The continuum of states effectively "grounds" the energetic electron before it can be transferred to adsorbed species[54]. In contrast to metals that have a continuum of states, semiconductors have a band gap separating a series of energetically closely spaced filled states, the valence band, from a series of energetically closely spaced unfilled states, the so-called conduction band. The Fermi level of semiconductors is located somewhere within the band gap. The position of the Fermi level depends on the effective mass of electrons and holes and the bandwidth of the material. The Fermi level might also shift within the band gap, e.g. through doping, where lattice atoms are substituted by atoms of different valency[55]. Unlike metals, in order for a semiconductor to absorb light, the incoming photon has to have a minimum energy equal or greater to the band gap in order to promote an electron from the valence band into the conduction band. Because of the lack of closely spaced states in the energy gap, excited-state

relaxation is much slower than in a metal. The lifetime of the so created free electron in the conduction band and the positive charge center, the electron hole, in the valence band is in the nanosecond regime[56]. This is sufficient time to undergo charge transfer to adsorbed species on the semiconductor surface where electron and hole may then react as reductant or oxidant, respectively.

The two different mechanisms of metals and semiconductors are illustrated in Figure 2-2.

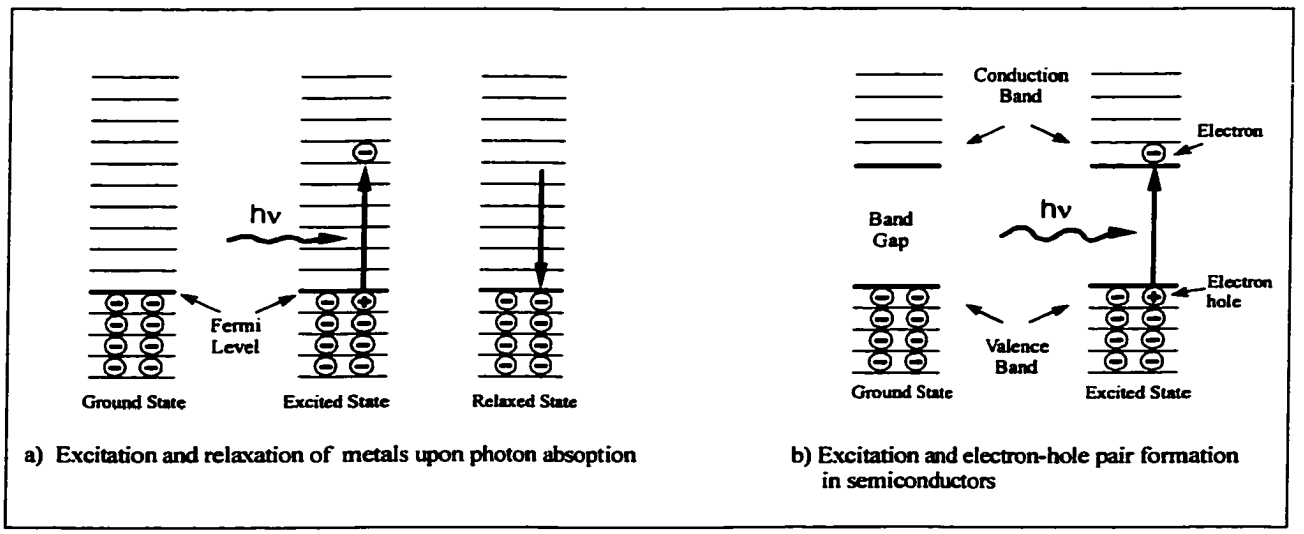

Figure 2-2 Photoexcitation (a) in a metal and (b) in a semiconductor (adapted from[5])

The photocatalytic mechanism for the excitation of TiO_2 can be described in three steps:

1. excitation throughout photon absorption followed by charge separation (electron/hole pair creation)
2. charge trapping and migration to surface
3. interfacial charge transfer to adsorbed surface species

When a photon with energy equal to or greater than the band gap of the semiconductor is absorbed, an electron is raised into the conduction band leaving an

electron hole in the valence band (Equation (2-1)). The electron-hole pair can then follow different pathways throughout its migration path to the surface. Throughout that migration process the electron and hole undergo a series of charge trapping and releasing processes. The hole will be trapped within the subsurface of the titanium dioxide cluster according to Equation (2-2) while the electron quickly reaches the surface where it is trapped as indicated in Equation (2-3)[6]. If the migration path to the surface is too long, recombination of electron and hole becomes likely on either the surface or within the bulk as described in paths A and B of Figure 2-3, respectively. This recombination is an undesired process as this represents a loss of just gained charge carriers and therefore a decrease in photon efficiency of the catalytic material. In the ideal case, electron and hole migrate separately to the solid surface where they then transfer their charges to the adsorbed species on the catalyst surface. The hole combines with an adsorbed hydroxyl group forming an OH^* radical (see Equation (2-4)) while the electron - released again from the $Ti^{3+}_{(surface)}$ - is usually tr=apped by an adsorbed oxygen forming a superoxide radical anion $O_2^-{}_{(ads)}$ (see Equation (2-5))[57]. Oxidation (electron acceptance) and reduction (electron donation) of adsorbed species are represented in paths C and D of Figure 2-3, respectively.

(2-1) $$TiO_2 \xrightarrow{UV} \text{exciton } (h^+/e^- \text{ pair}) \rightarrow h^+ + e^-$$

(2-2) $$(Ti^{4+} - O^{2-} - Ti^{4+})_{(subsurface)} + h^+ \rightarrow (Ti^{4+} - O^{\cdot} - Ti^{4+})_{(subsurface)}$$

(2-3) $$Ti^{4+}_{(surface)} + e^- \rightarrow Ti^{3+}_{(surface)}$$

(2-4) $$OH^-_{(ads)} + h^+ \rightarrow OH^*_{(ads)}$$

(2-5) $$O_{2(ads)} + e^- \rightarrow O_2^-{}_{(ads)}$$

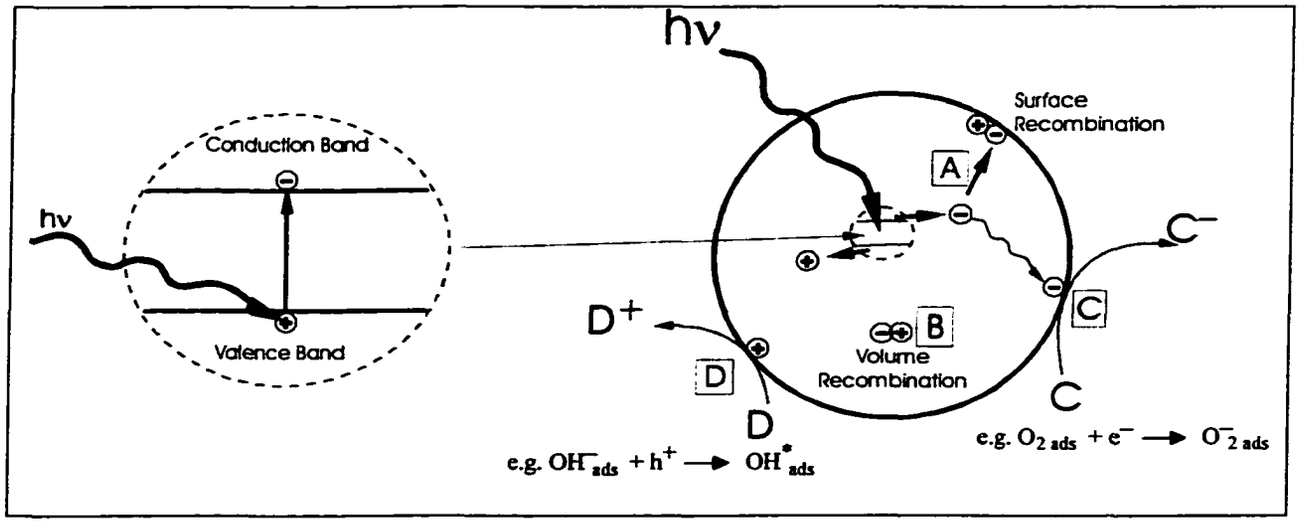

Figure 2-3 Schematic model of electron-hole pair generation in a solid upon absorption of a photon and pathways of electron-hole recombination (excitation and deexcitation). Adapted from[56]

Scientists are still not exactly sure which one of the activated sites is the actual active site for the photocatalytic conversion of various compounds[56, 58]. It is widely believed that mostly the OH* radical is responsible for the substrate transformation[42, 49, 59]. Complete degradation was reported throughout the attack of OH* radicals on adsorbed species where hydroxyl (OH) and perhydroxyl (HO_2) are considered as primary oxidants in the heterogeneous catalysis of organic molecules[60]. However, other researchers are still debating whether the superoxide radical would contribute to the substrate reaction as well, besides serving as electron traps. Cermanti and coworkers concluded from aromatic pollutants degradation studies in water that not only OH* radicals are involved in the oxidative steps in TiO_2 photocatalysis[61]. By introducing OH* scavengers to the reaction system they were able to show that species other than the OH* radical are contributing to the substrate conversion. They inferred that also the superoxide is chemically involved in

the photocatalytic oxidative steps. However, the majority of the literature states that the OH* radical would be the primary species entering the oxidation cycle[5, 62, 63].

2.3.3.3 Efficiency of Photocatalysts

In order to describe the efficiency of a catalyst the term of quantum yield is introduced. It can be described as the ratio of the rate of charge transfer over the sum of charge transfer rate and recombination rate[56]. Assuming diffusion of reactants and product to and from the catalyst surface is not a rate limiting process the above-defined quantum yield would take the value of one for the ideal case of no recombination occurring. However, in a real system, recombination does take place, thus reducing the quantum yield of the photocatalytic process. Another way to determine the efficiency of photocatalytic processes is the evaluation of the quantum yield introduced by Hennig et al.[51]. He described three different definitions of quantum yields (QY) values expressed as a ratio of the number of reactions per number of photons absorbed:

a) QY of substrate consumption, ϕ_s, which is the ratio of the number of substrate molecules reacted per number of absorbed photons,
b) QY of photochemical reaction, ϕ_u, which is number of reaction without catalyst per number of absorbed photons, and
c) QY of transformation of an initiator or catalyst, ϕ_c, which is number of activated catalyst sites per number of absorbed photons.

With the help of the values of the different quantum yields one may determine what type of photocatalytic reaction is present. A photocatalytic reaction (in contrast to photolytic reactions where no catalyst is necessary product transformation) is clearly indicated when $\phi_S > \phi_U$. Furthermore, photoinduced catalytic reactions are characterized

by $\phi_S > \phi_C$ while photoassisted reactions fulfill the condition of $\phi_S < \phi_C$. Additionally, for photoassisted reactions ϕ_S can not exceed unity ($\phi_S \leq 1$) whereas catalyzed photoreactions may achieve values of $\phi_S > 1$.

2.3.4 Catalyst Modifications to Enhance Photoefficiency

The major limitation of photocatalysis is the relatively low quantum efficiency of the oxidative substrate conversion. The catalysts efficiency is mainly limited due to the small range of the solar spectrum usable for excitation. TiO_2 is a quite stable catalyst though, but because of its relatively large band gap only light in the near UV range can photoexcite the catalyst. This does not exceed 10% of the solar energy available (see Figure 2-4).

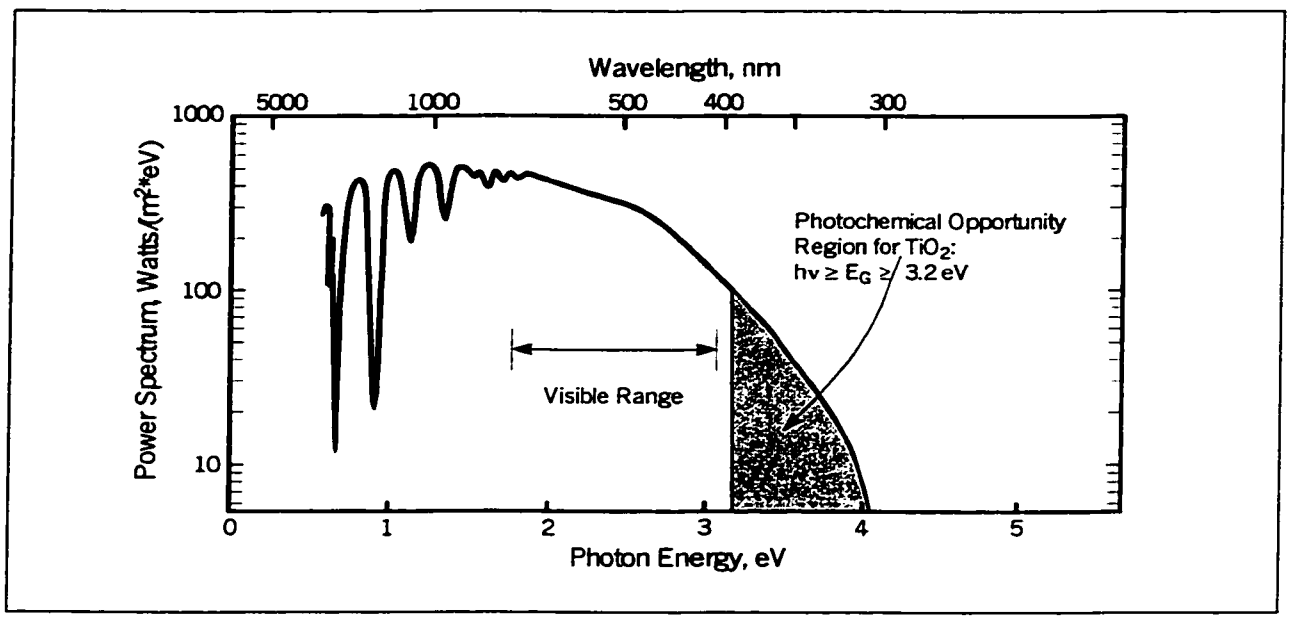

Figure 2-4 Solar spectrum at sea level with the sun at zenith[56]

As already mentioned at the end of Section 2.3.2.2 (Gas-Phase Heterogeneous Photocatalysis), much of research has aimed to find ways to improve the catalysts

performance. Some of the possible focal points for investigation include new or a combination of different semiconductor materials, the alteration of catalyst particle size, inclusion of dopants or co-catalysts, and the dispersion technique of the catalytic material in the reactor. Even though new semiconductor materials possessing photoinduced redox activity such as CdS have been investigated[5], however, those corrode under continued illumination. Besides losing photoactivity throughout an ongoing reaction, catalyst corrosion can create metal ions that are themselves toxic. An alternative would be using semiconductors with a narrower band gap thus permitting catalyst excitation and photoresponsiveness within in the visible range to utilize the solar spectrum more efficiently. Yet, those small band gap materials, in particular metal chalcogenides, are not sufficiently stable to be used for long-term photocatalytic applications. A different approach to enhance photoreactivity throughout a possible increase in light sensitivity would focus on the shift of the band-edge positions by using very small clusters (so-called quantum sized particles) rather than trying to match the band gap to the solar spectrum. The particles are tailored so small (10 –100 Å) that their size becomes comparable to the "de Broglie" wavelength of the charge carriers in the semiconductor. The separated electron and the hole in the Q-particles are confined in a potential well of very small geometric dimensions where they do not experience the electronic delocalization present in the bulk semiconductor. As a result, the confinement produces a quantization of discrete electronic states. This leads to an increase of the effective band gap of the semiconductor, enhancing the attainable potentials for oxidative or reductive reactions. Studies on quantum size particles had been performed for CdS, ZnO, and PbS. For example, as illustrated in Figure 2-5, the effective band gap of CdS increased from

2.6 eV, to 3.6 eV when the initial size of a particle larger than 100 Å was decreased to d~26 Å. This band gap shift was experimentally observed as a blue shift in the absorption spectra[56, 58]. As an additional result of the energy shift, the higher band-edge position can enhance the photoinduced electron transfer to adsorbed species on its surface. It is thermodynamically required that the relevant potential level of the acceptor species is below the conduction band potential of the semiconductor. Likewise, the potential level of the donor needs to above the valence band position of the semiconductor in order to donate an electron to the vacant hole. With the higher shifted band-edge position the latter mentioned conditions are more likely to be fulfilled.

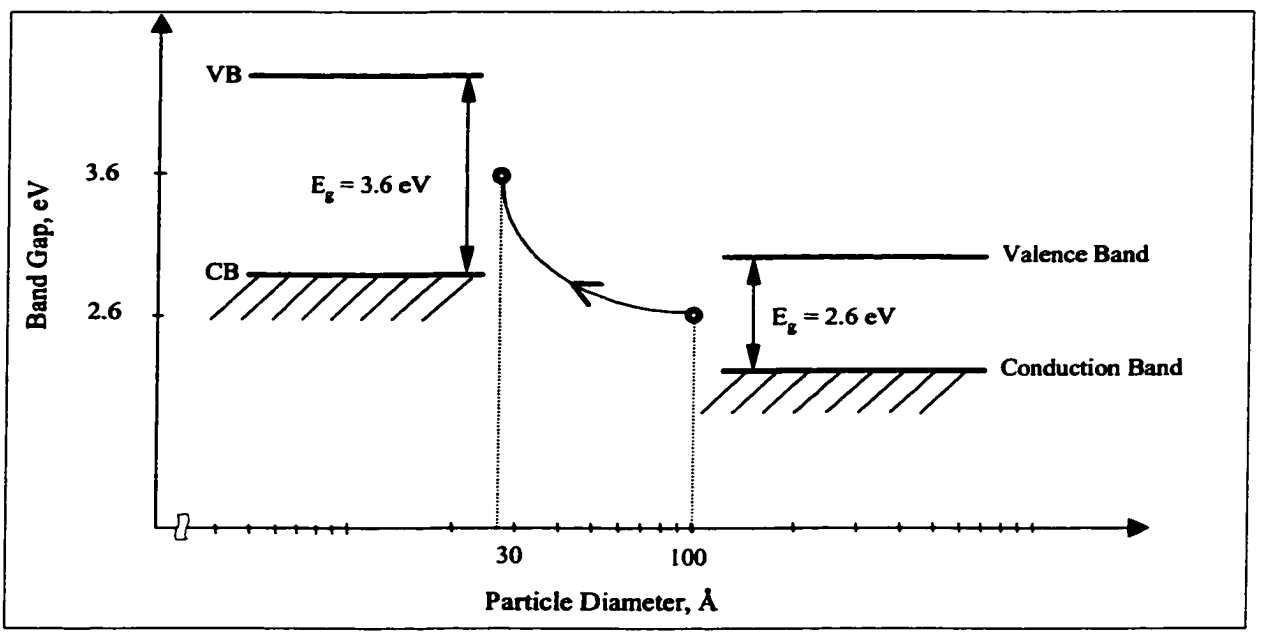

Figure 2-5 Quantum size effect on the CdS semiconductor band gap (modified from[56])

Photosensitization is another way to increase light absorption. Metal ion dopants within the bulk of the semiconductor or chemisorbed or physisorbed dyes increase the

efficiency of the excitation process by expanding the wavelength range of excitation. The sensitizer dyes are excited upon illumination and then transfer the charge into the semiconductor particle. The oxidized form can then undergo further reactions[64] and the electron from the semiconductor can be injected to an organic molecule adsorbed on the catalyst surface causing it to oxidize. The advantage of this process is that it responds to a larger fraction of the solar spectrum, e.g., into the visible range. However, some metal ions can leach from the photocatalysts or they act often as sites for efficient electron hole recombination causing in turn a decrease in photoactivity. The excitation step and charge transfer of sensitizers are shown in Figure 2-6.

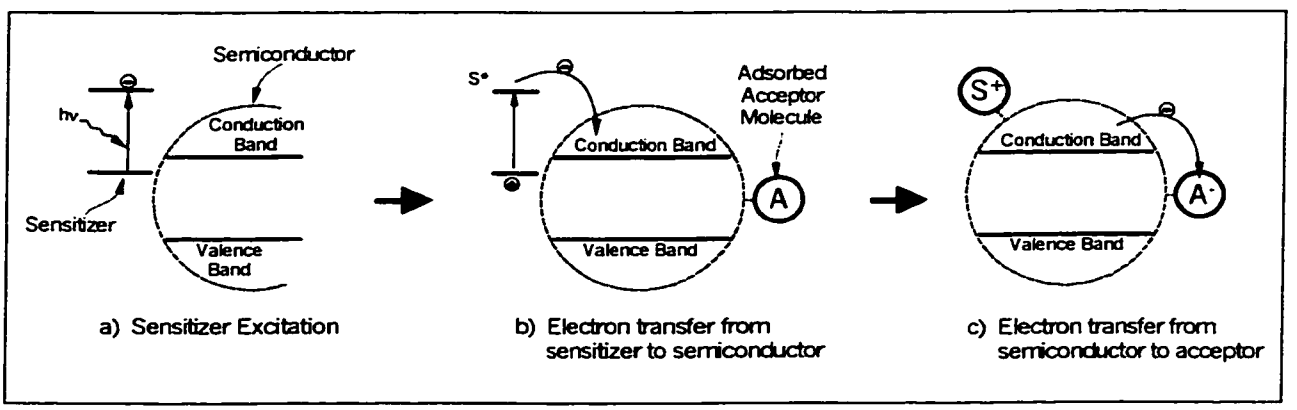

Figure 2-6 Sensitizer excitation and electron transfer (modified from[56])

Transition metal deposition on titanium dioxide is another form of semiconductor modification to achieve a better photocatalytic response. The main benefit results from an improvement in trapping electrons to inhibit electron-hole recombination. Iron and copper ions have shown to well serve as electron traps, while chromium ions create sites that promote recombination. Systems with noble metals, like silver or platinum, supported on titania has been very intensively investigated. Platinum proved to be a powerful catalyst, especially for water splitting and photodehydrogenation. In fact,

platinum is one of the best metal catalysts for dissociating or recombining hydrogen or hydrogenated compounds[7, 56]. The metal is, on one hand, important because of its own catalytic activity. On the other hand it alters the photocatalytic properties of the semiconductor by changing the distribution of electrons. A redistribution of electric charges and the formation of a double layer will take place at the contact point of semiconductor and metal (a process also happening at semiconductor-gas phase interface). Due to the transfer of mobile charge carriers to the metal-semiconductor interface and trapping the electrons on the surface a space charge layer is formed. This surface region will then become negatively charged. Since the concentration of negative charges at the interface is higher than in the interior of the semiconductor a positive space charge layer is created within the semiconductor in order to keep the material electrically neutral. This causes a shift in electrostatic potential, leading to a bending of the energy band upwards towards the surface region as depicted in Figure 2-7.

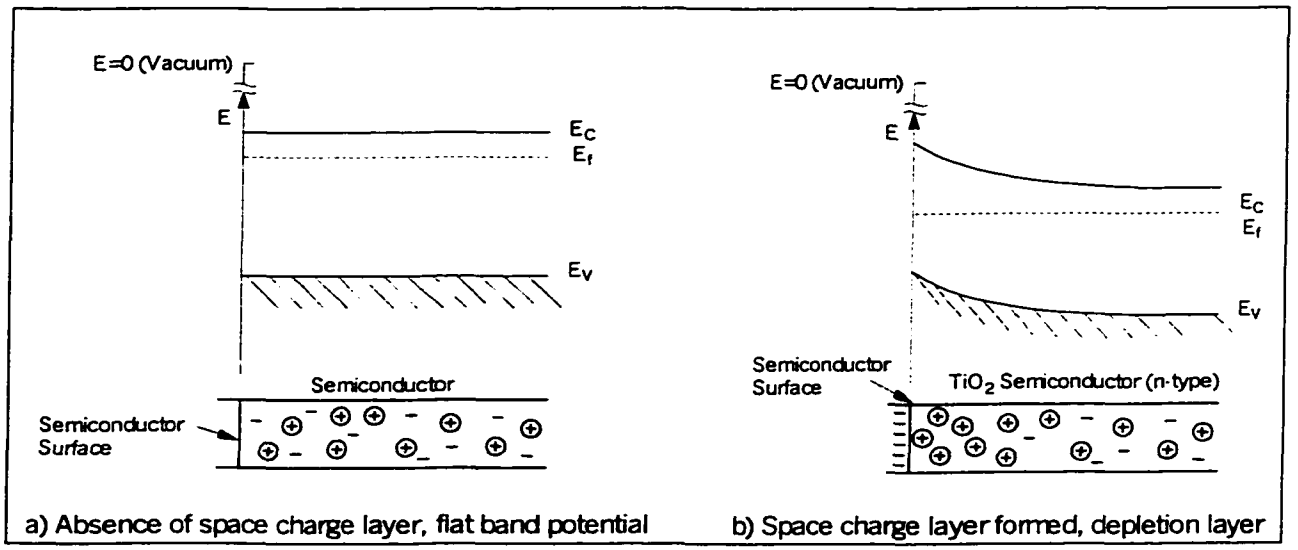

Figure 2-7 Space charge layer formation and band bending on an n-type semiconductor surface, such as TiO_2 (modified from[56])

When metal and semiconductor exist isolated from one another each component exhibits its own Fermi energy at a different level. However, when in contact with each other, electrons start to migrate from the semiconductor to the metal until both Fermi levels are aligned. The electrical contact makes electron migration possible away from the barrier region causing the formation of a space charge layer with an excessive negative charge on the platinum side and an excessive positive charge on the semiconductor. As a result, an upward energy band shift occurs on the semiconductor surface, the so-called depleted layer. This barrier at the metal-semiconductor interface is called the Schottky barrier and serves as an efficient electron trap preventing electron-hole recombination. The height of the Schottky barrier is given by subtracting the electron affinity E_x (measured from the conduction band edge to the vacuum level of the semiconductor) from the metal work function ϕ_m (energy necessary to raise an electron from the Fermi level up to the free space outside the solid). Figure 2-8 illustrates the Schottky barrier formation.

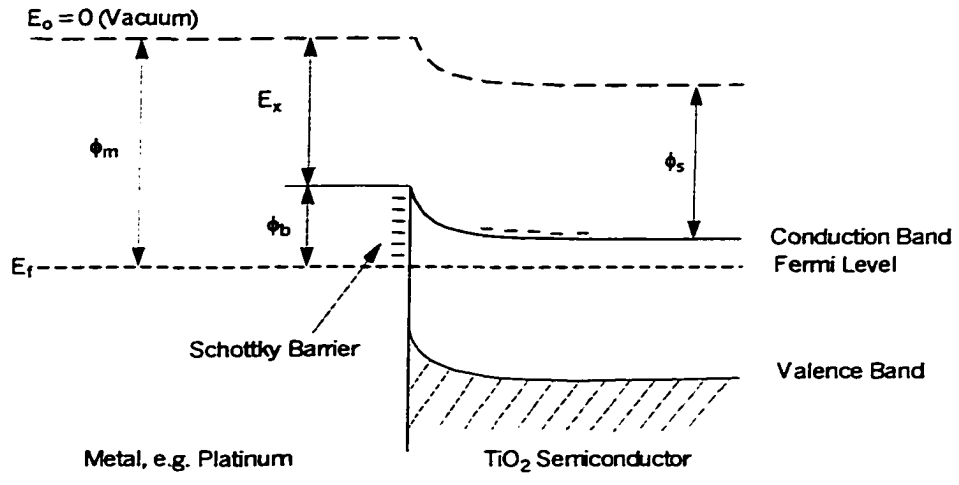

E_f = electron affinity, ϕ_m = work function of metal, ϕ_s = work function of semiconductor, ϕ_b = Schottky barrier, VB = valence band, CB = conduction band, E_f = Fermi level, E_o = vacuum level

Figure 2-8 Model of Schottky barrier[56]

Disdier et al. were able to demonstrate experimentally the existence of the Schottky barrier on platinum deposited on TiO_2[65]. They measured a reduction of photoconductance of TiO_2 with the addition of platinum due to electron migration to the metal (trapping) and the resulting formation of the Schottky barrier. With the electrons being "removed" the probability for electron-hole recombination is reduced which therefore increases the photoefficiency. The created holes are then free to diffuse to the TiO_2 surface to create reactive OH* radicals, the primary reactive site for the photocatalytic substrate conversion. Other researchers implied from the existence of the Schottky barrier that the hindered electron flow prevents the metal from acting as reduction centers[66]. In addition, they concluded from their photocatalytic dehydration study of methanol on metal loaded TiO_2 that the formed metal clusters give rise to

localized energy levels in the band gap of the titanium dioxide to which valence band electrons of TiO_2 are elevated at wavelengths above 390 nm. The increase in photocatalytic activity is therefore attributed to an extension of the energy absorbance in the visible region of 390 to 1000 nm[66, 67, 68]. An excellent paper by Choi and co-workers describes the photocatalytic effect of metal doping of quantum size TiO_2 particles[69]. Trichloromethane and tetrachloromethane oxidation was investigated over 21 metal ion-doped colloids. They observed that the photoactivity of doped TiO_2 varies widely depending on the specific dopant. While many of the dopants increased the photoactivity significantly, e.g. Fe^{3+} 15-fold, Mo^{5+} and Ru^{3+} 11-fold, Os^{3+}10 fold, V^{4+} 7-fold, and Rh^{3+} 5-fold, some dopants such as Al^{3+} and Co^{3+} reduced the activity. The difference in influencing the photoreactivity arises from the difference in energy levels compared to TiO_2 and as a result in the ability to trap electrons and holes which influences the electron/hole recombination rate. For example, Fe^{3+} has the ability to trap holes and electrons whereas Cr^{3+} can only trap holes. Photoexcited electrons in TiO_2 doped with Cr^{3+}, that cannot trap electrons and consequently recombine quickly with the trapped hole, while in Fe^{3+}doped TiO_2 recombination is less likely. The trapped hole in Fe^{4+} has a longer lifetime since the electron trapped in the Fe^{2+} is immobilized. In addition, the energy of charge release and migration within the lattice is of importance, in combination with the diffusion length. The charge carriers have to be transferred to the surface to be available for the photoreaction. Too strongly trapped electrons or holes would be detrimental. A combination of charge trapping, charge release and migration, and interfacial charge transfer is necessary to make the photoreaction possible. Once the electron is trapped by the iron ion, the created Fe^{2+} is relative unstable. Since the

Fe^{2+}/Fe^{3+} energy level lies close to the level of Ti^{3+}/Ti^{4+} the trapped electron in Fe^{2+} can easily be transferred to the surface Ti^{4+}, completing the interfacial electron transfer. Due to these different characteristics, the iron-ion is a more efficient dopant with respect to photoreactivity compared to the cromium-ion. Dopants with closed-shell configuration have only little effect on the photoreactivity as they are very stable and do not favor electron trapping. An important fact worth mentioning is that all afore described effects are only valid for dopants located close to the surface where interfacial charge transfers occur. With this kept in mind, quantum sized particles (as described above) possess the positive feature by always fulfilling this criterion, besides they demonstrate already good electronic properties. As Q-sized particles are so small that the wave function of the charge carrier spreads over the entire semiconductor cluster, the electron and the hole are readily available at the interface.

It is important to bear in mind that the effect of metal doping on the change in photoefficiency can not easily be predicted by only considering the above described criteria. An increase or decrease in efficiency depends also largely on the dopant concentration, the dopant dispersion, as well as the type of reactants to be converted. Most studies confirmed the existence of a maximum dopant concentration above which the photoactivity declines again. However, the value of this maximum concentration itself depends once more on the dopant metal and the reaction environment. The optimal dopant and dopant concentration have to be determined from experimental studies under the specific conditions of interest.

2.4 Photocatalytic Material

2.4.1 Introduction

Among other desirable properties, the appropriate catalyst for photodetoxification should have the following characteristics: it should not contain toxic elements, it needs to be stable in aqueous solutions containing extremely reactive and highly toxic chemicals (in case it is used for the liquid phase applications), and it should not be vulnerable to photo corrosion under constant bandgap illumination. Most metal oxides possess these characteristics, however, they have very large bandgaps or they are even insulators. One exception is Iron-III-oxide with a band gap of 2.2 eV. It absorbs light already in visible range below 560 nm, but the photocatalytic activity is too low compared to more effective semiconductors such as titanium or zinc oxides[3].

Of all the semiconductors investigated in regards to photocatalysis, titanium dioxide has been found to be the material with the highest efficiency for photocatalytic destruction. Only zinc oxide (ZnO) demonstrated a similar activity to TiO_2. But ZnO has a high deactivation rate, especially in acidic or alkaline liquid media, which makes this catalyst unsuitable for most technical applications.

However, depending on the final application, not only the catalyst's activity is a decisive factor for the choice of the appropriate photocatalyst. Low maintenance, deactivation, and high mechanical strength are also important characteristics that determine the usefulness of a catalyst. In the following sections two types of photocatalysts are introduced that were investigated for their usefulness for indoor air decontamination applications.

2.4.2 Titanium Dioxide and its Characteristics

Several studies on metal oxide photocatalysts have been performed in order to find an ideal catalyst for photooxidation. Ibusuki and Takeuchi studied the photocatalytic activity of ZnO in a butene-NO_2-dry air system and that of 16 other kinds of metal oxide for propylene-NO_2-dry air systems [Ibusuku, 1986]. They found that titanium dioxide revealed the highest photocatalytic activity compared to all other metal oxides. Other researchers came to the same conclusion that TiO_2 is the most destructive catalyst for a wide range of contaminants [Teichner, 1985].

TiO_2 is a semiconductor with a bandgap of approximately 3.2 eV and can absorb light below 400 nm to create electron/hole pairs. With this characteristic, TiO_2 is photoactive at wavelengths produced by the sun or other artificial photon sources. Titanium dioxide is comparatively inexpensive, non-toxic, insoluble, has a long lifetime and is safe[3, 7, 18, 38, 70]. For example, it can be found in toothpaste, paint, and sun block agents. Using molecular oxygen from air, which is available at enormous stoichiometric excess, it is able to completely mineralize a vast variety of organics in aqueous and gaseous reaction systems. Titanium dioxide does not deactivate during photoreactions[71] and no or only traces of water are needed to maintain the catalyst active[7]. Moreover, there is no or little formation of intermediates or side products. Even small amounts of side-products will eventually completely mineralize with sufficient residence time given.

These characteristics make titanium dioxide the most promising candidate for photocatalytic remediation processes of organic compounds. Nevertheless, as previously mentioned, the drawback of all presently available photocatalysts, including TiO_2, is their

low photoefficiency. For instance, only about 5-10% of the energy provided by the sun can be utilized as shown Figure 2-4. Due to the relatively large band gap, photon absorption resulting in an electron/hole pair formation occurs only at wavelengths starting at around 360 nm with a sharp drop to zero at 400 nm. Some approaches to increase photoefficiency have already been discussed in Section 2.3.3.3 Efficiency of Photocatalysts. Other variable photocatalyst properties that influence the photoreactivity or/and efficiency include crystalline structure, particle size, surface area, and surface OH-group density. Amorphous TiO_2 is mostly photocatalytically inactive. Of the three crystalline forms (brookite, rutile, and anatase) anatase is the modification with the highest activity with brookite showing no reactivity at all. Why rutile TiO_2 is active in some cases and virtually inactive in other cases is not clear yet and cannot be explained in a straightforward manner[72]. The different photoactivities between rutile and anatase cannot be attributed to different band gap values since the difference (E_g = 3.0 and 3.2 eV for rutile and anatase, respectively) is too small. Most researchers agree that the lower activity of rutile is due to a faster recombination of charge carriers. In addition, the amount of adsorbed reaction species on rutile is considerably lower compared to that of anatase due to a lower number of surface hydroxyl groups on rutile[6, 14]. Rutile and anatase are the two forms easily synthesized under ambient condition. Anatase is metastable and can transform to rutile at temperatures starting at 400 up to 1100°C[73].

The different structures of anatase and rutile are shown in Figure 2-9. Both structures are composed of a combination of octahedrons. They differ from each other by the degree of distortion and the assembly pattern. The octahedrons consist of Ti^{4+} ions surrounded by six O^{2-} ions. In rutile, the octahedron is not regular but it is slightly

orthorhombic distorted. In contrast, the octahedron of anatase shows a significant distortion so that its symmetry is lower than orthorhombic. The Ti-Ti distances in anatase TiO_2 are greater while the Ti-O distances are shorter compared to that of rutile. In the anatase structure each octahedron is in contact with eight neighbors, half of them sharing edge oxygen pairs, the other half sharing corner oxygen atoms. Rutile shares two octahedrons with an edge and eight octahedrons with a corner. These structural differences bring about the differences in mass densities and electron band configuration of rutile and anatase as pointed out above[56]. Anatase and rutile TiO_2 have band gap energies of 3.2 and 3.0 eV, respectively[10].

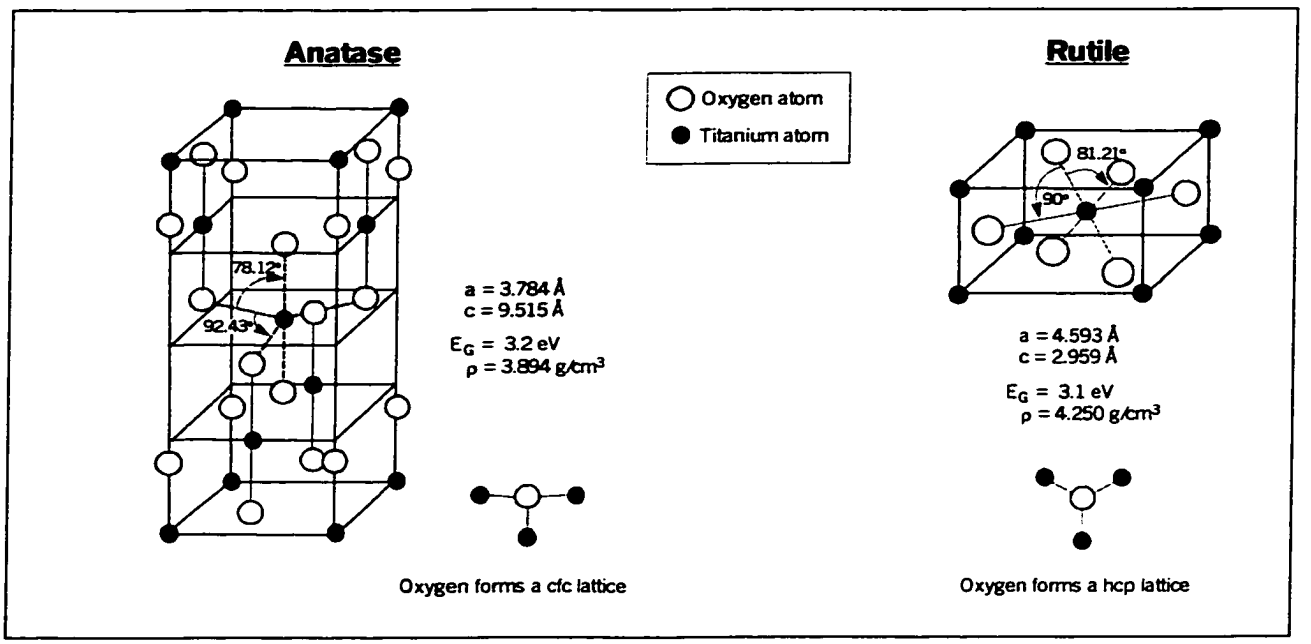

Figure 2-9 Anatase and rutile structure of titanium dioxide (adapted from[56])

Particular desired characteristics of a catalyst can be tailored either during synthesis by altering reaction conditions (starting material, thermal hydrolysis, sol-gel technique, pH of solution, additives etc.) or throughout post synthesis treatment such as thermal

treatment. Even though not necessarily related to the characteristics of the catalyst itself it might be mentioned at this point that the VOC degradation efficiency depends as well on adsorption/desorption rates of reactants and products, light intensity and rate of light absorption, and on the reactor design - in specific different methods of catalyst dispersion, e.g. like fixed bed versus coating of plates, or use of TiO_2 membranes, or TiO_2 beads.

Until now, the best commercially available catalyst is Degussa P25, a titanium dioxide powder subject to a vast amount of research performed in the field of photocatalysis.

2.4.2.1 Degussa P25 Catalyst

Degussa P25 is a pure titanium dioxide mixture of 70% anatase and 30% rutile, manufactured by Degussa Corporation. Although anatase has been found to be the crystalline structure with highest photoreactivity, however, most studies have shown that the P25-composition of 70/30 of anatase to rutile proved to be the most efficient catalyst with its reactivity significantly higher than that of a 100 percent anatase titanium dioxide. The particle size of P25 ranges from 15 to 40 nm[74] with an average primary particle diameter of 30 nm (300Å)[33]. Its surface area ranges between 35 and 65 m^2/g, the specific gravity is approximately 3.7 while the tapped density of the powder was determined to be 0.13 g/cc[75]. P25 is a white opaque nonporous material with a UV penetration depth of approximately 4.5 μm[29]. Even though the displayed characteristics of P25 would make it an ideal candidate for photocatalytic applications, there are still a number of problems that restrict the development of technologies employing photocatalysis. The available

surface area for catalytic reaction is relatively low, plus the limited accessibility of the incident UV light to the bulk material keeps the photoefficiency at a rather low level. With only 4.5 μm UV penetration depth most of the catalyst in a fixed bed is unavailable for photoexcitation. Competition of organic molecules for active surface sites becomes a rate-limiting factor. It is a challenge, therefore, to develop a photocatalyst or/and a photocatalytic reactor ensuring that most of the catalyst would be accessible to UV light.

2.4.2.2 TiO_2 Aerogel Catalyst

As outlined in the previous chapter, the current photocatalysts possess a low penetration depth for UV light keeping most of the bulk material in a catalyst bed unavailable for illumination. In addition, the low porosity of presently available catalytic materials causes diffusion problems, which hinder gas molecules to reach the active reaction sites. To have all of the catalytic material accessible to UV light very thin layers of catalyst material must be prepared in order to activate most of the implemented catalyst. Therefore, a challenge remains to be met by engineers and reactor designers.

One way to overcome the above-indicated problems would be a different kind of titanium dioxide catalyst, e.g., the form of an aerogel. An aerogel can be described as an open cross-linked metal oxide structure with a high void volume and fine pore size[76]. This novel material carries several desired catalyst characteristics such as high surface area (up to 2000 m^2/g), high porosity (up to 99%), low density (down to 0.03 g/cm^3)[77], and high transparency. These characteristics provide for easier gas diffusion, deeper penetration of UV light into the catalyst, and a larger number of available reaction sites. Furthermore, higher photo efficiencies could be expected since created electron/hole

pairs within the thinner aerogel walls are less likely to recombine due to the significantly shorter migration path to the solid-gas interface. Considering that more reactive sites are already provided by the aerogel due to its larger surface area, even more sites are available for activation because of the higher UV transparency of the material. Assuming the UV penetration depth (D) of 4.5 μm for a nonporous TiO_2 increased with porosity (ε) according to Equation (2-6)

(2-6) $$D = \frac{4.5}{1-\varepsilon}$$

then a titanium dioxide aerogel of 99% porosity, with all other variables being held the same, would exhibit a UV penetration 100 fold higher than compared to that of a nonporous material. It becomes clear that with a deeper penetration of UV light a higher fraction of the catalyst bulk (for a given particle size or film thickness) would be available for illumination and excitation as indicated in Figure 2-10.

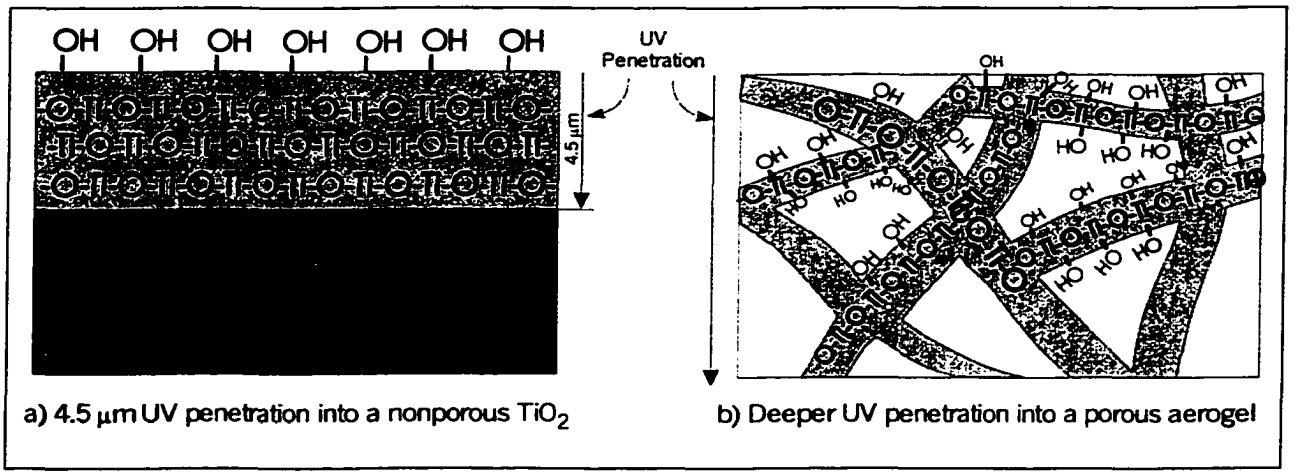

Figure 2-10 Difference in number of catalyst sites illuminated of nonporous TiO_2 and aerogel

It is especially noteworthy to examine the increase in UV accessible surface area with an increase in porosity of aerogels. Assuming one square centimeter of aerogel surface is illuminated as pictured in Figure 2-11 and furthermore that the aerogel pores can be considered as tubes with open ends, the surface area accessible to UV light (SA) can then be calculated according to equation (2-7) or (2-11).

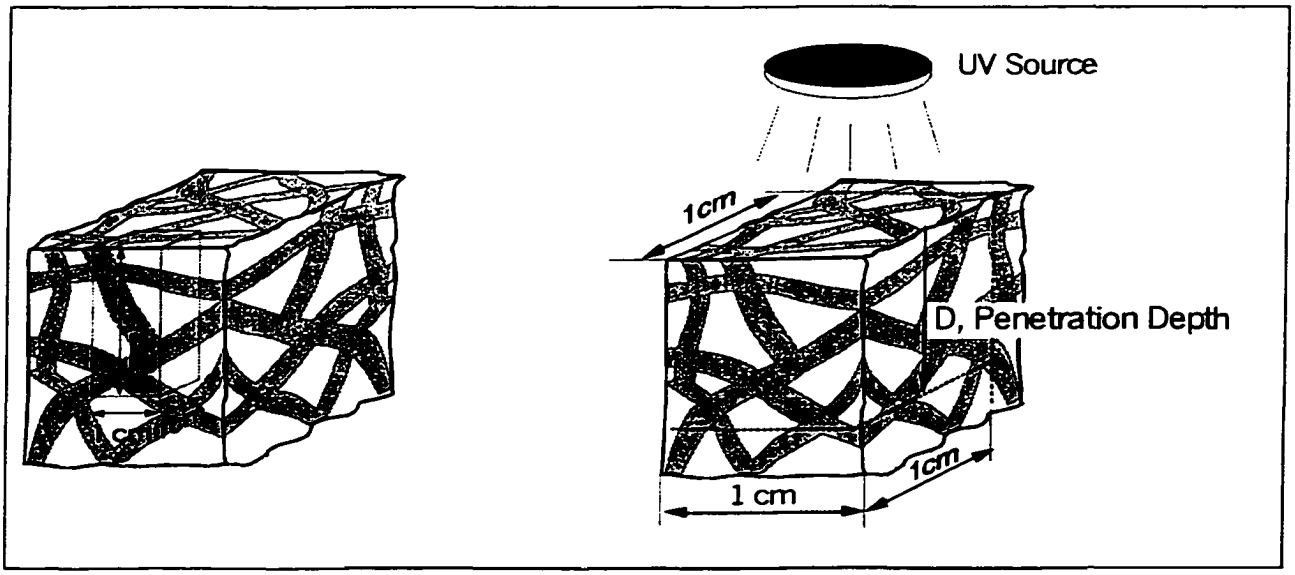

Figure 2-11 UV accessible Area in a porous aerogel

(2-7) $SA = \pi d_{pores} * l$ and

(2-8) $V_{void} = \frac{\pi}{4} d_{pores}^2 l$, thus

(2-9) $SA = \frac{4V_{void}}{d_{pores}}$.

with V_{void} = void volume of the pores, l = pore length, and d = aerogel pore diameter. Substituting Equations (2-10), (2-11) and (2-6) into Equation (2-7) will give equation (2-12), with which one can estimate the total illuminated surface area with respect to the porosity of the material.

(2-10) $V_{void} = \varepsilon * V_{total}$

(2-11) $V_{total} = 1\ cm^2 * D$

(2-6) $$D = \frac{4.5}{1-\varepsilon}$$

(2-12) $$SA = \frac{4 * 1cm^2 * 4.5\mu m}{d_{pores}} \frac{\varepsilon}{1-\varepsilon}$$

with ε = porosity, V_{total} = penetration volume, and D = penetration depth. For a material with no porosity, like Degussa, only 1 cm^2 SA is available for illumination, whereas an aerogel with 90% porosity and pores of 20 nm diameter the UV accessible surface area is increased by a factor of several thousands, as shown in Table 2-1.

	Porosity, ε	UV accessible Surface Area, SA
Non-porous Degussa P25	0	1 cm^2
Aerogel	0.90	7056 cm^2
Aerogel	0.99	77,613 cm^2

Table 2-1 UV accessible surface area for a nonporous and a porous material

Aerogels are synthesized via the sol-gel technology. Starting materials are a metal alkoxide, alcohol, and water. A series of hydrolysis and condensation reactions leads then to the gelation of the metal alkoxide compound through growth and crosslinkage of polymeric units. The net reactions leading to the formation of an anhydrous oxide are represented by[78]:

(2-13) $M(OR)_n + x\ H_2O \rightarrow M(OH)_x(OR)_{n-x} + x\ ROH$

(2-14) $M(OH)_x(OR)_{n-x} \rightarrow MO_{n/2} + x/2\ H_2O + (n-x)\ ROH,$

where M symbolizes a metal cation (e.g. Ti), and R an alkyl group (e.g., ethyl group C_2H_5). The hydrolysis reaction is catalyzed with either a base or an acid. Acid catalyzed

reactions result more in a gel with linear randomly branched chains, while base initiated reactions lead to a gel of highly branched polymeric clusters. The structure of an aerogel is primarily determined by the condensation process, which in turn depends on parameters such as composition of the initial solution, type of catalyst, pH of the initial solution, the presence of other ions, and temperature. Titanium dioxide gels prepared by Bischoff and Anderson, for example, were synthesized in an acidic or basic solution and produced amorphous materials, while the synthesis in a neutral medium resulted in a mixture of anatase and brookite[73]. In addition to the gelation conditions, aging of the gel as well as the drying process influence largely the gel characteristics. During the final step of the aerogel synthesis, the drying, the liquid in the pores of the so created continuous network is replaced with air. Kistler, who synthesized the first aerogels in 1931[79], removed the water in a liquid gel under supercritical conditions preventing thus the collapse of the gel-network, which is accompanied by a loss of a considerable amount of surface area. Drying a gel under ambient condition causes the gel to shrink significantly due to the surface tension at the liquid-vapor interface. When holding a liquid above its vapor pressure while raising the temperature to its critical point the liquid transforms into a gas which then can slowly be evacuated from the gel structure leaving a dry aerogel behind.

Teichner found in his study of isobutane oxidation over different TiO_2 catalysts that, when compared on a mass basis, the aerogels did not perform as well as the nonporous TiO_2 catalysts [22]. However, Dagan and Tomkiewicz concluded from photocatalytic oxidation studies of salicylic acid and other different organic contaminants in water that

the TiO_2 aerogels performed indeed at a much higher photocatalytic activity than Degussa P25 catalyst[80].

One of the challenges in developing catalytic reactors is to ensure that a high fraction of the catalyst surface area is accessible to UV light. Since UV light penetrates only about 4.5 microns into opaque titanium dioxide such as Degussa P25, either thin layers should be used, or the powder must be continuously stirred or mixed, such as in a fluidized bed reactor, to periodically expose the particles to UV light. Such reactor design is too complicated and costly for indoor air applications. An alternative to the fluidized bed is a packed bed. However, as the bed thickness is increased, the efficacy of the reactor is limited to the point until no longer more material is photoactivated (4.5 μm). At that point, additional thickness will simply allow the contaminant to bypass the photoactive portion of the bed, and efficiency of the reactor system consequently decreases. Therefore, the optimum bed thickness is restricted to the UV penetration depth of the photocatalytic material. Thus, in order to ensure that most of the catalyst is utilized for photooxidation it is necessary to prepare extremely thin catalyst beds or to spread thin layers of the photocatalyst evenly over a support. The highly porous aerogel, on the other hand, with ptentially extremely thin pore walls, has the ability to allow UV light to penetrate through hundreds of these thin pore walls, thus accessing reaction sites deeper within the catalyst bed and activating a large surface area without the necessity of thin layers or constant agitation.

Besides showing much promise for higher photocatalytic activity, aerogels are also considered to be suitable photocatalyst candidates due to other characteristics desired for

indoor air decontamination applications. One important aspect is the particle size. Depending on synthesis conditions, the aerogels may be tailored to have large particles with uniform particle size. This is especially of interest for their use in catalyst beds. A catalyst bed with larger particles allows for a better airflow thus limiting pressure drop across the catalyst bed for use in typical indoor air systems. In addition, aerogels can be synthesized in form of large blocks, as compared to a loose powder, while still allowing for the air to flow through due to its high porosity. Having solid pieces with high mechanical strength in a catalyst bed would greatly limit the occurrence of airborne particles.

Thus, the characteristics of the aerogel have potential for improvements in photocatalytic activity and for ease of utilization, e.g., less complicated reactor design. A simpler reactor design with the use of thicker beds makes relatively small scale applications such as indoor air decontamination much more likely for commercialization.

The work presented here will show that titanium dioxide aerogels (catalysts synthesized in our labs) are promising candidates for improving the photocatalytic oxidation technology.

2.4.3 Platinum Doped Titanium Dioxide

Already in Section 2.3.4 (describing Catalyst Modifications to Enhance Photoefficiency) was discussed that metal doping on titanium dioxide might alter the catalytic activity significantly. Several photocatalytic studies on metal-doped TiO_2 did not find the expected improvement in photocatalytic activity, though most of the reports stated an improvement of the photocatalytic performance after metal-doping of TiO_2[81].

Besides iron ions, platinum ions were the most investigated dopants with respect to photocatalytic oxidation. The effect that Pt ions exercise on the TiO_2 surface has not been fully investigated. Scientists agreed that the platinum dispersed on titanium dioxide enhances the photocatalytic efficiencies due to the shorter characteristic interfacial electron transfer time from the Pt-islands to adsorbed species compared to that from the TiO_2 surface trapping sites. However, it is still subject of controversial discussions if the created ohmic contact on the Pt-TiO_2 interface or the Schottky barrier is actually responsible for the photocatalytic enhancement[82, 83]. In any case, the major role of surface deposited Pt clusters has been attributed to the acceleration of electron trapping and O_2^- formation with a resulting decrease in electron/hole recombination and increase in h^+ and OH* radicals yield. The electron transfer can be described as[83]:

(2-15) $e^-_{CB} + Pt_n \rightarrow Pt_n^-$

(2-16) $Pt_n^- + O_2 \rightarrow Pt_n + O_2^-$

where n represents the number of platinum clusters, e^-_{CB} stands for the electron from conduction band. This process is again illustrated in Figure 2-12

If n is too large then the platinum clusters start to serve as recombination centers. Due to the higher Pt density the separation distance of charge carriers decreases making it for an electron easier to meet and recombine with a hole according to

(2-17) $Pt_n^- + h^+ \rightarrow Pt_n$

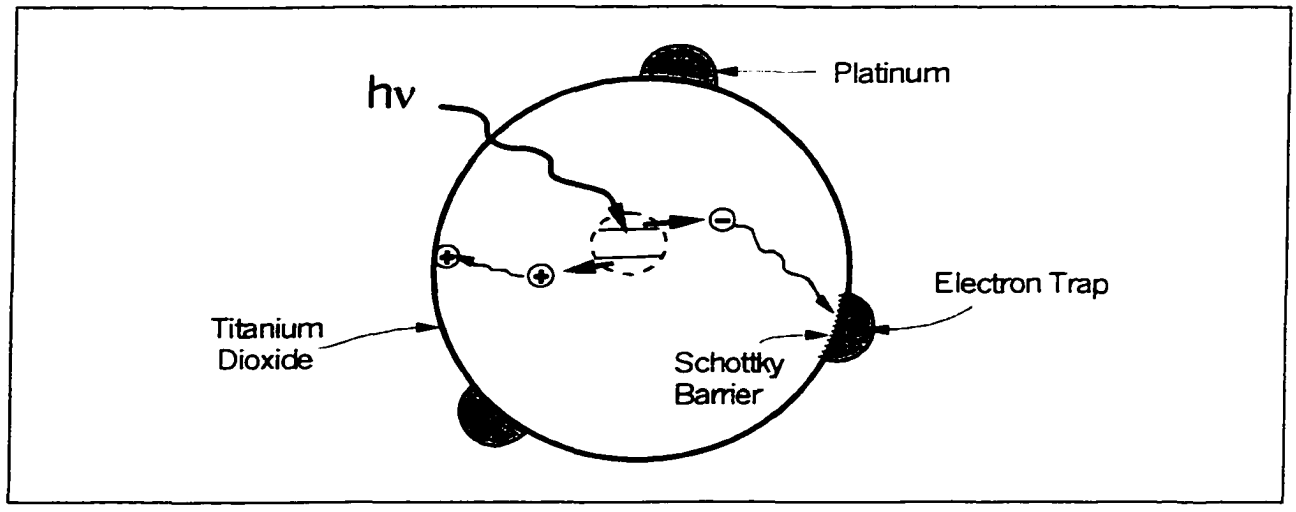

Figure 2-12 Effect of platinum on charge carrier separation

Figure 2-13 illustrates schematically the dependence of charge carrier separation distance on platinum loading. A low number of Pt deposits leads to an increase in charge carrier separation distance as seen in Figure 2-13a. With more Pt deposited on a TiO_2 particle, the distance of an electron to a Pt deposit is shorter and therefore closer to the hole.

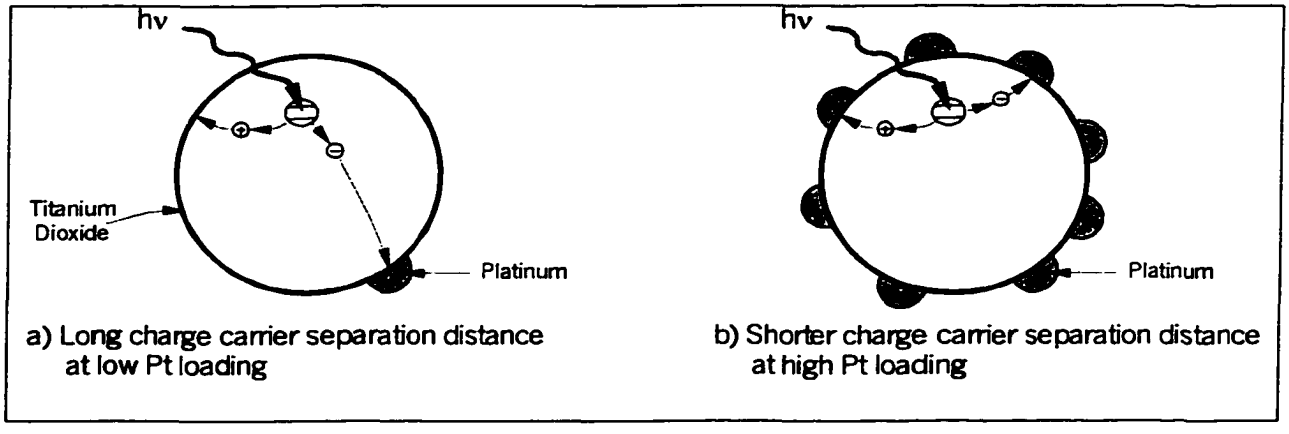

Figure 2-13 Effect of platinum deposit density on charge carrier separation distance (adapted from[83])

The optimum loading of platinum on a TiO_2 was found to be about 1.5wt%[66], however it varies with catalyst particle size and the specific oxidation application. Zang et al. reported a significant improvement in photoreactivity after depositing 0.5wt% Pt on TiO_2[84]. Another paper of Zang et al. reported that an otherwise inactive amorphous titanium dioxide material became photocatalytically active upon the modification with 1.3% platinum (IV) halides. Photodegradation of 4-chlorophenol was possible even within the range of visible light[81]. Chen at al. observed an increasing rate of alcohol conversion after the metallization of TiO_2 with 1% platinum[82], while Sadeghi and co-workers observed a maximum increase in methanol conversion at a dopant concentration of 8wt% Pt[83].

The photocatalytic activity is also affected by the preparation method of platinum deposition. The use of either photodeposition in a liquid slurry, chemical vapor deposition, or the incorporation of platinum during catalyst synthesis influences how well the Pt ions are dispersed in the catalyst and whether they are deposited only on the catalyst surface or within the pores or if they are even incorporated within the matrix.

Most of the research related to platinum doped TiO_2 for application of photocatalytic mineralization of organics has been performed for oxidation in an aqueous phase. The presented work, however, will illustrate that Pt-loaded TiO_2 can also enhance the photocatalytic destruction of organics (ethylene) in the gas phase.

3 Experimental

3.1 Catalyst Preparation

3.1.1 Degussa P25

The Degussa P25 photocatalyst, a titanium dioxide powder of 70% anatase and 30% rutile, was obtained directly from Degussa AG (GB AC, Frankfurt) and utilized as is for the photocatalytic studies.

3.1.2 Titanium Dioxide Aerogel Synthesis

Pure titanium dioxide aerogels were synthesized via the sol-gel method using titanium (IV) isopropoxide, ethanol, water, and acetic acid as starting material. An inorganic network is formed throughout a chain of hydrolysis and condensation reactions according to Equations (3-1) to (3-3), where R stands for an alkyl group such as a propyl-group. It should be kept in mind that these equations illustrated the substitution of solely one alkyl group (R). Hydrolysis and condensation would continue to occur until the remaining OR-groups on the Ti have been substituted, as shown in Equation

(3-4) for a completed overall reaction. Nonetheless, even after gelation is completed there will still remain some OR and OH groups in the final structure due to incomplete hydrolysis.

(3-1) $\text{Ti–OR} + \text{H}_2\text{O} \rightarrow \text{Ti–OH} + \text{R(OH)}$ (hydrolysis)

(3-2) $\text{Ti–OH} + \text{RO–Ti} \rightarrow \text{Ti–O–Ti} + \text{R(OH)}$ (alcohol condensation)

(3-3) $\text{Ti–OH} + \text{HO–Ti} \rightarrow \text{Ti–O–Ti} + \text{H}_2\text{O}$ (water condensation)

(3-4) $Ti(OR)_4 + 2\,H_2O \rightarrow TiO_2 + 4\,R(OH)$ (overall)

The hydrolytic condensation of titanium alkoxide is very complex and the quality of the final product depends on many variables[73]. For example, morphology and characteristics of the gel are strongly influenced by variables such as the choice of solvent, the ratio of reactants, the type of hydrolysis catalyst, the reaction temperature, and also the drying procedure[85]. A major problem with titanium (IV) isopropoxide is that it reacts vigorously upon the smallest addition of water forming undesired precipitates with a high degree of microstructural disorder. To prevent this fast precipitation, acetic acid was employed serving as a hydrolysis inhibitor. Additionally, it was surprisingly found that using excess water drastically slows down the hydrolysis reactions[86]. Consequently, the water/alkoxide ratio seems to play a role beyond that of the chemical requirement. Applying the excess water method did not only serve to influence the kinetics of gel formation but was also beneficial to reduce the density of the final aerogel.

Several aerogels with varying water/Ti-butoxide ratio were synthesized to obtain titanium dioxide aerogels with low and ultra-low densities.

3.1.2.1 Low-density titanium dioxide aerogel

Low density titanium dioxide aerogels (denoted as CEH2, CEH4, and CEH6) were prepared from titanium isopropoxide (97 %, Aldrich), ethanol (anhydrous, Aldrich), and acetic acid (99.5 %, Fisher Scientific). The compounds were mixed in a beaker according to a molar ratio of Ti : EtOH : HAc = 1 : 12 : 9. Under constant stirring, deionized water was added at a molar ratio of Ti : H_2O = 1 : 40. The gelation time was 4 - 5 days forming a translucent gel with a slightly cloudy appearance. The samples were

then dried under supercritical conditions as described later in Section 3.1.4 Supercritical Drying Procedure. A theoretical density (assuming no shrinkage during the drying procedure) of 0.18 g/cm^3 was calculated.

3.1.2.2 Ultra-low density pure titanium oxide aerogel

An ultra low density pure titanium oxide aerogel (denoted as T36) was prepared from a mixture of 14.6 ml ethanol (98% Aldrich), 3.08 ml titanium-isopropoxide (97 %, Aldrich), 24.0 ml distilled water, and 8.31 ml acetic acid (99.5 %, glacial, Aldrich) which is equivalent to a molar ratio of Ti : EtOH : HAc : DI = 1 : 22 : 13 : 120. In order to prevent precipitation, water was first mixed with acetic acid and then added to the titanium-isopropoxide ethanol mixture. After 5-6 weeks the gelation was complete with the gels having a milky appearance. The same drying procedure was applied as described in Section 3.1.4. A theoretical density (assuming no shrinkage during the drying procedure) of 0.032 g/cm^3 was calculated.

3.1.3 Binary Ti-Si aerogels

When two metallic compounds such as titanium-isopropoxide and tetraethoxysilane (TEOS) are involved in a sol gelation process then heterocondensation is possible according to:

(3-5) $\quad Ti{-}OH + Si{-}OH \rightarrow Ti{-}O{-}Si + R(OH)$ (adapted from [87])

The major problem of combining two different transition metal alkoxide precursors is their different rates of hydrolysis. Prehydrolysis of the alkoxide possessing the lower rate (TEOS) would be one way to overcome this difficulty. Another way would be to adjust

the ratio of water/alkoxide to reduce the hydrolysis rate of the faster reacting species (Ti-butoxide). The later method was applied to prepare binary Si-Ti- oxide aerogels.

A binary silica-titania aerogel with a molar ratio of Si : Ti = 1 : 4.5 was prepared from 0.5 ml tetraethoxysilane, 0.14 ml titanium-isopropoxide, 1.92 ml ethanol, 1.50 ml acetic acid, and 3.0 ml distilled water. All reactants were added at the same time. Ammonium hydroxide was added as a hydrolysis catalyst. Gelation occurred within two days, resulting in a slightly cloudy translucent gel, followed by the acetone wash procedure and supercritical drying.

3.1.4 Supercritical Drying Procedure

The supercritical drying procedure involved a two-step solvent replacement within the wet sol-gels. First, the gels were placed in a metal mesh container and then washed in acetone to replace solvent and water in the pores of the gel. A continuous acetone recycling apparatus as shown in Figure 3-1 was utilized to assure that the wet gels were always exposed to fresh acetone. The gel samples that were contained in a metal mesh were placed in the 5-Liter-sample holder filled with 4 L of acetone. The solvent from within the pores migrated into the acetone while acetone migrated into the pores. The now impure acetone passed into the acetone reservoir where heat was provided by a heating element to vaporize only the acetone. Pure acetone vapor then left the acetone reservoir, was condensed while passing across the cooling element, and was combined with the acetone in the sample holder. This refluxing cycle was continued for about two weeks until all of the solvent from the gel pores had been replaced by acetone.

The acetone within the gels was then replaced with liquid carbon dioxide using a similar purging system as for the acetone. A computer controlled apparatus as depicted in Figure 3-2 allowed for a continuous automatic flushing and degassing of CO_2 mixed with acetone purged from the gels. The initial acetone wash was necessary to fill the gel's pores with CO_2. Since CO_2 is immiscible in water without applying high pressures it would not be able to replace the water within the gel pores. Acetone served, therefore, as a binary solvent between water and carbon dioxide. After approximately two weeks, the acetone was entirely replaced with liquid CO_2. The temperature was slowly raised to 42°C, which is slightly above the critical point of CO_2, while holding the pressure at above 1100 psig. At those supercritical conditions the carbon dioxide has still a liquid-like density but it behaves like a gas, thus eliminating surface tension that a liquid would exert on the pore walls. The temperature was then held at this point for about two hours before the pressure was slowly released over a time period of 2-3 hours.

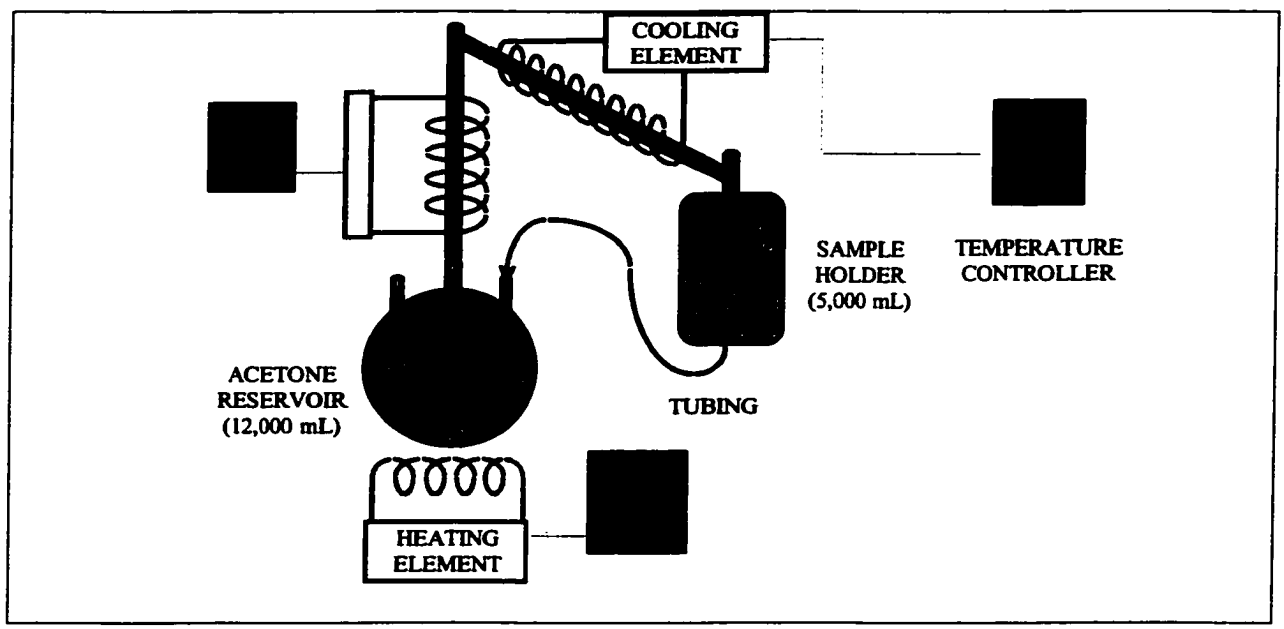

Figure 3-1 Acetone reflux apparatus for solvent replacement within the sol-gels[88]

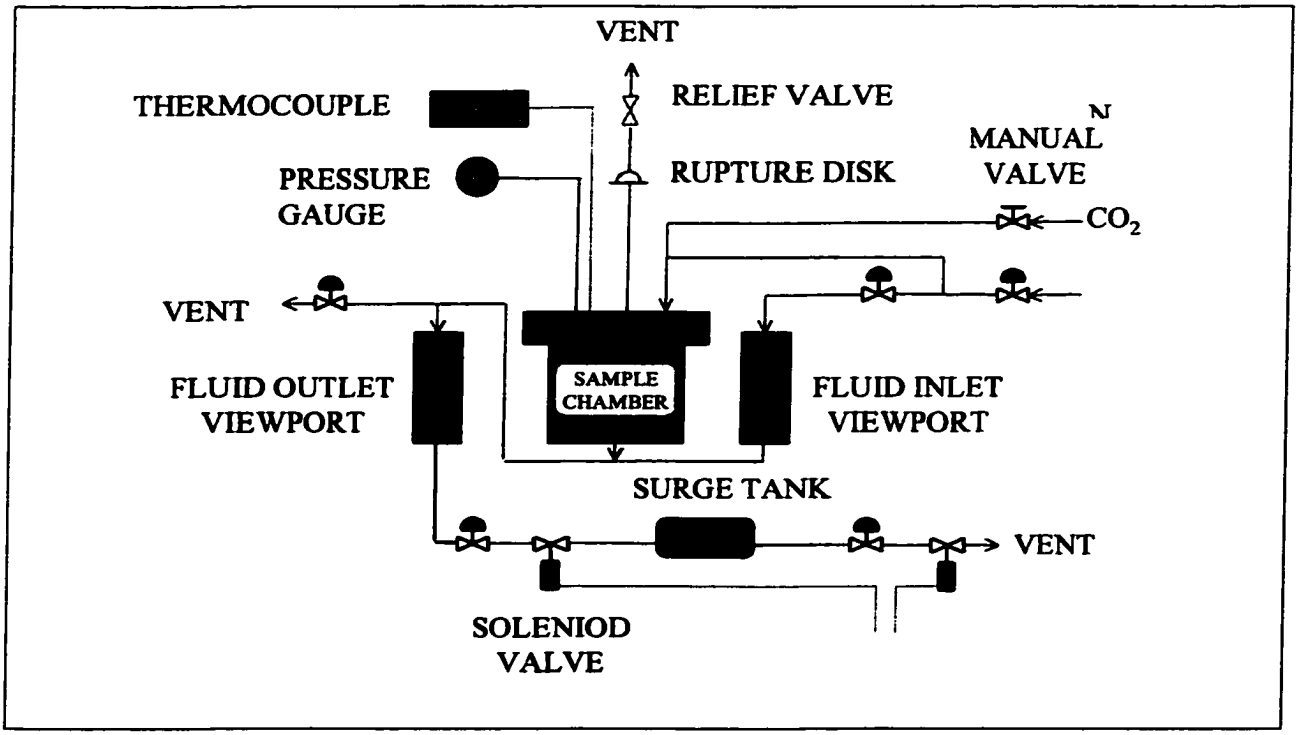

Figure 3-2 CO_2 solvent exchange and supercritical drying apparatus[88]

3.1.5 Platinum Doped Titanium Dioxide Catalyst

3.1.5.1 Photocatalytic Co-deposition of Platinum in Aqueous Slurry

Photocatalytic co-deposition of platinum on titanium dioxide is one of the possible methods to prepare a metal supported photocatalyst. This method is of advantage as it works under ambient pressure and temperature. Since the titania aerogel material loses a significant amount of surface area and porosity at temperatures above 200°C it was important to apply a metal deposition method that works at low temperatures. When a photosensitive semiconductor, such as titanium dioxide, in the presence of a noble metal salt is irradiated under UV light the metal will be deposited as small crystallites[89]. Platinum was first deposited on Degussa P25 by preparing the samples according to the method described by Herrman[90], to obtain samples of 0.01, 0.1, 0.5, and 3.0wt%

platinum. A defined amount of hydrogen hexachloroplatinate(IV) hydrate (Aldrich) was added to a quartz glass beaker containing a slurry of 100 ml deionized water mixed with 3 g of Degussa P25. This mixture was then agitated with a magnetic stirrer under constant illumination of UV light (450 W, Ace Glass) for about 10 hours. The slurry was then left to stand until the Degussa powder had settled. The supernatant was then discarded and the remaining material was dried in a vacuum oven at T = 110°C. The obtained yellow powder was then ground and placed in a photocatalytic quartz glass cell. After illumination under UV light for about 12 hours the yellow color of the powder changed to gray, which indicated a successful platinization. Since photocatalytic ethylene oxidation tests did not show an improvement of photocatalytic activity (see Chapter 4.7), no platinum doping was attempted using photocatalytic codeposition on the TiO_2 aerogels.

3.1.5.2 Photocatalytic Co-deposition of Ruthenium in Aqueous Slurry

The same method as described above (Paragraph 3.1.5.1) was applied to disperse ruthenium over Degussa P25. Starting material was Ruthenium(III)chloride (Aldrich), which was dissolved in 100 ml DI water. About 5 g of Degussa P25 was added and under constant stirring exposed to UV light for 6 hours utilizing the light source described in Section 3.5.1. The slurry was then heated under constant stirring until all water was evaporated. The obtained dry yellow-green powder was then placed in a vacuum oven at T = 180°C for about six to ten hours after which time the color of the powder had changed to gray.

3.1.5.3 Chemical Vapor Deposition of Platinum

Chemical vapor deposition (CVD) involves the use of sublimable organometallic components that are small enough to enter the pores of a catalyst. Even though it is known that under circumstances CVD may give deposited films contaminated with impurities, it is still an often practiced method for metal deposition as it is a low temperature process, the material can uniformly be covered with the dopant, and no acidity is created upon reduction.[91, 92, 93]. The CVD method as described by Dossi[94] and Jacobs[95] was applied under utilization of platinum hexafluoroacetlyacetonate ($Pt(AcAc)_2$) as sublimable compound. First, the white appearing TiO_2 catalyst powder catalysts (Degussa P25 and ultra-low density aerogel T36) were pre-calcined under vacuum at 150°C for at least 6 hours to remove adsorbed water. The catalyst was then combined with a defined amount of $Pt(AcAc)_2$ (Aldrich) to obtain catalyst loadings of 0.1, 0.5, and 1.2 wt% Pt. The compounds were well mixed with pestle and mortar under a helium atmosphere to assure a good dispersion of $Pt(AcAc)_2$ without introducing any humidity from the atmosphere. The mixture was then transferred into a quartz glass reactor tube that had one end sealed and placed in an oven. The quartz tube was then connected to a vacuum pump and evacuated down to 10^{-5} Torr over a period of about 10-12 hours. After that, the temperature was raised to 60°C at 5°C/minute and held at this temperature for two hours to remove eventual introduced water. The temperature was further increased to 80°C at 5°C/minute and then held at this temperature for one hour to remove remaining water and impurities of the $Pt(AcAc)_2$. Additional ramping to 100°C and holding at this temperature for one hour followed to sublime the $Pt(AcAc)_2$. After sublimation, the temperature was ramped to 135°C and held at this point for 15 minutes

to assure that all of the platinum acetyl acetonate was sublimed before cooling the system down to room temperature. The now yellow colored catalyst powder was removed from the quartz tube, placed in an oven under air flow of 100 cc/(minute * gram catalyst), heated to 180°C at 5°C/minute and held at this temperature for two hours to decompose the organometallic compound to platinum metal. After platinization, the catalyst had a gray colored appearance indicating a successful decomposition.

Due to technical difficulties the vacuum pump was not available for platinum deposition on all catalytic materials tested. The above-described method had to be altered slightly for the preparation of some of the aerogel samples. Instead of performing sublimation under vacuum it was performed under steady helium flow at 500 cm^3/minute[96]. The so obtained catalysts had the same appearance at all stages signifying a successful platinum vapor deposition.

3.2 Catalyst Characterization Methods

3.2.1 Surface Area Measurements

Surface area measurements were performed on all samples by using a Micromeritics ASAP 2000 utilizing N_2 adsorption and BET analysis. The samples were first degassed at 100°C for at least 6 hours. The sample weight varied usually between 0.2 to 0.3 g per run. Sample weights of the binary aerogel TS31b were around 0.03 g due to its low density and high surface area. The higher the surface area of a material the smaller amount of sample is recommended for the BET analysis.

3.2.2 X-Ray Diffraction studies

The X-Ray diffraction studies (XRD) were performed using a Siemens-D 501 Diffractometer with RX Kristalloflex 800 detector and copper anti-cathode tube (Monochromatisation using a Nickel filter, radiation at 1.5405 Angstrom (K-alpha 1 of copper)). The X-ray diffraction was measured in the range from $2\theta = 10°$ to 70°. The catalysts were not altered or specially treated in any form before the measurements.

3.2.3 Temperature Gravimetric Analysis

Temperature gravimetric analysis (TGA) was performed using the SHIMADZU TGA-50 Thermogravimetric Analyzer. A maximum amount of 20 mg of sample was placed into the sample holder, which was then attached to the microbalance of the TGA apparatus. The samples were heated at 5°C per minute.

3.2.4 Infra Red Spectra Analysis

Before measuring the infrared spectra, samples pellets were prepared from 200 mg of dry KBr and 2 mg of sample material. The spectra were obtained using the IR apparatus PERKIN-ELMER 16 PC, measuring light absorbency in the wave number range of 4000 to 400 cm-1.

3.2.5 The Ultra-Violet (UV) Spectra

The Ultra-Violet (UV) spectra were recorded with the Spectrometer lambda 2S (PERKIN ELMER UV/VIS/IR, Sphere integration detector, Range: 200 - 1100 nm). The UV diffuse reflection data were obtained in the wavelength range of 600 nm down to 200 nm without any prior alteration of the samples.

3.2.6 Particle Size Distribution

A Malvern Instruments Ltd., UK apparatus (Mastersizer 2000) was used to determine the particle size distribution for samples CEH6, T36, and TS31b. The catalysts in powder form were used as is and not specially treated before introducing into the vigorous stirred DI water bath of the apparatus.

3.2.7 Transmission Electron Microscopy

The samples for transmission electron microscopy (TEM) were prepared by first passing the material through a 325-mesh sieve and then dispersing a small sample of it into propanol. A droplet of this propanol/catalyst mixture was then applied to a perforated thin carbon film coated copper grid and left to dry in air. Diffraction-contrast TEM was performed using a JOEL Electron Optics Limited JEM-2000FX electron microscope.

3.2.8 Determining of Weight Fraction of Anatase in Catalyst Samples

In order to determine the amount of weight percent anatase in the catalyst samples the method of "Internal standard analysis for one component of a multi component system" was applied as described by Klug and Alexander[97, 98]. This method is based on the fact that when an internal standard is added in a constant portion x_S to a mixture of components of unknown amount (e.g, x_1, x_2, ...etc.), then the concentration of the unknown component is proportional to the intensity ratio of I_1/I_S according to

$$x_1 = k * \frac{I_1}{I_S} \qquad (3\text{-}6)$$

Since the aerogels were assumed to consist of a mixture of amorphous and anatase titanium dioxide in an unknown ratio, rutile titanium dioxide was then used as internal standard component. In order to determine first the factor k of Equation (3-6), ten samples of titanium dioxide mixtures with varying amounts of anatase (99.9%, Aldrich) and rutile (99%, Avocado Research Chemicals) titanium dioxide were prepared. Prior to weighing, the TiO_2 powders were dried at 110°C for at least 12 hours. Then, three XRD scans of each sample were performed. The peak areas of anatase to rutile were determined numerically using the trapezoidal method. Only the first appearing peaks at 2Θ = 25.5°, 38.0°, and 48.3° for anatase and 27.7°, 36.3, 41.5°, and 44.4° for rutile were used for the calculation. The peaks at 2Θ larger than 50° were omitted due to overlapping of the peaks of anatase and rutile. The ratio of the average values of the peak areas of anatase to rutile was then plotted against the amount of wt% anatase in the sample. The obtained data points were connected to obtain a calibration graph to determine the amount of anatase in the catalyst samples. Next, the catalyst samples were dried in an oven at 110°C for at least 12 hours. Then, about 15 to 30wt% of the same rutile TiO_2 as used for the calibration was added to the catalyst powder. The mixture was well ground and mixed with mortar and pestle before performing three XRD measurements of each of the prepared sample. The ratio of peak areas of anatase and rutile were determined in the same manner as done for the calibration curve. The obtained values were then compared with the calibration graph to determine the weight-percent of anatase with respect to rutile. Since the amount of added rutile to the catalyst sample was known, the weight percent of anatase with respect to the amount of catalyst without rutile could be calculated.

3.3 UV Light Penetration Through Catalyst Bed

3.3.1 Introduction

First discoveries concerning the penetration depth of UV into titanium dioxide where made by Formenti and co-workers in the early seventies[22]. In the early 90's, Peral and Ollis concluded from Courbon's work[23] that 99% of the UV light absorption occurs within the first 4.5 μm of nonporous anatase TiO2[29]. Otherwise, little literature exists reporting about the investigation of penetration depth of UV light into catalyst material. The here presented method is an attempt to evaluate the differences in UV light penetration of the different catalyst materials utilized for photocatalytic investigation.

The UV penetration through the catalyst bed was measured by dispersing the catalyst powder in an Agarose gel and measuring the light transmission through samples with varying amounts of dispersed catalyst.

Agarose comes from a family of polysaccharides, called agars, which is obtained from algae such as seaweed. It function in seaweed and algae is to provide some mechanical support so that cells do not collapse and to serve as anti-desiccation at low tide. Agarose is used extensively in food industry as ingredient stabiliser e.g. in ice cream and dessert jelly. Structurally, agarose is a galactan (galactose polymer) with extensive cross-linking forming two chains to join together and adopt a LH double helix. The two chains wrap tightly together closing the gaps and trapping water inside the helix. When agar is heated the cross-links break and the gel dissolves. Then, when poured into

a mould and the gel is cooled, the cross-links reform and the gel is set in the shape of the mould[99].

The advantage of using a gel to disperse the catalyst versus a dispersion of the catalyst in water is that a uniform distribution of catalytic material across the measured area could easily be established. Dipping methods or dropping of a material slurry on a sample holder (e.g. microscope slide) carry the risk of a non-uniform layer thickness. In addition, the gel could easily be handled throughout the measurements without disturbing the uniform distribution of the samples.

3.3.2 Sample Preparation

SeaKem Le Agarose (from Bioproducts), a product normally used for electrophoresis, was used to prepare the gels samples. Samples for the measurements were obtained by dispersing a known amount of catalyst powder in a 0.5wt% agar gel solution. The liquid gel was then poured into a mold and let stand to cool as shown in. The solution started to gel at temperatures around 35 to 37°C.

In order to prepare several gels with increasing loadings of TiO_2 the following procedure was applied: Before using the catalysts, the powder was ground, passed through a 45 μm sieve and dried for about 12-18 hours at 80°C in a vacuum oven. Then, approximately 0.03 g of catalyst sample was weighed in a small vial to which 5 ml of DI water was added (initial solution). One milliliter of this well mixed suspension (agitated by pumping with a syringe) was removed and placed into vial 1. Then, 4 ml of a 0.625 wt% Seakam gel solution (0.625g of agar powder per 1 ml of water) was added to vial 1, thus obtaining sample 1, a final gel solution of 0.5 wt%. One milliliter of DI water

was then added to the vial with the initial solution of dispersed catalyst and well mixed by pumping the liquid in and out of the syringe. Again, 1 ml from this now diluted initial solution was removed into vial 2 and combined with 4 ml of the 0.625wt% Seakam gel solution to obtain sample 2. This procedure was repeated until 12 samples were collected containing decreasing fractions of catalyst. The still liquid samples were then filled into rectangular containers of 26 x 45 mm and left to stand for gelation for about 15 minutes. The resulting gels had a thickness of about 3.5 mm. The quality of an even distribution of the material in the gel could be evaluated by visually observation and was later confirmed by the UV transmittance measurements at several different points across the entire gel area.

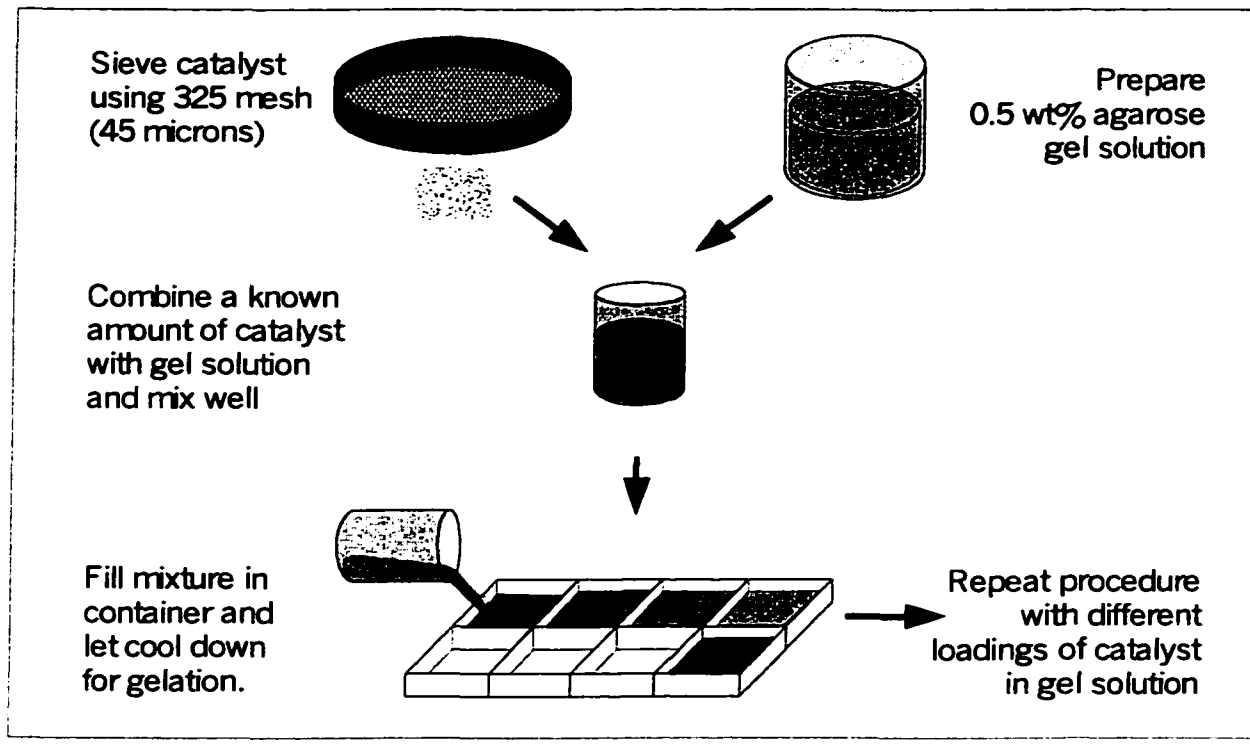

Figure 3-3 Agar gel sample preparation

3.3.3 Density Measurements

In order to determine the actual catalyst layer thickness in the different samples without the gel, the packing density of the material was determined. The catalyst density ρ_{cat} can be calculated using mass and volume of the catalyst according to Equation (3-7)

(3-7) $$\rho_{cat} = \frac{m_{cat}}{V_{cat}}, \qquad \text{therefore}$$

(3-8) $$\rho_{cat} = \frac{m_{cat}}{cat.height * width * length}$$

where width and length are equal to the mold dimensions of 26 x 45 mm. After rearranging equation (3-8), the catalyst height or effective layer thickness, D_{cat}, can be determined from Equation (3-9)

(3-9) $$D_{cat} = \frac{m_{cat}}{\rho_{cat} * width * length}$$

The following procedure was used to determine the density of a packed catalyst bed, which does not represent the actual bulk density of the material:

The nozzle of 1ml capacity syringes was cut off and the open end was then sealed using a glue gun. The ground, dried, and sieved (325 mesh) catalyst powder was then filled into a syringe. The catalyst weight was determined by weighing the syringes before and after filling with the catalyst. The sealed end of the syringes was 50 times tapped against a hard surface (counter) before placing them vertically into an ultrasound bath. Ultrasound was applied to the samples in four 15 minutes intervals each (maximum of timer) with about 15 to 20 minutes rest in-between. After that, the glued bottom of each

syringe was again tapped against the table for about 150 times after which no further settling was observed. The resulting volume was then determined by measuring the height of the catalyst bed. Equation (3-7) was used to calculate the density of each sample.

3.3.4 UV Transmittance Measurements

The experimental setup for measuring the UV transmittance is shown in Figure 3-4.

A specially constructed Plexiglas frame provided a fixed support for a UV detector (UVX Digital Radiometer UVP, San Gabriel, California (Serial # E 16614)) at the bottom of the frame. A UV lamp (Model UVG-11, Mineralight® Lamp, Short Wave UV – 254 nm (Serial # C083860) was held in place 4 cm above the UV sensor (Serial No. E20066). The UV sensor head was circular having a diameter of 9 mm and measured the energy of incoming UV light in the UV mid range of about 300 nm.

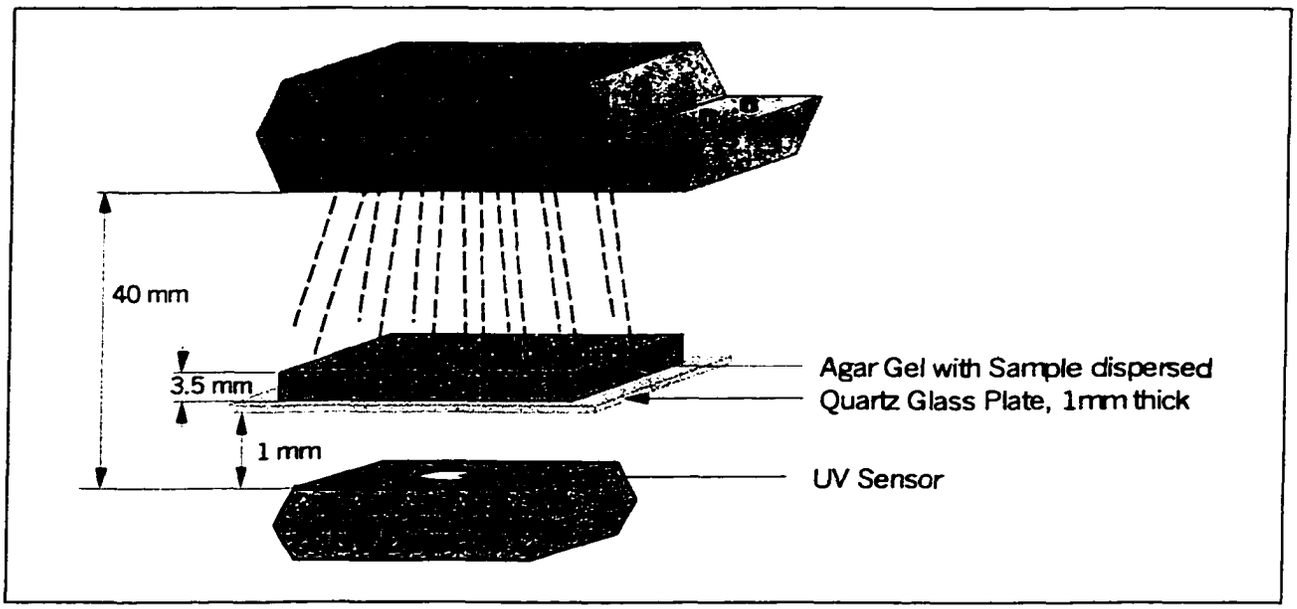

Figure 3-4 Experimental set-up to measure UV light penetration through a agar gel with catalyst samples dispersed in it

The UV lamp was adjustable to both sides in order to position the lamp such that a certain initial UV illumination (reading with no object between lamp and sensor) could be obtained for all measurements. The sample holder was designed to hold a quartz glass slide on which the gel sample was placed.

First, a gel sample containing no catalyst material was prepared and the UV intensity reported by moving the sample holder with the gel sample across the UV sensor at eight different locations and measuring the UV intensity. Using these data, the UV transmission, T, and UV absorbance, A, were calculated according to Equations (3-10) and (3-11)[100]

(3-10) $$T = \frac{I}{I_o},$$

(3-11) $$A = -\log(T),$$

where I = measured UV intensity of gel with dispersed catalyst
I_0 = measured UV intensity of gel with no catalyst.

3.4 Adsorption Study

The adsorption capacity of all studied catalytic materials was investigated to compare how much of the introduced gas had been removed from the gas phase due to adsorption on the catalyst. This study was particularly needed for acetone oxidation since acetone adsorbed very strongly on the catalyst. Furthermore, the adsorption data were needed to calculate reaction rates and reaction rate constants as described later in Section 0.

Successive increments of methane, ethylene or acetone were injected into the reactor loop, which included the reactor cell. The amount of acetone adsorbed on the catalyst,

m_{ads}, was determined from the difference of the gas phase concentration if no adsorption had occurred, C_{0ads}, and the actual measured concentrations, C_{meas}. C_{0ads} was determined according to Equation (3-12)

(3-12) $$C_{0ads} = \frac{m^{inj}}{V_{sys}},$$ which becomes

(3-13) $$C_{0ads(acetone)} = \frac{V^{inj}{}_{(acetone)} * \rho_{(acetone)}}{V_{sys}}$$ for acetone adsorption or

(3-14) $$C_{0ads(methane)} = \frac{V^{inj}{}_{(methane)} * P * MW_{(methane)}}{R * T * V_{sys}}$$ for methane adsorption,

since acetone was introduced to the reactor system as a liquid while the other organics (methane, ethylene) were injected as a gas. V^{inj} represents the volume of injected contaminant, V_{sys} is the volume of the reactor system, $\rho_{acetone}$ stands for the density of acetone, $MW_{acetone}$ is the molecular weight of acetone, R the universal gas constant, and P and T describe pressure and temperature, respectively, at ambient conditions. The amount of organic adsorbed on the catalyst was then calculated according to equation (3-15).

(3-15) $$m_{ads} = (C_{0ads} - C_{meas}) * V_{sys}$$

3.5 Photocatalytic Apparatus and Procedure

3.5.1 Experimental Set-Up

The flow diagram in Figure 3-5 pictures the reactor setup used for the photocatalytic oxidation experiments. The main components are a photocatalytic cell, a 450 W ultraviolet light source with power supply (7830, Ace Glass), a GC-Analyzer with flame

ionization detector (FID) (Sigma 300, Perkin Elmer), an integrator (Varian 4270), a circulation pump (Metal Bellows Corp. Model MB-41, stainless steel bellows), flow indicators (Cole Parmer), a pressure gauge, quick connects including a filter (Cajun 316 VCR), valves (Nupro), and stainless steel tubing (1/4 in OD). The bypass around the catalytic cell was put in place to adjust the pressure drop across the catalyst bed by varying the gas flow across the bypass. Quick connects with filter gaskets placed before and after the cell served to prevent catalyst powder from being purged into the system tubing and to allow for an easy change of the reactor cell. A separate loop, including a 6-port valve with sample loop and automatic sampler, was installed to repeatedly take data at defined time intervals. The external air supply served to purge the reactor loop and catalytic cell after each oxidation test.

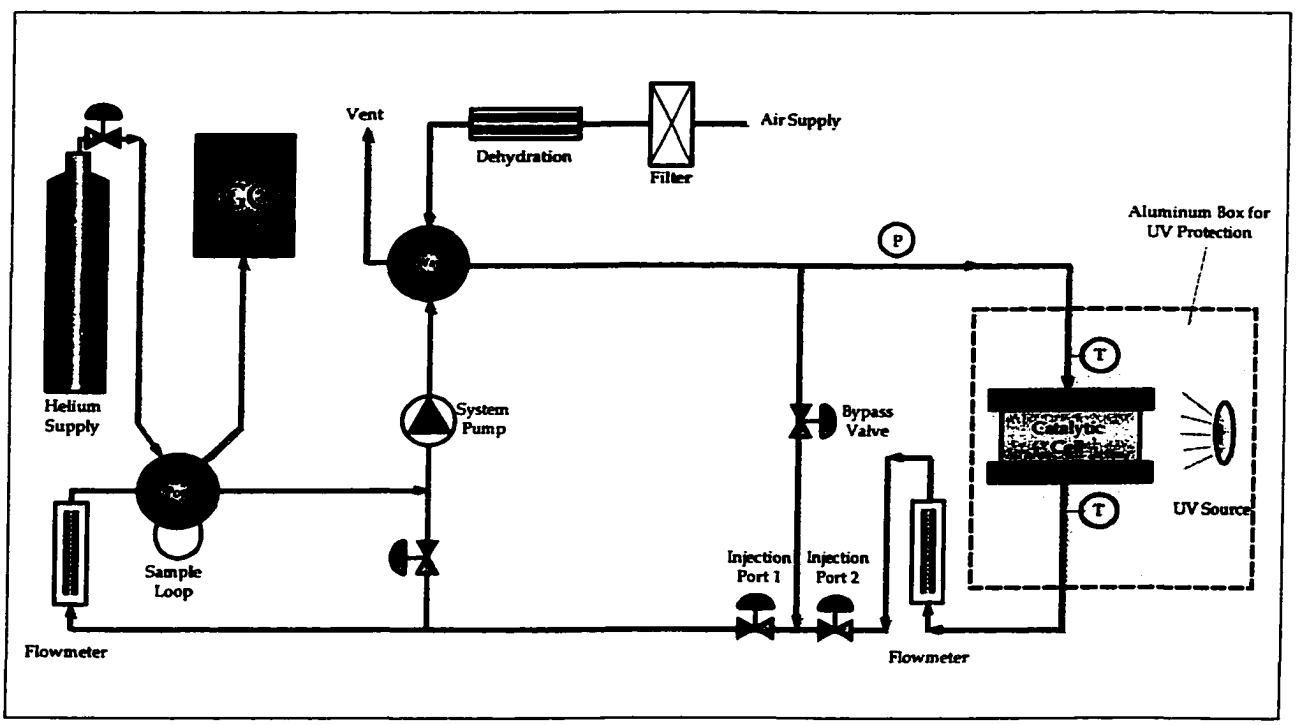

Figure 3-5 Simplified diagram of the photocatalytic reaction system

The numbers provided by the integrator represented peak areas that were converted to concentration values using a prior prepared calibration curve for each oxidized gas. The photocatalytic cell consisted of two flat 1/8-inch thick quartz glass plates of 6 x 3 inches positioned 1/32 inch apart to hold the catalytic material. After loading with a catalysts the reactor cell was sealed on top and bottom with metal joints that were held in place by eight screws as shown in Figure 3-6. The catalytic cell was then placed in the re-circulating reactor system one foot away from the UV light source to conduct the photocatalytic experiments. The volume of the reactor system changed between 212 ml and 316 ml. The change in volume occurred due to various modifications carried out to improve the experimental set-up.

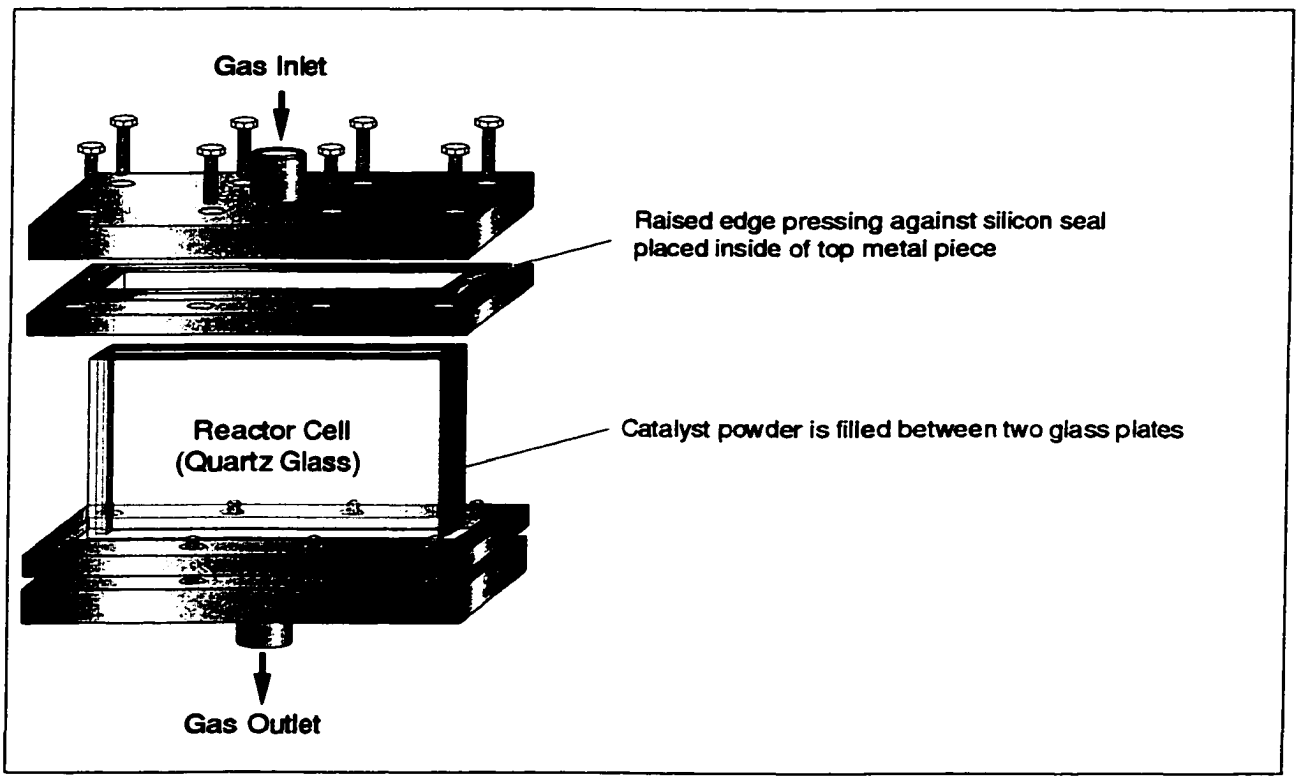

Figure 3-6 Photocatalytic Cell

3.5.2 Reactor Volume Determination

The volume of the reactor system, V_{sys} , was determined by helium expansion as indicated in Figure 3-7.

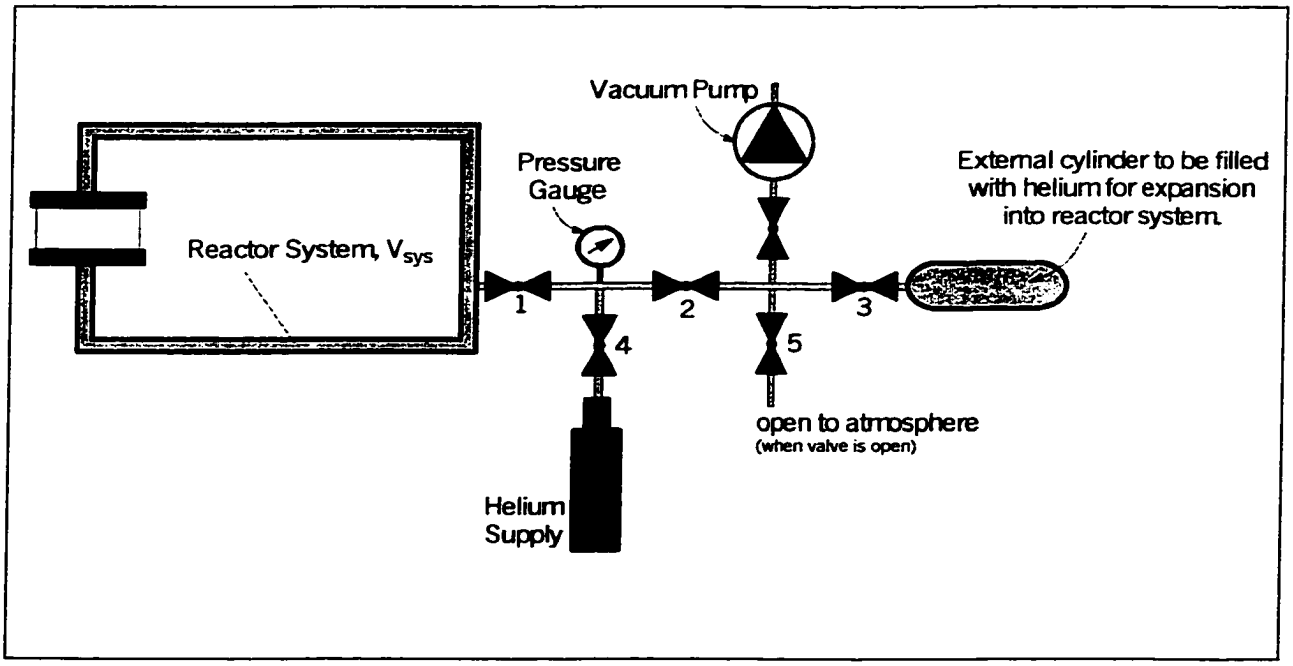

Figure 3-7 Helium expansion set-up to determine the reactor system volume

The reactor system was initially purged with helium and then evacuated using a vacuum pump (Fisher Scientific Mod. 5KH32FG 115E). The pressure, P_{vac}, was recorded. An external cylinder of known volume, V_{cyl}, was filled with helium at atmospheric pressure, P_1. The cylinder was then connected to the system allowing the helium to expand into the evacuated reactor system. The new system pressure, P_2, was recorded. By applying a simple mass balance, the volume of the reactor system was determined using the pressure difference of the expanded gas and applying the ideal gas law (Equation (3-16):

(3-16) $$PV = nRT$$

where P = Pressure, V = Volume, T = Temperature, n = number of moles, R = Universal gas constant.

Considering the fact that the number of moles, n_1, in the cylinder before expansion is the same as the number of moles in both the cylinder and reactor system after expansion, n_2

(3-17) $$n_1 = n_2$$

then we find by applying of Equation (3-16) and (3-17) that

(3-18) $$P_1 V_{cyl} = P_2 (V_{cyl} + V_{sys}) - P_{vac} (V_{sys})$$

Since it was not possible to draw an absolute vacuum to the system, the term $\{P_{vac} (V_{sys})\}$ in (3-18) had to be added to the equation to account for the mass of helium that was left in the reactor system after evacuation. The only unknown in Equation (3-18) is V_{sys}, which can easily be solved for.

3.5.3 Photocatalytic Oxidation Procedure

After the catalytic cell was filled with a catalyst powder (Degussa P25 or aerogel), the cell was placed into the reactor system and purged with dry air for at least 30 minutes. Then, the pump was switched on to start re-circulating dry air across the cell. The flow rate was adjusted to about 510-600 ml/min, which corresponded to a face velocity (flow velocity across the cross section of the catalytic cell) of approximately 300 cm/s (see Appendix Table 7-3). Depending on the catalyst, a higher flow rate increased the

pressure drop across the catalyst cell significantly. At this flow rate, effects of mass transfer from the bulk to the near-surface of the catalyst was negligible[33]. An organic compound (methane, ethane, acetone, and ethylene) as the contaminant was introduced into the system using injection port 1 (see Figure 3-5). The contaminated air was allowed to circulate in the reactor system for at least two hours (or longer if necessary) until the concentration within the reactor system came to equilibrium. The catalyst cell was covered to avoid temporarily UV exposure and the UV source was switched on. After circa five minutes, the intensity of the UV light had reached its maximum and the cell cover was removed. Even though a fan provided cooling by blowing air at room temperature across the cell, the temperature around the cell had increased from room temperature to 35°C due to heating by the UV lamp. This temperature increase, however, should not have had a significant influence on the reaction rate since generally the temperature does not affect the photocatalytic VOC oxidation rate[6]. The gas phase contaminant concentration was measured at initially five-minute intervals and then at 30 or 60-minute intervals depending on the rate of reaction. When no contaminant was detected anymore the light was then switched off and the reactor system including the cell was purged with dry air to prepare for a consecutive catalytic run.

3.6 Photocatalytic Oxidation Under Humid Conditions

Besides testing the catalysts for ethylene oxidation under initial dry conditions, another set of tests was performed to investigate how humidity would affect the reactivity of the different catalytic materials.

3.6.1 Humidity Caiibration

Commercially available humidity testers were too large to fit into the existing reactor system and most gel-chromatography columns do not tolerate water. Thus, the humidity in the reactor system was measured using a D8-WAX 1 micron 15x0.53 high resolution GC column (20-240°C, J&W Scientific) in a HP 5890 Series II gas chromatograph with a TCD (thermal conductivity detector). A calibration curve was prepared as described below according to an ASHRAE standard procedure using saturated salt solutions[101].

Saturated salt solutions are used to generate a certain humidity, where the ambient temperature determines the equilibrium water vapor pressure. The theory of the concentrated salt solutions is very complex. Generally, solutes reduce the solvent vapor pressure in portion to the amount of dissolved material. In the case for salt in water, the maximum vapor pressure depression is achieved when the solution is saturated, resulting in equilibrium relative humilities in the range of 5 to 100% depending on the salt and the ambient temperature. Due to the complexity of the theory, vapor pressure curves of saturated salt solutions were determined experimentally. Table 3-1 contains these results based on a number of studies.

Salt	Temperature, °C										
	0	10	20	30	40	50	60	70	80	90	100
Lithium Bromide	7.8	7.1	6.6	6.2	5.8	5.5	5.3	5.2	5.2	5.3	5.4
Lithium Chloride	11.2	11.3	11.3	11.3	11.2	11.1	11.0	10.8	9.4	10.3	12.1
Magnesium Chloride	33.7	33.5	33.1	32.4	31.6	30.5	29.3	27.8	26.1	24.1	22.0
Potassium Carbonate	43.1	43.1	43.2	43.2		40.9	39.2	37.4	35.4	33.4	31.3
Magnesium Nitrate	60.4	57.4	54.4	51.4	48.4	45.4					
Sodium Nitrate									48.5	44.9	41.0
Sodium Bromide		62.2	59.1	56.0	53.2	50.9	49.7	49.7			
Sodium Nitrate				75.1					63.0	60.7	58.3
Sodium Chloride	75.5	75.7	75.5	75.1	74.7	74.7	74.5	75.1	73.9	73.8	73.9
Potassium Chloride	88.6	86.8	85.1	83.6	82.3	81.2	80.2	79.5			
Barium Chloride									85.1	83.9	82.6
Potassium Sulfate	98.8	98.2	97.6	97.0	96.4	95.8	96.6	96.3	95.8	95.2	94.5

Table 3-1 Equilibrium relative humidities over saturated salt solutions[101]

The following salts were used to generate a calibration curve in the range of 10 to 80% relative humidity: LiCl, $MgCl_2$, KCO_3, $Mg(NO_3)_2$, NaBr, NaCl, and KCl. In a sealed jar each salt was mixed with a sufficient amount of DI water to obtain a sluggish mixture. The top seal of each jar was prepared with a Swagelog fitting holding a rubber septum, which served as sampling port. Using a syringe, 0.1 ml from the humid air right above the salt-water mixture phase was withdrawn and injected into the HP gel chromatograph. Table 3-1 was then utilized to determine for each injected sample its relative humidity according the temperature (room temperature). Using the recorded data from the GC measurements and the data for the relative humidities a calibration curve was obtained, which was then used to determine the relative humidity created in the reactor system for the photo-oxidation tests under humid conditions.

3.6.2 Preparation for Catalytic Oxidation under Humid Conditions

First, the reactor system, including the catalytic cell, was purged with dry air for at least two hours. Then, 0.1 ml of gas was withdrawn from one of the sampling ports of the reactor system using a syringe and injected into the HP GC analyzer. When zero humidity was confirmed, 25, 50, or 75 ml of DI water, depending on the desired humidity, were introduced to the reactor system through one of the sample ports using a micro-syringe. The air with the introduced contaminant and water was then allowed to recirculate for about two to three hours until equilibrium was observed (verified by GC measurements). Then, the UV lamp was switched on and data were collected automatically with the GC SIGMA 300 to record the change in contaminant concentration as was described before (Section 3.5.3 Photocatalytic Oxidation Procedure) and manually with the HP 5890 to collect humidity data.

4 Results and Discussion

4.1 Catalyst Preparation

4.1.1 Aerogel Synthesis

Several low-density and ultra-low density aerogels were synthesized as described in Section 3.1.2. The low-density aerogels are designated CEH1 to CEH6, the ultra-low density aerogels are designated T1 to T36. The greatest difficulties during synthesis occurred during the drying procedure. Many of the aerogels had collapsed due to unknown reasons. Small changes in pressure fluctuation, time of CO_2 exchange, or slight differences in the releasing speed of the supercritical carbon dioxide influence greatly the quality of the final product. From all the synthesized gels, CEH2, CEH4, CEH6, and T36 were investigated with respect to photocatalytic activity. CEH6 and T36 showed the highest reactivity, therefore research concentrated only on these two catalysts. A binary Si-Ti aerogel was investigated as well (TS31b). Even though it did not show any catalytic reactivity for the gases investigated, as discussed later in Section 4.6.4.1, the material was nevertheless characterized as described in the following sections.

All aerogels had an off-white appearance. The samples were more or less broken into small pieces after the drying procedure and exhibited a low mechanical strength. When handling, the pieces broke easily into smaller pieces.

4.1.2 Platinization of Degussa P25 and Aerogels

Three different concentrations of platinum were applied to Degussa, namely 0.1, 0.5, and 3.0wt% Pt with respect to TiO_2, using impregnation and photodeposition.

Furthermore, three more Degussa samples were prepared with platinum using chemical vapor deposition (CVD) with loadings of 0.1, 0.5, and 1.2wt% platinum. Higher concentrations where not investigated since most research papers agreed that 0.5mol% Pt (or 1.2wt%) was the optimal concentration at which highest photoreactivity was achieved[69, 81, 83, 84].

All samples had a light yellow appearance after CVD, which changed to gray after calcination/platinization as it is seen in Figure 4-1. The gray tone of the final samples increased in darkness with increasing platinum concentration as shown in Figure 4-2 and Figure 4-3.

Figure 4-1 T36 after Pt-CVD (top) and after calcination/platinization (bottom)

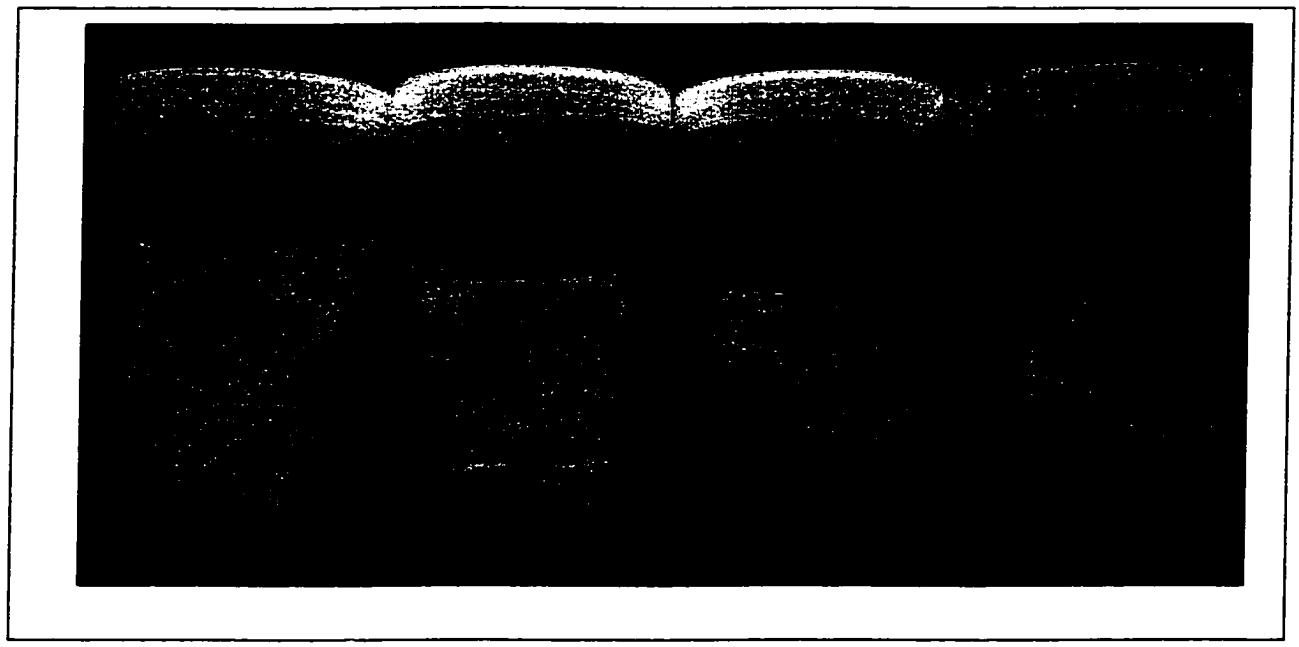

Figure 4-2 Untreated Degussa P25 and P25 with 0.1, 0.5, and 3.0wt% Pt using impregnation and photodeposition

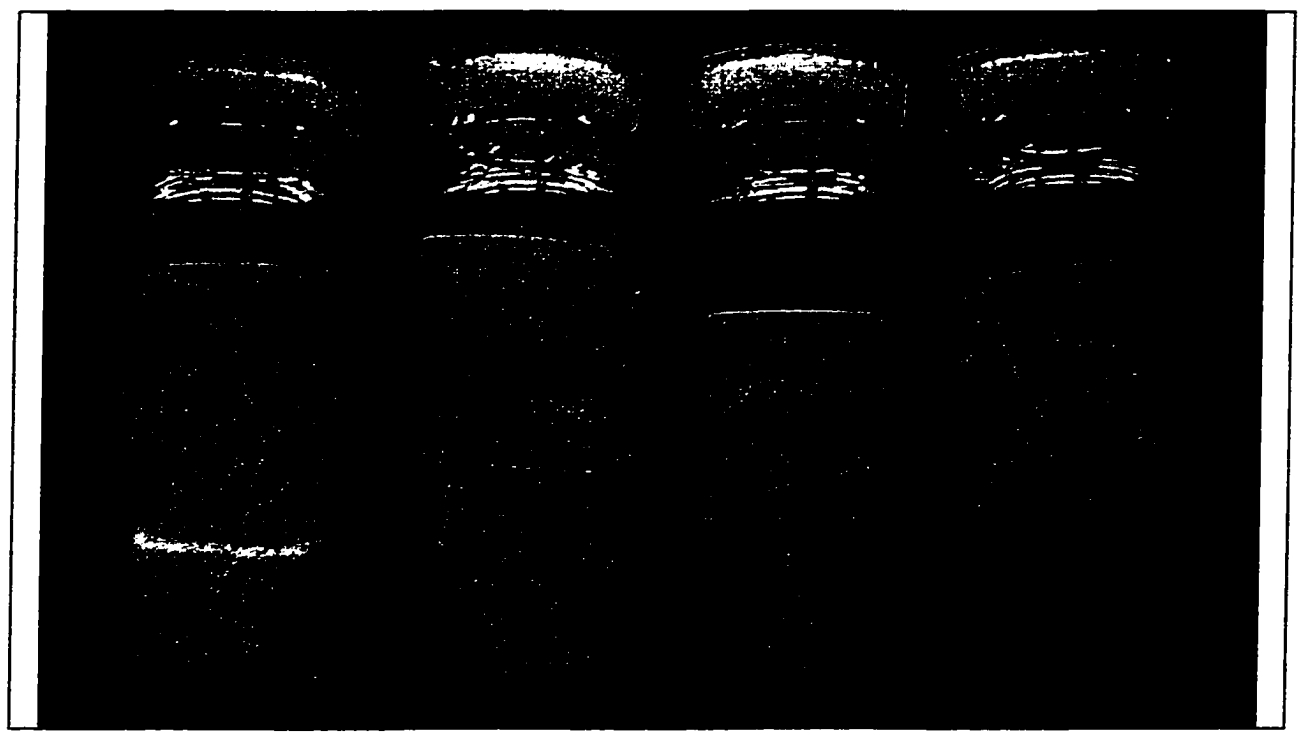

Figure 4-3 Untreated Degussa P25 and P25 with 0.1, 0.5, and 1.2wt% platinum deposited using chemical vapor deposition

The aerogel T36 was initially deposited with 1.2wt% platinum which corresponded to 0.5 mole%. It was also of interest to investigate the photocatalytic activity of T36 having the same platinum coverage per cm^2 surface area of the catalyst, as in the case for the 1.2wt% Pt on Degussa sample. Therefore, a second T36 sample was prepared with a loading of 7.7wt% Pt corresponding to approximately 0.025 g of platinum per cm^2 of catalyst. Another sample was prepared with a concentration of 3.5wt% Pt by applying a second CVD procedure to the T36 sample with 1.2wt% Pt. The aerogels had the same gray appearance after platinization as the platinum doped P25. With more platinum on the surface the samples were increasing dark. The sample with 7.7wt% Pt was almost black as shown in Figure 4-4.

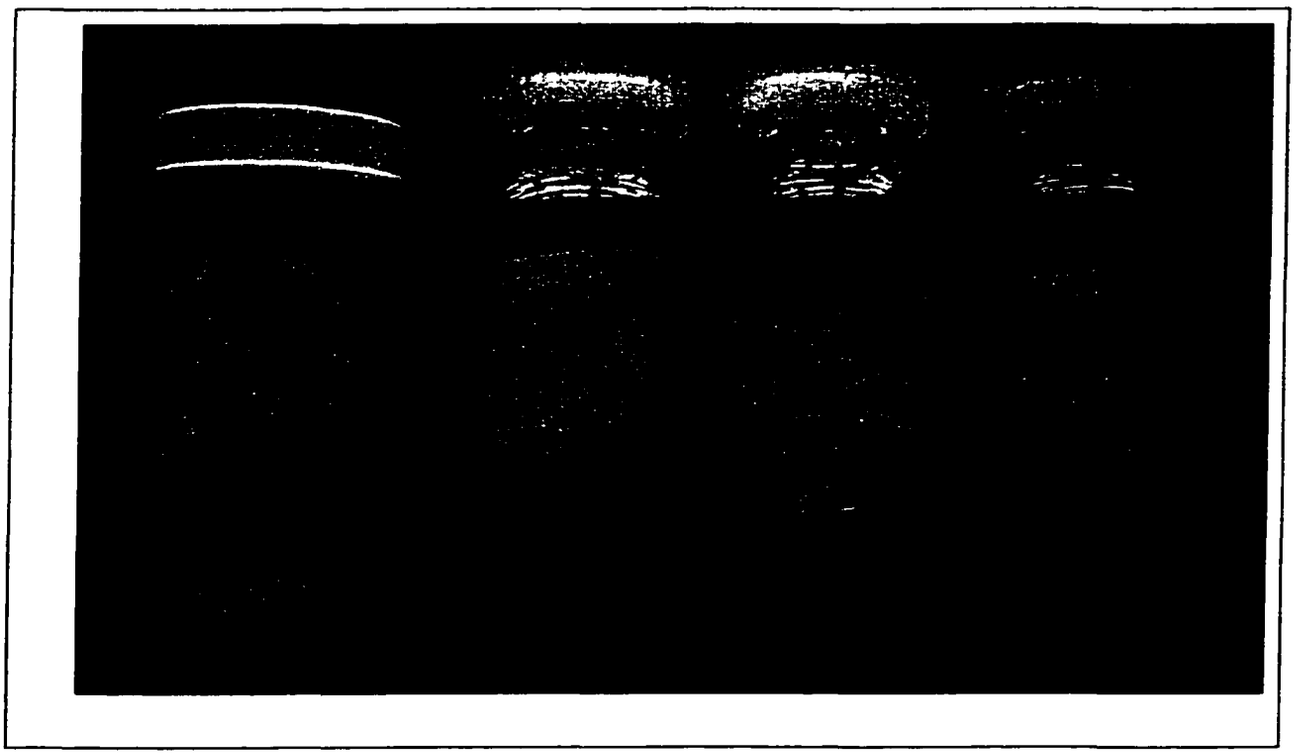

Figure 4-4 Untreated T36 and T36 with 1.2, 3.5 and 7.7wt% platinum deposited using chemical vapor deposition

4.1.3 Ruthenium Deposition on Degussa P25

Two samples of Degussa P25 were prepared with ruthenium (0.1wt% and 3.0wt%) and one sample combined with 0.1wt% ruthenium and 0.1wt% platinum. All catalyst powders had a gray colored appearance after calcination as shown in Figure 4-5.

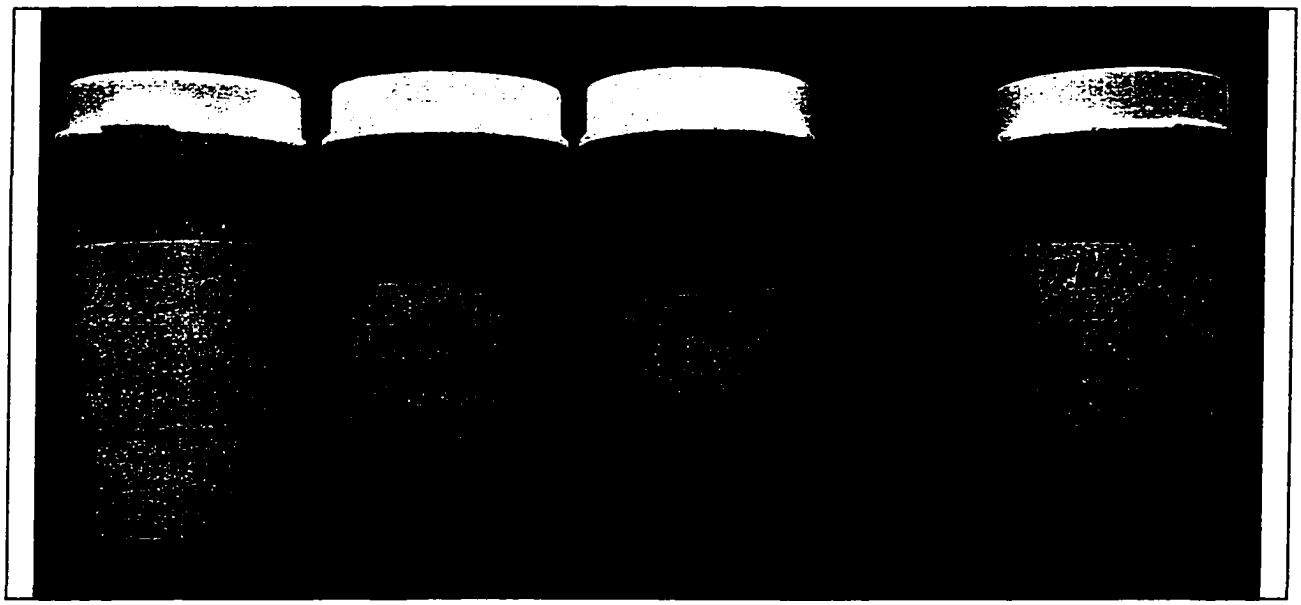

Figure 4-5 Untreated Degussa P25 and P25 with 0.1 and 3.0wt% ruthenium (three samples to the left) and combined 0.1wt% Pt and 0.1wt% Ru deposited using impregnation and photodeposition (right)

4.2 Aerogel Characterization

4.2.1 BET - Measurements

The specific surface area values of the catalyst materials, including the values for the samples after heat treatment, are summarized in Table 4-1. Other data, such as pore volume and average pore diameter are included in the table.

Heating the aerogels at a temperature of 150°C for 6 hours slightly decreased the specific surface area by 4 to 15%. In contrast, heating the samples up to 450°C for six

hours dramatically reduced the surface areas of the pure titanium dioxide aerogels. The low-density aerogels CEH2, CEH4, and CEH6 lost up to 60 % of its original surface area, while the ultra-low density aerogel T36 retained only 28 % of its original surface area. A similar observation was made for the pore volume, which decrease remarkably by up to 50% for the low-density gels and 60% for the utra-low density T36. These findings are comparable to the results of Campbell and co-workers who observed a similar behavior with thermal treatment of TiO_2 prepared via sol-gel synthesis[102]. High temperatures caused the porous network to collapse resulting in a decrease in surface area characteristic to a value of a xerogel. The average pores size of the TiO_2 aerogels was about 20 nm for the ultra-low density aerogels and less than 10 nm for the ultra-low density areogel T36. Even though the pore volume and the surface area decreased in a similar fashion upon heat treatment, the pore diameter did not remain the same as found by Campbell. In this work, the average pore size increased by 46 % for e.g. CEH6 and even 87 % for T36.

In contrast to the pure TiO_2 aerogels, the binary SiO_2-TiO_2 aerogel showed a higher mechanical stability against high temperatures with only a small decrease in surface area of about 14% and only about 3% decrease in pore volume after thermal treatment of 450°C. The average pore size was less than 10 nm and increased to about 12 nm after subjecting the sample to 450°C.

	P25 raw	P25 + 0.1 wt% Pt	P25 + 0.5 wt% Pt	P25 + 3 wt% Pt
BET SA , m^2/g	47.9	50.4	48.6	52.3
Change in surface area after thermal treatment , %		5.3	1.6	9.2
mulative pore volume of pores between 17 and 3000 Å diameter , cm^3/g	0.10	0.34	0.24	0.24
Change in pore volume after thermal treatment , %		233.8	127.8	132.5
Average pore diameter (4V/A) by BET , Å	83.09	251.82	176.57	168.63
Change in pore diameter after thermal treatment , %		203.1	112.5	102.9

	CEH2 raw	150°C 6 hrs	450°C 6hrs
BET SA , m^2/g	394.3	373.8	144.5
Change in surface area after thermal treatment , %		-5.2	-63.4
mulative pore volume of pores between 17 and 3000 Å diameter , cm^3/g	2.00	2.12	1.02
Change in pore volume after thermal treatment , %		5.7	-49.2
Average pore diameter (4V/A) by BET , Å	190.13	219.89	278.18
Change in pore diameter after thermal treatment , %		15.7	46.3

	CEH4 raw	150°C 6 hrs	450°C 6hrs
BET SA , m^2/g	358.8	326.9	126.0
Change in surface area after thermal treatment , %		-8.9	-64.9
mulative pore volume of pores between 17 and 3000 Å diameter , cm^3/g	2.04	1.12	0.95
Change in pore volume after thermal treatment , %		-45.2	-53.3
Average pore diameter (4V/A) by BET , Å	213.81	125.82	272.72
Change in pore diameter after thermal treatment , %		-41.2	27.5

	CEH6 raw	150°C 6 hrs	450°C 6hrs
BET SA , m^2/g	303.7	251.3	147.6
Change in surface area after thermal treatment , %		-17.3	-51.4
mulative pore volume of pores between 17 and 3000 Å diameter , cm^3/g	1.49	1.22	1.05
Change in pore volume after thermal treatment , %		-17.9	-29.3
Average pore diameter (4V/A) by BET , Å	185.68	191.77	271.21
Change in pore diameter after thermal treatment , %		3.3	46.1

	T36 raw	165°C 24hrs	220°C 25hrs	450C 6hrs
BET SA , m^2/g	337.0	318.0	304.4	91.8
Change in surface area after thermal treatment , %		-5.6	-9.7	-72.8
mulative pore volume of pores between 17 and 3000 Å diameter , cm^3/g	0.86	0.80	0.93	0.35
Change in pore volume after thermal treatment , %		-7.3	7.7	-59.7
Average pore diameter (4V/A) by BET , Å	96.68	94.82	113.93	181.23
Change in pore diameter after thermal treatment , %		-1.9	17.8	87.5

	T36 raw	T36 + 1.2wt% Pt	T36 + 3.5wt% Pt	T36 + 7.7wt% Pt
BET SA , m^2/g	337.0	287.4	136.9	136.4
Change in surface area after thermal treatment , %		-14.7	-59.4	-59.5
mulative pore volume of pores between 17 and 3000 Å diameter , cm^3/g	0.86	0.97	0.74	0.61
Change in pore volume after thermal treatment , %		12.3	-14.6	-29.7
Average pore diameter (4V/A) by BET , Å	96.68	128.19	197.48	160.65
Change in pore diameter after thermal treatment , %		32.6	104.3	66.2

	TS31b raw	185°C 6 hrs	220°C 48 hrs	450°C 6hrs
BET SA , m^2/g	501.5	445.8	428.9	430.8
Change in surface area after thermal treatment , %		-11.1	-14.5	-14.1
mulative pore volume of pores between 17 and 3000 Å diameter , cm^3/g	1.27	1.37	1.58	1.23
Change in pore volume after thermal treatment , %		8.2	24.7	-2.8
Average pore diameter (4V/A) by BET , Å	88.11	110.47	132.42	111.29
Change in pore diameter after thermal treatment , %		25.4	50.3	26.3

Table 4-1 BET data for Degussa P25 and aerogels CEH2, CEH4, CEH6, and T36

4.2.2 UV diffuse reflection studies

The UV absorption spectra for the pure titanium oxide aerogels are shown in **Figure 4-6** to Figure 4-11. These figures include also the spectra for 100 % anatase (44 μm particle size, purchased from Alfa Aesar) for comparison purposes. No significant difference was observed compared to 100% anatase TiO_2. All materials begin to absorb energy of light at about 400 nm. At wavelengths above 400 nm up to 1100 nm (maximum measured range) no light adsorption was measured. Absorption of light of about 85% continued from 400 nm down to 200 nm (within the UV range). It appears that the aerogel samples absorbed light also in the visible range above 400 nm (indicated by only 80-90% reflection in Figure 4-8 to Figure 4-11). A similar observation was made for the Degussa P25 containing the metal deposition (**Figure 4-6**and Figure 4-7). With increasing platinum content less light in the visible range from 1000 nm down to about 700 nm was reflected; about 95% for 0.1% Pt loading, about 90% for the 0.5% loading and 85% for the sample with 3% platinum loading. Starting at 700 nm, all platinum loaded samples showed a decrease in light reflection (or increase in absorption) with a similar sharp drop as for the pure Degussa and anatase at about 400 nm. The reduced light reflection for the Degussa samples loaded with ruthenium was even stronger; about 55% for 0.1% Pt + 0.1 Ru loading, about 50% for the 0.1% Ru loading and 40% for the sample with 3% ruthenium loading. Vorontsov and co-workers also observed a UV reflectance near 40% in the visible region with platinized TiO_2 samples obtained by photo-depositon using chloroplatinic acid.[103]. But they concluded that the platinum particles are translucent to visible light and would not alter the characteristic penetration depth of the platinized samples. Therefore, it is doubtful if the fraction of apparent light

absorbtion in the visible range would contribute to an enhancement of photocatalytic reactivity. Rather it is likely that the reduced UV reflectance is a result of light diffusion effects of the catalyst powder during the UV diffuse reflection measurements. Photocatalytic oxidation tests with energies of wavelengths of only above 400 nm would need to be performed to show if the platinized material is photocatalytically active under these conditions.

The binary aerogel, in contrast, showed a shift of UV absorption to lower wavelengths starting only at around 350 nm as seen in Figure 4-12. It appears to be an indication that the material would absorb energy from a smaller range of light than anatase titanium dioxide. This reduction of UV absorption is most likely due to the large amount of silica in the binary aerogel. The UV diffuse spectrum for amorphous silica, also included in this figure, shows clearly a stronger UV reflection at any wavelength compared to all other investigated catalysts.

In conclusion, the UV reflectance studies did not reveal any difference in the light absorption range of the aerogels, the P25 , or the platinized catalysts.

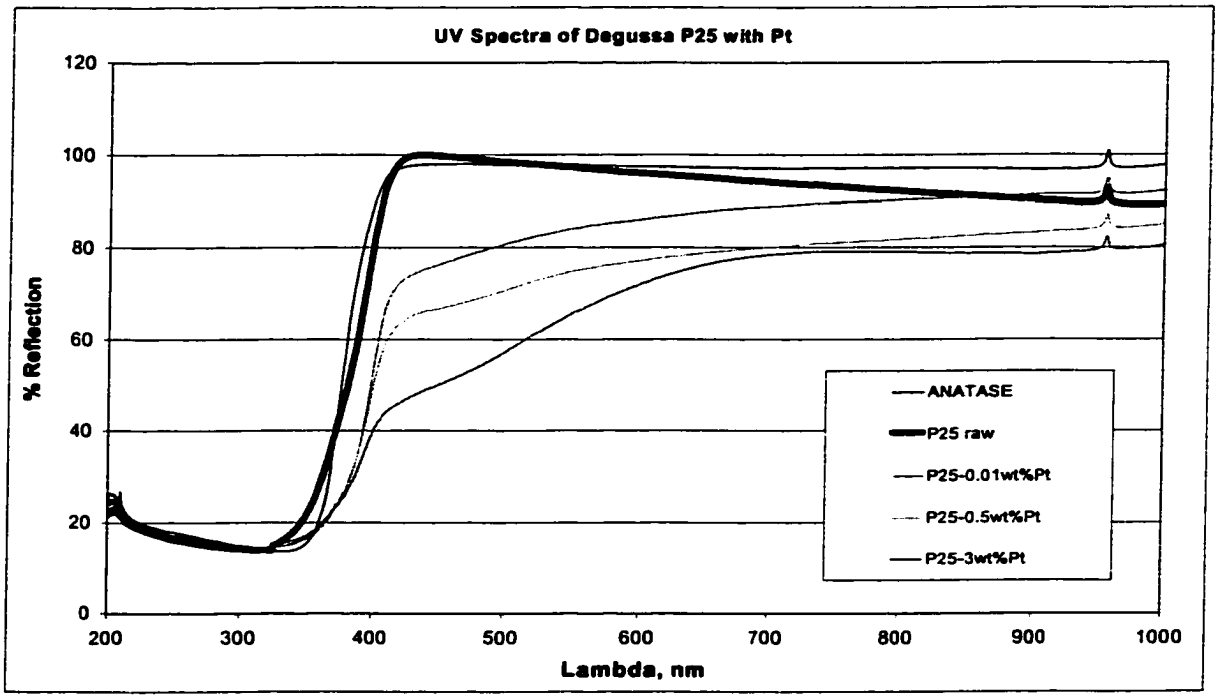

Figure 4-6 UV diffuse reflection spectra of Degussa P25 and P25 with platinum (photodeposition)

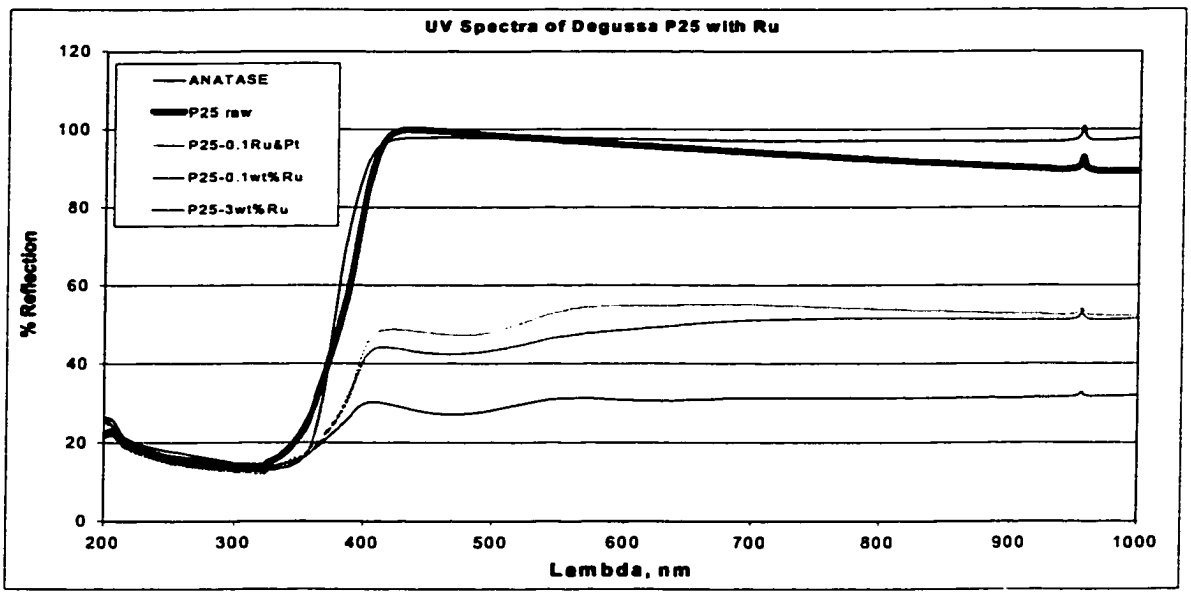

Figure 4-7 UV diffuse reflection spectra of Degussa P25 and P25 with ruthenium (photodeposition)

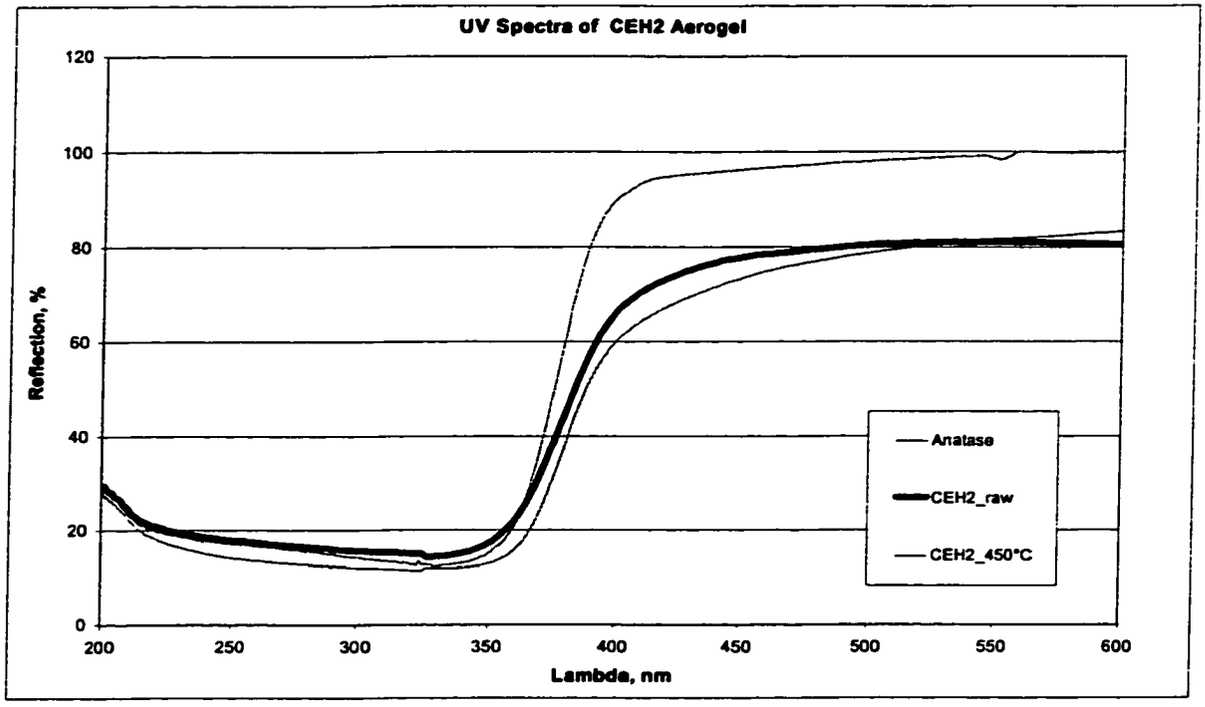

Figure 4-8 UV diffuse reflection spectra of aerogel CEH2

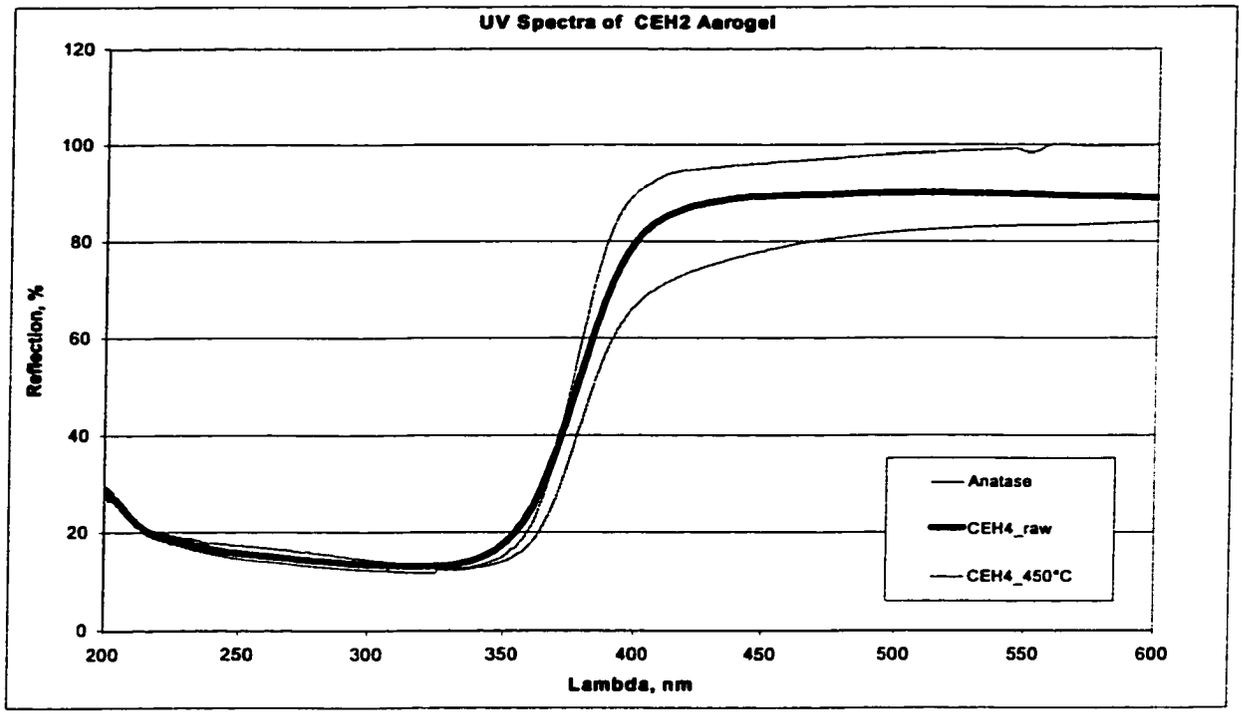

Figure 4-9 UV diffuse reflection spectra of aerogel CEH4

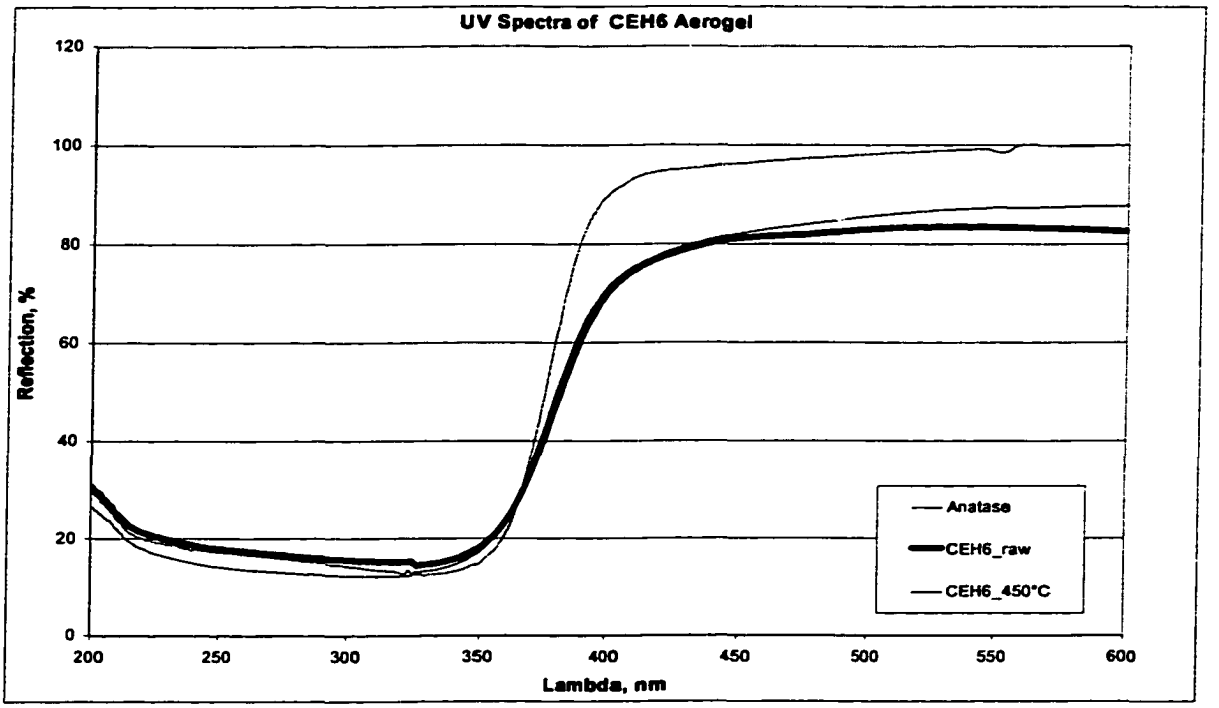

Figure 4-10 UV diffuse reflection spectra of aerogel CEH6

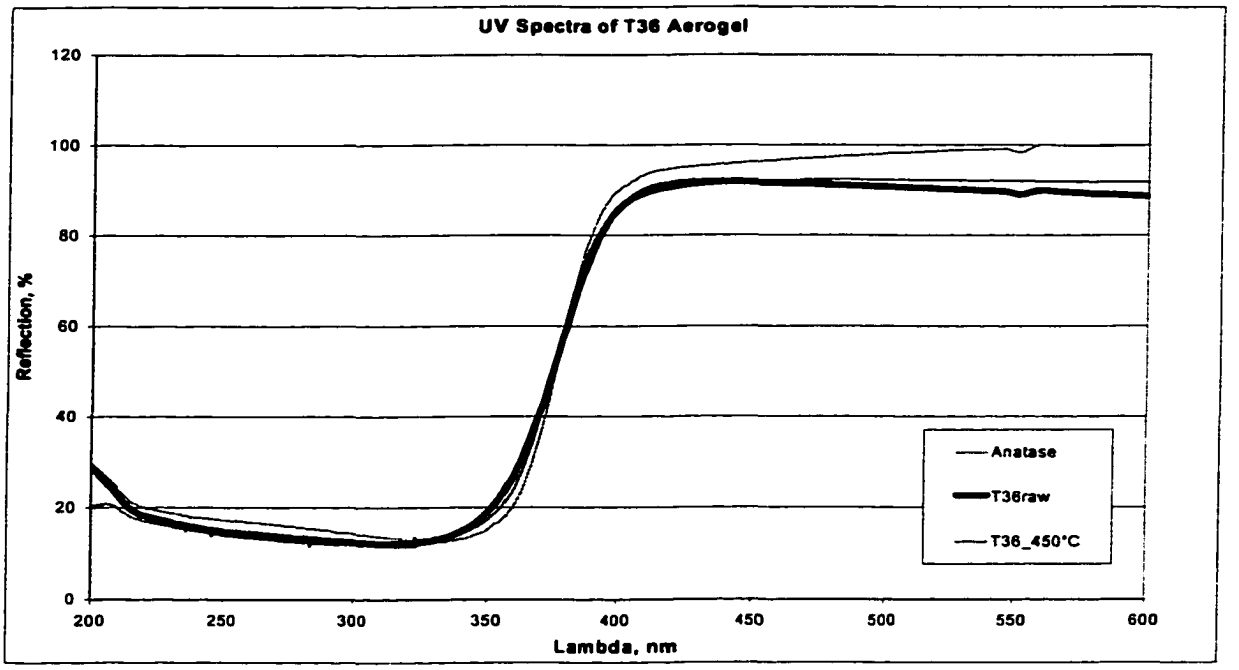

Figure 4-11 UV diffuse reflection spectra of aerogel T36

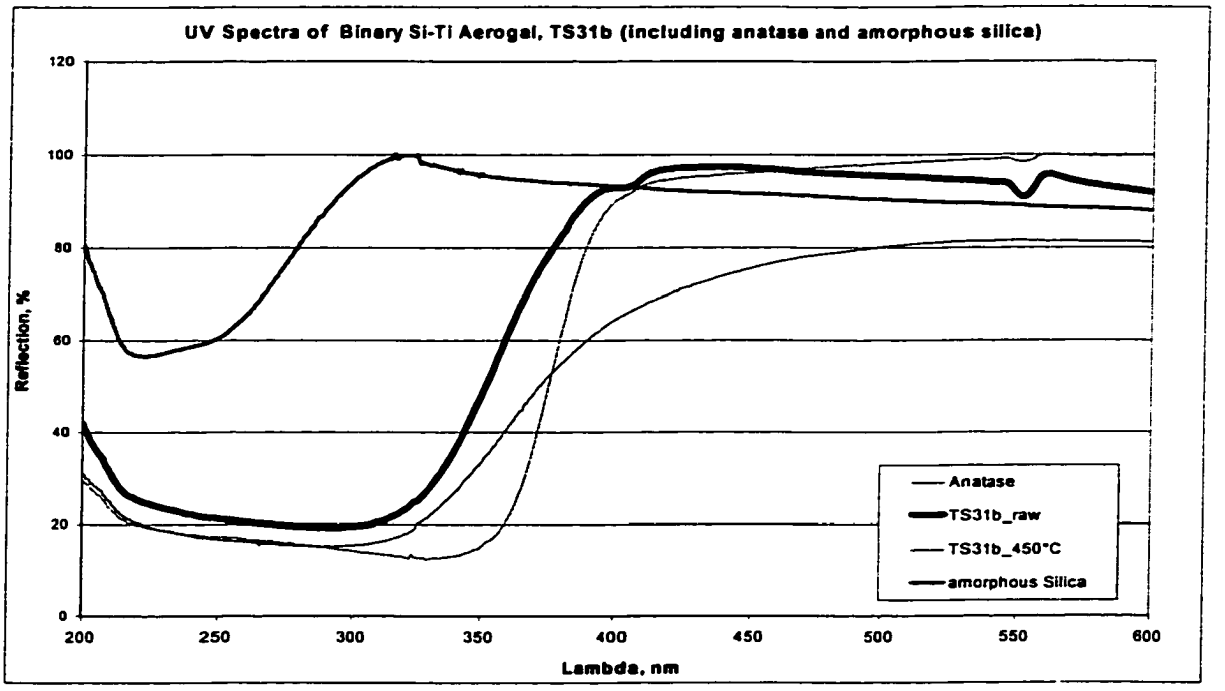

Figure 4-12 UV diffuse reflection spectra of binary aerogel TS31b

4.2.3 Temperature Gravimetric Analysis

The results of the TGA measurements are summarized in Figure 4-13 to Figure 4-18. The initial weight reduction upon heating at a rate of 5°C/minute was recorded for the untreated aerogels (indicated as "raw") as well as for the aerogels heated to 150°C and 450°C for 6 hours, respectively and is shown in the graph on top. The bottom graph indicates the change in mass with change in time (1st derivative) signifying how much of catalyst mass is lost at a given temperature. Figure 4-18 shows the TGA profile for Degussa P25 and Degussa doped with platinum and ruthenium.

All aerogels showed an initial weight reduction of about 10%, which was completed at 200°C. This initial weight loss can be attributed to the loss of weakly adsorbed water

on the surface. The second weight loss of about 15% at around 300°C might be due to additional water loss from deeper inside the pores and/or from reduced surface OH groups as throughout the condensation and polymerization gelation process of the aerogels non-polymerized OH groups remained within the gels structure. For the samples heat treated to 450°C, the second weight loss up to 300°C was reduced to about 2-3% indicating that the surface OH-groups as well as remaining adsorbed organic residuals from the synthesis deep inside the pores had been removed during the thermal treatment. This assumption can be supported by the findings indicated by the infrared spectra, which will be discussed in the following paragraph, 4.2.4 Infrared Analysis. In addition, Campostrini et al. found a similar presence of two weight losses with their sol-gel derived TiO_2 samples and attributed the first weight loss to loss of solvent and water[104]. The second weight loss was assigned to oxidation of residual organic moieties and condensation of terminal hydroxyl groups. This observed weight loss during thermal treatment was in agreement with other works in this field[86]. The binary aerogel TS31b similarly showed the first initial fast drop in weight of about 5% after heating up to 100°C, representing the elimination of weakly adsorbed water. However, no second sharp drop was observed as with the titanium dioxide gels, but rather a very slow decrease up to 1000°C. Piaggio and colleagues observed the same behavior but no explanation was attempted [105].

Degussa P25 did not show this drastic weight loss (see Figure 4-18) as observed with all aerogels. Less than one percent of adsorbed water was eliminated until a temperature of 100°C and less than 1% of other compounds (e.g. stronger adsorbed OH-groups) were removed throughout the continued heating up to 400°C. This was not surprising since

only a small amount of water or other organics will adsorb or the adsorption on this nonporous material is not as strongly as for the aerogels. The additional minor weight loss of the metal deposited Degussa samples, illustrated in the superposed graph showing a smaller range of the y-axis, resulted most likely from the removal of other organics left on the material after photo deposition of the hexachloroplatinate and ruthenium chloride, respectively.

The TGA results presented were repeatable which is shown for the aerogel CEH6 in Figure 4-15. The profiles for the 150°C treated aerogel are identical and lie closely on top of each other.

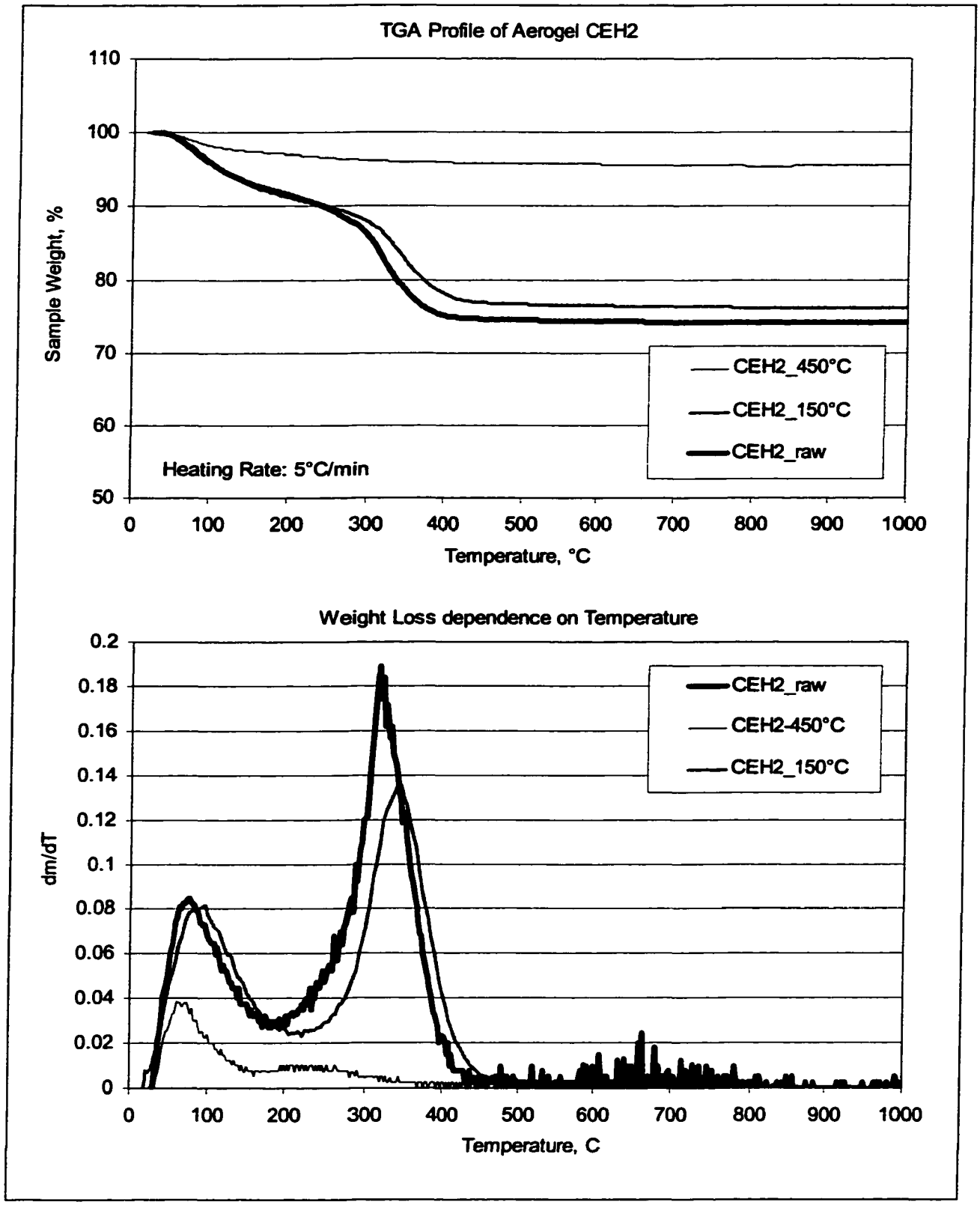

Figure 4-13 TGA profile and the weight loss (dm/dT) profile for aerogel CEH2

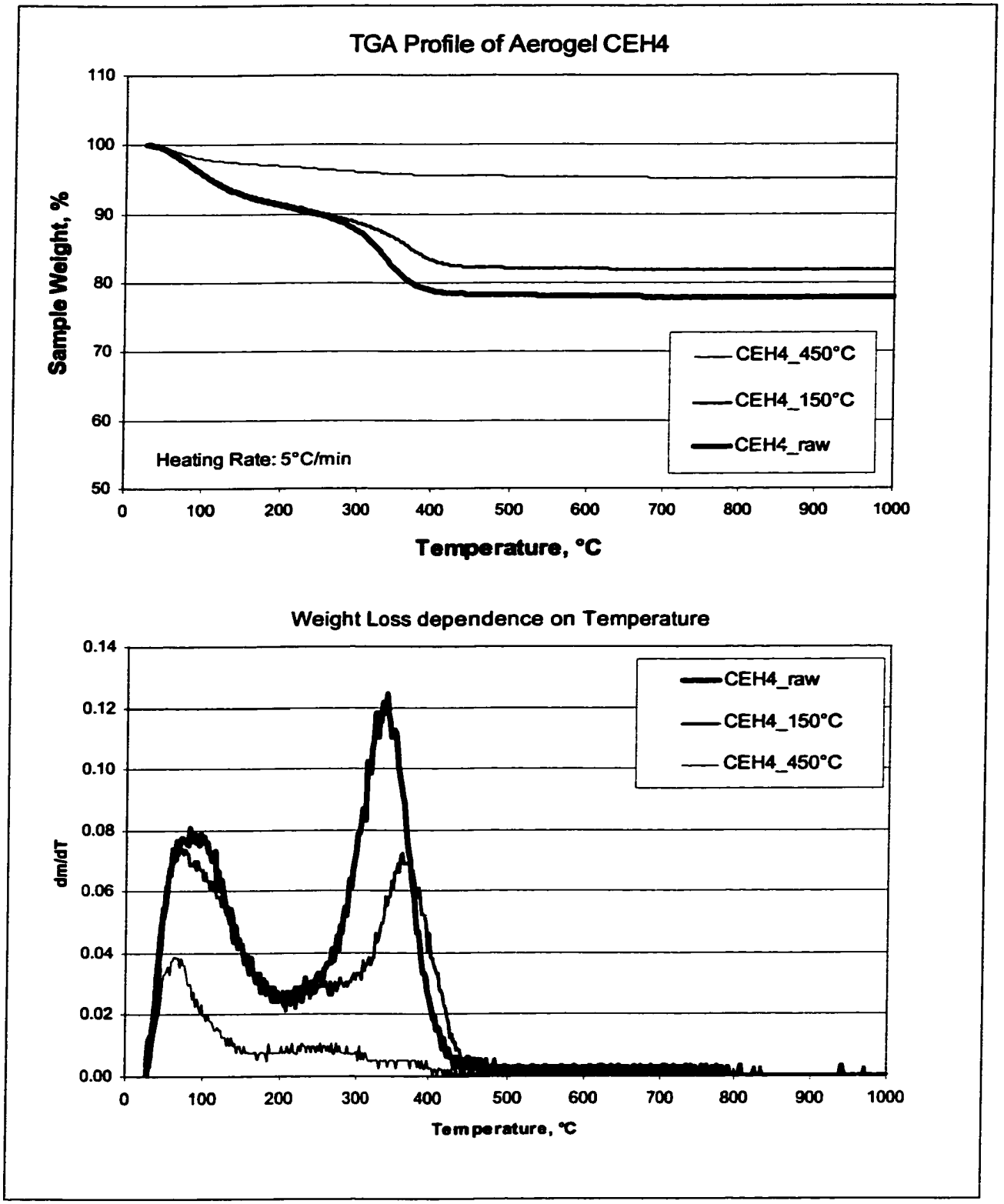

Figure 4-14 TGA profile and the weight loss (dm/dT) profile for aerogel CEH4

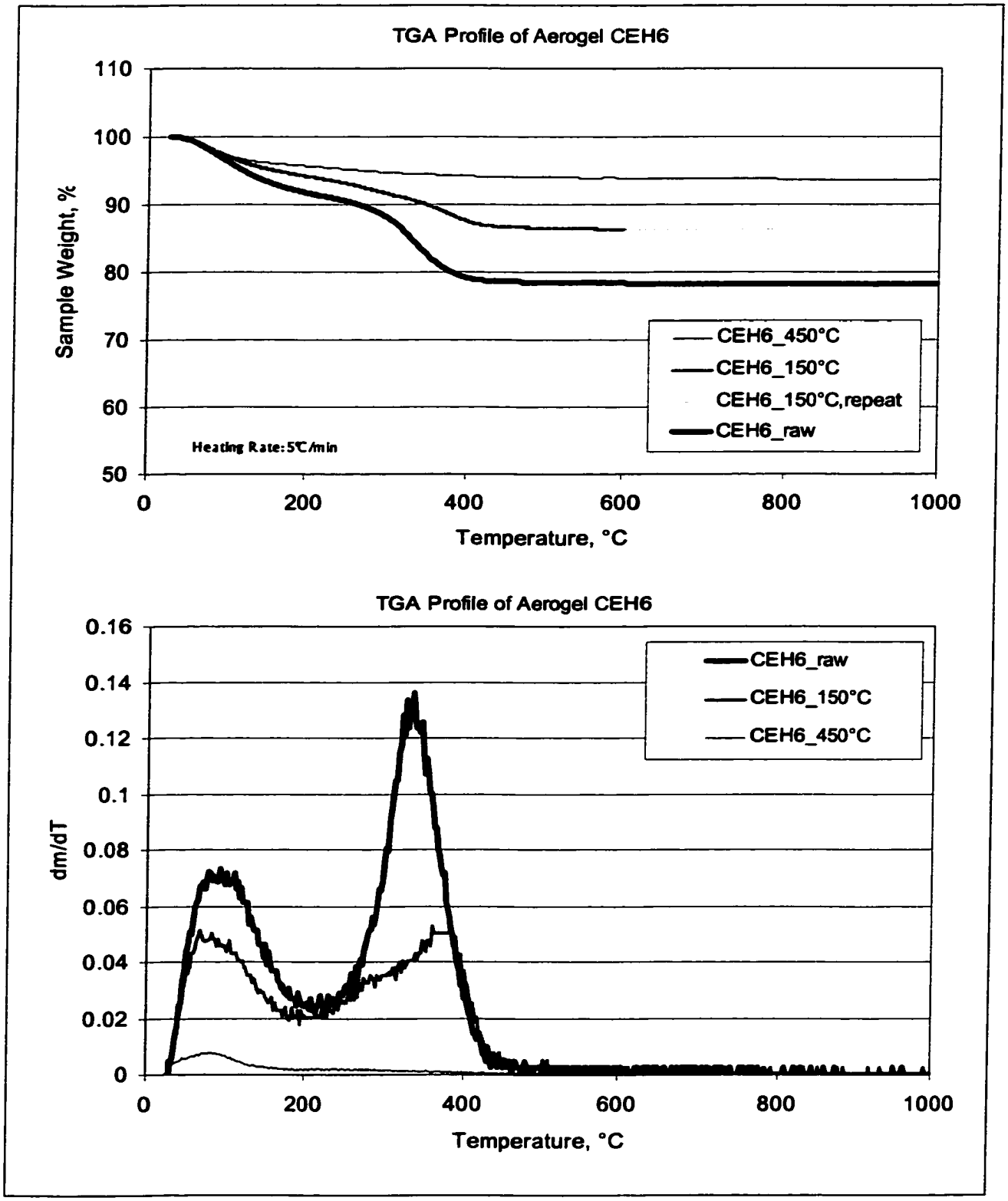

Figure 4-15 TGA profile and the weight loss (dm/dT) profile for aerogel CEH6

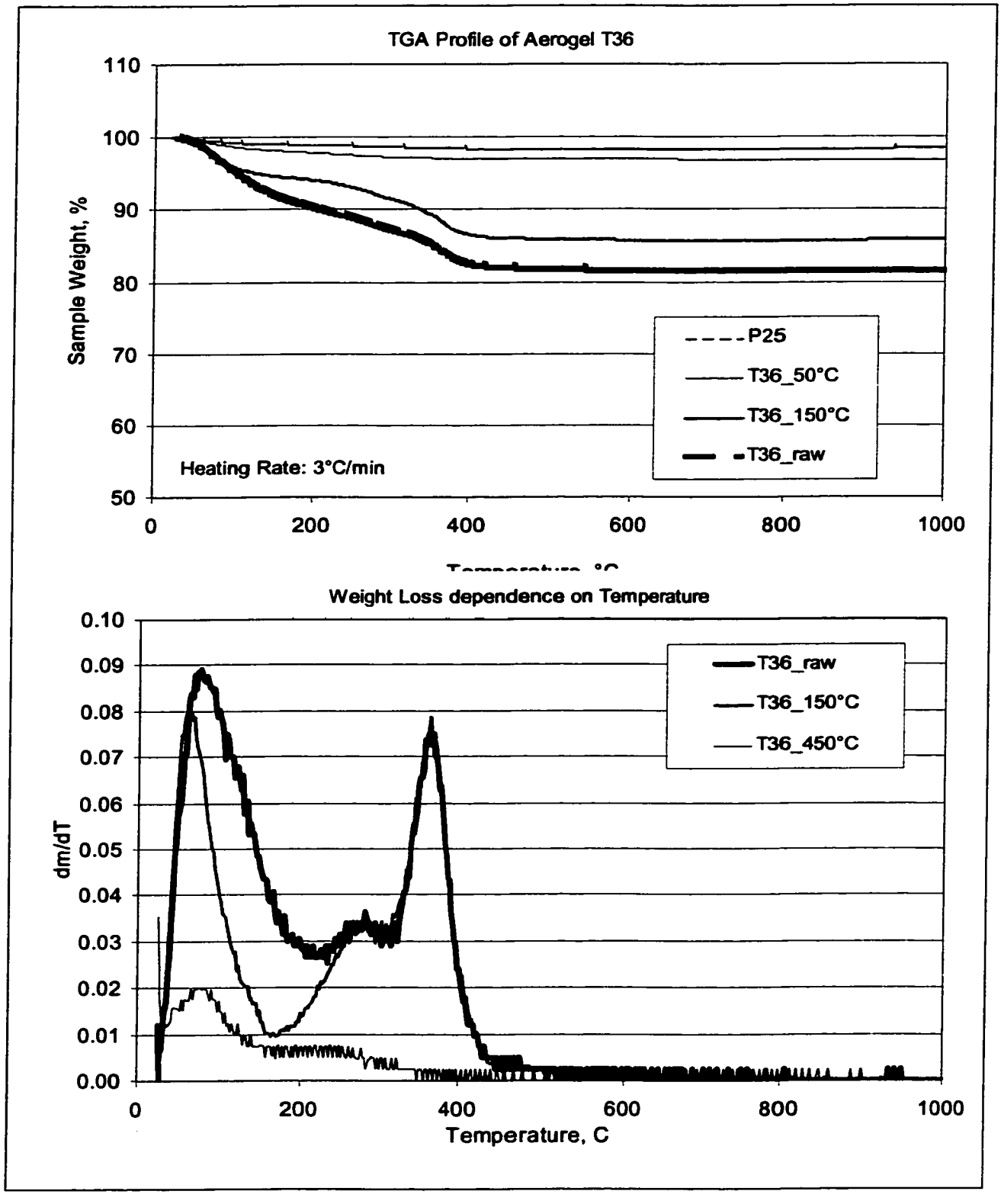

Figure 4-16 TGA profile and the weight loss (dm/dT) profile for aerogel T36

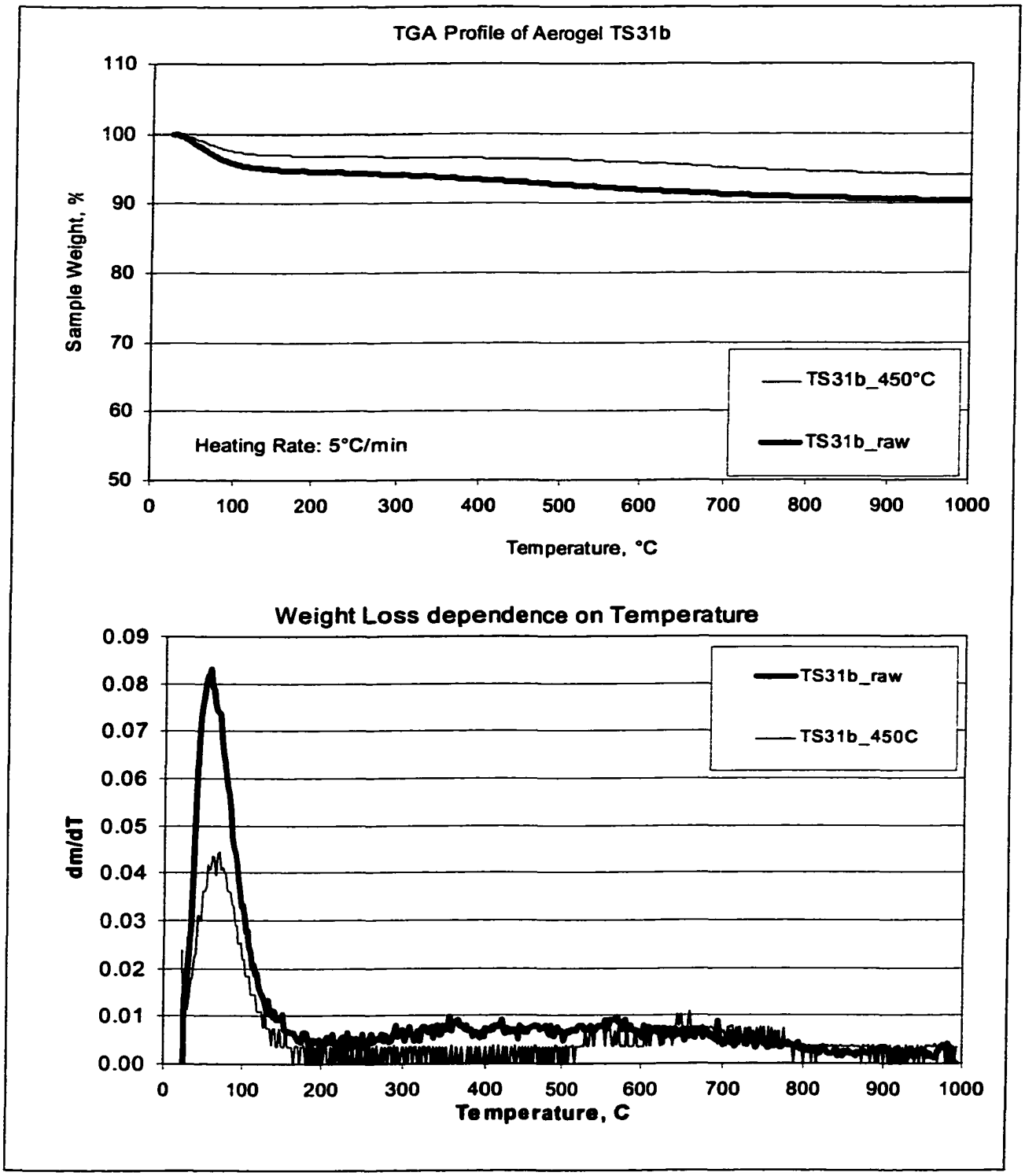

Figure 4-17 TGA profile and the weight loss (dm/dT) profile for binary aerogel TS31b

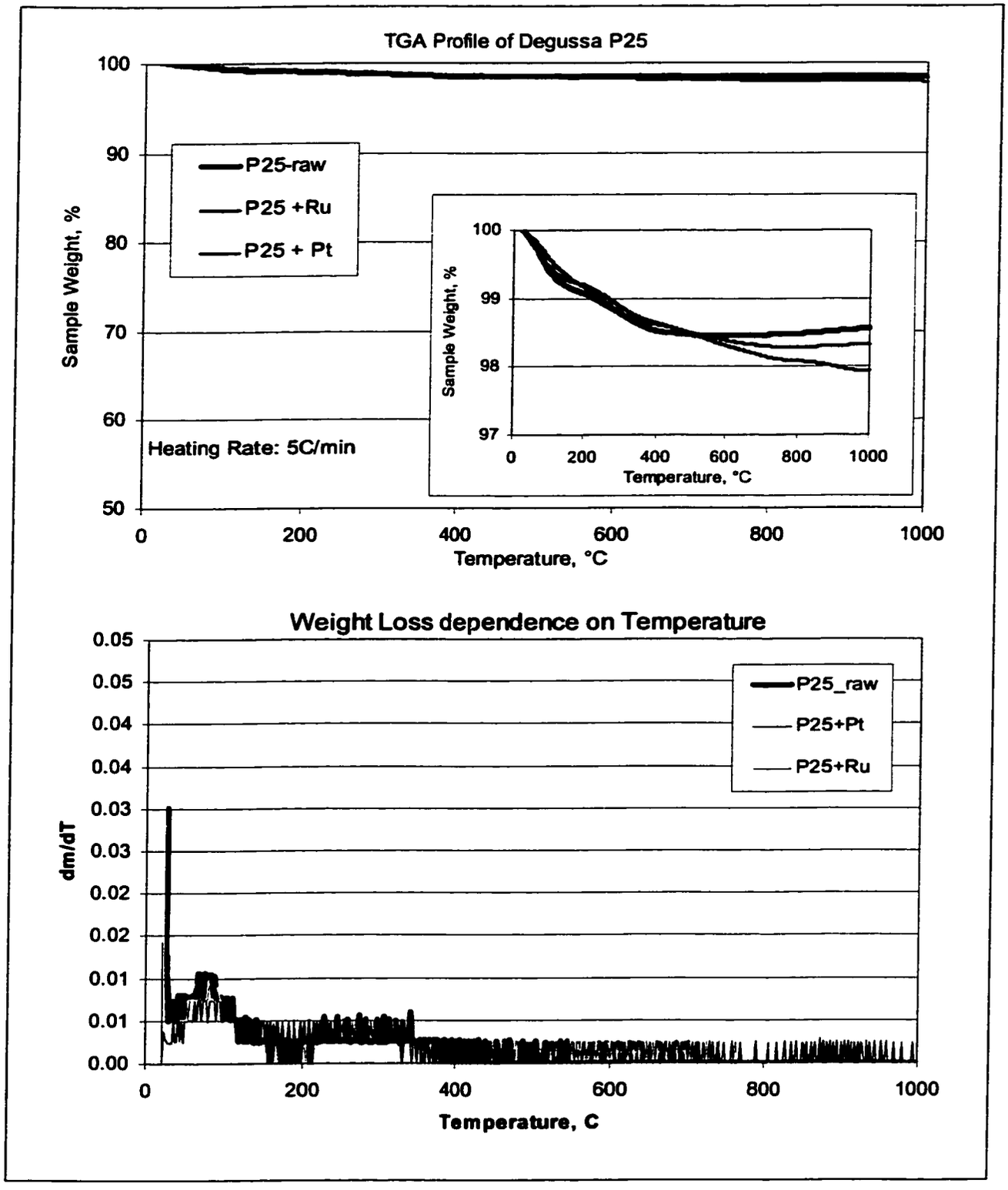

Figure 4-18 TGA profile and the weight loss (dm/dT) profile for Degussa P25 and Degussa loaded with platinum and ruthenium

4.2.4 Infrared Analysis

The infrared spectra of the titanium dioxide aerogels are combined in Figure 4-19. No noteworthy differences in appearing peaks were observed among the different samples. All samples had the significant strong absorption band from 460 to about 800 cm^{-1}, representing the Ti-O bond[104] and an asymmetric wide absorption band between 2500 and 3700 cm^{-1} resulting from the overlap of two OH related peaks at about 3400 and 3200 cm^{-1}. The peak at 3200cm^{-1} is a result of O-H stretching vibrations of hydroxyl groups bonded to Ti^{4+} [104, 106, 107]. The neighboring peak at 3400 cm^{-1} can be assigned to bending vibrations of adsorbed water on the TiO_2[104, 108] or, as Primet et al. described it, as stretching of hydrogen bonded OH-groups[109]. The same OH stretching vibration produced the peak at 1620 cm^{-1}. Next to the peak at 1620 cm^{-1} were two peaks observed at about 1540 and 1440 cm^{-1}. Some disagreement was found among researchers to what bonds those peaks were ascribed. Campostrini[104] assigned these peaks to bending vibrations of Ti-OH, whereas Munuera[108] and Augugliaro[110] assumed those peaks, including the peak at 1360 cm^{-1}, to be due to some carbon-like groups, produced by reaction of CO_2 with basic centers on the TiO_2 surface during storage of the catalyst powders in air. Primet and co-workers, in contrast, related those peaks at around 1450 cm^{-1} to bending vibrations of methyl groups. Lin-Vien and co-authors confirm that antisymmetric and symmetric CH_3 bendings occur at about 1470-1460 cm^{-1} as well as at 1395-1365 cm^{-1} [111]. Similarly, Marta et al. assigned adsorbed organics to the 1450 cm^{-1} peak. The latter explanation appears also to be closer related to the findings in this work. The peaks in questions reduced remarkably after degassing at 150°C for six hours and completely disappeared after heating the aerogel samples to 450°C for six hours, as it is

seen for the example of CEH6 in Figure 4-20. Therefore, CO_2 could not be responsible for those peaks since during heating under air the material is still exposed to CO_2 and could not have been removed. Figure 4-21 illustrates the IR spectra for all aerogels after heating to 450°C. All samples showed only the water band around 3500 and 1620 cm^{-1} besides the broad band between 400 and 800 cm^{-1}. This suggests that these peaks could rather correspond to frequencies related to Ti-OH bonds, or to vibrations of OH-groups from residual alcohol, and/or CH_3-groups left behind from incomplete hydrolysis reactions during synthesis as those components were removed throughout the heating process. The same peaks were found by Chen and Ruckenstein[106], who assigned them to the bending vibration of hydroxyl groups bound to titanium atoms on the surface of the gel. This assumption would also support the findings from TGA measurements in Section 0, showing a reduced weight loss for the heat-treated aerogels during TGA measurements starting at about 300°C. Another small peak at 1730 cm^{-1} evolved from weakly adsorbed water[108] , which also disappeared after thermal treatment.

It might be interesting to note that the last discussed peaks between 1350 and 1550 cm^{-1} were not as strong for the ultra-low density aerogel T36 compared to the low-density aerogels CEH2, CEH4, and CEH6. From this one might conclude that either hydrolysis and polycondensation reactions during gel synthesis were more complete or that during the washing procedure of the drying process residual organics were more thoroughly removed. The opposite was the case for the low-density aerogel CEH2. The peaks between 1350 and 1550 cm^{-1} were very strong, probably indicating a large amount of adsorbed or residual organics.

The infrared spectrum for Degussa P25 is shown in Figure 4-22. The same peaks as discussed for the aerogels appeared except the peaks between 1350 and 1550 cm^{-1}. This is another indication that those peaks could be related to adsorbed organics or to OH groups or water deep inside pores (as Degussa is a nonporous material). The IR spectrum of P25 was essentially identical to that of pure anatase TiO_2 with the added small water band around 3500 cm^{-1} from a small amount of adsorbed water. Even the platinum deposition did not result in any additional peaks. Most likely this peak was covered by the broad asymmetric peak of the water band and the OH stretching signal between 2800 and 3600 cm^{-1}.

Comparing the IR spectra of the binary aerogel with that of amorphous silica in Figure 4-23 shows that the IR spectrum of the aerogel agreed in all major peaks with that of the amorphous silica. None of the characteristic peaks of TiO_2 was observed. This could suggest that the amount of titanium incorporated into the silica structure is insignificant and could therefore explain the low photocatalytic reactivity of this material as described later. Concentration measurements using atomic absorption have shown that the TS31b sample contained only five percent titanium by weight in contrast to 20wt% when preparing the initial gel solution during synthesis. Similar to the TiO_2 aerogels, the asymmetric water peak around 3600 cm^{-1} and the peak at 1620 cm^{-1} was present, which is related to the water band and the Si-OH stretching band[112]. The broad peak at a frequency between 1050 and 1200 cm^{-1} as well as the peak close to 850 cm^{-1} are related to Si-O-Si silicon bonds[111, 113, 114]. A peak at 910 cm^{-1} signifying the Si-O-Ti bond could not be found. Either no such bond was established during synthesis, i.e. only Ti-O-Ti bonds or Si-O-Si bonds were established, or the peak at 910 cm^{-1} was hidden by the Si-

OH peak at 980 cm^{-1} [115]. The peak around 850 cm^{-1} resulted from Si-OH bonds[112]. The peak at 850 cm^{-1} could be an indication for Si-O bonds. The same peak appeared in the SiO_2 spectra collected by Nyquist and Kagel[116]. The peaks at 550 and 500 cm^{-1} have not been identified. The small peak present in all IR spectra at 2340 cm^{-1} corresponded to weakly adsorbed CO_2[106].

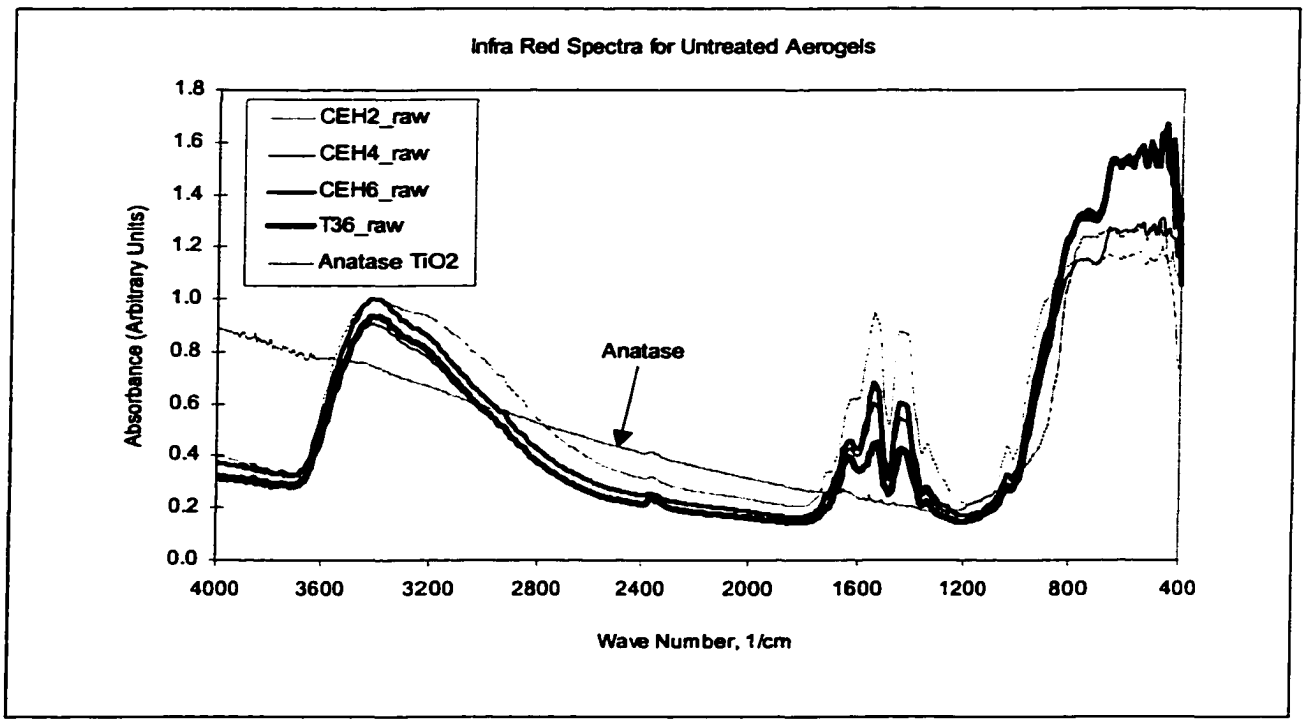

Figure 4-19 Infra red spectra of different TiO_2 aerogel samples

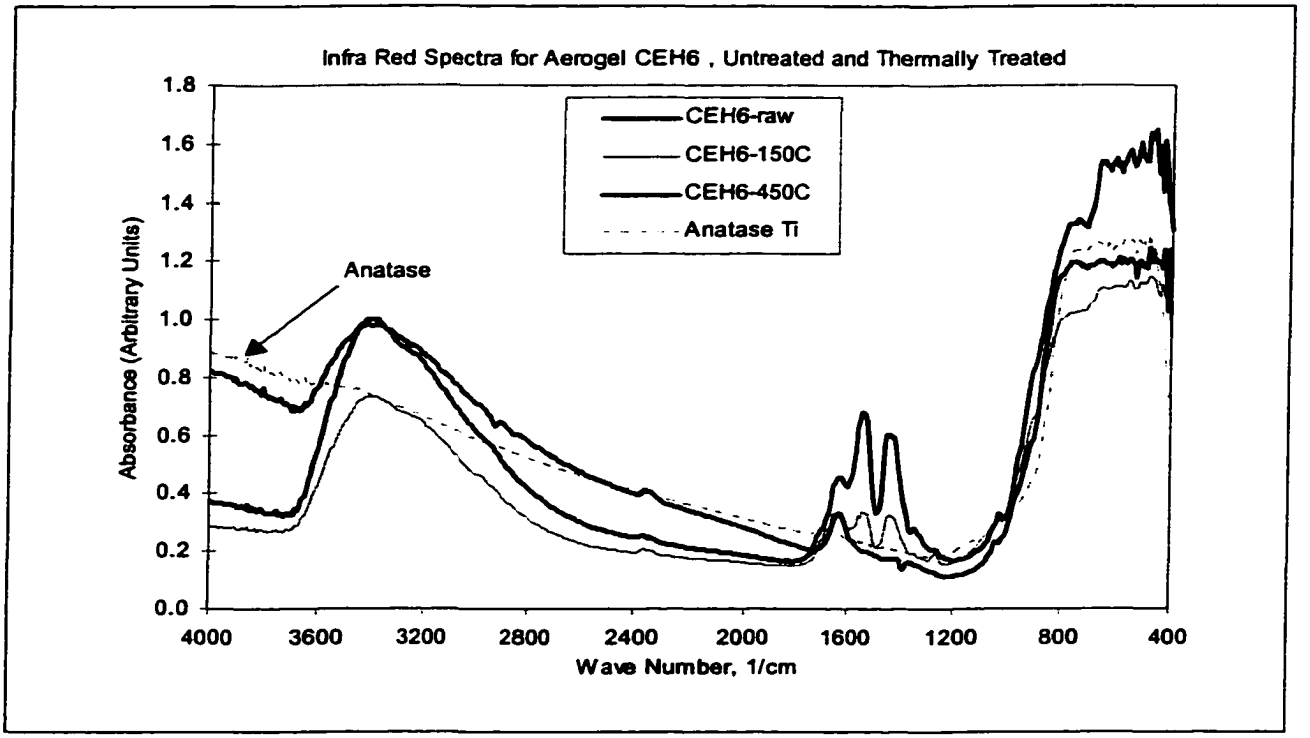

Figure 4-20 Infrared spectra of TiO_2 aerogel CEH6_raw and heat treated to 150 and 450°C

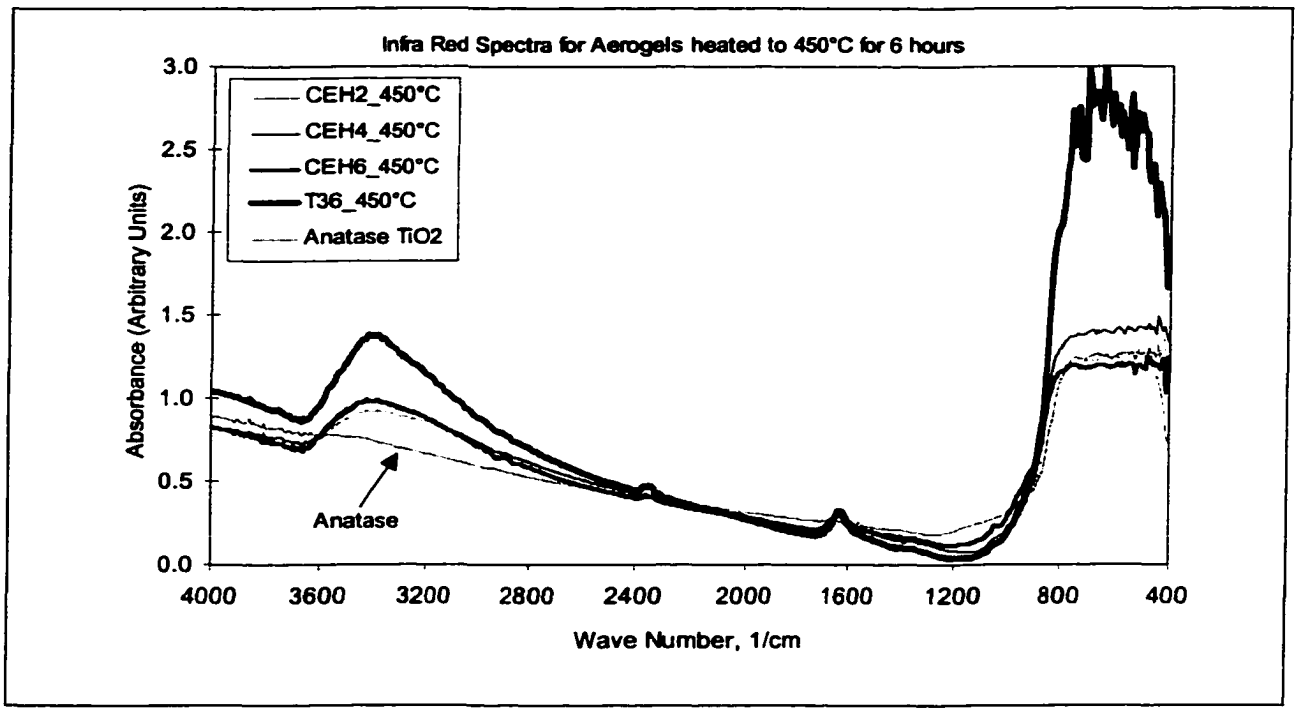

Figure 4-21 Infra red spectra of different TiO_2 aerogel samples heated at 450°C

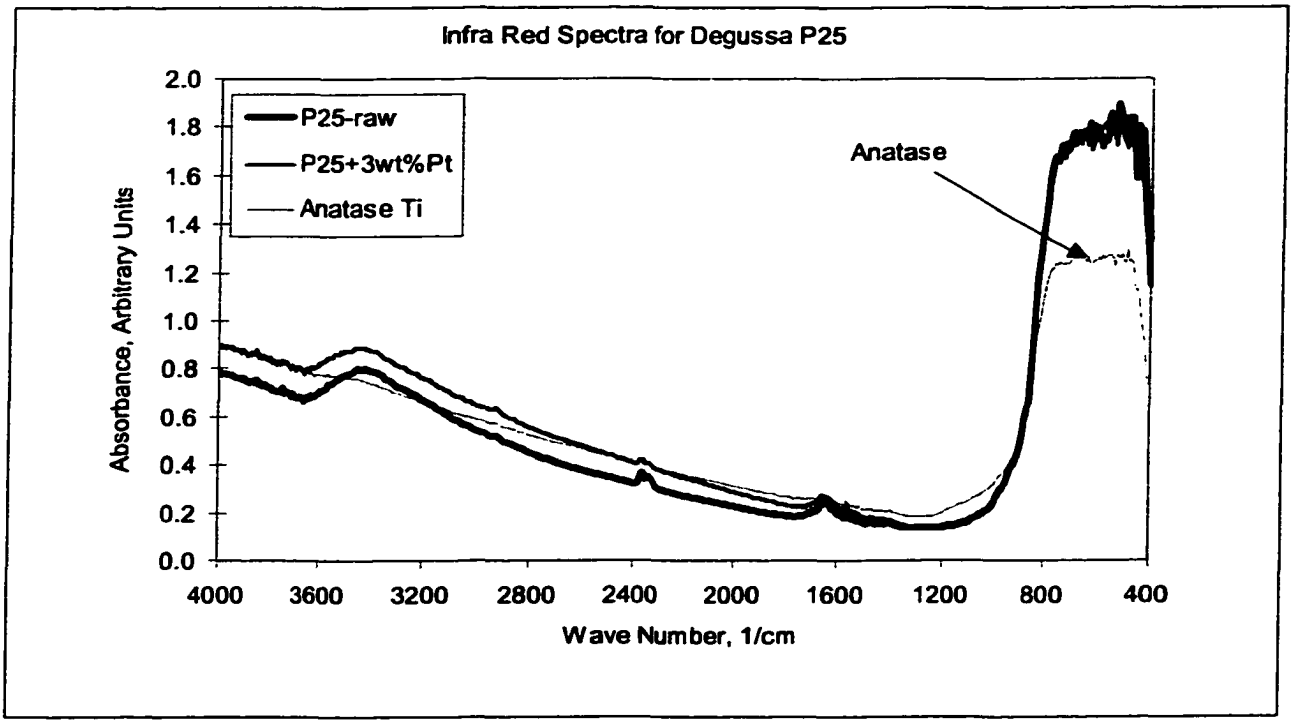

Figure 4-22 Infra red spectra of Degussa P35, including P25 with 3wt% platinum

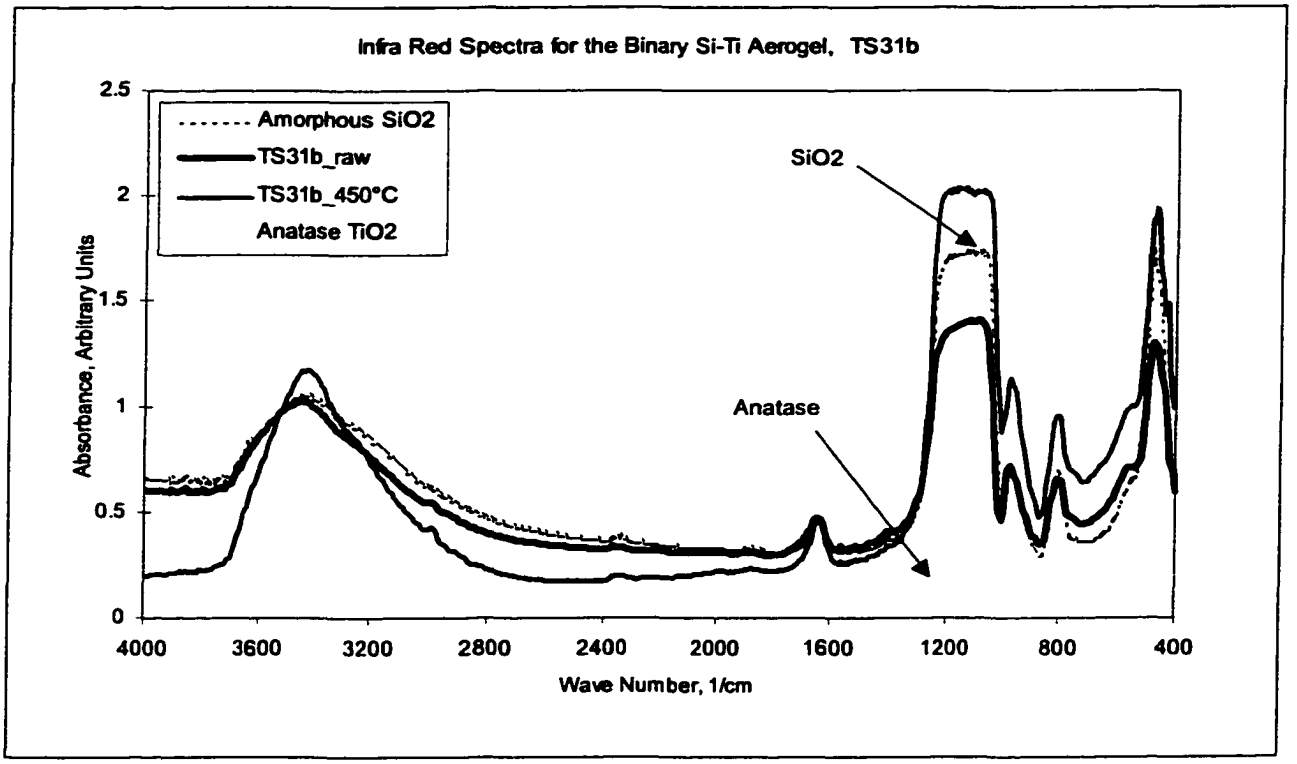

Figure 4-23 Infra red spectra of binary aerogel TS31b

4.2.5 X-Ray Diffraction

The XRD powder spectra of Degussa P25 and the aerogel materials are shown in Figure 4-24 to Figure 4-28, which include the spectra for 100% anatase for comparison purposes. As seen in Figure 4-24, Degussa P25 exhibits most of the characteristic peaks for rutile and anatase TiO_2. This was expected since Degussa is a mixture of 30% rutile and 70% anatase. The pure titanium dioxide aerogels showed a hump-like baseline shift between 20 and 30°, representing the amorphous structure, as well as a number of short wide peaks at the same angles where the anatase peaks are located. This suggests that the synthesized aerogels were not completely amorphous but contained a small amount of anatase crystallinity already prior to calcination. Heating up to 150°C did not change the crystalline structure or the amount of anatase. Only heating to 450°C for six hours showed a decrease of the amorphous portion in the material resulting in a gain of anatase crystallinity, which was indicated by an increase in peak height and a decrease in peak width. Of all the titanium aerogels, the ultra-low density aerogel T36 appeared to have the highest amount of anatase when comparing the XRD spectra. The anatase peaks were highest for T36 as seen in Figure 4-29. Also after heat treatment up to 450°C for 6 hours, it appeared that the spectra of T36 had the best defined anatase peaks compared to the other spectra as indicated in Figure 4-30. Calculations of the amount of anatase in section 4.2.6 confirmed these initial observations. It was also observed that none of the pure titanium dioxide aerogels showed any rutile crystallinity. The binary aerogel TS31b showed no crystallinity at all, even after thermal treatment no crystallinity was observed. The XRD spectrum of TS31b is identical to that of the amorphous silica as illustrated in Figure 4-31.

Furthermore, the Degussa samples with ruthenium and the platinized samples of Degussa and T36 were investigated with respect to crystallinity. Figure 4-32, Figure 4-33 and Figure 4-34 confirm that the crystallinity of those catalysts was not altered during the platinum deposition. A similar observation was made for the ruthenium deposited Degussa sample. All major peaks of the XRD spectra of the platinized samples look similar as those of the raw material. Only one aerogel sample, the one that underwent the platinization procedure twice (3.5wt% Pt), had more developed anatase peaks (Figure 4-34).

Lastly, X-ray scans were performed of a heat-treated Degussa P25 and a T36 aerogel to a temperature of 550°C for 12 hours. After exposure of Degussa P25 to 550°C the percentage of rutile crystallinity increased significantly in the P25, reducing the amount of anatase crystallinity (see Figure 4-35). The areogel T36, in contrast, showed a remarkable increase in anatase with no development of any rutile crystallinity.

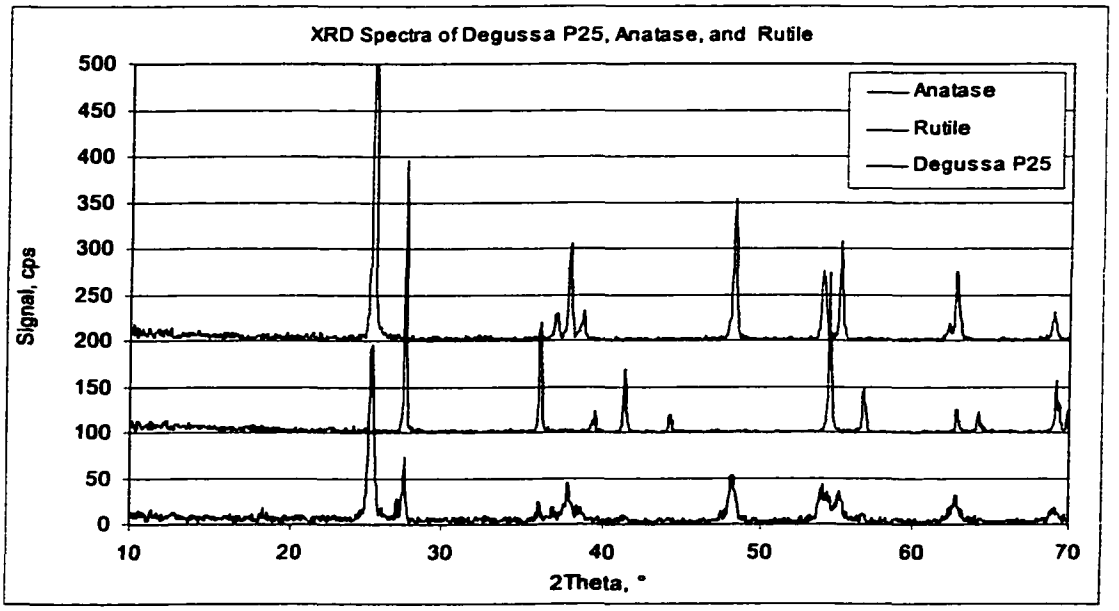

Figure 4-24 XRD profiles for Degussa P25, including that of anatase and rutile TiO_2

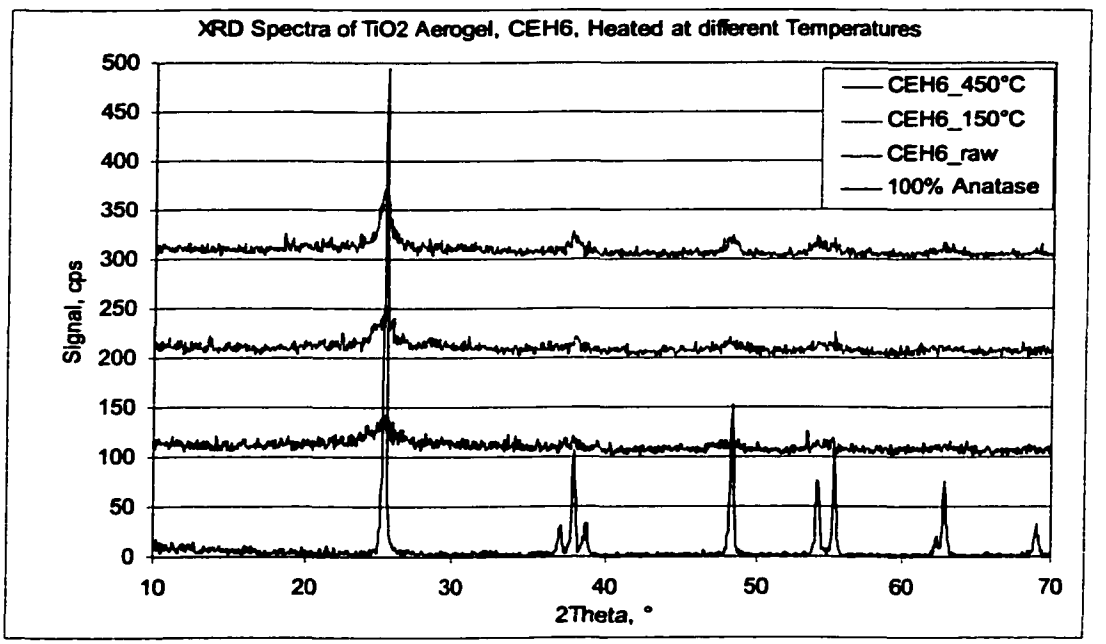

Figure 4-25 XRD profiles for low-density aerogel CEH2, untreated and heat treated to 150 and 450°C

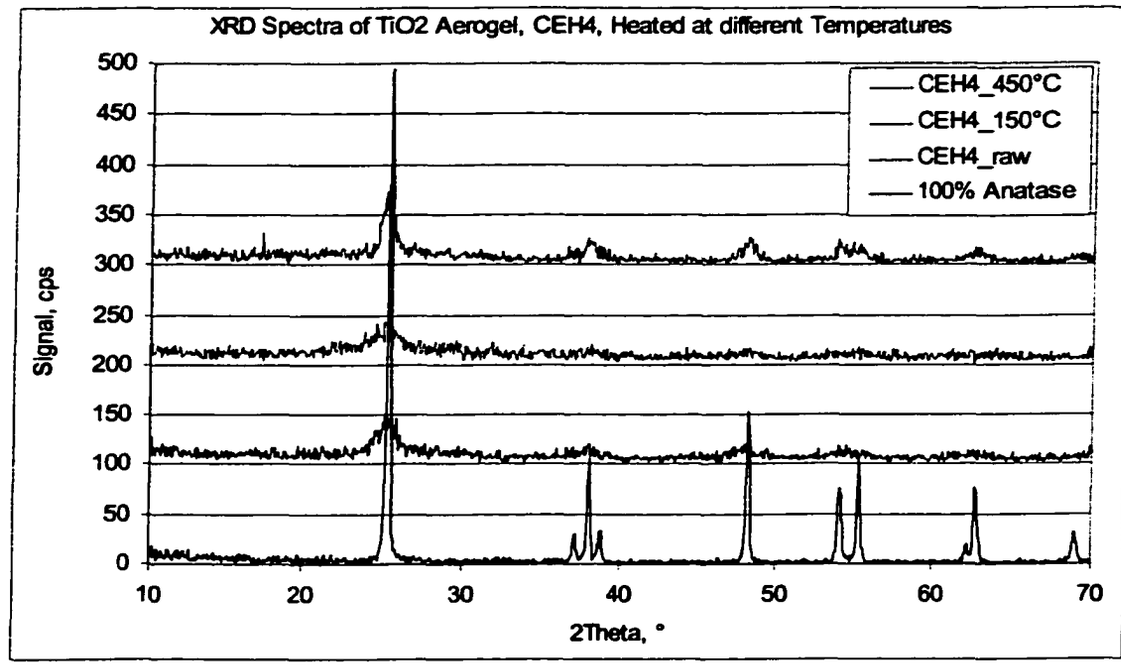

Figure 4-26 XRD profiles for CEH4, untreated and heat treated to 150 and 450°C

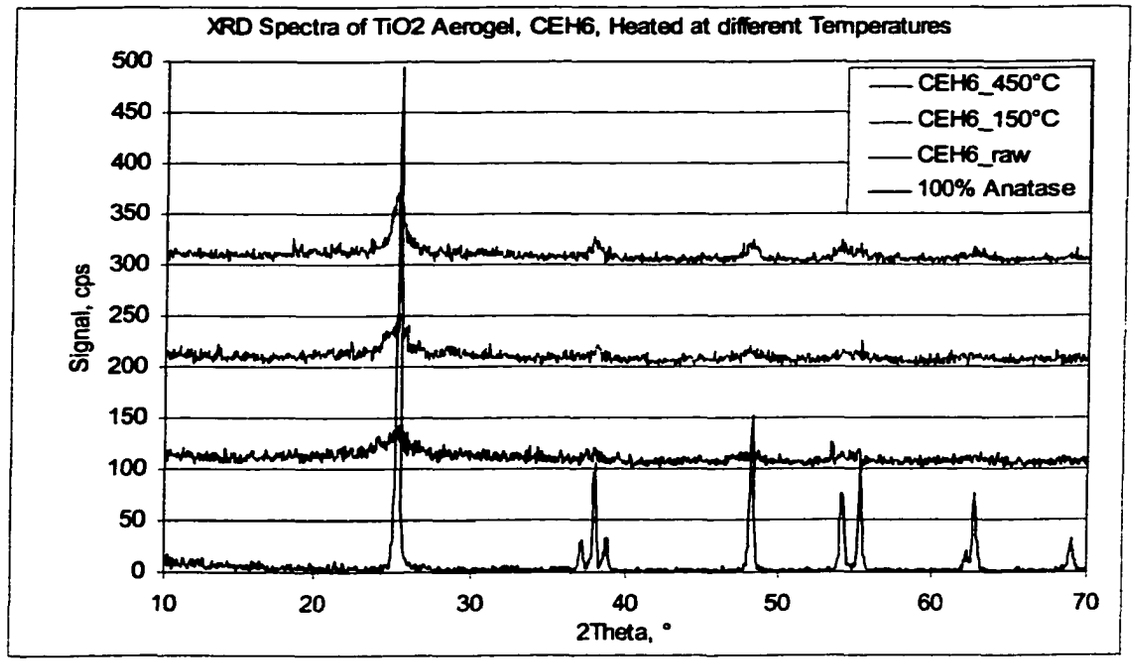

Figure 4-27 XRD profiles for CEH6, untreated and heat treated to 150 and 450°C

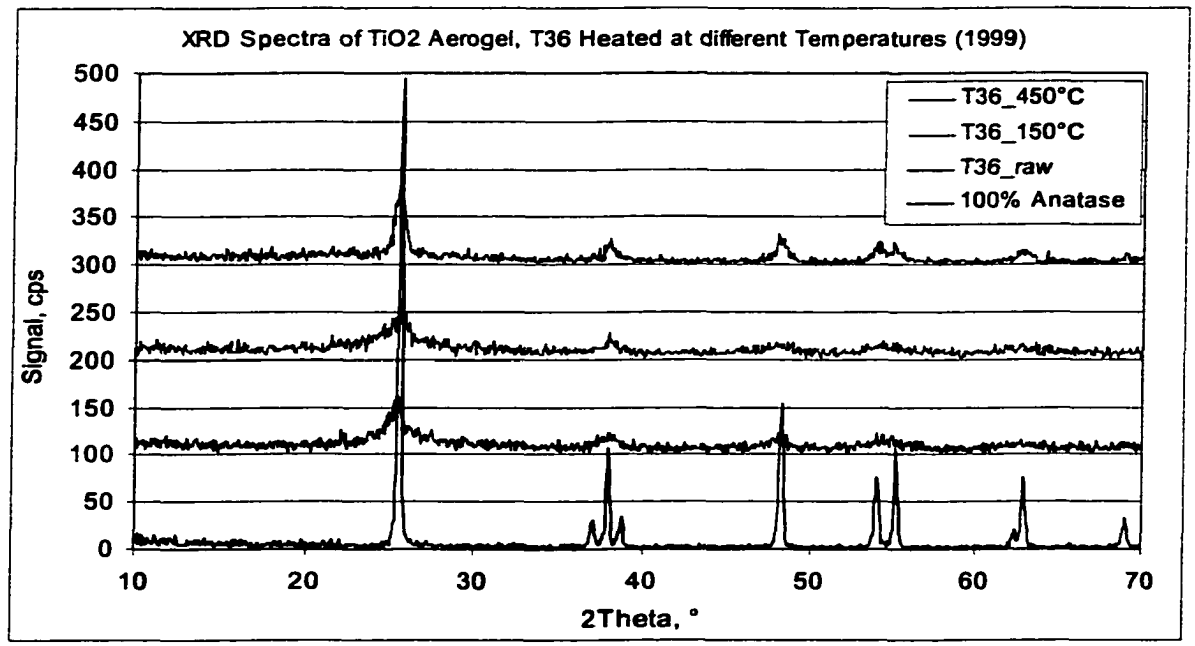

Figure 4-28 XRD profiles for ultra low-density aerogel T36, untreated and heat-treated to 150 and 450°C

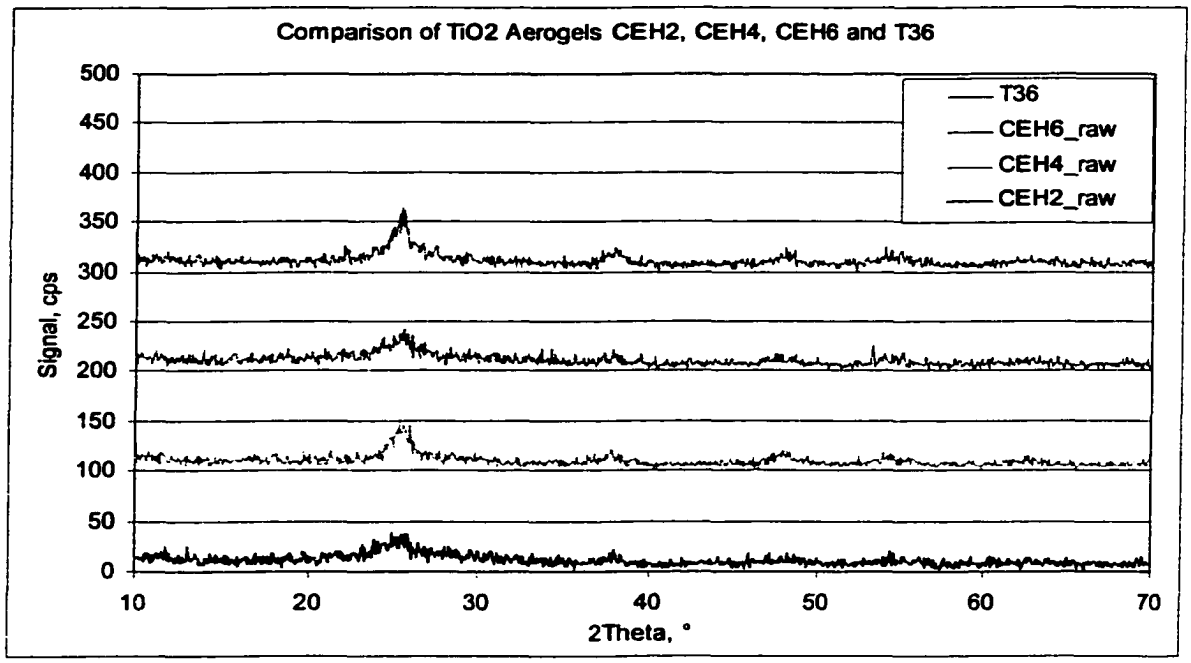

Figure 4-29 Comparison of XRD profiles of all pure TiO_2 aerogels (raw material)

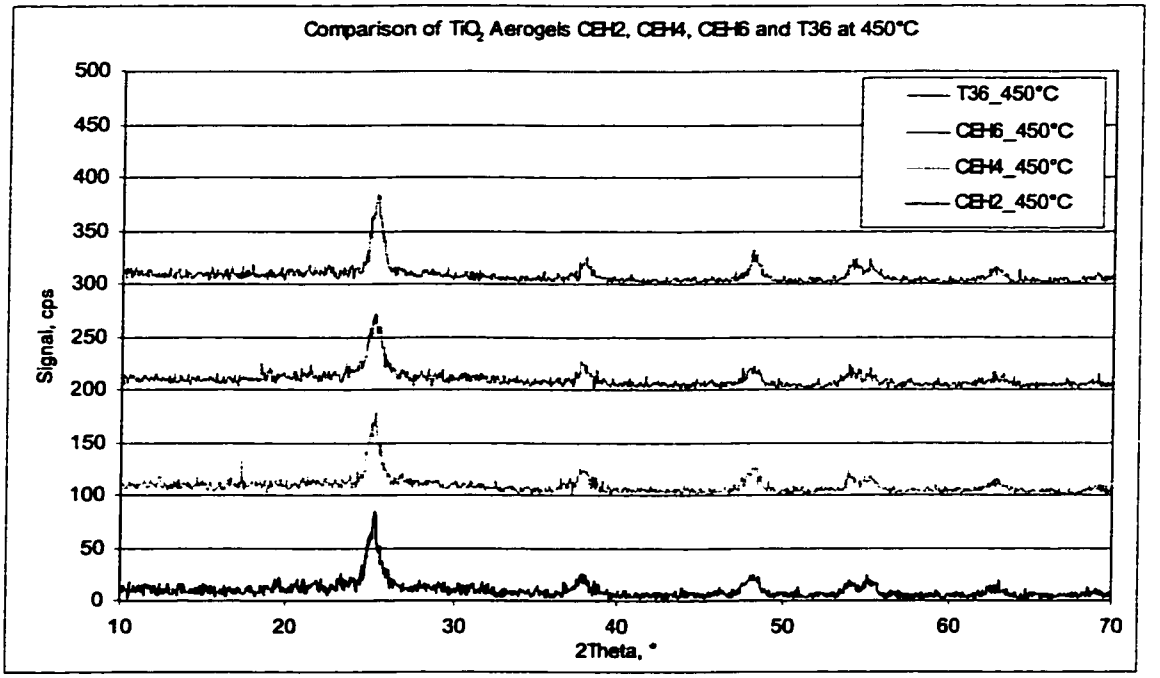

Figure 4-30 Comparison of XRD profiles of all heat treated pure TiO_2 aerogels

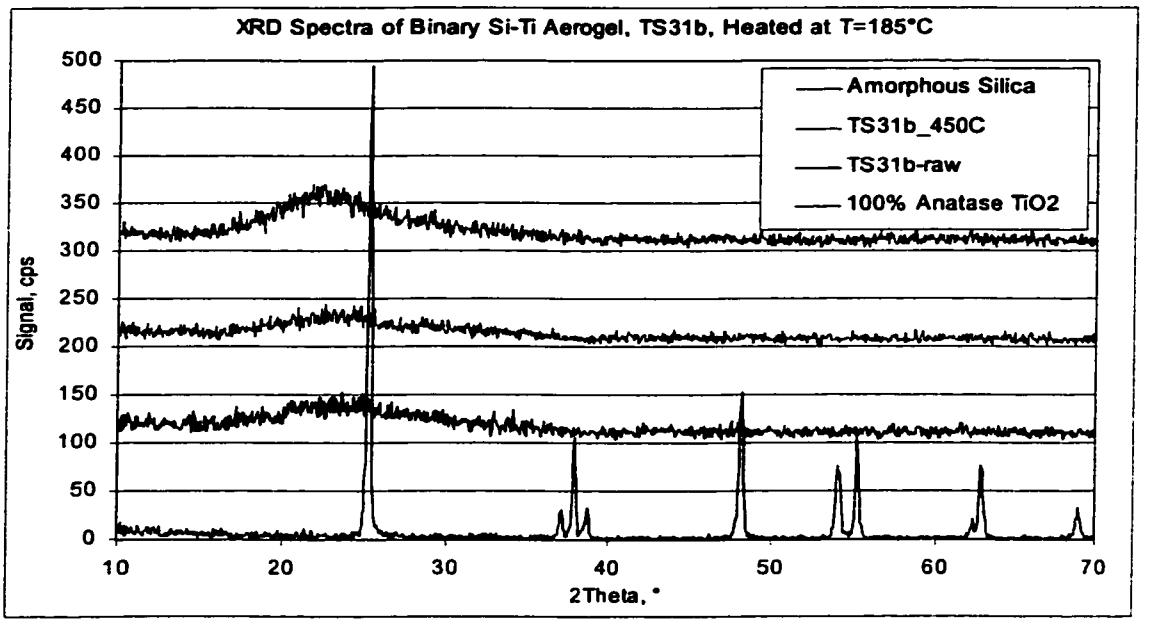

Figure 4-31 XRD profiles for binary aerogel TS31b, untreated and heat treated to 450°C as well as the profile for amorphous silica (top graph) and anatase titanium dioxide (bottom graph)

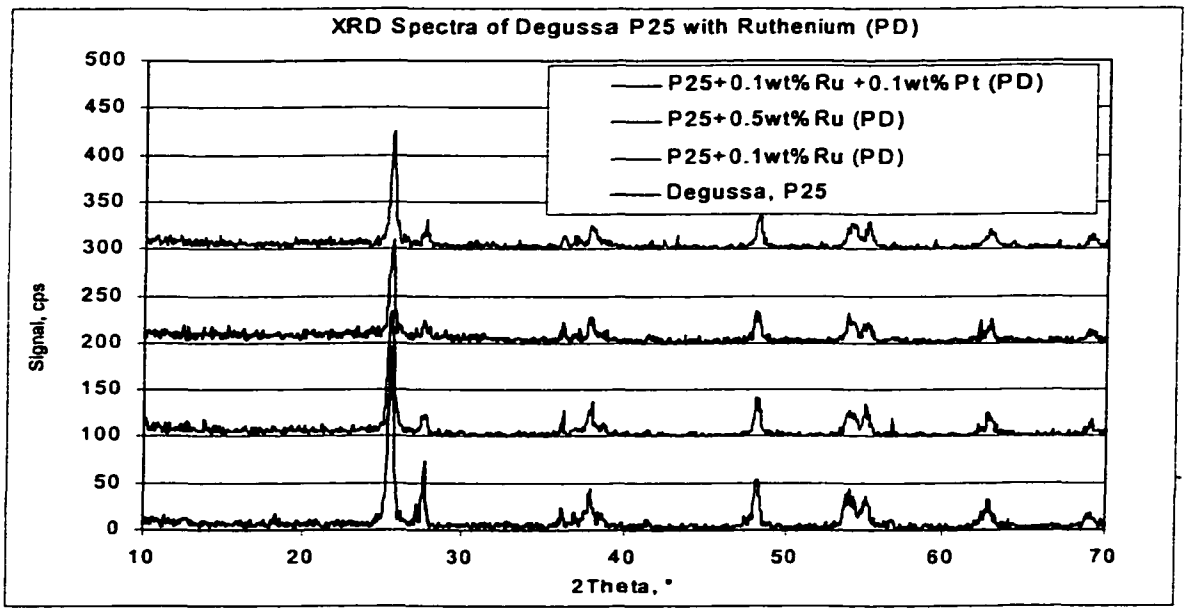

Figure 4-32 XRD profiles for Degussa P25 with ruthenium (PD = photo deposition)

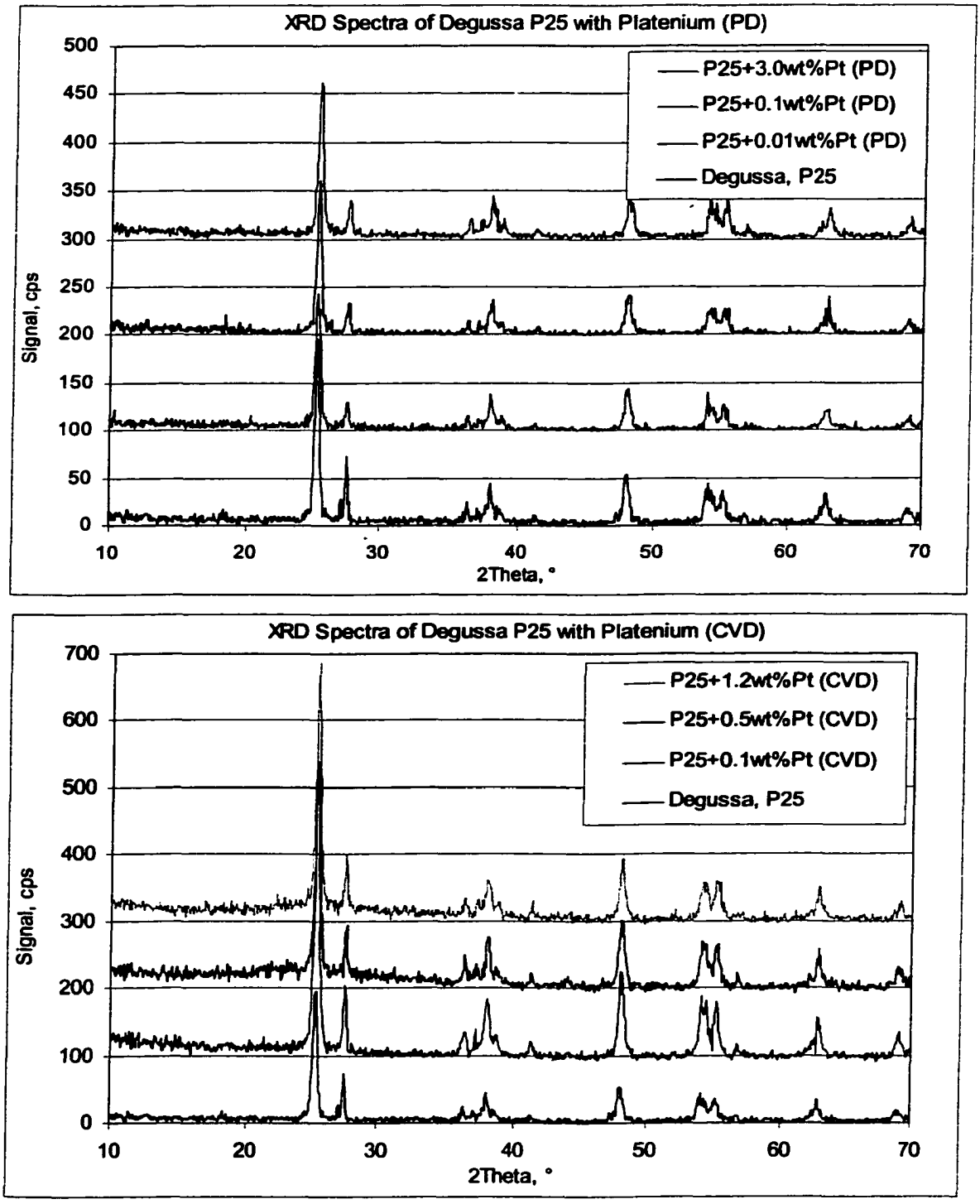

Figure 4-33 XRD profiles for Degussa P25 with platinum (top graph: PD = photo deposition; bottom graph: CVD = chemical vapor deposition)

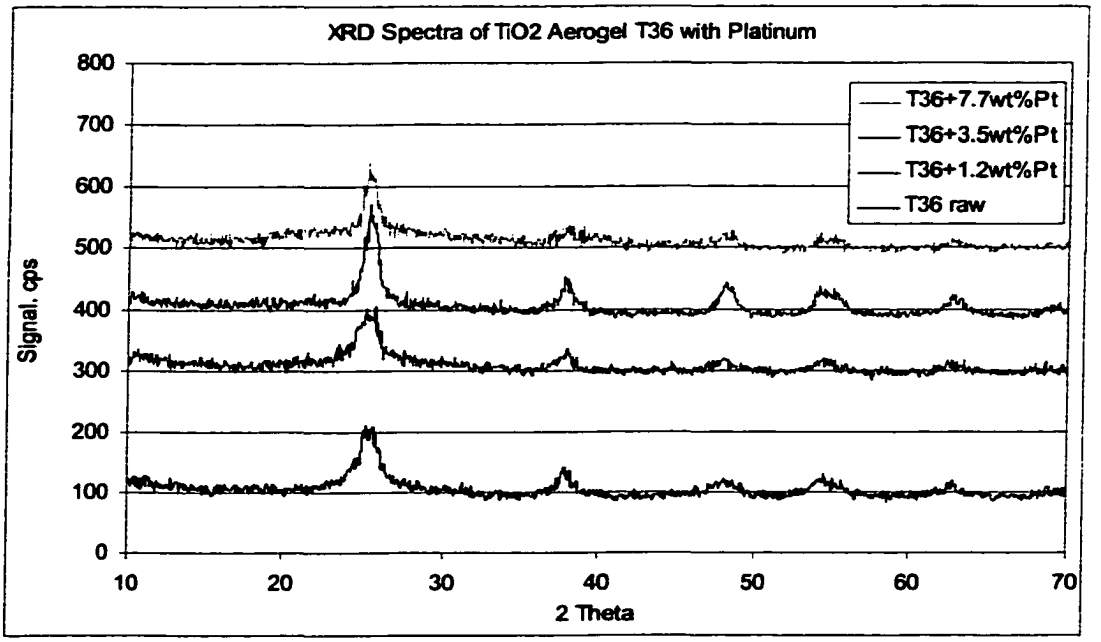

Figure 4-34 XRD profiles for aerogel T36 with platinum

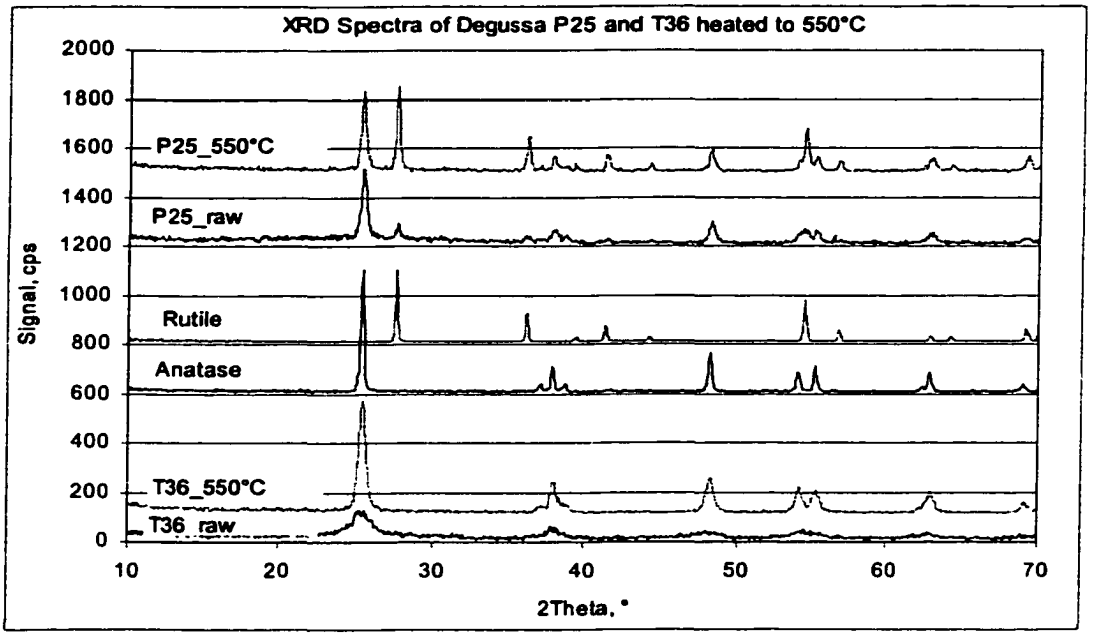

Figure 4-35 XRD profiles for heat treated Degussa and T36 to 550°C (including the raw materials and 100% anatase and 100% rutile)

4.2.6 Fraction Anatase in Aerogel Samples

As discussed in Section 3.2.8, Klug and Alexander described a method using X-ray diffraction to quantitatively analyze the amount of one component in a multi-component system ("Internal standard analysis for one component of a multi component system")[97] by adding a standard compound that has clearly distinguished peaks from the component to be analyzed. Using rutile titanium dioxide as standard component and comparing the integrated areas of the major peaks of rutile with the integrated areas of the major anatase peaks the amount of anatase could be determined.

First, a calibration curve was developed. Ten samples of varying amounts of anatase and rutile titanium dioxide were prepared as shown in Table 4-2, the XRD spectra were obtained and the first major peaks of each component were integrated.

Anatase, g	Rutile, g	wt% Anatase	Intensity Ration, I_A / I_R			average	stdevp
			Run 1	Run 2	Run 3		
0.0209	0.2147	**8.9**	0.32	0.44	0.32	**0.36**	0.06
0.0572	0.3047	**15.8**	0.50	0.43	0.48	**0.47**	0.03
0.1289	0.3950	**24.6**	0.64	0.80	0.58	**0.67**	0.09
0.1990	0.3122	**38.9**	1.05	1.09	1.02	**1.05**	0.03
0.3351	0.1943	**63.3**	2.19	2.04	2.24	**2.16**	0.09
0.3327	0.1122	**74.8**	5.68	5.91	5.74	**5.78**	0.10
0.4187	0.1056	**79.9**	6.20	4.46	5.76	**5.47**	0.74
0.3622	0.0475	**88.4**	7.84	6.35	6.13	**6.77**	0.76
0.3372	0.0297	**91.9**	11.73	11.93	12.20	**11.95**	0.19

Table 4-2 Calibration sample data from XRD

Then, the intensity ratios of anatase to rutile, I_A/I_R, were plotted against weight percent anatase of the anatase/rutile mixture as illustrated in Figure 4-36. Each data point in this figure is the average of three different measurements. The data points up to 50wt% anatase follow a linear trend with insignificant deviation. For anatase fractions larger than 70wt% the data points became more scattered and the slope of the curve

increased fast going up to infinity when approaching an anatase content of 100wt%. Since the obtained data points followed neither a linear nor an exponential trend within the range of 50 to 100wt% anatase a graph was manually superposed such that it would best fit the data to form calibration curve as seen in Figure 4-36.

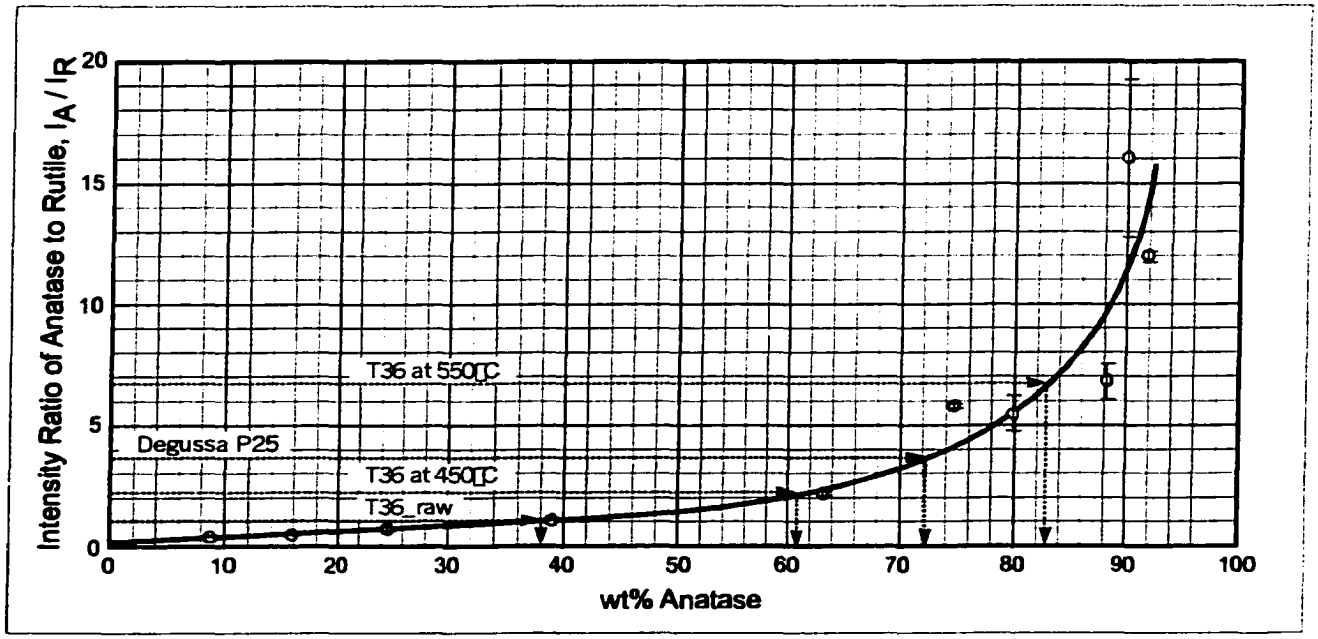

Figure 4-36 Calibration curve for determining the weight percent of anatase in aerogels

In order to determine the amount of anatase in the catalysts, the samples were first dried at 100°C for at least 12 hours. Then, about 15-30wt% of rutile TiO_2 was added to the dried samples. After thorough grinding and mixing, three XRD scans per one sample were performed and the peak areas were calculated as described above for the calibration samples. As an example, Figure 4-37 shows the three XRD scans for T36 with added rutile TiO_2 used to calculate the peak area. The narrow peak at around $2\Theta = 28°$, e.g., originates from the rutile that was added to the T36 sample added.

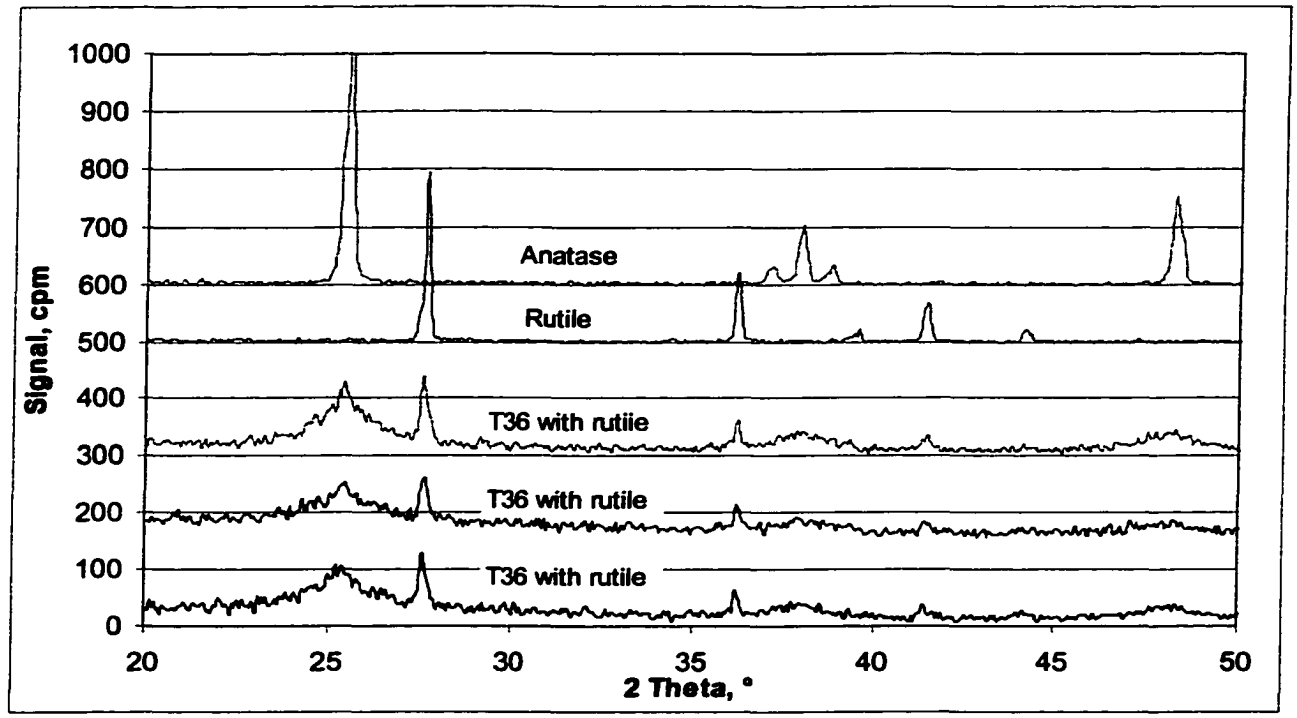

Figure 4-37 XRD spectra of T36_raw with added rutile for determining wt% anatase

The values obtained for the ratio of anatase to rutile were then utilized to find the amount of anatase under use of the calibration curve in Figure 4-36. The so obtained numbers, however, did not represent the actual amount of anatase in the catalyst (since a known amount of rutile was added to the sample) but indicated how much anatase was present with respect to rutile. Since the amount of added rutile was known, the actual weight percent of anatase could then be calculated as outlined for T36 (untreated) in the Appendix (Table 7-4).

The above calculations were not necessary for the Degussa since rutile was already present in the samples. Since no rutile was added, the values read from the calibration graph represented the amount of anatase in the sample.

Table 4-3 summarizes the results obtained for the aerogel T36, CEH6, Degussa P25, and for the samples with platinum deposition. A good agreement was found with the literature value of anatase for Degussa with 73wt% and 72wt%, respectively. The untreated aerogels had an anatase fraction of about 10wt%. After heat treatment to 450°C the amount of anatase increased to 89% for T36 and 50wt% for CEH6. The anatase fraction for the heat treated T36_450°C with 89wt% appears to be surprisingly high since the XRD spectra did not show that much very well developed peaks (narrow and high peaks) as the pure anatase. Also, questionable is reliability of the amount of anatase crystallinity found for the platinum doped T36. The XRD scans from Figure 4-34 did not show a significant change in crystallinity after CVD. Calculations for the amount of anatase, however, showed an increase of anatase from 11 to 45, and 40wt% after deposition of 1.2 and 7.7wt%, respectively. There are several reasons that might explain the unexpected data. First, weighing errors were possible during preparations of the samples when adding rutile since only small amounts of catalyst were available for the measurements. Another possibility for errors lies in the integration of the peak areas. The peaks for anatase are not very well defined and the baseline is partly shifted to higher values due to the amorphous portion of the aerogels. In addition, the calibration curve for anatase fractions larger than 50 % was not as accurate since the data points were more scattered in this range. Slight shifts of the superposed trend line can change the result of the amount of anatase largely; especially in the steep-slope range at high anatase/rutile ratios close to 90wt% anatase.

In any case, even though the values obtained are not of highest accuracy they still provide an estimate about the crystallinity of TiO_2 catalyst samples, confirming thus

observations made from looking at the XRD spectra. The still broad peaks might indicate that the crystalline regions were relatively small and are discontinuous. This might explain why even after thermal treatment the aerogel's mechanical strength (judged from visual observation) did not increase. Even though the heat-treatment did increase the fraction of crystallinity the created crystalline regions, however, were still broken up by amorphous regions. In order to increase the mechanical strength, in addition to the photocatalytic activity, a long-range crystalline would be desired.

Sample	Sample Sample weight, g	added Rutile weight, g	added Rutile wt%	Intensity Ratio, I_A / I_R Run 1	Run 2	Run 3	I_A / I_R average	Standard deviation, I_A / I_R stdev	from graph anatase wt%	rutile wt%	Factot to find actual anatase	actual anatase wt%
T36_raw	0.0239	0.0041	14.6	1.10	1.11	1.25	**1.16**	0.07	40	60	0.67	**11**
T36_150	0.0202	0.0065	24.3	1.02	1.07	0.98	**1.02**	0.04	34	66	0.52	**17**
T36_450	0.0206	0.0120	36.8	1.93	2.27	2.56	**2.25**	0.26	61	40	1.53	**69**
T36_550	0.0313	0.0059	15.9	6.62	6.69	7.09	**6.80**	0.20	83	17	4.88	**92**
T36_1.2wt%Pt	0.0140	0.0034	19.5	2.90	3.13	2.43	**2.82**	0.29	65	35	1.86	**45**
T36_3.5wt% Pt	0.0654	0.0108	14.2	4.39	4.51	4.47	**4.46**	0.05	76	24	3.17	**52**
T36_7.7%Pt	0.0248	0.0043	14.8	3.70	2.87	3.21	**3.26**	0.34	70	30	2.33	**40**
CEH6_raw	0.0211	0.0036	14.6	0.91	0.92	1.05	**0.96**	0.06	34	66	0.52	**9**
CEH6_450	0.0193	0.0045	18.9	3.17	2.21	2.73	**2.70**	0.39	68	32	2.13	**50**
P25_raw	–	–	–	3.64	3.36	4.47	**3.82**	0.47	73			**73**
P25_after react	–	–	–	3.60	3.73	3.94	**3.76**	0.14	72			**72**
P25_1.2%Pt	–	–	–	3.38	3.98	3.90	**3.75**	0.26	72			**72**
P25_550	–	–	–	1.55	1.58	1.50	**1.54**	0.03	52			**52**

Table 4-3 Data to determine weight percent anatase in catalyst samples

4.2.7 Laser Gravimetry

The particle size distributions seen in Figure 4-38 show the distributions for the untreated low-density TiO_2 aerogel samples CEH4, CEH6, the ultra-low density aerogel T36, and the binary aerogel TS31b. The three pure TiO_2 aerogels had similar distributions with two distinguished major accumulations of particle sizes one ranging from 1 to 30 μm with a maximum around 5 μm and another ranging from 80 to 200 μm in diameter with a maximum at 150 μm. All three titanium dioxide aerogels consisted

primarily of particles smaller than 20 μm, with only a small fraction (10-15%) of larger particles of a size around 100 μm. The ultra-low density T36 had the least amount of large particles with about 7% large than 50 or 4% larger than 100 μm compared to 20% larger than 50 or 15% larger than 100 μm for the low density aerogel CEH6 as seen in Figure 4-39. The binary aerogel had also a binary particle size distribution, however, with a significantly larger fraction of large particles. Only 20% of all particles were smaller than 20 μm. Approximately 50% of the TS31b particles were larger than 50 μm, with still more than 35% of all particles larger than 100 μm. Heat treatment to 450°C for six hours resulted in a drastic change in particle size distribution. Almost no particles larger than 100 μm remained in the aerogel samples as it can be seen in Figure 4-40.

The maximum at the small particle size had disappeared for all gels except for T36. Only 33 % of all particles were less than 10 μm while 50% of all particles were between 20 and 100 μm for the low-density gels CEH4 and CEH6 as shown in Figure 4-41. Likewise for the binary aerogel, 75% of all the particles were between 20 and 100 μm. Only the ultra-low density aerogel did not change its particles size to larger values after thermal treatment. More than 93% of all particles were less than 20 μm with the remainder of particles not exceeding a diameter of 65 microns. Figure 4-42 illustrates again how the particle size distribution had considerably changed for the aerogels CEH4, CEH6, and TS31b after thermal treatment. The ultra-low density aerogel T36, in contrast, shifted only the distribution within the small range of particles below 20 microns.

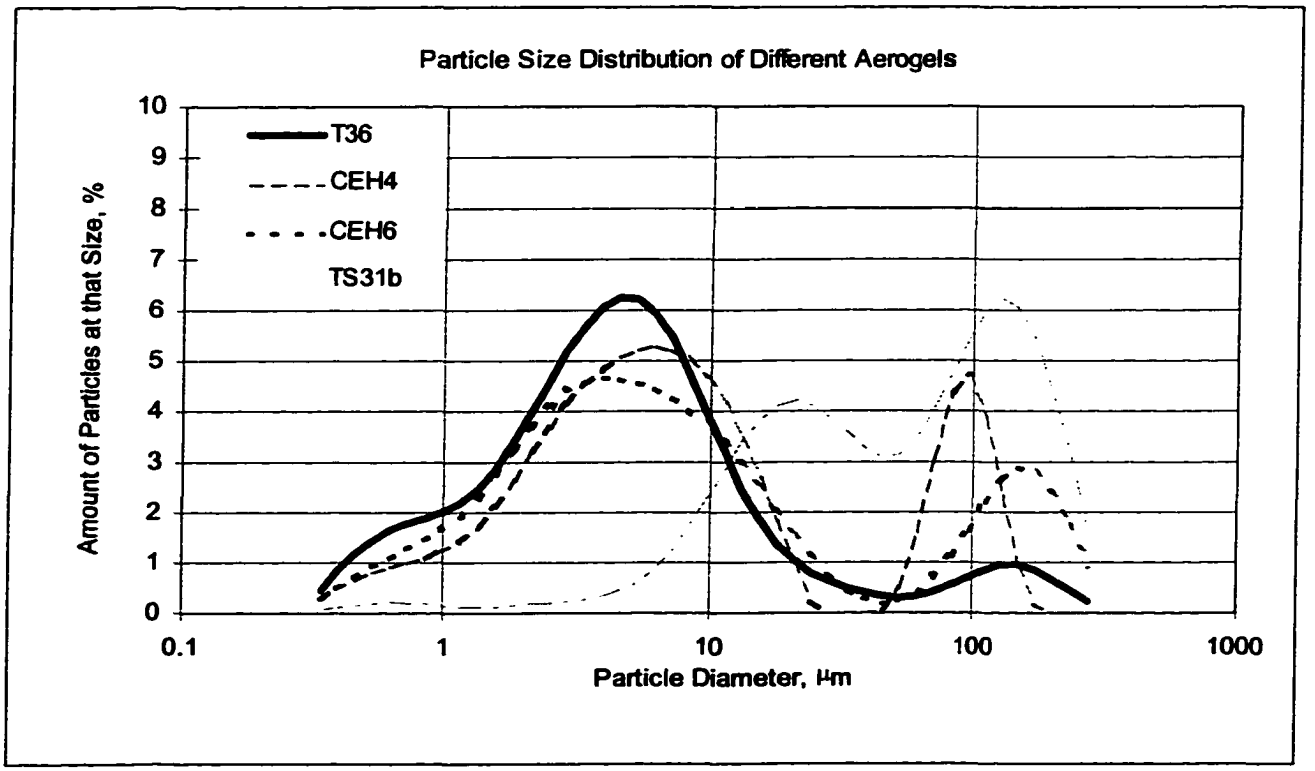

Figure 4-38 Particle size distribution of untreated TiO_2 aerogels

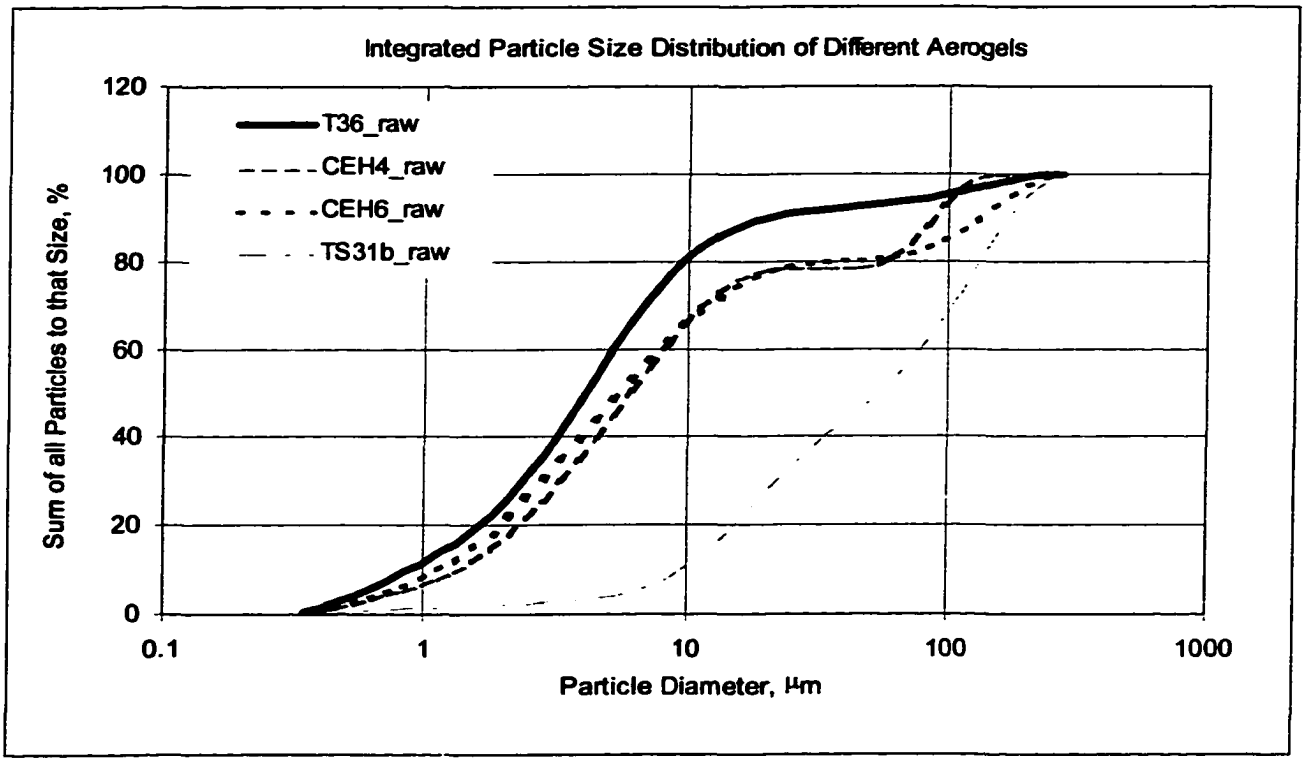

Figure 4-39 Integrated particle size distribution of untreated aerogels

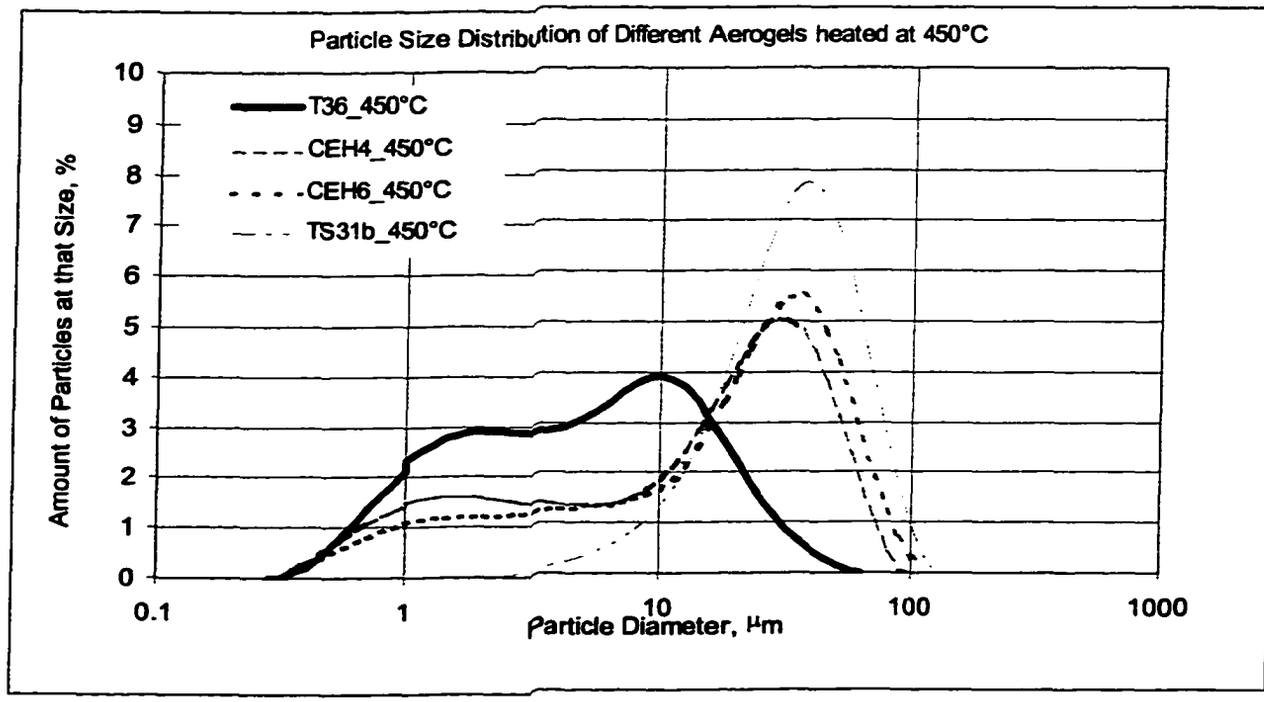

Figure 4-40 Particle size distribution of heat-treated TiO_2 aerogels at 450°C for 6 hours

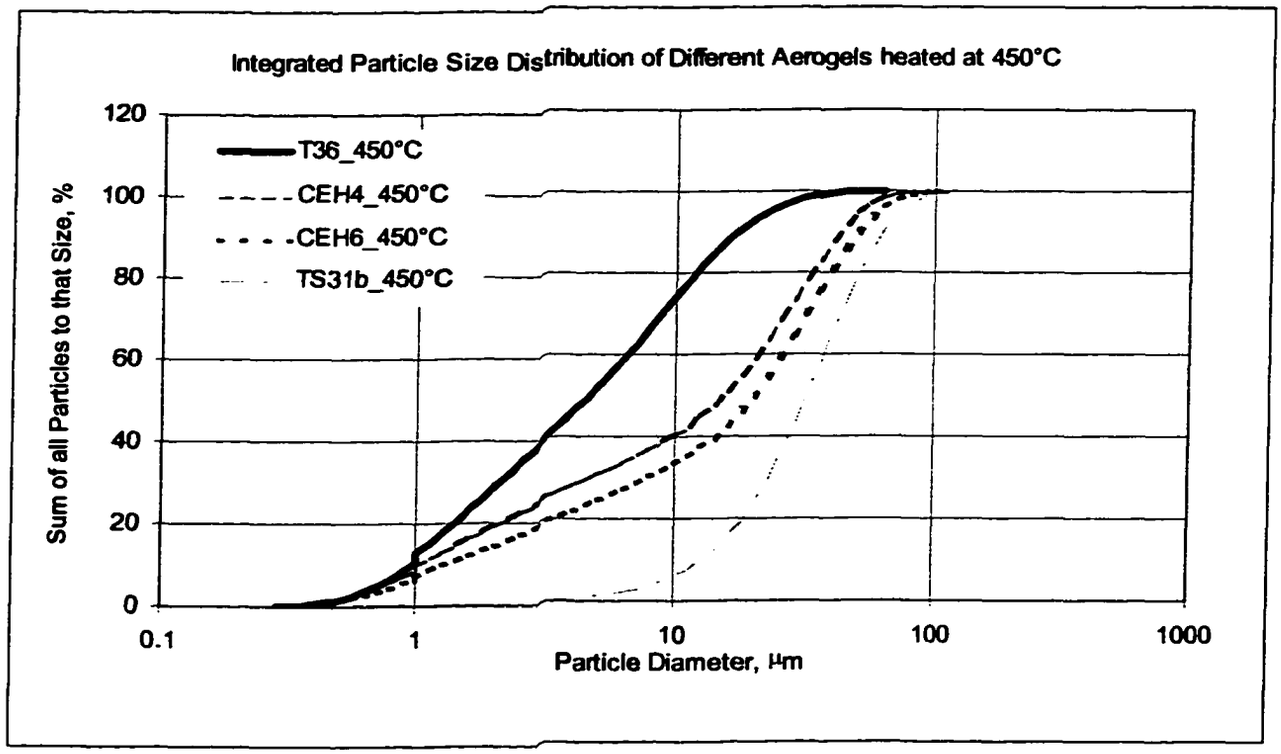

Figure 4-41 Integrated particle size distribution of heat-treated aerogels at 450°C for 6 hours

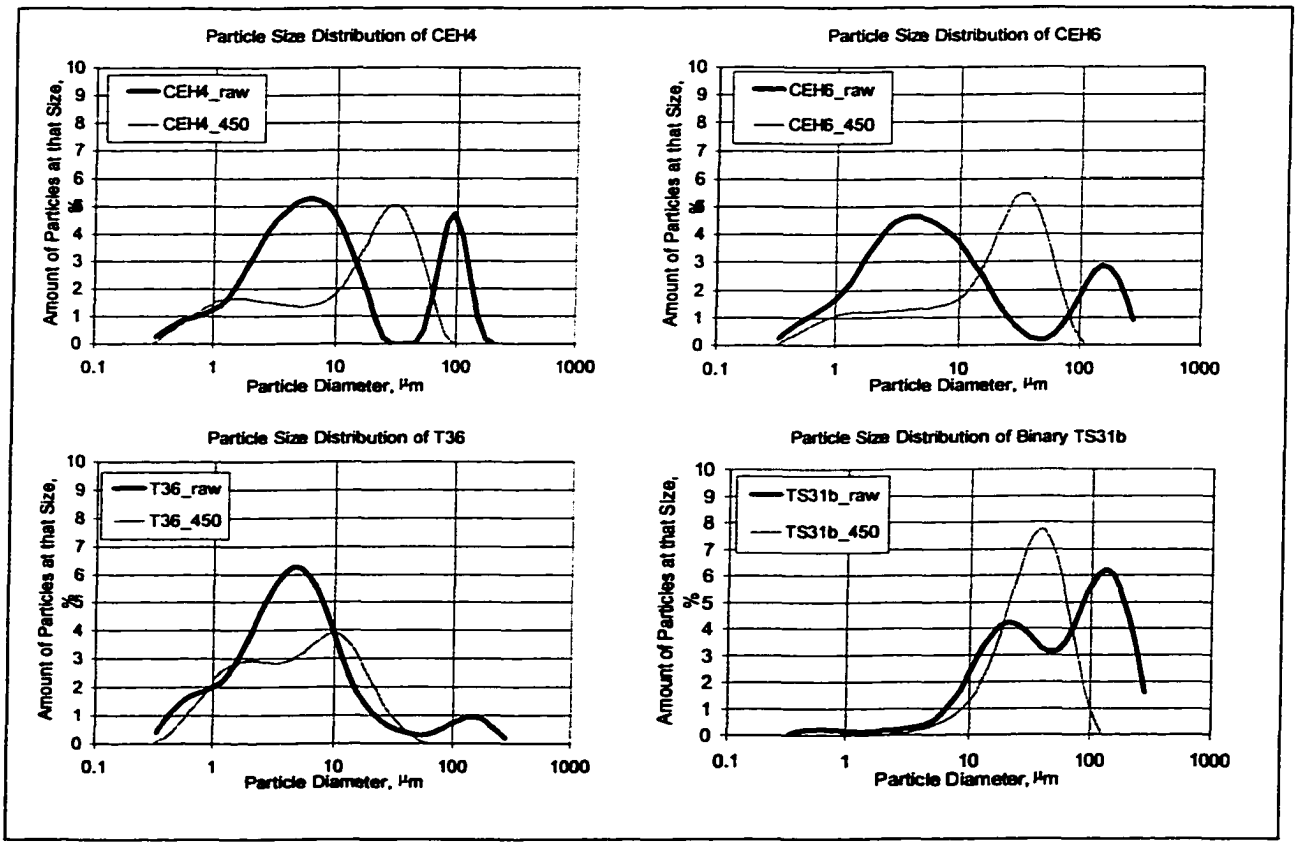

Figure 4-42 Comparison of change in particle size distribution of aerogels CEH4, CEH6, T36, and TS31b

A different and perhaps more precise (but very tedious) method to determine the particle size distribution would be taking about 20-50 different TEM snapshots of a sample and counting the number of particles of different sizes. This type of analysis, however, was not performed at this time. Only a few TEM images were taken (see Chapter 4.2.8) to exemplify structure differences and particle sizes of the different catalyst samples

4.2.8 Transmission Electron Microscopy Images (4.2.8)

4.2.8.1 Pure Degussa, Aerogels CEH6 and T36, and Binary Aerogel TS31b

The TEM photographs for Degussa P25 and the aerogels T36 and CEH6 (untreated and thermal treated to 450°C) are shown in Figures Figure 4-43 through Figure 4-45. The crystalline structure can clearly be seen for the Degussa P25 (Figure 4-43). XRD graphs and calculations (Chapter 4.2.6) had revealed that the aerogels did show some anatase crystallinity but were mostly amorphous. Therefore, when looking at the TEM images most of the regions observed did not show any crystalline structure. However, in some areas a few crystalline structures were visible (circled areas in top pictures of Figure 4-44 and Figure 4-45). When comparing the surface structure of the aerogels to the one of Degussa it was obvious that the crystal size of both aerogels were remarkably smaller (around 2-5 nm compared to about 20-30 nm for P25). After heating of the aerogel the crystal size of the T36 had increased to almost the same size of the Degussa while the increase in crystal size of the heat-treated CEH6 was not as significant (approximately around 10 nm). Both heat-treated aerogel samples, however, showed a remarkable increase in crystallinity. Most regions observed under the microscope showed crystalline structures as it can be seen from looking at the bottom photograph in Figure 4-44 and Figure 4-45. The binary aerogel TS31b, in contrast, showed already no anatase or rutile peak in the XRD spectra. Accordingly, none of the regions observed under the TEM microscope showed crystallinity (Figure 4-46). Heating to 450°C did not change the structure of the TS31b at all as seen in the bottom photograph of Figure 4-46. Only one small area seemed to show any crystallinity (circled area).

Figure 4-43 TEM photograph of Degussa P25

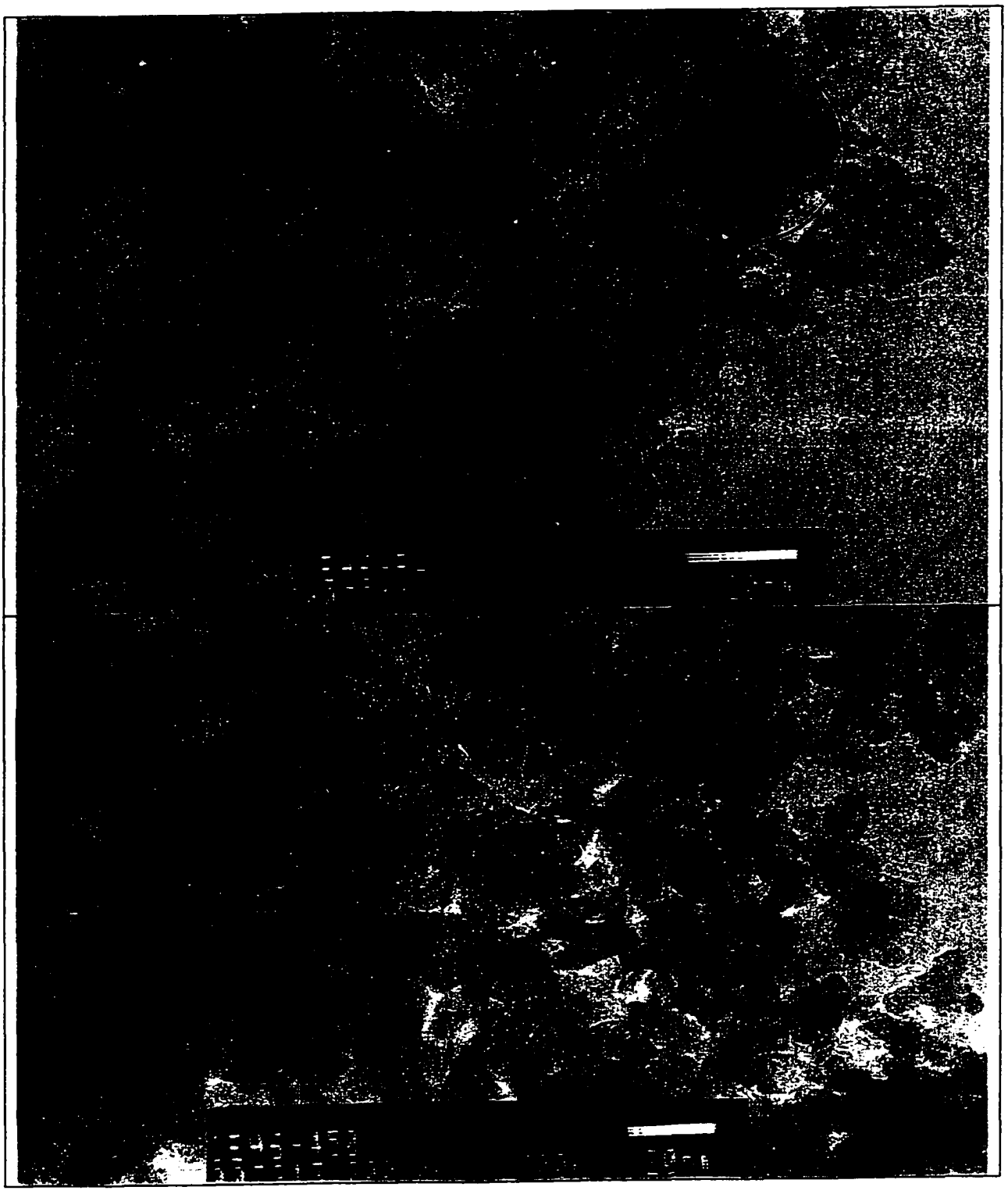

Figure 4-44 TEM photograph of low aerogel CEH6 untreated (top) and heated to 450°C (bottom)

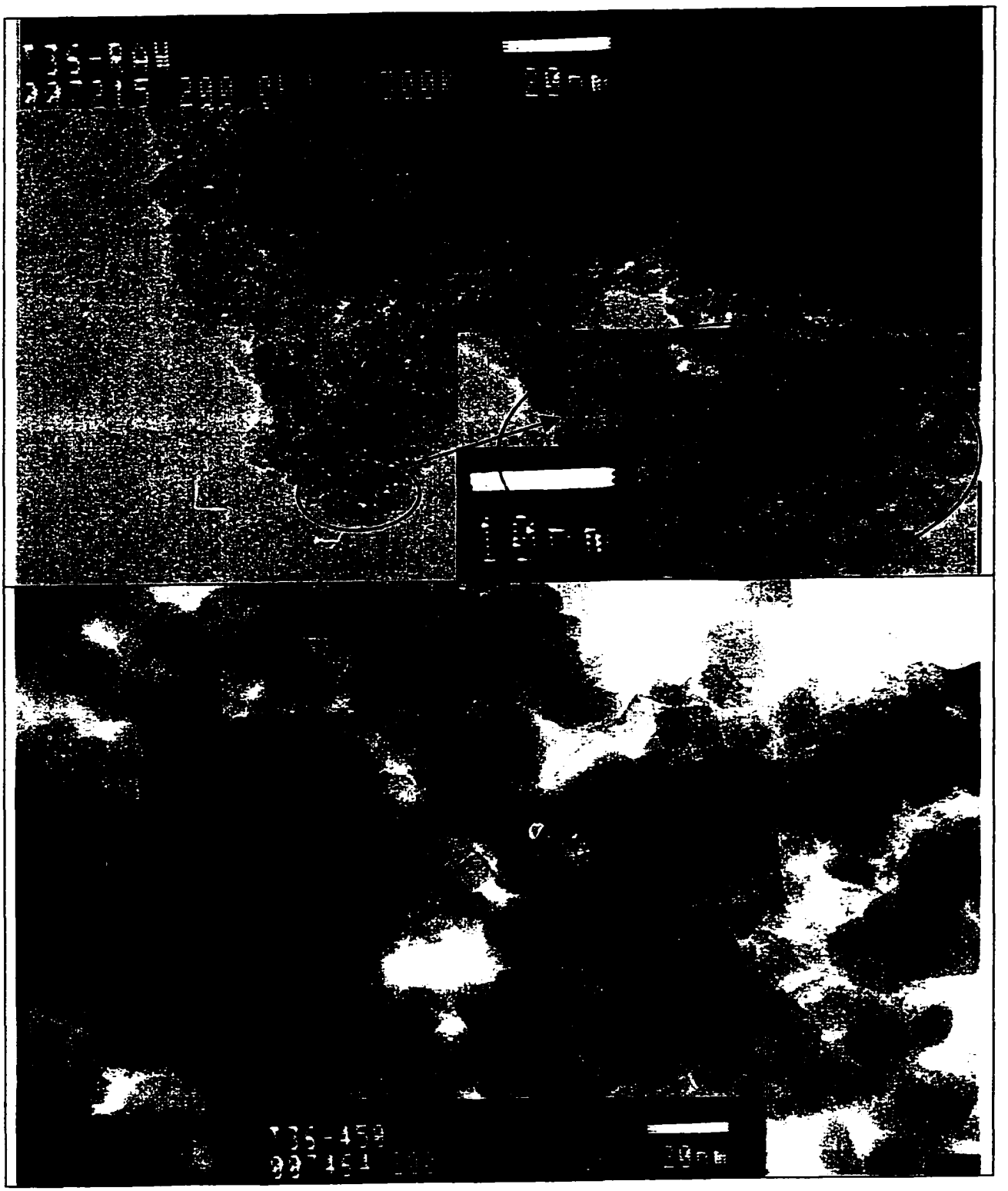

Figure 4-45 TEM photograph of ultra-low aerogel T36 untreated (top) and heated to 450°C (bottom)

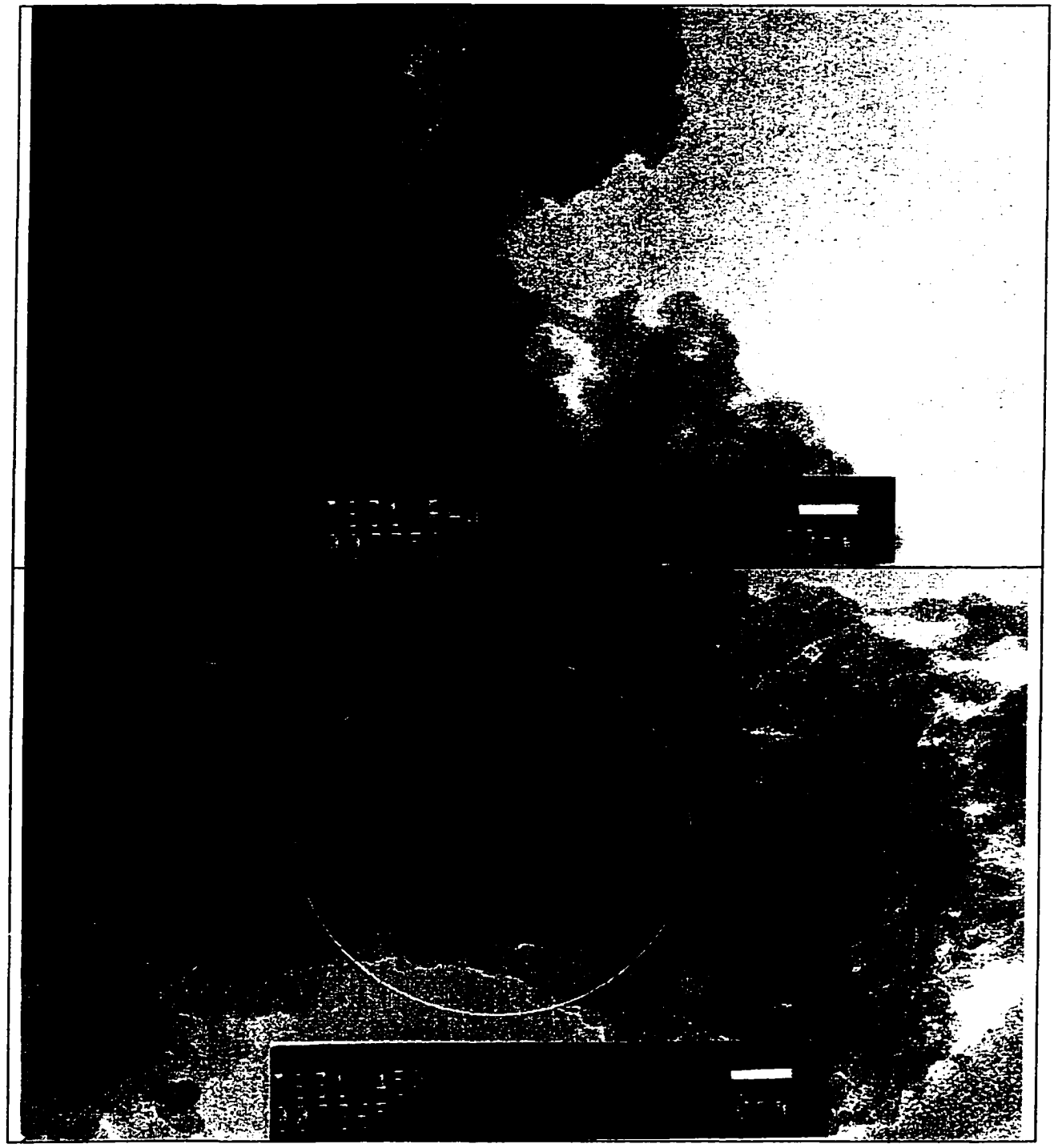

Figure 4-46 TEM photograph of binary aerogel TS31b untreated (top) and heated to 450°C (bottom)

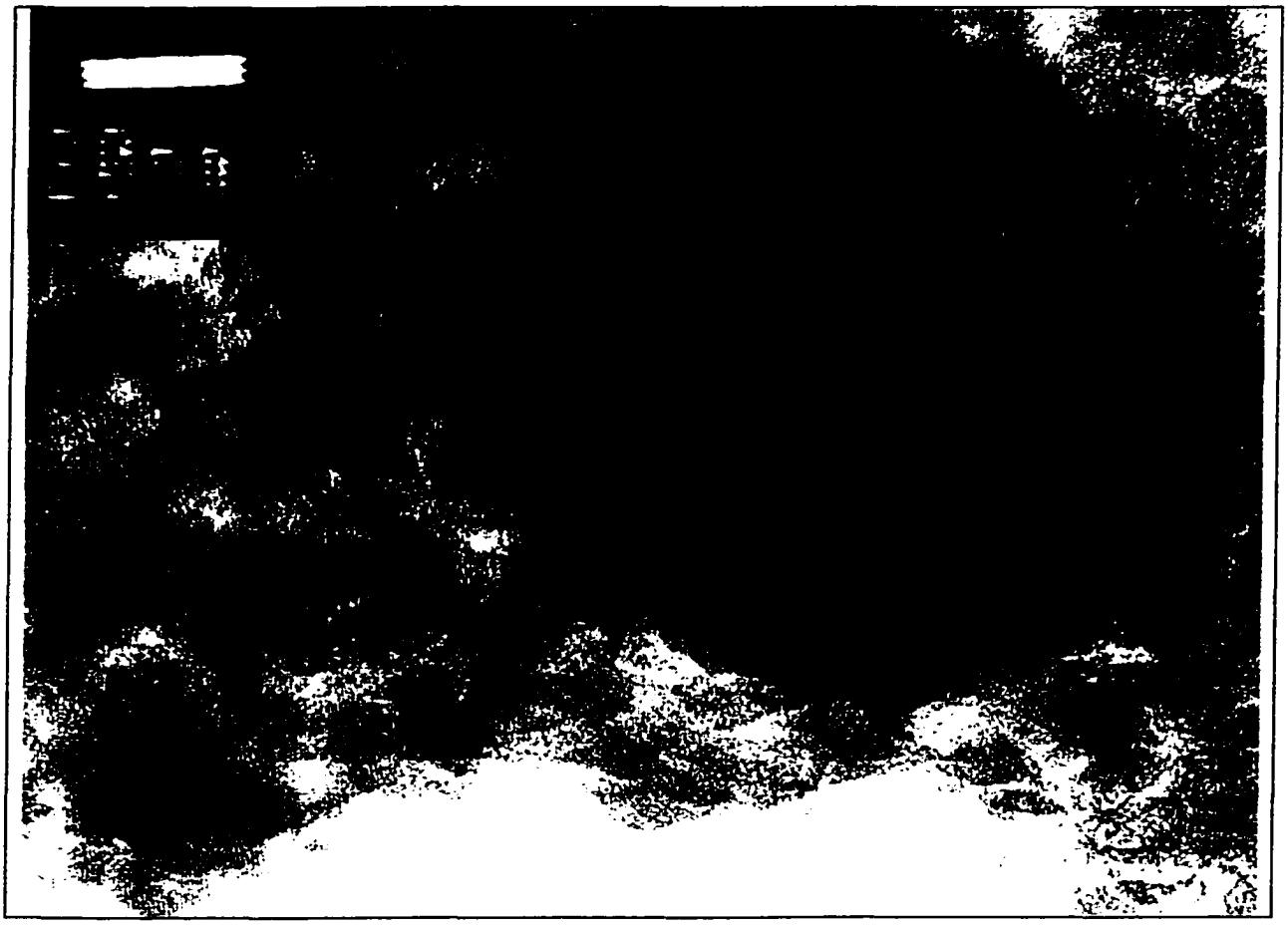

Figure 4-47 Enlarged image of circled area of TEM photograph of binary aerogel TS31b heated to 450°C in Figure 4-46 (bottom)

4.2.8.2 Platinum Deposited Catalysts Degussa P25 and Aerogel T36

A TEM photograph of Degussa with 0.5wt% platinum deposited via photo co-deposition (see Chapter 3.1.5.1) is seen in Figure 4-48 and shows an even distribution of platinum clusters across the surface of the catalyst. The same observation was made for 0.1 and 3wt% platinum. The case was different for the platinum deposited Degussa samples prepared via chemical vapor deposition. Platinum clusters were not observed at all places of the material. However, the regions that were found to have platinum clusters had a uniform coverage of small, well-distributed Pt clusters (Figure 4-50 to

Figure 4-52). Of all three samples, the one with 1.2wt% of platinum showed the most uniform platinum coverage of the catalyst surface.

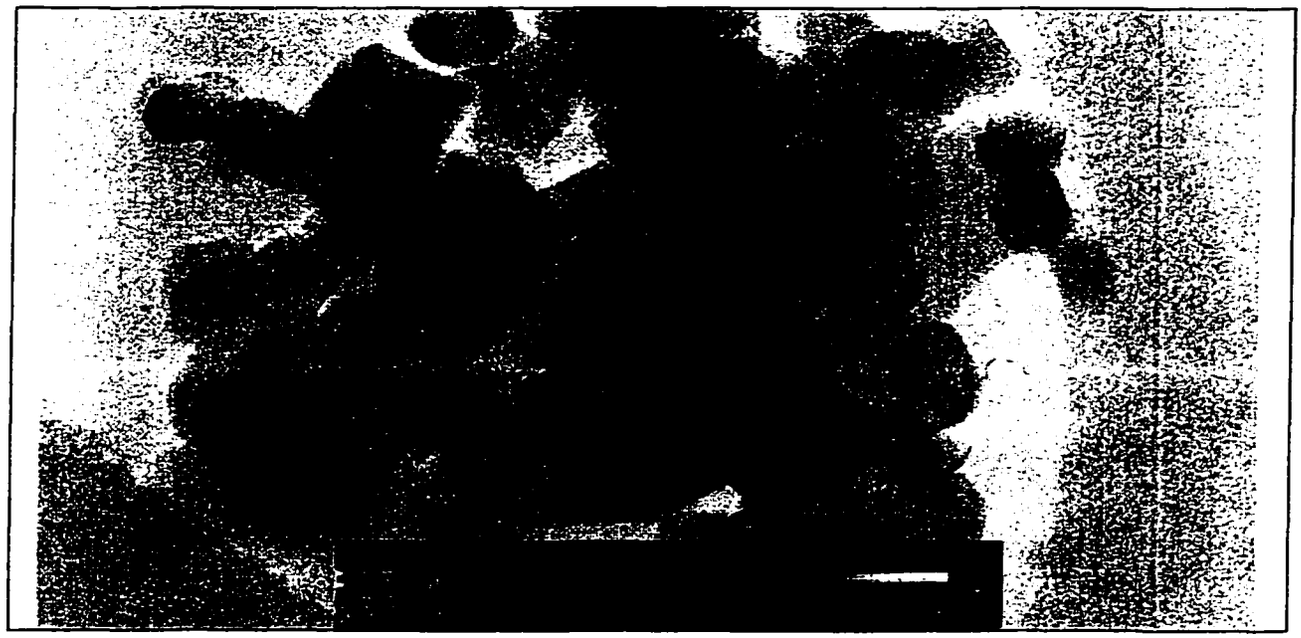

Figure 4-48 TEM photograph of Degussa P25 with 0.1wt%Pt (impregnation)

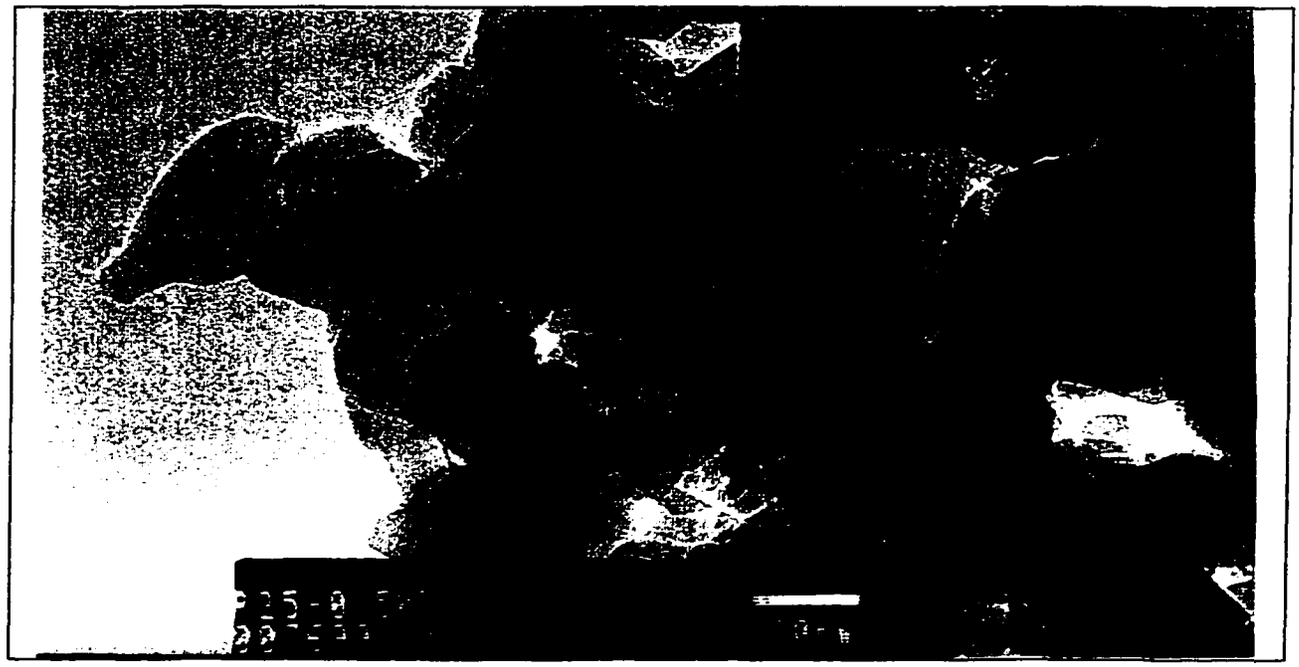

Figure 4-49 TEM photograph of Degussa P25 with 0.5wt%Pt (impregnation)

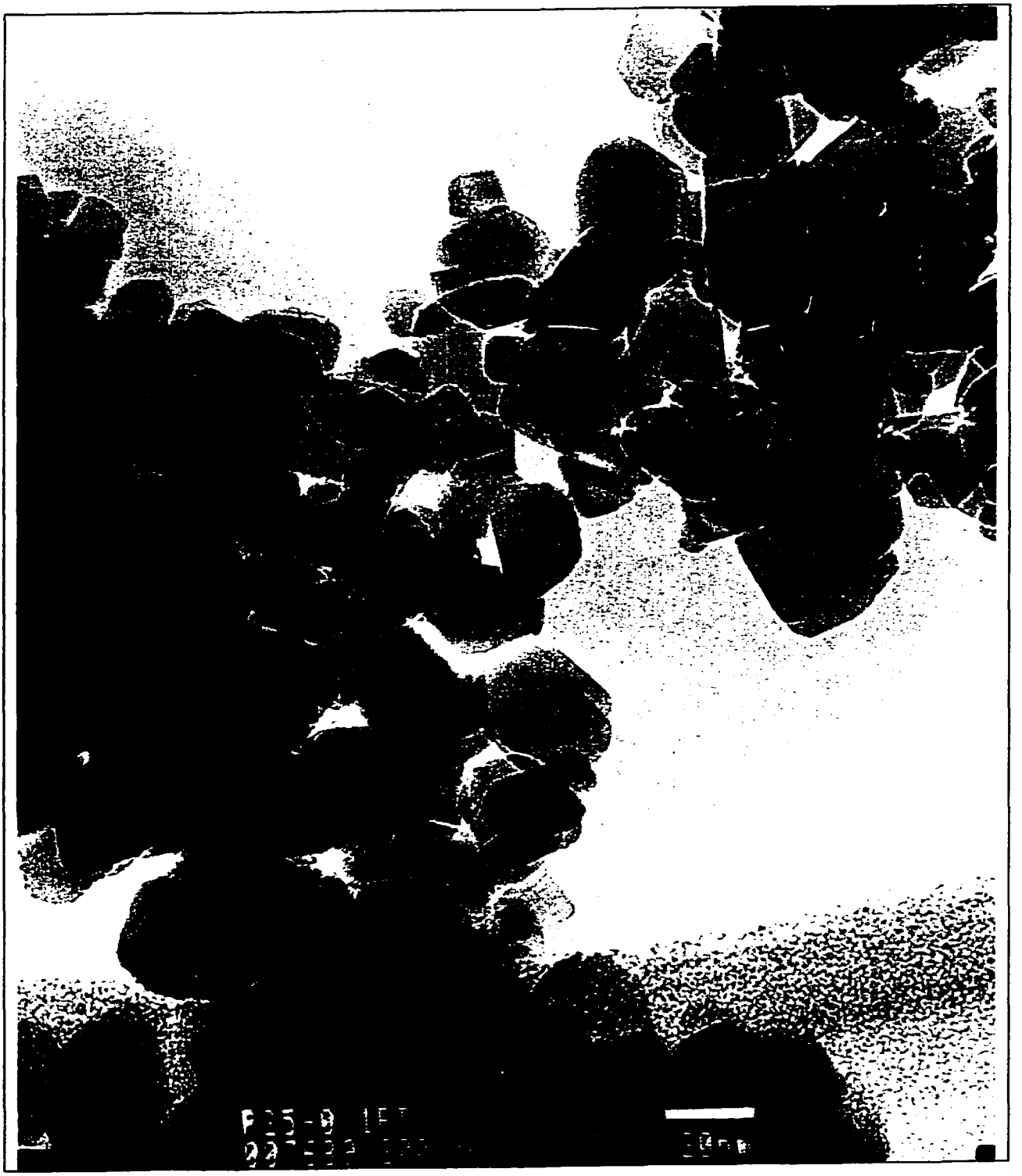

Figure 4-50 TEM photograph of Degussa P25 with 0.1wt%Pt (CVD)

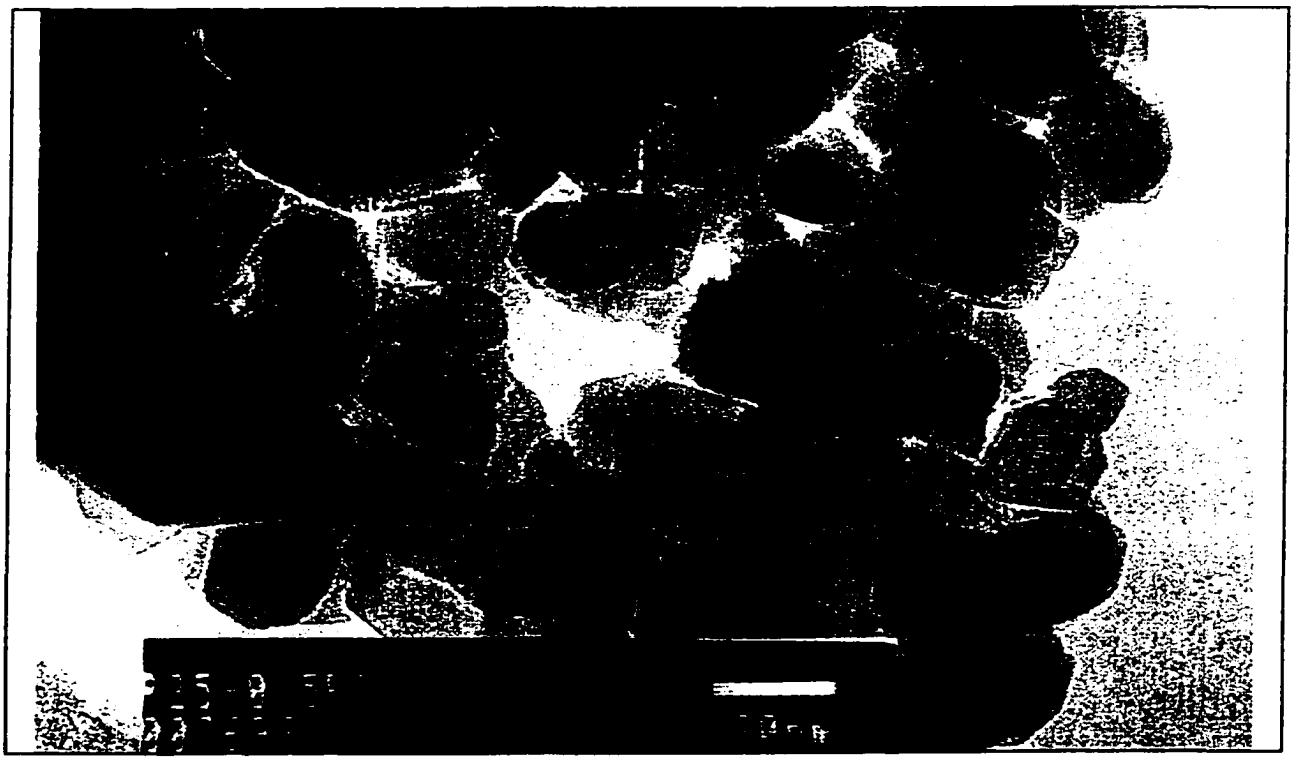

Figure 4-51 TEM photograph of Degussa P25 with 0.5wt%Pt (CVD)

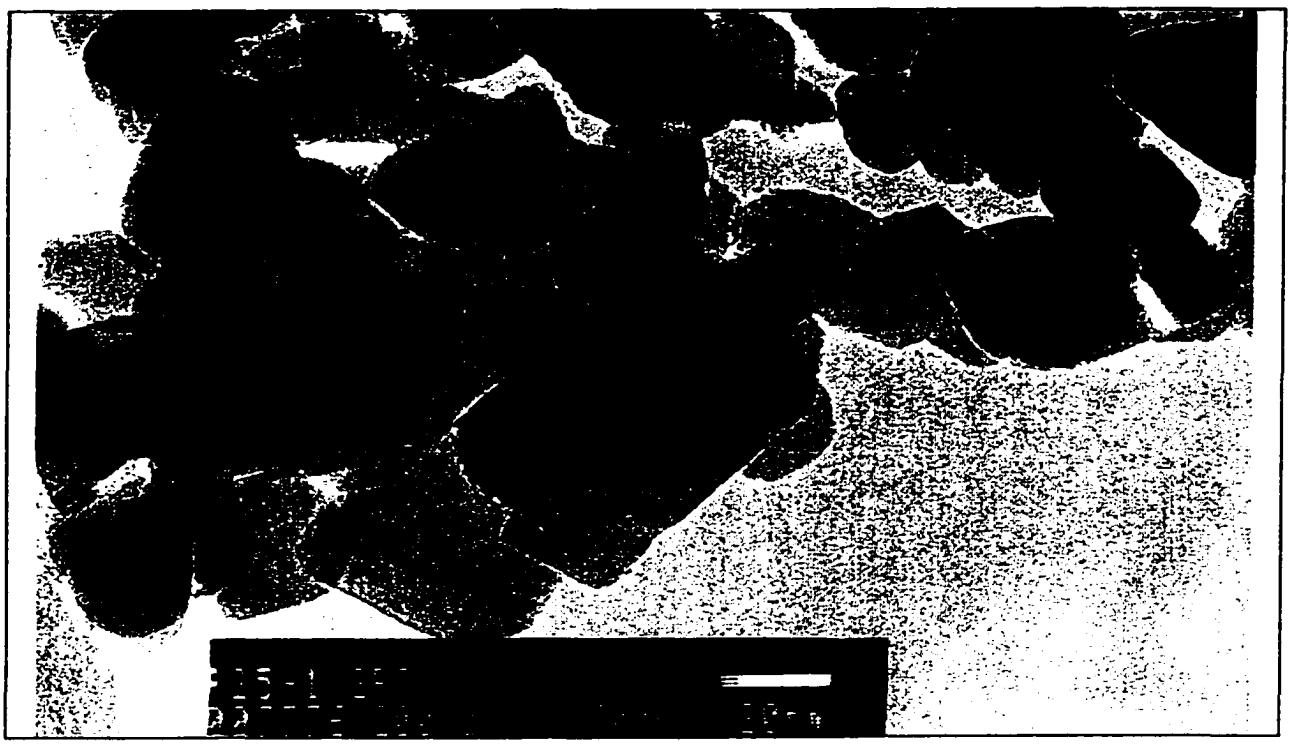

Figure 4-52 TEM photograph of Degussa P25 with 1.2wt%Pt (CVD)

Since the particle size of the aerogel T36 was small (ranging approximately from 2 to 5 nm) it was difficult to see the platinum clusters on the TEM images of the T36 sample with 1.2wt% platinum. However, looking at Figure 4-53 one can recognize the platinum as small dots mostly located on the right site of the photograph. Similarly to the Degussa P25, the CVD procedure did not uniformly cover the aerogel surface.

A sample of T36 with 3.5wt% platinum was prepared by stepwise addition of the platinum. First, 1.2wt% Pt was deposited using CVD, then a second CVD procedure followed to obtain a final platinum concentration of 3.5wt%. Figure 4-54 illustrates the T36 sample with 3.5 wt% Pt. Remarkably, parts of the material showed larger particle sizes close to the size of Degussa even though the same procedure was followed as during the first step. This was also the case for a second prepared sample of T36_3.5wt% Pt as seen in Figure 4-55. Even though it was found that the aerogel was relative stable at temperatures up to 185°C (see Chapter 4.2.1) it is possible the heating procedure (150°C for pre-calcination before CVD and 180°C for platinization – see Chapter 3.1.5.3) applied to the catalyst for a second time might have caused the TiO_2 particles to grow in size. As already seen with the T36, when heated to 450°C the particle size increased appreciably. Therefore, even though the temperature did not exceed 185°C, a prolonged heating might have caused the change in particle size of the T36_3.5wt% Pt samples.

The particle size of the aerogel sample with 7.7wt% Pt also increased slightly after the CVD procedure. However, the increase was not as extensive as with the T36_3.5wt% Pt sample. In addition, the sample with 7.7wt% Pt displayed a more

uniform size of the TiO_2 particles. It was furthermore observed that the platinum clusters were significantly larger compared to the Pt clusters on all samples with lower Pt concentration. Different in the preparation of the previously discussed samples was that the amount of 7.7wt% platinum was deposited in one single CVD step. This must have led to an accumulation of larger platinum clusters, which can be seen in the superposed photograph taken at 500x resolution in the upper part of Figure 4-56. This is in agreement with the findings by Vorontsov et al.[103]. They were able to determine from acetone thermal oxidation test over TiO_2 with varying amounts of platinum (CVD deposited) that an increasing platinum content led to an increase in the size of the platinum particles instead in an increase in the number of particles. If the size of the particle remained the same and only the number of platinum particles increased with increasing platinum content then the reaction rate would be directly proportional to the platinum concentration. However, if only the size of the Pt particles increased but the number of particles remained the same then the reaction rate would be proportional to the Pt-concentration to the power of 2/3. An equivalent calculation was performed as described later in Section 4.7.2 confirming an increase in platinum particle size.

Figure 4-53 TEM photograph of aerogel T36 with 1.2wt%Pt (CVD)

Figure 4-54 TEM photograph of aerogel T36 with 3.5wt%Pt (CVD)

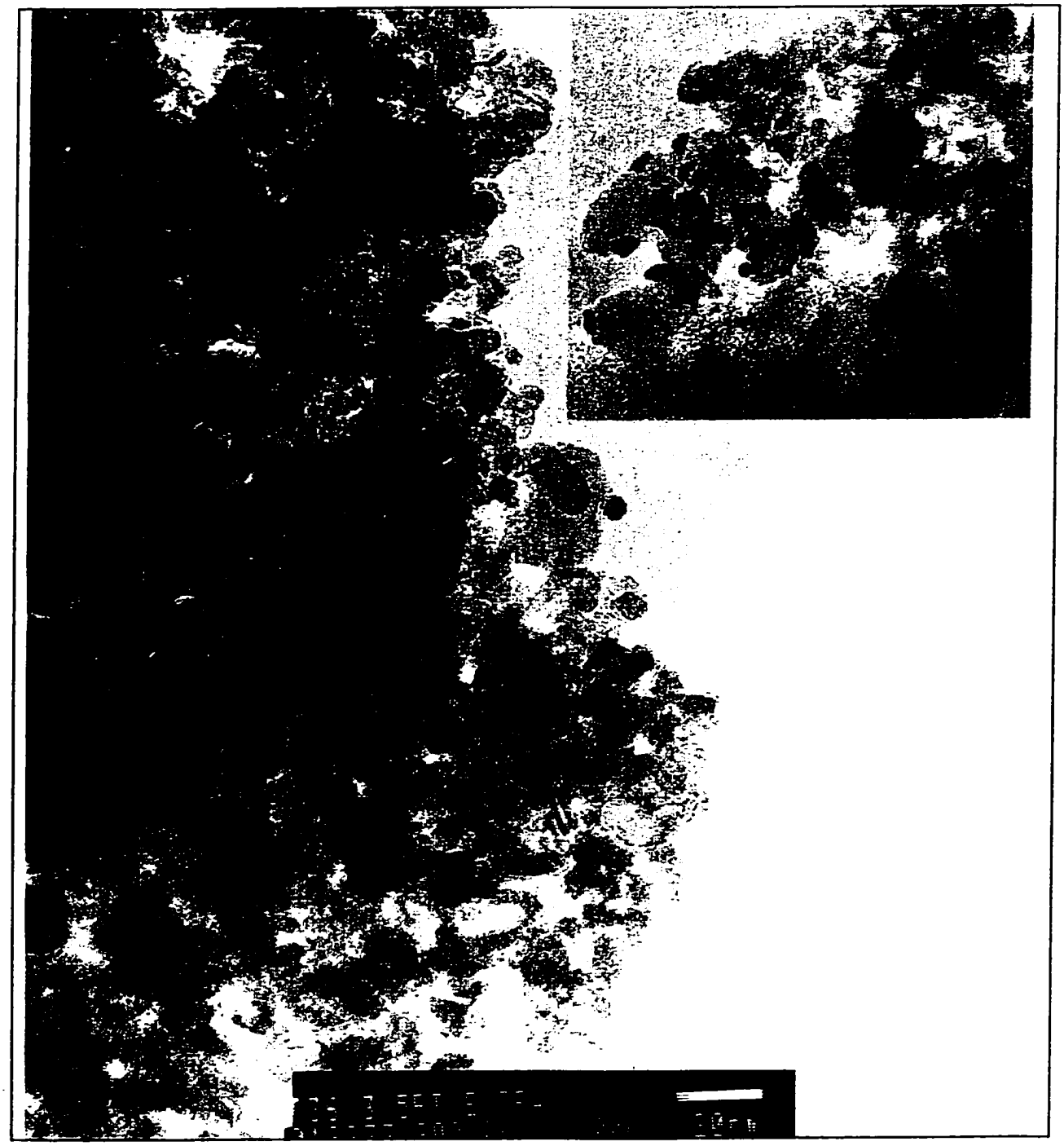

Figure 4-55 TEM photograph of aerogel T36 with 3.5wt%Pt (CVD), repeated sample

Figure 4-56 TEM photograph of aerogel T36 with 7.7wt%Pt (CVD)

4.3 Investigation of UV Transparency of TiO_2-Catalysts

4.3.1 UV Penetration into Pure Titanium Dioxide

First, the catalyst bed packing density was determined as described in Section 3.3.3. The densities for Degussa P25 and the aerogels CEH6 and T36 are summarized in Table 4-4. Then, the UV transmittance was determined as outlined in Section 3.3.4. The results of the UV measurements is pictured in Figure 4-57 and illustrates the UV transmittance through different aerogel catalysts and Degussa P25 dependent on the mass of catalyst in the prepared agar gel.

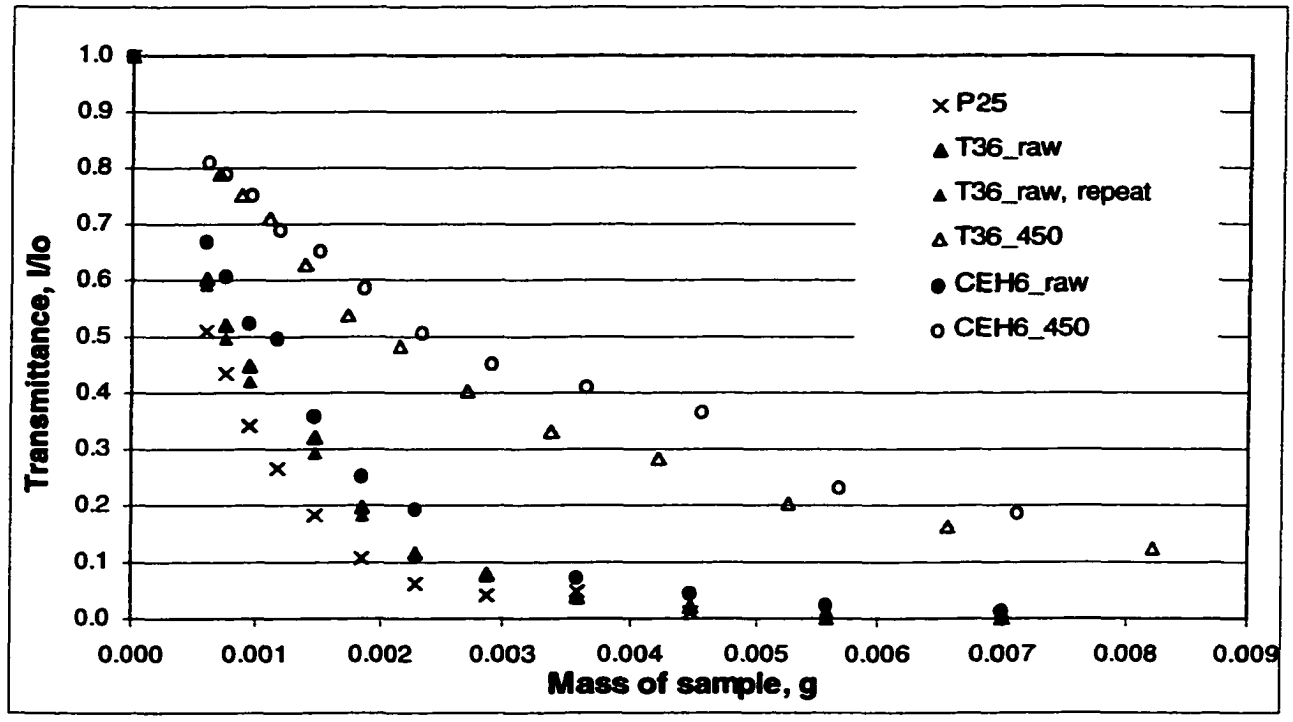

Figure 4-57 UV Transmittance of P25 and different aerogels dependent on catalyst mass distributed in the agar gel

Catalyst	Mass of catalyst, g	Volume of catalyst, ml	Density of catalyst, g/cm^3
Degussa P25	0.254	0.50	0.51
T36_raw	0.071	0.55	0.13
T36_450	0.152	0.57	0.27
CEH6_raw	0.079	0.65	0.12
CEH6_450	0.098	0.38	0.26

Table 4-4 Data to determine the packing density of catalyst materials

The data show that the UV transmittance through an agar gel layer loaded with Degussa P25 reduced very rapidly with increasing mass of catalyst. The absorption decreased also quickly for the aerogels T36 and CEH6, however the decrease was slower. For example, 50% of the UV light was absorbed by a gel sample containing 6 mg of Degussa whereas 8 and 12 mg of T36 and CEH6, respectively, were needed to absorb 50% of the UV light. The slower decrease was more significant for the aerogels that had been heat-treated to 450°C. More than 20 mg of the heat-treated aerogel was necessary to absorb 50% of UV light.

Since the densities of the different catalysts varied, the volume of catalyst dispersed within the agar gel varied also considerably. The density of Degussa was nearly twice that of the untreated aerogel; therefore accordingly more volume of aerogel catalyst (about twice as much) was added to the initial solution during the agar gel preparation. Taking the density of the catalyst into account, as well as the dimensions of the gel sample, the actual catalyst bed thickness of each sample without the agar gel was calculated. Comparing the UV transmittance on the basis of catalyst bed layer thickness revealed the difference in UV transmittance between the Degussa P25 and the aerogels

more clearly. The transmittance dependence on catalyst layer thickness is shown in Figure 4-58.

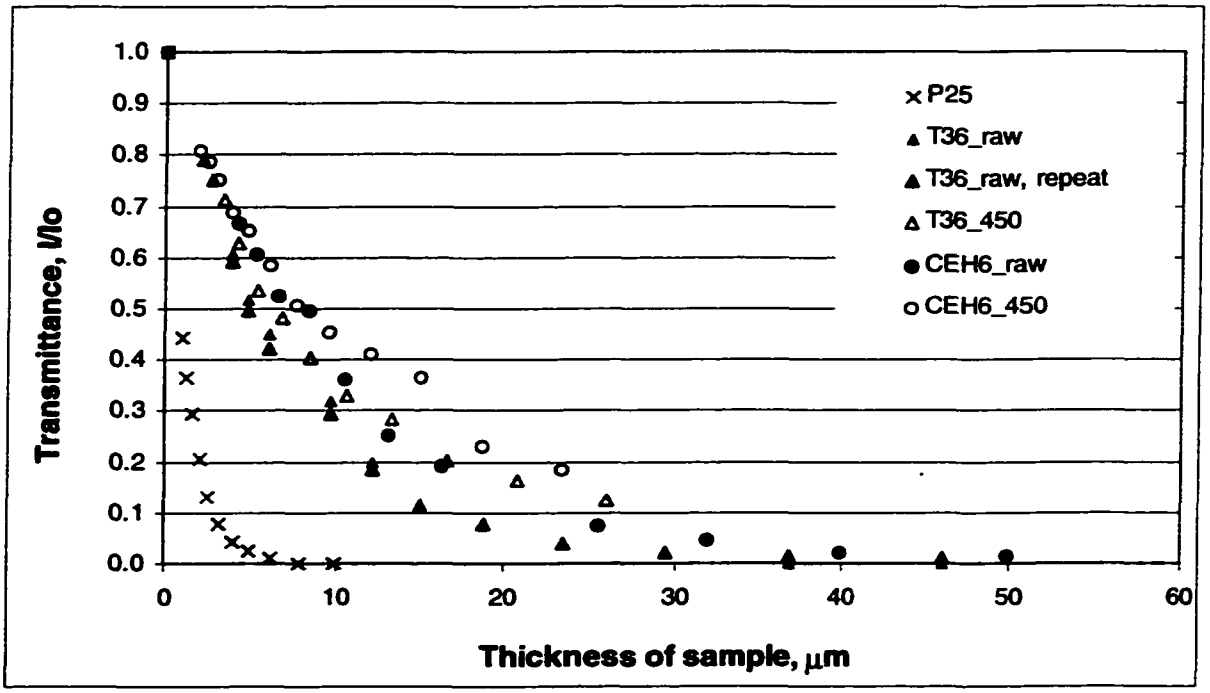

Figure 4-58 UV Transmittance of P25 and different aerogels dependent on catalyst layer thickness without the agar gel

At about 10 μm the UV transmittance for P25 was essentially zero whereas the aerogel samples still transmitted light through a catalyst bed of up to 50 μm deep as illustrated in Figure 4-58. Figure 4-59 and Figure 4-60 depict the UV absorbance dependence on catalyst mass and catalyst bed thickness. In these illustrations the difference of Degussa P25 and the aerogel is more clearly demonstrated.

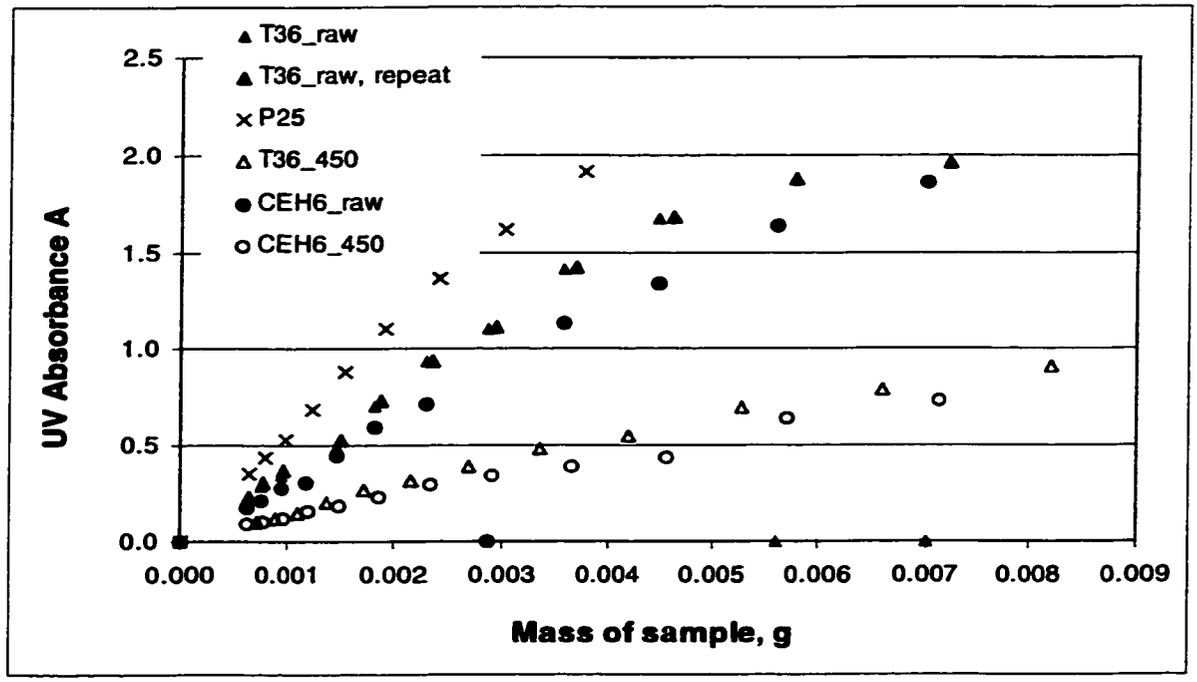

Figure 4-59 UV absorbance of P25 and different aerogels dependent on catalyst mass in agar gel sample

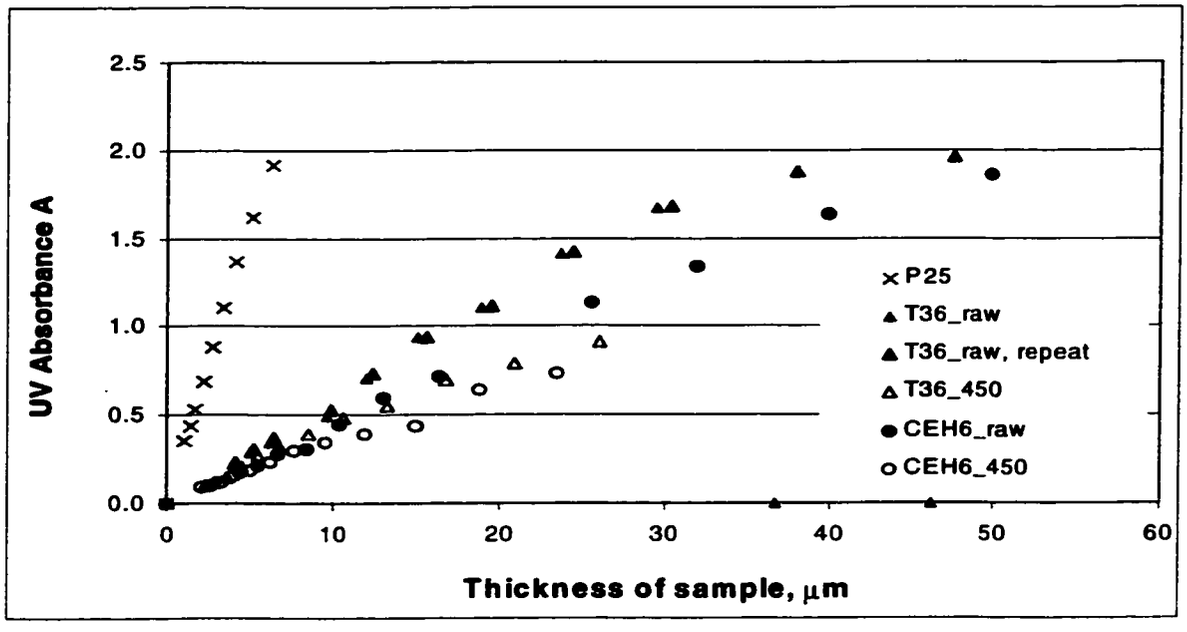

Figure 4-60 UV absorbance of P25 and different aerogels dependent on catalyst layer thickness without the agar gel

All aerogel samples showed a higher UV penetration through the catalyst layer compared to that of Degussa. Furthermore, the heat-treated samples showed the lowest UV absorbance at any specific catalyst weight or catalyst bed thickness, thus showing that UV light is allowed to penetrate deeper into the catalyst bed. These findings support the trend estimated from UV penetration depth calculations of Equation (2-7). Table 4-5 summarizes the so calculated values of penetration depth as a function of porosity. The porosity was determined using pore volume data obtained from BET measurements and Equation (4-1).

$$\varepsilon = \frac{m_c V_g}{m_c V_g + \frac{m_c}{\rho_{skeletal}}} \quad \text{(adapted from Hill}^{117}\text{)}, \tag{4-1}$$

where m_c = mass of catalyst in g, V_g = void volume in cm^3/g, and $\rho_{skeletal}$ = true density of the bulk solid. The density was assumed to be 3.84 g/cm^3 according to the density of nonporous anatase TiO_2[118]

Even though the experimental values did not coincide with the exact value of the predictions of Equation (2-7) (experimental values are approximately twice the values of the prediction), however, the order of magnitude of the increase in penetration depth for the experimental data are similar to the predicted values. The penetration depth determined from the experiment increased by the same factor as was predicted from calculations. The UV light penetrated four to seven times deeper into the porous aerogel than into Degussa P25.

It is still unclear what counted for the improved UV transmittance through a layer of heat-treated aerogel catalyst compared to the untreated aerogel. Possible explanations could be the difference in particle size as the heat-treated samples have a noticeably larger particle size compared to the untreated material as mentioned in Section 4.2.7 (Laser Gravimetry). However, tests on UV transmittance through 100% anatase material at different particle sizes have not supported this assumption. No obvious trend was observed when investigating anatase TiO_2 of 44 μm, 0.9 μm (Aldrich), and 0.2 μm (Acros) particle size as seen in Figure 4-61.

	P25	T36 raw	T36 450°C	CEH6 raw	CEH6 450°C
Mass of catalyst, g		0.1176	0.28555	0.1741	0.26505
BET surface area, m^2/g	47.8554	336.976	94.21305	303.7328	136.7987
Single Point Total Pore Volume of pores less than 900 Å at P/Po 0.98 cm^3/g	0.099407	0.814438	0.403491	1.409896	0.929909
Cumulative Pore Volume of pores between 17 and 3000 Å diameter cm^3/g	0.103209	0.861974	0.386739	1.487022	1.0027095
Porosity, %	0	80	61	84	78
Penetration depth, μm	4.5	22.8	11.5	28.9	20.6
Factor of increase in penetration depth compared to Degussa P25:		5	3	6	5

i

Table 4-5 Estimated penetration depth of UV light through different aerogels and Degussa P25

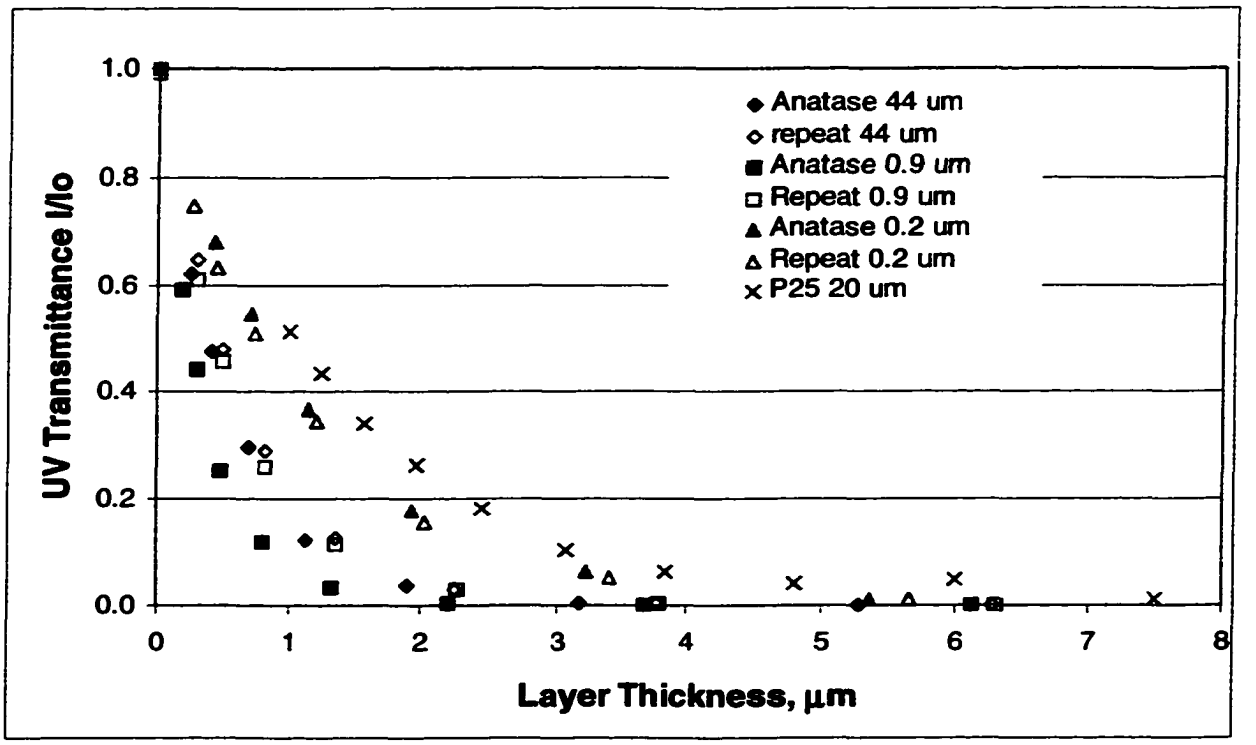

Figure 4-61 UV transmittance through TiO_2 layers of different particle size

Another possible reason for the difference in UV transmittance is the effect of light scattering. Platzer and Bergkvist investigated bulk and surface light scattering from transparent silica aerogels[119]. They reported that light scattering of the bulk depends on several aerogel properties such as porosity, mean free path within the pores, and geometrical building block shape of the particles. They also mentioned that among other factors the chemistry (e.g., solvent content) influences bulk scattering considerably. This would support the hypothesis that remaining organics and/or water on the surface of the untreated aerogels might contribute to a restricted UV penetration. In addition, they found out that the reflected light intensity depends largely on the roughness of the surface showing higher scattering on smooth surfaces. The scanning electron microscope images

of T36 and T36 heated at 450°C in Figures 6 and 7 verify that the surface of the heat-treated sample has become distinguishably smoother. With this smoother surface, reduced surface light scattering might also contribute to a deeper UV penetration into a packed bed.

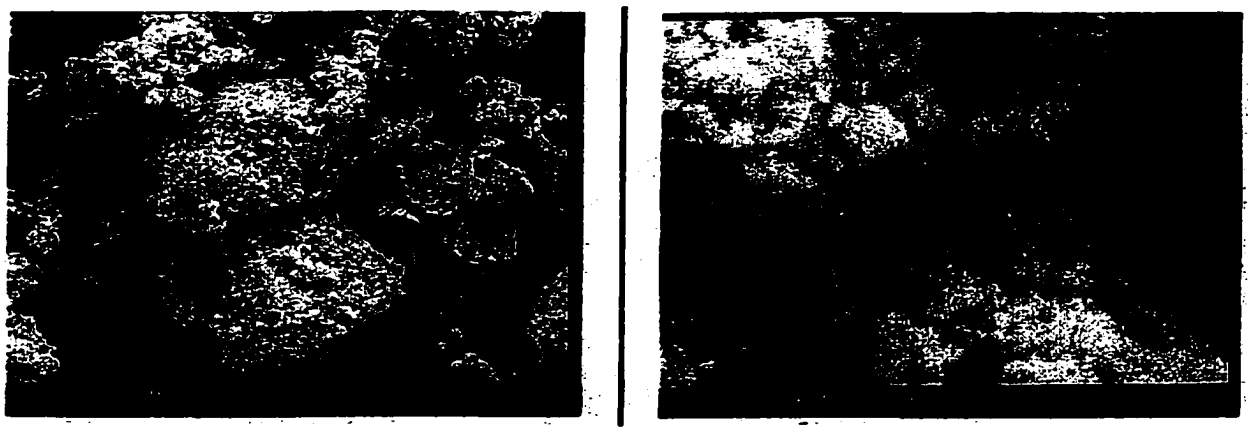

Figure 4-62 Scanning electron microscope images of untreated low density pure TiO_2 aerogel T36 at different magnifications

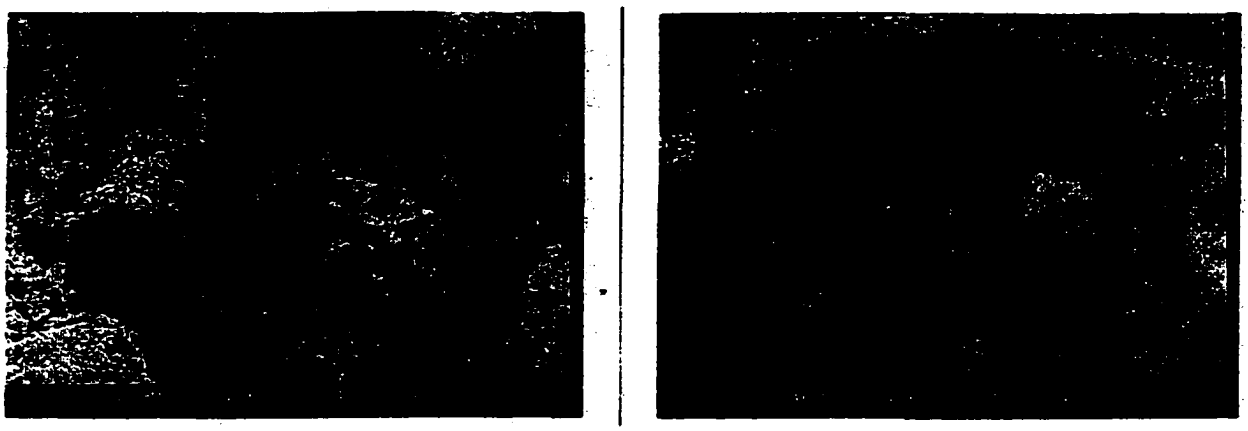

Figure 4-63 Scanning electron microscope images of heat-treated (450°C for 6 hours) low density pure TiO_2 aerogel T36 at different magnifications

4.3.2 UV Penetration into Platinum Deposited Titanium Dioxide

In order to find out if the platinum deposition has an influence on the light absorbance, the same experiments as above were performed. Table 4-6 summarizes the

data used to determine the packing density. The platinum deposition did not alter the packing density notably for the Degussa. The aerogel T36, however, showed an increase in density by 2-3 times. As already observed before (see Section4.2.8 Transmission Electron Microscopy Images), the heating process applied during the platinum deposition caused the gel structure to collapse, resulting in a loss of surface area as well as an increasing the density of the material.

As it can be seen in Figure 4-64, the platinum deposition did not alter the UV light absorption of Degussa P25 significantly. Since the density of P25 did not change after the platinum deposition there was no difference observed between the samples when evaluating the UV transmittance dependence on the catalyst layer thickness (Figure 4-65). Also when comparing the UV absorbance data in Figure 4-66, only a small difference could be noticed between the pure and the platinum deposited Degussa sample. Platinum deposition appeared to increase the UV absorbance slightly

Platinum deposited on Degussa P25				
	Mass of catalyst, g	Volume of catalyst, ml	Density of catalyst, g/cm^3	Factor increase
Degussa P25	0.254	0.50	0.51	
0.1wt% Pt on P25	0.282	0.52	0.54	1.1
0.5wt% Pt on P25	0.242	0.47	0.52	1.0
1.2wt% Pt on P25	0.208	0.41	0.51	1.0
Platinum deposited on Ultra-low Aerogel T36				
	Mass of catalyst, g	Volume of catalyst, ml	Density of catalyst, g/cm^3	Factor increase
T36_raw	0.071	0.55	0.13	
1.2wt% Pt on T36	0.124	0.44	0.28	2.2
3.5wt% Pt on T36	0.178	0.45	0.40	3.1
7.7wt% Pt on T36	0.154	0.37	0.42	3.2

Table 4-6 Data to determine the packing density of platinum deposited P25 and T36. The last column indicates the increase in density of the P25 and the T36, respectively, after platinization

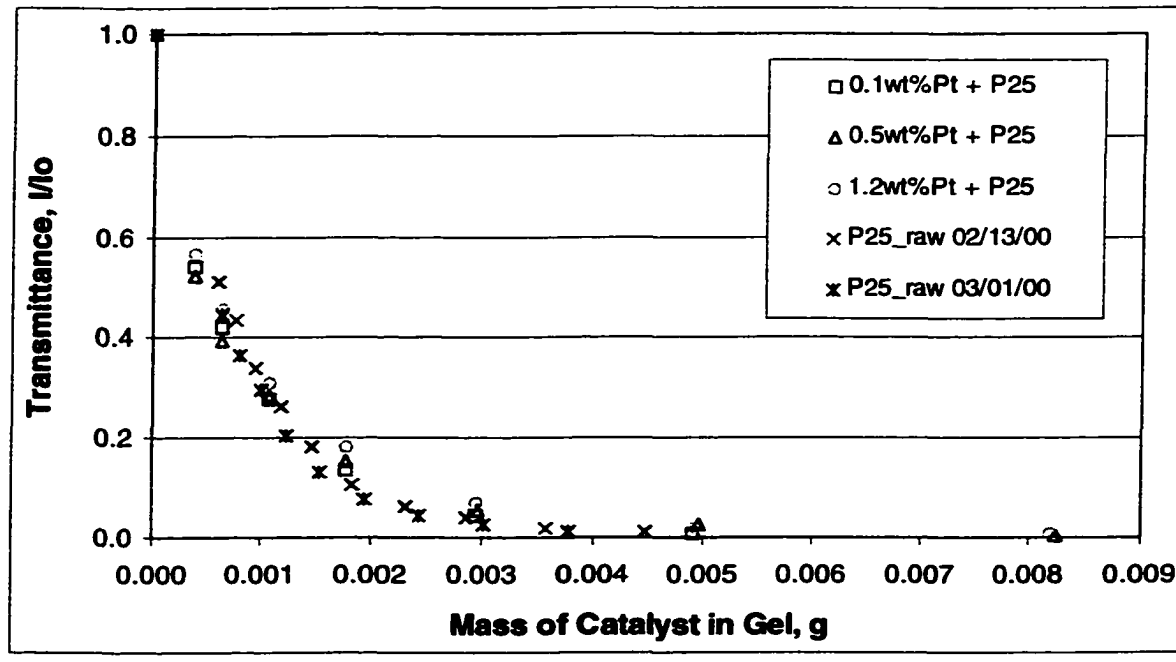

Figure 4-64 UV Transmittance of platinum deposited Degussa P25 dependence on catalyst mass in the agar gel layer

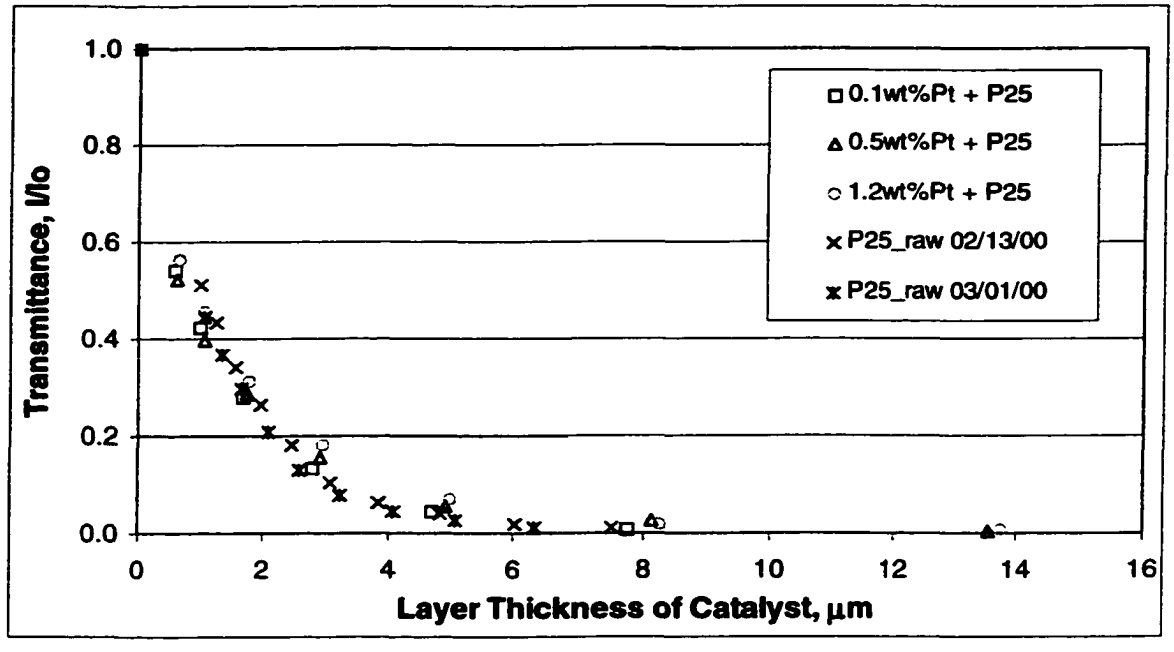

Figure 4-65 UV Transmittance of platinum deposited Degussa P25 dependence on catalyst layer thickness without the agar gel

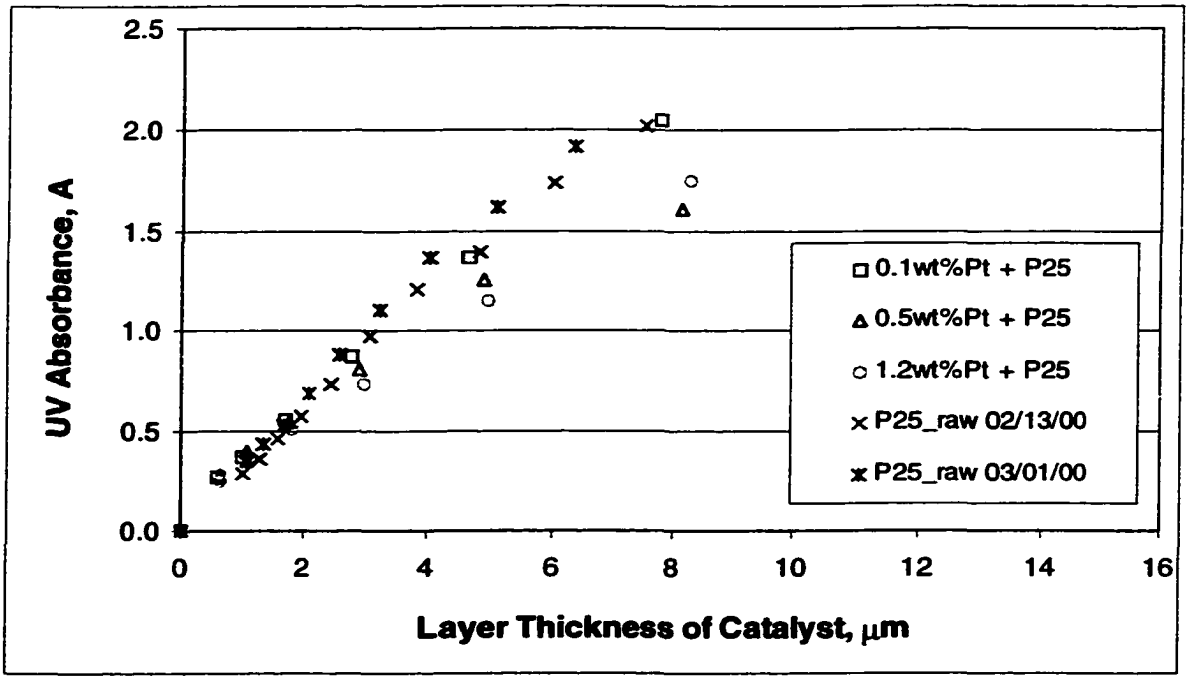

Figure 4-66 UV absorbance of platinum deposited Degussa P25 dependence on catalyst layer thickness without the agar gel

4.3.3 UV Transparency

Another way to evaluate the UV transparency is to determine the diffuse attenuation coefficient as Vincent et al. measured it during investigations of the UV transparency of four Antarctic lakes[120]. They found that a low concentration of chromophoric dissolved organic matter or dissolved organic carbon (DOC) was responsible for the water to be unusually transparent to solar ultraviolet radiation. The diffuse attenuation coefficients (K_d) were determined from linear regressions of the natural logarithm of the radiation against depth of the lake using only those data points within the log-linear portion of the curve for the upper layer. The inverse of the diffuse attenuation coefficient, $1/K_d$, was accounted as a direct measure of UV transparency. Applying the same method for the

catalyst powder dispersed in agar gel provided a means of comparison of the UV transparency of the different titanium dioxide materials. The natural logarithm of the transmitted energy, ln (I), was plotted against the catalyst layer thickness as shown in Figure 4-67 for Degussa P25, in Figure 4-68 for the ultra-low density aerogel T36, in Figure 4-69 for the low-density aerogel CEH6, and in Figure 4-70 for the platinum doped P25. A linear plot with $R^2 > 0.99$-0.98 was obtained using only the data points in the linear range. No more than two to three data points related to the largest layer thickness per experimental set had to be omitted in order to obtain $R^2 > 0.98$. Based on the assumption that ln (I) is linear to the catalyst layer thickness, the following relation (Equation (4-2)) can be specified where the diffuse attenuation coefficient K_d can be found from the slope. As defined by the work of Vincent and co-workers, 1/Kd can be seen as a measure for transparency[120]. Table 4-7 summarizes the results for the Degussa P25 and the different aerogels.

(4-2) $$\ln (I) = - K_d * D_L + \ln (I_o)$$

with I = measured UV intensity of gel with dispersed catalyst
I_0 = measured UV intensity of gel with no catalyst.
D_L = catalyst layer thickness
K_d = diffuse attenuation coefficient

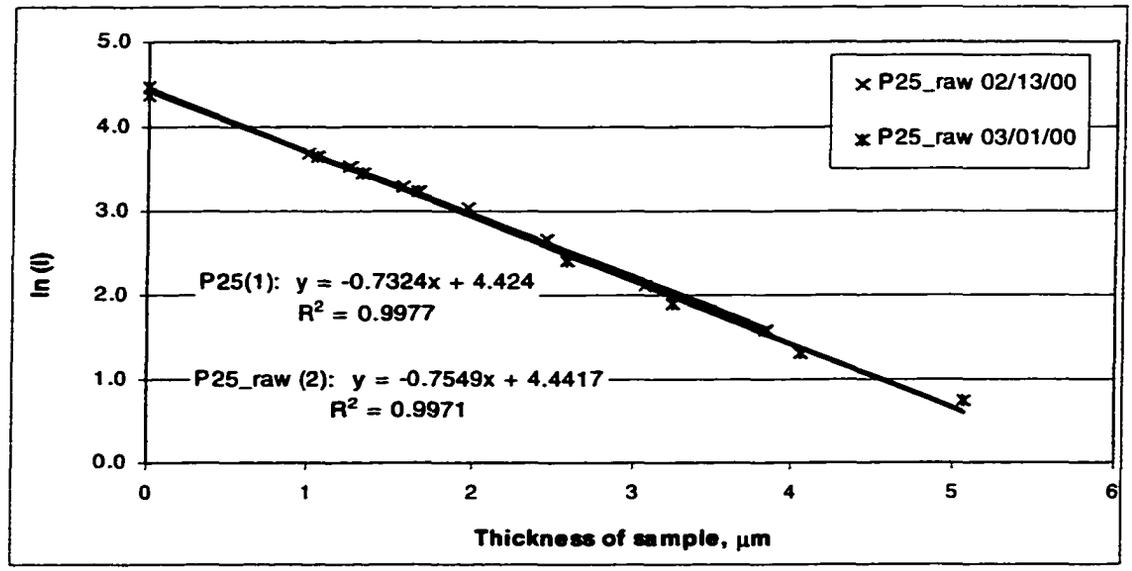

Figure 4-67 Graph to determine the diffuse attenuation coefficient K_d: Natural logarithm of transmitted energy through agar gel layers dependant on the catalyst layer thickness of Degussa P25

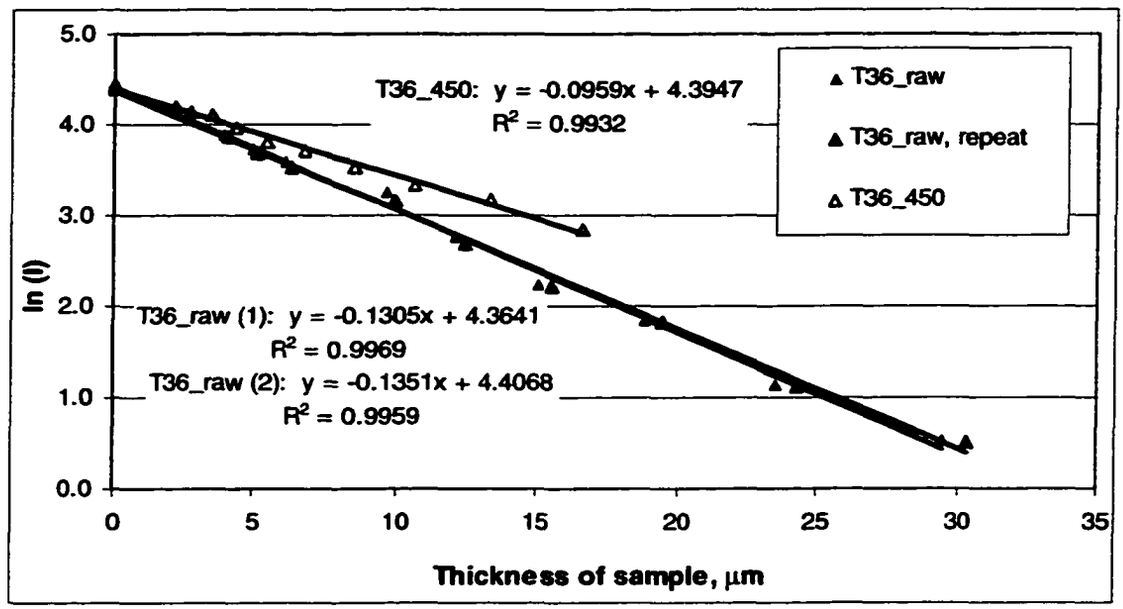

Figure 4-68 Graph to determine the diffuse attenuation coefficient K_d: Natural logarithm of transmitted energy through agar gel layers dependant on the catalyst layer thickness of ultra-low density aerogel T36

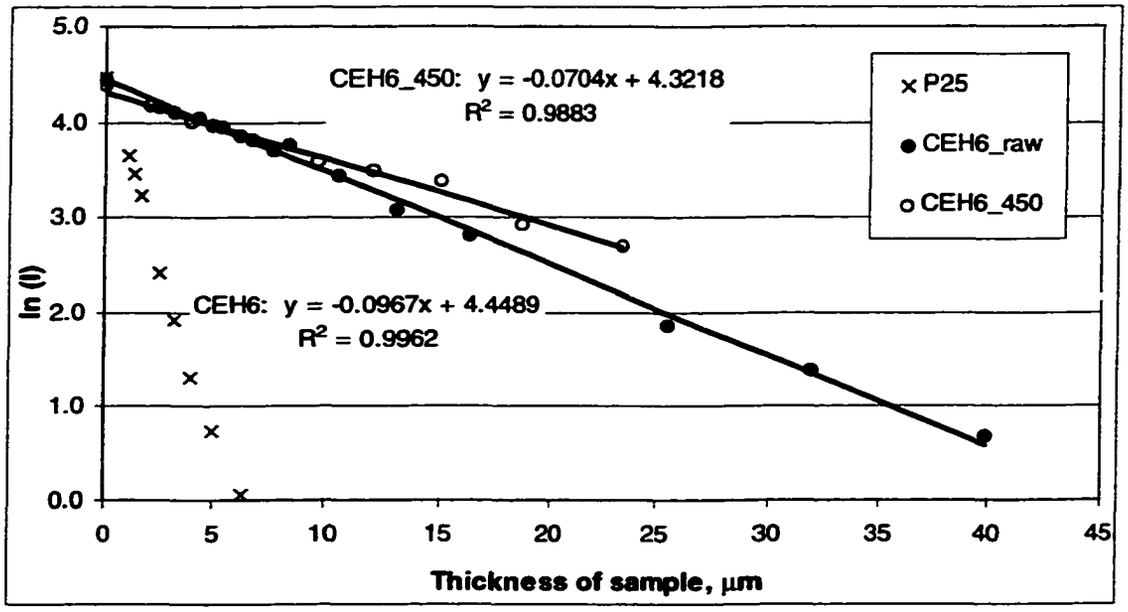

Figure 4-69 Graph to determine the diffuse attenuation coefficient K_d: Natural logarithm of transmitted energy through agar gel layers dependant on the catalyst layer thickness of low density aerogel CEH6

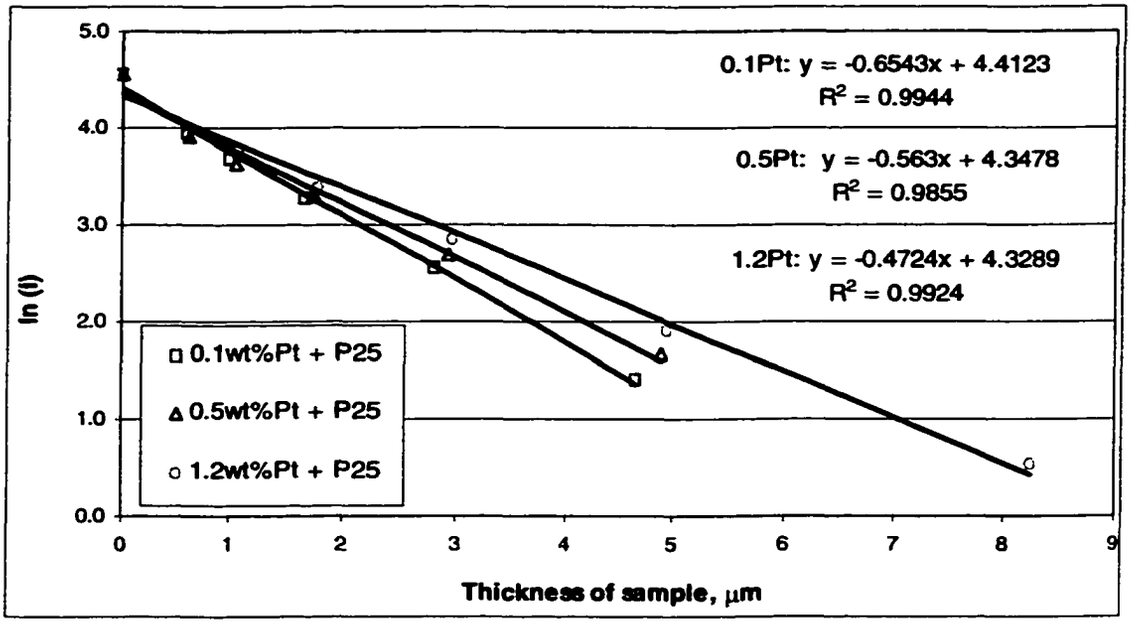

Figure 4-70 Graph to determine the diffuse attenuation coefficient K_d: Natural logarithm of transmitted energy through agar gel layers dependant on the catalyst layer thickness of Pt-doped Degussa P25

Catalyst	-Slope	Regression R^2	Transparency = 1/Kd	Factor Increase to P25	Factor Increase to T36
P25_raw (1)	0.7549	0.9971	1.32		–
P25_raw (2)	0.7324	0.9977	1.37		–
T36_raw (1)	0.1305	0.9969	7.66	5.7	–
T36_raw (2)	0.1351	0.9959	7.40	5.5	–
T36_450	0.0959	0.9932	10.43	7.7	1.4
CEH6_raw	0.0967	0.9962	10.34	7.7	1.4
CEH6_450	0.0704	0.9883	14.20	10.5	1.9
P25+0.1wt% Pt	0.6543	0.9944	1.53	1.1	–
P25+0.5wt% Pt	0.5630	0.9855	1.78	1.3	–
P25+1.2wt% Pt	0.4724	0.9924	2.12	1.6	–
T36+1.2wt% Pt	0.2245	0.9945	4.45	3.3	0.6
T36+3.5wt% Pt	0.2099	0.9851	4.76	3.5	0.6
T36+7.7wt% Pt	0.1656	0.9803	6.04	4.5	0.8

Table 4-7 Linear regression data and transparency results for Degussa P25 and the different aerogels. The last two columns indicate the factors by which the transparency increased compared to that of Degussa P25 and T36, respectively.

These data show clearly that the aerogels have a higher transparency than Degussa P25. The transparency of the untreated T36 increased by a factor of five, while CEH6 demonstrated a sevenfold increase in transparency. These experimental findings are similar to those data estimated from earlier calculations using Equation (2-6) and the porosity data (see Table 4-5). Heat treatment increased the transparency of the aerogels by an additional factor of 1.4 compared to the untreated aerogel leading to an increase of up to tenfold compared to P25. This, however, does not coincide with the estimates from Table 4-5. However, as was stated before, other factors like surface smoothness, particle size, or adsorbed organics play also an important role in as how deep the UV light can penetrate into the catalyst material.

It is noteworthy to point out that a good repeatability of the UV penetration measurements was achieved as illustrated by two different measurements of both untreated Degussa P25 and T36 as seen in Table 4-7.

The UV transparency of P25 did not change significantly after platinum deposition. An increase of transparency by a factor of only up to 1.6 was observed (see Table 4-7). Platinum deposition on the aerogel T36 also led to a slight increase in UV light penetration when compared on a mass basis of catalyst (see Figure 4-71), however, when comparing the catalysts on the basis of layer thickness (Figure 4-72), the UV transmittance showed a decrease. Nonetheless, the penetration depth is still higher compared to that of Degussa. When compared to the untreated T36, the UV transparency decreased by a factor of 0.6 to 0.8 because the platinum is UV transparent. Even though the porosity of the aerogel samples did not decrease as shown in Table 4-8, but the densities became significant higher (increase by a factor of two to three times). Perhaps the change in density may be an influencing factor for the UV transparency.

	T36 raw	T36 + 1.2wt% Pt	T36 + 1.2wt% Pt	T36 extra 1.2wt% Pt	T36 + 3.5wt% Pt	T36 extra + 3.5wt% Pt	T36 + 7.7wt% Pt
m cat, g	0.1176	0.5855	0.2384	0.3296	0.4854	0.3987	0.5796
BET Surface Area m2/g	337.0	287.4	291.5	298.9	136.9	166.0	136.4
Cumulative Pore Volume cm3/g	0.8620	0.9680	1.0064	1.0840	0.7363	0.7776	0.6060
porosity ,%	77	79	79	81	74	75	70

Table 4-8 Calculated porosity of T36 and platinized T36 (including repeated measurements indicated by "extra").

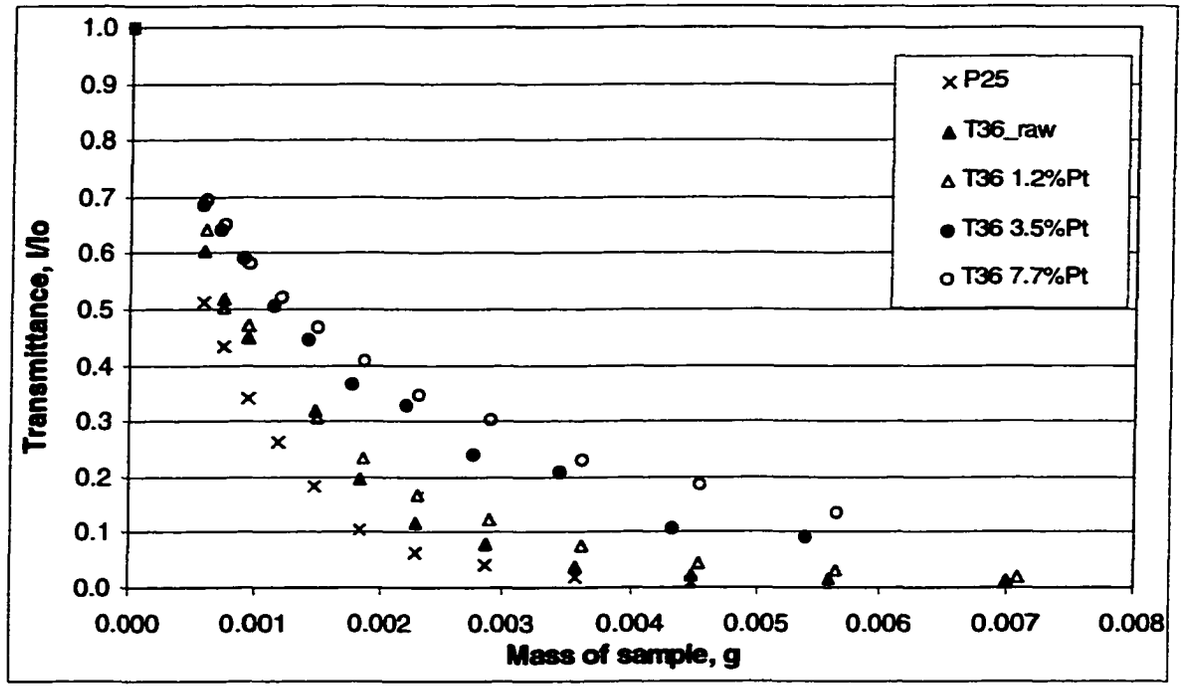

Figure 4-71 UV Transmittance of ultra-low density aerogel T36 with platinum dependent on catalyst mass in the agar gel

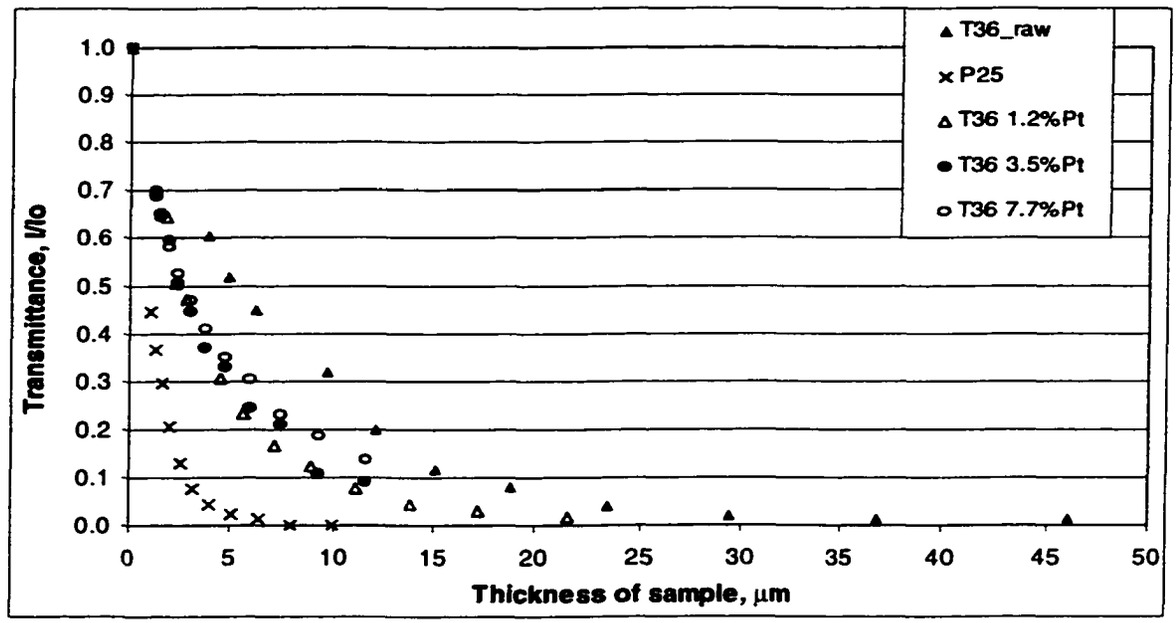

Figure 4-72 UV Transmittance of ultra-low density aerogel T36 with platinum dependent on layer thickness

Since the binary silica/titanium dioxide aerogel TS31b did not show any catalytic activity, it was not of interest to determine the UV transmittance for this material. However, measurements of encapsulated anatase TiO_2 in SiO_2 (both synthesized via the sol-gel method)[121] were performed and have shown a remarkable increase in UV penetration depth as seen in Figure 4-73. The striking increase in UV penetration is due to the large amount of silica (7wt%) in the catalyst. Silica has a very high UV transparency as confirmed by measurements of mixtures of SiO_2 and TiO_2 (see Figure 4-74). With increasing amount of silicon dioxide in the mixture the UV transmittance increased. Table 4-9 shows the values for UV transmittance (determined from Figure 4-75 and Figure 4-76) of the encapsulated material as well as the anatase TiO_2 in SiO_2, indicating that silica had a 100 times higher UV transparency compared to P25 or anatase titanium dioxide. Thus, titanium dioxide dispersed in a porous silica structure might be more effectively utilized as a result of the deeper UV penetration into the catalyst material allowing for more of the TiO2 to be reached by photons for activation.

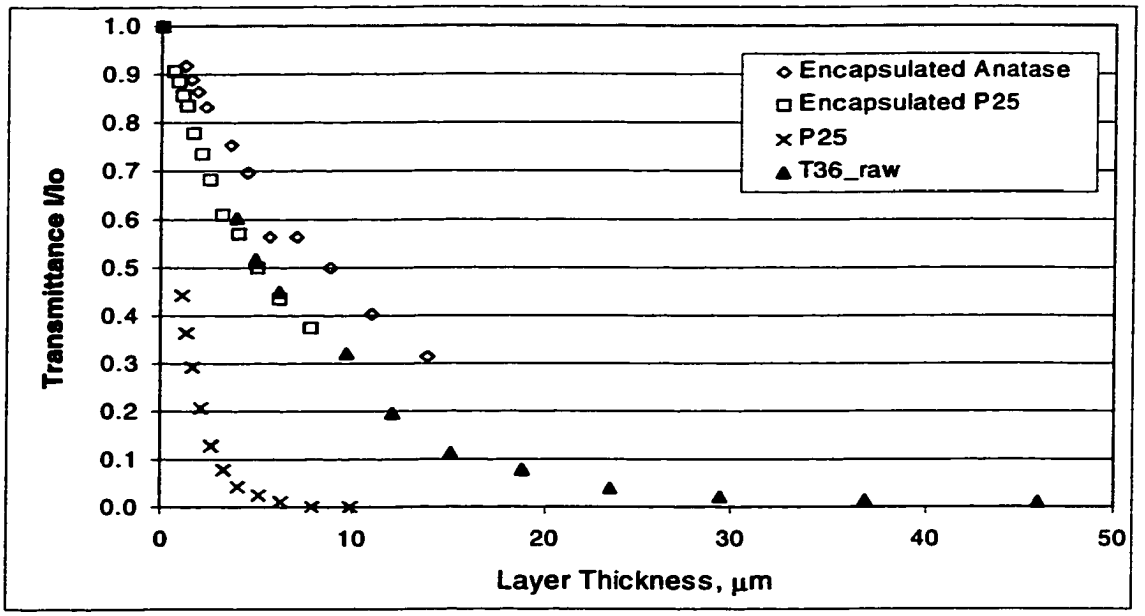

Figure 4-73 UV Transmittance of encapsulated anatase TiO_2 and P25 in SiO_2 dependent on layer thickness

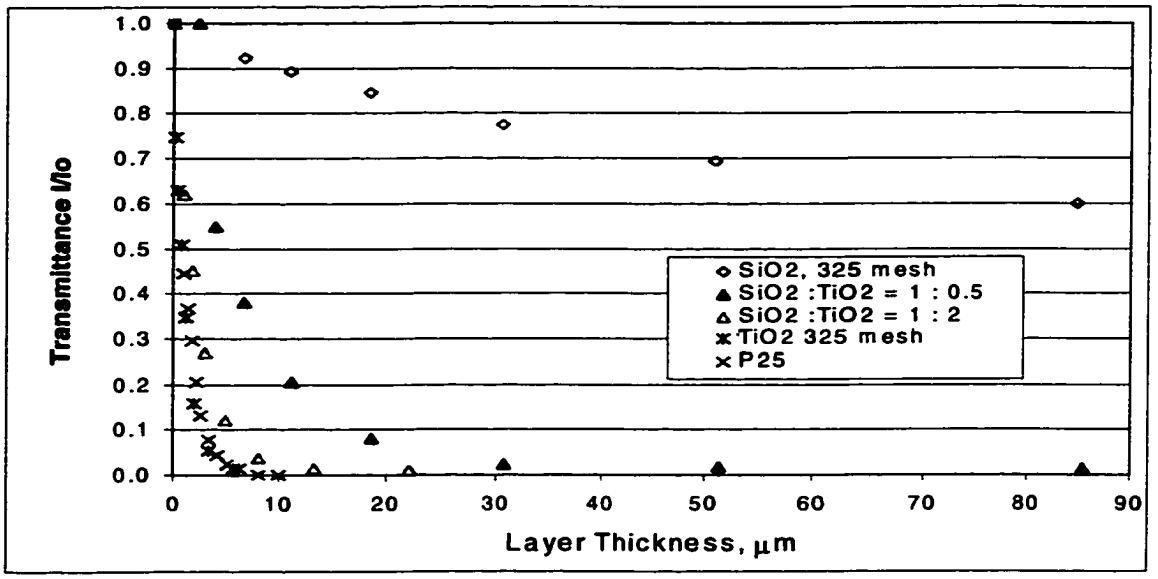

Figure 4-74 UV transmittance of SiO_2, anatase TiO_2, and mixtures of SiO_2 and anatase TiO_2, dependent on layer thickness

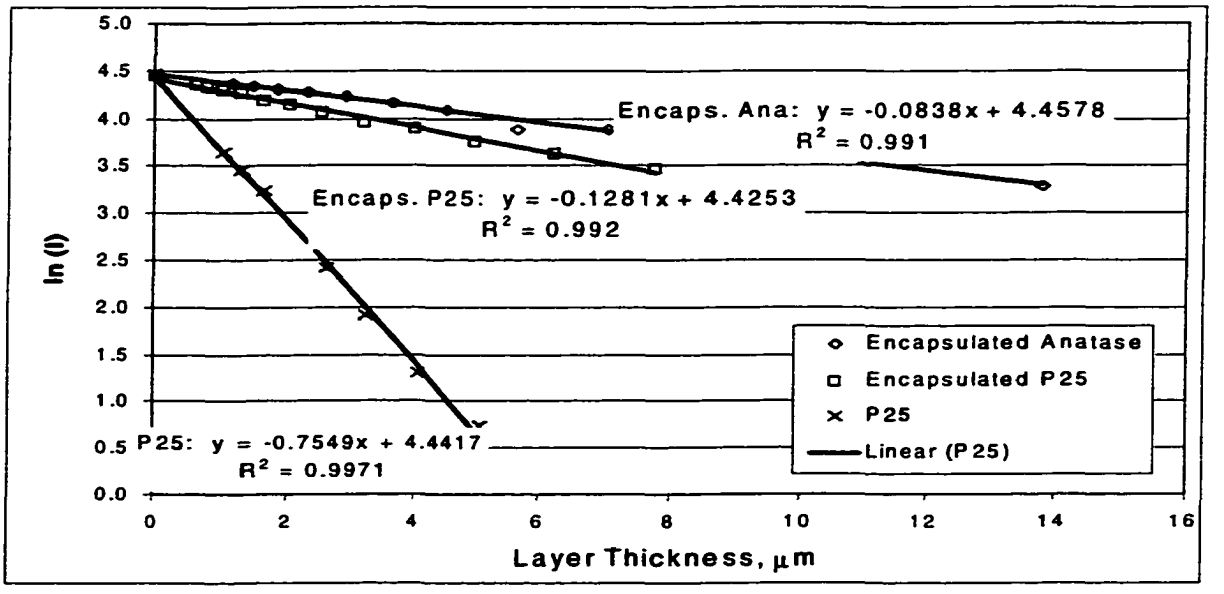

Figure 4-75 Graph to determine the diffuse attenuation coefficient K_d: Natural logarithm of transmitted energy through agar gel layers versus the catalyst layer thickness of encapsulated anatase TiO_2 in SiO_2 (both synthesized via sol-gel route) and encapsulated Degussa P25

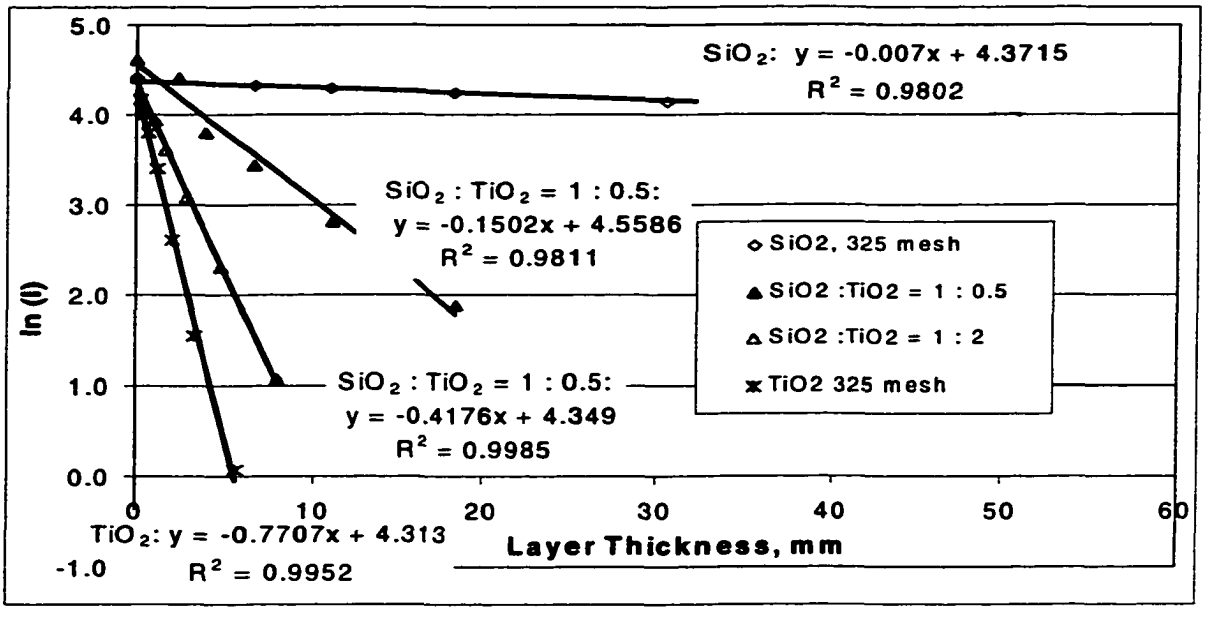

Figure 4-76 Graph to determine the diffuse attenuation coefficient K_d: Natural logarithm of transmitted energy through agar gel layers dependant on the catalyst layer thickness of anatase TiO_2, amorphous SiO_2 and mixtures of both

Catalyst	-Slope	Regression R^2	Transparency = 1/Kd	Factor Increase
P25	0.7549	0.9971	1.32	
anatase in SiO_2	0.0838	0.9910	11.93	9.0
P25 in SiO_2	0.1281	0.9920	7.81	5.9
SiO_2	0.0070	0.9802	142.86	107.8
$SiO_2 : TiO_2 = 1 : 0.5$	0.1502	0.9811	6.66	5.0
$SiO_2 : TiO_2 = 1 : 2$	0.4176	0.9985	2.39	1.8
anatase TiO_2	0.7707	0.9952	1.30	1.0

Table 4-9 Linear regression data and transparency results for P25 and encapsulated anatase (sol gel synthesis) TiO_2 and P25 in SiO_2 (sol gel synthesis). The last column indicated the factor by which the transparency increased compared to that of Degussa P25

4.4 Photocatalytic Reactor System

4.4.1 Volume of Reactor System

The reactor volume was determined as described in Section 3.5.2. However, before determining the reactor system volume, the volume of the external cylinder, V_C, and the manifold, V_M (space inside tubing and valves between reactor system and external cylinder, see Figure 3-5), had to be determined first, which was done according to the procedure as follows.

The external cylinder was evacuated and then the manifold was filled with helium (Valves 1 and 3 were closed) at P_{atm} = atmospheric pressure. After slowly opening valve 3, the gas expanded into the cylinder for which Equation is valid. Since it was not possible to draw an absolute vacuum to the system, the term (P_{vac} V_C) in Equation (4-3) had to be added in order to account for the mass of helium that was still left in the external cylinder after evacuation. Then, the same procedure was repeated but with the

external cylinder filled with a known amount of tin pieces, V_{tin}. For this case, Equation (4-4) applies.

(4-3) $P_{atm} V_M = P_1 (V_M + V_C) - P_{vac} V_C$

(4-4) $P_{atm} V_M = P_2 (V_M + V_C) - (P_{vac} V_C + V_{tin})$

where P_1 and P_2 are the pressures in manifold and cylinder after helium expansion. This is a system of two equations with two unknowns and can be solved for V_M and V_C.

At least five repeated helium expansions were performed and the average value of the recorded pressures was used to calculate the volume. The volume of the external cylinder was found to be 424.5 ml. Since some modifications had been performed on the reactor system throughout the duration of the research project the volume of the manifold had changed from initially 44.8 ml to 37.6 ml. The reactor system setup, however, was modified several times and the volume was again determined after each adjustment. The system volume varied between 280 and 320 ml. The exact value for each catalytic experiment will later be indicated on each individual data spreadsheet in the Appendix.

4.4.2 Test-Contaminants and Calibration of GC for Contaminants

The following contaminants were used for testing and comparing the different catalysts:

Methane, CH_4, a representative of alkanes, is a colorless, odorless gas that occurs abundantly in nature as the main constituent of natural gas (85%)[122]. Methane is also known to be one of the major greenhouse gases (besides water vapor and carbon dioxide) that cause global warming. Methane pollution occurs during the production and transport

of coal, natural gas, and oil, from rotting organic waste in landfills, and it is released from certain animals, especially cows, as a byproduct of digestion. The amount of methane in the atmosphere has more than doubled since the beginning of the Industrial Revolution in the mid-1700s[123].

Ethane, C_2H_6, a second representative of the alkane group, is a colorless, odorless, gaseous compound. It is the second most important component of natural gas (9%)[122], it also occurs dissolved in petroleum oils and as a by-product of oil refinery operations and of the carbonization of coal[124]. As of January 1999, emissions of ethane must be included in permit applications for all sources of emitted pollutants to the Department of Environmental Quality[125].

Acetone (2-Propanone), CH_3COCH_3, a representative of ketones, is a volatile organic compound identified as one of the impurities of waste-gas from intensive animal husbandry, fermentation, pharmaceutical and sewage treatment processes, and landfill sites[126]. Acetone is a colorless flammable liquid manufactured to make plastic, fibers, drugs, and other chemicals. It is also found in vehicle exhaust and tobacco smoke. Even though it is also found in the natural environment, industrial processes contribute mainly to the acetone release into the environment than natural processes. Most of the acetone released during manufacturing and use goes into air (97%). It takes not less than about 22 days to break down one-half of the total amount of acetone from sunlight exposure[127].

Ethylene, C_2H_4, a representative of alkenes, is an odorless, colorless, tasteless gas released during the natural ripening process of particular fruits and vegetables[128]. In some applications ethylene gas is used (under controlled conditions) as a ripening agent.

However, when present in small amounts, it can shorten the life of particular cut flowers, inhibit the development of immature flower buds, or cause fresh produce to deteriorate faster during shipping and storage. Ethylene gas levels as low as 1 part per million (ppm) can destroy an entire shipment in a single day[129]. Some examples of high ethylene producing fruits include apples, avocados, peach, pear, plum, and nectarines, as well as banana, mango, and tomatoes. Controlling ethylene levels in storage and shipping devices is therefore of high importance.

Before performing the photocatalytic oxidation tests the GC integrator, that was connected to the gas chromatograph and provided numbers for integrated peak areas, had to be calibrated for each specific contaminant. The integrator was calibrated simply by assigning a pollutant gas concentration to the peak area number provided by the integrator.

First, the reactor system - not including the photocatalytic reactor cell - was purged with air. Then, consecutive known amounts of contaminant gas were introduced to the system. The gas was allowed to circulate for one hour and the peak area value was recorded for each new concentration interval. The concentration of contaminant within the reactor system was determined using Equation (4-5) where the number of moles injected, $n_{injcted}$, was calculated using the ideal gas law (Equation (4-6)).

$$C = \frac{n_{injected}}{V_{system}} \quad (4\text{-}5)$$

$$n_{injected} = \frac{PV_{injected}}{RT}, \quad (4\text{-}6)$$

where $V_{injcted}$ = injected volume of contaminant, V_{system} = reactor system volume, P = atmospheric pressure, T = room temperature, R = ideal gas constant.

An example calibration graph for methane is shown in Figure 4-77. The equations of each individual calibration for each contaminant is included in the spreadsheet data of the respective photocatalytic run.

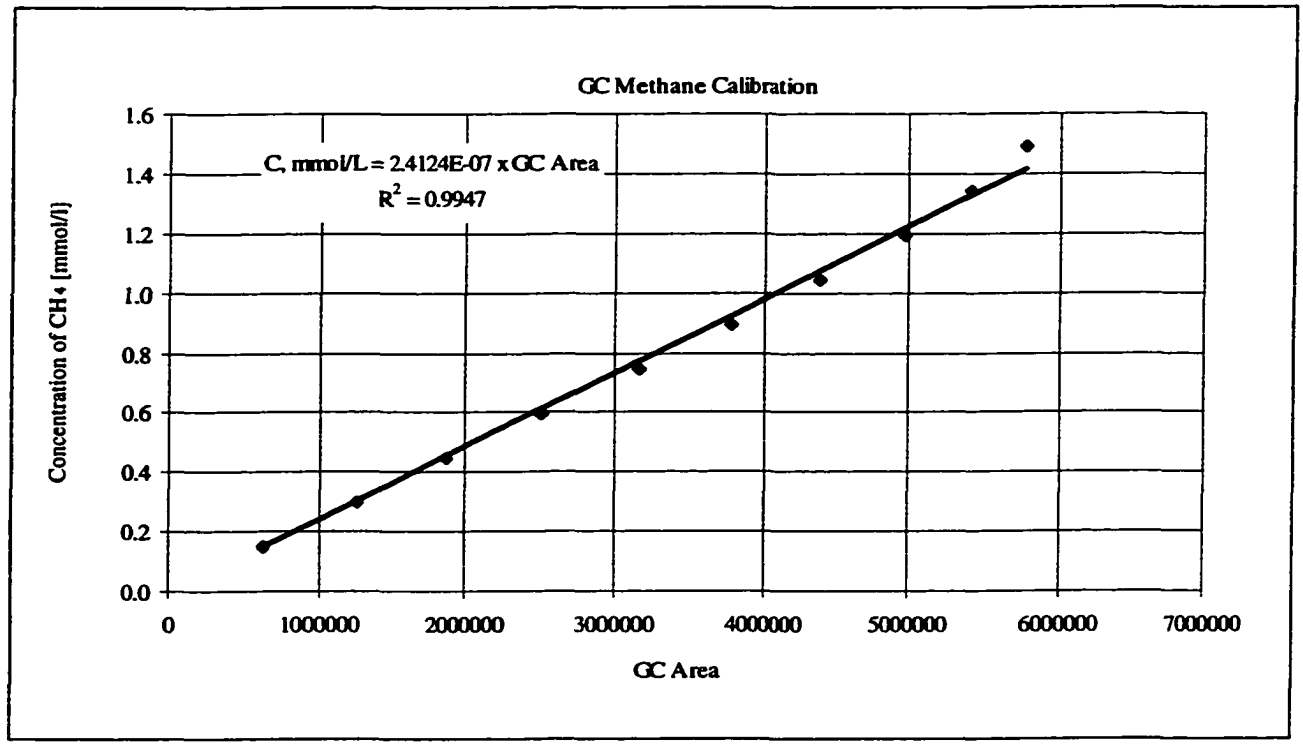

Figure 4-77 GC calibration for methane

4.5 Study of Gas Adsorption on Catalysts

Adsorption studies of acetone, ethylene and water were performed as outlined by Sauer and Nimlos[36, 40]. The amount of adsorbed gas was determined by first adding a known amount of gas to the reactor system with the catalyst present and measuring the signal and then comparing that value to the concentration calculated for the case if no

catalyst was present. Adsorption parameters were then calculated based on the Langmuir adsorption mechanism using Equation (4-7)[41].

$$\Theta_i = \frac{m_i}{\mu_{i\max}} = \frac{K_i C_i}{1 + K_i C_i} \quad (4\text{-}7)$$

where Θ_i = surface adsorption coverage of contaminant i (dimensionless), m_i = adsorbed amount of contaminant i per gram of catalyst, $\mu_{i\max}$ = maximum amount of ontaminant adsorbed in a monolayer, K_i = adsorption equilibrium constant, and C_i = gas concentration of contaminant i.

After rearranging Equation (4-7) and plotting $1/m_i$ versus $1/C_i$, the monolayer constant $\mu_{i\,max}$ and the adsorption equilibrium constant K_i can be determined from the slope and intercept of a straight line fit.

4.5.1 Acetone Adsorption

Acetone is a volatile gas that adsorbed very strongly on the catalytic materials. Kinetic rate calculations using the Langmuir-Hinshelwood rate form take only gas phase concentrations into account; however, they do not include the mass of acetone reversibly adsorbed on the catalyst. In order to account for physical adsorption/desorption of acetone from the catalyst powders, adsorption studies were performed to determine the monolayer adsorption constant, $\mu_{i\,max}$, to be used for kinetic evaluations discussed in a later Chapter (4.6.3 Acetone Photo-Oxidation).

Figure 4-78 illustrates the difference in acetone adsorption between a 100 % anatase powder and the aerogel CEH6 by plotting the final gas phase acetone concentration in the system after adsorption versus the amount of acetone injected ($C_{theoretical}$) and comparing

these data with the same measurement with no catalyst present in the system. While anatase reduced the acetone concentration by only 16 to 25 % (with highest fraction of acetone feed removal at lowest feed), the aerogel adsorbed already 70 to 96 % of the initial acetone feed (with 96% at the lowest feed concentration) as summarized in Table 4-10. It is important to point out that the four-fold higher adsorption by the aerogel compared to anatase was achieved with only one third of the mass of catalyst (1.08 g aerogel compared to 3.74 g of anatase).

A linear regression was performed of the inverse of mass of acetone adsorbed versus the inverse of the gas phase concentration (see Figure 4-79) to determine $\mu_{a\,max}$ and K_a for acetone adsorption on anatase TiO_2 and aerogel CEH6. Table 7-5 in the Appendix shows the raw data and the results of the calculations. Table 4-11 summarizes the values for $\mu_{a\,max}$ and K_a. The adsorption constant K_a^{CEH6} of the aerogel with 0.020 g/m^3 was about three times higher than that of anatase with $K_a^{ana} = 0.007$ g/m^3. The maximum amount of acetone adsorbed for the aerogel was almost 30 times higher for the aerogel with $\mu_{a\,max}^{CEH6} = 106.8$ mg per gram of catalyst compared to $\mu_{a\,max}^{ana} = 4.4$ mg acetone/g-cat. Figure 4-79 exhibits the comparison of actual adsorption data with the determined Langmuir model.

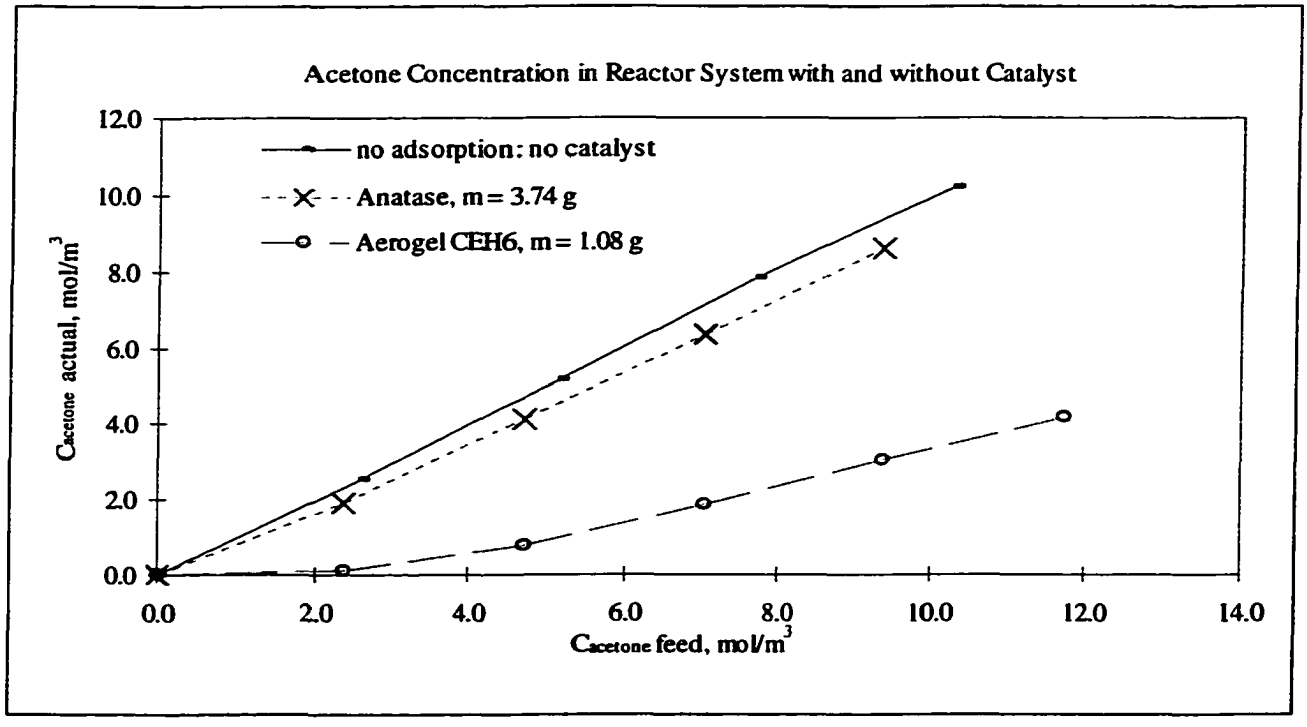

Figure 4-78 Comparison of the gas phase acetone concentration in the reactor system after adsorption on anatase and aerogel.

C theoretical mmol/l	C, mmol/l			reduction of acetone concentration, %		
	empty system	sytem with anatase	aerogel	reactor system	anatase	aerogel CEH6
0.0	0.0	0.0	0.0			
2.6	2.5	1.9	0.1	2.5	25.5	96.5
5.1	5.1	4.1	0.8	0.0	19.8	85.4
7.7	7.8	6.3	1.8	-1.6	17.6	76.4
10.3	10.2	8.6	3.0	0.8	16.5	70.1

Table 4-10 Reduction of acetone concentration due to adsorption

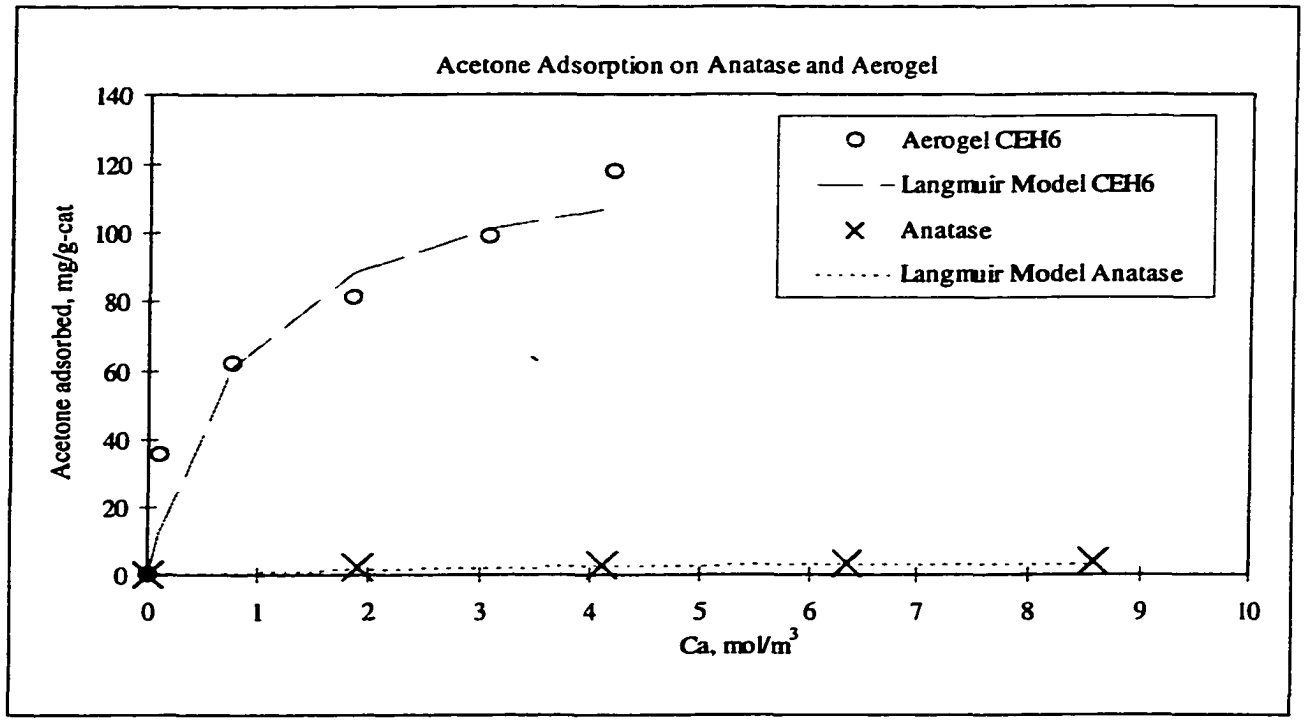

Figure 4-79 Acetone adsorption on anatase and aerogel: experimental data and model fit using a Langmuir expression

4.5.2 Adsorption of other Hydrocarbons (Ethane, Ethylene)

The adsorption behavior for ethane and ethylene was also studied for comparison purposes. Figure 4-80 illustrates that the adsorption of ethane on anatase was insignificant. The determined amount of adsorbed C_2H_6 was very small resulting in data that were too scattered ($R^2 = 0.3751$ for linear regression) to provide reasonable data for calculating $\mu_{c\,max}$ and K_{ca} for ethane adsorption on anatase TiO_2. However, ethane adsorption on the aerogel CEH6 was more clearly defined for which adsorption data were determined as summarized in Table 7-6 in the Appendix.

Figure 4-81 shows the fit of the Langmuir isotherm to the experimental data. Ethylene adsorption on both catalyst types was stronger than ethane adsorption, however, not as strong as the adsorption of acetone. Similar to acetone adsorption, anatase TiO_2

had a lower adsorption constant ($K_e^{ana} = 0.005$ g/m^3) of about one third that of the aerogel CEH6 ($K_e^{CEH6} = 0.019$ g/m^3) as seen in Table 4-11. The adsorption constant for the ultra-low density aerogel T36 was more than eight times higher than that of anatase with $K_e^{ana} = 0.0446$ g/m^3. The maximum amount of ethylene adsorbed per gram of catalyst was about one third lower for anatase with $\mu_{e\,max}^{ana} = 9.94$ mg compared to $\mu_{e\,max}^{CEH6} = 13.66$ mg for the aerogel CEH6. (Table 7-7 in the Appendix summarizes the data for ethylene adsorption on anatase and the aerogel. Figure 4-82 shows the comparison of ethylene adsorption for anatase and the aerogels per gram of catalyst. The Langmuir adsorption isotherms are included in the same graph showing a good agreement with experimental data.

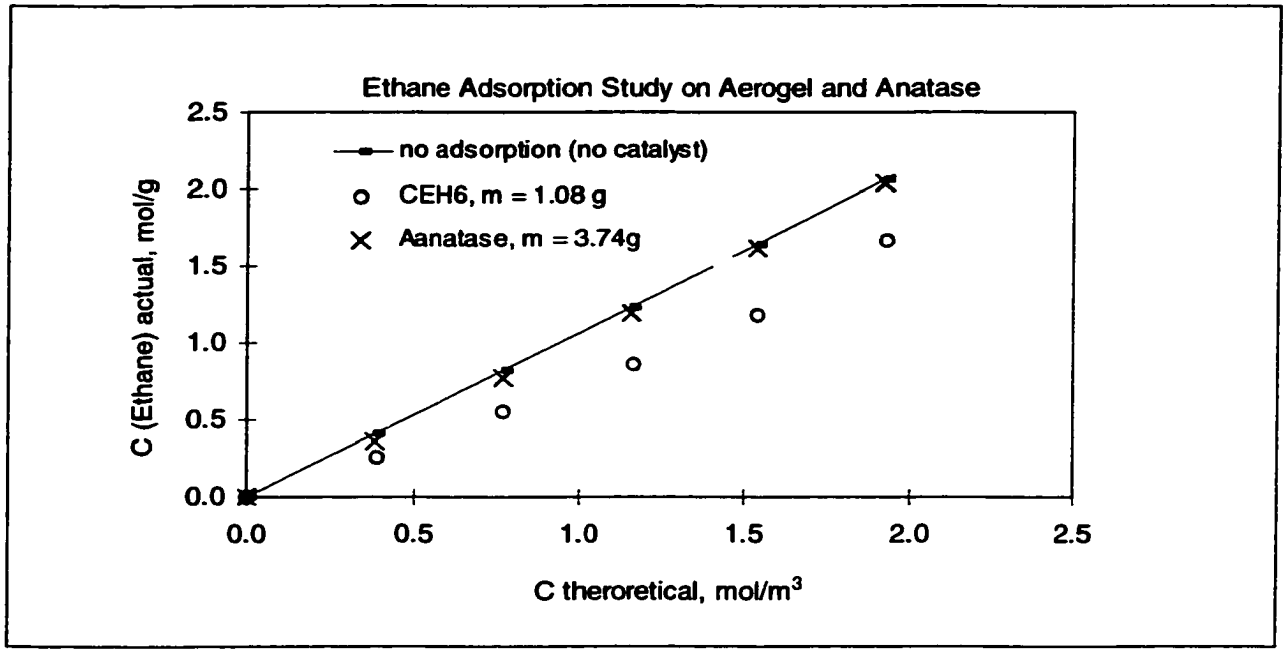

Figure 4-80 Comparison of ethane gas phase concentrations in the reactor system after adsorption on anatase and aerogel

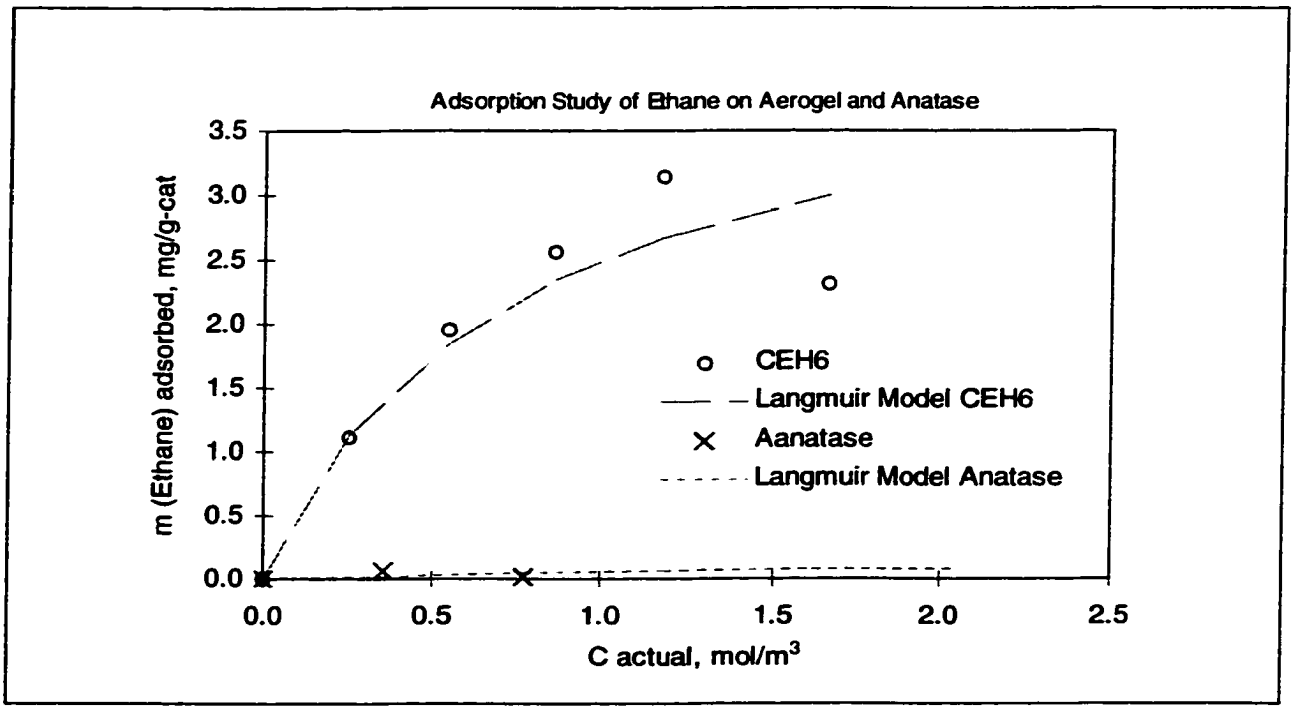

Figure 4-81 Ethane adsorption on anatase and aerogel CEH6: experimental data and model fit using a Langmuir expression

	Acetone Adsorption		Ethane Adsorption		Ethylene Adsorption	
	μa mg/g cat	Ka m^3/g	=> μ ea mg/g cat	Kea m^3/g	με mg/g cat	Ke m^3/g
Anatase	4.4	0.007	0.20	0.013	9.9	0.005
CEH6	106.8	0.020	4.32	0.049	13.7	0.019

Table 4-11 Adsorption constants K_x and maximum amount of acetone (μa), ethane (μea), and ethylene (με), respectively, in a monolayer for anatase and aerogel CEH6

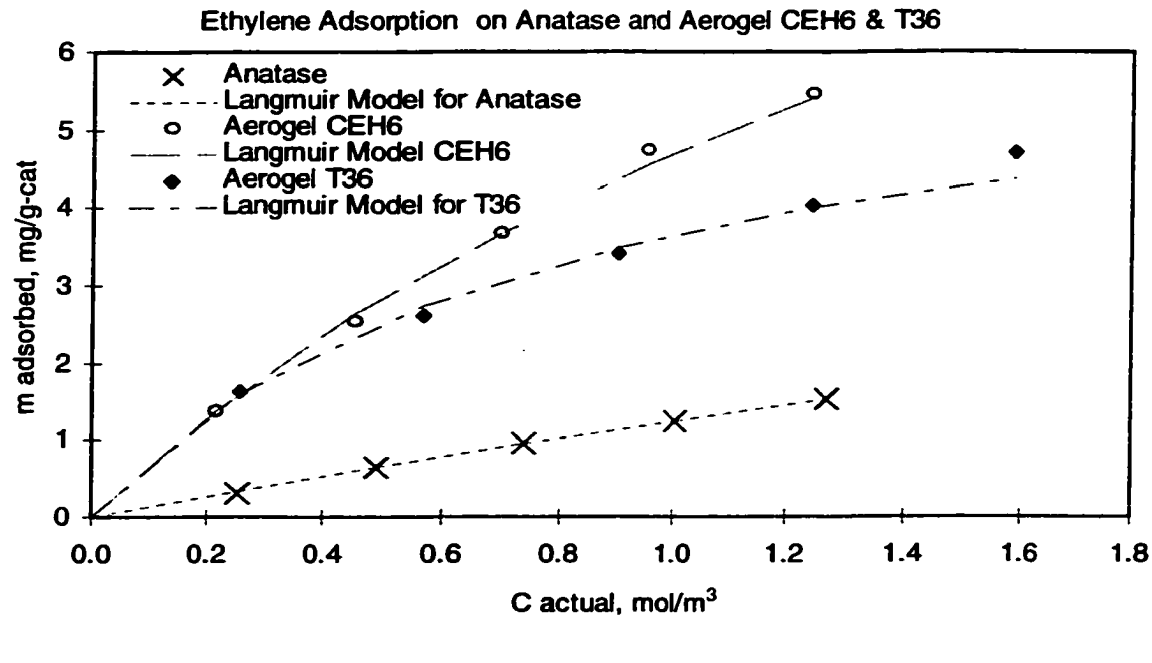

Figure 4-82 Ethylene adsorption on anatase and aerogels CEH6 and T36: experimental data and model fit using a Langmuir expression

4.5.3 Ethylene Adsorption under Humid Conditions

In order to see if water has any influence on the ethylene adsorption characteristic the heat-treated aerogel T36_450 was investigated for ethylene adsorption under humid conditions. Three different humidity levels were established in the reactor system with 1.3 g of T36_450 catalyst present. As described above for ethylene adsorption, the amount of ethylene adsorbed was determined for 33, 48, and 60% relative humidity. As seen in Figure 4-83 the adsorption of ethylene decreased only slightly after subjecting the catalyst to humid conditions. Once the catalyst was exposed to water the adsorption of ethylene was nearly the same at all humidity levels. The values for the ethylene adsorption constants, K_c, also changed little with increasing humidity as shown in Table 4-12. One possible explanation for this result is that the catalyst – once exposed to

humidity - may still be saturated with adsorbed water from the preceding adsorption test even though the system was purged with dry air before each new experiment. Even though water did competitively adsorb on the catalyst it did not alter the ethylene adsorption capability of T36_450 significantly. The increase of humidity from 0 to 60 % resulted in a decrease of ethylene adsorption by about 20% (compare also K_e in Table 4-12).

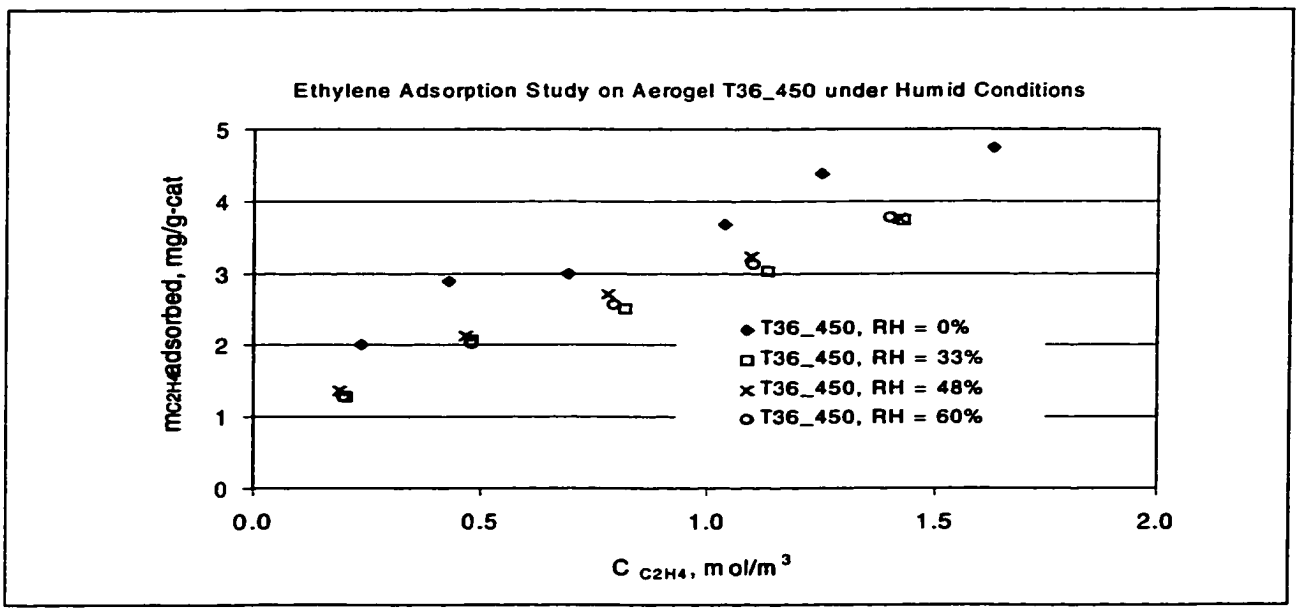

Figure 4-83 Ethylene adsorption aerogels T36 at different humidity levels

Catalyst	RH, %	=> μe = mg/g cat	=> Ke = m^3/mol
T36_raw, RH=0%	0	6.59	1.25
T36_450, RH=0%	0	3.94	2.65
T36_450, RH=33%	33	4.34	2.07
T36_450, RH=48%	48	4.36	2.39
T36_450, RH=60%	60	4.38	2.12

Table 4-12 Ethylene Adsorption constants and maximum amount of ethylene in a monolayer (μe) for the aerogel T36_450 under humid conditions

4.6 Photocatalytic Oxidation Tests and Results

4.6.1 Methane Photo-Oxidation

The complete reaction for methane oxidation is:

$$CH_4 + 2\,O_2 \rightarrow CO_2 + 2\,H_2O$$

Photocatalytic tests of methane oxidation were performed according to the procedure described in Section 3.5. The activity of the low-density aerogel CEH6 was tested and compared to the activity of Degussa P25. The catalytic cell filled with anatase contained 3.7 g of catalyst while the catalytic cell containing aerogel held only 1.3 g due to the lower density of the aerogel. Figure 4-84 shows a representative graph describing the decrease in methane concentration with time during oxidation over the aerogel CEH6. In order to test if the catalyst is active without illumination the UV lamp was switched off. No methane oxidation was observed during the dark periods. When continuing to illuminate the reaction continues at the same rate were the oxidation was interrupted before. A second graph, indicating the methane concentration under UV illumination with no catalyst present, shows that methane is not oxidized under UV illumination only. The methane oxidation results over the aerogel was compared to anatase in Figure 4-85. Clearly, the aerogel oxidized methane significantly faster than the commercially available 100% anatase. Additionally, in the same figure is indicated that a reasonably good repeatability of the oxidation results was achieved. Similar experiments were performed testing both catalysts at several different initial methane concentrations ranging from 900 ppm to 20 000 ppm corresponding to 0.5, 1.0, 2.0, 6.0, and 10 ml feed at ambient conditions to the reactor system having a volume of 298 ml. In order to compare the

performance of the two catalysts, the change in concentration versus time for both catalysts was plotted for each initial concentration. These data are summarized in the Appendix (Table 7-11). At all initial concentrations the aerogel oxidized methane at a faster rate than anatase.

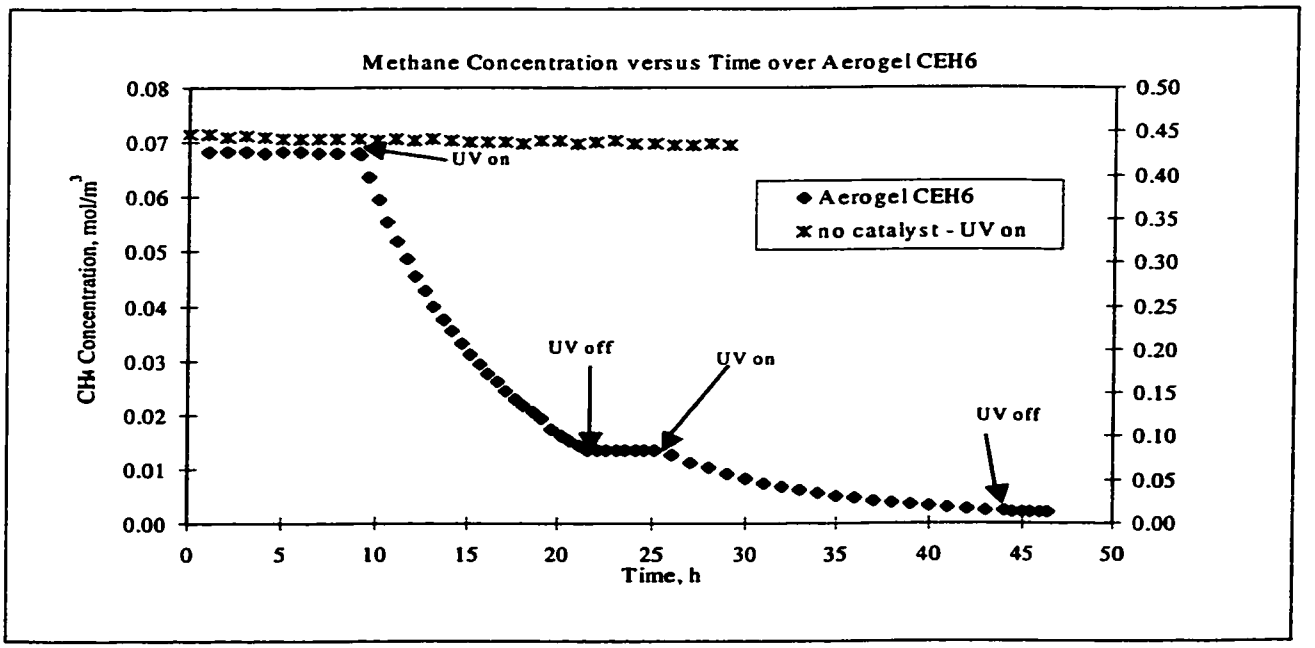

Figure 4-84 Methane oxidation over aerogel CEH6

Since methane adsorption on the catalyst is very low (see Chapter 4.5), nearly all of the methane in the system is in the gas phase. Therefore, the rates of methane oxidation were simply calculated by the ratio of change in methane gas phase concentration over change in time as in equation (4-8):

(4-8)
$$rate = \frac{dC}{dt} = \frac{C_{i+1} - C_i}{t_{i+1} - t_i}$$

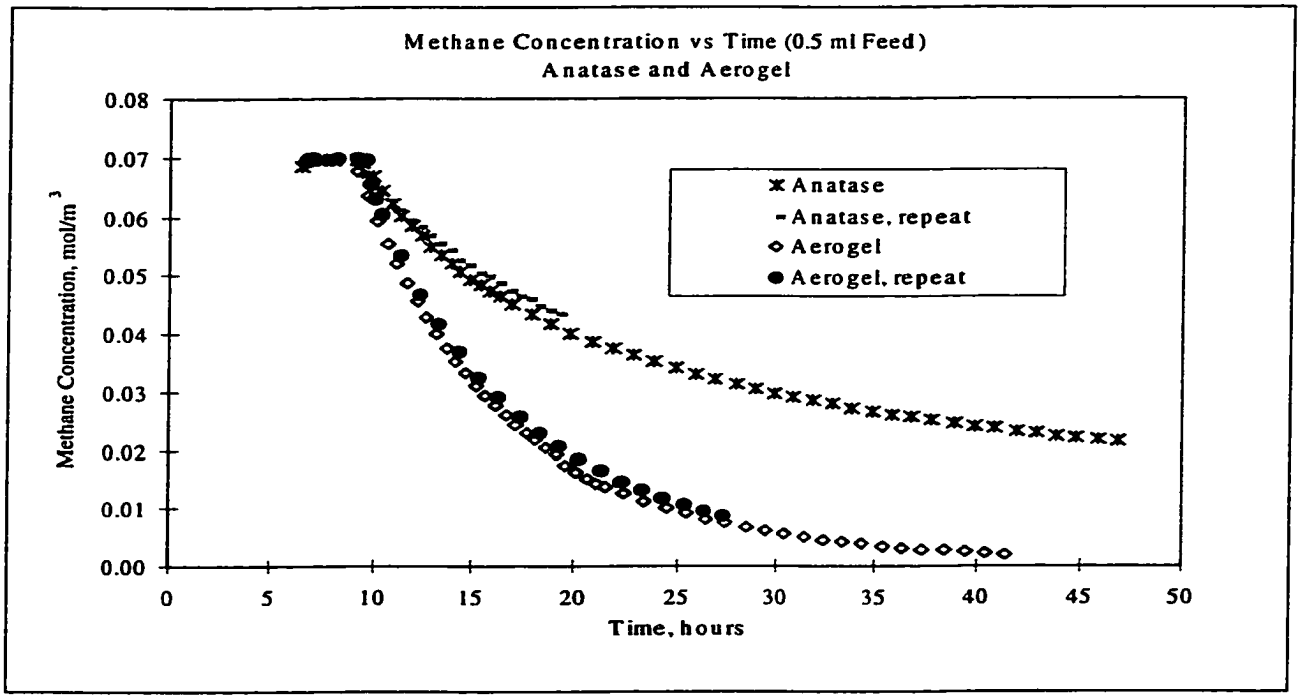

Figure 4-85 Photocatalytic CH_4 oxidation over 100% anatase and aerogel CEH6

When looking only at the initial rates based on the amount of catalyst in the catalytic cell, as seen in Figure 4-86, it becomes clear that the initial rates of the aerogel are significantly higher than the initial rates of the anatase. The same was the case when comparing the initial rates based on the illuminated cell window area of the catalyst cell as seen in Figure 4-87. However, comparing the initial rates based on the actual illuminated catalyst volume (i.e., from estimates of the penetration depth of UV light into the bulk) indicates that the anatase demonstrates a better performance. This implies that the actual reaction sites of the anatase have a higher activity than the aerogel sites or that the number of active sites per surface area on the anatase is higher. Considering the very low anatase crystallinity of the synthesized aerogel (as already discussed in Chapter 4.2.6) this result was not surprising.

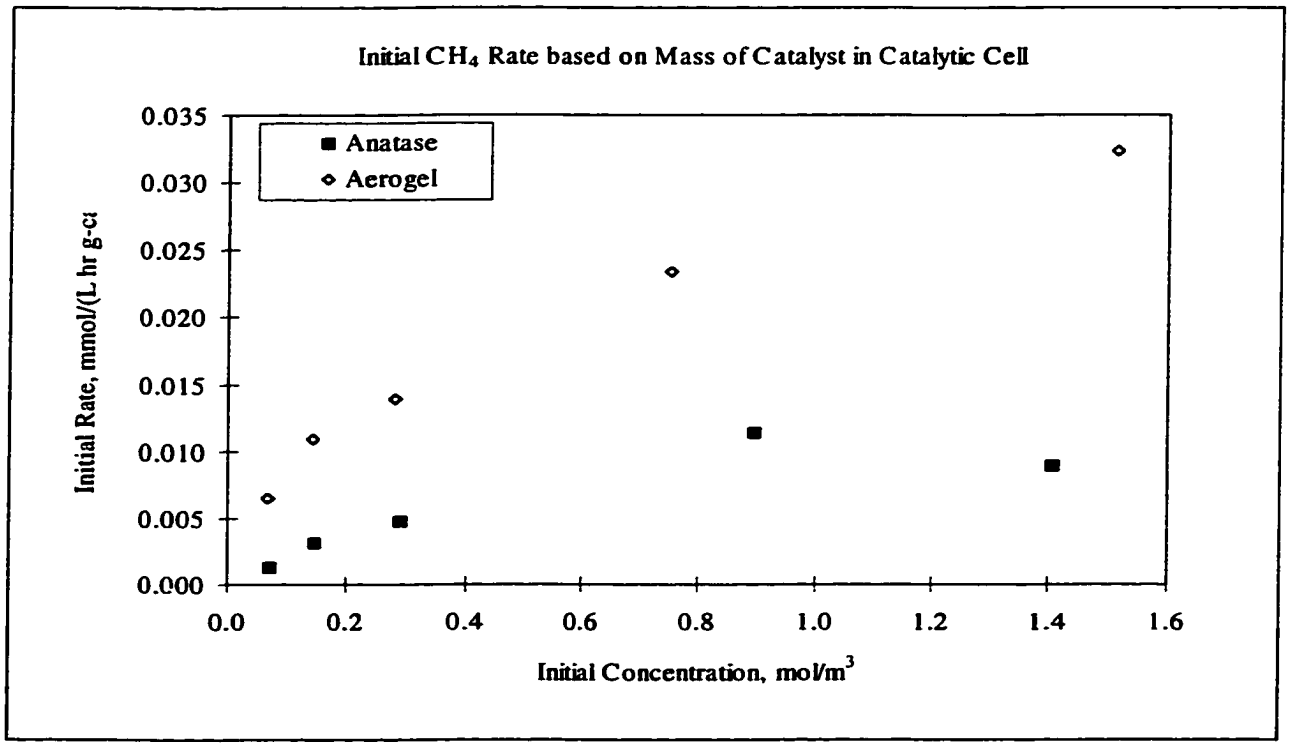

Figure 4-86 Initial CH_4 oxidation rates based on weight of catalyst in catalytic cell

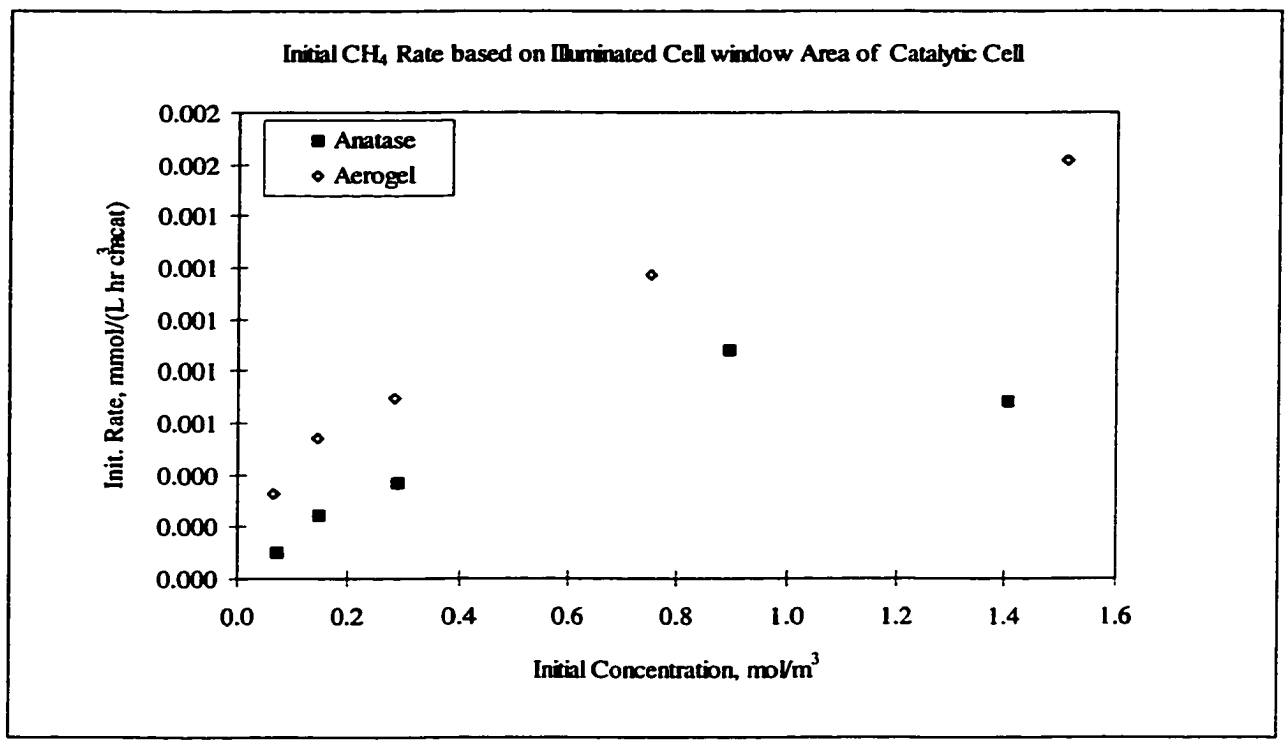

Figure 4-87 Initial methane oxidation rates based on illuminated cell window area

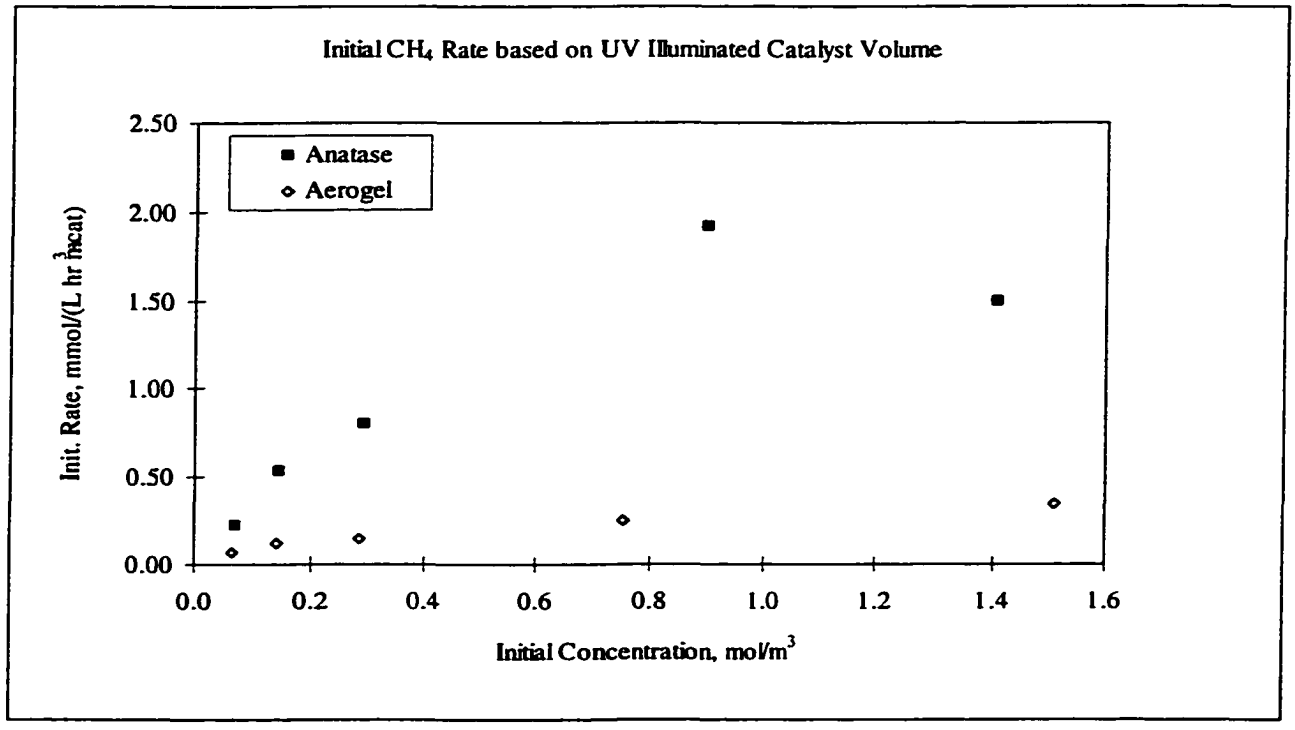

Figure 4-88 Initial methane oxidation rates based on actual illuminated catalyst bed (UV penetrated catalyst volume)

In order to evaluate and compare reaction rate constants, initial rate data were utilized based on catalyst mass, catalyst volume, and illuminated catalyst bed volume. The reaction rate constants for both catalysts were determined based on a Langmuir-Hinshelwood expression according to equation (4-9)

$$\frac{dC_{CH_4}}{dt} = \frac{k_{CH_4} K_{H_2O} K_{CH_4} C_{CH_4}}{1 + K_{H_2O} C_{H_2O} + K_{CH_4} C_{CH_4}} \quad \textbf{(4-9)}$$

where C_{CH4} = gas phase concentration of methane
C_{H2O} = gas phase concentration of water
t = time
k_{CH4} = reaction rate constant for methane oxidation
K_{CH4} = adsorption constant for methane
K_{H2O} = adsorption constant for water

Before conducting a new experimental run, the reactor system was purged with dry air in order to remove any water. However, it was possible that adsorbed water from previous runs were not removed by the dry air and may still have remained adsorbed on the catalyst. Assuming that this water was strongly adsorbed and that those sites are not involved in the reaction equation (4-9) can be simplified to (4-10):

$$(4\text{-}10)\quad -\frac{dC_{CH_4}}{dt} = r = \frac{k_{CH_4} K_{CH_4} C_{CH_4}}{1 + K_{CH_4} C_{CH_4}}$$

Rearranging of equation (4-8) leads to (4-11)

$$(4\text{-}11)\quad \frac{1}{dC_{CH_4}/dt} = \frac{1}{k_{CH_4}} + \frac{1}{k_{CH_4} K_{CH_4}} \frac{1}{C_{CH_4}} \quad .$$

When plotting the inverse of the initial rate (dC_{CH4}/dt) versus the inverse of the initial concentration the data should give a straight line. The reaction rate constant k_{CH4} can then be determined from the intercept, which is $1/k_{CH4}$. The methane adsorption constant was determined from the slope, which is $1/k_{CH4}K_{CH4}$. The data for the aerogel CEH6 and the anatase are shown in Figure 4-89. Table 4-13 summarizes the determined rate constants.

Rate Constants $k_{x\ methane}$ (lin. integration)	Anatase	Aerogel
k mass, mol/(m^3 hr g-cat)	0.024	0.030
k ill. Cell window area, mol/(m^3 hr cm^2-cat)	0.0018	0.0015
k ill. cat-Volume, mol/(m^3 hr cm^3-cat)	4.28	0.52
k ill. cat-SA, mol/(m^3 hr m^2-cat)	0.086	0.003
Methane Adsorption Constant K, m^3/mol	0.89	4.15

Table 4-13 Rate constants for anatase and CEH6 based on mass, illuminated cell window area, UV accessible catalyst volume and UV accessible catalyst surface area.

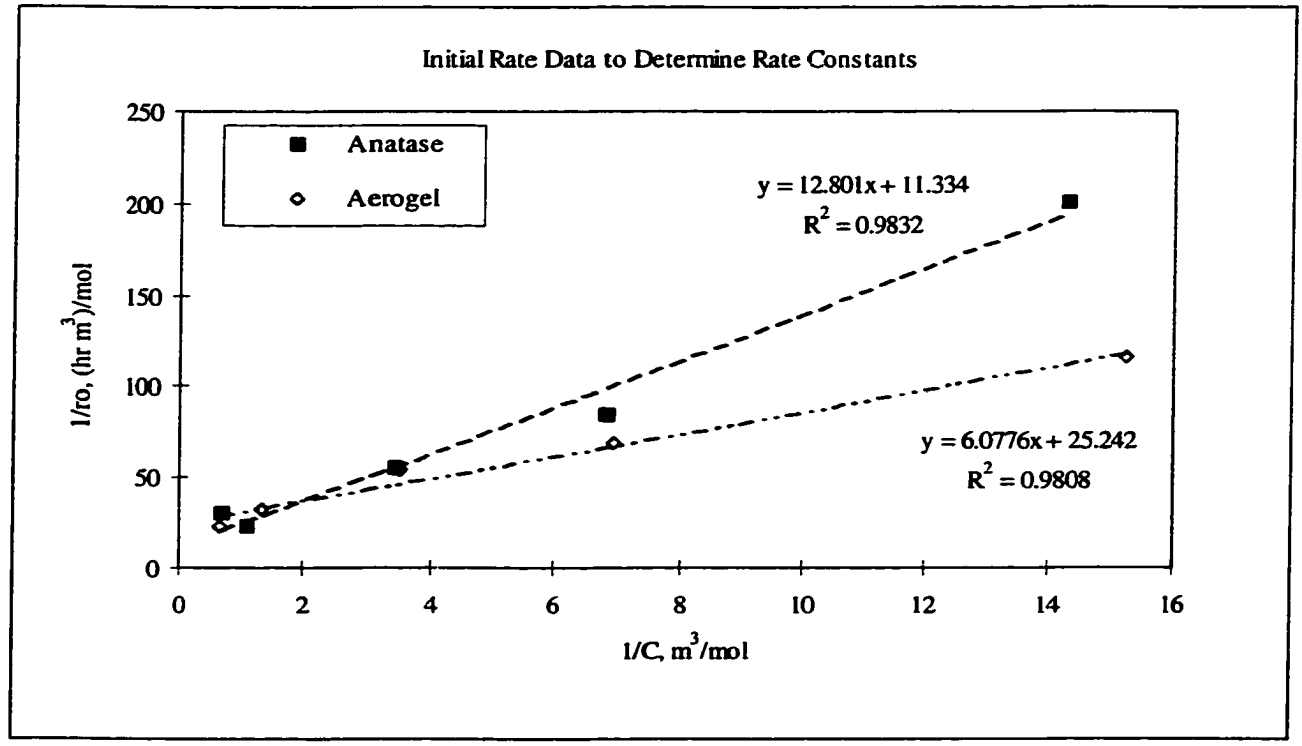

Figure 4-89 Linear regression of 1/rate versus 1/C to determine the rate constants k_{CH4} for anatase and aerogel CEH6

A more accurate way of determining the rate parameters, however, is using a nonlinear regression method as described in more detail in Section 4.6.4.2. This is done by maximizing the non-linear regression parameter R^2 (see Equation (4-20)) over the experimental initial rate data of each set fitted to the Langmuir-Hinshelwood reaction rate model such as described in equation (4-10). The values of the rate parameters using this method are tabulated in Table 4-14 and show a good agreement of the Langmuir-Hinshelwood model with the initial rate data as shown in Figure 4-90 for the experiments over the anatase and the aerogel CEH6.

Rate Constants $k_{x\ methane}$	Anatase	Aerogel
k mass, mol/(m^3 hr g-cat)	0.014	0.042
k ill. Cell window area, mol/(m^3 hr cm^2-cat)	0.0011	0.0021
k ill. cat-Volume, mol/(m^3 hr cm^3-cat)	2.52	0.72
k ill. cat-SA, mol/(m^3 hr m^2-cat)	0.050	0.004
Methane Adsorption Constant K, m^3/mol	2.16	2.00

Table 4-14 Rate constants for anatase and the aerogel CEH6 based on mass in catalytic cell, illuminated cell window area, illuminated catalyst volume in catalyst bed, and UV illuminated catalyst surface area using the method of maximizing R^2

The reaction rate constant of the aerogel CEH6 based on catalyst mass was about three times higher than that of 100% anatase. However, as already predicted from the initial rate data based on actual illuminated catalyst bed (see Figure 4-88), the performance of anatase based on how much surface area was accessed by UV light is still considerably better than that of the areogel. The related k-value for anatase (based on illuminated catalyst volume) was about three times higher compared to the one of the aerogel and when based on the total illuminated catalyst surface area the respective k-value for anatase was about 13 times higher. This confirms that the actual reaction sites of the aerogel are considerably less photocatalytically reactive than the anatase sites and/or that the number of active sites per surface area in the catalyst bed of the anatase is very much higher.

The Langmuir-Hinshelwood models using equation (4-10) and the rate parameters from Table 4-14 were also calculated for each individual run. The so calculated models did not describe the experimental rate data satisfactorily as it can be seen in Figure 4-92

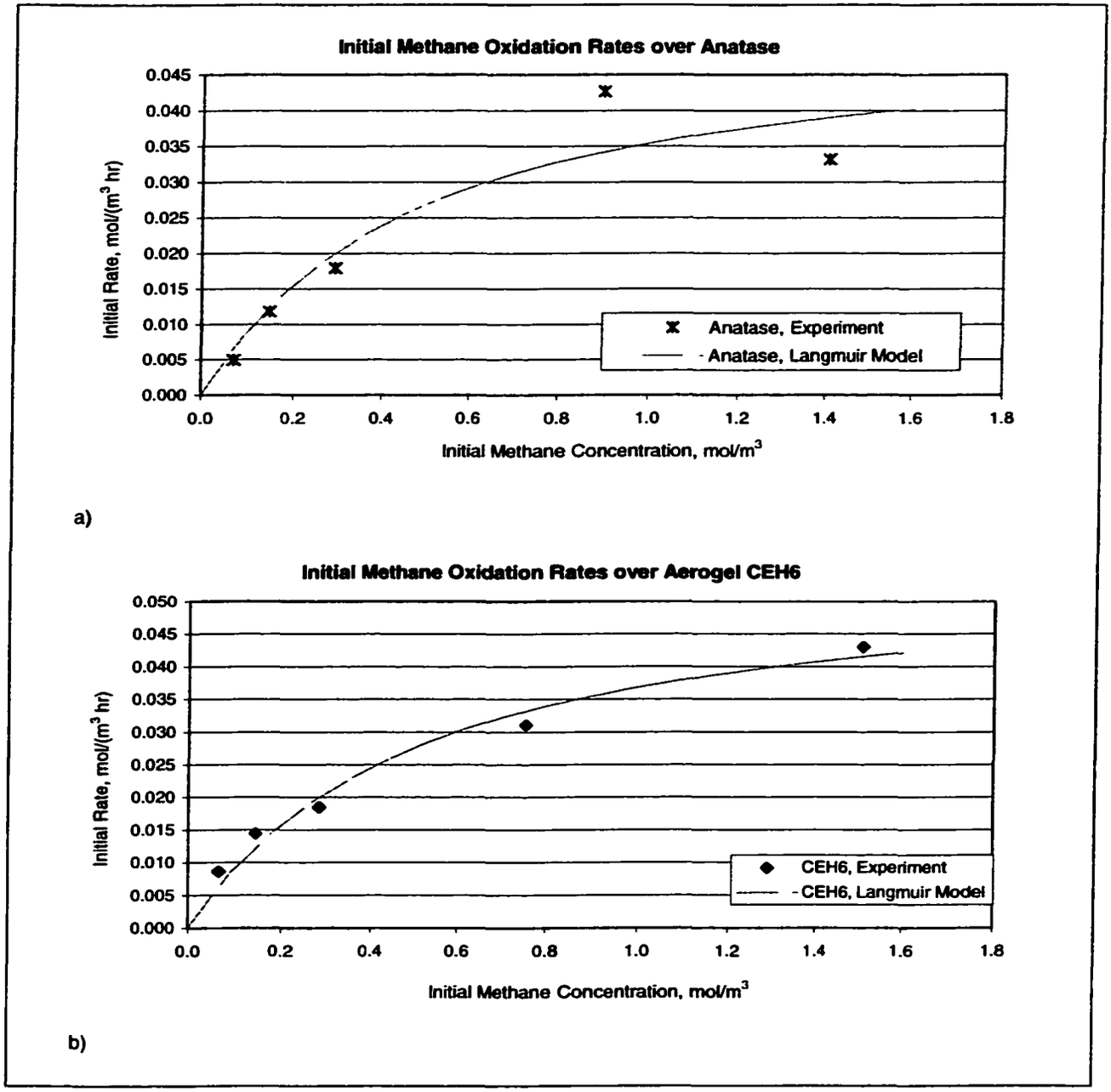

Figure 4-90 Initial rate data and Langmuir-Hinshelwood model of methane oxidation over anatase (a) and aerogel CEH6 (b)

The reason behind this behavior lies in the fact that water was generated throughout the oxidation of methane, but equation (4-10) did not take any water in the reactor system into account. Not surprisingly, then, the predicted rates were higher than the actual rates.

To account for the effect of water, the water adsorption constants K_W were determined as outlined in Section 4.6.4.2, which are tabulated for anatase and the aerogel CEH6 in Table 4-15. When applying the so found values for K_W in equation (4-9), the predicted rates described the experimental data better. It needs to be pointed out that for the aerogel the water did not have such a strong effect on the reaction rate than for the anatase. For all individual photooxidation experiments over CEH6, the non-linear regression parameter could be maximized for values of K_W in the range of $5*10^7$. However, it was found that applying smaller values for K_W resulted in the same rate predictions. In fact, values for K_W greater than 0.1 m^3/mol did not affect the predicted Langmuir-Hinshelwood rate significantly. For that reason, all values for K_W for the aerogel CEH6 in Table 4-15 were set to 0.1 m^3/mol. When comparing the magnitudes of the term K_WC_W with the term K_MC_M in equation (4-9) as illustrated in Figure 4-91 it is clear that the water term K_WC_W was considerably smaller (which was even the case for $K_W = 5*10^7$ m^3/mol) thus the influence of the generated water became negligible for the methane oxidation rate prediction over aerogel CEH6. Even though the determined rate parameters provided a reasonably good fit to the experimental data. However, the behavior is not that of a typical Langmuir-Hinshelwood trend. Therefore, it must be assumed that some other - more complex - reaction mechanism might be present than simple competitive adsorption for the same site.

Catalyst	Feed Methane ml	C Methane mol/m^3	Kw m^3/mol	R^2	Kw avg m^3/mol
Anatase					
	0.5	0.0699	5.37	0.64	
	1	0.1459	23.42	0.77	
	2	0.2915	11.34	0.57	
	6	0.8957	4.00	0.87	
	10	1.4075	9.65	0.61	10.76
CEH6					
	0.5	0.0656	0.10	0.95	
	1	0.1440	0.10	0.97	
	2	0.2839	0.10	0.88	
	6	0.7538	0.10	0.78	
	10	1.5099	0.10	0.91	0.10

Table 4-15 Water adsorption constants for each individual methane oxidation experiment over anatase and aerogel CEH6.

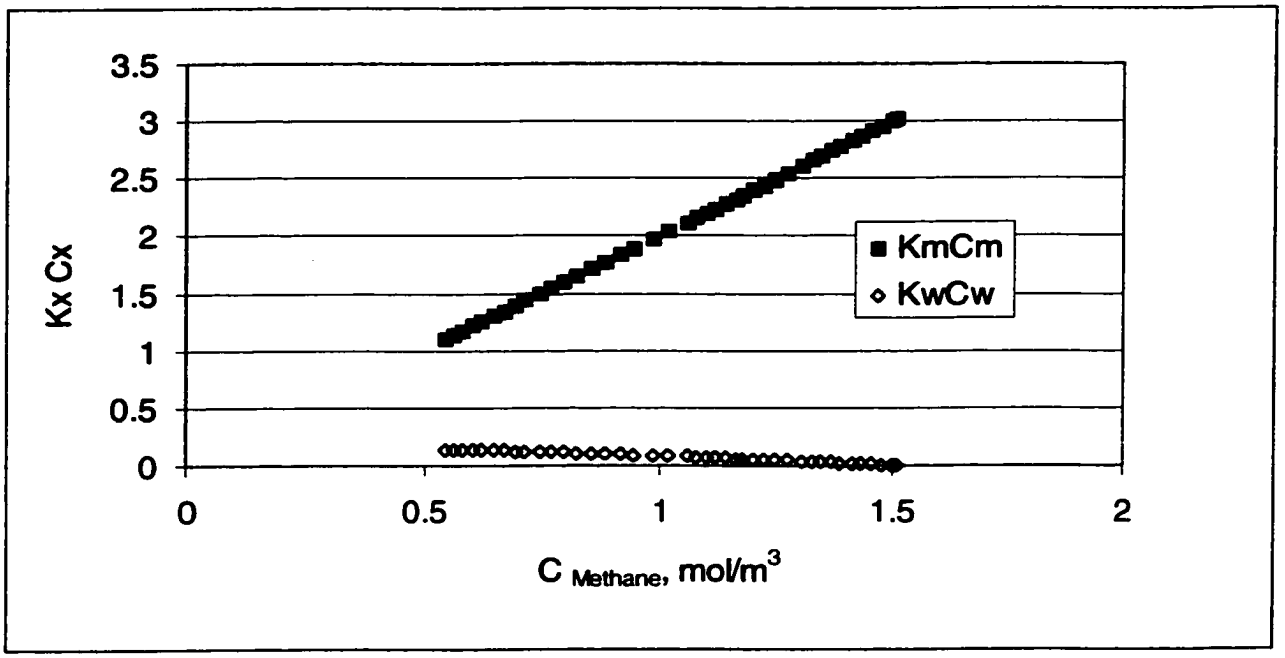

Figure 4-91 Comparison of magnitudes of the water term K_WC_W and the methane term K_MC_M in equation (4-9) for methane oxidation over the aerogel CEH6

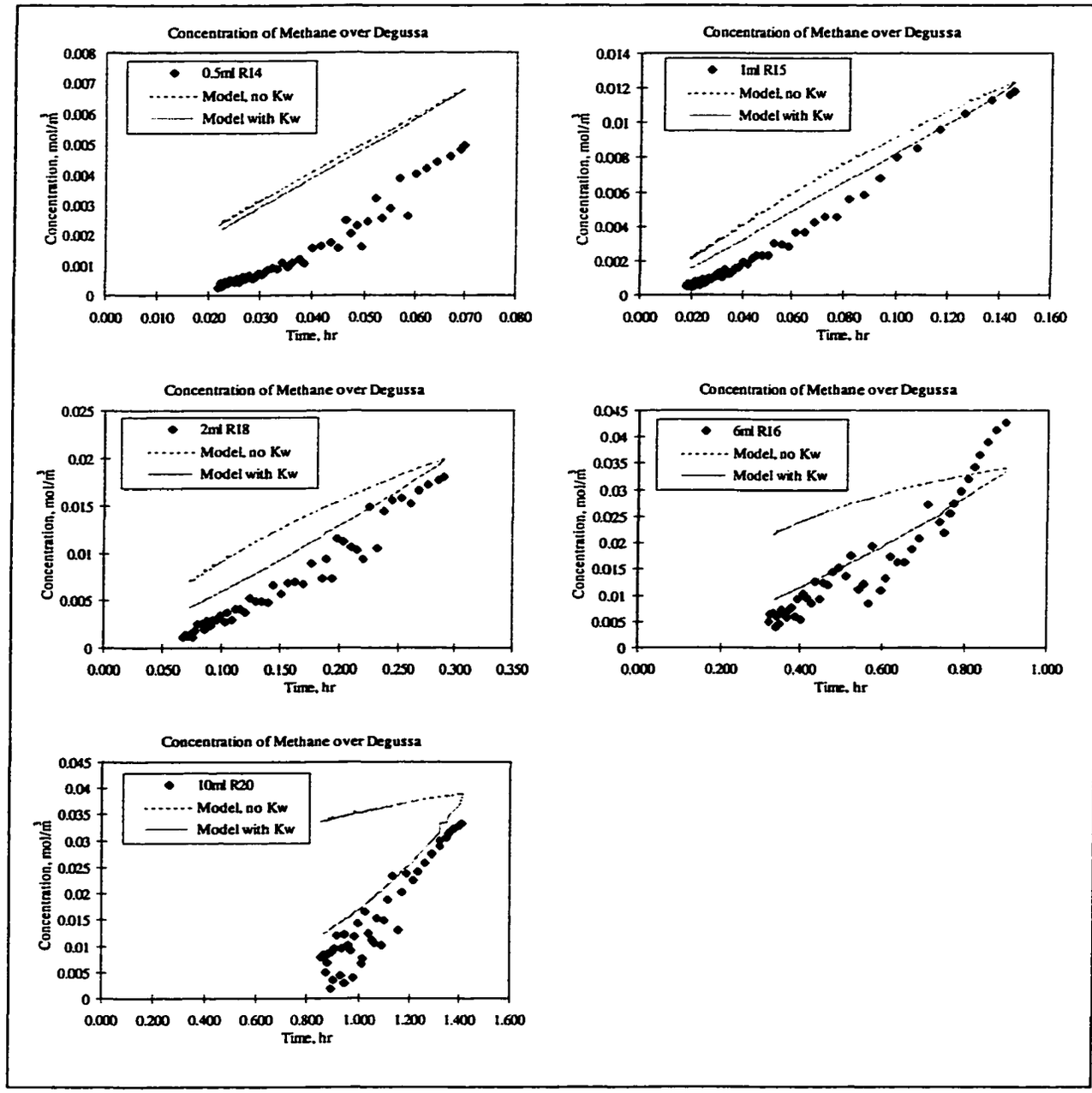

Figure 4-92 Reaction rates versus methane concentration and Langmuir-Hinshelwood models of individual methane oxidation tests over anatase CEH6 at initial feeds of 0.5, 1, 2, 6, and 10 ml methane feed at ambient conditions. The dotted lined indicate models ignoring the water term, the dashed lines include the water term in the model.

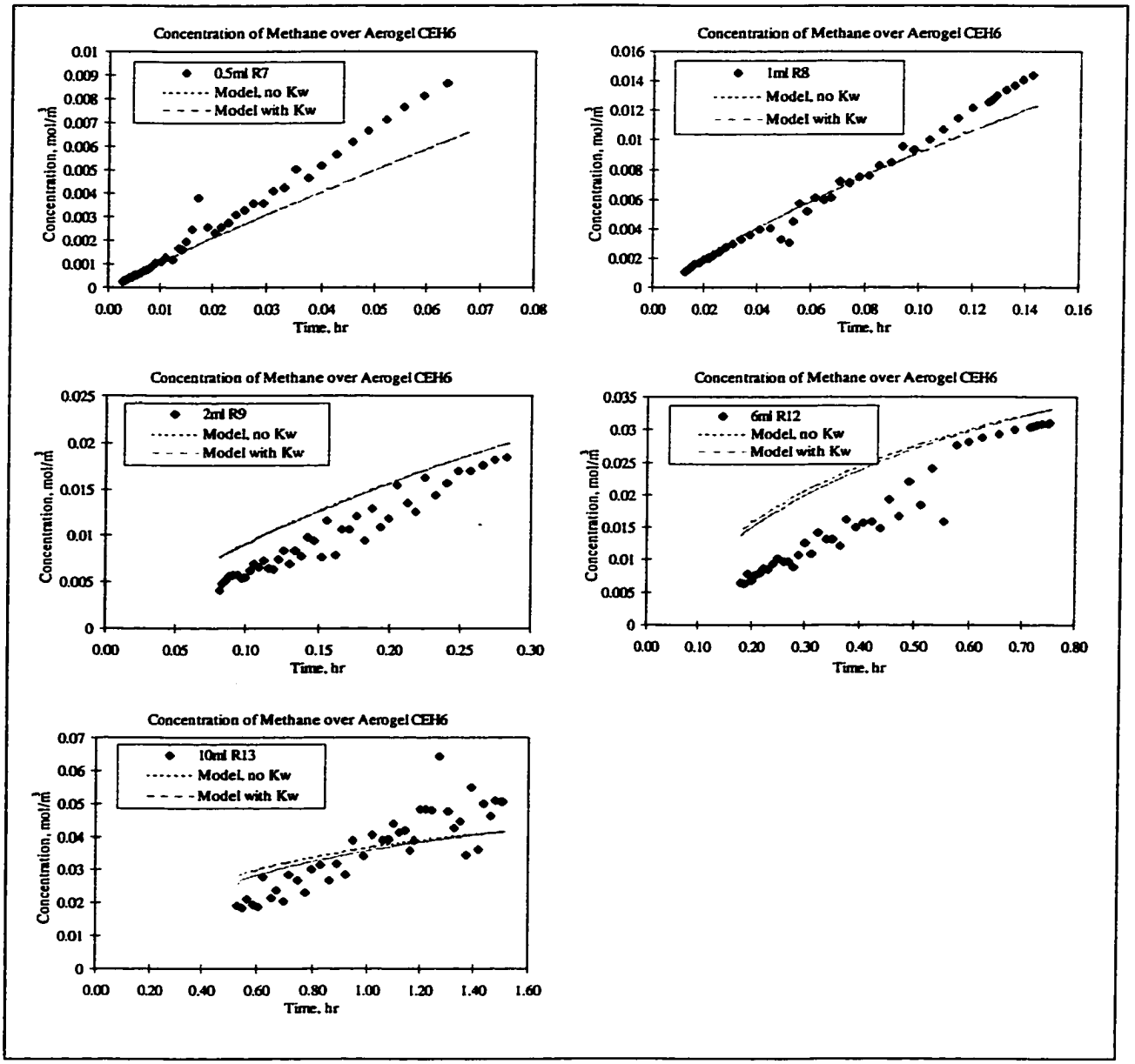

Figure 4-93 Reaction rates versus methane concentration and Langmuir-Hinshelwood models of individual methane oxidation tests over aerogel CEH6 at initial feeds of 0.5, 1, 2, 6, and 10 ml methane feed at ambient conditions. The dotted lined indicate models ignoring the water term, the dashed lines include the water term in the model.

4.6.2 Ethane Photo-Oxidation

The complete oxidation reaction for ethane is:

Ethane Oxidation: $C_2H_6 + 7/2\ O_2 \rightarrow 2\ CO_2 + 3\ H_2O$

Photocatalytic tests of ethane oxidation were conducted in the same manner as described in Section 3.5. The catalytic cell filled with anatase contained 3.7 g of catalyst while the catalytic cell containing the aerogel held only 1.1 g. Oxidations tests were performed at initial ethane concentrations ranging between 8000 and 50,000 ppm according to 3, 5, 8, 11, and 15 ml of ethane feed at ambient conditions. Figure 4-94 shows the decrease in ethane concentration of both catalysts at 5 ml feed. Both experimental runs were performed twice and showed good repeatability. It can also be observed that the aerogel oxidized ethane at a much faster rate than the anatase. The experimental results for all other initial concentrations are summarized in the Appendix (Table 7-12). At any initial ethane concentration the aerogel outperformed the anatase by a significant margin. Ethane oxidation over the aerogel was completed within about one third time less than over the anatase. It was also tested if ethane would oxidize without the presence of any catalyst. This was not the case as seen in Figure 4-95.

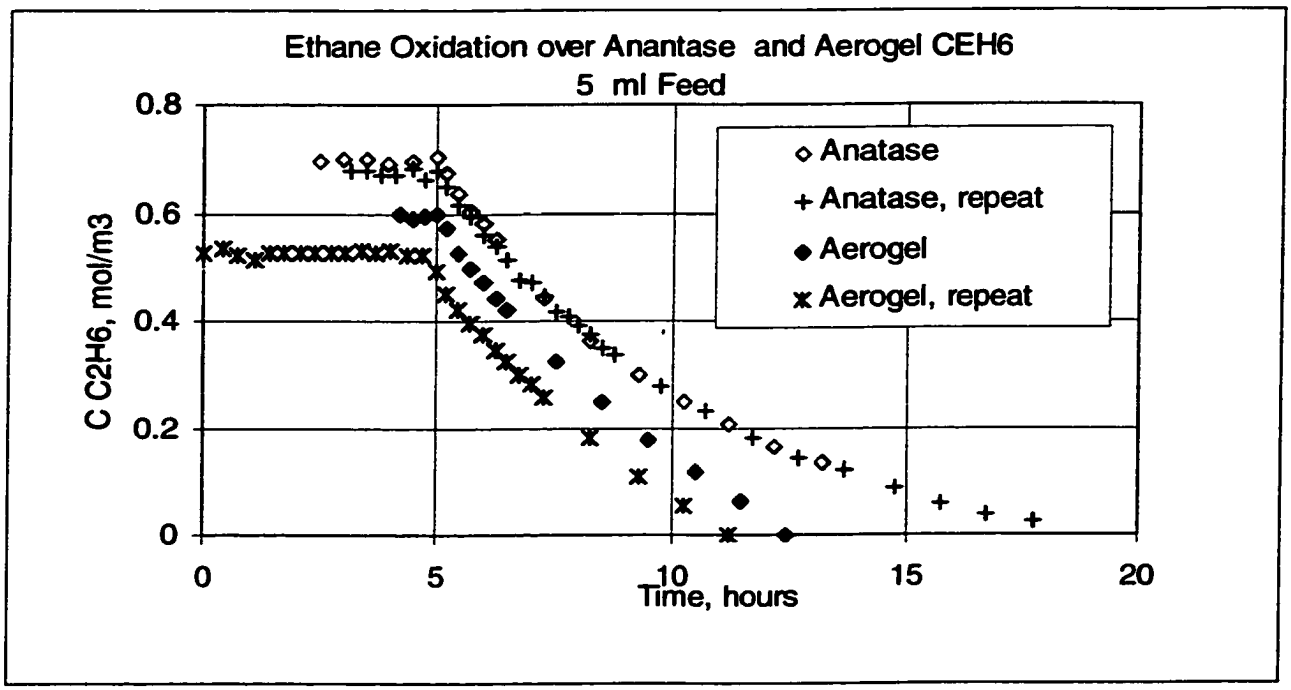

Figure 4-94 Ethane oxidation over aerogel CEH6 and 100% anatase

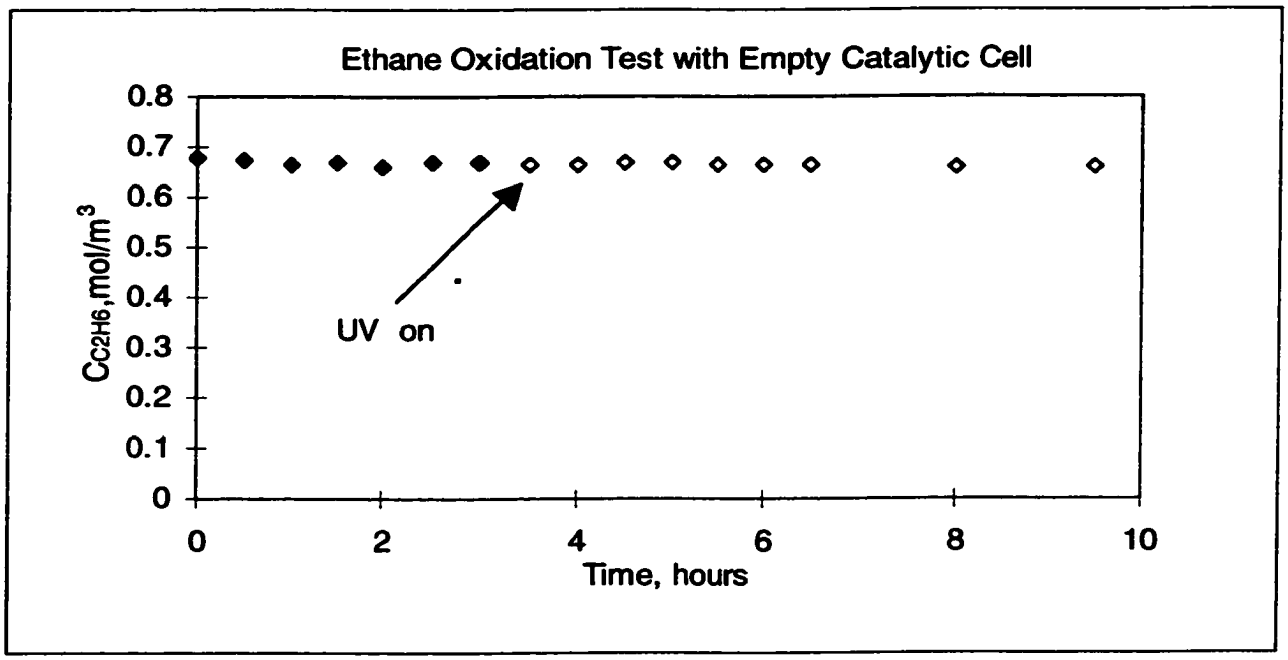

Figure 4-95 Ethane concentration under UV illumination without the presence of a catalyst

The initial rate data are shown in Figure 4-96 to Figure 4-98. Based on mass of catalyst in the system, the initial rates over the aerogel were about three times higher than over the anatase, while based on illuminated catalytic cell window area the aerogel exceeded the performance of the anatase by a factor of two. However, similar to the observations from methane oxidation tests, when comparing the initial rates based on actual illuminated catalyst volume, the anatase showed a four times higher activity. And normalizing the initial rates to the total UV illuminated surface area of the catalyst showed a 40 fold higher initial rate for the anatase. This, again, is indicative of the higher reactivity of an activated site or the higher number of active sites per total illuminated surface area.

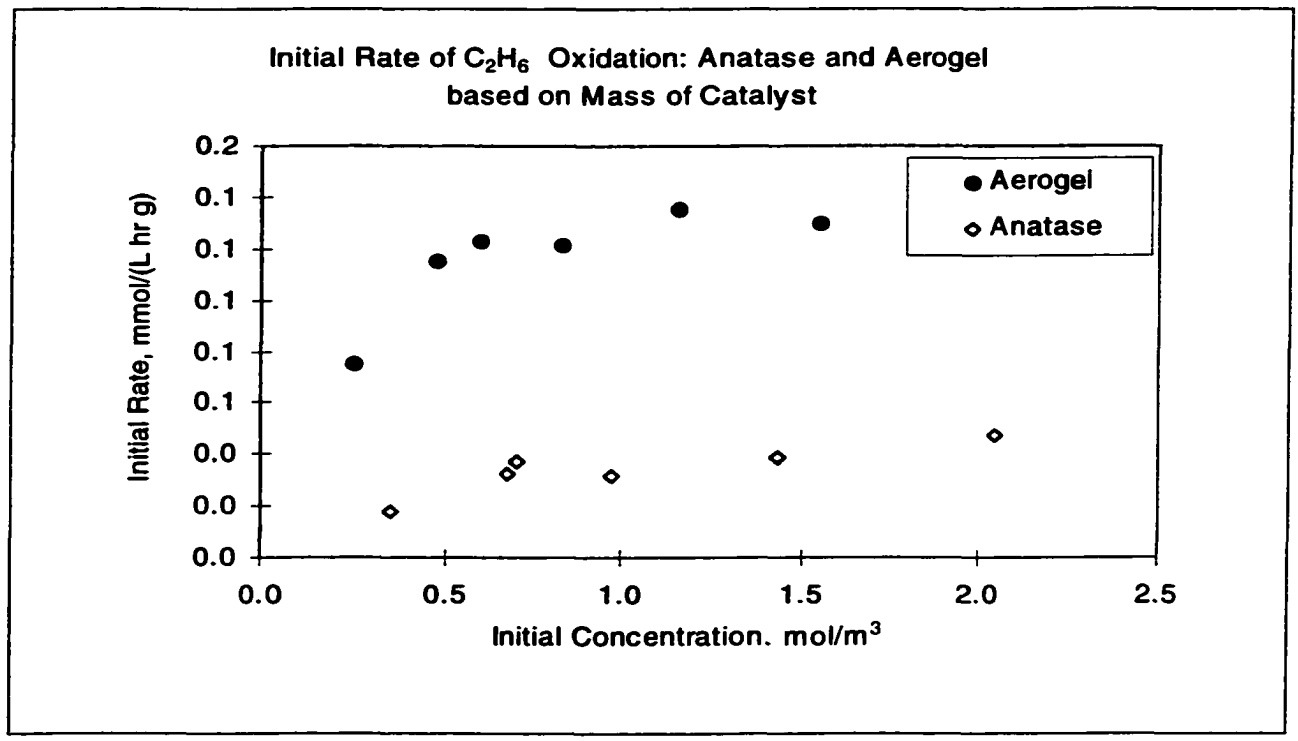

Figure 4-96 Initial ethane oxidation rates based on mass of catalyst in catalytic cell

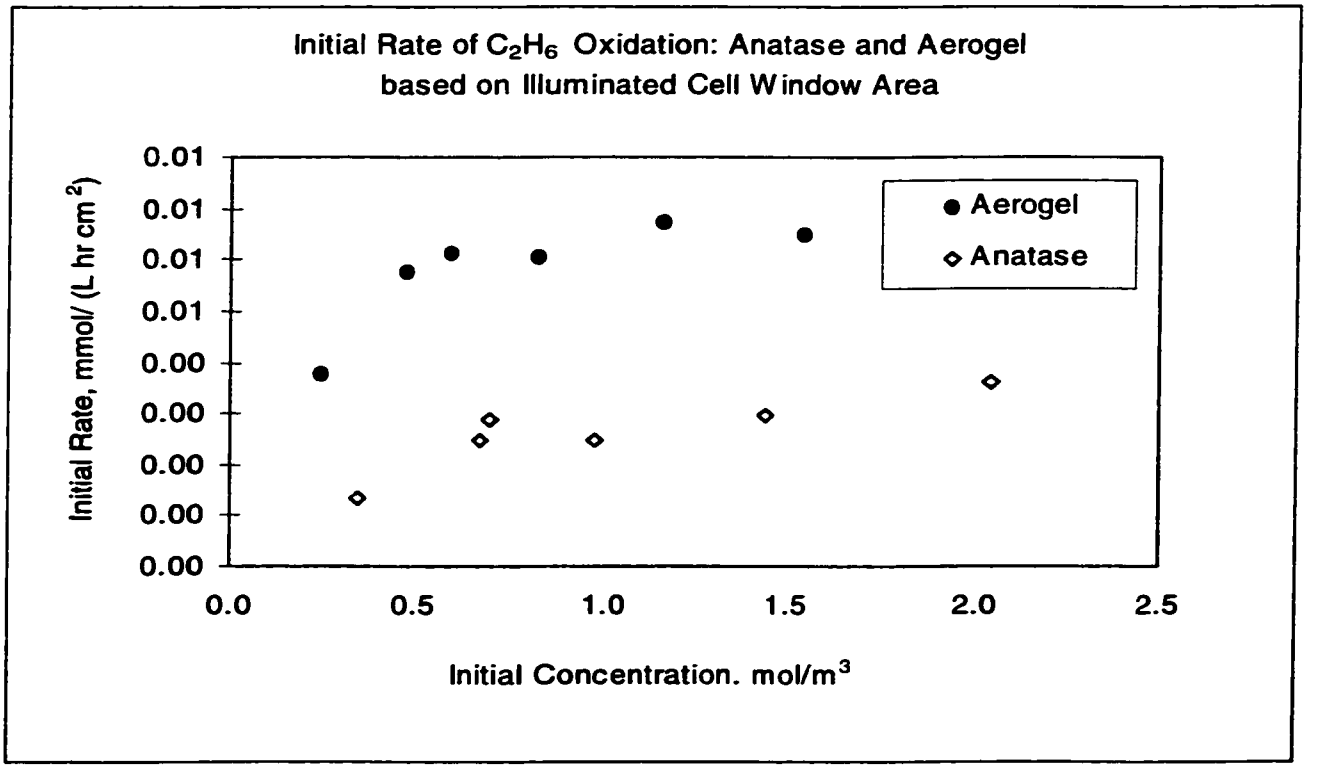

Figure 4-97 Initial ethane oxidation rates based on illuminated cell window area

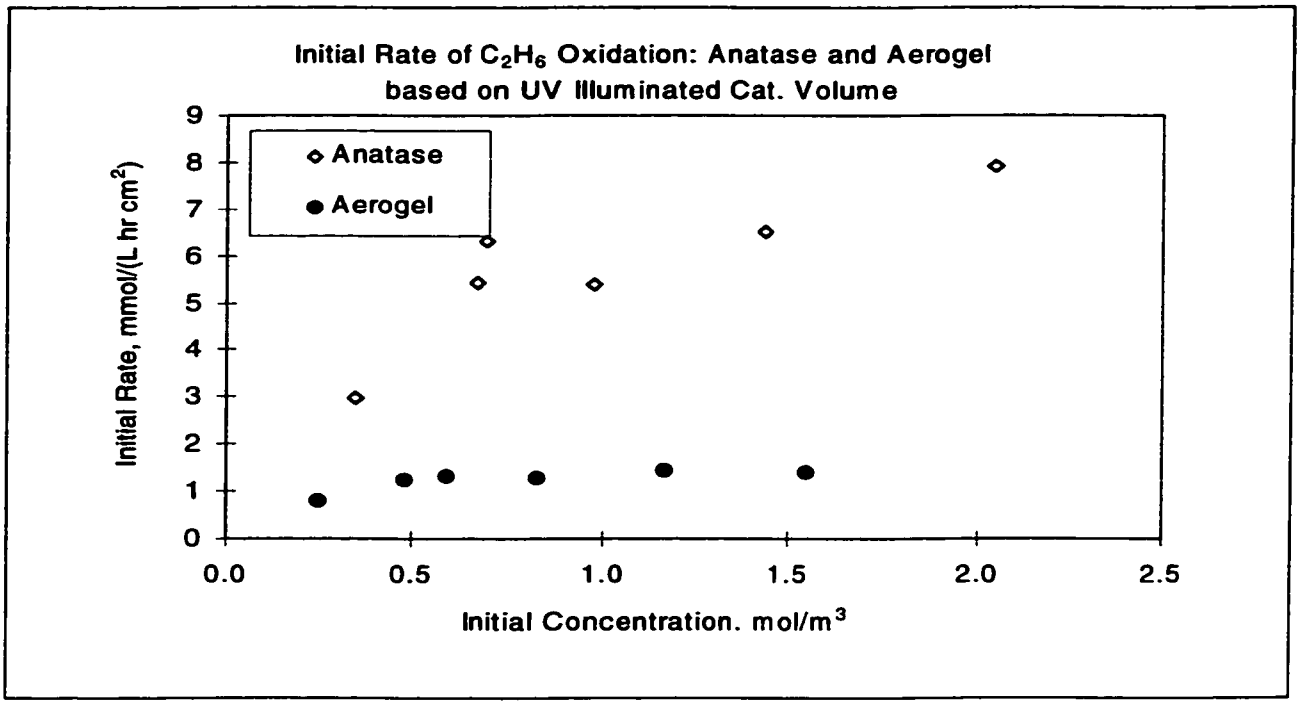

Figure 4-98 Initial ethane oxidation rates based on actual UV penetrated catalyst volume

The reaction rate constants for ethane oxidation were determined using the same calculations steps as introduced for the methane oxidation in the previous section. The rate constants for ethane oxidation were determined by maximizing R_2 of the Langmuir-Hinshelwood model over the experimental initial rate data. The so determined values are summarized in Table 4-16. Figure 4-99 shows a good agreement of models with the initial rate data for both catalysts. Comparison of the initial rates already indicated that the aerogel oxidized ethane at a faster rate than anatase on the basis of mass and illuminated cell window. The obtained rate constants confirmed those observations with a k_{C2H6} of aerogel almost three times higher based on mass or a k_{C2H6} of aerogel about 1.6 times that of the k_{C2H6} of anatase based on illuminated cell window. This is an interesting result from the engineering point of view as the amount of catalyst and the cell size are important parameters in reactor design calculations. However, the intrinsic reactivity of the aerogel is still lower by a factor of 3.8 smaller based on the amount of actual UV illuminated catalyst volume or about 17 times smaller based on actual illuminated catalyst surface area.

Rate Constants $k_{x\ ethane}$	**Anatase**	**Aerogel**
k mass, mol/(m^3 hr g-cat)	0.054	0.135
k ill. Cell window area, mol/(m^3 hr cm^2-cat)	0.0041	0.0067
k ill. cat-Volume, mol/(m^3 hr cm^3-cat)	9.03	2.33
k ill. cat-SA, mol/(m^3 hr m^2-cat)	0.21	0.0122
Ethane Adsorption Constant K, m^3/mol	1.97	3.92

Table 4-16 Rate constants for ethane oxidation over anatase and aerogel CEH6

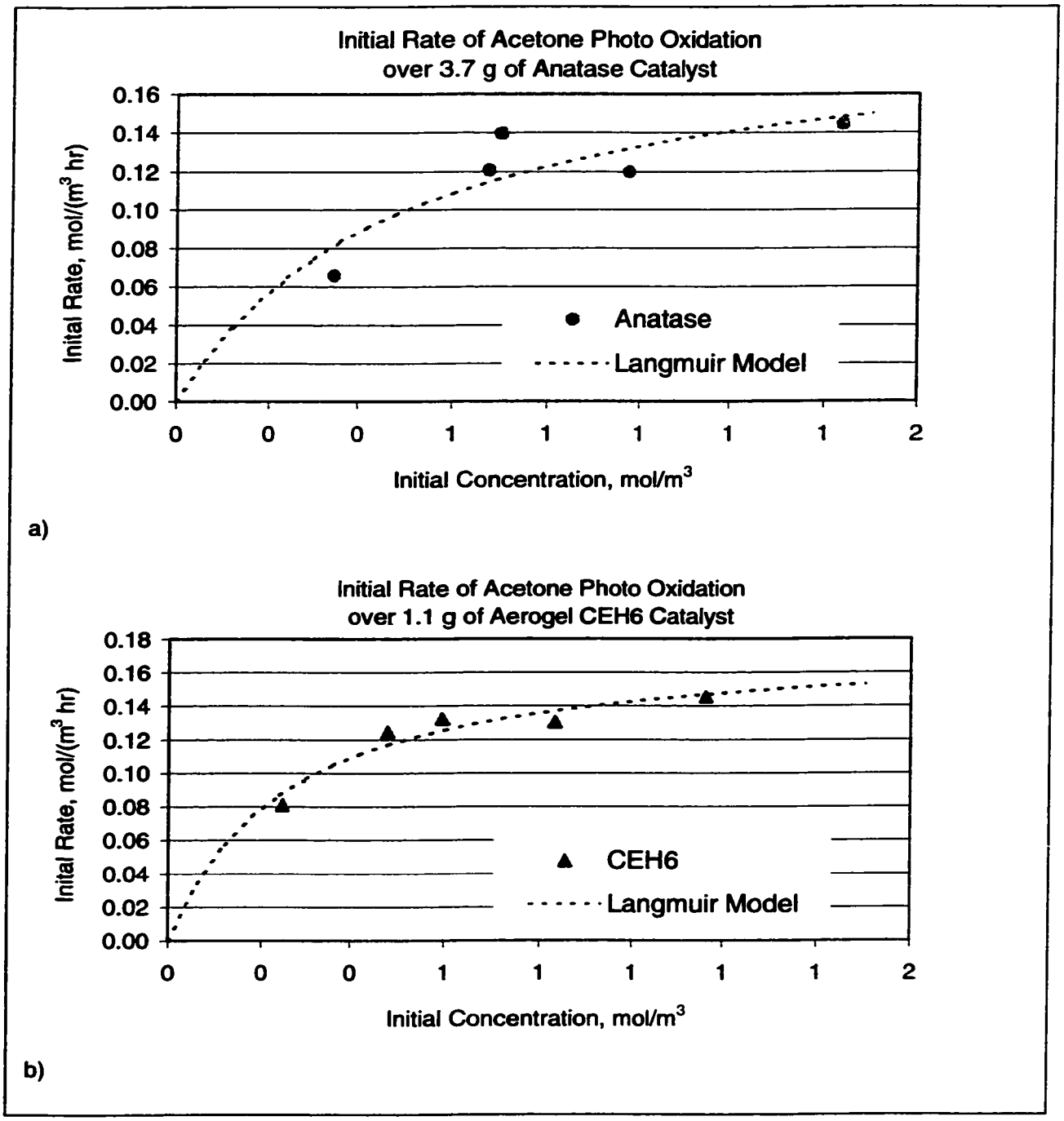

Figure 4-99 Initial rate data and Langmuir-Hinshelwood model of ethane oxidation over anatase (a) and aerogel CEH6 (b)

The water adsorption constants listed in Table 4-17 were determined as outlined in Section 4.6.4.2. Similar to the finding from the methane oxidation test, the rate

dependence on generated water was stronger for the anatase than for the aerogel. Again, for the aerogel, the trend of the Langmuir-Hinshelwood model did not change notably for any value of the water adsorption constant K_W greater than 1. The little influence of the generated water on the Langmuir prediction can be understood when considering the fact that the value for the water term of the Langmuir-Hinshelwood relation (K_WC_W) is much smaller compared to the ethane term (K_EC_E) as seen in Figure 4-100. In contrast, the water term for the anatase catalyst is of significant magnitude to influence the rate prediction considerably. One of the reasons for the different behaviors between the two catalyst could be that generated water adsorbed mainly on non-reactive sites on the aerogel (since the intrinsic activity is much lower for the aerogel), while many reactive sites of the anatase were blocked by competitively adsorbed water. It is also noteworthy to point out that the anatase showed a trend in reaction rates, which was slightly different from a typical Langmuir-Hinshelwood behavior. This is best seen at higher initial ethane feed concentrations (8, 11, and 15 ml) as in Figure 4-101 where the rates do not level out at higher concentrations but rather seem to increase sharply. A possible explanation for this performance could be that the catalyst was quickly deactivated by strongly adsorbed byproducts that were not detected in the gas phase and that were eventually also oxidized. Another argument could be that anatase might have different sites on which generated water adsorbs differently strong. Therefore, assuming a Langmuir-Hinshelwood expression for competitive adsorption for the same sites (as assumed for the rate parameter calculations in this work) might not be applicable. It is also possible that some other reaction mechanism than Langmuir-Hinshelwood determines the reaction rate. In

contrast, the Langmuir-Hinshelwood models provided acceptable predictions for ethane oxidation over the aerogel CEH6.

Catalyst	Feed Ethane ml	C Ethane mol/m^3	C Water mol/m^3	Kw m^3/mol	R^2	Kw avg m^3/mol
Anatase						
	3	0.346	0.3454	1.58	0.54	
	5	0.701	0.8392	0.41	0.82	
	8	0.674	1.1198	2.83	0.73	
	11	0.974	1.6754	1.89	0.95	
	15	1.437	2.1549	1.92	0.93	1.73
CEH6						
	3	0.246	0.0509	1.00	0.76	
	5	0.595	0.1683	1.19	0.56	
	8	0.479	0.3492	1.00	0.71	
	11	0.832	0.6104	1.00	0.86	
	15	1.163	0.6390	1.50	0.60	1.14

Table 4-17 Water adsorption constants for each individual ethane oxidation experiment over anatase and aerogel CEH6. The non-linear regression parameter R^2 and the average value of K_W are included

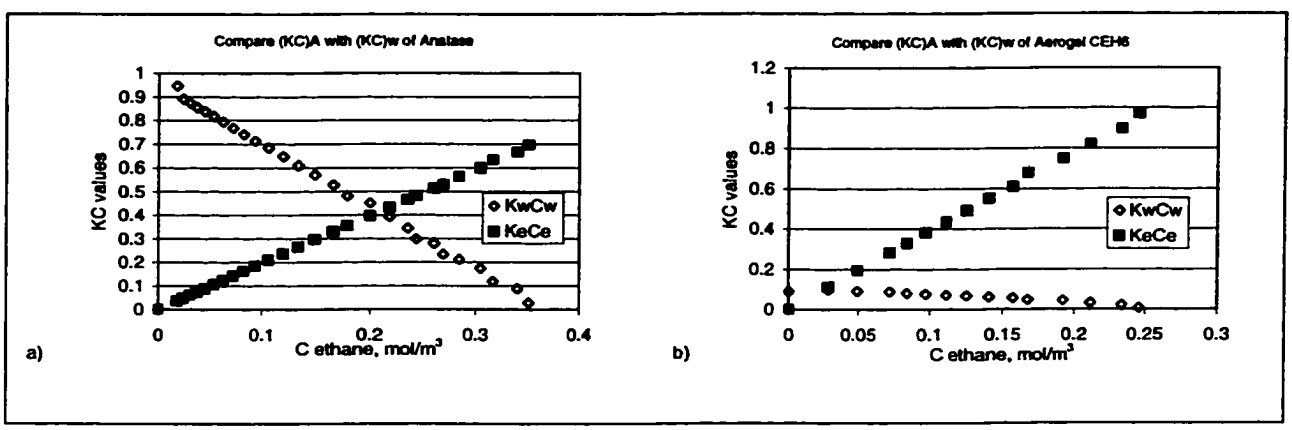

Figure 4-100 Comparison of magnitudes of the water term K_WC_W and the ethane term K_EC_E in equation (4-9) for methane oxidation over anatase (a) and the aerogel CEH6 (b)

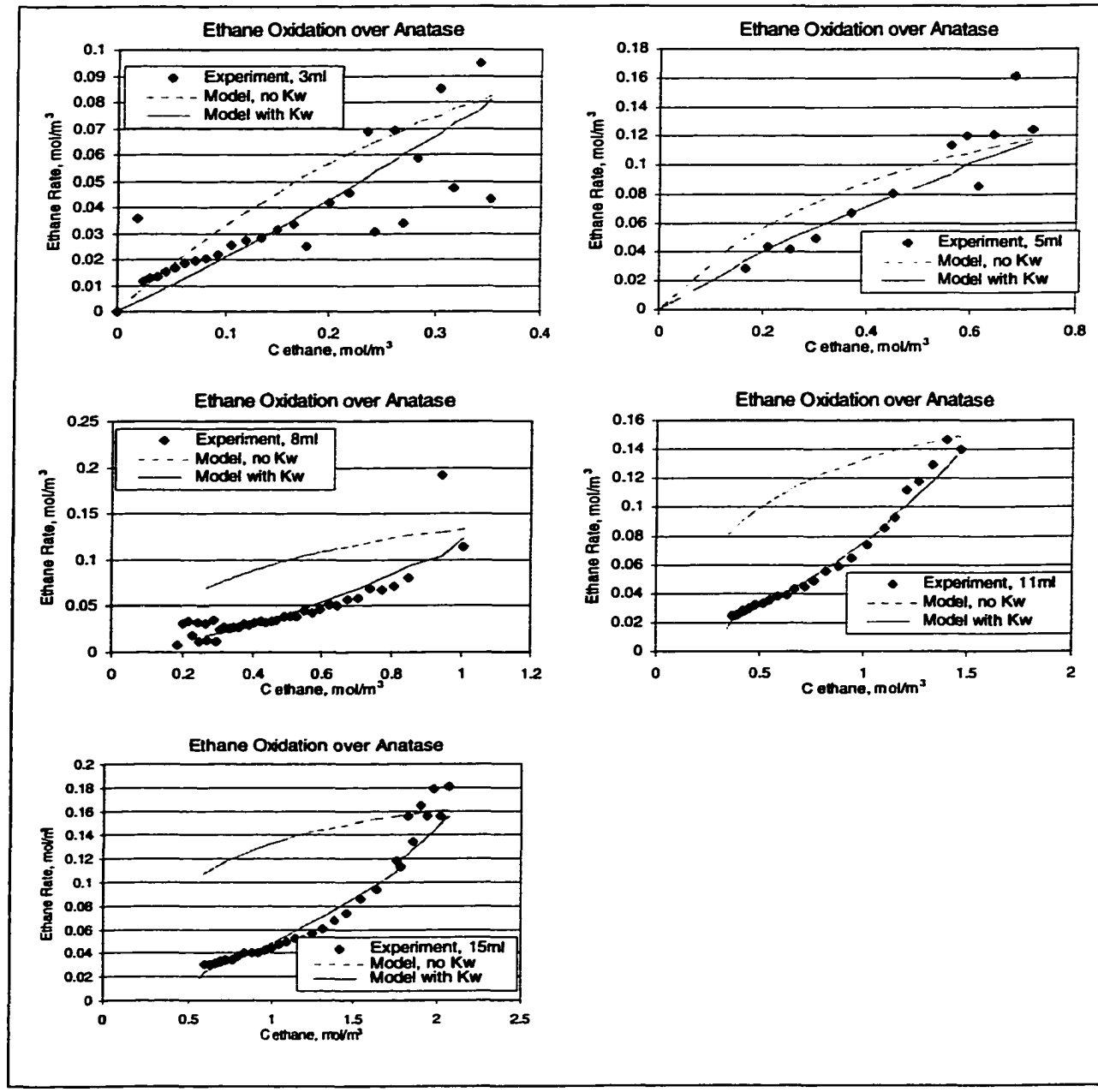

Figure 4-101 Reaction rates versus ethane concentration and Langmuir-Hinshelwood models of individual methane oxidation tests over anatase at initial feeds of 3, 5, 8, 11, and 15 ml of methane feed at ambient conditions. The dotted lines indicate models ignoring the water term, the dashed lines include the water term in the model.

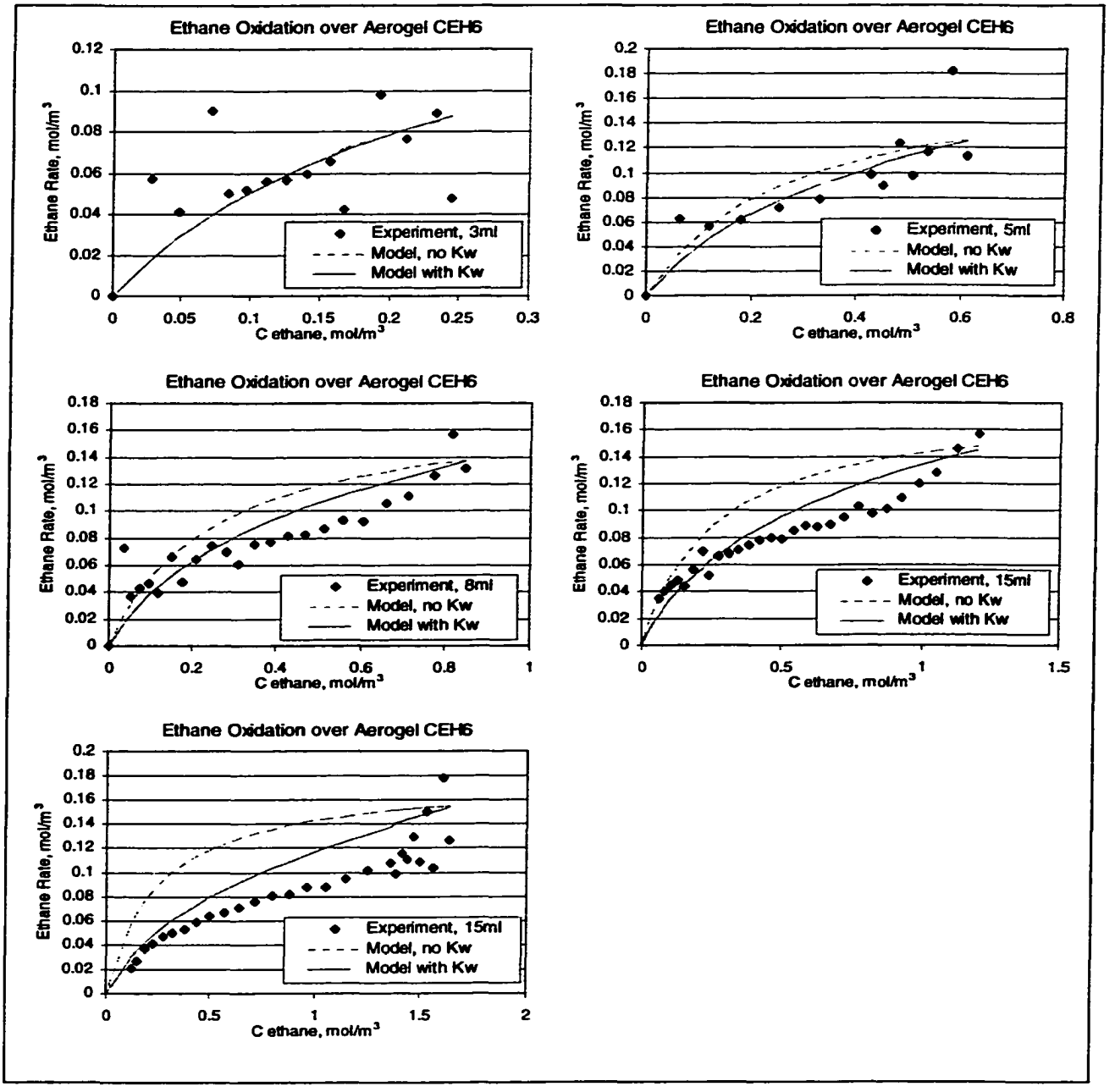

Figure 4-102 Reaction rates versus ethane concentration and Langmuir-Hinshelwood models of individual methane oxidation tests over aerogel CEH6 at initial feeds of 3, 5, 8, 11, and 15 ml of methane feed at ambient conditions. The dotted lines indicate models ignoring the water term, the dashed lines include the water term in the model.

4.6.3 Acetone Photo-Oxidation

The complete oxidation reaction for acetone is

$$CH_3\text{-}CO\text{-}CH_3 + 4\ O_2 \rightarrow 3\ CO_2 + 3\ H_2O$$

Photocatalytic oxidation of acetone was performed over four catalysts: anatase TiO_2 (Aldrich, 99.9 % anatase titanium IV oxide), Degussa P25 (Degussa Corporation New Jersey), the low-density aerogel CEH6, and the ultra-low density aerogel T36 (both aerogels synthesized in our labs (see 3.1.2). The reactor cells were loaded individually with 3.74 g of anatase (corresponding to a bed volume of 3.8 cm^3), 1.3 g of CEH6 (corresponding to a bed volume of 2.1 cm^3), 2.2 g of Degussa P25 (corresponding to a bed volume of 2.8 cm^3), and 0.75 g of T36 (corresponding to a bed volume of 3.8 cm^3). The varying amounts of catalyst loadings were mainly due to the varying densities of the different catalyst powders (see 4.3.1). Since the aerogels had the lowest densities a lesser amount of this material was needed to fill the cell. Even though the catalyst cells were initially filled to approximately the same height the final catalyst bed volume for each catalyst varied due to the different packing ability of each catalyst after exposing it to the airflow in the reactor system. Acetone oxidation tests were performed for initial gas phase concentrations ranging from 0.2 to 2.5 mmol/L. Since more acetone adsorbed on the high surface area aerogels than on the anatase and the Degussa P25 (see Chapter 4.5.1) the initial gas phase concentration was remarkably lower with the aerogels present in the system even though an equivalent amount of acetone had been injected for both types of catalysts (see Figure 4-103).

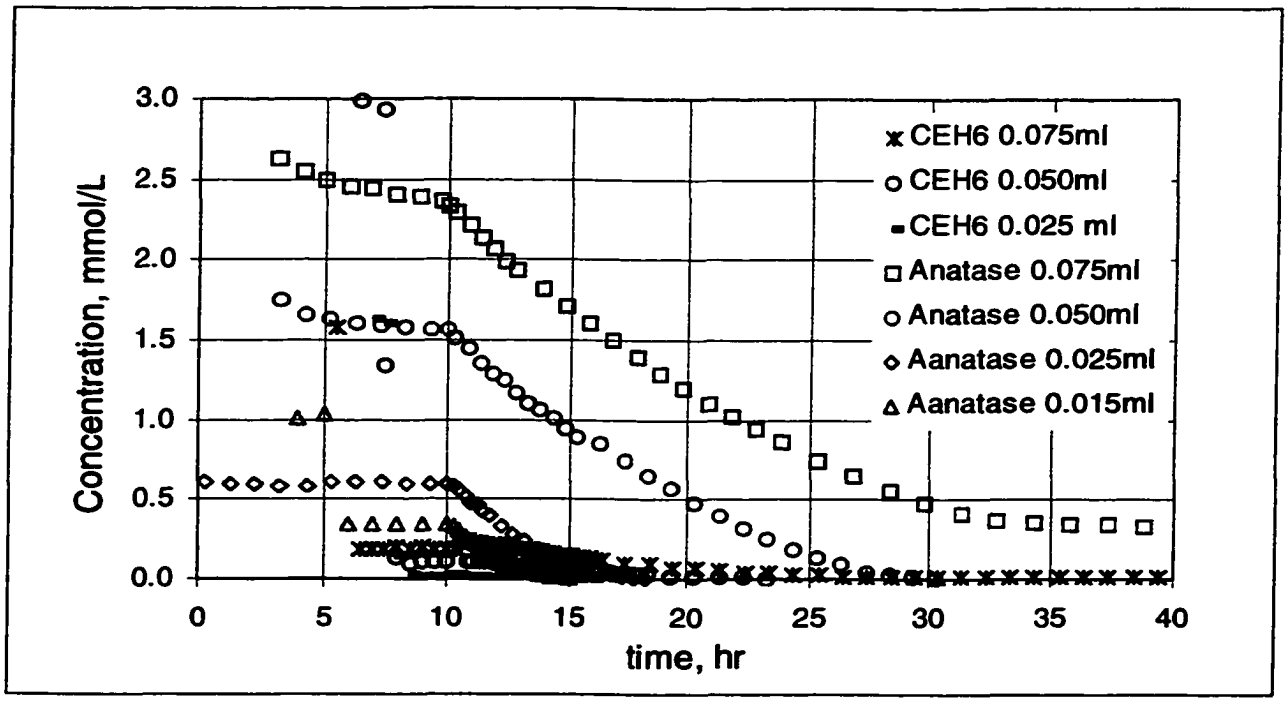

Figure 4-103 Acetone oxidation results (acetone gas phase concentration dependent on time) over anatase and the low-density aerogel CEH6 at different initial concentrations. The UV light was switched on at time = 10 hours.

Another noticeable irregularity was a spiking in gas phase acetone concentration in the system after switching the UV lamp on. This temporary increase in concentration resulted from desorption of acetone due to the slight temperature increase from the UV light. This increase in concentration was not as strongly observed for the anatase catalyst as in the case with the Degussa and the aerogel present in the reactor system (see Figure 4-103 and Figure 4-105). In order to evaluate acetone reaction rate parameters only those data were taken into consideration for rate calculations that indicated a decrease in concentration. Additionally, due to a partly broad scattering of the initial data of some of the experimental runs a second order fit was performed for the initial data points. Those fitted data were then used to determine the initial acetone oxidation rates.

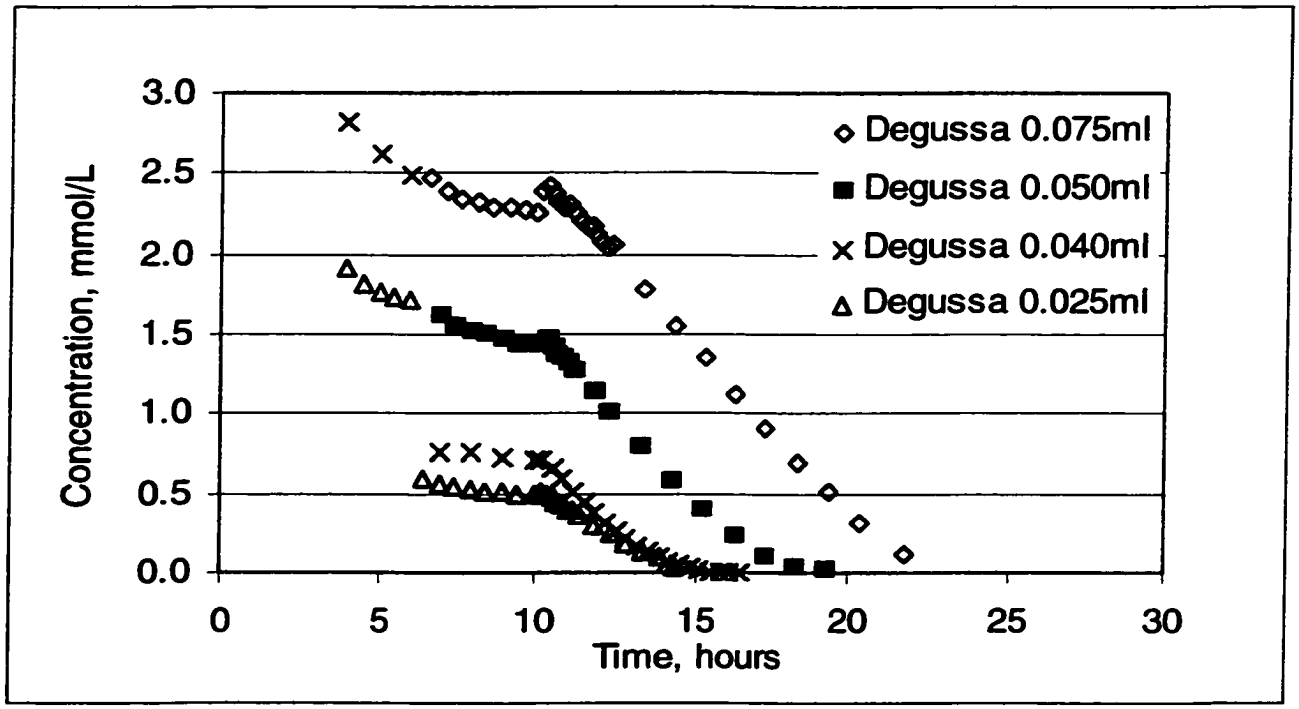

Figure 4-104 Acetone oxidation results (acetone gas phase concentration dependent on time) over Degussa P25 at different initial concentrations. The UV light was switched on at time = 10 hours.

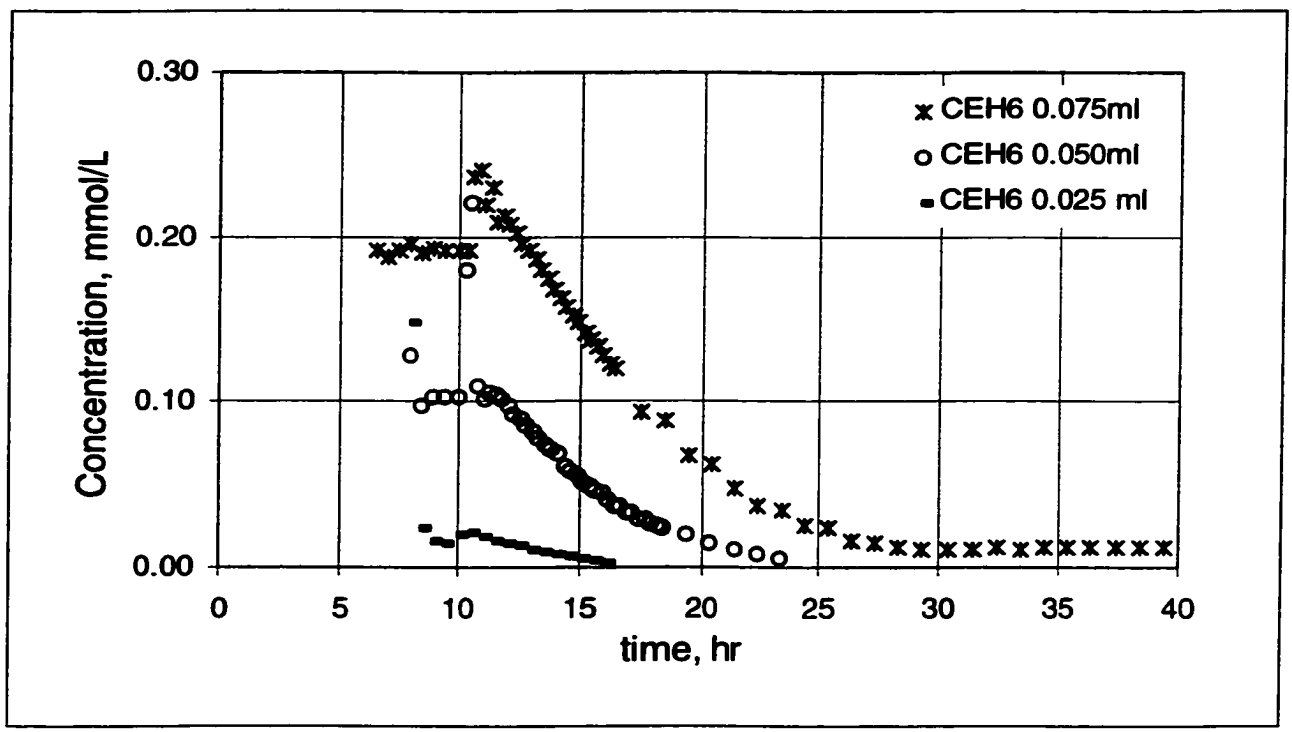

Figure 4-105 Acetone oxidation results over the low density aerogel CEH6

As described earlier, acetone adsorbed strongly on the catalyst thus removing a large portion of the acetone from the gas phase. That means that the Langmuir-Hinshelwood rate expression, which takes only the gas phase concentration into account, is not applicable in its simple form to be used for evaluating the kinetic parameters. Sauer and Ollis[40] outlined a procedure for calculating the rate constant by also taking the amount of acetone adsorbed on the catalyst into account. The starting point for developing a rate expression was the Langmuir-Hinshelwood rate expression (4-12) assuming that only acetone is adsorbed on the surfaces, that there are no kinetically significant intermediates or products, that the adsorption of carbon dioxide was negligible, and that no water was present in the system at initial conditions.

$$\textbf{(4-12)} \quad -r_A = \frac{k_A Kb_A C_A}{1 + Kb_A C_A}$$

where k_A is the acetone reaction rate constant, Kb_A is the acetone adsorption constant, C_A is the acetone gas phase concentration, and r_A is the acetone reaction rate. The reaction rate, r_A, however, is not only accounted for by the change in acetone concentration in the gas phase (dC/dt). Since about 70-95 % of the injected acetone was initially adsorbed on the catalyst the consumed amount of the reversibly adsorbed acetone on the catalyst (dM/dt) must be included in the kinetic rate evaluation as well. A full mass balance on the acetone in the system can then be described by Equation (4-13)

$$\textbf{(4-13)} \quad r_A = V_g \frac{dC_A}{dt} + \frac{dM_A^{ads}}{dt},$$

where V_g is the gas volume of the reactor system and M_A^{ads} is the mass of acetone adsorbed on the catalyst (mg) given by Equation (4-14) as already introduced in Chapter 4.5.1.

$$\Theta_A = \frac{M_A^{ads}}{\mu_A^{overall}} = \frac{K_A^{overall} C_A}{1 + K_A^{overall} C_A} \quad \textbf{(4-14)}$$

$_A$ represents the acetone surface adsorption coverage on the catalyst (dimensionless), $_A^{overal}$ is the maximum number of acetone molecules in a monolayer (mg), $K_A^{overall}$ is the acetone adsorption constant. Combining equations (4-12) and (4-14) with (4-13) leads to Equation (4-15)

$$-\frac{k_A Kb_A C_A}{1 + Kb_A C_A} = \left. d\left(V_g C_A + \frac{\mu_A^{overall} K_A^{overall} C_A}{1 + K_A^{overall} C_A} \right) \right/ dt \quad \textbf{(4-15)}$$

If the total mass of acetone, , is defined according to (4-16)

$$\Psi = V_g C_A + \frac{\mu_A^{overall} K_A^{overall} C_A}{1 + K_A^{overall} C_A}, \quad \textbf{(4-16)}$$

Equation (4-15) can then be simplified to (4-17)

$$-\frac{k_A Kb_A C_A}{1 + Kb_A C_A} = \frac{d\Psi}{dt}, \quad \textbf{(4-17)}$$

which upon rearranging to equation (4-18) can be used to determine the acetone reaction rate.

(4-18) $$\frac{1}{-d\Psi/dt} = \frac{1}{k_A Kb_A} * \frac{1}{C_A} + \frac{1}{k_A}$$

Plotting of the initial rates $-1/(d\ /dt)$ versus initial concentrations $1/C_{Ao}$ can then be represented by a straight line using a linear least square fit model with the slope = $1/k_A Kb_A$ and the intercept = $1/k_A$.

Experiments were performed with 15, 25, 50, and 75 ml acetone (12, 20, 40, 60 mg) injected. Table 4-18 summarizes the initial rate data for anatase TiO_2, Degussa P25, and the aerogel CEH6 and Figure 4-106 shows the initial rates based on one gram of catalyst. As expected, the pure anatase sample had a lower activity compared to Degussa. Degussa P25, which contains only 70% anatase (the crystalline form with the highest reactivity for the gas phase photo-oxidation) is generally accepted as the commercially available photocatalyst with the highest photoactivity. The aerogel CEH6 showed initial rates in the same order of that of Degussa. However, since the initial gas phase concentrations with CEH6 in the reactor system were much lower than with the Degussa present, a direct comparison of the initial rate data with respect to the initial gas phase concentration could not be made. As mentioned earlier, more acetone adsorbed on the aerogel thus removing up to 98 % of the initial acetone feed out of the gas phase. This resulted in considerably lower initial gas phase concentrations. Anatase reduced the initial acetone concentration due to adsorption by only up to 58 % as summarized in Table 4-19. Therefore, two additional oxidation tests were performed with the CEH6 catalyst at acetone feed rates of 0.2 and 0.3 ml, which resulted in higher acetone gas phase concentrations that were comparable to those for Degussa P25 in the reactor system. Those tests are included in Figure 4-106 and are labeled with "CEH6 – xhigh C".

At these high acetone concentrations within the reactor system the initial rate did not increase any further.

ANATASE μa = 16.29 mg (max adsorbed Acetone for 3.7g cat.)
Ka = 0.42 L/mmol
V sys = 306.96 ml

Anatase		Acetone Feed ml	avgCo mg/L	ro = d(Psi)/dt mg/min	-ro mass mg / (min g-cat)	o ill Cell windo mg / (min cm2)	-ro ill.cat-SA mg / (min cm2-ill.)	-ro ill.cat-V mg / (min cm3-cat)
m cat, g =	3.7							
ill. cell window area, cm^2=	48.5							
Vcat, cm^3 =	3.8	0.015	16.217	0.0262	0.0070	0.00054	0.5285	1.1810
BET SA, m^2/g =	2.3	0.025	34.266	0.0311	0.0083	0.00064	0.6270	1.4010
porosity =	0.0	0.050	89.297	0.0453	0.0121	0.00093	0.9124	2.0386
d pore, um =	8.2	0.075	124.081	0.0448	0.0120	0.00092	0.9028	2.0173
ill. cat SA, m^2=	0.05							
d penet, um =	4.6							
penet. Vol, cm^3=	0.022							

DEGUSSA P25 μa = 4.5 mg (max adsorbed Acetone for 2.2 g cat.)
Ka = 0.00021 L/mmol
V sys = 308.98 ml

Degussa P25		Acetone Feed ml	avgCo mg/L	-ro = -d(Psi)/dt mg/min	-ro mass mg / (min g-cat)	o ill Cell windo mg / (min cm2)	-ro ill.cat-SA mg / (min cm2-ill.)	-ro ill.cat-V mg / (min cm3-cat)
m cat, g =	2.2							
ill. cell window area, cm^2=	32.9							
Vcat, cm^3 =	2.6	0.025	53.48	0.0472	0.0215	0.0014	0.0792	3.1893
BET SA, m^2/g =	47.8	0.040	64.97	0.0652	0.0296	0.0020	0.1093	4.4010
porosity =	0.00	0.050	110.30	0.0720	0.0327	0.0022	0.1208	4.8627
d pore, um =	0.0	0.750	165.03	0.0769	0.0349	0.0023	0.1290	5.1929
ill. cat SA, m^2=	0.60							
d penet, um =	4.5							
penet. Vol, cm^3=	0.015							

AEROGEL CEH6 μa = 138.890 mg (max adsorbed Acetone for 1.3 g)
Ka = 1.2 L/mmol
V sys = 306.96 ml

AEROGEL		Acetone Feed ml	avgCo mg/L	-ro = -d(Psi)/dt mg/min	-ro mass mg / (min g-cat)	o ill Cell windo mg / (min cm2)	-ro ill.cat-SA mg / (min cm2-ill.)	-ro ill.cat-V mg / (min cm3-cat)
m cat, g =	1.3							
ill. cell window area, cm^2=	26.6	0.025	1.04	0.0114	0.0086	0.0004	0.0008	0.1482
Vcat, cm^3 =	2.1	0.050	6.04	0.0325	0.0244	0.0012	0.0022	0.4226
BET SA, m^2/g =	303.73	0.075	11.89	0.0372	0.0280	0.0014	0.0025	0.4841
porosity =	0.84	0.025	1.96	0.0255	0.0192	0.0010	0.0017	0.3314
d pore, um =	185.7	0.075	9.51	0.0264	0.0199	0.0010	0.0018	0.3436
ill. cat SA, m^2=	14.72	0.200	108.97	0.0339	0.0255	0.0013	0.0023	0.4413
d penet, um =	28.9	0.300	178.13	0.0357	0.0268	0.0013	0.0024	0.4641
penet. Vol, cm^3=	0.077							

Table 4-18 Initial acetone rate data over anatase TiO_2, Degussa P25, and low-density aerogel CEH6

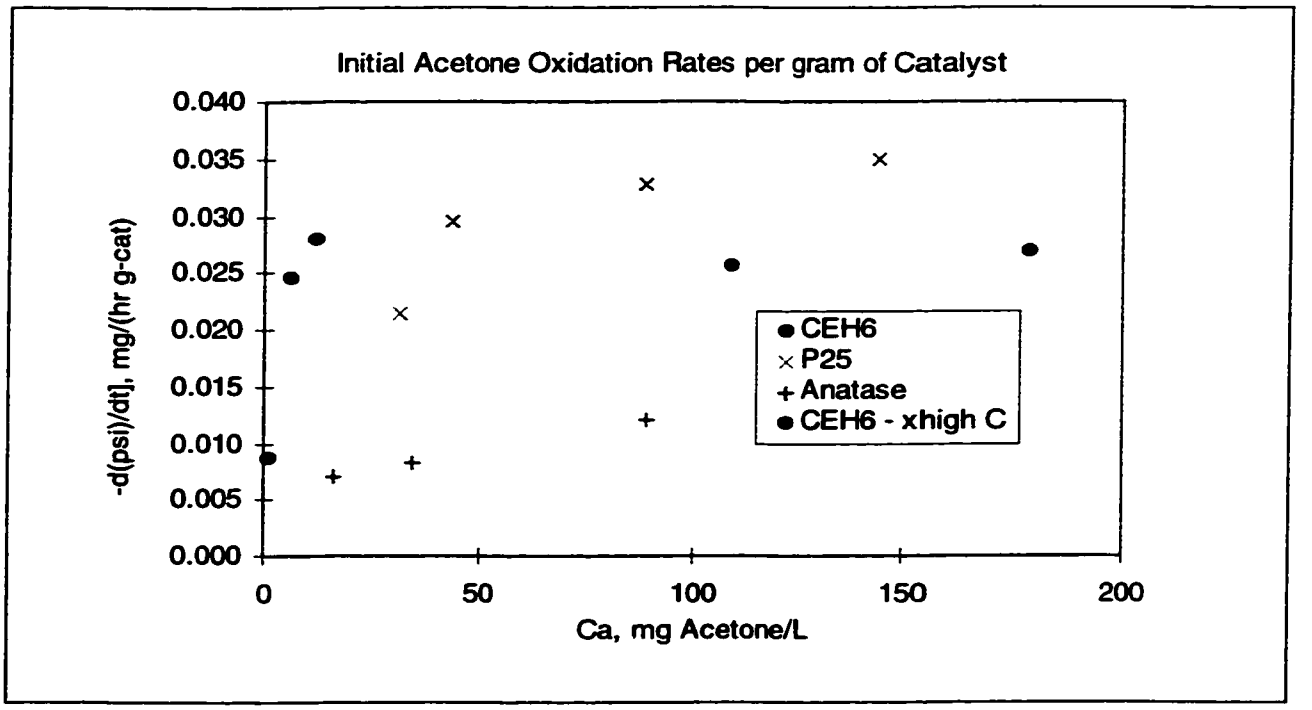

Figure 4-106 Initial acetone rates based on one gram of catalyst

Feed	Feed	theoretical	Anatase		CEH6	
ml	mg	C, mg/L	C act.	% adsorbed	Cact.	% adsorbed
0.015	11.9	38.6	16.2	58	-	-
0.025	19.8	64.3	34.3	47	1.0	98
0.050	39.5	128.7	89.3	31	6.0	95
0.075	59.3	193.0	124.1	36	11.9	94
0.200	158.0	514.7	-	-	109.0	79
0.300	237.0	772.0	-	-	178.1	77

Table 4-19 Reduction of initial acetone gas phase concentration in reactor system

A better approach of comparing both catalysts is given by means of reaction rate constants. The calculations were performed as outlined in Chapter 4.6.4.2. The non-linear regression parameter R^2 was maximized by fitting the initial rate data to Equation (4-17). The results are summarized in Table 4-20. Figure 4-107 and Figure 4-108 show a good agreement of models with the experimental initial rate data for

anatase, Degussa P25, and the aerogel CEH6, respectively. Besides calculating the rate constants based on mass of catalyst as seen in the first row of Table 4-20, the rate constants were also determined based on illuminated cell window area, actual illuminated catalyst volume and actual illuminated catalyst surface area. Degussa P25 displayed the highest acetone reaction rate constant with $k_{P25}^{Acetone} = 0.044$ mg/min g-catalyst on a basis of mass of catalyst. The rate constant of the aerogel was $k_{CEH6}^{Acetone} = 0.027$ mg/min g-catalyst, which is less than 40% lower than that of Degussa. The difference between the two catalysts is much more visible for the constants based on actual UV accessible catalyst surface area. The constant for P25 was about 60 times higher than the one for the aerogel CEH6. A similar observation was also made for the methane and ethane oxidation tests that on a UV accessible basis the Degussa outperformed the aerogel by a big margin signifying the still much lower intrinsic activity of the aerogel.

Acetone Rate Constants	Anatase	P25	CEH6
k mass, mg/(min g-cat)	0.014	0.044	0.027
k ill. Cell window area, mg/(min cm^2-cat)	0.0011	0.0029	0.0014
k ill. cat-Volume, mg/(min cm^3-cat)	0.014	6.524	0.017
k ill. cat-SA, mg/(min m^2-cat)	0.054	0.162	0.002
Acetone Adsorption Constant K, L/mg	0.05	0.034	0.42

Table 4-20 Acetone reaction rate constants for anatase, Degussa P25, and CEH6

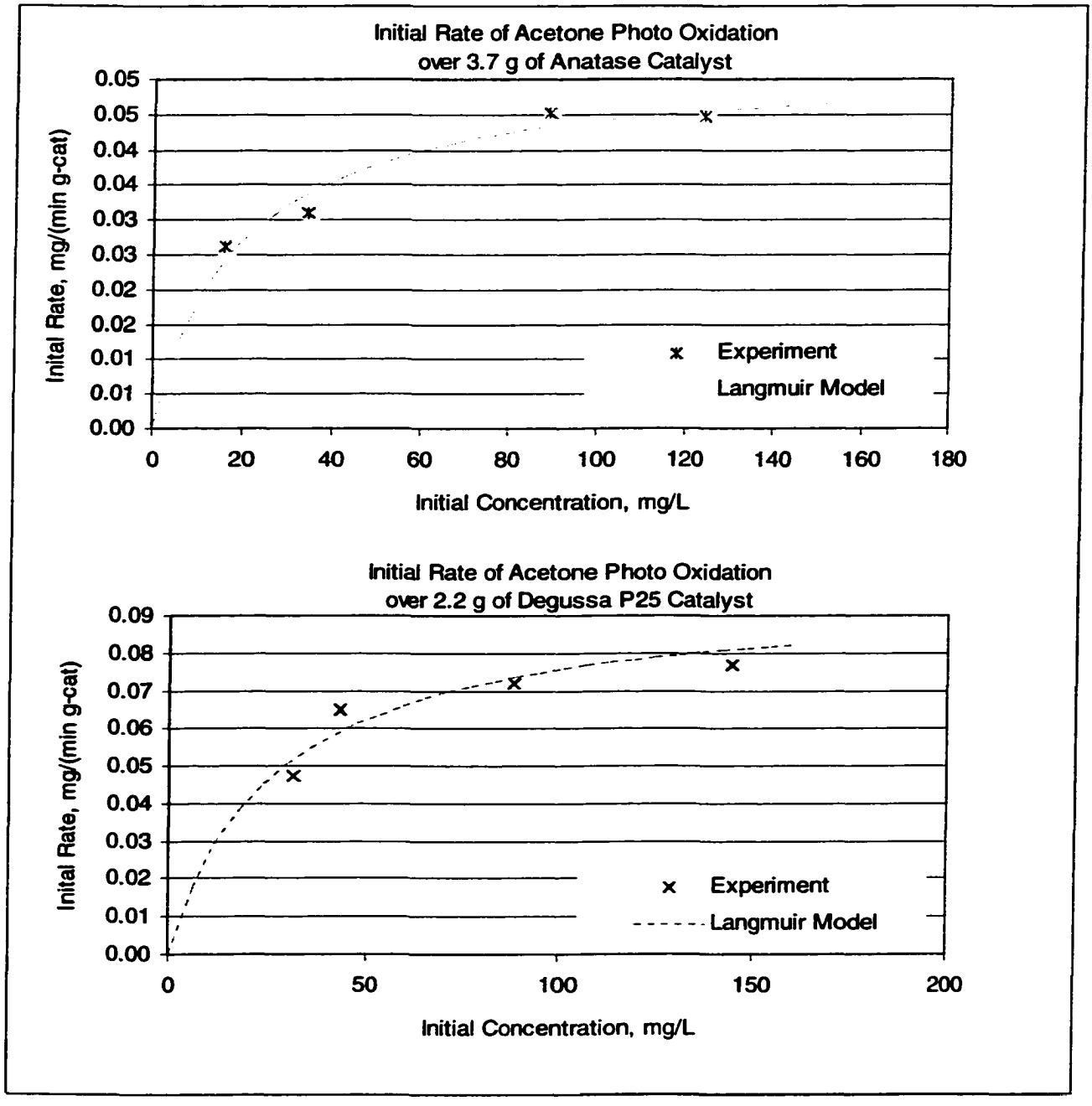

Figure 4-107 Initial acetone photooxidation rate data for anatase (top) and Degussa P25 (bottom)

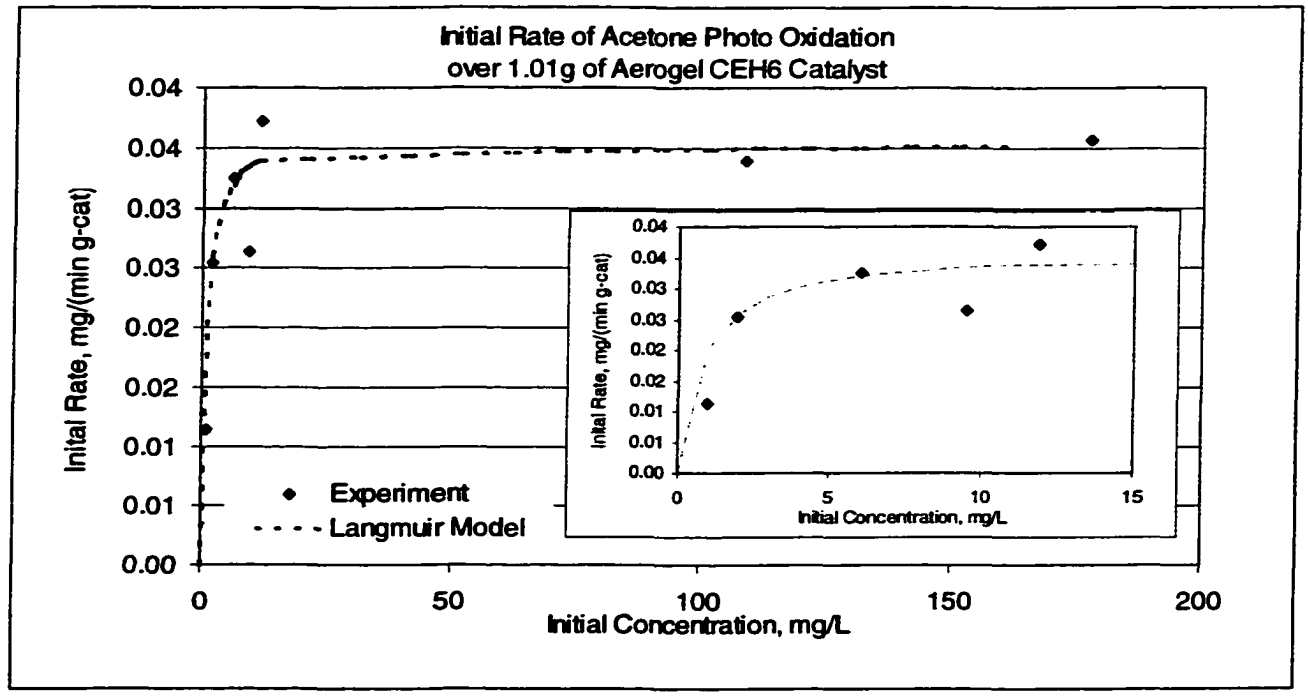

Figure 4-108 Initial acetone photooxidation rate data for the aerogel CEH6. The superimposed graph is the same graph with enlarged x-axis.

A few non-identified side-products at very low concentrations compared to the acetone concentration (about 1:2000 when comparing the GC integrated peaks areas) were generated during acetone oxidation. Their appearance is illustrated in Figure 4-109. One intermediate generated over the anatase (at retention time (RT) = 0.46) was completely oxidized at the end of each single experiment. The other side-product at RT = 73 increased in concentration throughout the experimental run but it can be assumed that – given sufficient time - it would also eventually have been eliminated. The Degussa P25 did not generate any measurable side-products.

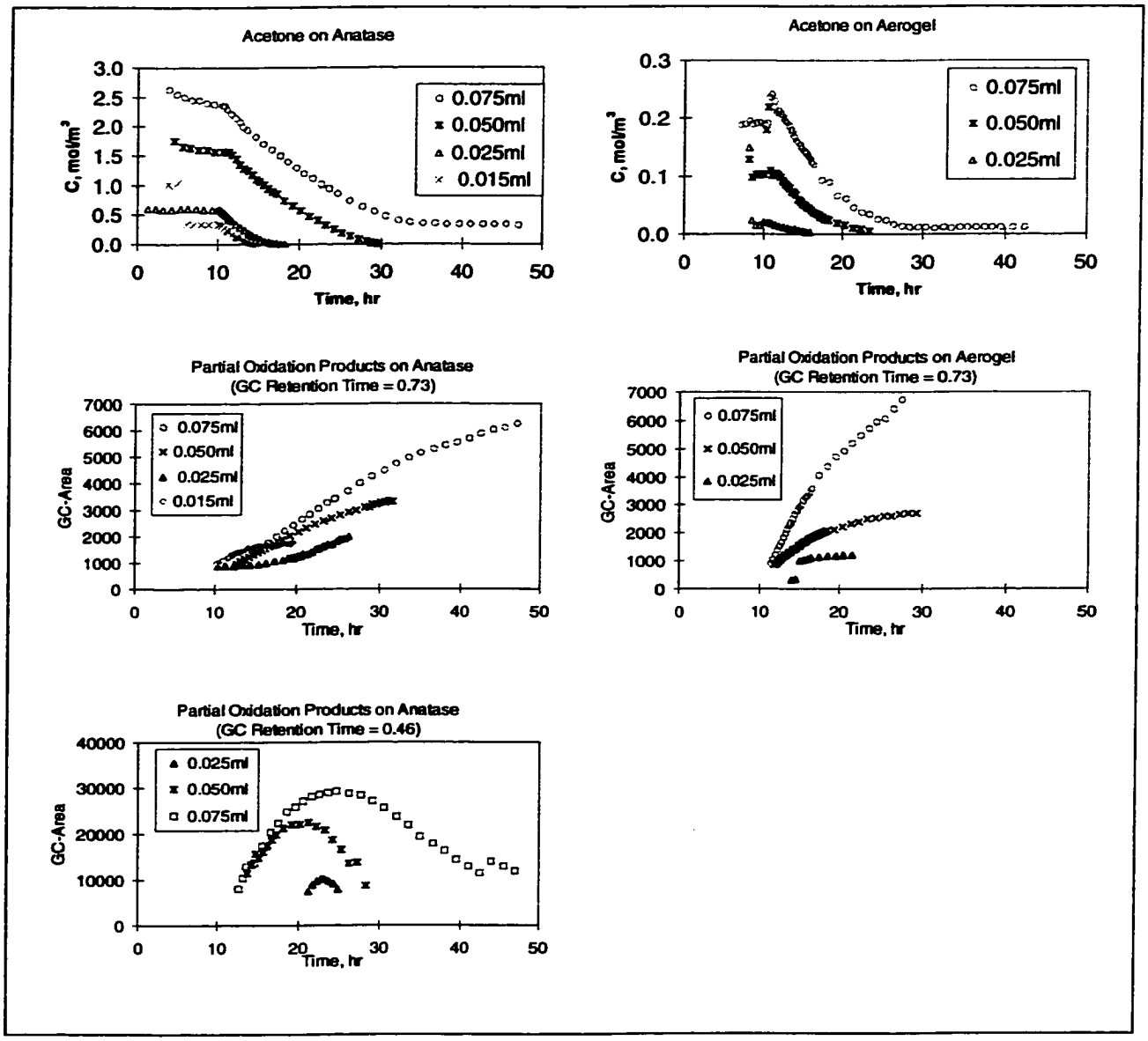

Figure 4-109 Partial oxidation products of acetone oxidation over Anatase (2 lower left graphs) and aerogel CEH6 (lower right graph). Both graphs on the top indicate the acetone concentration in the reactor at different acetone feeds.

A second series of acetone oxidation tests was performed with Degussa (2.2 g), the low-density aerogel CEH6 (1.01 g), and the ultra-low-density aerogel T36 (0.75 g). Those tests were performed at lower feed rates than the previous test, specifically at 5, 10, 15, 20, and 25 l of acetone feed. In addition, the experimental procedure was slightly altered. The catalyst cell was first covered before the UV light was switched on. After approximately 30 minutes of UV illumination, the cover was removed. This allowed for the UV lamp to reach its maximum illumination power, for the temperature of the reactor cell to adjust to its final value and for the gas phase concentration to reestablish equilibrium. As already mentioned before, even though a fan provided cooling during the experimental run the heat generated from the UV light caused nonetheless a slight temperature increase of the reactor cell from about 25°C to maximum 33-35°C. This led to an acetone desorption from the catalyst causing a spike in gas phase acetone concentration. A representative graph for the photo oxidation of 15 l acetone feed is pictured in Figure 4-110. For all other initial concentrations the same trend was observed, principally showing that the Degussa decreased the concentration in the reactor system at a higher initial rate than the aerogel. However, the ultra-low density aerogel T36 oxidized the acetone within the same time frame as the Degussa P25.

In order to evaluate of the kinetic rate parameters the same procedure was used as described earlier in this section. The initial rates based on mass of catalyst, illuminated cell window area, and UV accessible catalyst surface area for the three catalysts are shown in Figure 4-111, Figure 4-112, and Figure 4-113, respectively; while the data for the related reaction rate constants are summarized in Table 4-21. As seen in Figure 4-114

the determined reaction rate parameters resulted in a prediction of initial rates close to the experimental data.

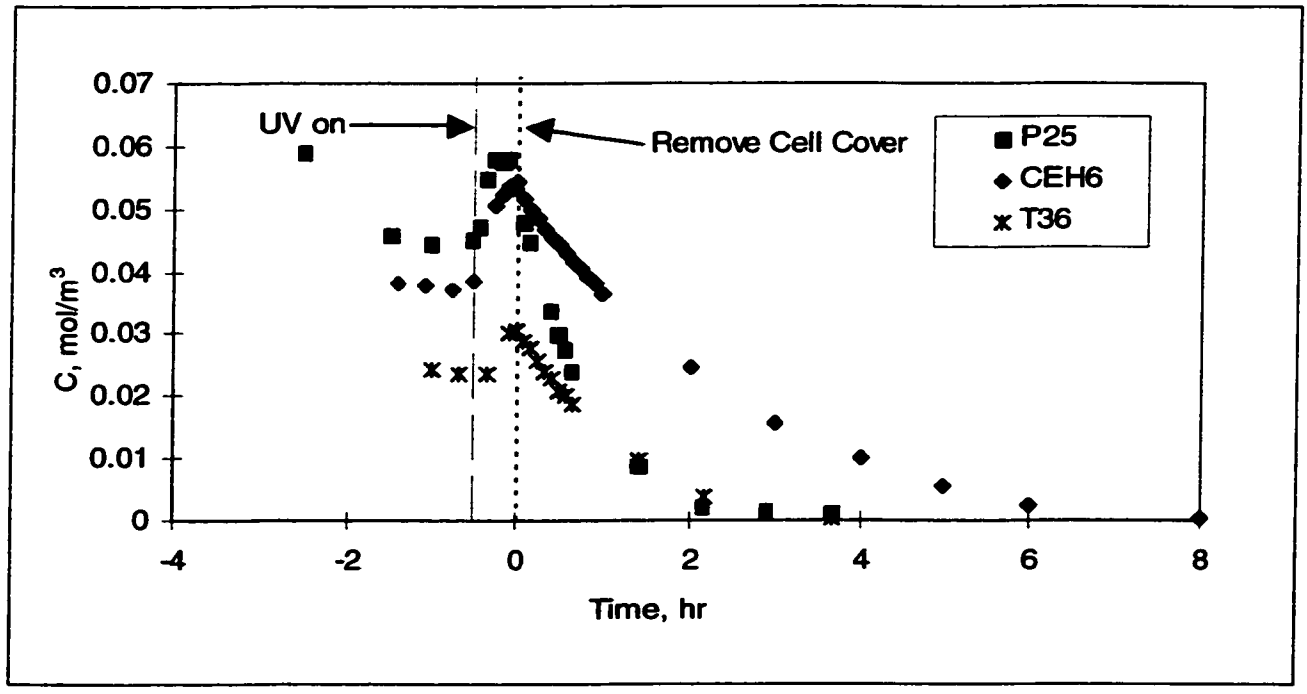

Figure 4-110 Photo-oxidation of acetone over Degussa P25 and the aerogels CEH6, and T36

Rate Constants $k_{x\ acetone}$	P25	T36	CEH6
k mass, mg/(min g-cat)	0.014	0.093	0.086
k ill. Cell window area, mg/(min cm^2-cat)	0.0008	0.0019	0.0863
k ill. cat-Volume, mg/(min cm^3-cat)	1.7780	1.04	0.09
k ill. cat-SA, mg/(min m^2-cat)	0.0499	0.0118	0.0863
Acetone Adsorption Constant K, L/mg	0.295	0.688	0.297

Table 4-21 Acetone reaction rate constants for lower initial concentrations for Degussa P25, T36, and CEH6

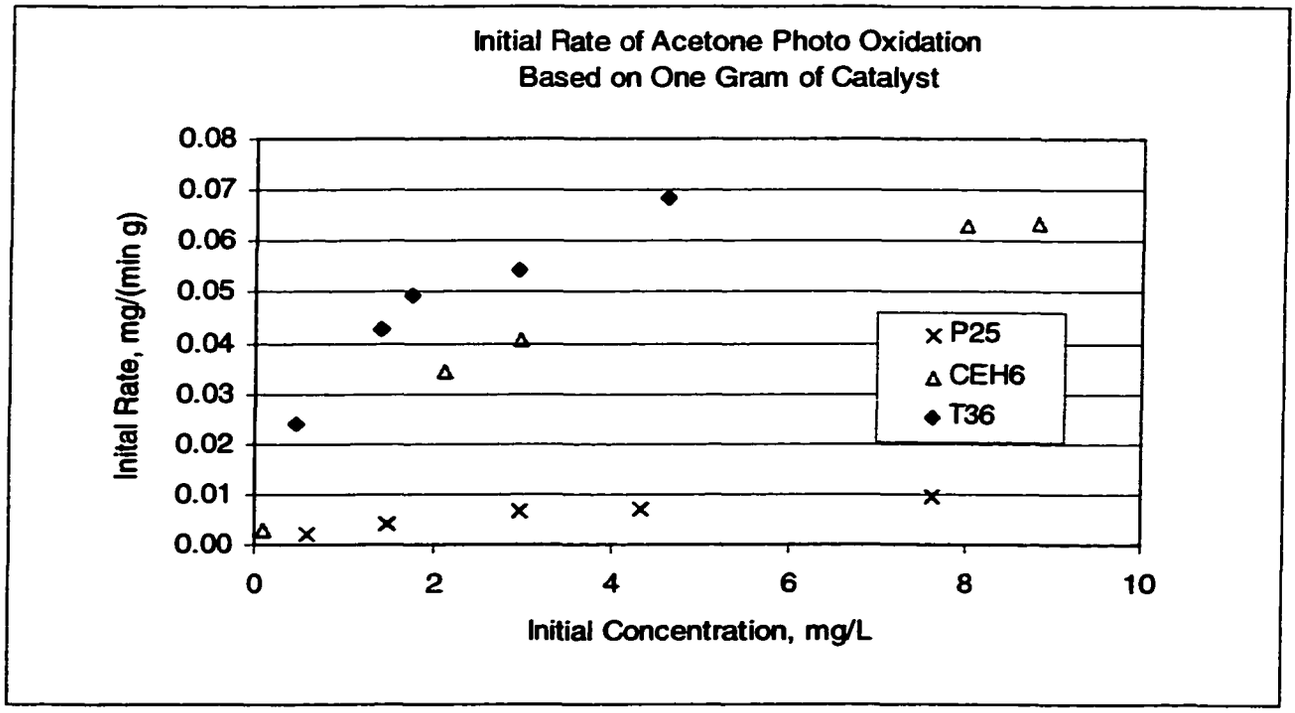

Figure 4-111 Initial acetone oxidation rates at lower initial concentrations for P25, CEH6, and T36 based on 1 g of catalyst

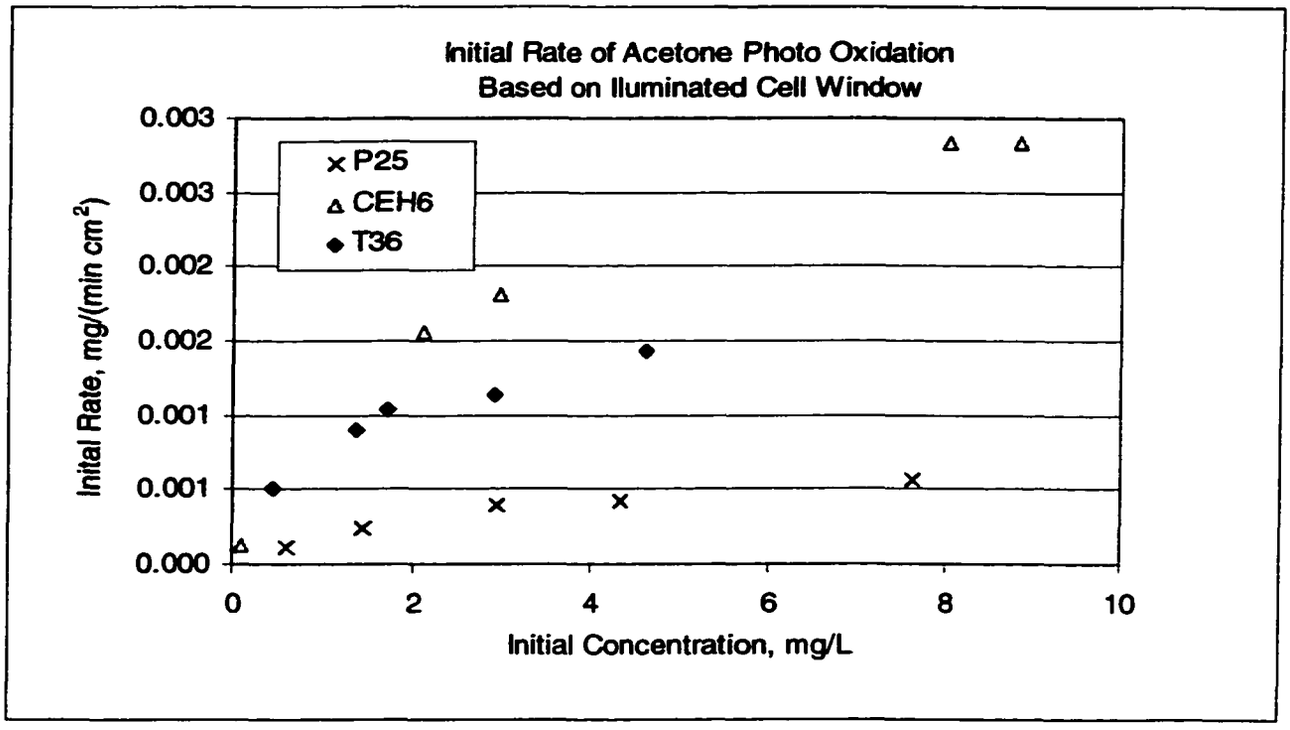

Figure 4-112 Initial acetone oxidation rates at lower initial concentrations for P25, CEH6, and T36 based on illuminated cell window area

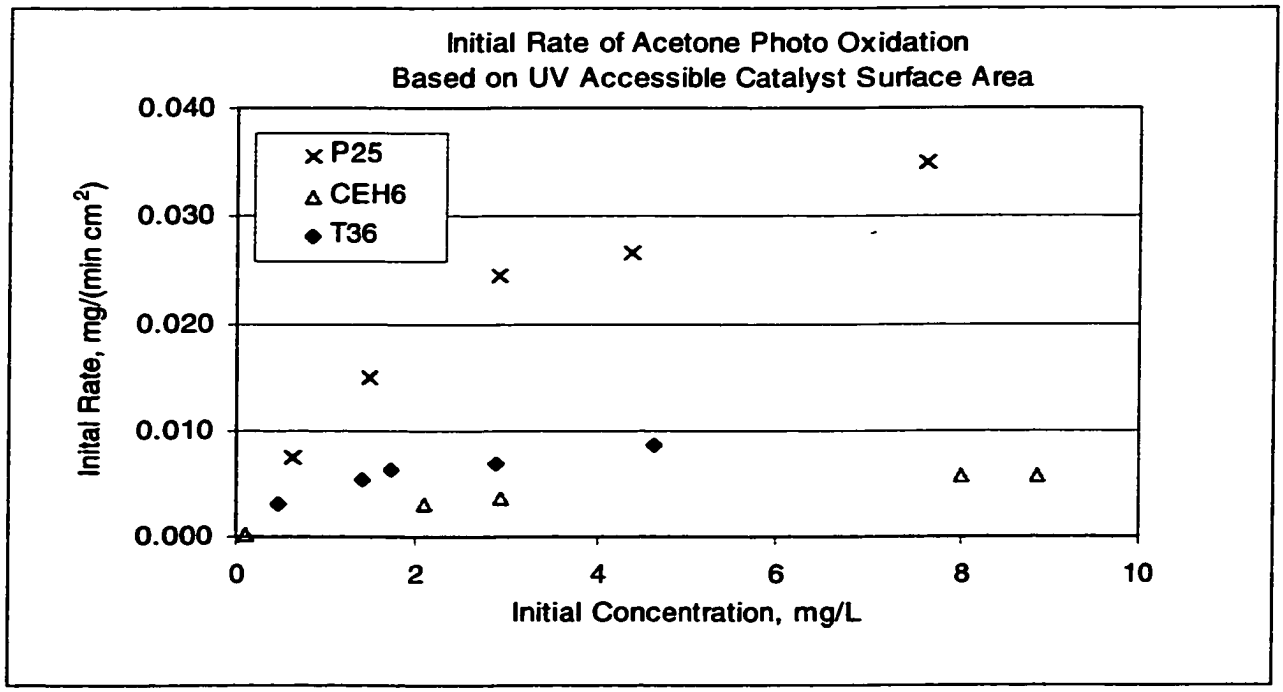

Figure 4-113 Initial acetone oxidation rates at lower initial concentrations for P25, CEH6, and T36 based on UV accessible catalyst surface area

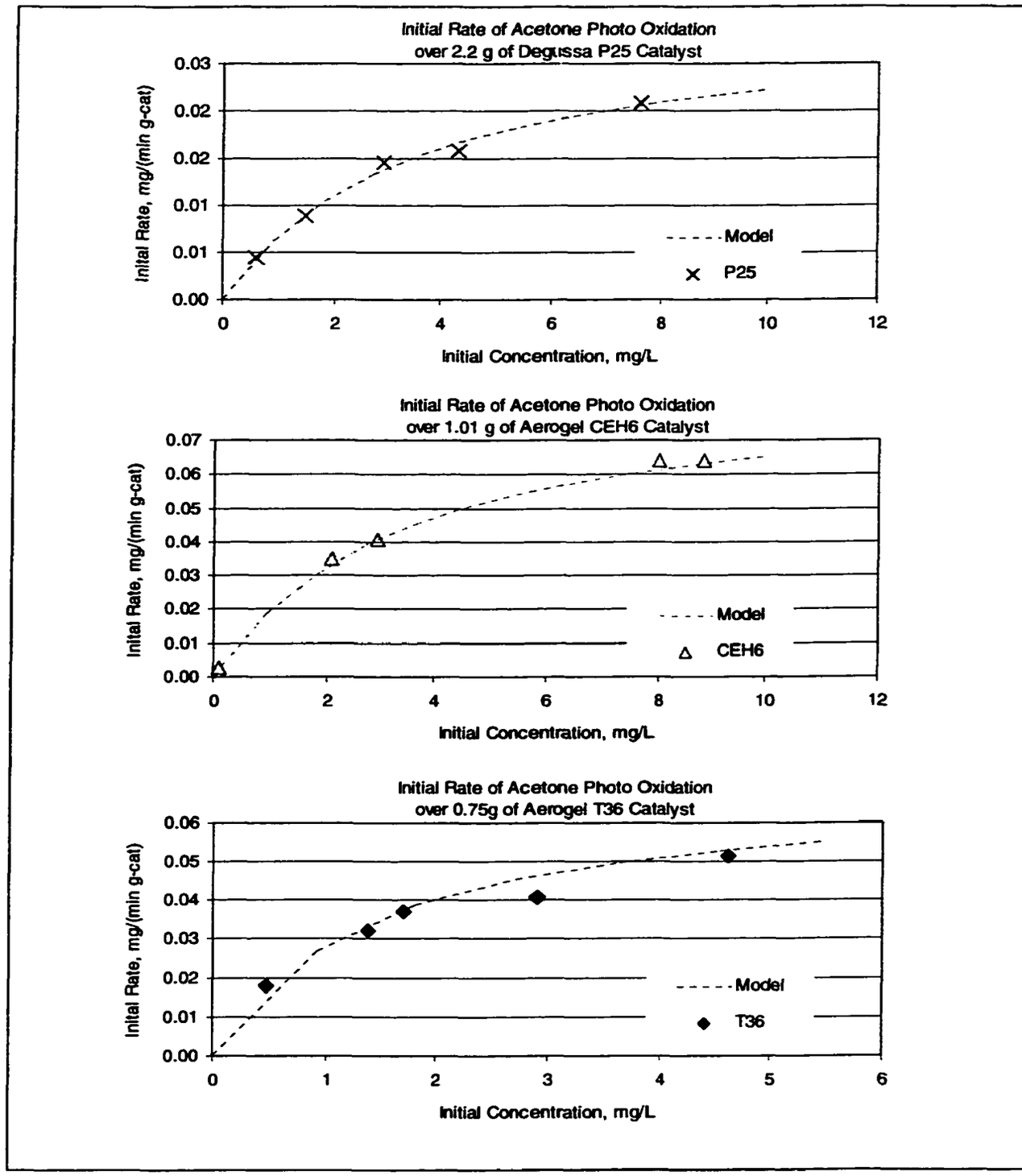

Figure 4-114 Initial acetone photooxidation rate data and Langmuir-Hinshelwood models for Degussa P25, CEH6, and T36 for experimental runs at lower initial concentrations

As shown in Figure 4-111 and Figure 4-112, the aerogels demonstrated significantly higher initial rates on a per mass basis and per illuminated cell window area basis. The initial rates were higher by a factor of about five. This is also reflected in the rate constants where the aerogel T36 had a $k^{T36}_{acetone}$ of 0.093 mg/min g-cat and the $k^{CEH6}_{acetone}$ of CEH6 was 0.086 mg/min g-cat which was almost six times higher compared to the rate constant of Degussa P25 with 0.014 mg/min g-cat. A similar observation was made when comparing the rate constants on a basis of illuminated cell window area. The rate constants of T36 and CEH6 were higher by a factor of two and four, respectively. When comparing the rate data based on UV accessible surface area of the catalyst, the Degussa demonstrated a better performance with initial rates up to six times higher than that of the aerogels, a clear indication for the higher intrinsic activity of the commercial Degussa P25.

When comparing the initial acetone rate data of P25 at different initial acetone concentrations as shown in Figure 4-115 it was observed that the rates did not increase proportionally with the concentration. At low concentrations of up to 10 mg/L the initial rate depended strongly on the concentration, while at higher initial concentration the dependence of the initial rate is less, following Langmuir-Hinshelwood kinetics according to equation (4-12). This trend was especially observed for the aerogel CEH6 as seen in Figure 4-108. At low initial acetone feeds the initial rate depended strongly on the initial concentration. At higher acetone feeds the initial reaction rate did not change at all.

No measurable byproducts were recorded during acetone oxidation at these low initial acetone concentrations over Degussa P25, the aerogel CEH, and the aerogel T36.

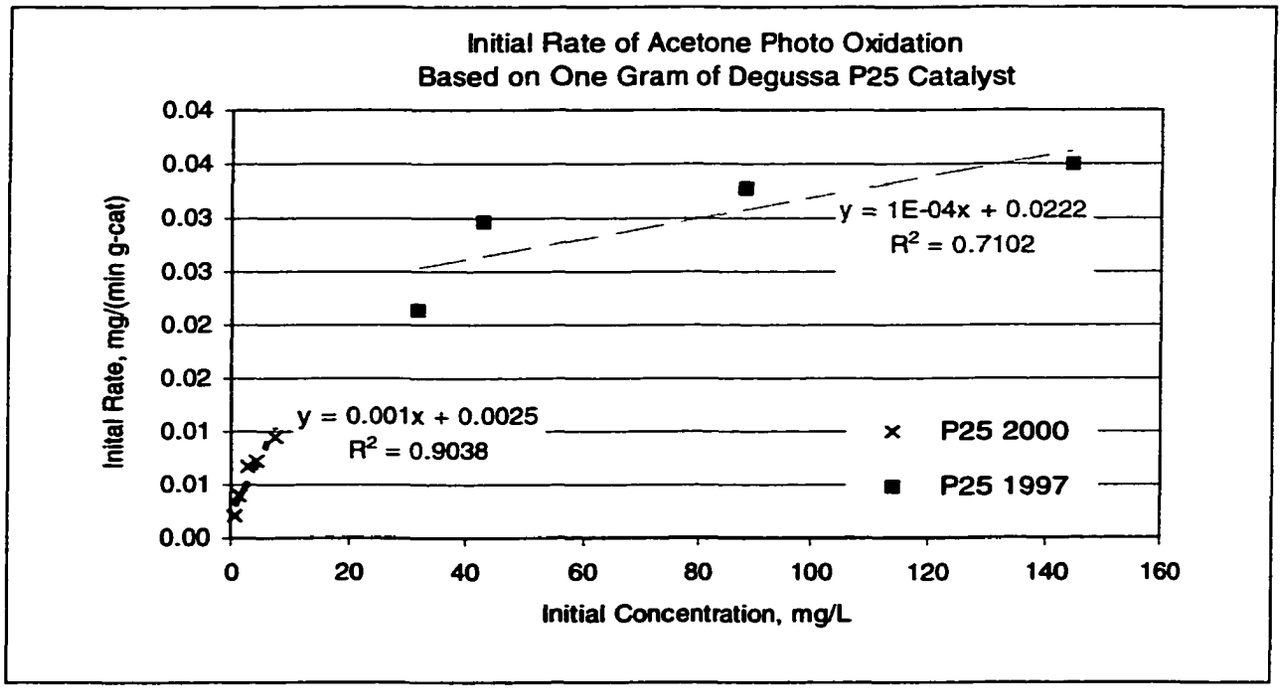

Figure 4-115 Initial rate of acetone oxidation over Degussa P25 at different initial concentrations. P25 1997 denotes the set of experiments at higher feed rates, while P25 2000 stands for the photoxidation tests at lower acetone feeds.

The Langmuir-Hinshelwood models using the rate parameters from Table 4-21 and Equation (4-17) were determined for each individual acetone photooxidation test and are shown together with the experimental rate data in Figure 4-116, Figure 4-117, and Figure 4-118 for anatase, Degussa P25, and the aerogel T36, respectively. The predicted rates from the model agreed already well with the experimental data (for all three catalysts) even though the water term (K_WC_W) was not included in the calculations. In order to determine the influence of generated water the adsorption constant K_W was evaluated - as outlined in Section 4.6.4.2 - by maximizing R^2 over the rate data of each individual experimental run using Equation

(4-19) $$-\frac{k_A K_A C_A}{1+K_A C_A+K_W C_W}=\frac{d\Psi}{dt},$$

with K_A and C_A the rate constant and the adsorption constant, respectively, for acetone and K_W and C_W the rate constant and the adsorption constant, respectively, for water.

Maximizing R^2 resulted for most of the experiments in values for K_W in the range of about $5*10^8$ m^3/mol, which was similar to the findings for ethane photooxidation over the aerogel CEH6. In spite of this, it was observed that the Langmuir-Hinshelwood models changed only insignificantly when using a much smaller K_W value of 0.001 or 0.01 m^3/mol instead of $5*10^8$ m^3/mol as is summarized in Table 4-22. This signifies that the generated water during the reaction did not greatly alter the reaction kinetics of acetone photooxidation, which was the case for either catalyst: anatase, Degussa P25, or the aerogel T36. The Langmuir-Hinshelwood models evaluated with or without the water term did not show any significant difference as seen in Figure 4-116, Figure 4-117, and Figure 4-118 for Degussa P25, the low-density aerogel CEH6, and the ultra- low density aerogel T36, respectively. Figure 4-119 supports this finding by illustrating that the water term (K_WC_W) in Equation (4-17) was negligibly small compared to the acetone term (K_AC_A), hence indicating that adsorbed acetone only determined the acetone photooxidation rate. This agrees with the investigations by Bickley and co-workers[15] who concluded from their studies that acetone - once adsorbed on the catalyst - is not displaced by water from the surface. Consequently, adsorption of acetone is stronger than water and the amount of generated water did not reduce the reactivity by blocking of reaction sites.

Catalyst	Feed acetone um	C acetone mg/L	Cw avg mol/m^3	Kw m^3/mol	R^2	Kw avg m^3/mol
P25						
	5	0.6051	0.0254	0.00	0.87	
	10	1.4663	0.0531	0.00	0.74	
	15	2.9358	0.1094	0.00	0.82	
	20	4.3472	0.1243	0.00	0.65	
	25	7.6201	0.1020	0.00	0.83	0.00
CEH6						
	5	0.0907	0.0272	0.00	0.31	
	10	2.0954	0.4061	0.01	0.12	
	15	2.9491	0.6477	0.01	0.72	
	20	8.0102	0.8771	0.04	0.72	
	25	8.8424	1.0068	0.32	0.72	0.08
T36						
	5	0.4614	0.1648	0.00	0.63	
	10	1.3921	0.3362	0.00	0.57	
	15	1.7199	0.3688	0.00	0.63	
	20	2.9100	0.7334	0.00	0.97	
	25	4.6224	0.5698	0.38	0.42	0.08

Table 4-22 Water adsorption constants for each individual acetone oxidation experiment over Degussa P25, the aerogel CEH6, and T36. The non-linear regression parameter R^2 and the average value of K_W are included.

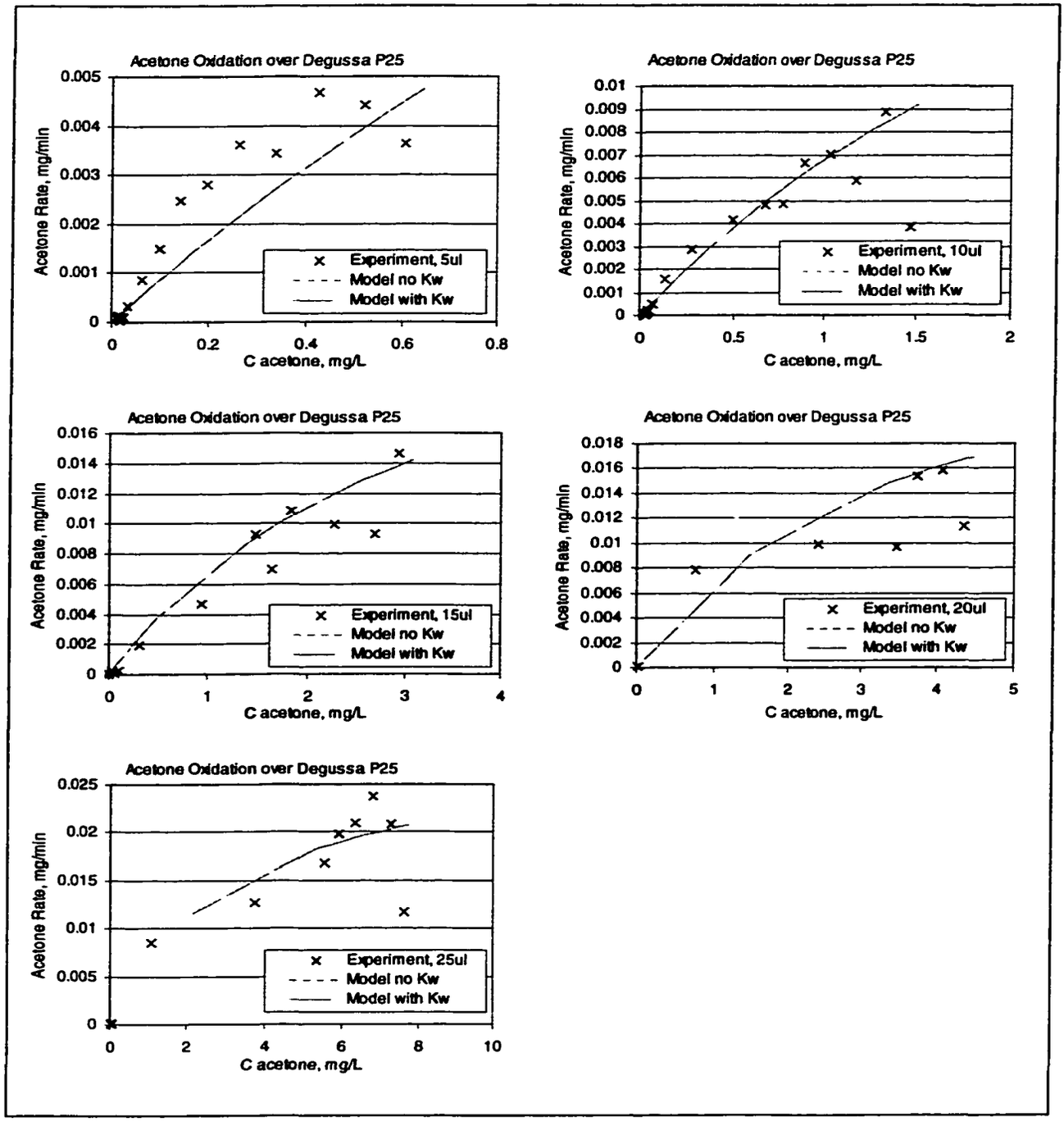

Figure 4-116 Reaction rates versus acetone concentration and Langmuir-Hinshelwood models of individual acetone photooxidation tests over Degussa P25 at initial feeds of 5, 10, 15, 20, and, 25mm acetone feed. The dotted lines indicate models ignoring the water term; the dashed lines include the water term in the model.

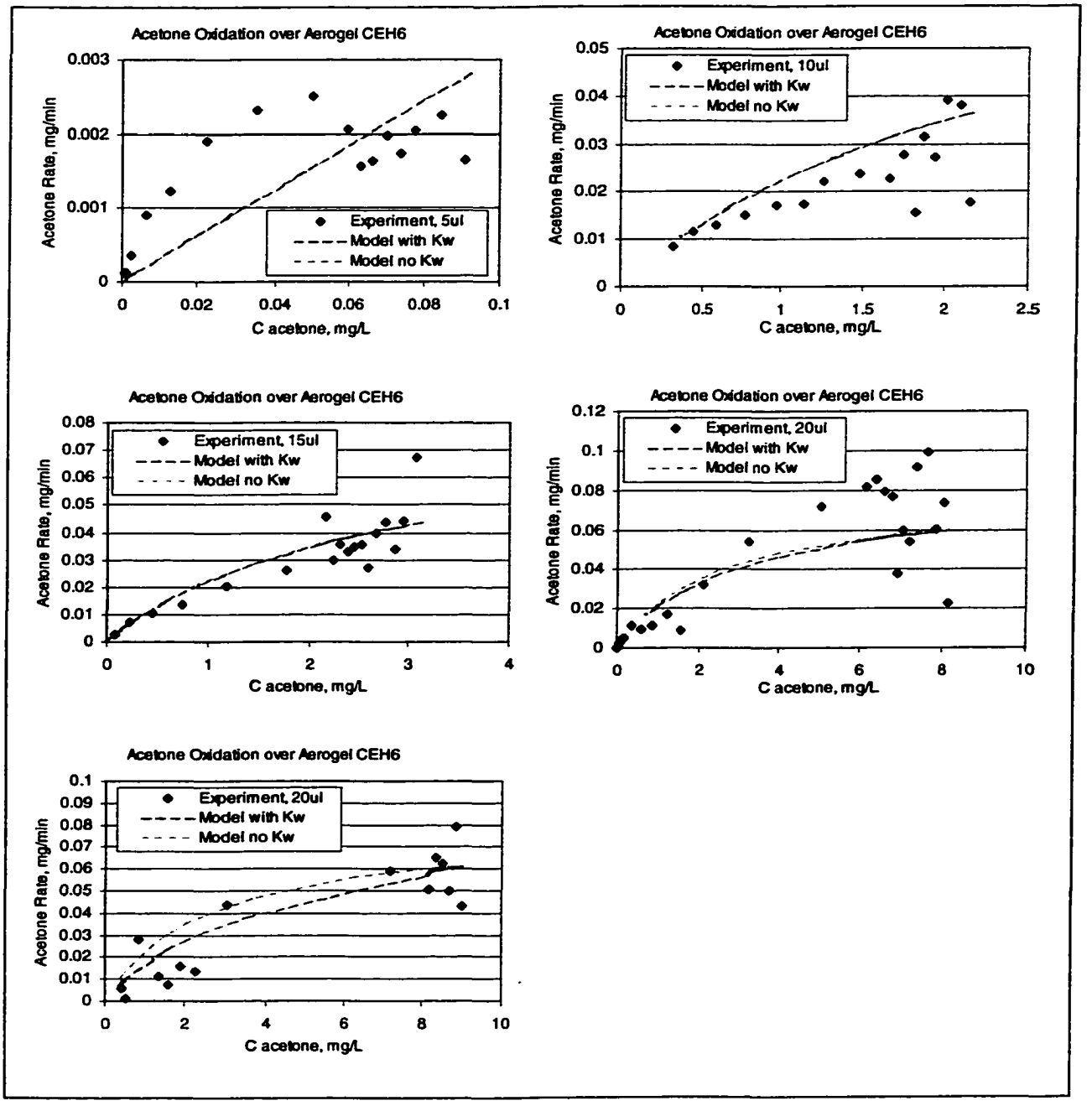

Figure 4-117 Reaction rates versus acetone concentration and Langmuir-Hinshelwood models of individual acetone photooxidation tests over aerogel T36 at initial feeds of 5, 10, 15, 20, and, 25 mm acetone feed. The dotted lines indicate models ignoring the water term; the dashed lines include the water term in the model.

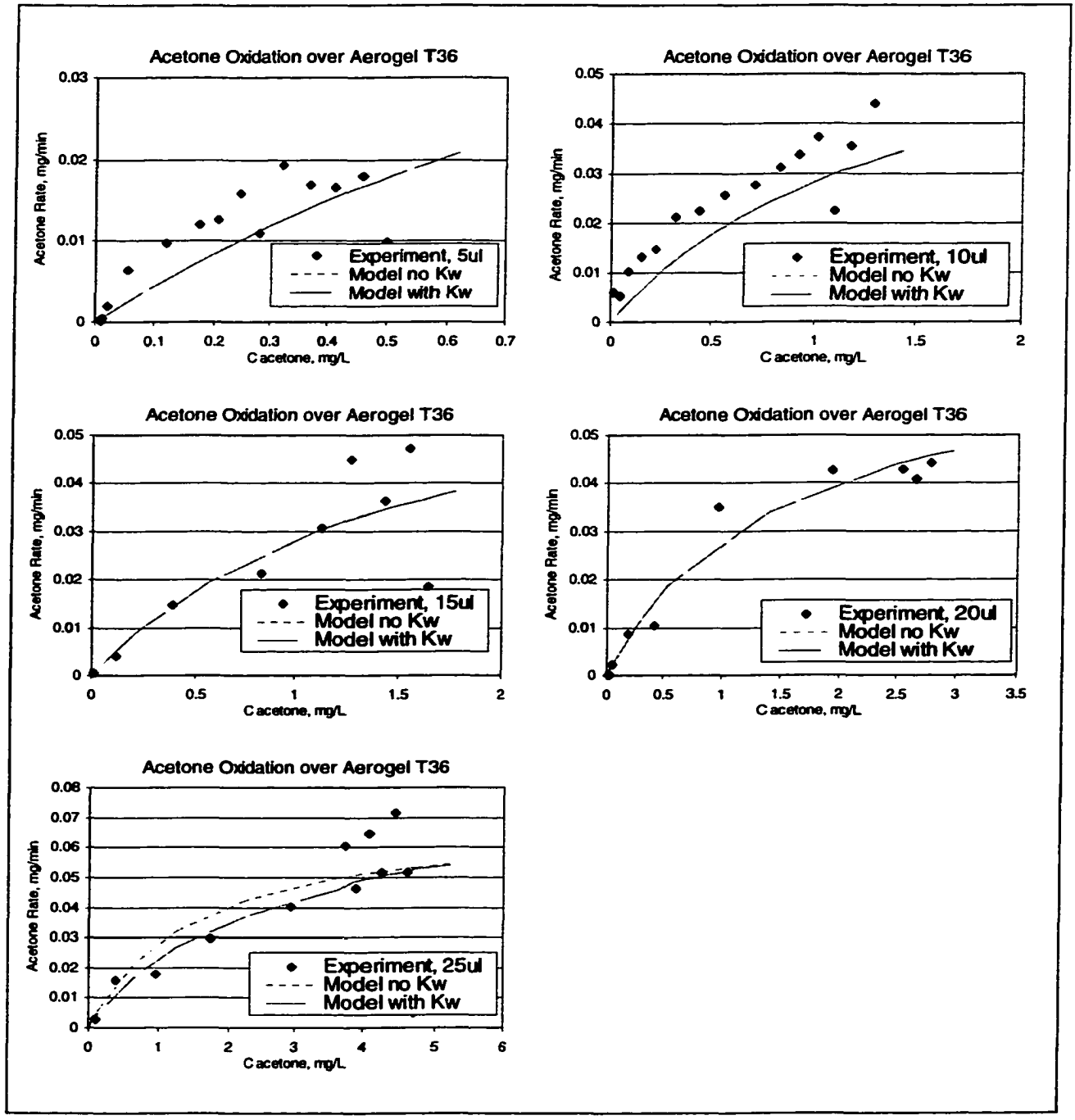

Figure 4-118 Reaction rates versus acetone concentration and Langmuir-Hinshelwood models of individual acetone photooxidation tests over Degussa P25 at initial feeds of 5, 10, 15, 20, and, 25mm acetone feed. The dotted lines indicate models ignoring the water term, the dashed lines include the water term in the model.

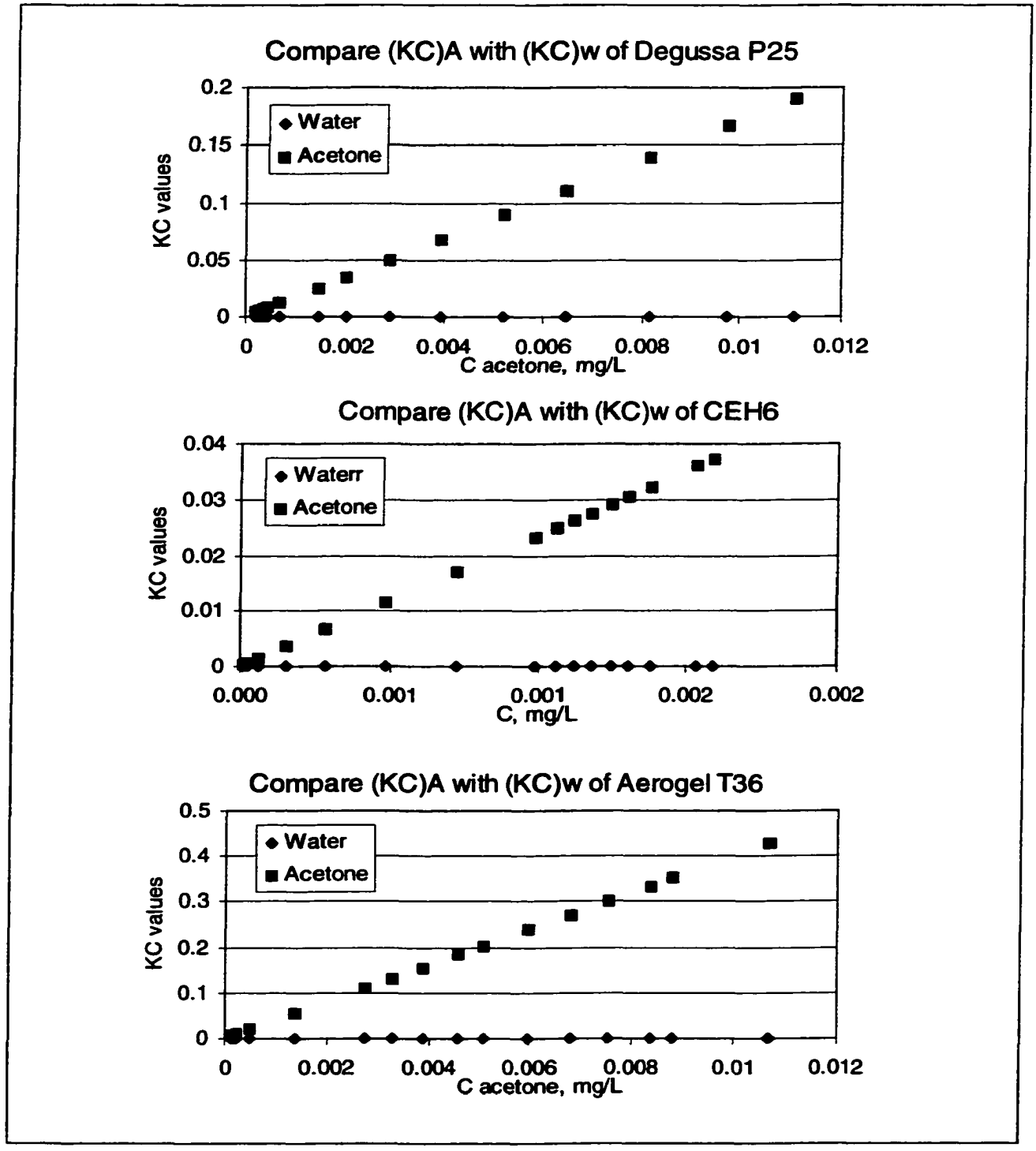

Figure 4-119 Comparison of magnitudes of the water term K_WC_W and the acetone term K_AC_A in equation) for acetone oxidation over anatase (a) and the aerogel CEH6 (b)

4.6.4 Ethylene Photocatalytic Oxidation under initial dry conditions

Photocatalytic oxidation tests using ethylene as contaminant were performed over the commercially available Degussa P25 (2.2 g), the low-density aerogel CEH6 (1.1 g), the ultra-low-density aerogel T36, the binary aerogel TS31b (0.8 g), and rutile TiO_2 (2.2 g) purchased from Alfa Aesar. In addition to these tests, ethylene oxidation under humid conditions over P25 and T36 was studied. Furthermore, Degussa P25 and the aerogel T36 were modified with platinum in order to investigate the influence of metal deposition on the photocatalytic activity. The results of these studies will be presented in a following section (4.7).

The complete oxidation reaction for ethylene is

Ethylene Oxidation: $C_2H_4 + 3\,O_2 \rightarrow 2\,CO_2 + 2\,H_2O$

First, an oxidation test with an empty catalytic cell was performed in order to verify that ethylene would not photolytically oxidize. Figure 4-121 shows that the gas phase concentration in the reactor system remained unchanged indicating that ethylene cannot be oxidized under merely UV illumination.

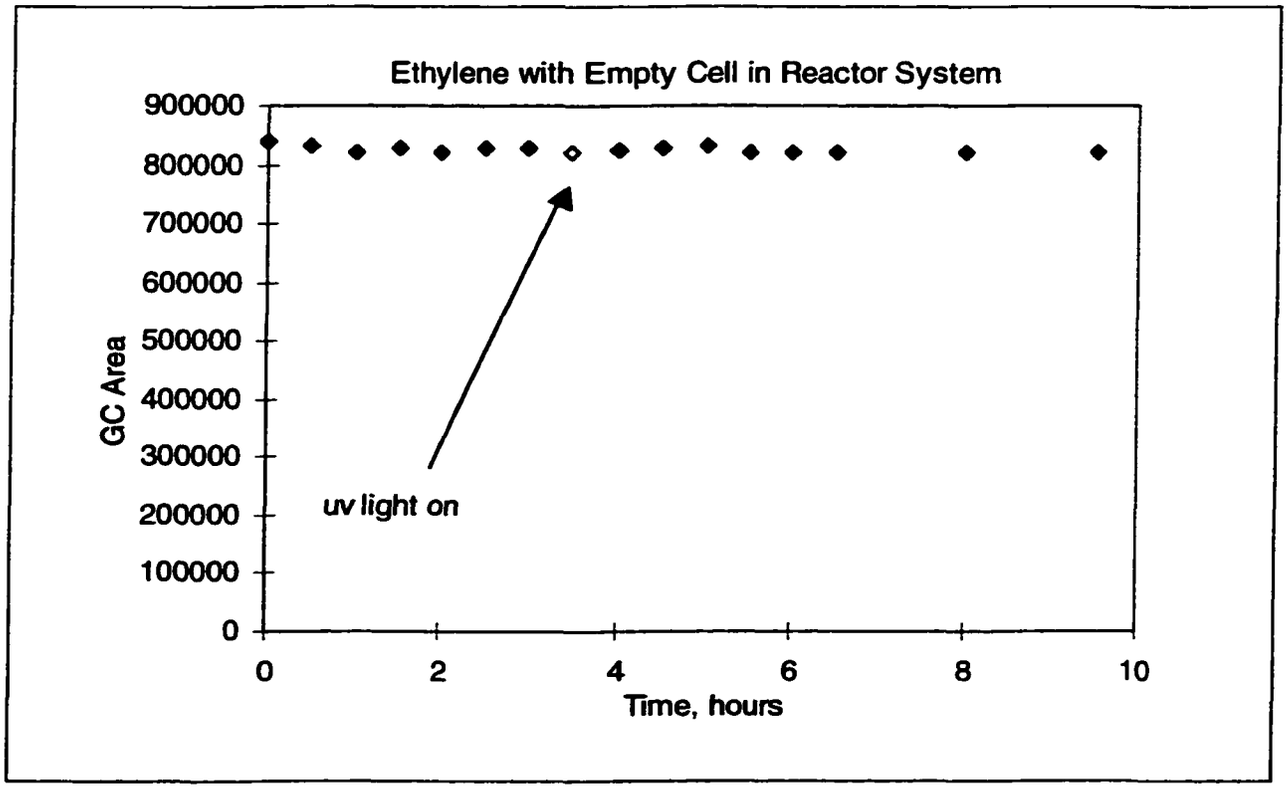

Figure 4-120 Ethylene concentration in reactor system under UV illumination and no catalyst present

4.6.4.1 Binary Aerogel TS31b

Since in previously discussed photocatalytic experiments the 100% anatase TiO_2 showed the least activity of all tested catalysts this catalyst was not further investigated for ethylene oxidation. However, it was of interest to see if 100% rutile TiO_2 would show any activity. As it can be seen in Figure 4-121, rutile did not show any significant photoactivity. Also, the binary aerogel TS31b did not photocatalyze ethylene oxidation considerably. Even thermal treatment of the aerogel to 450°C did not lead to any improvement of its photocatalytic activity which - in contrast - was the case for the pure titanium dioxide aerogel as discussed later in this chapter. A possible reason for the low activity of the binary aerogel might be the low concentration of titanium dioxide within

the material. Atomic absorption measurements were performed (see appendix) indicating only 4wt% of titanium in the aerogel. This small amount of titanium in the silica structure was probably insufficient to show a noteworthy reactivity of this aerogel material. In addition, no anatase crystalliny was detected from the XRD studies (4.2.6), which implied already that this material would not be photocatalytic active.

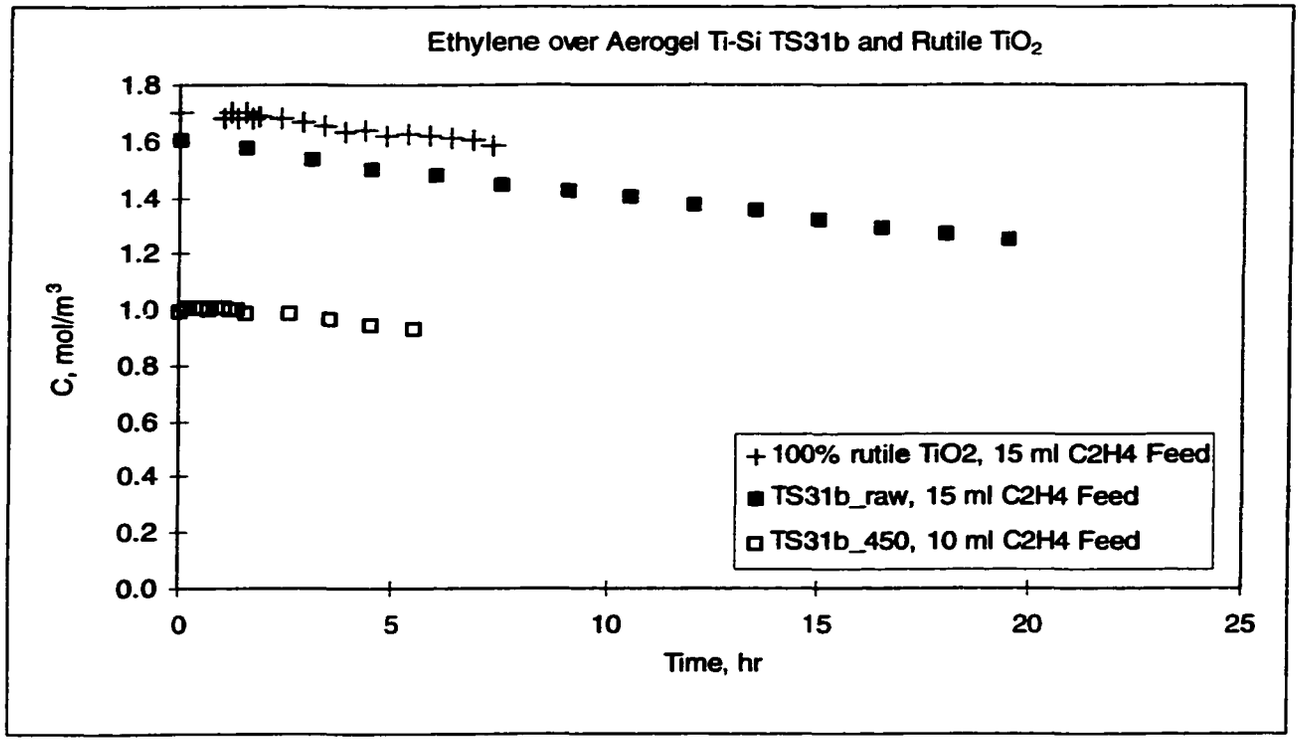

Figure 4-121 Ethylene concentration dependence on time upon UV illumination over 100% rutile TiO_2, the binary Ti-Si aerogel TS31b, and the TS31b thermal treated to 450°C.

First, ethylene oxidation tests were performed at initial gas phase concentrations ranging between 0.2 and 2.2 mol/m^3. The decrease in concentration with time for all catalysts showed a similar trend as was observed for the methane or ethane oxidation. A representative graph at 10 ml ethylene feed is shown in Figure 4-122. Data at other initial concentrations (summarized in the Appendix Table 7-15 and following) showed a similar

behavior. all the catalysts the ultra-low density aerogel T36 reduced the ethylene concentration in the system at the highest rate. Even though the difference of the oxidation rate did not appear very significant it needs to be pointed out that only 0.75 g of T36 was used compared to 1.3 g of CEH6 or 2.2 g of Degussa P25. The different catalytic activities are compared on various bases and discussed later.

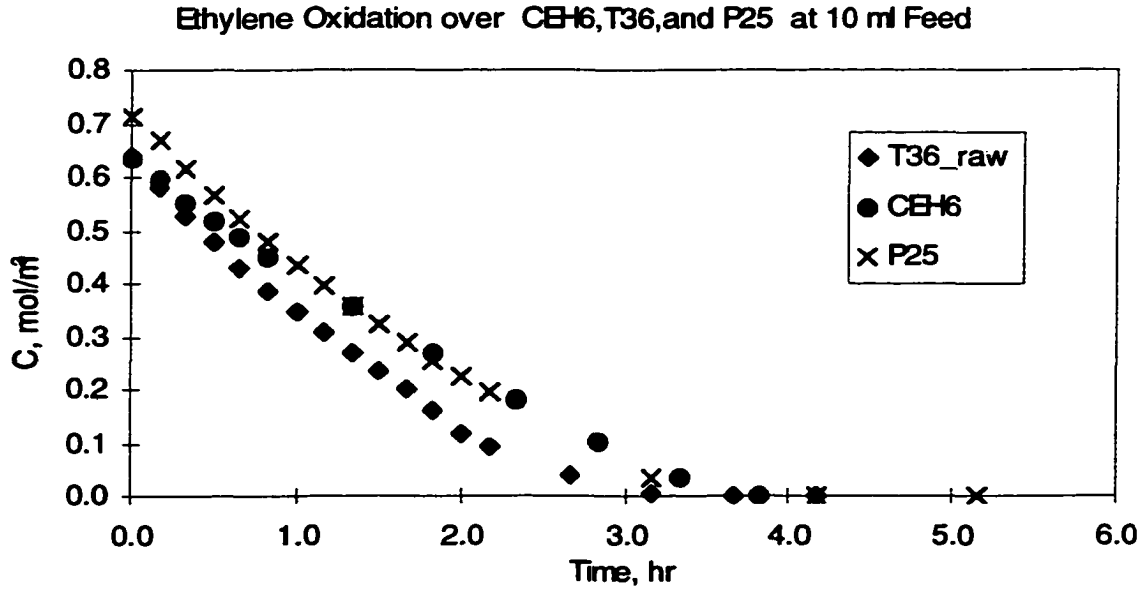

Figure 4-122 Ethylene oxidation over aerogels T36, CEH6 and the Degussa P25

4.6.4.2 Degussa P25 Catalyst

The photocatalytic activity of Degussa P25 was investigated twice at initial concentrations ranging between 0.2 and 2.2 mol/m^3. The second set of experiments was performed with a redesigned reactor system having a volume of one third less than before (213 ml compared to 316 ml). The kinetic results, however, are similar as it can be seen

by comparing the rate constants of both sets of experiments in Table 4-23 and when comparing the initial rates as shown in Figure 4-123.

Rate Constants $k_{x\ ethylene}$	P25	P25_new
k mass, mol/(m^3 hr-cm^3cat)	0.251	0.238
k ill. Cell window area, mol/(m^3 hr cm^2-cat)	0.0168	0.0141
k ill. cat-Volume, mol/(m^3 hr cm^3-cat)	37.30	31.31
k ill. cat-SA, mol/(m^3 hr m^2-cat)	0.93	0.88
Ethylene Adsorption Constant K, m^3/mol	1.7319	3.6130

Table 4-23 Kinetic results of ethylene oxidation of two sets of experimental runs over Degussa P25 at higher initial concentrations (using method linear regression to find the rate parameters)

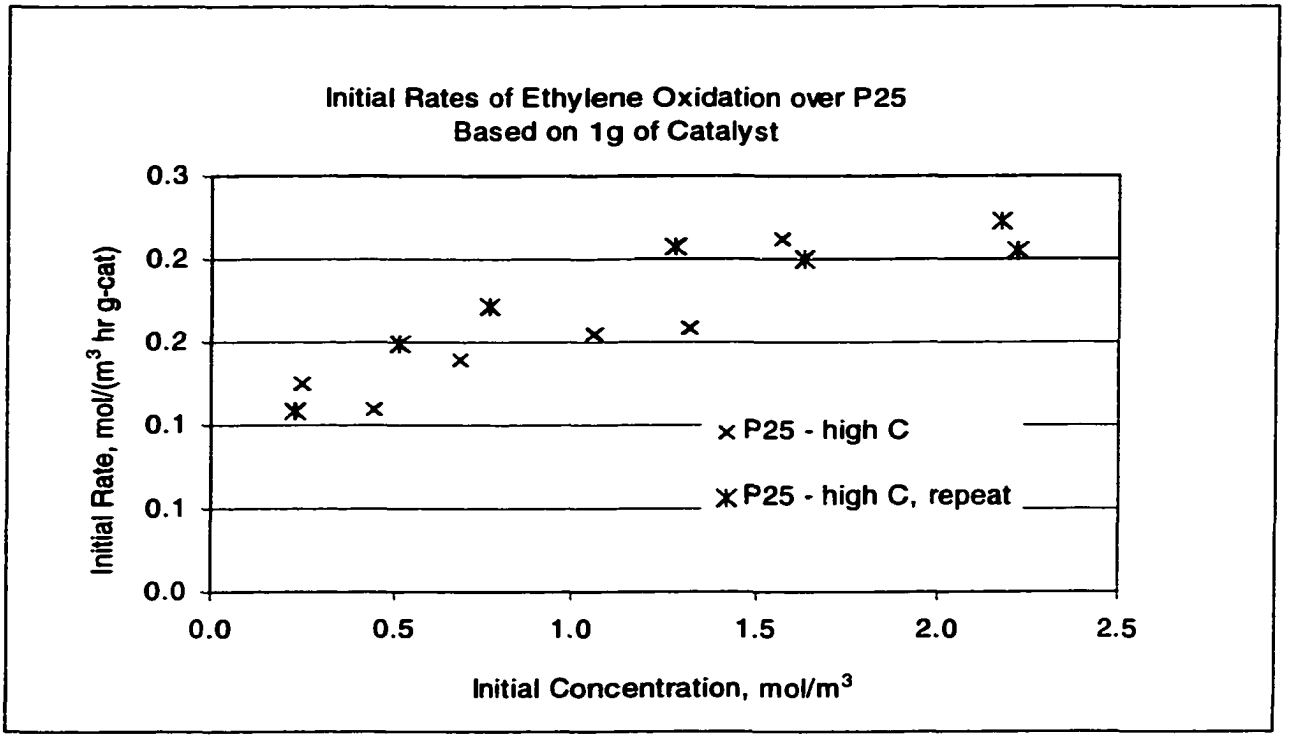

Figure 4-123 Initial mass based ethylene oxidation rates over Degussa P25 of two sets of experimental runs over Degussa P25. Each set was performed at initial concentrations between 0.2 and 2.2 mol/m^3 corresponding to 3, 5, 7, 10, 12, and 15 ml ethylene feed to the reactor system. The first set of experiment was performed with a reactor system of 316 ml, the repeated set in a 216 ml system.

No apparent reason could be found, however, why the adsorption constant K_E of both sets of experiments differed significantly. A scattering of the data could be a reason for this effect. Since the evaluation of the adsorption constant K using linear regression depends on the intercept as well as on the slope (K = intercept/(slope), a small variation in the value for the slope due to a largely scattered data can result in a substantial difference in K since the intercept is also affected by a change in slope. It was suspected that using nonlinear regression might avoid this problem. Therefore, another way to evaluate the rate constants was attempted. This was done by maximizing the non-linear regression parameter R^2 (Equation (4-20)[40]) over the experimental initial rate data of each set fitted to the Langmuir-Hinshelwood reaction rate model such as described before with equation (4-10) for methane oxidation.

$$R^2 = 1 - \frac{\Sigma(r_{experiment} - r_{model})^2}{\Sigma(r_{experiment} - r_{average})^2} \qquad (4\text{-}20)$$

The so obtained rate parameter values are summarized in Table 4-24. For easy comparison the values obtained from linear regression are again included in the same table. The adsorption constants obtained from maximizing R^2 were in the same range of about 3 m^3/mol, which was close to the value obtained of the set P25_new using linear regression. Figure 4-124 shows the initial rate data from both experimental sets plotted against initial ethylene concentration and includes the model fits for both evaluation methods. Even though the K_E-value from linear regression for the first set of experiments was by a factor of two smaller compared to the value obtained from maximizing R^2 this model fit nevertheless well to the experimental data with predicted initial rates only

slightly lower. This suggests that the model is not very sensitive to the adsorption constant K_E when applied within the range of concentrations it was determined.

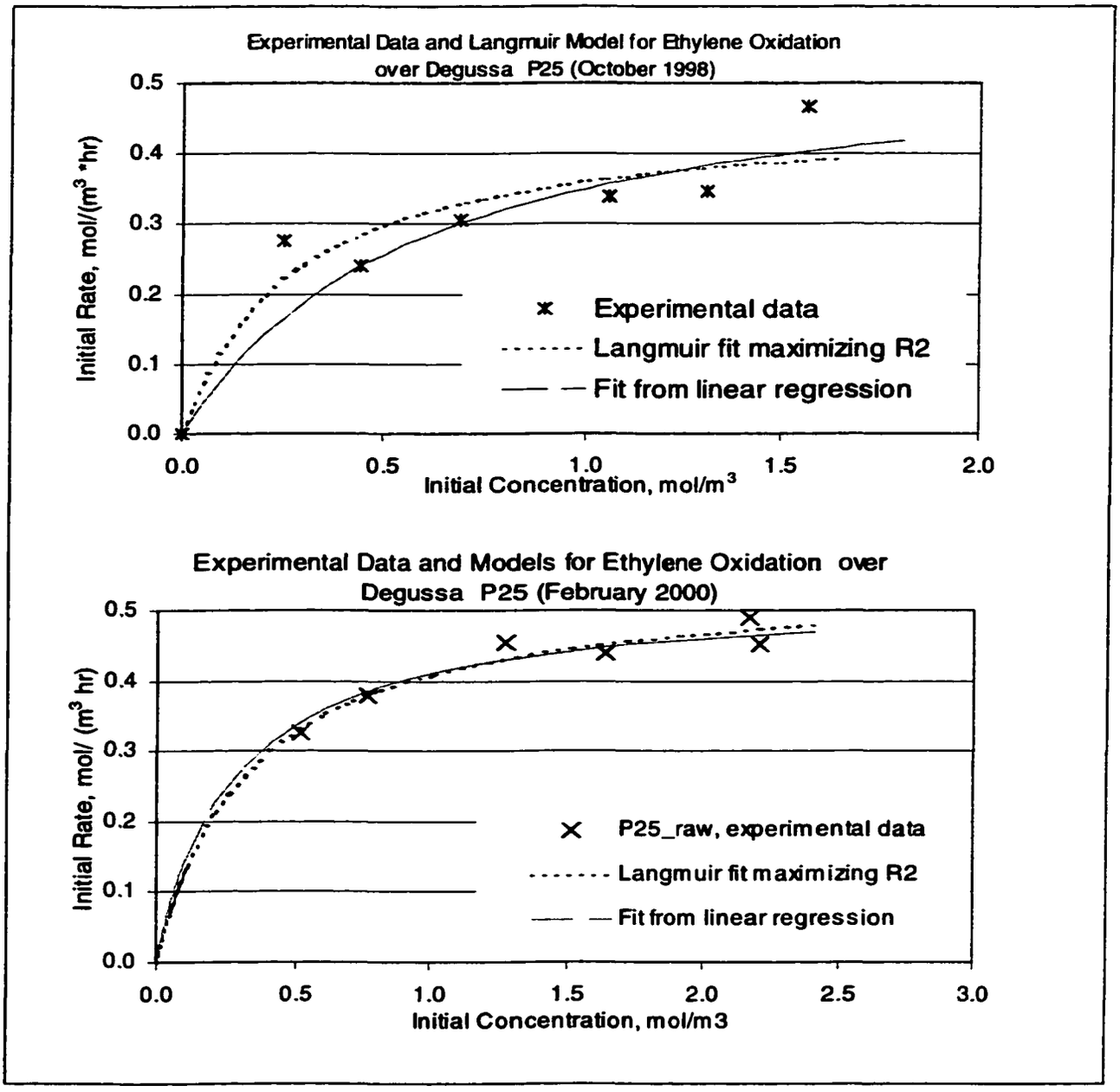

Figure 4-124 Initial ethylene oxidation rates over P25 of two sets of experiments (per 2.2 g of catalyst in the catalytic cell) and the model fit using linear regression and maximizing R^2. to find the kinetic parameters k and K.

Rate Constants $k_{x\ ethylene}$	P25 R2 max	P25_new R2 max	P25 Lin Regr.	P25_new Lin Regr.
k mass, mol/(m^3 hr g-cat)	0.208	0.237	0.251	0.238
k ill. Cell window area, mol/(m^3 hr cm^2-cat)	0.0139	0.0140	0.017	0.0141
k ill. cat-Volume, mol/(m^3 hr cm^3-cat)	30.941	31.1121	37.299	31.31
k ill. cat-SA, mol/(m^3 hr m^2-cat)	0.77	0.874	0.926	0.88
Ethylene Adsorption Constant K, m^3/mol	3.7245	3.876	1.732	3.6130

Table 4-24 Kinetic rate parameters for ethylene oxidation over Degussa P25 using different evaluation procedures (maximizing R^2 over Langmuir-Hinshelwood rate expression or using linear regression).

In addition to the previous set of experimental runs at high initial ethylene concentrations a second set of experiments was performed to investigate the catalyst's performance at lower initial concentrations ranging from 0.08 to 0.1 mol/m^3 corresponding to injected amounts of 0.1, 0.3, 0.5, 0.7, and 1.0 ml of ethylene at room temperature and atmospheric pressure. Initial ethylene oxidation rates and the obtained rate parameters related to this set of experimental runs are seen in Table 4-25 (the values determined for the experiments performed at higher concentrations are included in this table for easier comparison) and Figure 4-125. The rate parameters obtained from linear regression and from maximizing R^2 were found to differ by about 20%. The results from linear regression are probably subject to larger deviation since the position of intercept and slope are significantly influenced by scattered data, which have a stronger impact on the resulting values of k and K. The method of using the experimental data to maximize R^2 over the Langmuir-Hinshelwood rate expression was the method applied and discussed from here on.

P25_new Rate Constants $k_{x\ ethylene}$	low C lin. Reg.	low C R^2 max	high C lin. Reg.	high C R^2 max	all C R^2 max
k mass, mol/(m^3 hr g-cat)	0.064	0.086	0.238	0.248	0.237
k ill. Cell window area, mol/(m^3 hr cm^2-cat)	0.004	0.005	0.014	0.015	0.014
k ill. cat-Volume, mol/(m^3 hr cm^3-cat)	8.41	11.29	31.31	32.533	31.11
k ill. cat-SA, mol/(m^3 hr m^2-cat)	0.24	0.32	0.88	0.913	0.87
Ethylene Adsorption Constant K, m^3/mol	46.73	24.72	3.61	3.01	3.88

Table 4-25 Kinetic parameters of ethylene oxidation calculations for experimental runs over Degussa P25 at higher and lower initial concentrations. The label "lin.Reg" stands for the evaluation method using linear regression, "R^2 max" stand for the method of maximizing R2 over the experimental data.

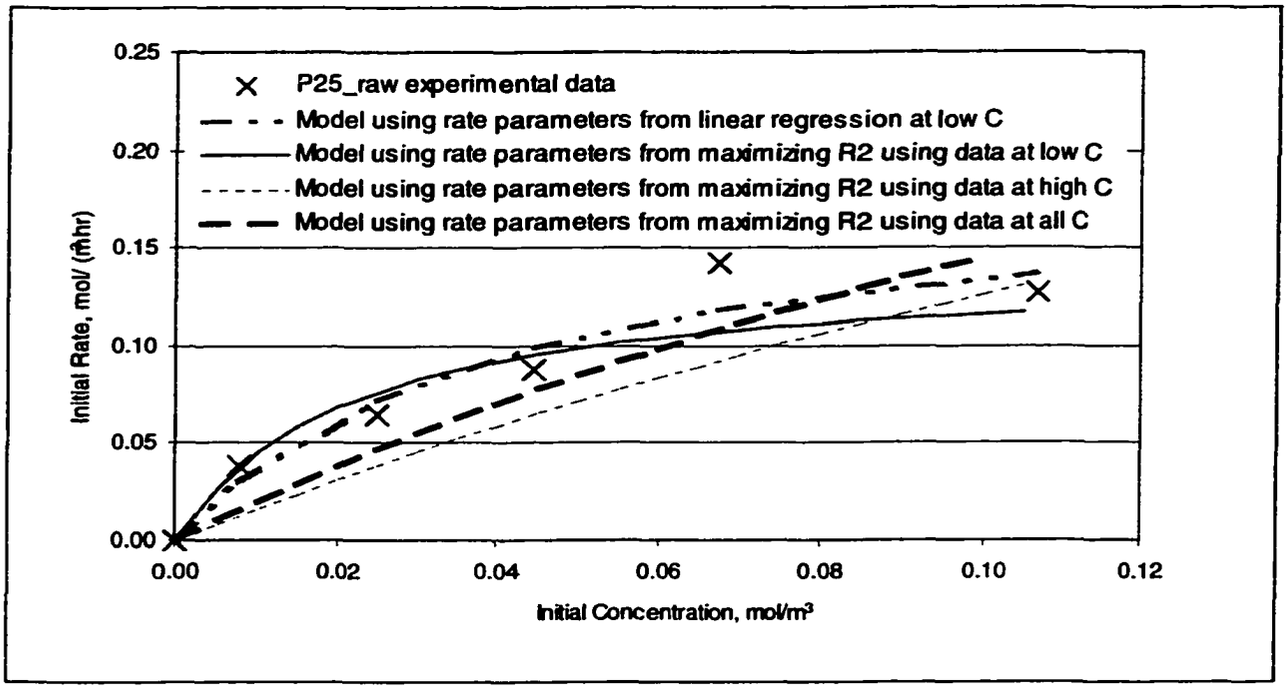

Figure 4-125 Initial ethylene oxidation rates over Degussa P25 at low initial ethylene concentrations of up to 0.1 mol/m^3. Models using rate parameters obtained from different evaluation methods are included.

It was also observed that the reaction rate constants at low concentrations differed notably (about three times) from the values found at higher concentrations. As seen in Figure 4-125, the rate parameters found using only the data from experiments performed at low initial concentrations provide a good prediction of initial rates in the range of

lower initial concentrations. The Langmuir-Hinshelwood models using rate data obtained from experiments at higher initial concentrations (Figure 4-124 and Table 4-24) were also plotted in the same graph (dashed and dotted lines). The models using the rate parameters obtained from experiments with higher initial concentration resulted as well in predictions close the experimental initial rate data. However, it did not show as clearly the typical trend of a Langmuir prediction (rather a nearly straight line) as in the case for the models using the rate parameters obtained from the tests with low initial concentrations. Another comparison was carried out by plotting different Langmuir-Hinshelwood predictions over all initial rate data (data of both sets of experimental runs at lower and higher initial concentrations) using the different determined rate parameters for calculating the model fit. This is shown in Figure 4-126. The models calculated from rate parameters obtained from initial rate data at high initial concentrations or from using all initial rate data (including the ones at low initial concentrations) were in very good agreement with all experimental data. The models calculated by using the rate parameters obtained from only the data at low initial concentrations, however, predicted initial rates far below the actual data in the range of high initial concentrations. This indicates that a Langmuir-Hinshelwood rate expression determined from experiments at low initial concentrations cannot be applied for an entire range of exposed concentrations. Obee and Brown[33], who also applied the Langmuir-Hinshelwood rate form for the evaluation of toluene reaction rate constants, found this model to be a good correlation within the applied range of their experiments at very low concentrations of 0.5 to 2.0 ppmv. However, they stated that the extrapolation of oxidation performance data collected at higher concentrations might not be valid for any intended application at

significantly different concentrations. This is especially true when the oxidation process is complex and critically dependent on the contaminant concentration. They showed that in particular in the presence of water the oxidation was crucially dependent on humidity level and contaminant concentration. They reasoned that there are two distinguishable oxidation regions: one was defined in which the hydroxyl radical population (adsorption site population) determines the oxidation rate and one in which competitive adsorption (co-adsorption) determines the oxidation rate. The location of those two regions depends on the relative adsorption affinity of the TiO_2 for water and the contaminant plus it is dependent on the mechanism of radical attack, which in turn depends on the specific contaminant. This observation agrees with the finding of the ethylene and acetone oxidation of this work. The obtained rate parameters differed notably between the two sets of experiments of lower and higher initial concentrations (more generated water during oxidation tests with high initial concentrations). Hence, the rate parameters found in this work will only be applicable for the range of concentrations it was determined from.

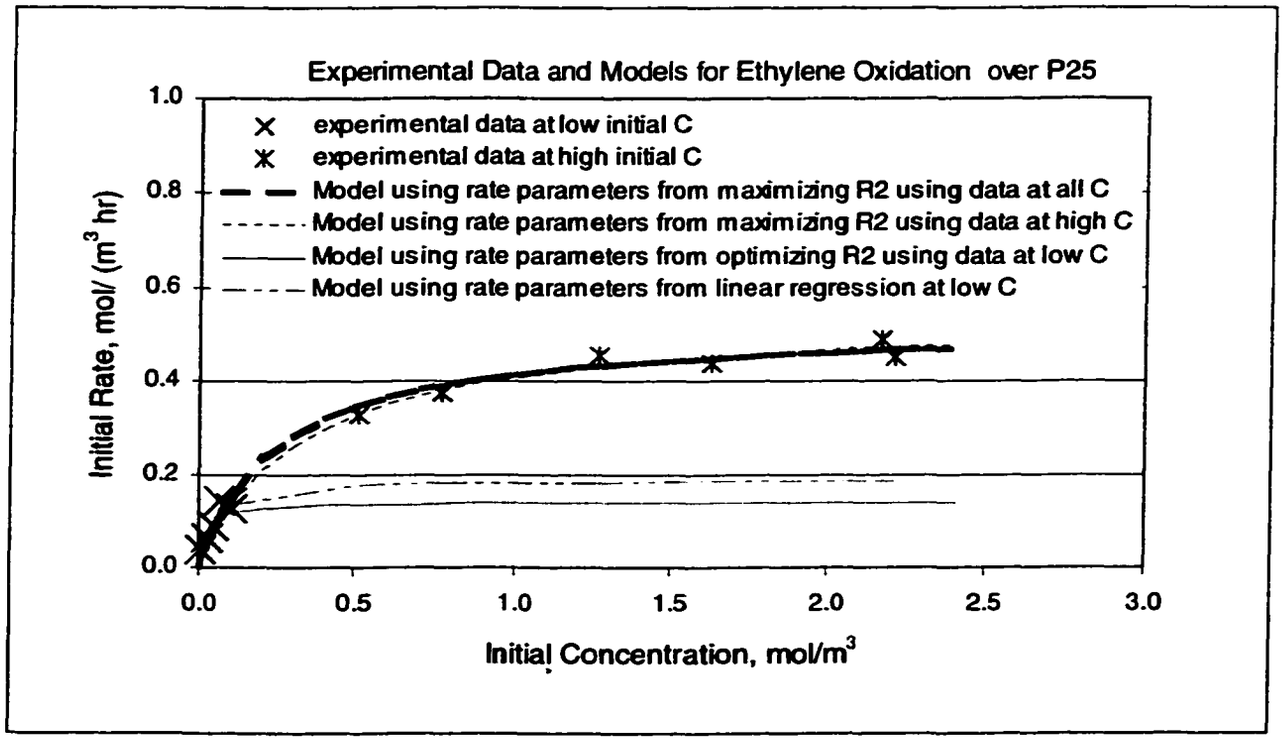

Figure 4-126 Actual initial ethylene oxidation rates (based on mass) over Degussa P25 at lower and higher initial ethylene concentrations and the comparison of different reaction rate model predictions

The Langmuir-Hinshelwood predictions according to equation (4-21) while using the rate parameters determined from the initial rate data were calculated to find out how well those rate predictions would fit the rates of all of the experimental data of an individual experiment (not just initial rates). The actual reaction rates at any point in time were calculated by dividing the change in concentration by the change in time for each data point interval according to (4-22).

(4-21) $$-r_E = \frac{k_E K_E C_E}{1 + K_E C_E},$$

where k_E stands for the ethylene reaction rate constant, K_E the ethylene adsorption constant, and C_E the gas phase concentration of ethylene.

(4-22) $$rate_{actual} = \frac{dC}{dt}$$

Comparing the predictions with the actual rate data in Figure 4-127 and Figure 4-128 show that the predicted rates according to equation (4-21) were higher than the actual rates, especially for the experiments at higher initial concentrations (see Figure 4-128). This signifies that the generated water during the reaction played an important role and needed to be included in the rate prediction. Therefore, in order to take the influence of generated water during the ethylene oxidation into account the water adsorption constants were determined as follows.

Since the water concentration was not measured during the experimental runs the amount of water was estimated from the ethylene concentration. For each mol of ethylene consumed two moles of water were generated according to the chemical ethylene oxidation rate equation: $C_2H_4 + 3\,O_2 \rightarrow 2\,CO_2 + 2\,H_2O$. The water gas phase concentrations C_W was then calculated with the aid of the generalized Langmuir adsorption expression for multicomponent adsorption where ethylene and water adsorb competitively according to equation (4-23)

(4-23) $$\Theta_W = \frac{(K_W^{RH} C_W)}{1 + K_E^{dry} C_E^{RH} + (K_W^{RH} C_W)}$$

where Θ_W is expressed as in (4-24)

(4-24) $$\Theta_W = \frac{V_W^{adsorbed}}{V_m} = \frac{C_W^{generated} - C_W}{V_m}$$

with V_m = water adsorbed in a complete monolayer and $V_W^{adsorbed}$ = the amount of water adsorbed on the catalyst. Data for monolayer coverage of water were not available. Since water adsorbs strongly, the assumption was made, that water would adsorb similarly to acetone. The monolayer coverage of acetone on the aerogels was determined from acetone adsorptions studies (see Section 4.5.1) and the value for P25 was taken from the literature[40]. The value for V_m was then determined from the μ_a values from the adsorption studies, which represent the maximum amount of acetone adsorbed in a monolayer (see Table 4-26).

$$V_m = \frac{\mu a * mass_{catalyst}}{MW * V_{system}}$$

	Anatase	P25	CEH6	T36	T36_450
μa mg/g cat	4.4	2.0	106.8	106.8	30.5
m cat, g	3.7	2.2	1.33	0.75	1.3
$MW_{acetone}$, g/mol	58	58	58	58	58
V system, L	0.309	0.2951	0.313	0.3087	0.2951
==> V_m, mmol/L	0.909	0.263	7.828	4.476	2.319

Table 4-26 Estimate of amount of water in a monolayer adsorbed on a catalyst

After combining (4-23) and (4-24), the equations can then be rearranged leading to a quadratic expression than can be solved for the water gas phase concentration C_W as in (4-25)

(4-25) $$0 = K_W C_W^2 + (1 + K_E C_E + K_W V_m - C_W^{generated} K_W)\, C_W + C_W^{generated}(K_E C_E - 1)\,.$$

After finding the water gas phase concentration, the water adsorption constant, K_W, was determined by maximizing R^2 over the experimental rate data of each individual run

according to the Langmuir-Hinshelwood expression including the term for water adsorption as indicated in (4-26)

$$(4\text{-}26) \quad -r_E = \frac{k_E K_E C_E}{1 + K_E C_E + K_W C_W}$$

The obtained water adsorption constants K_W for each individual experimental run are summarized in Table 4-27. The values for R^2 are included in the same table as well as the R^2 for the same Langmuir-Hinshelwood model using the average value of $K_W = 0.60$ mol/m^3. At some of the individual tests (0.1, 0.7, and 3.0 ml feed) the value for R^2 could only be maximized by obtaining a negative value for K_W (indicated by the value of 0 in Table 4-27). At those test, the rate models ignoring the term for water adsorption fit already reasonable well to the experimental data. Therefore, the models with and without using KW were identical in Figure 4-129 and Figure 4-130. Since this was mainly the case for the experiments at lower ethylene feeds (0.1 to 3 ml) and the values for K_W varied appreciably without showing a trend it may suggest that the amount of generated water did not have an effect as strongly on the overall reaction model as seen in the case for tests with higher ethylene feed (5 to 15 ml) in which necessarily more water was generated. The Langmuir-Hinshelwood models using the average value for $K_W = 0.60$ m^3/mol (ignoring the tests at low initial concentrations) provided rate predictions that fit well to the experimental rate data over the whole range of applied initial concentrations (including the lower concentrations) as it can be seen in Figure 4-129 and Figure 4-130. This suggests that the term of $K_W C_W$ in the denominator of the Langmuir-Hinshelwood model does not change much compared to the term $K_E C_E$..

Figure 4-131 shows the relative magnitude of K_WC_W compared to K_EC_E. The term K_WC_W was for most of experiment relatively small compared to K_EC_E and therefore did not dominate the rate prediction. This explains why the use of the average value of K_W for the Langmuir rate prediction provided still a good fit to all experimental runs.

Feed, ml ml	C ethylene mol/m^3	Cw avg mol/m^3	Kw m^3/mol	R2 with calcul. Kw	R2 with avg Kw	% R2 deviation
0.1	0.0077	0.0147	0.00	0.93	0.93	0.4
0.3	0.0249	0.0539	1.87	0.94	0.94	0.1
0.5	0.0444	0.0930	3.48	0.96	0.94	1.9
0.7	0.0676	0.1113	0.00	0.98	0.98	0.3
1	0.1067	0.0843	5.28	0.97	0.74	23.7
3	0.2259	0.0000	0.00	0.83	0.65	21.7
5	0.5159	0.0000	0.64	0.84	0.84	0.6
7	0.7700	0.0000	0.18	0.90	0.80	11.1
10	1.2720	0.0000	0.68	0.86	0.86	0.0
12	1.6297	0.0000	0.54	0.99	0.96	3.2
15	2.1721	0.0000	0.53	0.83	0.82	1.1
		average K_w -->	0.60	m^3/mol		

Table 4-27 Determined water adsorption constants for ethylene oxidation over P25 for each individual experimental run. Included are the values for R^2 of the Langmuir-Hinshelwood models using each individual run.

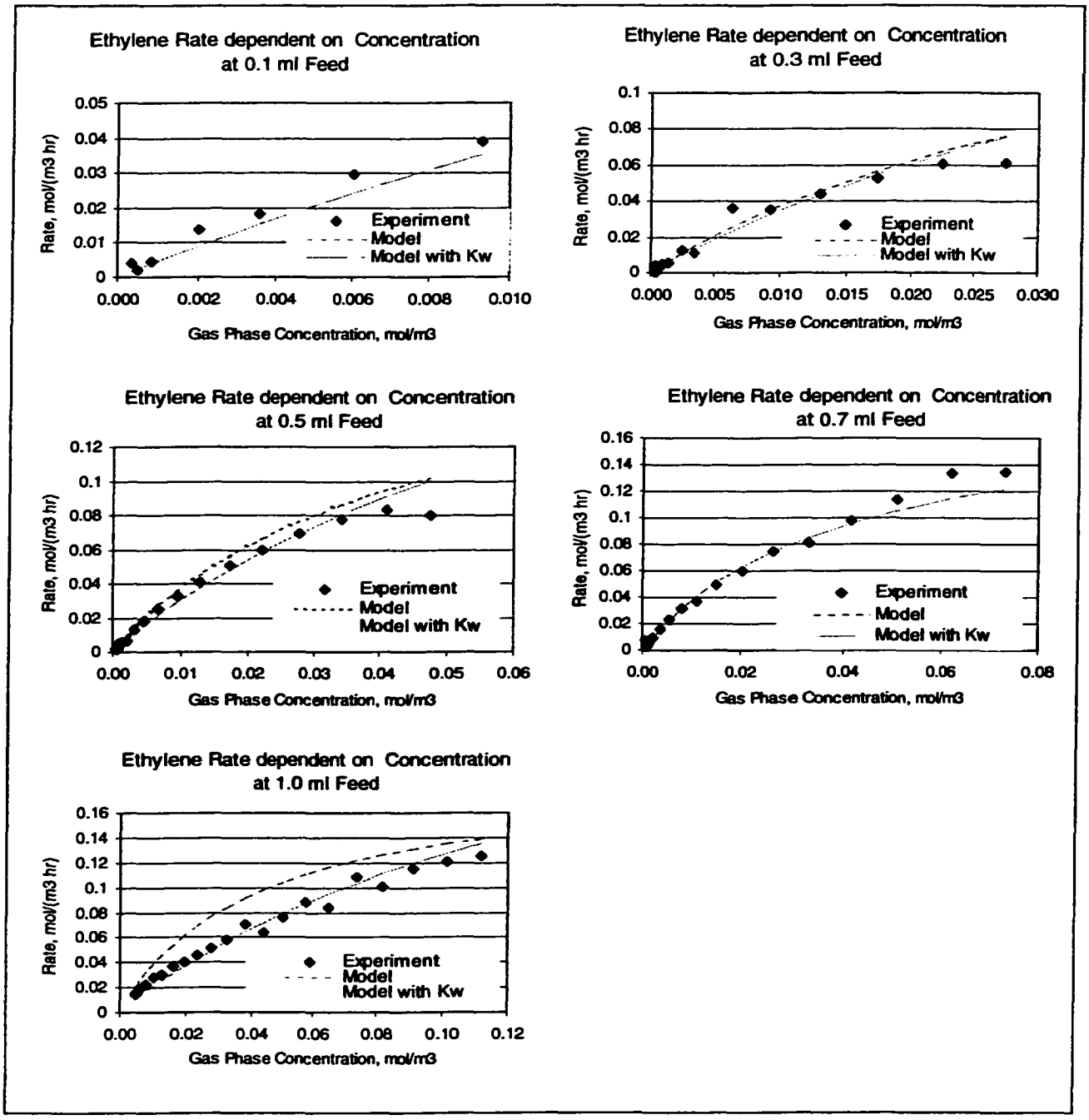

Figure 4-127 Experimental rates and Langmuir-Hinshelwood rate models (used rate parameters are listed in Table 4-25 and Table 4-27) for each individual ethylene oxidation test over Degussa P25 at lower initial concentrations

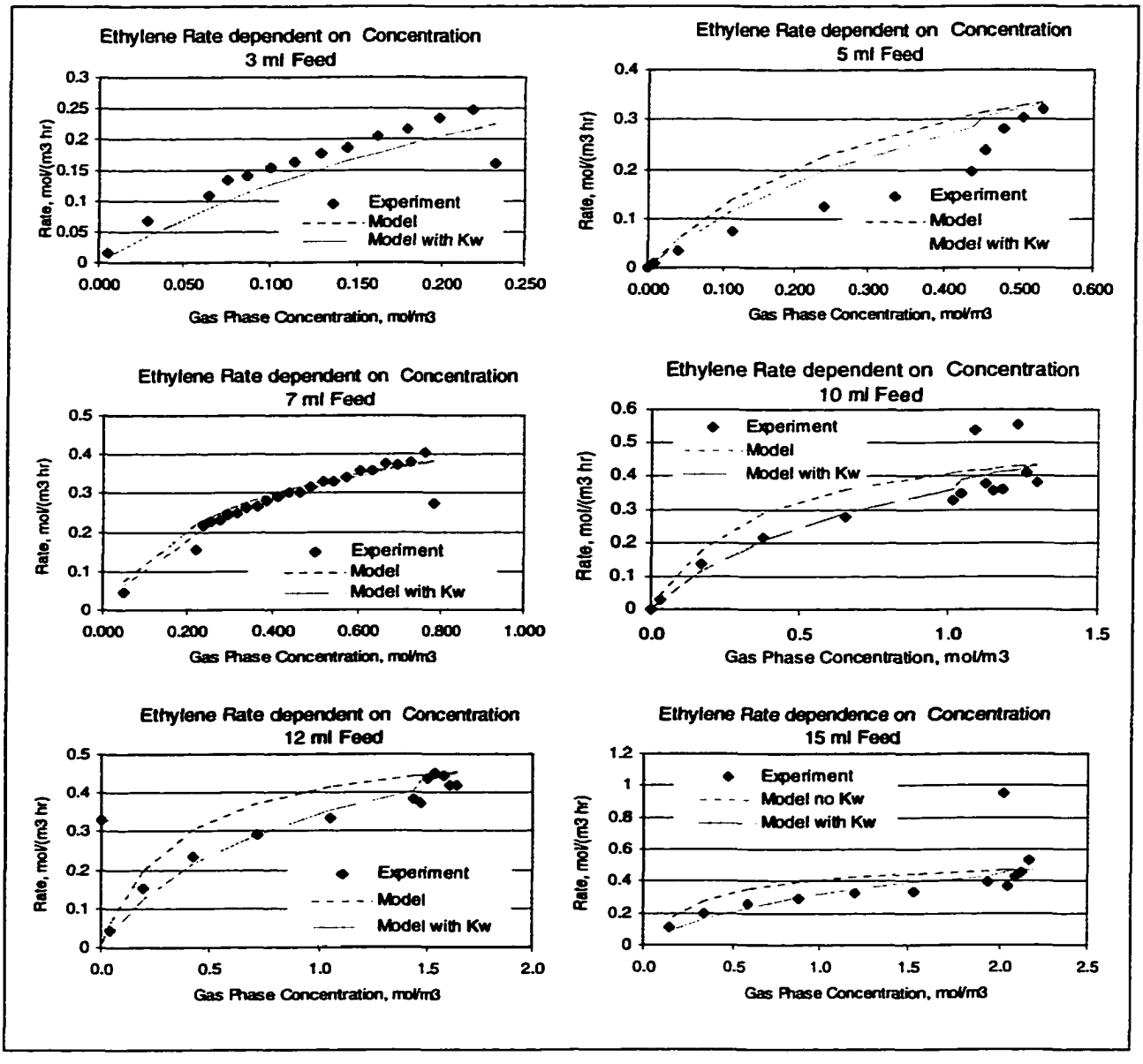

Figure 4-128 Experimental rates and Langmuir-Hinshelwood rate models (used rate parameters are listed in Table 4-25 and Table 4-27) for each individual ethylene oxidation test over Degussa P25 at higher initial concentrations. The dotted lines indicate the model without K_W, while the dashed line represents the model including the water term $K_W C_W$.

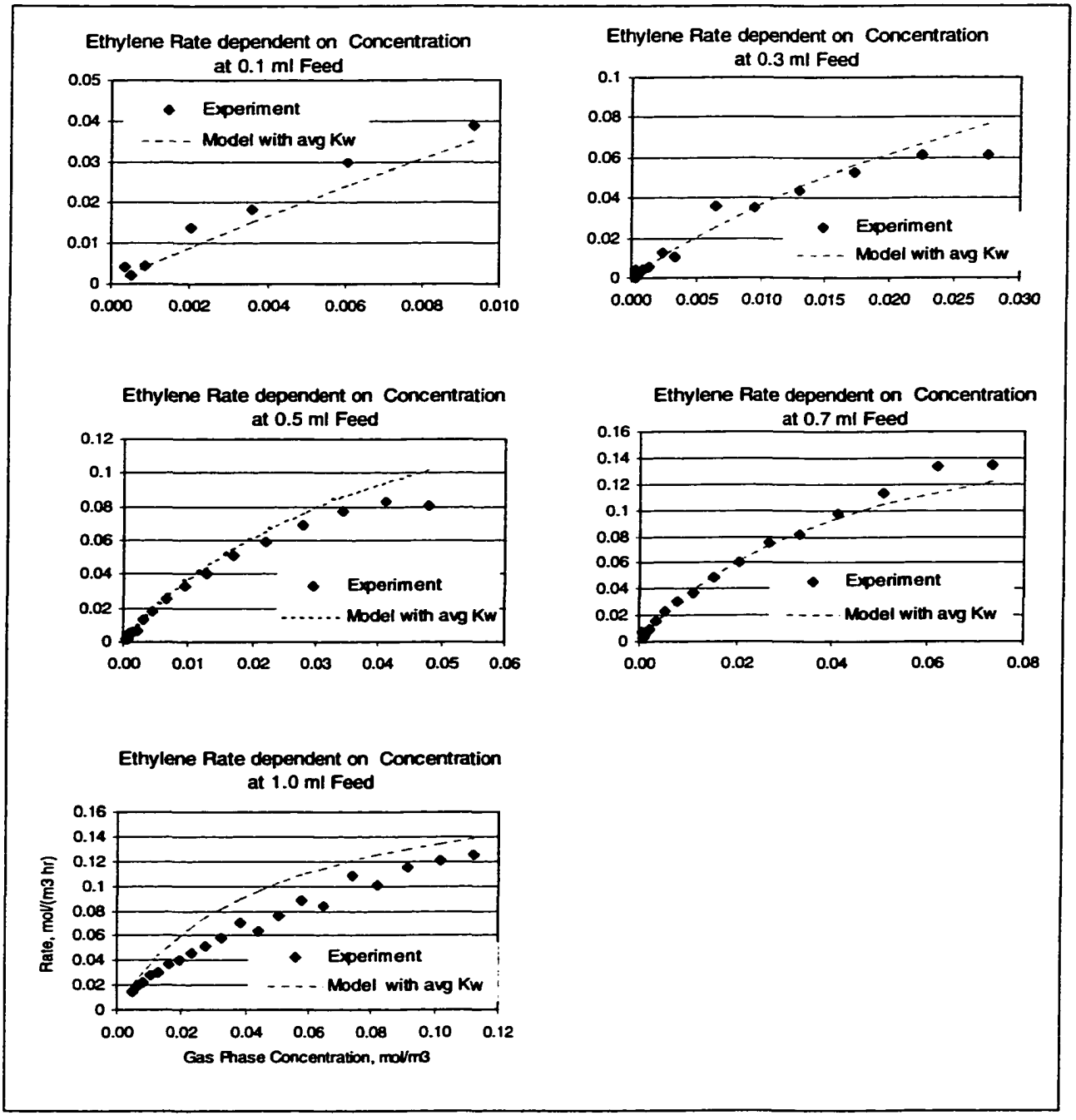

Figure 4-129 Comparison of Langmuir-Hinshelwood rate models using average value for $K_W = 0.60\ m^3/mol$) with experimental rates for each individual ethylene oxidation test over Degussa P25 at lower initial concentrations

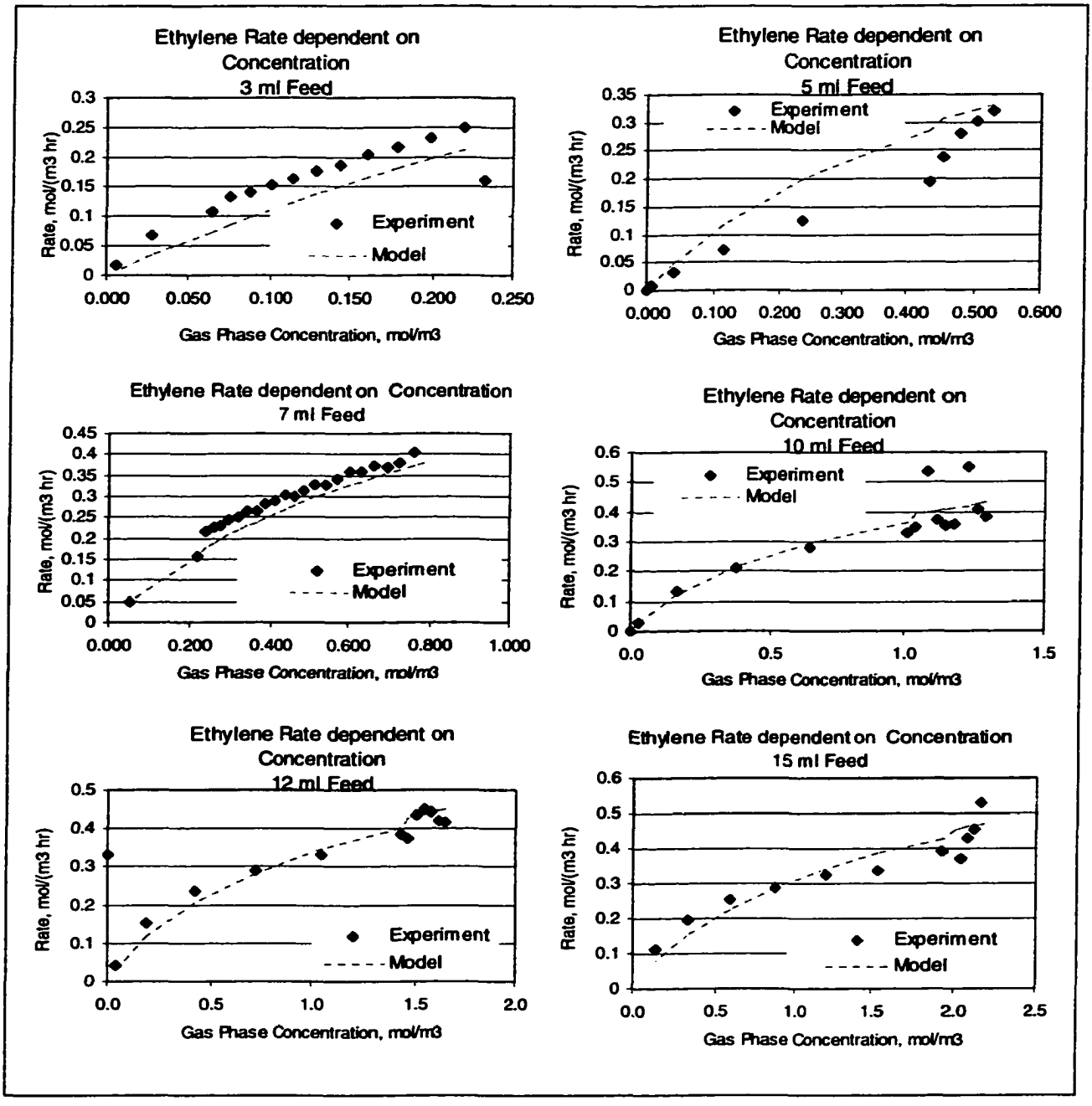

Figure 4-130 Comparison of Langmuir-Hinshelwood rate models using the average $K_W = 0.60\ m^3/mol$ with experimental rates for each individual ethylene oxidation test over Degussa P25 at higher initial concentrations.

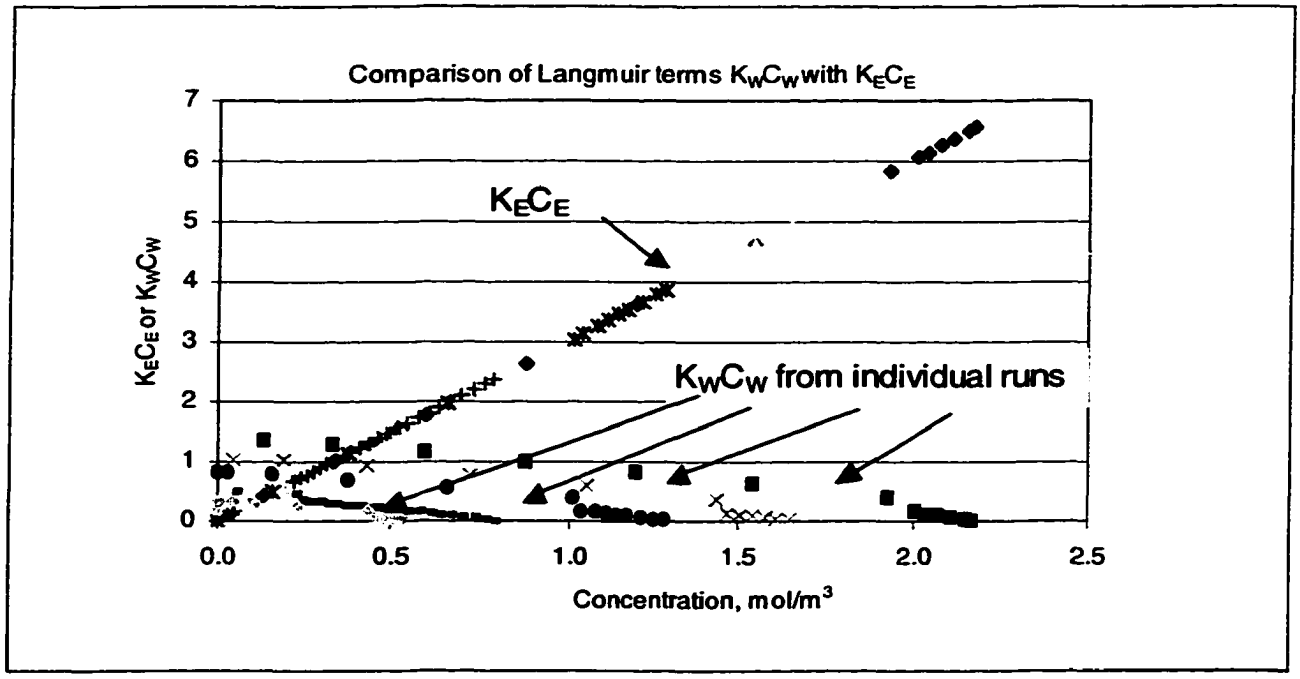

Figure 4-131 Comparison of denominator terms in the Langmuir-Hinshelwood expression

4.6.4.3 Ultra-low-density Aerogel T36

Similar ethylene oxidations test as described for the Degussa P25 were performed for the ultra-low-density aerogel T36. A similar trend as seen with P25 was observed for this aerogel catalyst when comparing the initial reaction rates of the data set performed at lower and the set at higher initial ethylene concentrations. The increase in initial rate with initial concentration slows down towards higher initial concentrations starting at 0.2 mol/m^3 (corresponding to 3 ml ethylene feed and up) as seen in Figure 4-132, which is typical for a Langmuir-Hinshelwood rate expression. The reaction rate parameters were determined by maximizing R^2 to fit the Langmuir-Hinshelwood rate model over the experimental data as previously described for the Degussa P25 catalyst. The results are summarized for both sets of experiments (at lower and higher initial ethylene concentrations) in Table 4-28. In

addition, the method of maximizing R^2 was applied over all data covering both sets of experiment (last column labeled with "all C R2 max" in Table 4-28). The rate parameters for the experiments at high concentrations and the parameters determined over the whole range of initial concentrations (last two columns of Table 4-28) were of the same scale showing a reaction rate constant based on mass of catalyst of $k_E^{T36} = 0.59$ mol/(m^3 hr g-cat) and an ethylene adsorption constant $K_E^{T36} = 7.3$ m^3/mol. At low concentrations the value for the rate constant was lower by about 30 percent. The plots in Figure 4-132 and Figure 4-133 show the experimental initial rate data and rate models using different evaluation criteria. Similar to the observation from the Degussa tests, predicted rates for high concentrations using the rate parameters determined from experiments at lower initial concentrations were about 50 % too low supporting the theory that data collected at lower concentrations might not be valid for any intended application at significantly different concentrations. In contrast, however, using rate parameters determined from experiments at high initial concentrations provided reasonable well fits to the initial rates at low initial feed concentrations.

T36_raw Rate Constants $k_{x\ ethylene}$	low C R2 max	high C R2 max	all C R2 max
k mass, mol/(m^3 hr g-cat)	0.395	0.601	0.589
k ill. Cell window area, mol/(m^3 hr cm^2-cat)	0.008	0.013	0.011
k ill. cat-Volume, mol/(m^3 hr cm^3-cat)	4.244	6.456	5.900
k ill. cat-SA, mol/(m^3 hr m^2-cat)	0.048	0.073	0.074
Ethylene Adsorption Constant K, m^3/mol	15.694	6.894	7.803

Table 4-28 Kinetic results of ethylene oxidation calculations for experimental runs over aerogel T36 at lower and higher initial concentrations

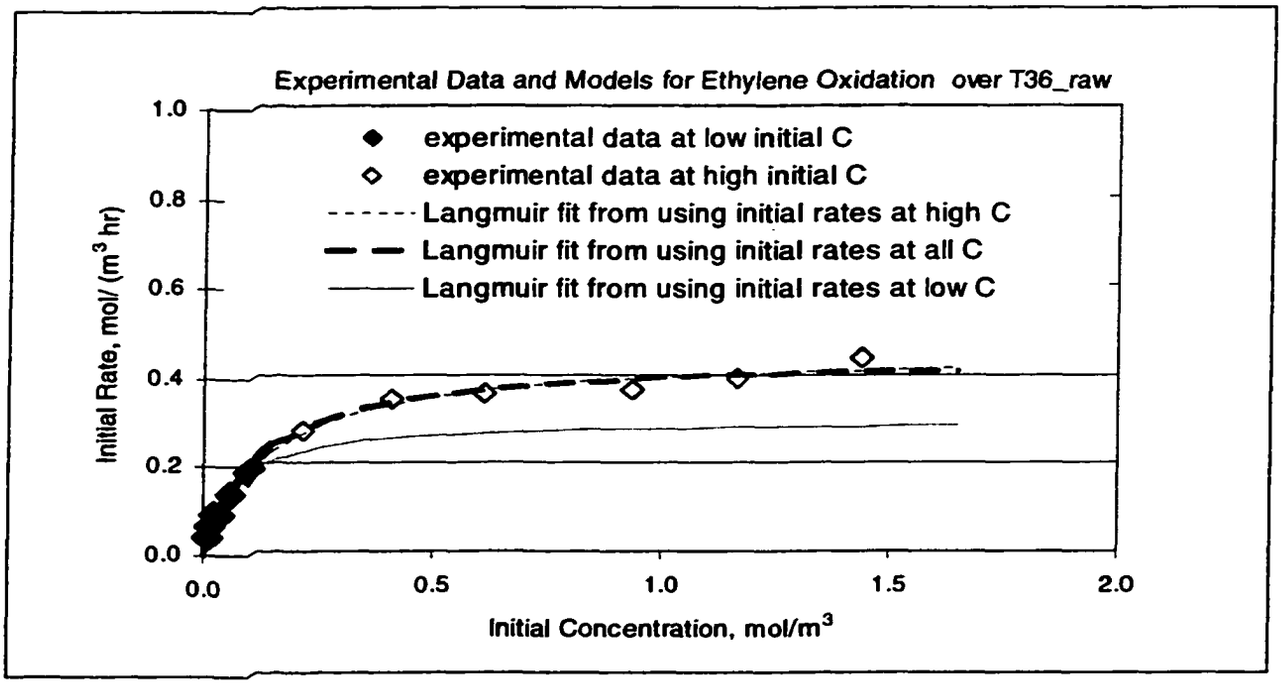

Figure 4-132 Initial ethylene oxidation rates over 0.75 g of T36 and comparison of Langmuir-Hinshelwood models using rate parameters from different evaluation criteria

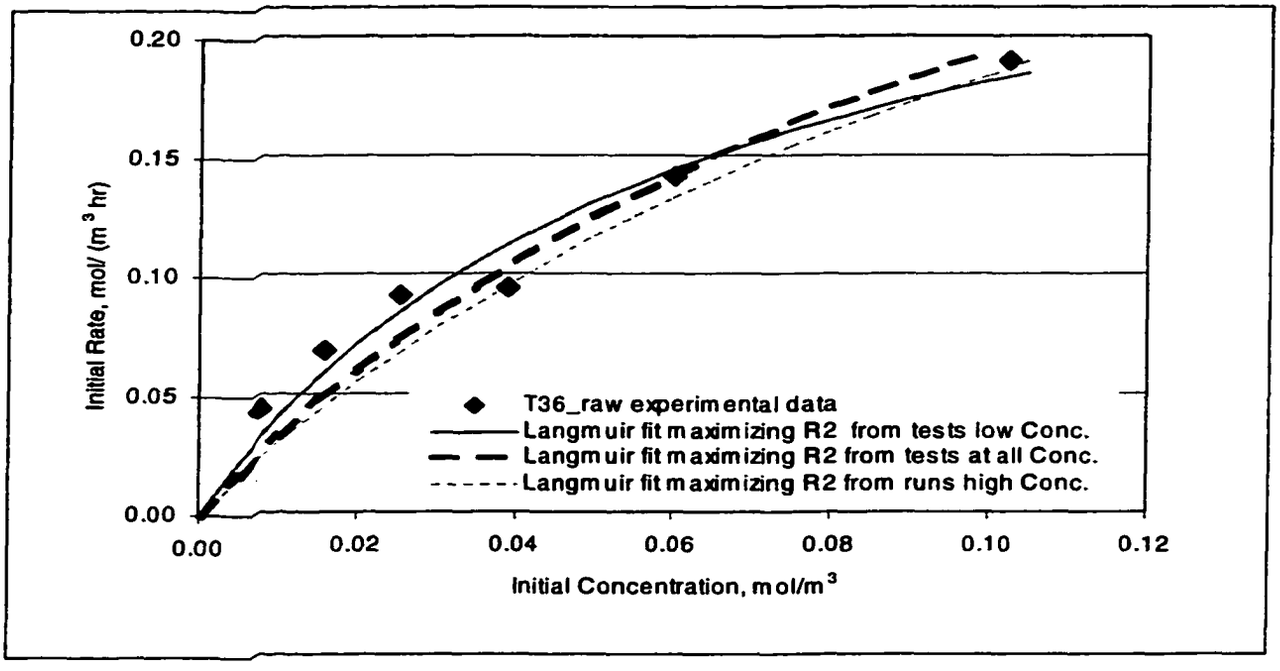

Figure 4-133 Initial ethylene oxidation rates over 0.75 g of T36 at lower initial ethylene concentrations and comparison of Langmuir-Hinshelwood models using rate parameters from different evaluation criteria

Langmuir-Hinshelwood approximations using the values for k_E and K_E from maximizing R^2 were performed for each individual experiment and the models are compared to the actual data in Figure 4-134 and Figure 4-135. A good agreement between experimental data and model was observed for the tests at low concentrations. However, similar as was observed for the Degussa P25, the deviation of the model data from the experimental data is more apparent in the case of higher initial ethylene concentrations. The rate inhibiting effect of water might explain this deviation. The amount of water generated during the reaction was determined in a similar manner as described for the Degussa P25 and those data were used to find the adsorption constant K_E^{T36} for each individual oxidation test using the method of maximizing R^2. The obtained rate parameters are summarized in Table 4-29 and include the values for R^2 for each run and the R^2 for the same Langmuir-Hinshelwood model using the average value of $K_E^{T36} = 1.20$ mol/m^3. The determined water adsorption constants varied between 0.6 and 1.9 m^3/mol. For the individual tests performed at low initial concentrations (0.1, 0.2, 0.3, and 0.5 ml feed) the value for R^2 could only be maximized for $K_W = 0$ suggesting that generated water did not significantly influence the reaction kinetics in these cases. The models ignoring the water term in the Langmuir-Hinshelwood expression resulted already in reasonable fits to the experimental data as seen in Figure 4-134. At higher initial ethylene feeds the influence of generated water became more apparent as it is shown in Figure 4-135. Models ignoring the water term deviated largely from the experimental data resulting in predictions of higher values and show that the rate models using the average value of K_W were in most cases close to the rate models using the individual K_W. Therefore, the average value of $K_W^{T36} = 1.25$ mol/m^3 was used in any subsequent calculations.

Feed, ml ml	C ethylene mol/m^3	Cw avg mol/m^3	Kw m^3/mol	R2 with calcul. Kw
0.1	0.0079	0.0130	0.00	0.92
0.2	0.0160	0.0280	0.00	0.99
0.3	0.0254	0.0420	0.00	0.99
0.5	0.0389	0.0711	0.00	0.98
0.7	0.0603	0.1015	1.91	0.99
1	0.1025	0.1665	1.43	0.99
3	0.2181	0.2888	0.00	0.95
5	0.4114	0.5662	0.76	0.97
7	0.6106	0.7934	0.90	0.88
10	0.9391	1.3144	1.21	0.96
12	1.1698	1.1281	1.63	0.92
15	1.4402	1.5978	2.18	0.99
		avg -->	1.25	m^3/mol

Table 4-29 Determined water adsorption constants for ethylene oxidation over aerogel T36 for each individual experimental run. Included are the values for R^2 of the Langmuir-Hinshelwood models using each individual run (calcul. Kw).

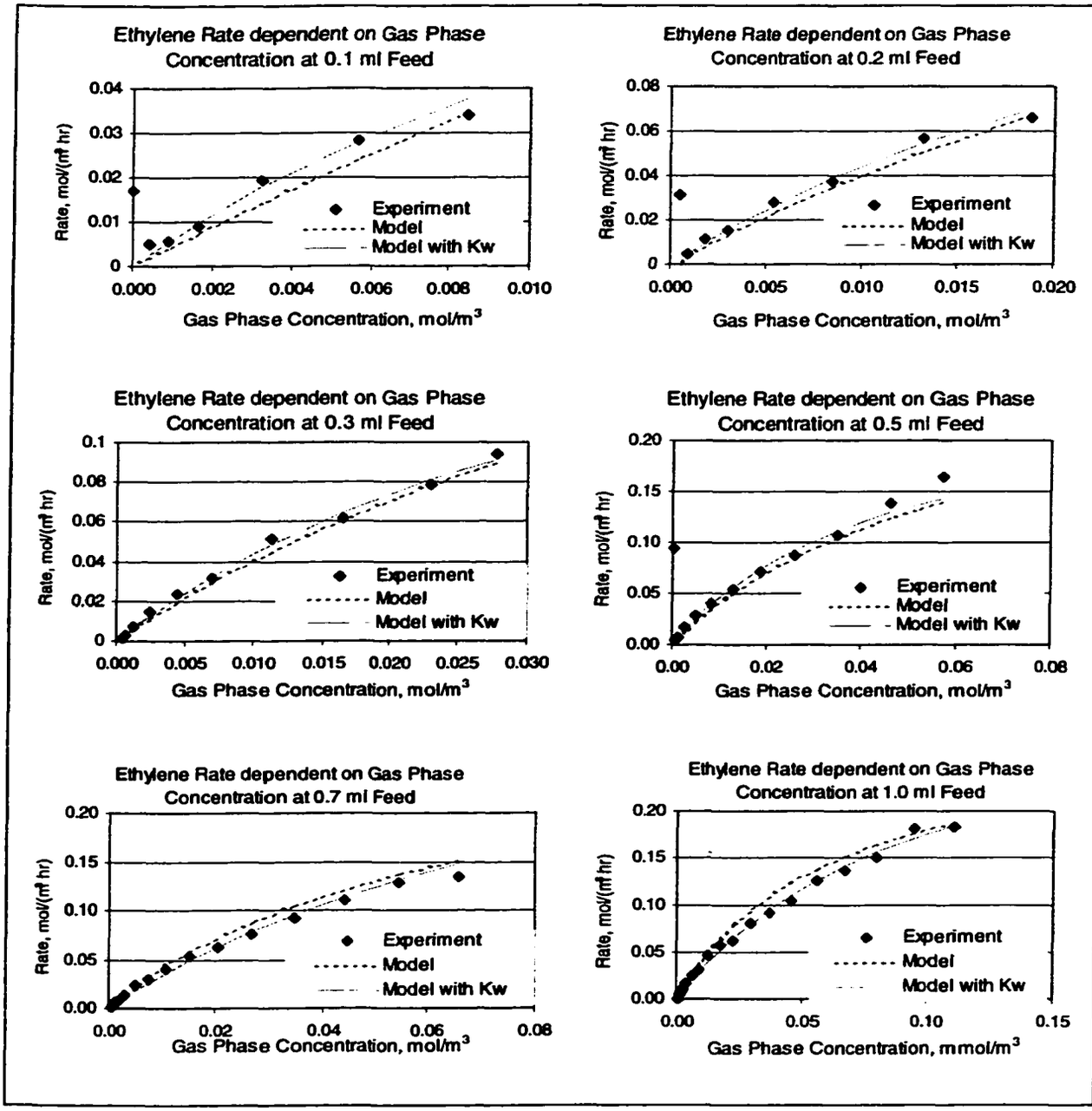

Figure 4-134 Experimental rates and Langmuir-Hinshelwood rate models (used rate parameters are listed in Table 4-28 and Table 4-29) for each individual ethylene oxidation test over T36 at lower initial concentrations

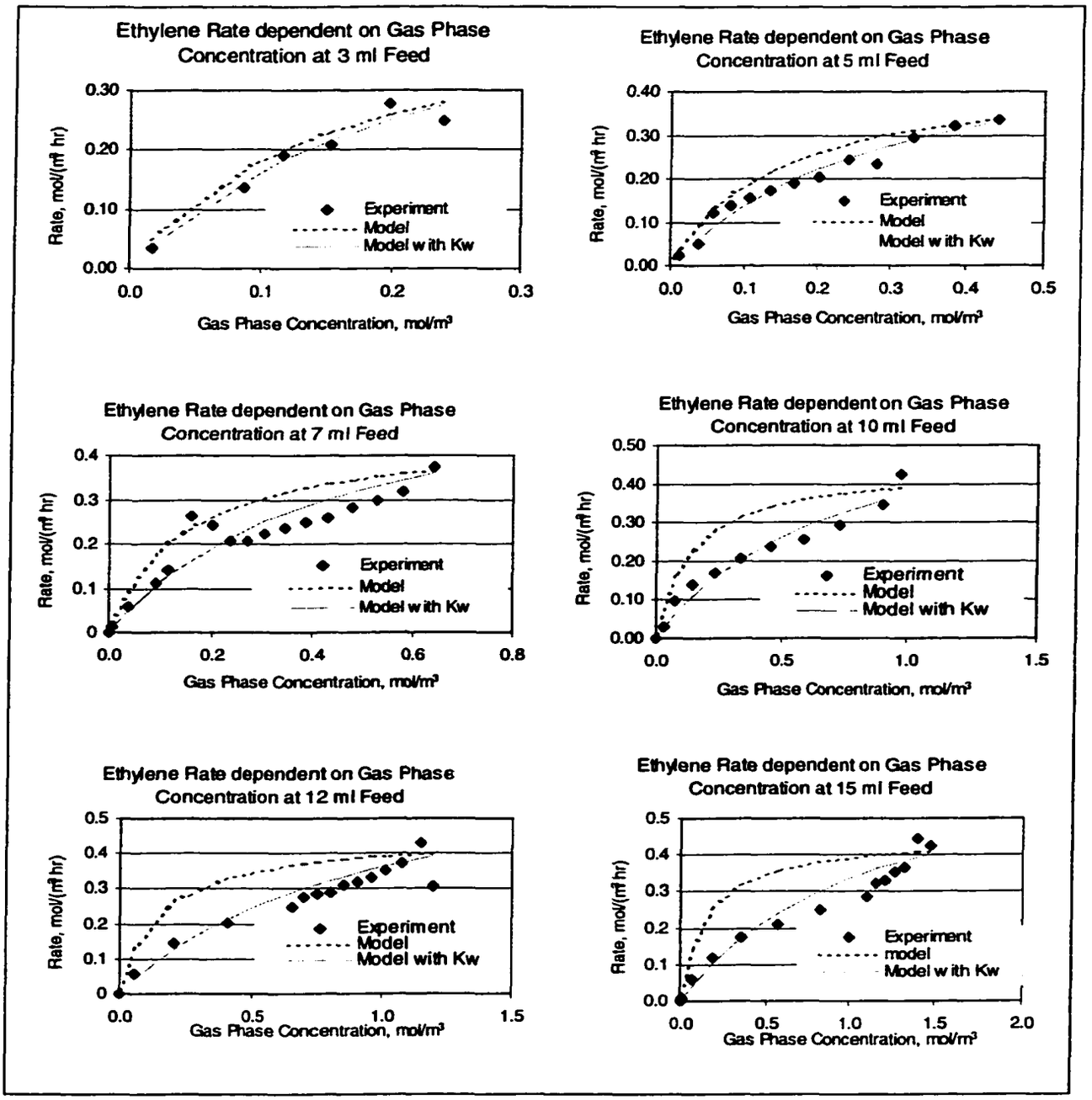

Figure 4-135 Experimental rates and Langmuir-Hinshelwood rate models (used rate parameters are listed in Table 4-28 and Table 4-29) for each individual ethylene oxidation test over Degussa P25 at higher initial concentrations

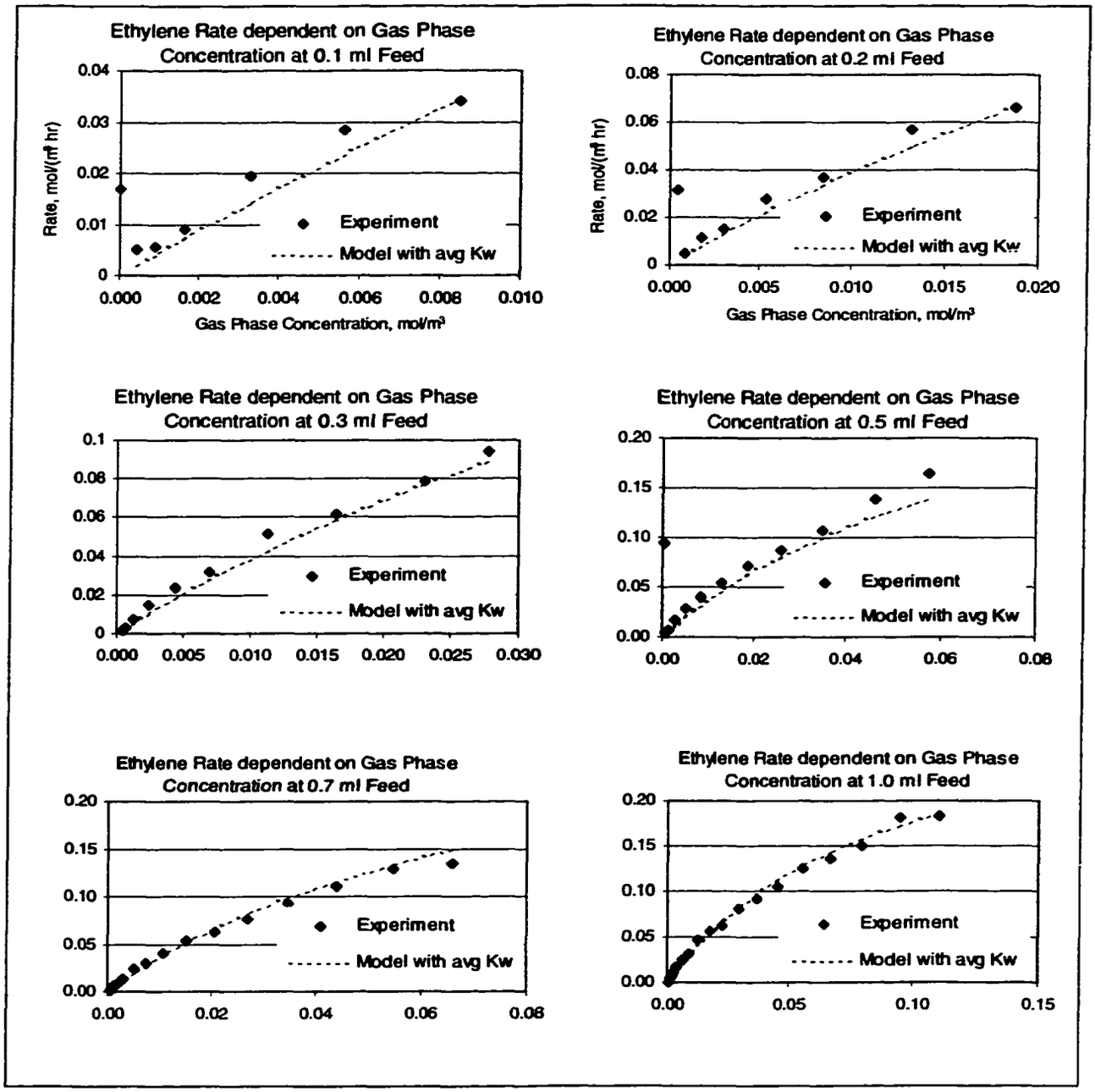

Figure 4-136 Comparison of Langmuir-Hinshelwood rate models (using the average Kw = 1.25 m^3/mol) with experimental rates for each individual ethylene oxidation test over Aerogel T36 at lower initial concentrations

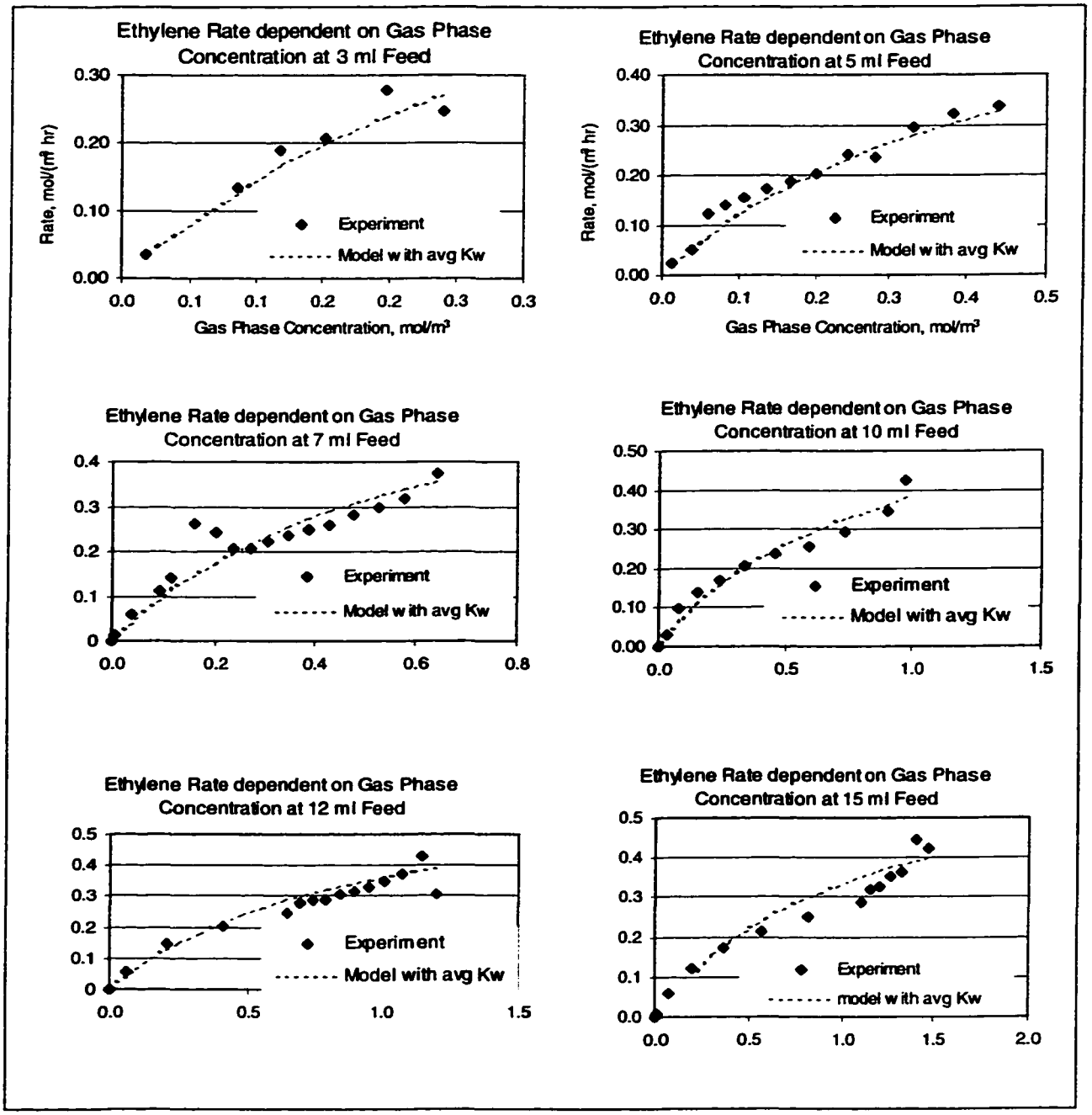

Figure 4-137 Comparison of Langmuir-Hinshelwood rate models (using the average Kw = 1.25 m^3/mol) with experimental rates for each individual ethylene oxidation test over aerogel T36 at higher initial concentrations

4.6.4.4 Thermal-Treated Aerogel T36_450

In Chapter 2.4.2 was discussed that anatase is the crystal form of TiO_2 catalyst with the highest activity. One possible way to increase the activity of the aerogel form of TiO_2 would be to increase its anatase crystallinity, for example through thermal treatment. The ultra-low density aerogel T36 was heat treated to 450°C, which did also increase the percentage of anatase as shown in Section 4.2.6. It was now of interest to find out if this thermal treatment of the aerogel T36 would in fact lead to an increase in photocatalytic activity. The same experimental procedure as described for P25 was applied in order to test the heat-treated T36, denoted by T36_450. The catalytic cell was loaded with 1.3 g of aerogel, thus occupying 40.2 cm^2 of the cell window area. Figure 4-138 shows the result for the oxidation at 7 ml ethylene feed to the reactor. All other tests with different initial concentrations showed a very similar behavior (see Appendix). However, it needs to be kept in mind that almost twice as much catalyst powder (1.3 g) was in the reactor cell compared to the untreated T36 (0.75 g). Since the density of T36_450 had increased during the thermal treatment from 0.13 to 0.27 g/cm^3 (see Section 4.3.1) more mass was needed in order to fill the catalytic cell. Thus, when comparing the rates on a mass basis, the heat-treated aerogel did not exceed the performance of the untreated material as was initially indicated by the decrease in concentration as seen in Figure 4-138. The determined reaction rate constants summarized in Table 4-30 (and Figure 4-139 shows a satisfactory agreement of the model with experimental data) confirmed this finding showing a rate constant on a mass basis with $k_{T36\_450} = 0.472$ mol/m^3 hr g-cat for T36_450, which was about 20% smaller than the rate constant for the raw material T36 with $k_{T36\_raw} = 0.593$ mol/m^3. Therefore, only the higher amount of catalyst in the reactor

system led consequently to a faster oxidation of ethylene in the reactor system. But when normalizing the initial rates to one gram of catalyst it shows that the untreated T36 had still a higher activity as is also illustrated in Figure 4-140. In contrast, when comparing the efficiency of both catalysts based on illuminated cell window area the heat-treated material with $k_{T36\_450} = 0.015$ mol/m^3 hr cm^2 showed an improvement by almost 40% compared to $k_{T36\_raw} = 0.011$ mol/m^3 hr cm^2. This difference in reactivity is also displayed in Figure 4-141 showing higher initial rates based on illuminated cell window area for the T36_450. The increased activity resulted from two effects of the heat-treatment. First, more of the catalyst volume per illuminated cell window area was accessible to UV light since the UV light could penetrate about 40% deeper into the catalyst bed of the T36_450 compared to the untreated T36. (see Chapter 0 UV Transparency). Therefore more of the catalyst material in the reactor cell was available for UV activation. Secondly, the anatase crystallinity increased by a factor of seven. This increase in activity is again illustrated in Figure 4-142. Even though the surface area did greatly decrease due to the high temperature exposure from 336 m^2/g down to 94.2 m^2/g the activity of the catalyst surface illuminated by the UV of the heat-treated aerogel turned out to be two times higher than before exposing the catalyst to 450°C (Figure 4-142). That would indicate that despite the 73% loss in surface area either the number of active sites on the TiO_2 or the intrinsic activity per site had increased significantly. This confirmed that – as expected - increasing the anatase crystalline did increase the photocatalytic activity.

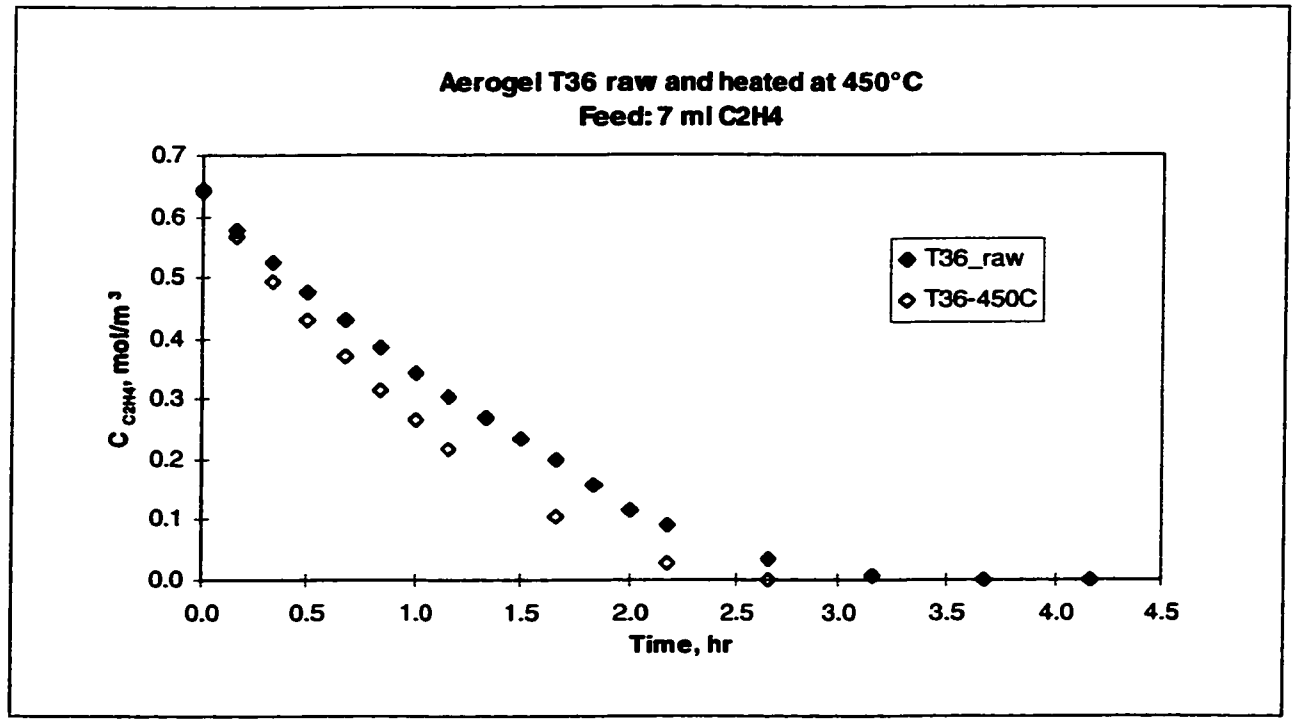

Figure 4-138 Ethylene oxidation over untreated T36 and T36 heat-treated to 450°C

Rate Constants $k_{x\ ethylene}$	T36_450 max. R^2	T36_raw max. R^2
k mass, mol/(m^3 hr g-cat)	0.505	0.593
k ill. Cell window area, mol/(m^3 hr cm^2-cat)	0.0163	0.011
k ill. cat-Volume, mol/(m^3 hr cm^3-cat)	6.27	5.942
k ill. cat-SA, mol/(m^3 hr m^2-cat)	0.16	0.075
Ethylene Adsorption Constant K, m^3/mol	4.183	7.330

Table 4-30 Rate parameters for ethylene oxidation over the ultra-low-density aerogel T36 thermal treated to 450°C

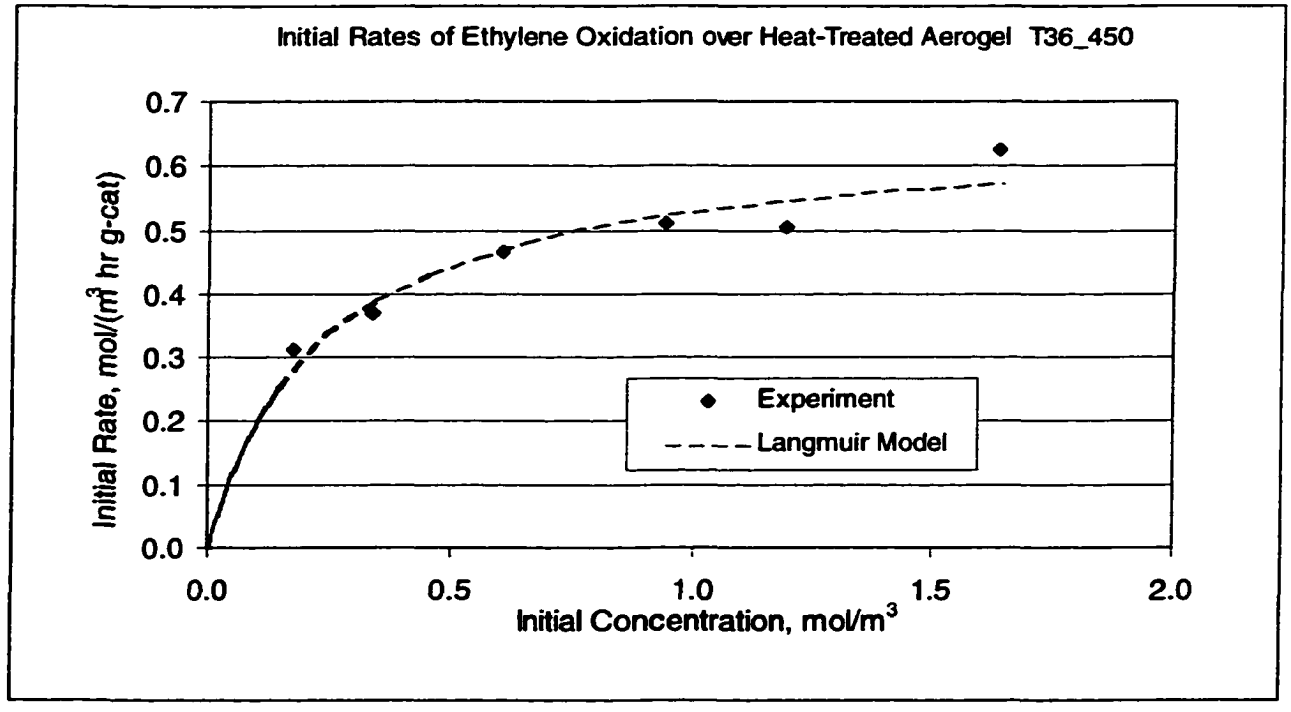

Figure 4-139 Initial rate data and Langmuir-Hinshelwood model of ethylene oxidation over the heat-treated aerogel T36_450

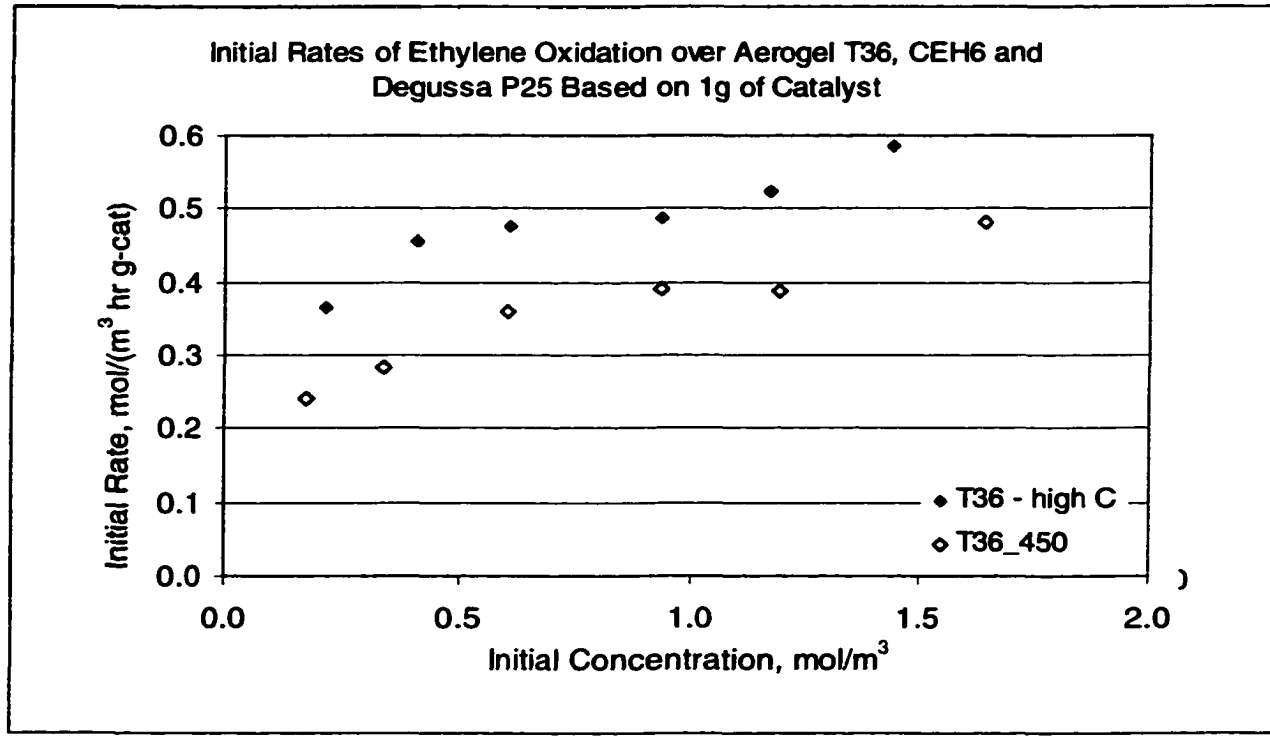

Figure 4-140 Comparison of initial ethylene oxidation rates (based on mass) over T36 untreated and thermal treated to 450°C.

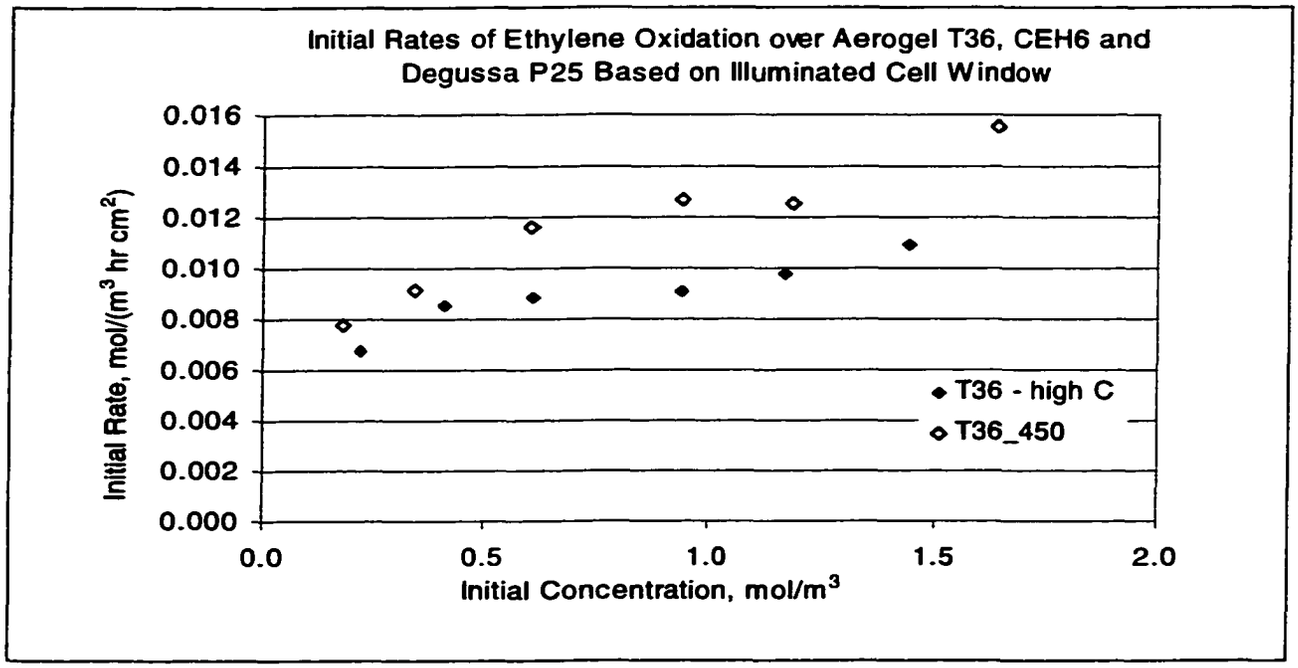

Figure 4-141 Comparison of initial ethylene oxidation rates (based illuminated cell window area) over T36 untreated and thermal treated to 450°C.

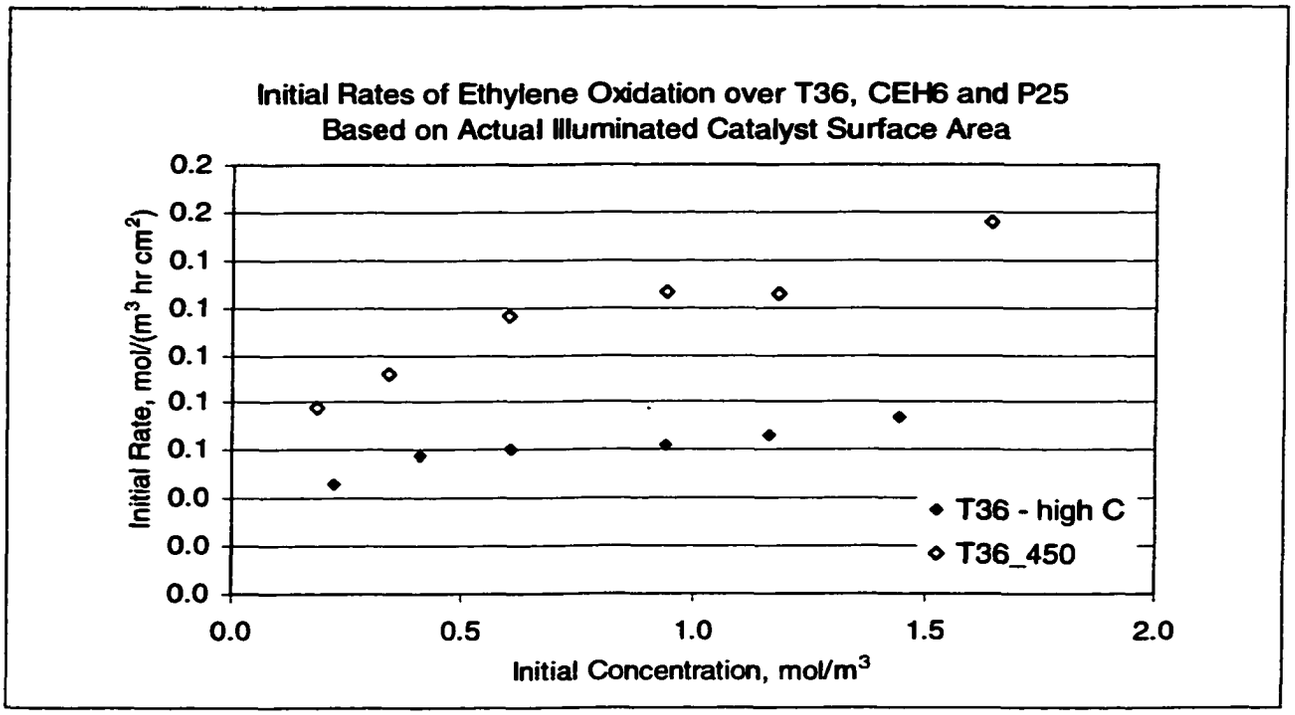

Figure 4-142 Comparison of initial ethylene oxidation rates (based actual illuminated catalyst surface area) over T36 untreated and thermal treated to 450°C.

The rate constant and adsorption constant determined from maximizing R^2 was then used to predict the rates for each individual experimental run. A comparison of the experimental rate data with the predicted Langmuir-Hinshelwood rates (ignoring the water term $K_{H2O}*C_{H2O}$, where K_{H2O} stands for the adsorption constant of water and C_{H2O} for the concentration of water) is shown in Figure 4-143. Only at low initial concentrations did the model fit well with the actual data indicating that generated water or water still adsorbed on the catalyst from the atmosphere or from previous oxidation tests did not change the oxidation rate significantly. Again, similarly as observed from tests with P25 and T36, at higher initial feed rates the photocatalytic activity of the catalyst was appreciably lower than predicted, which most likely resulted from the generated water during the ethylene oxidation. In order to account for the water generation, the water adsorption constant was then calculated for each individual experiment in a similar fashion as described before for the Degussa P25. Table 4-31 shows the K_W for each individual run and includes the average value. Only at the lowest ethylene feed of 3 ml was K_W found to be negative indicating that at this concentration any generated water did not have a notable influence on the reaction rate. The reaction rate models including the water term $K_{H2O}*C_{H2O}$ in the Langmuir-Hinshelwood equation are included in Figure 4-143. Figure 4-144 depicts for each individual experimental run the Langmuir-Hinshelwood models calculated using the average $K_W = 2.29\ m^3/mol$, which produced a rate models that fit reasonably well to the experimental data of the individual runs and was used as kinetic parameter for the T36_450 catalyst.

All tests discussed previously were performed under initially dry conditions. The following Chapter 4.6.5, however, will investigate the influence of water on the ethylene photo oxidation under humid conditions.

Feed ml	C_{C2H4} mol/m^3	C_w avg mol/m^3	K_W m^3/mol	R^2 with calcul. Kw
3	0.179	0.3096	0.00	0.9942
5	0.342	0.4538	2.28	0.9972
7	0.605	0.7309	2.62	0.9880
10	0.939	1.1053	2.89	0.9800
12	1.189	1.3961	2.60	0.9639
15	1.642	1.8474	1.07	0.9551
		average K_W --->	2.29	m^3/mol

Table 4-31 Determined water adsorption constants for ethylene oxidation over aerogel T36_450 for each individual experimental run. Included are the values for R^2 of the Langmuir-Hinshelwood models using each individual run (calcul. Kw) and using the average K_w (avg K_w).

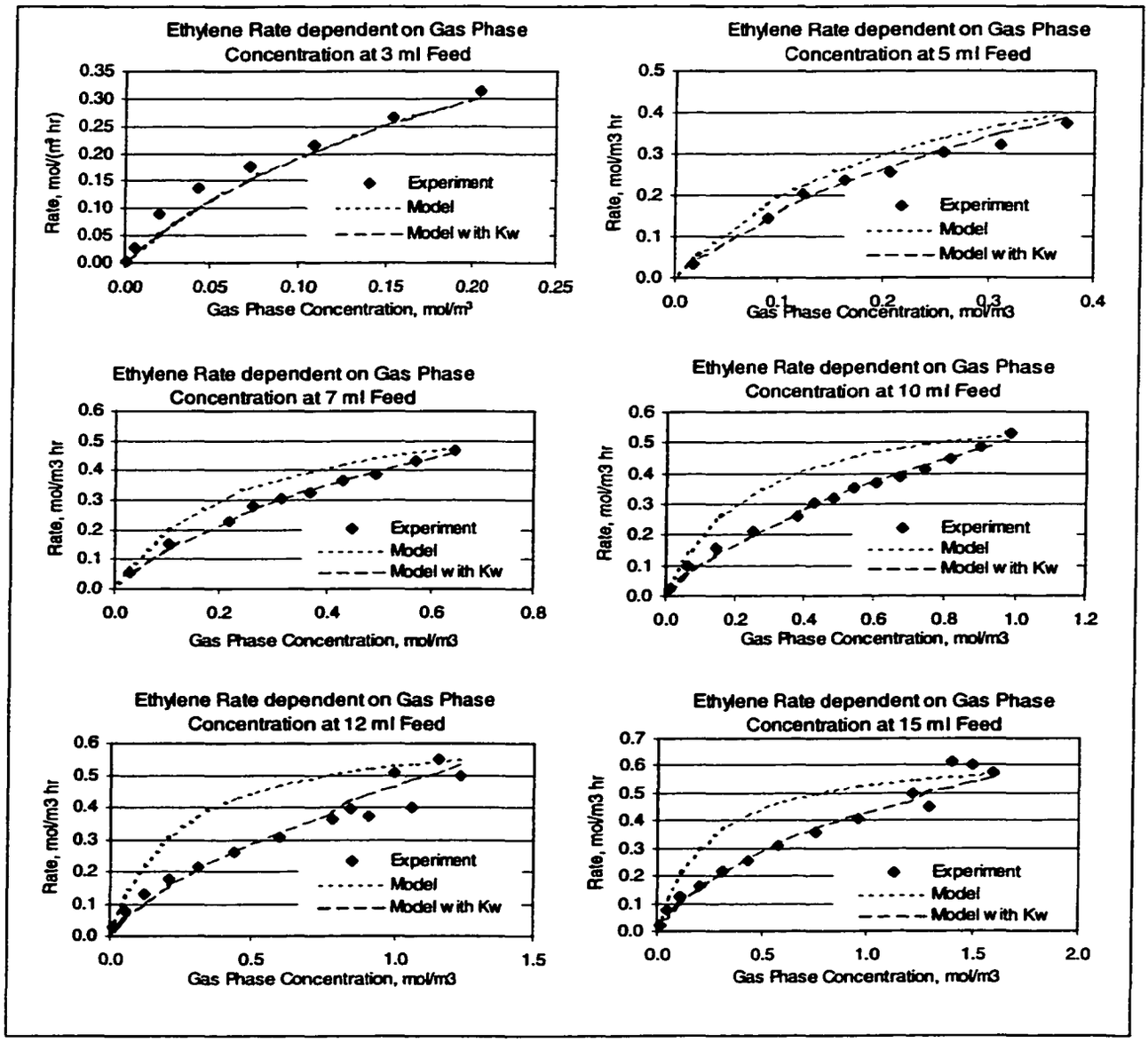

Figure 4-143 Experimental rates and Langmuir-Hinshelwood model rates for each individual ethylene oxidation test over the aerogel T36_450 at higher initial concentrations

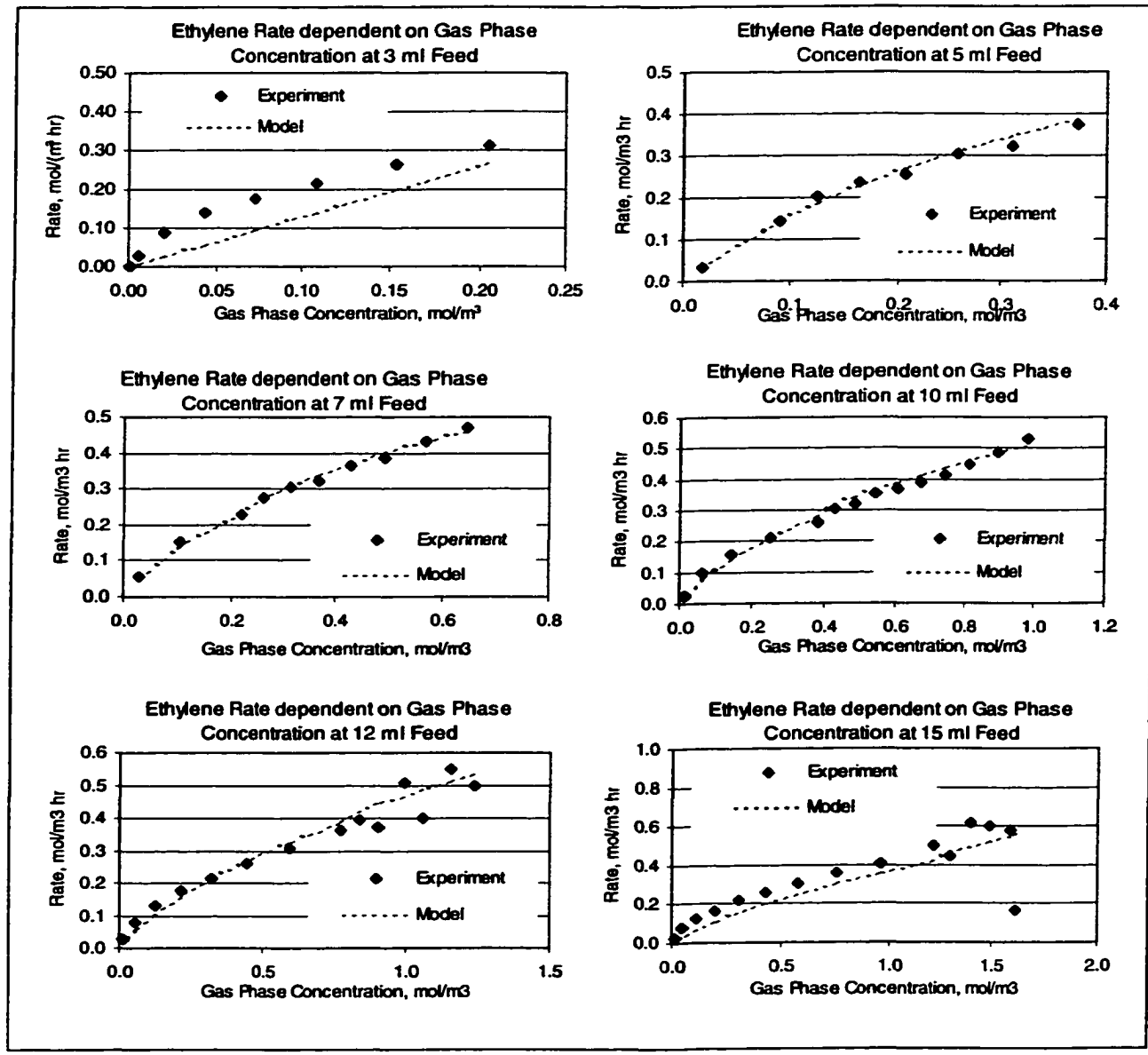

Figure 4-144 Comparison of Langmuir-Hinshelwood rate models calculated using the average $K_W = 2.29\ m^3/mol$ for each individual ethylene oxidation test over thermal treated aerogel T36_450 at higher initial concentrations

4.6.4.5 Low-density aerogel CEH6

The low-density aerogel CEH6 was also investigated regarding its photocatalytic activity for ethylene oxidation. The same procedure was applied as previously described with Degussa P25. The initial rate data for 1.3 g of CEH6 in the reactor system are shown in Figure 4-145.

The reaction kinetic parameters are summarized in Table 4-32. Both evaluation methods (linear regression and maximizing R^2) gave similar results. The reaction rate constants are all lower than that of the ultra-low density aerogel T36 or T36_450 indicating that the low-density aerogel CEH6 possesses a lower photocatalytic activity than the ultra-low-density aerogel T36. Figure 4-146 compares the actual reaction rates at any time throughout the reaction with the predicted data from the Langmuir-Hinshelwood expression. The prediction fits the experimental data reasonable well even without including the term of $K_W * C_W$ in the rate model. Apparently, generated water seemed to have no or only very little effect on the reaction rate.

Rate Constants $k_{x\ ethylene}$	CEH6 lin.Reg.	CEH6 max. R^2
k mass, mol/(m^3 hr g-cat)	0.332	0.347
k ill. Cell window area, mol/(m^3 hr cm^2-cat)	0.017	0.092
k ill. cat-Volume, mol/(m^3 hr cm^3-cat)	5.74	6.00
k ill. cat-SA, mol/(m^3 hr m^2-cat)	0.03	0.03
Ethylene Adsorption Constant K, m^3/mol	2.0	1.8

Table 4-32 Rate parameters for ethylene oxidation over the low-density aerogel CEH6

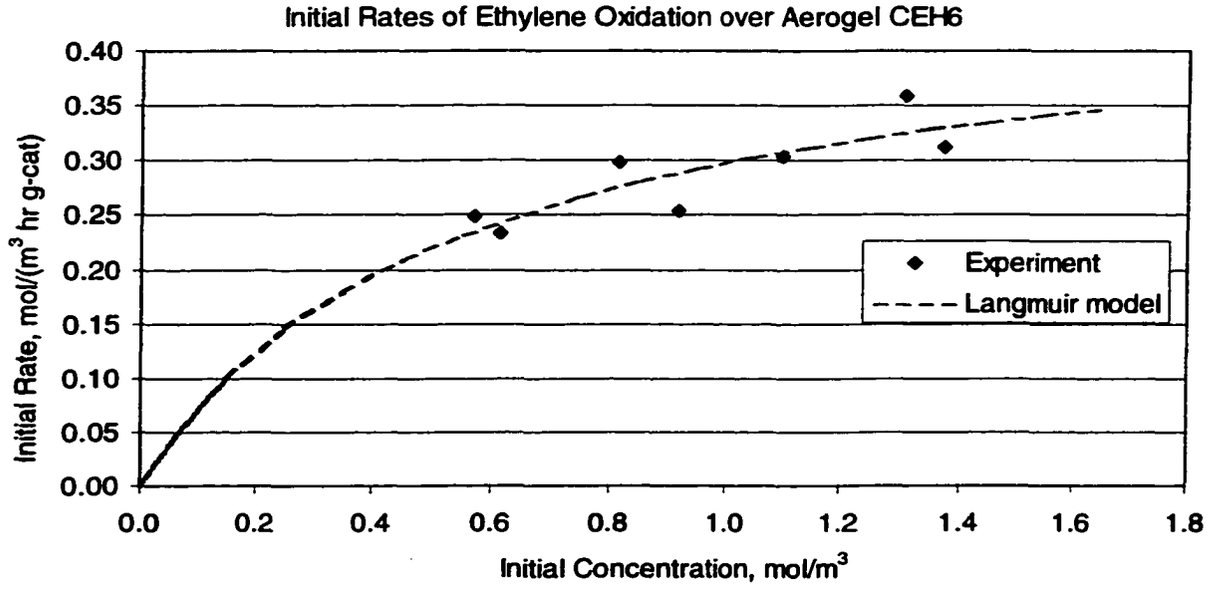

Figure 4-145 Initial rates of ethylene oxidation over the aerogel CEH6 and the Langmuir-Hinshelwood model

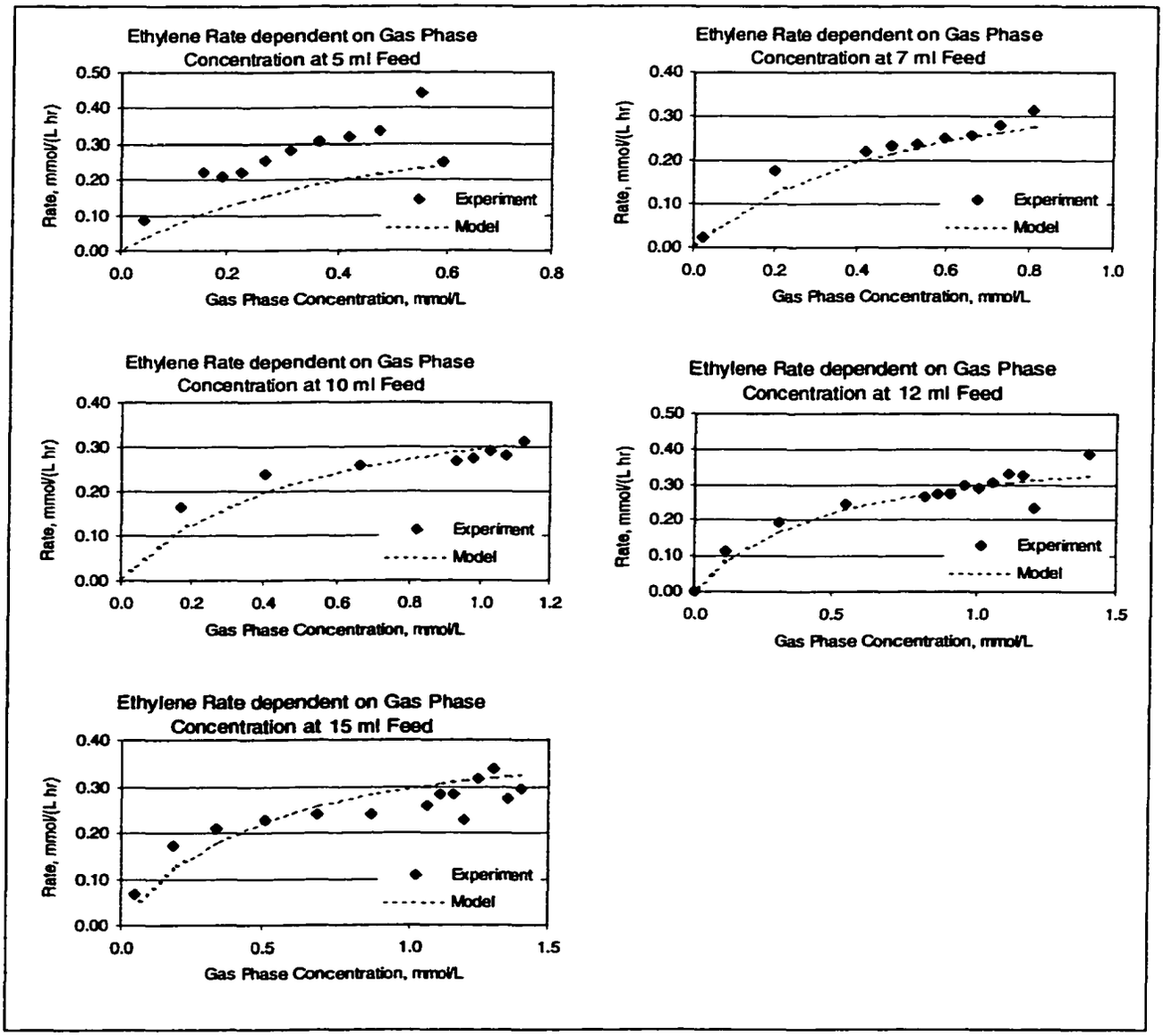

Figure 4-146 Comparison of initial ethylene oxidation rates (based on mass) over the low-density aerogel CEH6

4.6.4.6 Comparison of Catalysts

The performance of the aerogels is compared to Degussa P25 in Figure 4-147, Figure 4-148, Figure 4-149, and Figure 4-150, which depicts the initial oxidation rates based on mass, based on illuminated cell window area, based on actual illuminated catalyst surface area, and based on UV accessible catalyst volume, respectively. Clearly, when

comparing on a mass basis the ultra-low-density aerogel T36 showed the best performance of all tested catalysts. However, when comparing the activity on how much cell window area was occupied by the catalyst and exposed to UV light then the difference in performance was not as significant (Figure 4-148). The heat-treated T36_450 appeared to have only a slightly higher rate than the Degussa P25. A striking difference in catalyst performance was observed when looking at the efficiency of the catalyst based on UV accessible catalyst volume and surface area (Figure 4-150, and Figure 4-149). Clearly, the Degussa P25 has a remarkably higher intrinsic activity per activated surface area compared to all aerogels. Nevertheless, it had been shown with the T36 sample that there is a potential to enhance the activity of the aerogel sites.

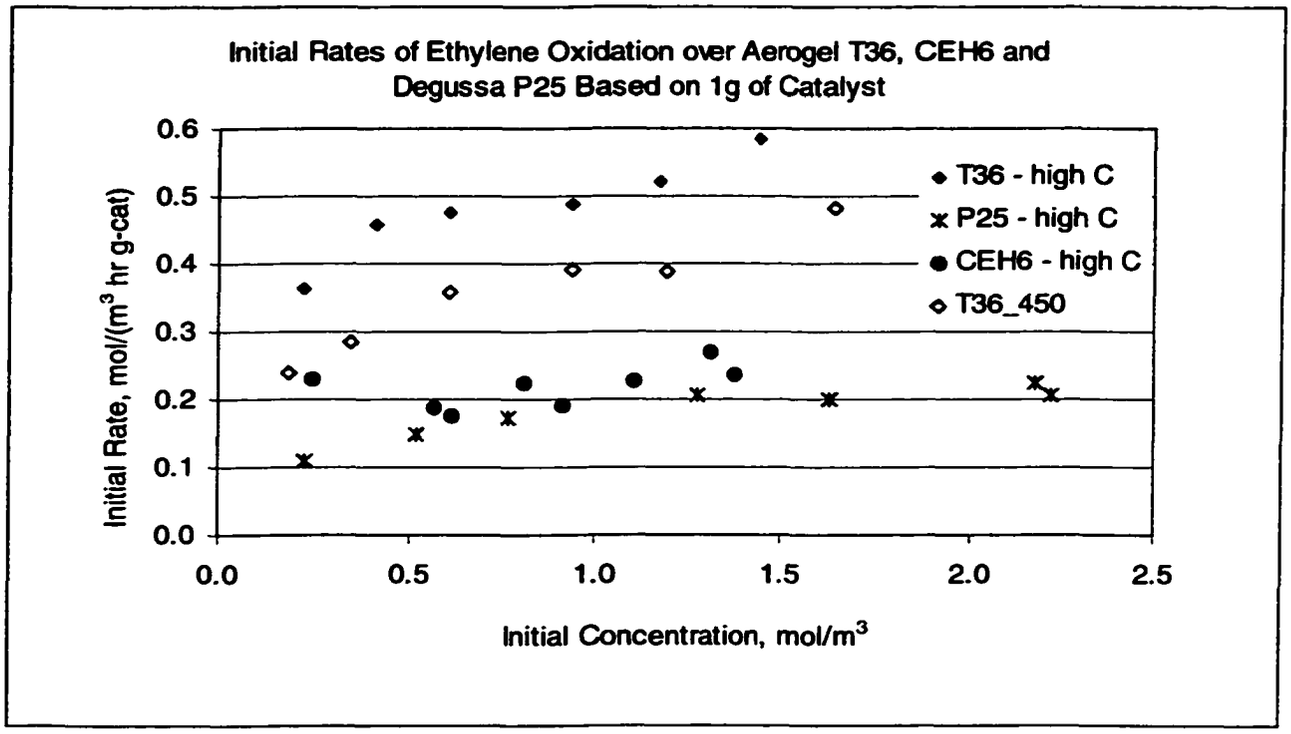

Figure 4-147 Comparison of initial ethylene oxidation rates (based on mass) over T36 untreated and thermal treated to 450°C, the aerogel CEH6, and the Degussa P25.

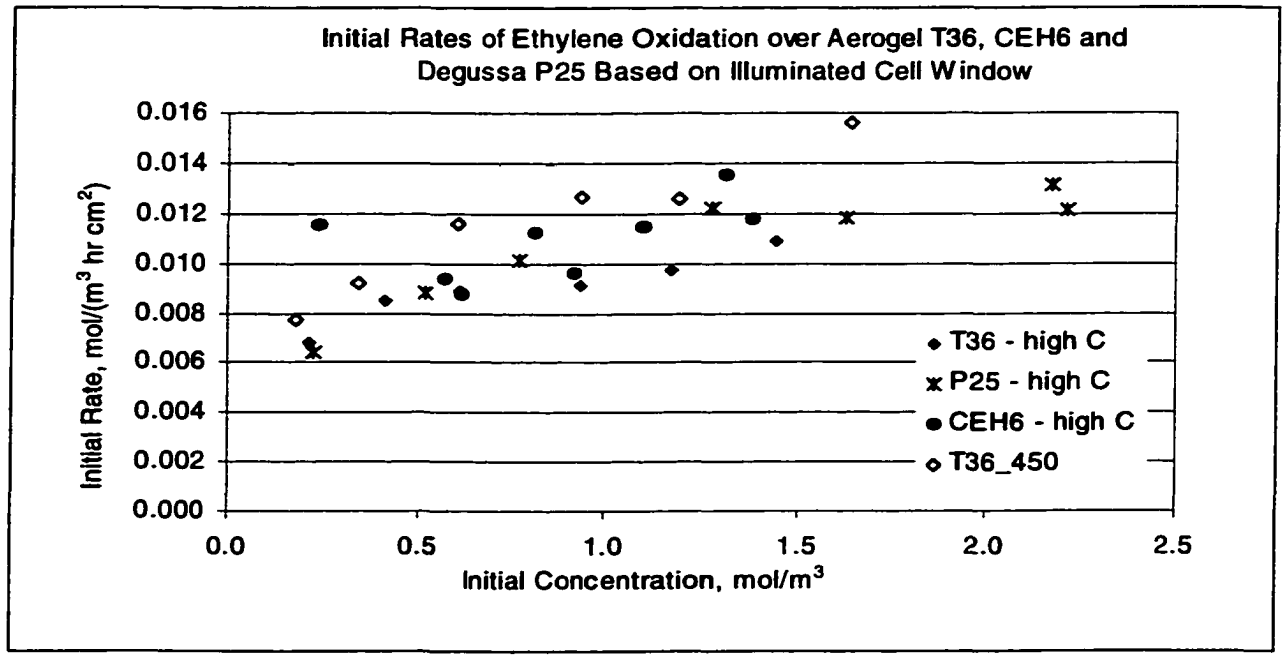

Figure 4-148 Comparison of initial ethylene oxidation rates (based illuminated cell window area) over T36 untreated and thermal treated to 450°C, the aerogel CEH6, and the Degussa P25.

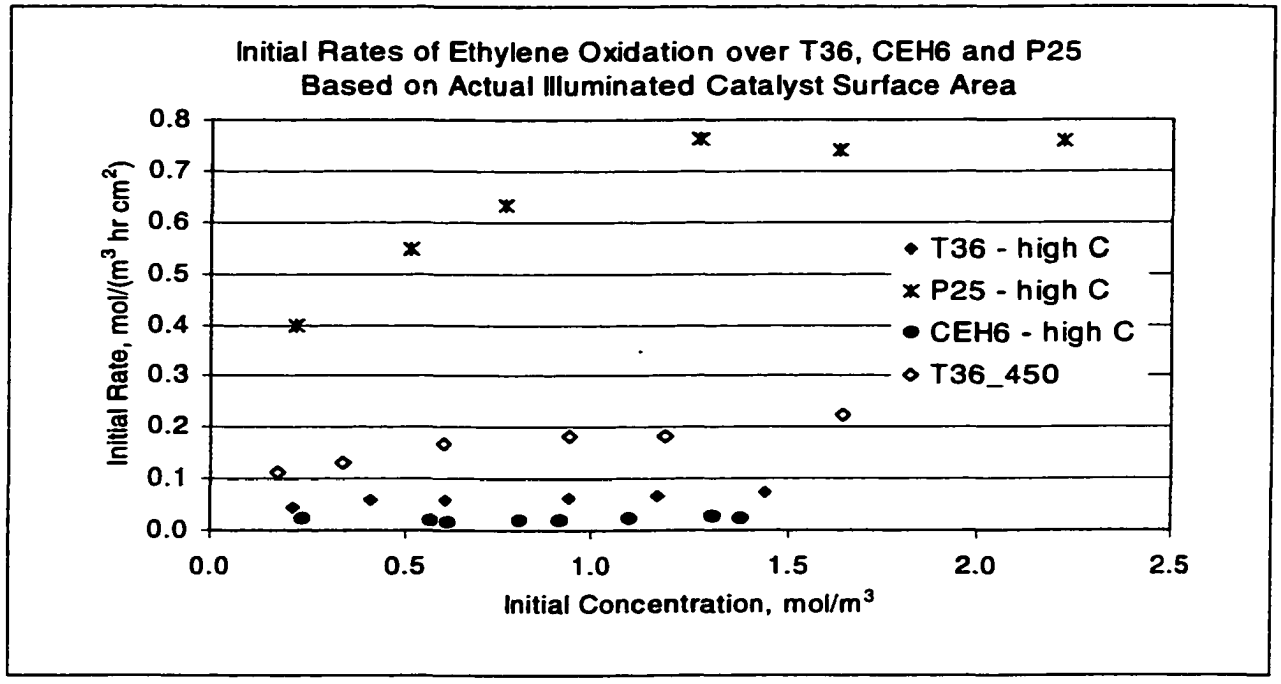

Figure 4-149 Comparison of initial ethylene oxidation rates (based actual illuminated catalyst surface area) over T36 untreated and thermal treated to 450°C, the aerogel CEH6, and the Degussa P25.

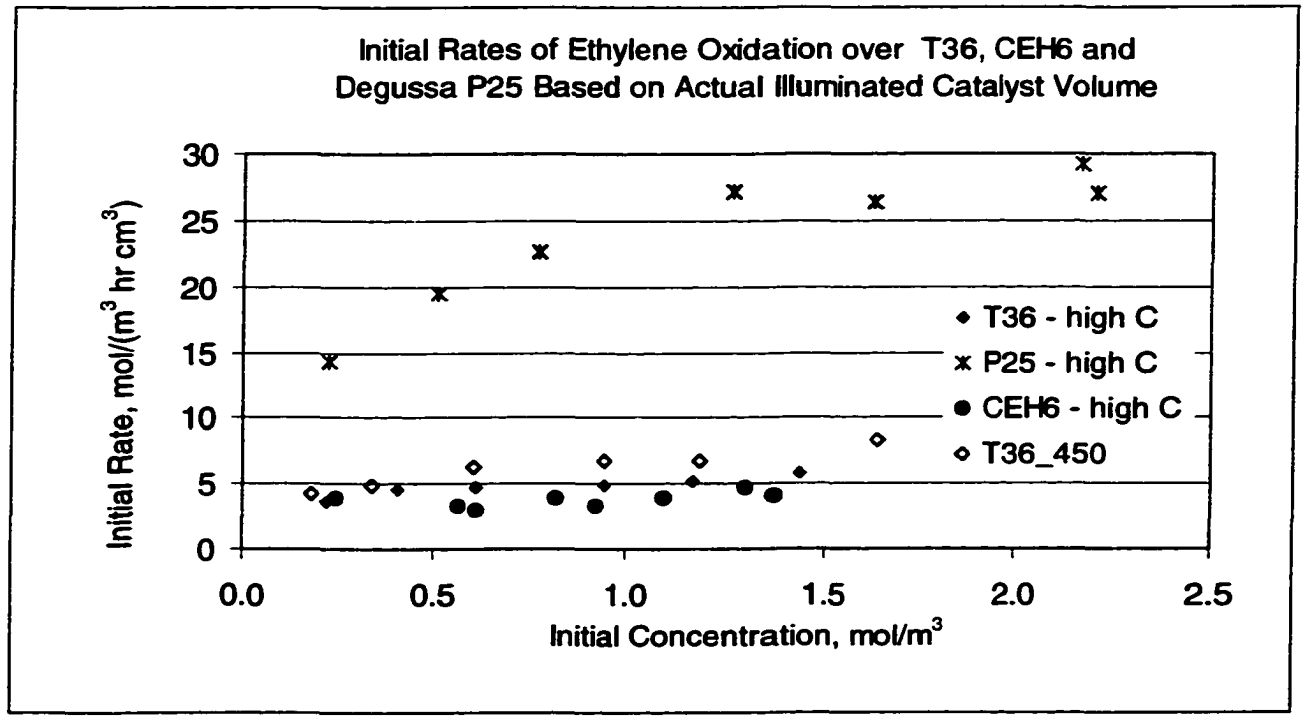

Figure 4-150 Comparison of initial ethylene oxidation rates (based actual illuminated catalyst volume) over T36 untreated and thermal treated to 450°C, the aerogel CEH6, and the Degussa P25.

4.6.5 Ethylene Photocatalytic Oxidation under Humid Conditions

Ethylene photo-oxidations test under humid conditions were performed with Degussa P25, the aerogel T36, and the thermal treated aerogel T36_450. The experimental procedure as described in Sections 3.5 and 3.6.2 was applied to perform the experiments.

4.6.5.1 Degussa P25_RH

The individual oxidation test results under humid conditions (change in concentration with time) over Degussa P25 (2.2 g) are summarized in the Appendix and is shown for one representative graph at 12 ml ethylene feed and 40% relative humidity in Figure 4-151. Data related to tests under humid conditions were labeled as P25_RH (RH = relative humidity). At all other individual initial ethylene concentrations the result

was essentially the same, showing that the ethylene oxidation was slower for the tests that had already water present at initial conditions. Thus, as concluded already from the pervious experiments without added water, water showed to have a negative impact on ethylene oxidation under these specific reaction conditions of relative humidities from 40 to 50% and initial ethylene concentrations ranging between 0.16 and 1.4 mol/m^3. The decrease in activity is again illustrated in Figure 4-152 showing lower initial rates for the tests under humid conditions.

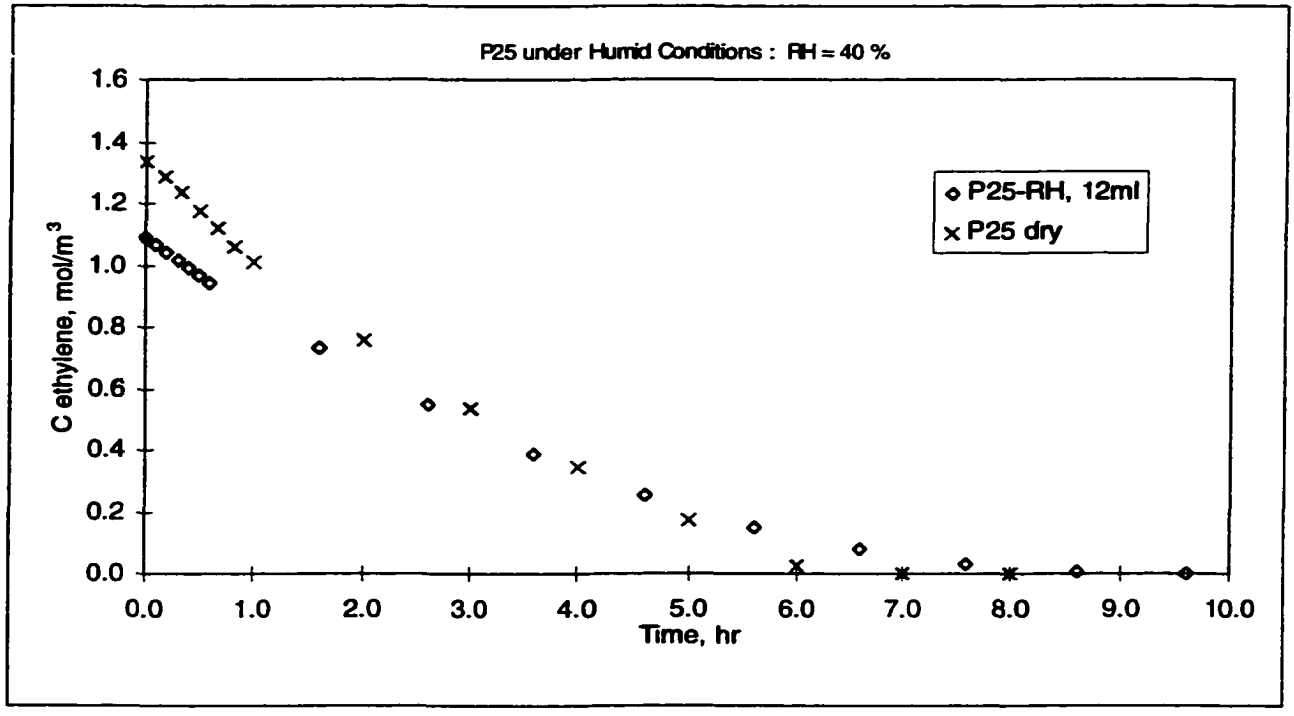

Figure 4-151 Ethylene photo-oxidation over Degussa P25 under humid conditions compared to the oxidation under initial dry conditions at 12ml ethylene feed

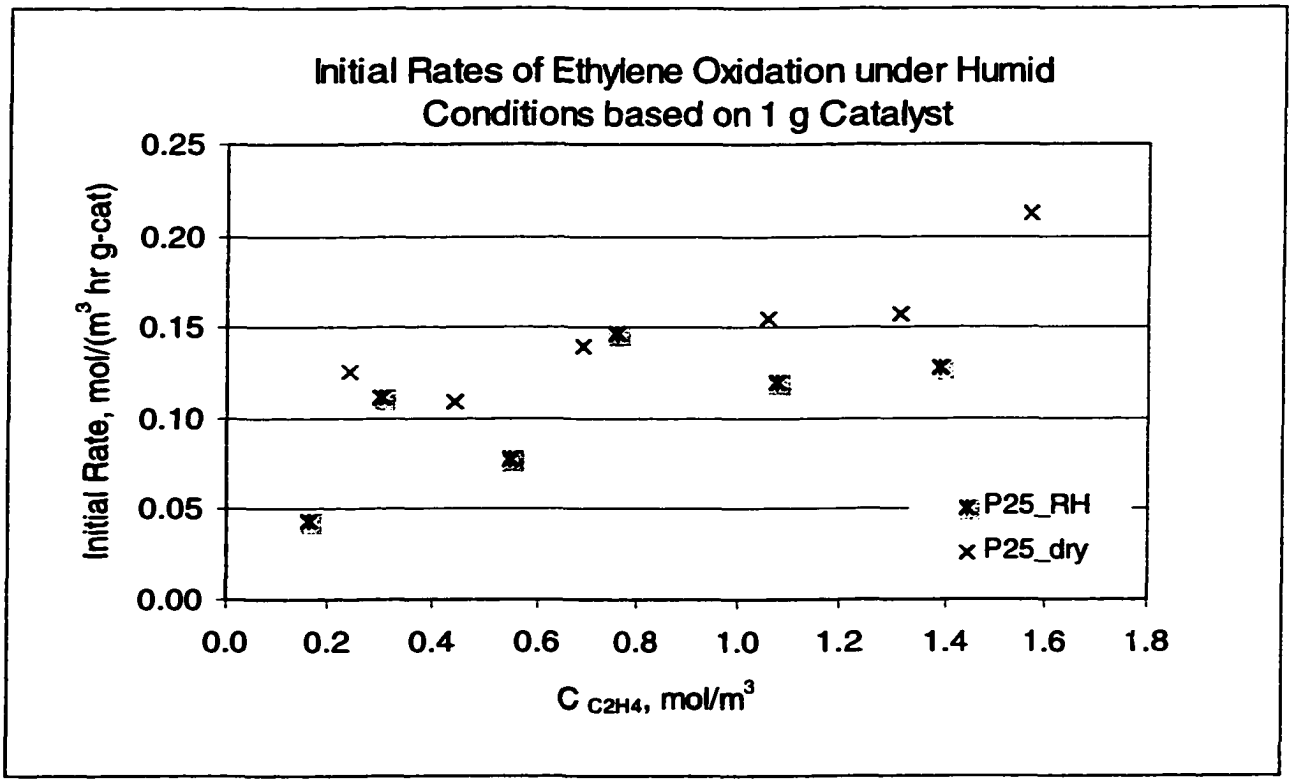

Figure 4-152 Initial rates of ethylene oxidation based on one gram of Degussa P25 under initial dry (P25_dry) and initial humid (P25_RH) conditions

An attempt was made to determine the reaction rate parameters according to the following procedure. First, the Langmuir-Hinshelwood model was calculated using all rate parameters (k_E, K_E, and K_W) determined from experiments under initial dry conditions and compared to the experimental data. This is illustrated in Figure 4-153 and shows that the so predicted rates were slightly higher than the actual data. This can be explained from the fact that the water concentration was determined under the assumption that water adsorbed similarly strong as acetone (see Section 4.6.4.2). This might have resulted in estimated water concentrations that were too high. Since the assumed water gas phase concentration for the model calculations was higher, the value of the calculated adsorption constant was therefore found to be lower than would have

been predicted at lower water gas phase concentrations (looking at the denominator term $C_W K_W$). Therefore, a K_W being too small in the Langmuir-Hinselwood expression resulted in a rate overprediction.

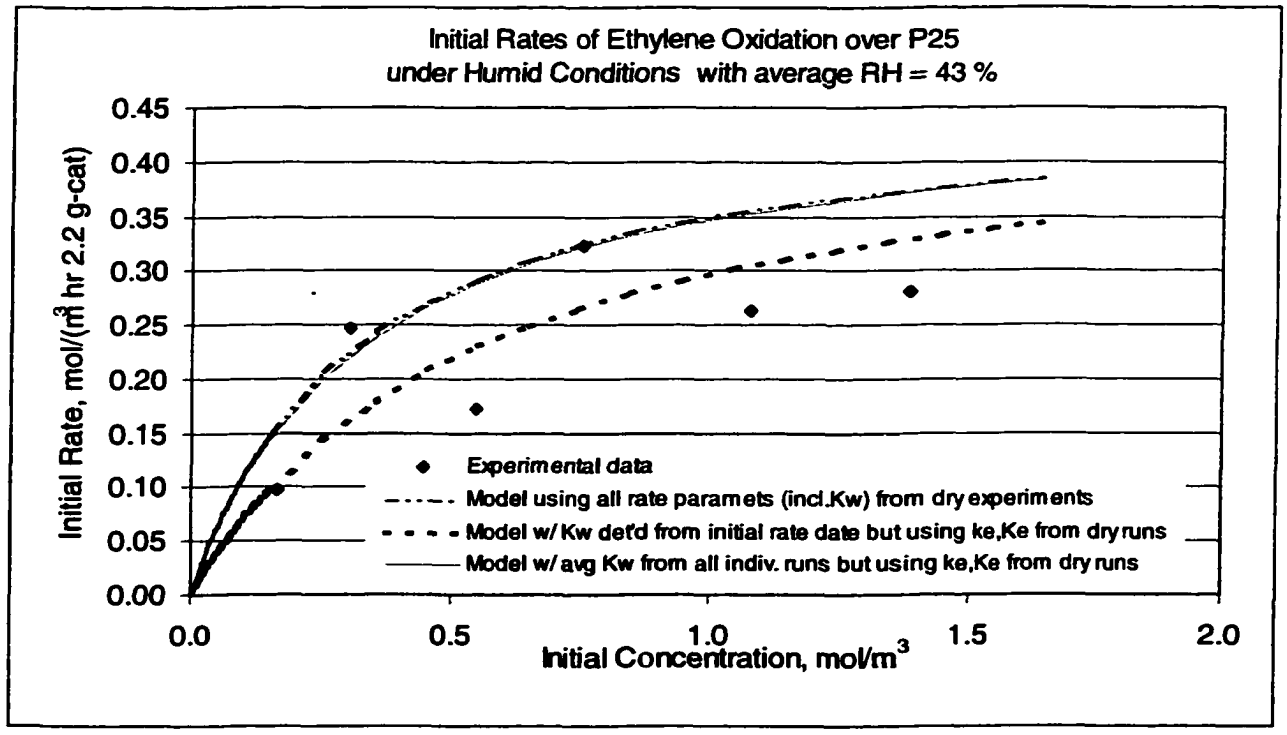

Figure 4-153 Initial rate data over Degussa P25 under humid conditions and Langmuir-Hinshelwood models using different rate parameters.

To find a K_W closer to the actual value the following calculation was performed. Using the values of k_E^{dry} and K_E^{dry} that were determined from tests under initial dry conditions the water adsorption constant K_W^{RH} was determined from equation (4-27) by maximizing R^2 over the initial rate data.

$$(4\text{-}27) \quad -r_E = \frac{k_E^{dry} K_E^{dry} Co_E^{RH}}{1 + K_E^{dry} Co_E^{RH} + K_W^{RH} Co_W^{RH}}$$

Co_E and Co_W stand for the initial gas phase concentrations of ethylene and water, respectively. The initial water concentration in the system was determined from the measured relative humidity values, RH (see equation (4-28)).

$$\textbf{(4-28)}\quad RH = \frac{P'_{H_2O}}{P^*_{H_2O}},$$

where P'_{H2O} represents the actual water partial pressure in the system and P^*_{H2O} the water vapor pressure at any given temperature. The saturation water vapor pressure was determined from the Antoine equation (4-29)[130]

$$\textbf{(4-29)}\quad \log_{10} P^*_{H_2O} = A - \frac{B}{T + C}$$

with A, B, and C are dimensionless constants[130], P^*_{H2O} in mmHg and the temperature, T, in °C.

The concentration of water was then estimated from (4-31) which was derived from the Ideal Gas Law[130] (4-30)

(4-30) P V = n R T,

where P, V, n, and T stand for system pressure, volume, and temperature, respectively and R is the gas constant.

$$\textbf{(4-31)}\quad C_W = \frac{n}{V} = \frac{P'_{H_2O}}{RT}$$

The initial experimental conditions of each run are summarized in Table 4-33. The last column of this table contains data for K_W of each individual run which will be

discussed later in this chapter. Table 4-34 holds the data for the rate constants and the water adsorption constants K_W obtained from two evaluation procedures. Note again that the ethylene adsorption constant K_E was not determined from this set of data, the values of k_E^{dry} and K_E^{dry} determined from experiments under initial dry conditions were rather utilized to find the water adsorption constant related to this set of experiments under humid conditions. The value for the water adsorption constant found from initial rate data with $K_W = 2.12$ m^3/mol was by a factor of five higher compared to the one from initial dry conditions but provided nevertheless a Langmuir-Hinshelwood model that agreed with the experimental initial rate data as seen in Figure 4-153.

Ethylene Feed, ml	Temp, °C	RH, %	log10(P*)	P^*_{H2O}, mmHg	P'_{H2O} mmHg	Co_W, mol/m^3	Kw m^3/mol
3	22.80	43	1.32	20.81	9.01	0.49	0.77
5	23.20	40	1.33	21.32	8.53	0.46	0.16
7	23.20	47	1.33	21.32	10.11	0.55	0.65
10	22.90	42	1.32	20.94	8.71	0.47	0.15
12	22.90	41	1.32	20.94	8.49	0.46	0.59
15	22.80	63	1.32	20.81	13.21	0.72	0.54
	average RH =	43	%		average C_W, K_W =	0.49	**0.54**

Table 4-33 Experimental initial conditions of ethylene oxidation over P25 under humid conditions. The calculated values of the water adsorption constant K_W for each individual run are included in the last column.

Ethylene rate constant from tests at initial dry conditions, k_E		0.458	mol/(m^3 hr)
Ethylene adsorption constant from tests at initial dry conditions, K_E		3.72	m^3/mol
Average Kw from individual tests at initial dry conditions		0.60	m^3/mol
Kw from initial rate data at initial humid conditions	K_{W1} new-->	2.12	m^3/mol
Average Kw from individual tests at initial humid conditions	K_{W2} new-->	0.54	m^3/mol

Table 4-34 Rate constants and water adsorption constants determined from two evaluation procedures for ethylene oxidation under humid conditions over P25

The water adsorption constants were also determined for each individual experiment of different initial ethylene concentration using the method of maximizing R^2 of the Langmuir-Hinshelwood model over the experimental data as was described for P25 under initial dry conditions in Section 4.6.4.2. The water gas phase concentration C_W was also determined as outlined in Section 4.6.4.2. First, the total amount of water in the system at any point in time was estimated by using the injected amount of water (0.025 ml) and adding the amount of water generated from the ethylene oxidation. Then, C_W, the water gas phase concentration, was determined at any point in time in the reactor system from equation (4-25), followed by solving for K_W using the rate expression (4-27). The so obtained values for K_W^{RH} of each experimental run are tabulated in Table 4-33 (last column). The average of the K_W values with $K_W = 0.54$ m^3/mol was close to the value found from the experiments under initial dry conditions (0.60 m^3/mol), thus confirming the validity of the evaluated kinetic parameter. The higher value of K_W determined from the initial rate data is probably due to the fact that the initial water concentration was eventually much higher than determined from relative humidity measurements.

The Langmuir-Hinshelwood models for each individual run using these data are illustrated in Figure 4-154 and show a good agreement with the experimental data in most of the cases (dotted lines). The dashed lines represent the Langmuir-Hinshelwood models using all parameters determined from experiments under initial dry conditions (including the value of K_W, which also led to rate predictions that were close to the experimental the experimental data. Therefore, the value of 0.54 m^3/mol for the water adsorption constant

provided models describing the kinetics well and is considered to be the best available kinetic parameter for ethylene oxidation over the Degussa P25 catalyst.

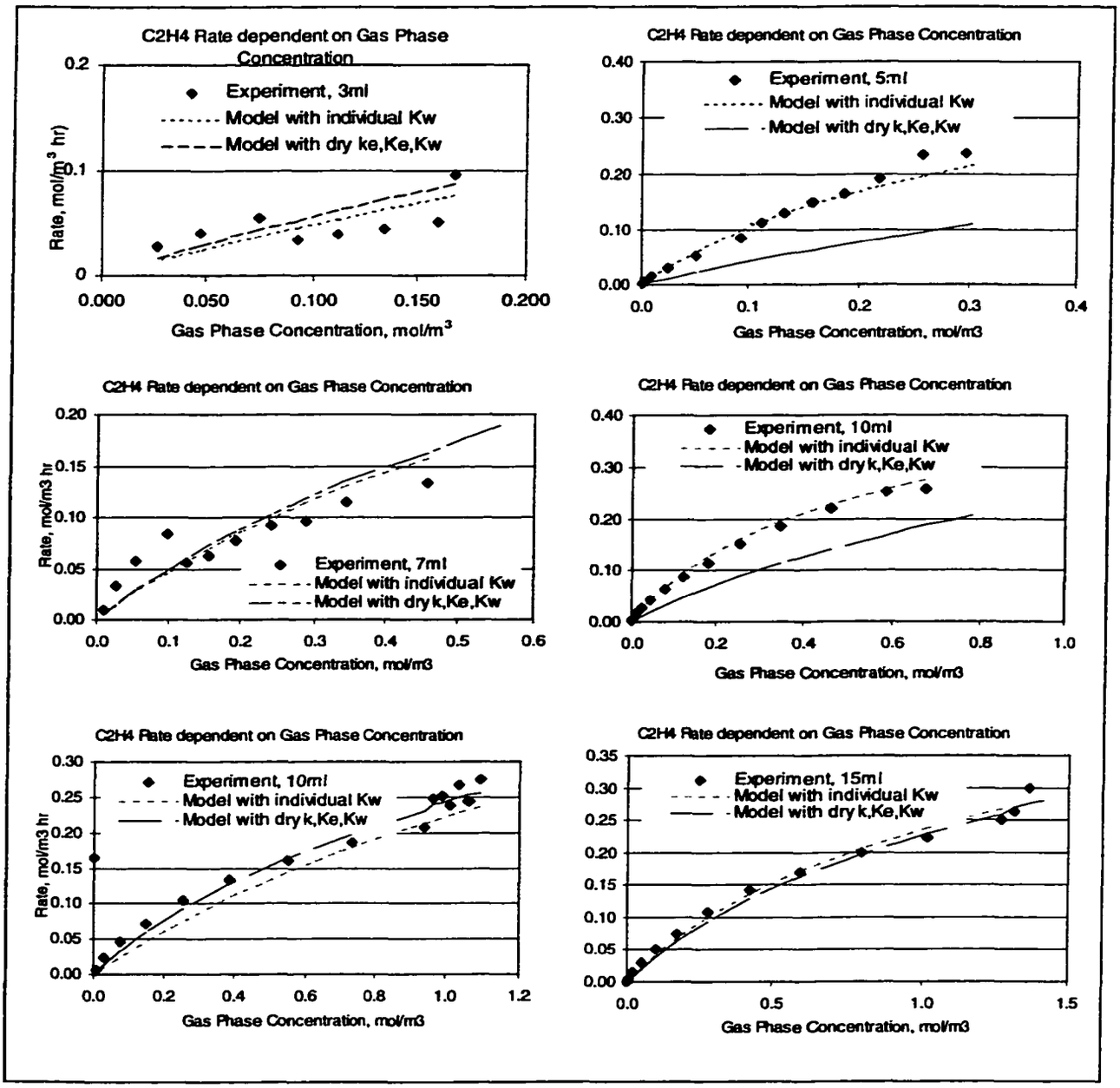

Figure 4-154 Langmuir-Hinshelwood model and experimental data of ethylene oxidation over Degussa P25 at different initial ethylene concentrations. Dotted graphs represent models using the water adsorption constant K_W determined from K_W of each individual run, while dashed lines represent the models using rate parameters (including K_W) from experiments under initial dry conditions.

4.6.5.2 Aerogel T36_RH

The results (change in concentration with time) of one ethylene oxidation test under humid conditions over the aerogel T36 (0.75 g) is shown for one representative graph at 3 ml ethylene feed and 36% relative humidity in Figure 4-155. The data for the individual tests at other initial ethylene feed concentrations are summarized in the Appendix. The data related to tests under humid conditions were denoted as T36_RH while T36_dry stands for the ethylene oxidation tests under initial dry conditions. Even though the same amount of water was introduced into the reactor system the relative humidity in the system varied between 36 and 49% (see Table 4-35). This variation might be due to an inaccuracy of water injection into the system as the amount of DI injected was very small (25 µl). Another possible reason might be that the catalyst had still some water adsorbed on its surface, which was not completely removed after purging of the system. Thus, less water could be adsorbed from the gas phase resulting in a higher water gas phase concentration.

As seen in Figure 4-155, ethylene was oxidized at a lower rate under initial humid conditions than under initial dry conditions. This is again shown by the lower initial oxidation rates for all tests under humid conditions compared to the tests under initial dry conditions as illustrated in Figure 4-156.

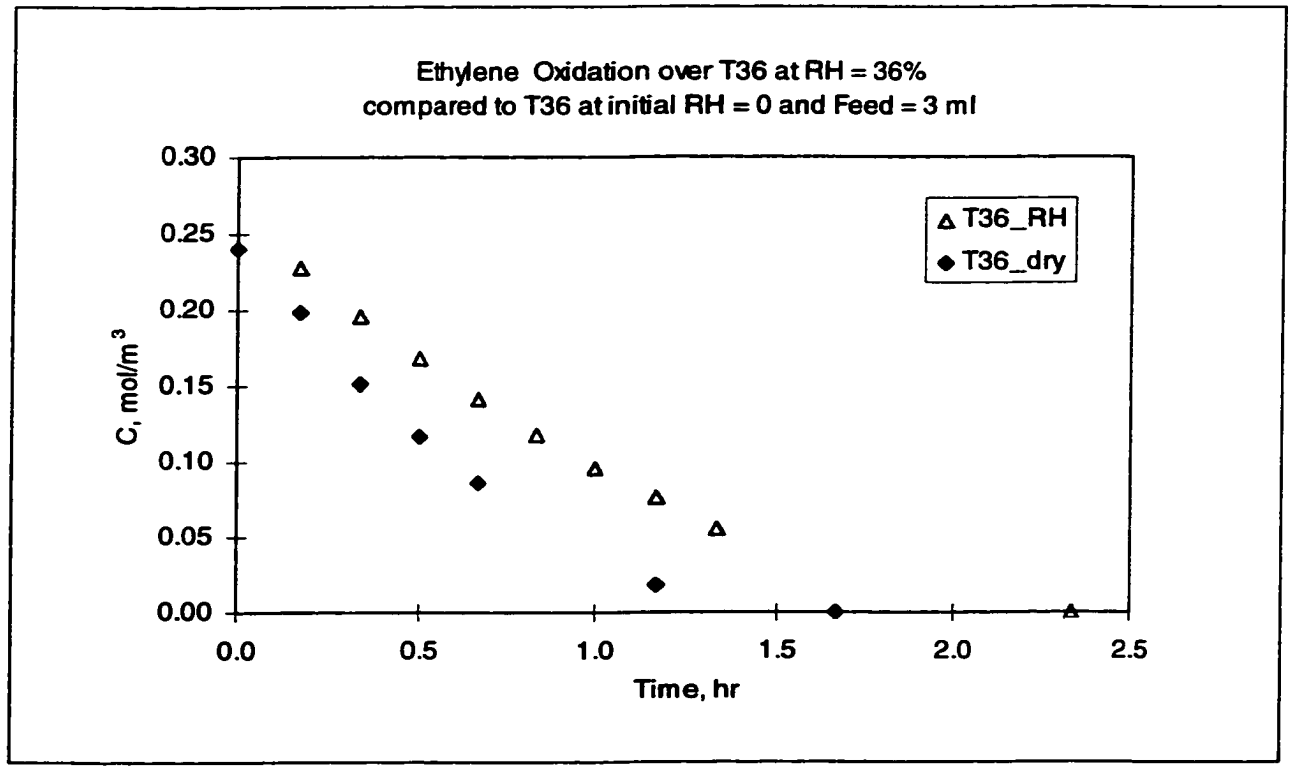

Figure 4-155 Ethylene photo-oxidation over Degussa P25 under humid conditions compared to the oxidation under initial dry conditions at 12ml ethylene feed

Ethylene Feed, ml	Temp, °C	RH, %	log10(P*)	P^*_{H2O}, mmHg	P'_{H2O} mmHg	Co_W, mol/m^3	K_W, m^3/mol
3	22.40	35.8	1.31	20.31	7.28	0.39	0.41
5	22.40	38.2	1.31	20.31	7.76	0.42	1.02
7	24.30	30.4	1.36	22.78	6.93	0.37	1.23
10	21.70	44.5	1.29	19.46	8.67	0.47	1.05
12	22.70	43.2	1.32	20.69	8.94	0.48	2.04
15	20.50	48.6	1.26	18.08	8.79	0.48	1.43
	average RH =	40.1	%		avg C_W, K_w	0.44	1.35

Table 4-35 Experimental conditions of ethylene oxidation over T36 under humid conditions. The calculated values of the water adsorption constant K_W for each individual run are included in the last column.

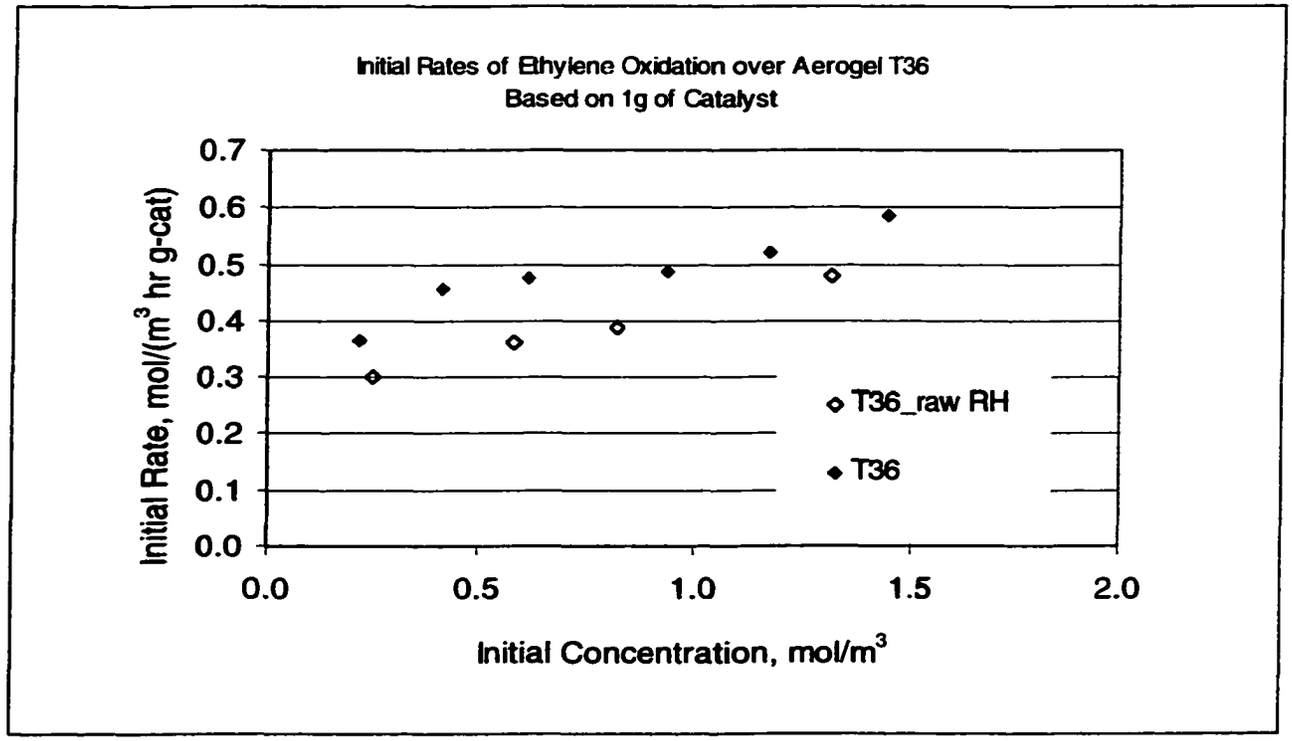

Figure 4-156 Initial ethylene oxidation rates over the aerogel T36 at initial dry (T36) and humid conditions (T36_raw RH)

Analogous to the calculations performed for the Degussa P25 under humid conditions, the initial rate data were first used to determine the water adsorption constant K_W. Applying the reaction rate constant k_E^{dry} and the ethylene adsorption constant K_E^{dry} from the ethylene oxidation tests with T36 under initial dry conditions, R^2 was maximized for the Langmuir-Hinshelwood equation over the initial rate data. The resulting K_{WI} and the utilized rate parameters for its evaluation are summarized in Table 4-36. Similar to the observation made with the Degussa P25, the water adsorption constant found from the initial rate data under humid conditions was higher compared to the value of K_W from the tests under initial dry conditions. It is possible that the actual initial water gas phase concentrations were higher than determined from relative humidity measurements, which therefore resulted in lower K_W value. Nonetheless,

comparing the Langmuir-Hinshelwood models using the different K_W's demonstrated that both rate predictions showed an equivalent trend (evidently with the model using the K_W^{dry} showing the highest predictions) as it can be seen when comparing the dotted with the dashed curve in Figure 4-157.

Ethylene rate constant from tests at initial dry conditions, k_E	0.441	mol/(m^3 hr)
Ethylene adsorption constant from tests at initial dry conditions, K_E	7.80	m^3/mol
Average water adsorption constant from tests at initial dry conditions	1.25	m^3/mol
Kw from initial rate data at initial humid conditions K_{W1} new-->	2.20	m^3/mol
Average Kw from individual tests at initial humid conditions K_{W2} new-->	1.35	m^3/mol

Table 4-36 Rate constants and water adsorption constants determined from two evaluation methods for ethylene oxidation under humid conditions over aerogel T36

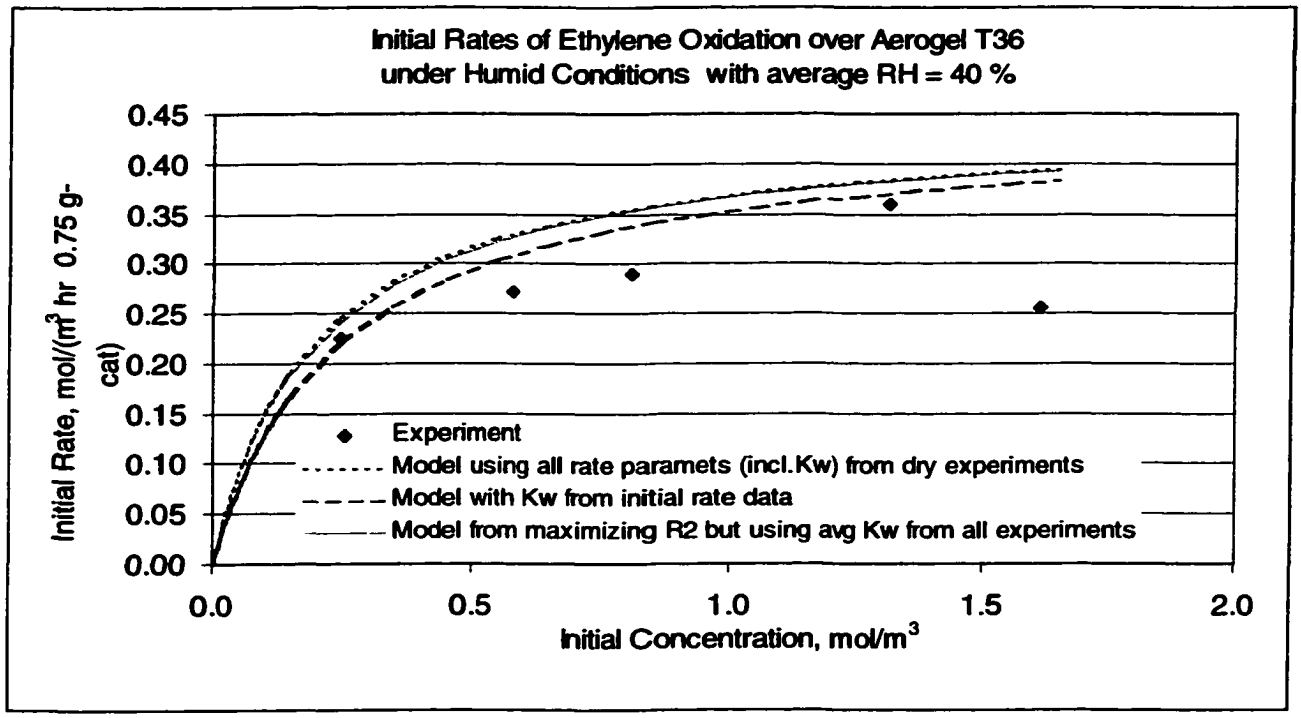

Figure 4-157 Initial rate data under humid conditions over aerogel T36 and Langmuir-Hinshelwood models from two evaluation methods.

Similar as performed for the Degussa P25, the values for K_W were determined for each individual run. The results are listed in Table 4-35 (last column) and the Langmuir-Hinshelwood models of each individual experiment are shown in Figure 4-158 together with the experimental data. The K_W values for each individual run ranged from 1.0 to 2.0 m^3/mol with an average value of 1.35 m^3/mol. This value was close to the K_W found from the experiments under initial dry conditions (1.25 m^3/mol). The models calculated with the different values of K_W agreed well with the set of initial rate data as well as with the rate data of each individual experiment as seen in Figure 4-158The dashed lines represent the models using the water adsorption constant K_W determined from the experiments under dry conditions. Both models (calculated from K_W^{dry} = 1.25 m^3/mol and the K_W^{RH} = 1.35 m^3/mol from each single experiment) agreed satisfactorily with the experimental data, confirming the legitimacy of the values of the adsorption constant as kinetic parameter for ethylene oxidation.

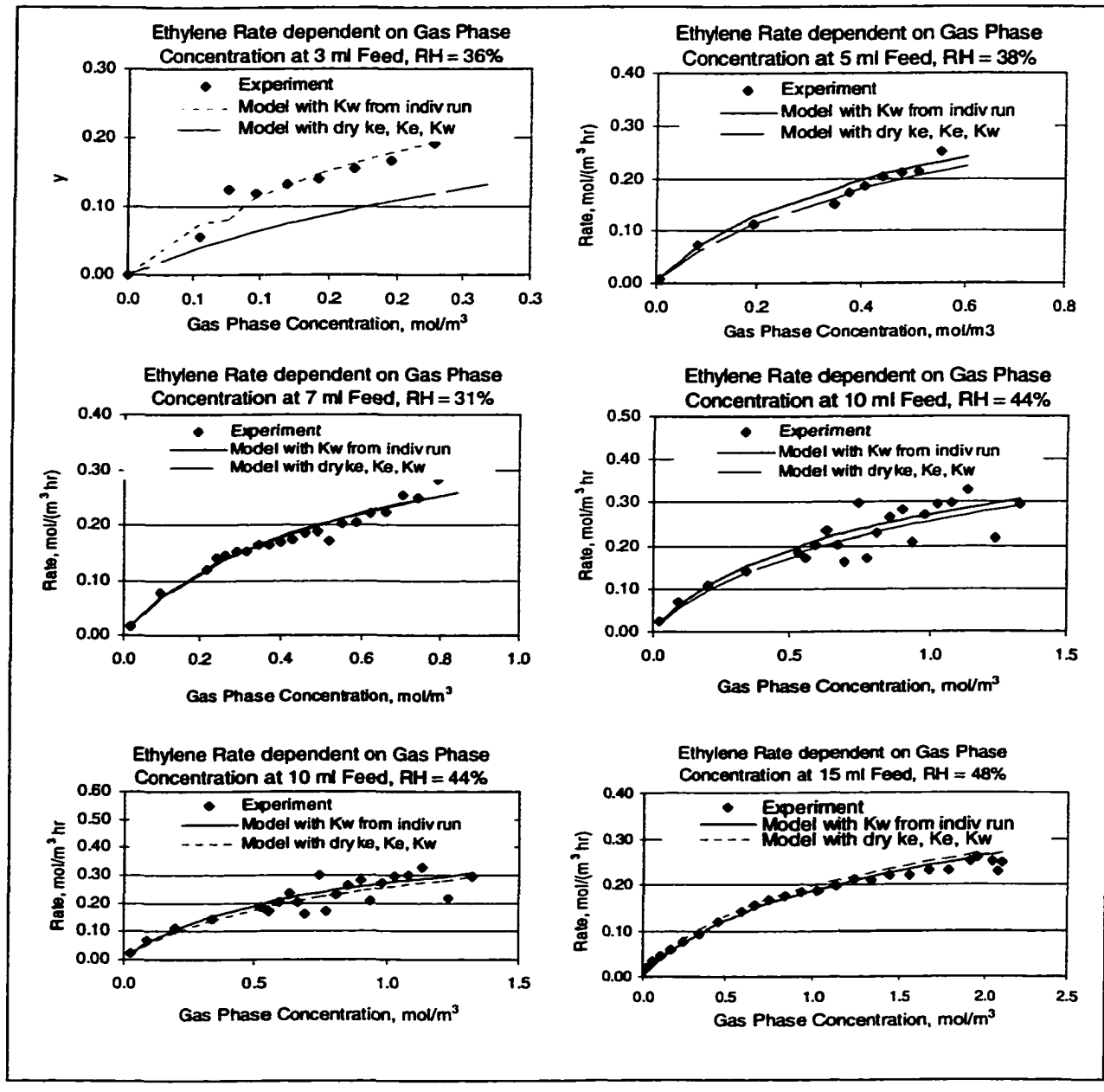

Figure 4-158 Langmuir-Hinshelwood model and experimental data of ethylene oxidation under humid conditions over aerogel T36 at different initial ethylene concentrations. The solid lines represent the Langmuir-Hinshelwood models calculated from K_W of each individual run, and the dotted lines represent the models using all rate parameters (including K_W) determined from experiments under initial dry conditions.

4.6.5.3 Aerogel T36_450 RH

Figure 4-159 shows the result of ethylene oxidation at different humidity levels over the heat-treated aerogel T36, labeled as T36_450 RH. The presence of water at initial conditions drastically reduced the reactivity of the catalyst. It took about three times longer to oxidize the initial ethylene feed compared to oxidizing the same amount under initial dry conditions. In addition, it was noticed that the level of humidity did not influence the reaction velocity significantly. At 28% or 40% relative humidity approximately the same time was needed (13 hours) to completely oxidize 0.9 mol/m^3 of ethylene (Figure 4-159.a). A comparable trend was observed for another test at 12 ml ethylene feed under 20% and30% relative humidity (see Figure 4-159.b) Therefore, the rate parameters determined for this set of experiments can be considered valid for a humidity range between 20 to 40% relative humidity according to the range of humidity levels the experiments were conducted (see Table 4-37). All other tests at different initial ethylene concentrations are summarized and compared to the tests under initial dry conditions in the Appendix.

Figure 4-160 illustrates that the initial rates under initial humid conditions were almost three times lower than the rates at initial dry conditions. This reduction in reactivity resulted possibly from the water blocking some of the reaction sites due to competitive adsorption.

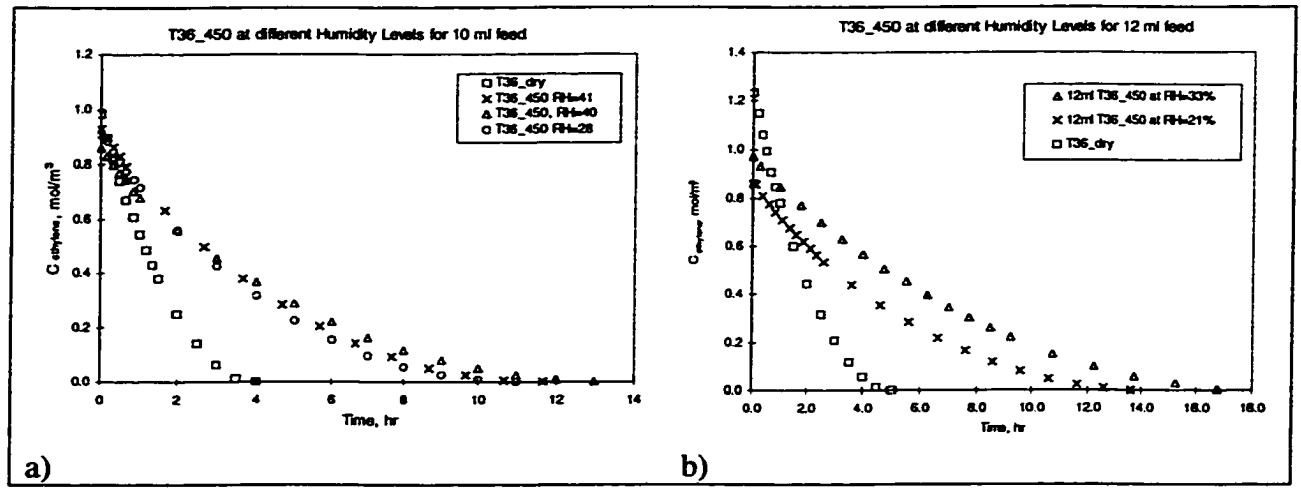

Figure 4-159 Ethylene photo-oxidation over heat-treated aerogel T36 under humid conditions compared to the oxidation under initial dry conditions at 10 and 12 ml ethylene feed

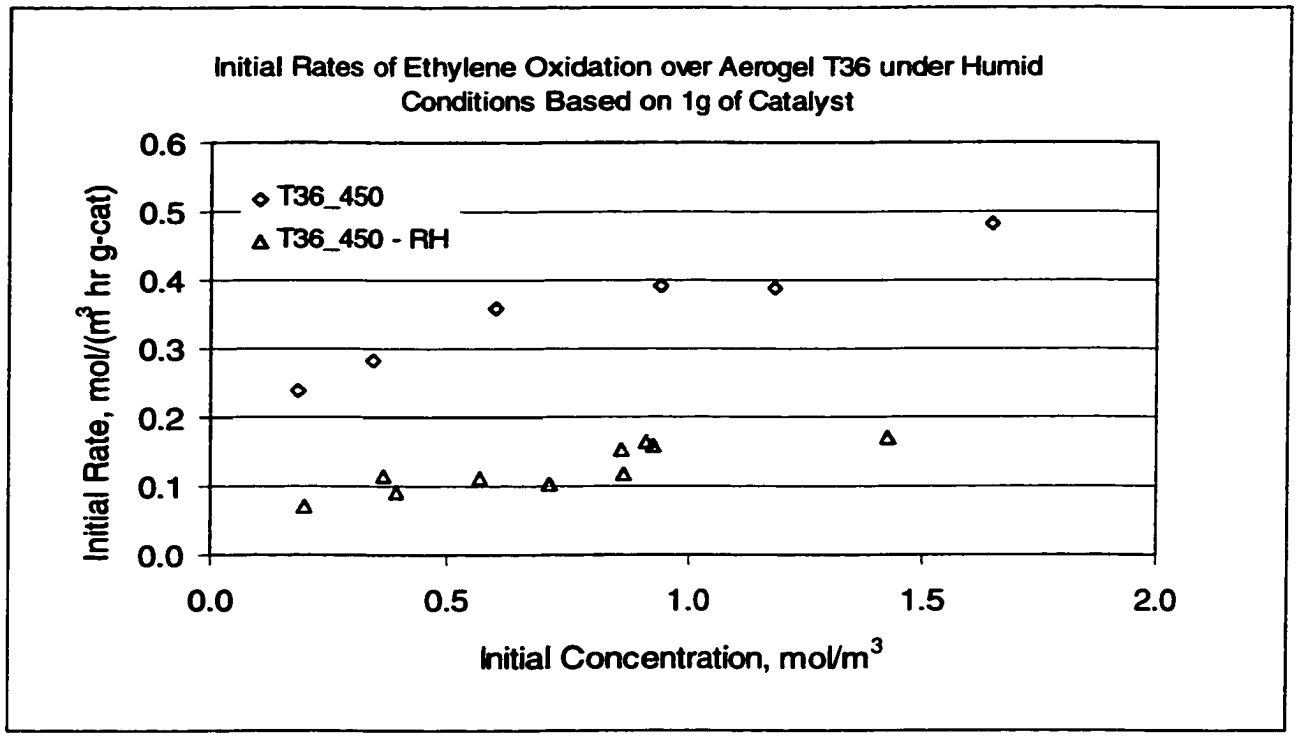

Figure 4-160 Initial ethylene oxidation rates over T36_450 at initial dry (T36_450) and humid conditions (T36_450 RH)

Ethylene Feed, ml	Temp, °C	RH, %	log10(P°)	P°_{H2O}, mmHg	P'_{H2O} mmHg	Co_W, mol/m^3	K_W, m^3/mol
3	22.6	30.0	1.31	20.56	6.18	0.33	1.36
5	22.5	29.2	1.31	20.44	5.97	0.32	1.83
5x	22.8	20.7	1.32	20.81	4.30	0.23	2.29
7	22.7	31.8	1.32	20.69	6.58	0.36	2.30
10	22.5	27.3	1.31	20.44	5.58	0.30	2.19
10x	24.0	39.7	1.35	22.38	8.89	0.48	2.19
10xx	22.3	40.8	1.31	20.19	8.23	0.45	2.86
12	25.1	23.7	1.38	23.90	5.67	0.30	4.14
15	22.6	28.8	1.31	20.56	5.93	0.32	3.06
	average:	30.2			avg C_W, K_w =	0.34	2.47

Table 4-37 Experimental conditions of ethylene oxidation under humid conditions over thermal treated aerogel T36_450. The calculated values of the water adsorption constant K_W (using the method of maximizing R^2) for each individual run are included in the last column.

First, the Langmuir-Hinshelwood model calculated using the rate parameters from initial dry conditions (including K_W) was plotted against the experimental initial rates, which can be seen in Figure 4-161. The so predicted rates were higher than the actual initial rates under humid conditions. This may be because water initially introduced to the system adsorbed competitively strongly onto the catalyst surface thus blocking a high fraction of reaction sites that were initially available in the case for the experiments under initial dry conditions. With many sites not being available for photooxidation anymore the actual initial rates under humid conditions were lower. Therefore, a new K_W was determined from the initial rates under humid conditions (maximizing R^2 of Langmuir-Hinshelwood using k_E^{dry} and K_E^{dry}). The so obtained value (21.9 m^3/mol) was almost ten times higher than K_W^{dry} = 2.29 m^3/mol). It is possible that water might adsorb differently on this catalyst, i.e., with stronger bonds during pre-adsorption when exposed to humid conditions and with weak bonds from generated water. Similar to the procedure

discussed for the Degussa P25 for the Degussa P25 (Section 4.6.5.1), K_W was also determined for each individual experiment under humid conditions. The average value of the individual K_W of 2.47 m^3/mol was close to the value obtained from initial dry conditions. The utilized kinetic rate parameters for ethylene oxidation under humid conditions over the thermal treated aerogel T36_450 are tabulated in Table 4-38.

Ethylene rate constant from tests at initial dry conditions, k_E		0.657	mol/(m^3 hr)
Ethylene adsorption constant from tests at initial dry conditions, K_E		4.18	m^3/mol
Average water adsorption constant from tests at initial dry conditions		2.29	m^3/mol
Kw from initial rate data at initial humid conditions	K_{W1} new-->	21.92	m^3/mol
Average Kw from individual tests at initial humid conditio	K_{W2} new-->	2.47	m^3/mol

Table 4-38 Rate parameters including water adsorption constants determined from different evaluation methods for ethylene oxidation under humid conditions over the heat-treated aerogel T36_450

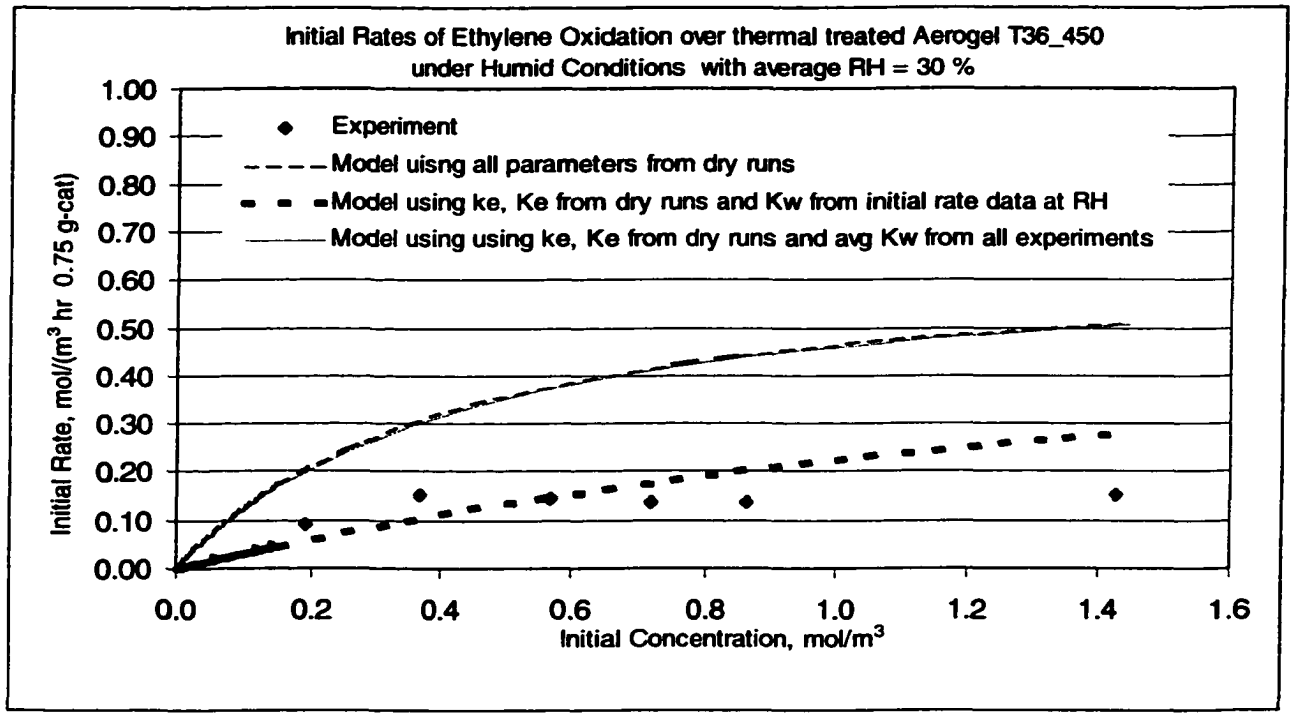

Figure 4-161 Initial ethylene oxidation rate data under humid conditions over the heat-treated aerogel T36_450 and Langmuir-Hinshelwood models using different rate parameters

Figure 4-162 summarizes two rate predictions and the actual data. The solid lines represent the model assuming initial dry conditions. The predicted rates agreed mostly with the actual data. The dotted lines are the models calculated using the average value of all individual runs with $K_W^{RH} = 2.47\ m^3/mol$. This value of K_W^{RH} was close to the one found from initial dry conditions ($K_W^{dry} = 2.29\ m^3/mol$), confirming the validity of this kinetic parameter. Even though the models did agree reasonably well with the experimental data, it was yet observed that the trend of the Langmuir model using the determined rate parameters did show a slight different behavior than for a typical Langmuir model. Normally, a Langmuir-Hinshelwood prediction shows a fast rate increase at low concentrations while at high concentration the predicted rates approach an asymptote. The models for the T35_450 catalyst, in contrast, do not show this trend as clearly, which can best be seen when looking at the experiment at 15 ml ethylene feed in Figure 4-162. This could imply that there may eventually be a different mechanism involved besides simple Langmuir-Hinshelwood kinetics. Possibly, there are different adsorption sites on the T36_450 catalyst, which adsorb ethylene with different strength[103]. Those reactive sites may have become available after the thermal removal of strongly adsorbed water and/or organics (left from synthesis). At non-humidity oxidation tests, those sites were still available and not reoccupied from reaction products. However, when exposing the catalyst to high levels of humidity, those sites might have been blocked again by strongly adsorbed water. In addition, heating of the aerogel did increase the anatase crystallinity and therefore the number of active sites; however, the surface area was drastically reduced at the same time. Therefore, the fraction of active

sites compared to all available sites of the catalyst was much higher for the heat-treated aerogel compared than for the untreated material. Thus, with the T36 catalyst a higher fraction of water could adsorb on non-reactive site, while in contrast to the T36-450 catalyst with the higher density of active sites per surface area the adsorbed water necessarily blocked a higher fraction of reactive sites since not as many non-reactive sites (percentage wise) were available for water adsorption. For this reason, the percent decrease in photoreactivity of the heat-treated aerogel T36_450 was observed to be three times higher compared to the untreated T36.

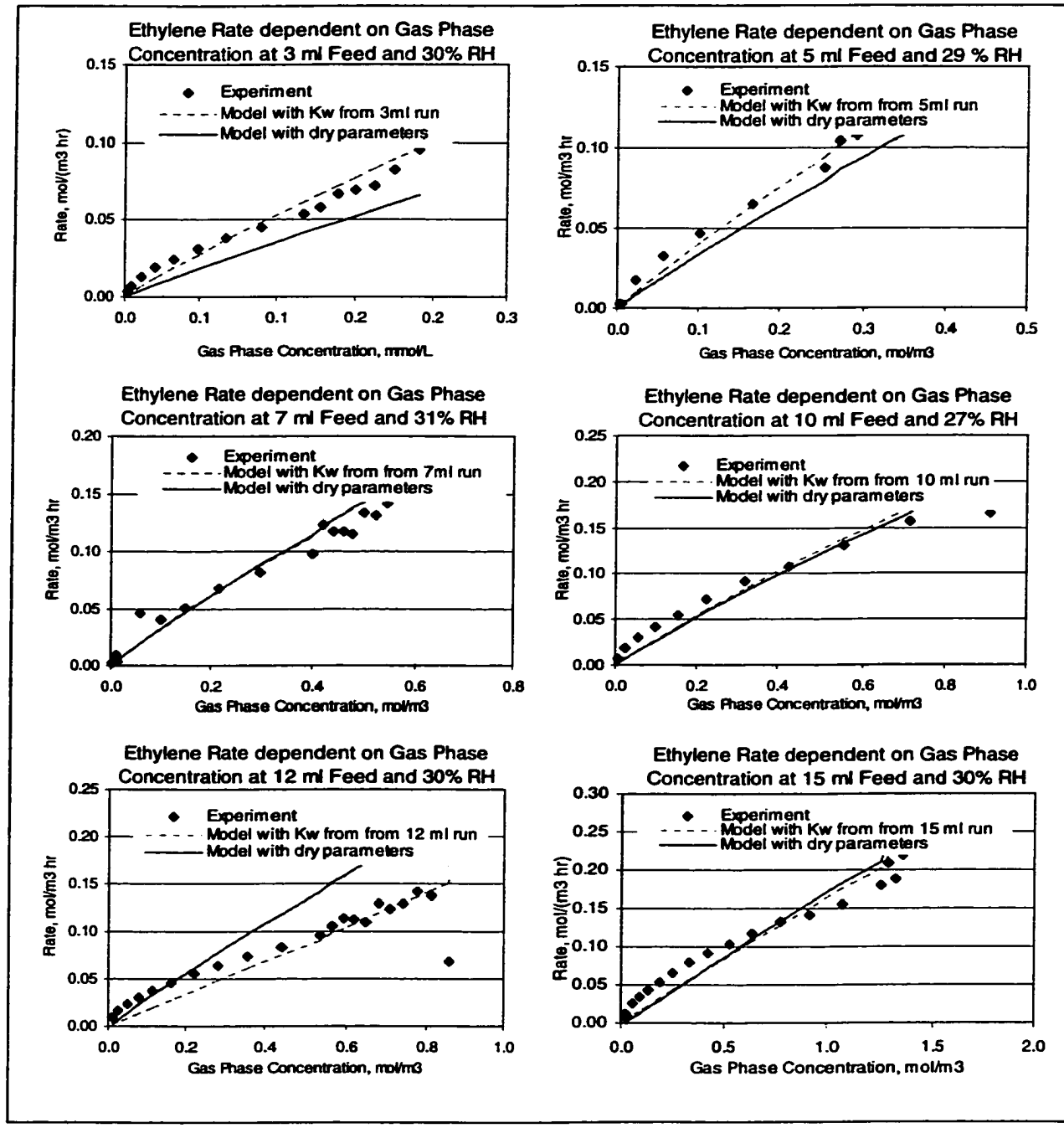

Figure 4-162 Experimental rate data of ethylene oxidation under humid conditions over heat-treated aerogel T36_450 for individual tests at different initial ethylene concentrations. The dashed lines represent the Langmuir-Hinshelwood models calculated using k_E, K_E, and K_W from tests under initial dry conditions. The dotted line represents the model using k_E, K_E, from tests under initial dry conditions and K_W calculated from initial rate data of tests under humid conditions.

4.6.5.4 Comparison/Summary of Test under Humid Conditions

Since no separate reaction rate constants were determined for the oxidation under humid conditions the performance of the three investigated catalysts Degussa P25, the untreated aerogel T36 and the heat-treated aerogel T36_450 was compared on basis of initial rate data. Figure 4-163 again illustrates the initial rates (based on one gram of catalyst) for the three catalysts by comparing the rates under initial dry conditions to the rates under humid conditions. The presence of initial water in the reactor system inhibited the ethylene oxidation over all three catalysts. Since the initial rates showed a near linear behavior in the range of concentrations a linear fit was performed in order to quantitatively describe the differences in reactivity. Table 4-39 summarizes the initial rate data estimated from the linear regression expressions. Averaging the decrease in initial rates over the six data points within the range of initial concentrations of 0.2 to 1.4 mol/m^3 showed that the Degussa demonstrated a 24% decrease while the initial rates of the aerogel T36 was decrease by only 19%. In contrast, the heat-treated T36_450 diminished its reactivity by about 2/3 under the influence of water. It was also observed that the T36_450 had the highest water adsorption constant, indicating that water adsorbed more strongly on this catalyst compared to the untreated T36 and the Degussa P25. This could be one of the possible explanations for the higher fraction of loss in reactivity under humid conditions.

The presence of water can have different effects on the oxidation rate. This depends, among other factors, on the organic to be oxidized, on the type of catalyst employed as well as on the degree of humidity level and the contaminant concentration. Peral and Ollis[29] found that the photooxidation rate of m-xylene increased with increasing water

concentrations between 1000 to 1500 mg/m^3 and decreased thereafter rapidly to eventually level out at water concentrations above 3000 mg/m^3. Toluene oxidation is promoted by water whereas TCE oxidation is inhibited, this also depending on the degree of humidity. Acetone oxidation was clearly inhibited by the presence of water[40], [15], while for n-butanol water is neither an inhibitor nor a promotor[131]. The main reason for this differing behavior lies in the fact that water can serve either as regenerator for depleted OH-groups on the catalyst surface (which are believed to be vital for the photoreaction) or it can competitively adsorb on the catalyst thus blocking reaction sites. Other researchers found that water can also contribute to actually displacing surface-adsorbed species.[15]

In the case of ethylene oxidation of this study it was clearly shown that water acted as an oxidation inhibitor mostly due to the stronger adsorption of water compared to ethylene. It should be noted, however, that even though the oxidation rate was reduced under humid conditions, the introduced ethylene was nevertheless completely oxidized without measurable by-products.

P25

experiment initial rates, mol/m³ hr g-cat					fit initial rates, mol/m³ hr g-cat					
					slope	0.151	0.082			
Ethylen	dry		wet		intercept	0.237	0.066			
Feed, ml	C, mol/m³	Rate	C, mol/m³	Rate	C, mol/m³	dry fitRate	RH fitRate	Rate difference	Factor decrease	Percent decrease
3	0.244	0.126	0.164	0.044	0.200	0.107	0.078	0.029	1.371	27.1
5	0.441	0.109	0.299	0.112	0.400	0.119	0.089	0.031	1.348	25.8
7	0.690	0.140	0.548	0.078	0.600	0.132	0.099	0.033	1.329	24.8
10	1.059	0.154	0.758	0.147	0.900	0.151	0.115	0.035	1.308	23.6
12	1.312	0.158	1.078	0.120	1.100	0.163	0.126	0.037	1.297	22.9
15	1.566	0.212	1.385	0.127	1.400	0.182	0.142	0.040	1.283	22.1
							average -->	0.035	1.323	**24.4**

T36_raw

experiment initial rates, mol/m³ hr g-cat					fit initial rates, mol/m³ hr g-cat					
					slope	0.151	0.082			
Ethylen	dry		wet		intercept	0.237	0.066			
Feed, ml	C, mol/m³	Rate	C, mol/m³	Rate	C, mol/m³	dry fitRate	RH fitRate	Rate difference	Factor decrease	Percent decrease
3	0.008	0.058	0.248	0.299	0.200	0.393	0.292	0.102	1.348	25.8
5	0.016	0.090	0.579	0.362	0.400	0.423	0.325	0.098	1.301	23.1
7	0.025	0.121	0.817	0.386	0.600	0.452	0.359	0.094	1.262	20.7
10	0.039	0.125	1.314	0.480	0.900	0.497	0.409	0.088	1.216	17.7
12	0.060	0.187	1.613	0.341	1.100	0.526	0.442	0.084	1.191	16.0
15	0.103	0.252	2.093	0.348	1.400	0.571	0.492	0.079	1.160	13.8
							average -->	0.089	1.246	**19.5**

T36_450

experiment initial rates, mol/m³ hr g-cat					fit initial rates, mol/m³ hr g-cat					
					slope	0.151	0.082			
Ethylen	dry		wet		intercept	0.237	0.066			
Feed, ml	C, mol/m³	Rate	C, mol/m³	Rate	C, mol/m³	dry fitRate	RH fitRate	Rate difference	Factor decrease	Percent decrease
3	0.179	0.240	0.191	0.069	0.200	0.267	0.083	0.185	3.233	69.1
5	0.342	0.284	0.367	0.116	0.400	0.297	0.099	0.198	3.001	66.7
7	0.605	0.359	0.571	0.112	0.600	0.328	0.116	0.212	2.835	64.7
10	0.939	0.392	0.718	0.104	0.900	0.373	0.140	0.233	2.659	62.4
12	1.189	0.389	0.865	0.118	1.100	0.403	0.157	0.246	2.573	61.1
15	1.642	0.482	1.428	0.171	1.400	0.449	0.181	0.267	2.472	59.6
							average -->	0.231	2.708	**62.9**

Table 4-39 Initial rate data and linear fit data of ethylene oxidation for Degussa P25, and the aerogels T36 and T36_450 at initial dry and humid conditions

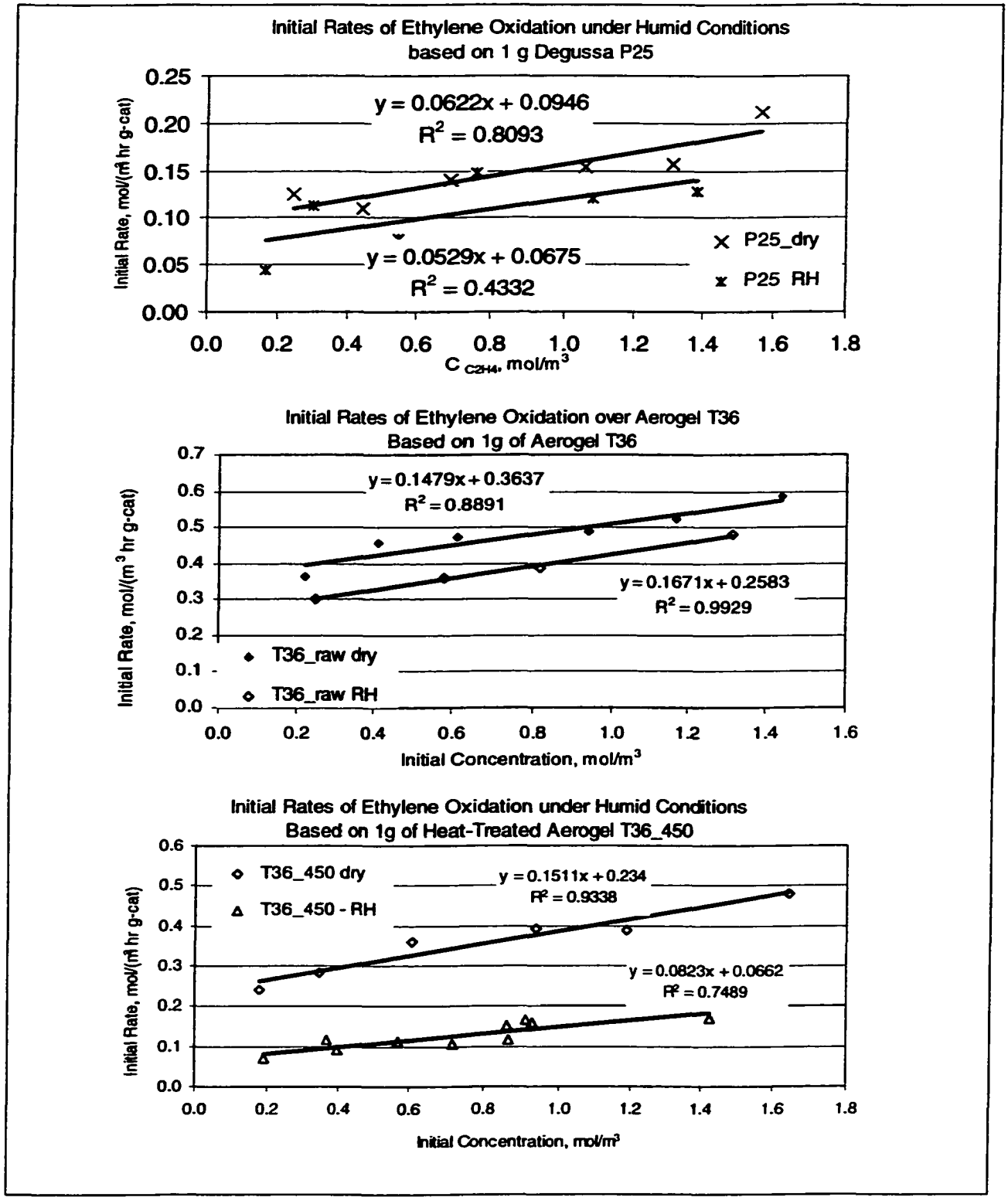

Figure 4-163 Comparison of initial ethylene oxidation rates of Degussa P25, and aerogels T36 and heated T36_450 under initial dry and humid conditions

4.7 TiO_2 Modified with Platinum and its Photocatalytic Activity

Platinum (and also ruthenium) was deposited on Degussa P25 in order to investigate if the addition of noble metals leads to an improvement in its photocatalytic activity. The two methods of metal deposition were described previously in Section 3.1.5.

4.7.1 Aqueous Photocatalytic Co-Deposition of Platinum on Degussa P25

First, ethylene photo-oxidation tests were performed over Degussa P25 with 3wt% platinum deposited. Since the photocatalytic activity had drastically reduced (see Figure 4-164) as a result of the platinum deposition process, Degussa samples with less platinum (0.5 and 0.1 wt% Pt) were prepared and tested in order to see if a lower platinum content would lead to an increase in photocatalytic activity.

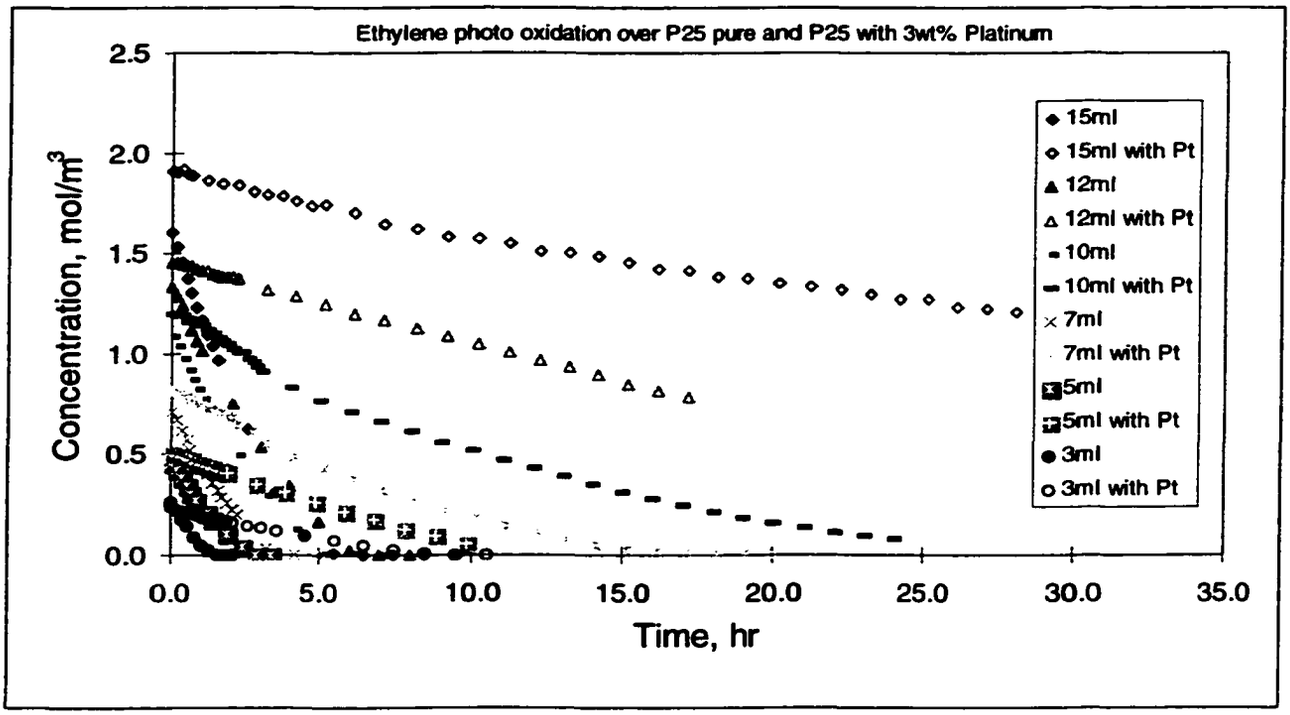

Figure 4-164 Ethylene photo oxidation over Degussa P25 with 3wt% Pt (photo deposition) and pure P25

The individual ethylene oxidation tests for both catalysts at ethylene feeds between 3 and 15 ml are summarized in Figure 4-165. For comparison purposes the results of the pure Degussa P25 tests are included. Figure 4-165 indicates that all platinum loaded catalysts had a lower activity than the pure P25 and that the ethylene oxidation rate decreased with increasing platinum amount.

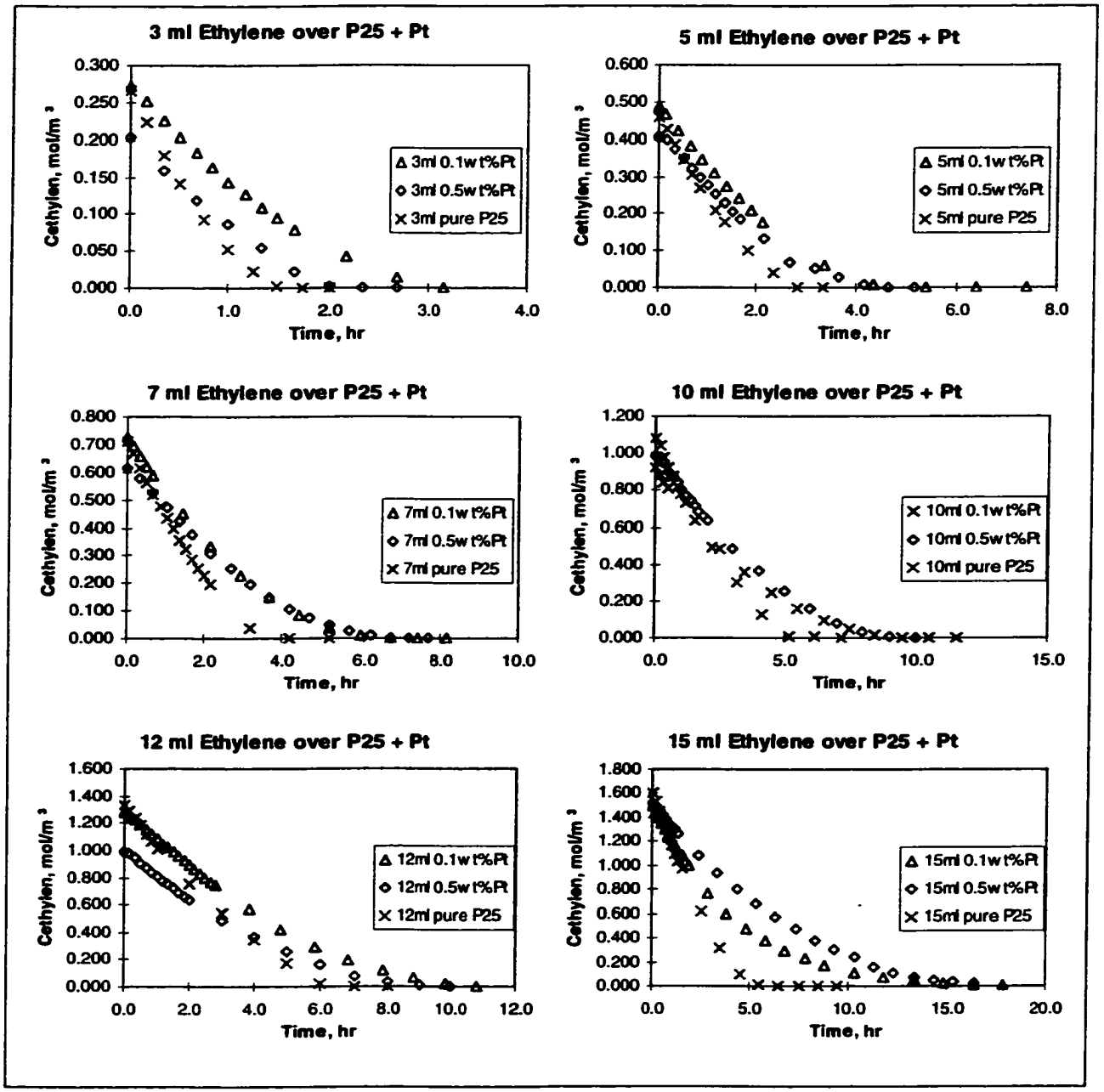

Figure 4-165 Ethylene photo oxidation over Degussa P25 with 0.1 and 0.5wt% Pt (impregnation and photo deposition) compared to the results of pure P25

The decreasing reactivity with increasing platinum content is also reflected in the reaction rate constants as listed in Table 4-40. With k = 0.14 mol/(m^3 hr cm^{3}cat) the rate

constant of the Degussa with 0.1wt% platinum was about 70% lower compared to the untreated Degussa.

Degussa with Platinum (Photodeposition)	0	0.1wt%	0.5wt%	3 wt%
k mass, mol/(m^3 hr g-cat)	0.545	0.140	0.120	0.063
Ethylene Adsorption Constant K_E, m^3/mol	3.0	2.8	4.2	1.8
Water Adsorption Constant K_W, m^3/mol	0.32	0.34	0.93	1.49

Table 4-40 Reaction rate constants for ethylene oxidation over Degussa P25 at different platinum loadings (applied by impregnation)

Degussa P25 was also loaded with ruthenium in an attempt to increase its photocatalytic activity. The ethylene oxidation results, however, showed a similar trend as was already found for the platinum deposited Degussa. This is illustrated in Figure 4-166 and can be observed from Table 4-41 showing a decrease in the rate constants with increasing ruthenium content.

Degussa with Ruthenium (Photodeposition)	0	0.1wt%	3wt%	0.1wt%Ru +0.1wt% Pt
k mass, mol/(m^3 hr g-cat)	0.545	0.156	0.072	0.132
Ethylene Adsorption Constant K_E, m^3/mol	3.0	1.7	3.7	3.6
Water Adsorption Constant K_W, m^3/mol	0.32	0.00	0.24	0.28

Table 4-41 Reaction rate constants for ethylene oxidation over Degussa P25 at different ruthenium loadings (applied by impregnation)

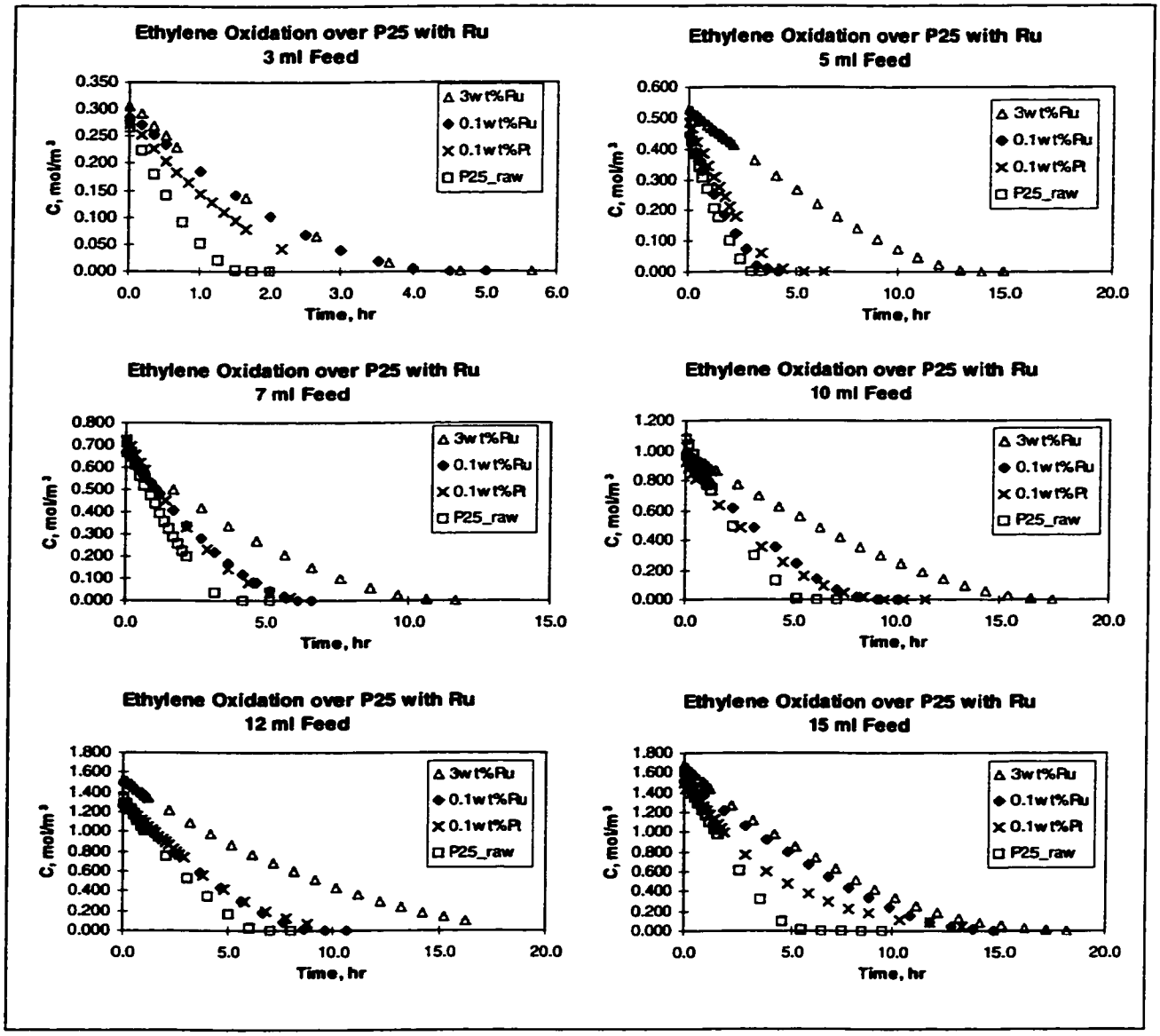

Figure 4-166 Ethylene photo oxidation over Degussa P25 with 0.1 and 3wt% Ru and 0.1Ru+0.1wt% Pt (impregnation and photo deposition) compared to the results of pure P25

No evident reason for the reactivity decrease could be found from the XRD data (Section 0) or when looking at the TEM images (Section 4.2.8). The anatase crystallinity did not change and the TEM photographs did not show any difference to the samples prepared using chemical vapor deposition that in contrast did show an increase in activity

as discussed in the following section (4.7.2). In 1977, Santacesaria et al. proposed an attack of the surface of Al_2O_3 by the H_2PtCl_6 impregnating solution and Fenoglio and coworkers investigated interactions taking place between the metal precursor species ($RhCl_3$ H_2O) and the catalyst support during the impregnation of a TiO_2 catalyst.[132] They found that the acidic solution attacked the surface of the support causing a partial dissolution of TiO_2 followed by a re-deposition, which may also result in a partial covering of the metal precursor. Since for the platinum and ruthenium deposition H_2PtCl_6 and $RuCl_3$ H_2O, both creating acidic solutions, were used to impregnate Degussa, the aforementioned effect might have taken place during the impregnation procedure causing the decrease in photoactivity of the Degussa. Vorontsov et al observed a similar decrease in photoactivity with increasing platinum content, which they attributed to etching of the TiO_2 surface by chloroplatinic acid[103]. Equivalent to this research, they concluded that only samples with chemically vapor-deposited platinum were more active than TiO_2. The following chapter (4.7.2) presents and discusses the results of ethylene oxidation over Degussa P25 and aerogel T36 with chemically vapor-deposited platinum showing an increased photoactivity.

4.7.2 CVD of Platinum on Degussa P25 and Aerogel T36

First, platinum was deposited on Degussa P25 using chemical vapor deposition (CVD). Three samples were prepared as described in Chapter 4.1.2 to contain 0.1, 0.5, and 1.2wt% platinum and were then tested for ethylene photooxidation at different initial feed rates ranging from 0.1 to 1.0 ml ethylene feed (as described in Section 3.5.3). The results of all tests for the three catalysts plus the untreated Degussa P25 are shown in

Figure 4-167. At almost all initial feeds the catalyst with 1.2wt% platinum (see connected data points in Figure 4-167) photooxidized ethylene at the fastest rate. The related reaction rate constants are listed in Table 4-42 and showed an increase with increasing platinum loading. With 0.1wt% Pt loading, the rate constant $k^{0.1} = 0.116$ mol/m^3 hr g-cat was about 35% higher compared to the untreated Degussa while for 1.2wt% loading the rate constant $k^{1.2} = 0.126$ mol/m^3 hr g-cat was about 45% higher.

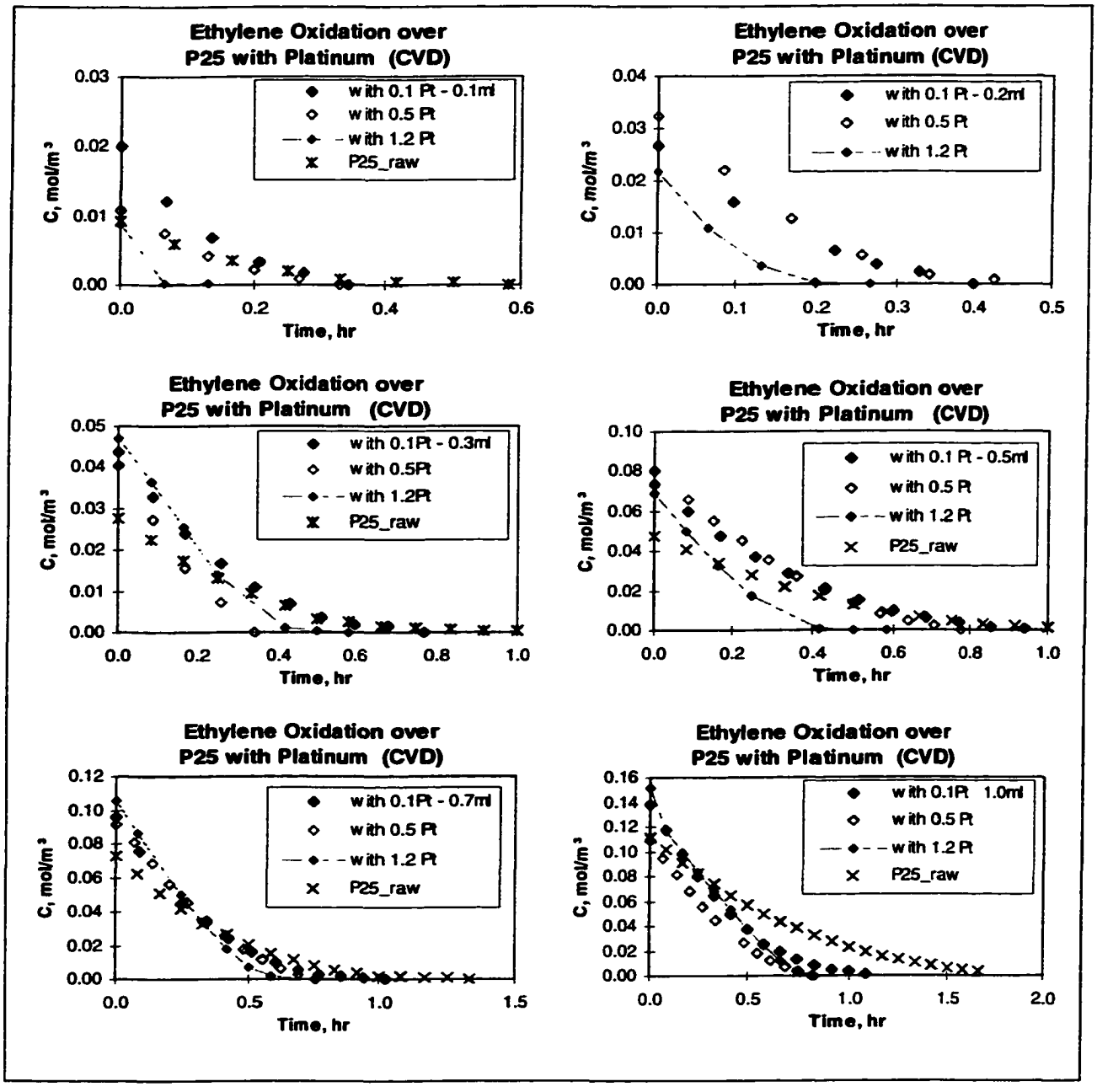

Figure 4-167 Ethylene photo oxidation over Degussa P25 with 0.1, 0.5 and 1.2wt% Pt (CVD) compared to the results of pure P25

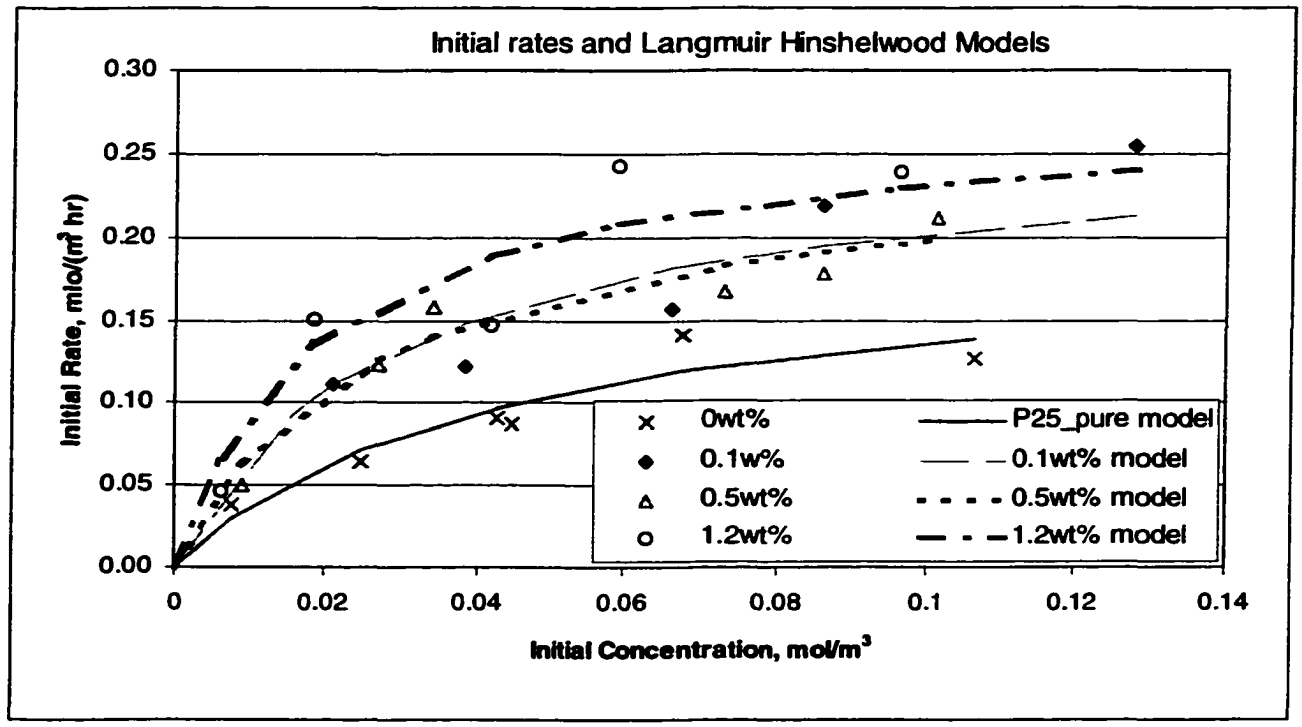

Figure 4-168 Initial rates and Langmuir-Hinshelwood of pure P25 and P25 loaded with 0.1, 0.5, and 1.2wt% platinum (CVD)

Degussa with Platinum (CVD)	0	0.1wt%	0.5wt%	1.2 wt%
k mass, mol/(m^3 hr g-cat)	0.086	0.116	0.114	0.126
Ethylene Adsorption Constant K_E, m^3/mol	46.7	35.2	36.0	49.1
Water Adsorption Constant K_W, m^3/mol	2.66	4.21	0.94	3.36

Table 4-42 Rate parameters (reaction rate constants and adsorption constants) for Degussa loaded with platinum via CVD

Since platinum deposition on P25 was successful in terms of increasing its photoactivity, platinum was also added to the aerogel with highest photocatalytic activity, the T36. Since 1.2wt% of platinum loading showed the highest activity for the Degussa P25, the same amount was added to T36 (CVD). It was also of interest to see if 7.7wt% platinum loading would further enhance the aerogel's activity. The 7.7wt% loading on the aerogel T36 is equivalent to 1.2wt% loading on Degussa P25 with respect to surface

coverage of platinum (0.25 mg Pt/m^2-catalyst). First, the amount for 7.7wt% Pt was deposited at once. Then, considering the fact that when depositing a large amount at once the platinum might not be evenly distributed over the surface but rather have deposited in clusters, it was attempted to add the platinum in increments to the catalyst. Therefore, the aerogel T36 with 1.2wt%Pt was subjected again to CVD to have a final platinum loading of 3.5wt%. A second platinum deposition obtaining a final 7.7wt% loading was not performed since the photocatalytic activity had decreased after the second CVD procedure and the catalyst showed a fast deactivation, as it will be discussed later. Figure 4-169 shows the results of ethylene concentration over T35 with 1.2wt% Pt at different initial ethylene concentrations. A good repeatability of experiments was achieved. In all cases, the platinum doped aerogel oxidized the ethylene introduced to the reactor system faster compared to the untreated T36. As mentioned before, the T36 with 3.5wt% Pt, however, had a lower activity, which can be seen in Figure 4-170. Repeated experiments at the same initial ethylene concentration are included in the same graph indicating a drastic deactivation of the 3.5wt% Pt catalyst. The initial lower activity might be a result of the loss in surface area, which was noticed after the second CVD procedure. It is not clear, why the surface area decreased after the additional deposition of platinum. The same experimental CVD procedure was perform and the catalyst was even prepared twice with the same result (see Table 4-43). However, only the loss of surface area could not be responsible for the loss in activity because the aerogel with 7.7wt% Pt (deposited in one step) also had a lower surface area by more than 50% from it's original value but demonstrated an increased activity after the platinum deposition, which can be seen in Figure 4-171. Possible reasons could be the accumulation of

intermediate products as found by Vorontsov et al.[103], any contamination of the catalyst from deposits from the second CVD step, i.e. organics of the platinum acetyl acetonate as argued by Dossi et al.[94] and Signoretto and co-workers[133], or any interactions of adsorbed water and/or reaction byproducts (the catalyst had undergone ethylene tests before the second step of CVD was applied). However, a surface analysis in depth would have to be performed in order to understand the exact mechanism behind the catalyst deactivation after the second CVD procedure.

Aerogel T36 with Platinum (CVD)	0	1.2wt%	3.5wt%	3.5wt% (2)	7.7 wt%
BET surface area, m^2/g	336.9	287.4	136.9	165.9	136.4
Percent SA reduction, %	-	14.7	59.4	50.8	59.5

Table 4-43 BET surface area of aerogel T36 and T36 with platinum

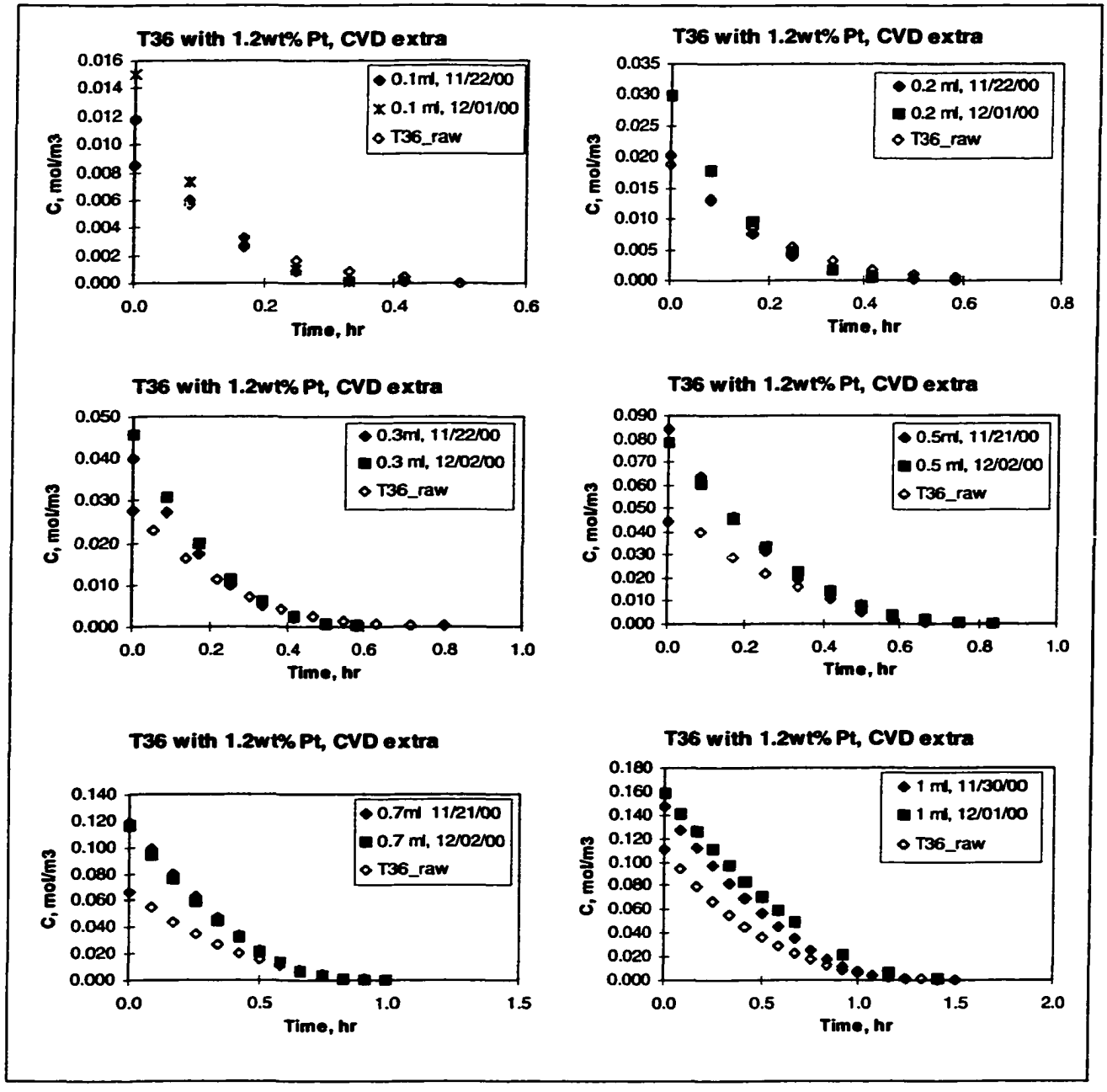

Figure 4-169 Ethylene photo oxidation over aerogel T36 with 0.1wt%Pt (CVD) compared to the results of pure T36

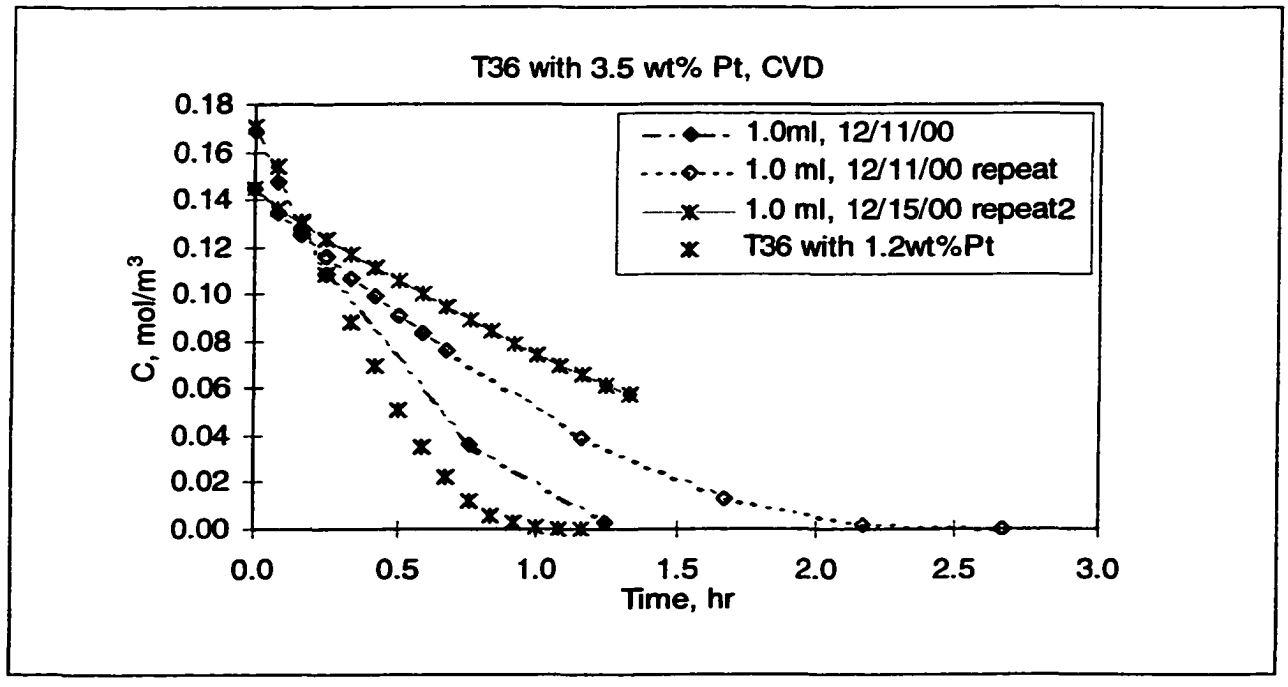

Figure 4-170 Ethylene photo oxidation of 1 ml feed over aerogel T36 with 3.5wt%Pt (CVD) compared to the results of T36 with 1.2wt%Pt

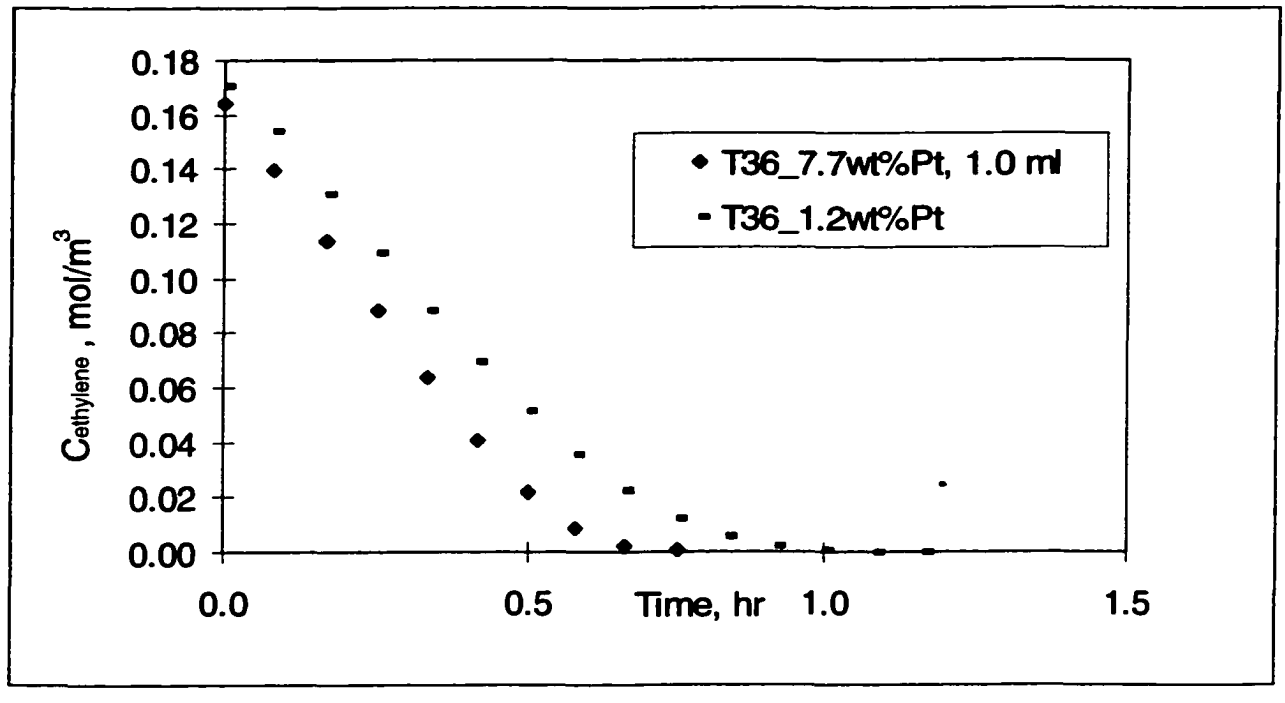

Figure 4-171 Ethylene photo oxidation of 1 ml feed over aerogel T36 with 7.7wt%Pt (CVD) compared to the results of T36 with 1.2wt%Pt

As previously pointed out, the aerogel with 7.7wt% platinum showed the highest activity of all platinum deposited aerogel samples which is depicted in Figure 4-171 for 1 ml ethylene feed. The results for all other tests are summarized in the Appendix (Table 7-27 and following tables. Table 4-44 summarizes the reaction rate parameters of all platinum altered aerogel samples and Figure 4-172 shows the initial ethylene rates together with the Langmuir-Hinshelwood models calculated from the found reaction rate parameters. Compared to the Degussa-Pt samples, the rate constant of the aerogel was about 3.5 times higher when compared on the same wt%-loading and about 4.5 times higher compared on the same platinum loading per surface area. This ratio is comparable to the ratio of rate constants of the untreated T36 and Degussa P25 (k_{T36} /k_{P25} was also about 3.5), signifying that the platinum deposition had the same positive effect for both catalysts. As discussed in Chapter 2.4.3 the platinum served probably as electron trap preventing the electron/hole recombination. It needs to be pointed out, however, that the increase in activity was not proportional to the amount of platinum on the catalyst. Even though about six times more platinum was on T36 with 7.7wt% compared to T36 with 1.2wt% Pt the rate constant was only about 33% higher. Similarly for the Degussa, P25_1.2wt%Pt with a loading of platinum of about 12 times higher than for the P25_0.1wt%Pt the rate increased by only about 9%. This supports the theory that with increasing amount of platinum the Pt-centers turn into electron/hole recombination centers, as the distance between platinum centers is smaller thus decreasing the separation distance of charge carriers and making it easier for an electron to meet and recombine with another hole.

Aerogel T36 with Platinum (CVD)	0	1.2wt%	3.5wt%	7.7 wt%
k mass, mol/(m^3 hr g-cat)	0.395	0.439	0.289	0.585
Ethylene Adsorption Constant K_E, m^3/mol	15.7	27.2	8.8	17.3
Water Adsorption Constant K_W, m^3/mol	1.20	1.83	0.94	0.00

Table 4-44 Rate parameters for the aerogel T36 loaded with platinum via CVD

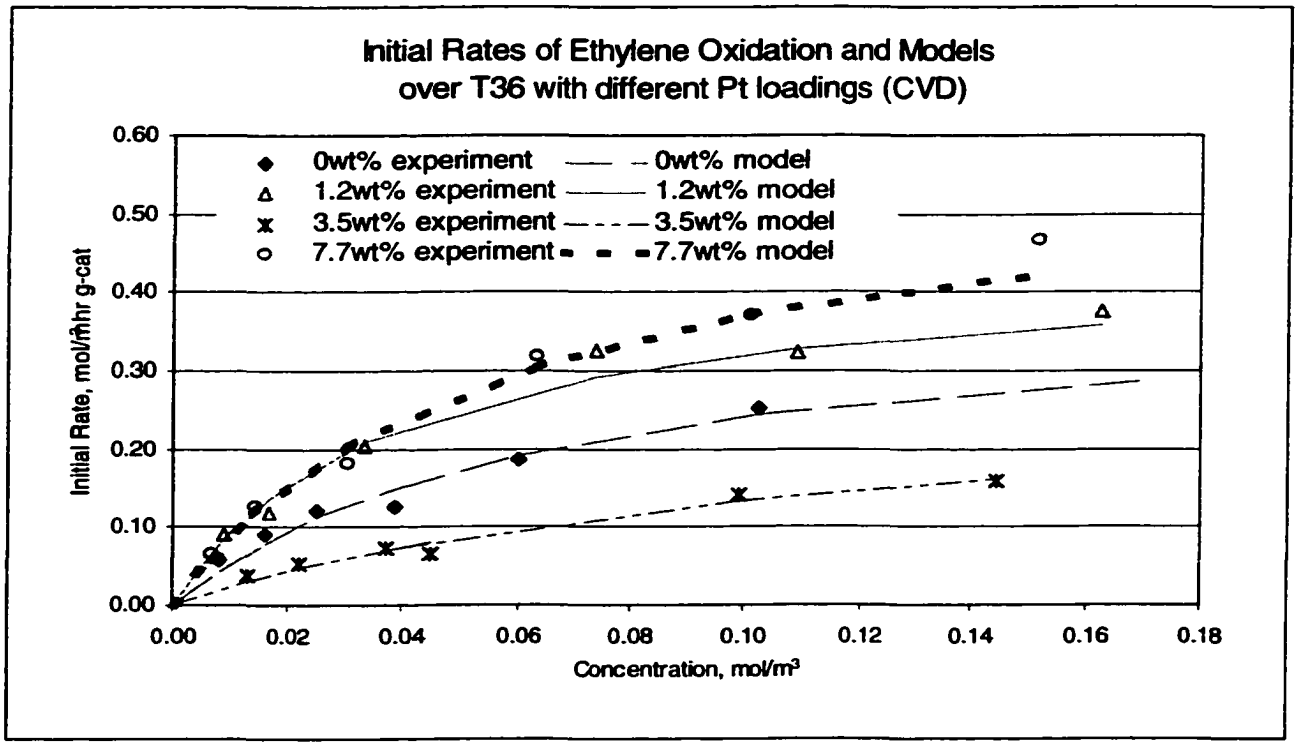

Figure 4-172 Initial rates and Langmuir-Hinshelwood of pure aerogel T36 and T36 loaded with 1.2, 3.5, and 7.7 wt% platinum (CVD)

As pointed out in Chapter 3.2.7, Vorontsov et al. were able to find out that an increasing platinum content led to an increase in the size of the platinum particles than rather in an increase in the number of particles. If the size of the particle remained the same and only the number of platinum particles increased with increasing platinum content then the reaction rate would be directly proportional to the platinum concentration. However, if only the size of the Pt particles increased but the number of

particles remained the same then the reaction rate would be proportional to the Pt-concentration to the power of 2/3. The same analysis was performed with the reaction rate constants obtained from ethylene tests over P25 and T36 deposited with platinum. Table 4-45 shows the results and confirms that for both catalysts (P25 and T36) the rate constants fit to a power of 2/3 of the Pt content resulted in a better value for R^2. This supports the findings from the TEM studies that the addition of more platinum to the catalyst did not lead to a higher number of platinum particles per Ti_O2 but instead resulted in the deposition of the same number but larger Pt particle clusters. This explains also why the reaction did nit linearly increase with the platinum content.

Degussa P25

wt% Pt	0	0.1	0.5	1.2
k_{ethyl} P25	0.086	0.116	0.114	0.126

rate contant = m * wt%Pt + n		rate contant = m*wt%$Pt^{2/3}$+n	
m =	0.0280	m =	0.0234
n =	0.0965	n =	0.0998
R^2 =	0.9880	R^2 =	0.5572

Aerogel T36

wt% Pt	0	1.2	3.5	7.7
kethyl T36	0.395	0.439	0.289	0.585

rate contant = m * wt%Pt + n		rate contant = m*wt%Pt2/3+n	
m =	0.0360	m =	0.024
n =	0.4016	n =	0.4016
R^2 =	0.9998	R^2 =	0.9943

Table 4-45 Two different regression models of the ethylene oxidation rate constant dependence on platinum content on Degussa P25 and aerogel T36

5 Conclusions

Several different pure TiO_2 aerogel samples (low density pure titanium oxide aerogel (CEH6) and ultra low density aerogel (T36)) as well as a binary Si-Ti-aerogel (TS31b) were prepared in our labs and characterized. Their photoctalytic activity was tested and compared to Degussa P25, a commercial nonporous photocatalyst with highest known photoactivity.

The specific surface area of the aerogel of up to 330 m^2/g (T36) was more than six times higher than that of Degussa P25 and had porosities varying between 60 and 80%. As a result of the high porosity of the aerogels the total UV accessible surface area of the aerogel material was found to be up to ten times higher than that of the nonporous Degussa P25.

UV penetration through aerogel layers was investigated and compared to that of Degussa P25 by dispersing the catalyst material in an agar based gel measuring the UV intensities through a number of catalyst beds with varying amounts of catalyst. All aerogel samples allowed a deeper UV penetration into the catalyst bed compared to Degussa P25. When comparing on a mass basis, the heat-treated pure titanium dioxide aerogels exhibited an even higher UV penetration than the untreated samples. This characteristic is an important feature of a catalyst to be utilized in photocatalytic applications since it would ensure that more of the material in a catalyst bed would be available for photoactivation.

XRD measurements revealed that the untreated aerogel were mostly amorphous with a very low crystallinity of about 10%. It is known that the anatase form of titanium dioxide is the highest photocatalytically active form. Thermal treatment led to an increase in fraction of anatase crystals, which was proved to increase the intrinsic activity of the aerogel material by more than 100% shown in the ethylene rate constant of $k^{T36\_450} = 0.163$ mol/(m^3 hr m^2-cat) compared to $k^{T36\_raw} = 0.073$ mol/(m^3 hr m^2-cat).

Photocatalytic test using ethylene as air contaminant showed no reactivity for the amorphous binary Si-Ti-aerogel TS31b. The pure titanium dioxide aerogels, however, successfully catalyzed the complete oxidation of methane, ethane, ethylene, and acetone. No measurable byproducts were detected during photooxidation of the methane, ethane, and ethylene. Acetone oxidation led to the production of unidentified intermediates that were also eventually oxidized.

Comparing the performance of the catalysts on a mass basis in the reactor system, the ultra-low density aerogel T36 was the most active, followed by the low-density CEH6 aerogel. The T36 aerogel was nearly three times as reactive at the Degussa P25 (on a mass basis), while the CEH6 was about 60% more active.

On the other hand, using the actual illuminated catalyst area as the basis for comparison showed that the intrinsic activity of the aerogel is still lower than that of Degussa P25. However, thermal treatments of the aerogel caused a significant increase in intrinsic activity by a factor of three in the case of the ultra-low density aerogel T36. When comparing the reactivity on the basis of catalytic cell window area illuminated – an important criterion for reactor design considerations - the aerogels demonstrated

equivalent initial reaction rates compared to P25, while the low-density aerogel CEH6 demonstrated a reactivity of even twice than that of Degussa.

Deposition of platinum on titanium dioxide is one of the methods to enhance the photocatalytic activity of a catalyst. Photocatalytic co-deposition using hexachloroplatinate, however, decreased the catalyst's activity mostly due to a catalyst surface attack by the acidic H_2PtCl_6 solution. Chemical vapor deposition, in contrast, did lead to an improvement in photocatalytic activity by 50% for the commercial Degussa P25 with 1.2wt% Pt loading and the aerogel T36 with 7.7wt% platinum deposited.

Since room air usually contains a certain humidity the effect of water on the catalyst performance was investigated for Degussa P25, the aerogel T36, and the thermal treated T36_450. The presence of water in the gas phase at initial conditions greatly reduced the photocatalytic activity for ethylene oxidation over all catalysts. The greatest reduction in photoactivity was observed for the heat-treated aerogel T36_450, which showed a decrease in initial ethylene rates by a factor of 2.7 (or 63%) while the initial rates decrease by about 20% for the untreated aerogel T36 and by 24% for the Degussa P25. Even though the intrinsic activity of the aerogel increased after thermal treatment, the number of active sites was reduced at the same time. Competitively adsorbed water thus occupied a larger fraction of active sites leading to a stronger reduction in photoactivity.

Another beneficial characteristic of aerogels is the high adsorption capacity, which was demonstrated during tests of acetone oxidation. Up to 98% of acetone feed to the reactor system was immediately removed from the gas phase. This capacity suggests that sudden high concentrations ('spikes') of a strongly adsorbing contaminant, such as

acetone, can quickly be removed from the gas stream and then subsequently completely oxidized, thus constantly regenerating the aerogel's adsorbent surface via photooxidation of the adsorbed contaminant.

Increasing the mechanical strength of the aerogels is still an issue that needs to be resolved. The use of catalysts in a catalyst bed or when applied on a catalyst support for the use in filters requires a material that is sufficiently mechanically stable to remain on the surface, thus preventing loss of material and releasing small particles into the air stream. The here-investigated aerogels, however, did not show this desired characteristic. Although larger particles along with an increase in crystallinity were obtained from thermal treatment, however the mechanical strength did not change significantly.

The results of this work indicate that the porous low-density aerogels were more effective in destroying the tested contaminants, despite their low anatase crystallinity. Based on mass, the aerogels outperformed the commercially available catalyst with the highest catalytic efficiency (Degussa P25). That the low-crystallinity aerogel performed so well has significance for improvements in photocatalytic activity. Even thought the intrinsic activity of the aerogels was still lower compared to that of the Degussa P25, however, the potential of the aerogels is enormous if the activity of all UV accessible sites could be increased to that of the Degussa.

This study has demonstrated that the TiO_2 aerogels are a competitive candidate for photocatalysis as they carry the potential for improvements in photocatalytic activity and have characteristics that simplifies their utilization for indoor air decontamination applications, e.g., less complicated reactor design.

6 Future Considerations

It was shown that increasing the crystallinity did significantly improve the intrinsic activity of the aerogel catalyst since crystalline structure shows the highest photocatalytic activity. However, a drawback of thermal treatment is that the exposure to heat also resulted in a loss of surface area and porosity. Different methods need to be researched in order to increase the crystallinity . In addition, a more uniform anatase structure is desired since this would lead to a higher mechanical strength of the catalyst. Therefore, if, if the crystallinity can be developed after the synthesis or if an aerogel can be synthesized already possessing a high crystallinity, the aerogel should have the advantages of higher activity plus a greater stability.

The preparation of binary Si-Ti-oxide or titania-coated silica aerogels carry the potential of providing photocatalysts that possess a high mechanical strength besides a high photocatalytic activity. Silica aerogels have shown very good stability at high temperatures, with porosities and surface areas virtually unchanged by treatments at several hundred degrees Celsius.

One imperative characteristic of a catalyst to be employed in indoor air-decontamination systems is a long catalyst life. Even though the aerogel was utilized in many consecutive experimental runs, no specific long-term oxidation studies had been performed on the aerogels yet. Future research should focus on the study of the catalyst life and its deactivation.

All photooxidation studies in this work were performed using a 450 W UV lamp as energy source. With the present reactor setup not all of the UV radiation was used for activating the catalyst. Furthermore, significant heat was generated, which required a constant flow of cool air across the reactor cell. Excessive heat generation downgrades the use of this process for indoor air ventilations and cooling systems. Additionally, conserving energy is as important as decontamination of air. It is therefore of interest to investigate what lower energy sources would lead to similar photocatalytic efficiencies of the aerogel in applications for air decontamination.

7 Appendix

7.1 Appendix to Chapter 3

	Li Cl	*MgCl2*	*KCO3*	*Mg (NO3)2*	*NaBr*	*NaCl*	*KCl*
T, °C	RH, %	RH, %	RH, %	RH, %	RH, %	RH, %	RH, %
0	11.2	33.7	43.1	60.4	62.2	75.5	88.6
10	11.3	33.5	43.1	57.4	59.1	75.7	86.8
20	11.3	33.1	43.2	54.4	56	75.5	85.1
30	11.3	32.4	43.2	51.4	53.2	75.1	83.6
40	11.2	31.6		48.4	50.9	74.7	82.3
50	11.1	30.5		45.4	49.7	74.7	81.2
60	11	29.3				74.5	80.2
70	10.8	27.8				75.1	79.5
80	9.4	26.1				73.9	
90	10.3	24.1				73.8	

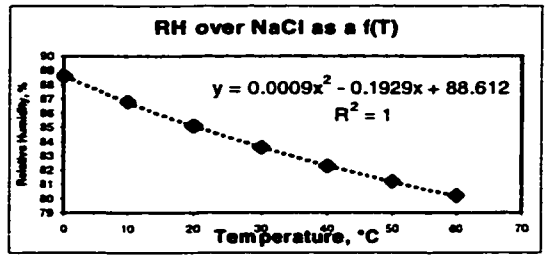

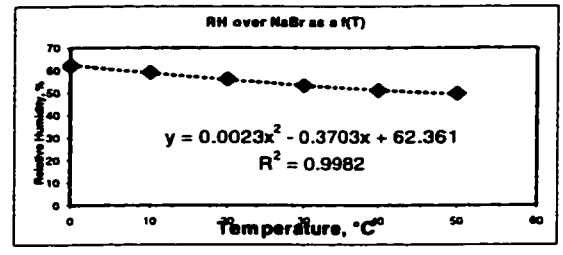

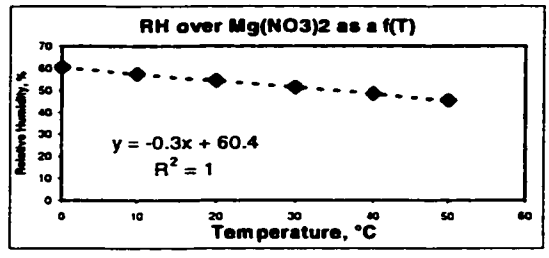

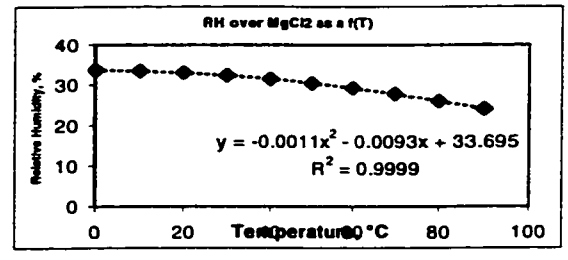

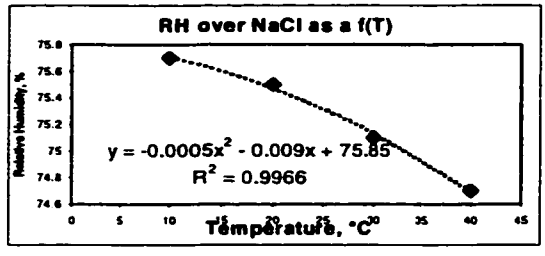

Table 7-1 Relative humidity dependence on temperature for various salt solutions (Data from ASHRAE STANDARD (ANSI/ASHRAE 41.6-1994)

25-Jan-99

P*(T) = 21.26 mmHg
P*(T) = 0.83 inHg
Patm = 29.24 in Hg
T = 23.15 C (was also Room Temperature)

Antoine:
logP*(T), mmHg = A - B/(TinC + C)
A = 8.10765
B = 1750.286
C = 235

	Injected,	GC Area							GC Area	y =	est. RH, %	to g
Room air	10	99	98						99	0.008112	28.6 <-- by calc.	
LiCl	20	71	79	77					76	0.003209	11.3	
by calc-->	10	35.5	39.5	38.5					38	0.003209	11.3 11.3 fixed for 10<T<30	
MgCl2	10	118	126	115	118	114	116		118	0.009341	32.9 y = -0.0011x2 - 0.0093x + 33.695	
KCO3	10	132	138	135					135	0.012269	43.2 43.2 fixed for 20<T<30	
Mg (NO3)2	10	177	188	183	179				182	0.015181	53.5 y = -0.3x + 60.4	
NaBr	10	197	182	191	195	184	199	191	191	0.015626	55.0 y = 0.0023x2 - 0.3703x + 62.361	
NaCl	10	251	271	244	259	258	267		258	0.021406	75.4 y = -0.0005x2 - 0.009x + 75.85	
KCl	10	289	293	305	303	288	312	300	299	0.024035	84.6 y = 0.0009x2 - 0.1929x + 88.612	

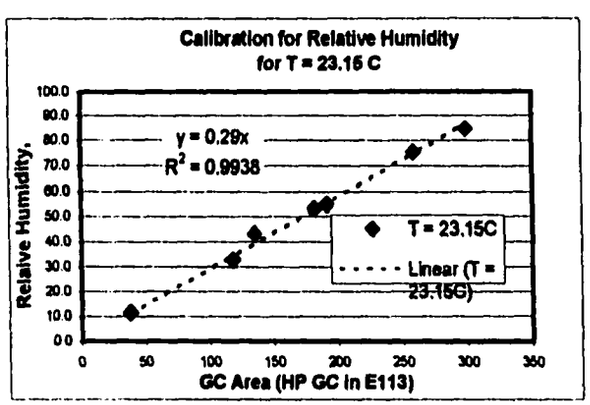

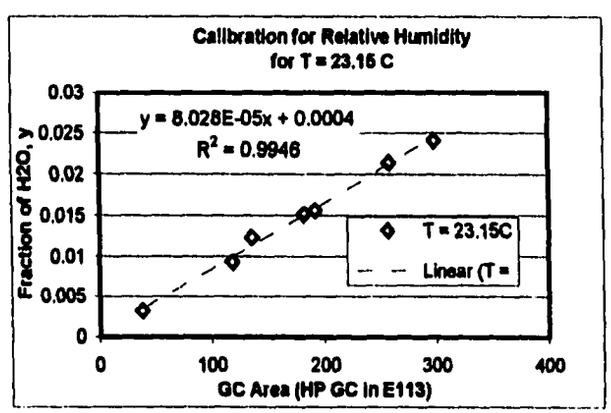

Table 7-2 Example for calibration of GC for relative humidity data.

Flowindicator 0 - 15

1-Feb-02

Scale reading	Volume ml	time, s test 1	test 2	test 3	t avg s	Flowrate ml/min
0						0
1	100	19.10	18.90	18.90	18.97	316.34
2	100	8.9	8.9	9	8.93	671.64
3	100	5.9	5.9	6.1	5.97	1005.59
4	100	4.4	4.4	4.2	4.33	1384.62

pump did not get higher flow rates

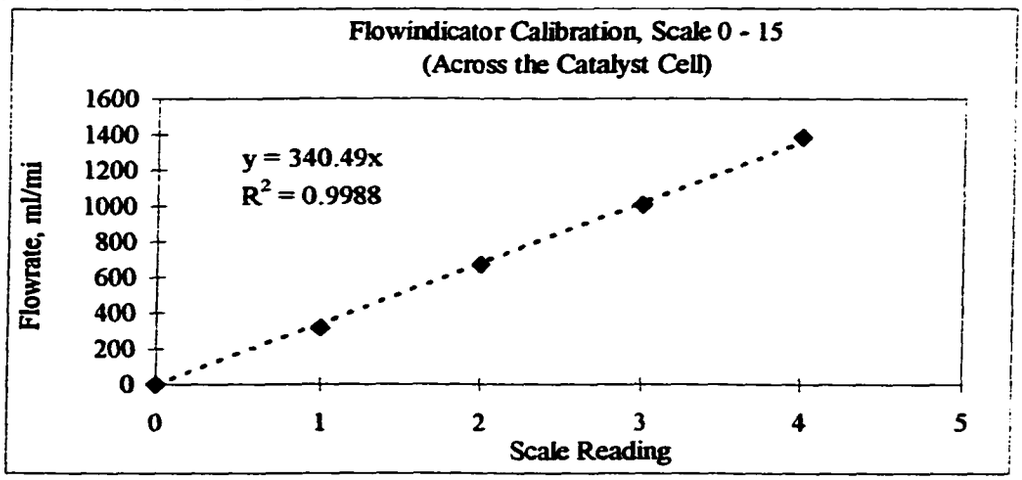

Face Velocity for Scale Reading = 1:

cell dimensions: width =	0.03	in (=1/32 in)
length =	5.80	in
cross section of Cell = 1/32 in * 5 3/8 inch =	0.028	cm^2
Face Velocity = V (ml/min) / A (cm^2) =	**202.0**	**cm/s**

Scale reading	V ml/min	Face Vel cm/s
1	340.5	202.0
1.5	510.7	303.0
2	681.0	404.0

Table 7-3 Flow rate measurement of air circulating in reactor system

7.2 Appendix to Chapter 4

weight of catalyst:		$m_{T36} = 0.0239$ g
weight of rutile added to catalyst:		$m_{rutile} = 0.0041$ g
therefore, weight percent of rutile added to catalyst:		= 14.6wt% rutile
from Integration of peak areas:		ratio anatase : rutile = 1.16
thus, from Figure 4-36:		wt% anatase = 42
	or	wt% rutile = (100-42) = 58
then		anatase : rutile = 42 : 58
		or anatase = 0.72 * rutile
		mass anatase = 0.72 * 0.0041 g
	⇨	mass anatase = $2.96 * 10^3$ g
	⇨	% anatase = mass anatase / mass catalyst
	⇨	% anatase = ($2.96 * 10^3$ g / 0.0239 g)* 100
		anatase = 12.4wt%

Table 7-4 Sample calculation to determine fraction of anatase by weight

Anatase Acetone Adsorption

Whole Reactor System with Anatase Reactor Cell
(no GC by-pass, with degussa cat.cell)
Date: 10/27/96

m cat =	3.74 g		
Volume =	290.57 ml	rho acetone =	0.79 g/cm3
Patm =	29.24 inHg	Mw acetone =	58.08 g/mol
T =	23.20 °C	n, mol = rho*V/Mw =	0.013636364 *V(feed)
C, mmol/L =	7.2004E-08 * GC-Area	Co = n/V sys * 10E6 =	mmol/l

n total, mmol	C theor. mmol/l	GC-Area actual	C actual, mmol/l	m ads., mg	m ads., mg/g-cat	1/Ca	1/m ads.	Langmuir Fit m ads = μ*KC/(1+KC) m ads., mg	m ads./g-cat
0.00	0.00	0	0.00	0.00	0.00	-	-	0.00	0.00
0.68	2.35	26549653	1.91	7.34	1.96	0.52	0.14	8.06	1.93
1.36	4.69	57209446	4.12	9.68	2.59	0.24	0.10	10.78	2.75
2.05	7.04	88140345	6.35	11.70	3.13	0.16	0.09	12.15	3.16
2.73	9.39	119133583	8.58	13.63	3.65	0.12	0.07	12.97	3.40

=> Intercept = 1/μa =	0.0614	=> μa =	16.29 mg
		=	4.35 mg/g-catalyst
=> Slope = 1/(Ka μa) =	0.1471	=> Ka =	0.42 L/mmol
		=	0.007 m^3/g

CEH6 Acetone Adsorption

Whole Reactor System with Aerogel CEH6 Reactor Cell
(no GC by-pass, with CEH6 aerogel cat.cell)
Date: 10/28/96

m cat =	1.30 g		
V system =	289.11 ml	rho acetone =	0.79 g/cm3
Patm =	29.26 inHg	Mw acetone =	58.08 g/mol
T =	23.10 °C	n, mol = rho*V/Mw =	0.0136364 *V(feed)
C, mmol/L =	7.2004 * GC-Area	Co = n/V sys * 10E6 =	mmol/l

n total, mmol	C theor. mmol/l	GC-Area actual	C actual, mmol/l	m ads., mg	m ads., mg/g-cat	1/Ca	1/m ads.	Langmuir Fit m ads = μ*KC/(1+KC) m ads, mg	m ads./g-cat
0.0000	0.00	0	0.00	0.00	0.00	-	-	0.00	0.00
0.6818	2.35	1202804	0.09	38.14	29.34	11.546456	0.0262203	12.88	9.91
1.3636	4.69	10422450	0.75	66.54	51.18	1.3325194	0.0150297	65.24	50.18
2.0455	7.04	25664655	1.85	87.61	67.39	0.5411379	0.0114138	95.23	73.25
2.7273	9.39	42310323	3.05	106.99	82.30	0.3282442	0.009347	108.67	83.59
3.4091	11.73	58273280	4.20	127.19	97.84	0.2383274	0.0078623	115.56	88.89

=> Intercept = 1/μa =	0.0072	=> μa =	138.89 mg
		=	106.84 mg/g-catalyst
=> Slope = 1/(Ka μa) =	0.0061	=> Ka =	1.18 L/mmol
		=	0.02032245 L/mg
		=	0.020 m^3/g

Table 7-5 Data for acetone adsorption on anatase and aerogel

Adsorption Study of Ethane on Anatase

Whole Reactor System with Anatase Reactor Cell
(no GC by-pass, with spiral)
Date: 3/25/97

m cat =	3.74 g		
Volume =	308.98 ml		
Patm =	28.75 inHg	=	0.96 atm
T =	22.20 °C	=	295.35 K
Mw =	30.00 mg/mmol		

Ethane calibration
C, mmol/L = 8.20609E-07x GC Area R2 = 0.9938
R = 0.08206 atm ml/(K mmol)
n, mmol =P,K*Vfeed,ml/(R T,K)
Co, mmol/l = n/Vsys, ml * 1000

V feed ml	n feed mmol	m feed mg	no adsorpt. C theor, mmol/l	actual GC-Area	w/ adsorpt C actual, mmol/l	m ads. mg	m ads. mg/g-cat	1/ C actual	1/m ads	Langmuir Model m ads = μ*KC/(1+KC) mg	mg/g-cat
0	0.00	0.00	0.00	0	0.00	0.00	0.00	–	–	0.00	0.00
3	0.12	3.57	0.38	440164	0.36	0.22	0.06	2.77	4.55	0.09	0.02
6	0.24	7.14	0.77	933849	0.77	0.03	0.01	1.30	30.48	0.16	0.04
9	0.36	10.70	1.15	1445272	1.19	-0.29	-0.08	0.84	-3.46	0.22	0.06
12	0.48	14.27	1.54	1973049	1.62	-0.74	-0.20	0.62	-1.36	0.27	0.07
15	0.59	17.84	1.92	2487827	2.04	-1.08	-0.29	0.49	-0.92	0.31	0.08

no cell in the system
Anatase => Intercept = 1/ μa = 1.3533 l/mg => μa= 0.739 mg
= 0.198 mg/g cat
=> Slope = 1/(Ka μa) = 3.7388 mg/g cat => Ka = 0.362 L/mmol
= 0.0129272 m3/g

Adsorption Study of Ethane on Aerogel CEH6

Whole Reactor System with Anatase Reactor Cell
(no GC by-pass, with spiral)
Date: 3/24/97

m cat =	1.078	g	
Volume =	313.21 ml		
Patm =	28.81 inHg	= 0.962868888	atm
T =	22 °C	= 295.15	K
Mw =	30 mg/mmol		

Ethane calibration
C, mmol/L = 8.20609E-07x GC Area R2 = 0.9938
R = 0.08206 atm ml/(K mmol)
n, mmol =P,K*Vfeed,ml/(R T,K)
Co, mmol/l = n/Vsys, ml * 1000

V feed ml	n feed mmol	m feed mg	no adsorpt. C theor, mmol/l	actual GC-Area	w/ adsorpt C actual, mmol/l	m ads. mg	m ads. mg/g-cat	1/ C actual	1/m ads	Langmuir Model m ads = μ*KC/(1+KC) mg	mg/g-cat
0	0.0000	0.0000	0.0000	0	0.0000	0.0000	0.0000	–	–	0.0000	0.0000
3	0.1193	3.5780	0.3860	313866	0.2576	1.1905	1.1044	3.8826	0.8400	1.2188	1.1306
6	0.2385	7.1559	0.7720	664154	0.5450	2.1040	1.9518	1.8348	0.4753	1.9959	1.8515
9	0.3578	10.7339	1.1580	1047177	0.8593	2.7685	2.5682	1.1637	0.3612	2.5231	2.3405
12	0.4771	14.3118	1.5440	1435980	1.1784	3.3890	3.1438	0.8486	0.2951	2.8803	2.6719
15	0.5963	17.8898	1.9300	2024806	1.6616	2.4880	2.3080	0.6018	0.4019	3.2395	3.0051

Aerogel => Intercept 0.2148 l/mg => μa = 4.66 mg
= 4.32 mg/g cat
=> Slope = 1/(0.156 mg/g cat => Ka = 1.38 L/mmol
= 0.849 m3/g

Table 7-6 Data for ethane adsorption on aerogel CEH6

Adsorption Study of Ethylene on *Anatase*

Whole Reactor System with Anatase Reactor Cell
(no GC by-pass, with spiral)
Date: 4/22-23/97

C, mmol/L = 8.0651E-07x GC Area

m cat =	3.74 g		
Volume =	308.98 ml		
Patm =	28.80 inHg =	0.96 atm	
T =	22.00 °C =	295.15 K	
Mw =	28.00 mg/mmol		

Ethylene calibration
C, mmol/L = 8.0651E-07x GC Area
R2 = 0.9938
n, mmol = P,K*Vfeed,ml/(R T,K)
Co, mmol/L = n feed/Vsys, ml * 1000
R = 0.082057 atm ml/(K mmol)

V feed ml	n feed mmol	m feed mg	no adsorpt. C theor, mmol/l	actual GC-Area	w/ adsorpt C actual, mmol/l	mads. mg	m ads, mg/g-cat	1/ C actua	1/m ads	Langmuir Fit per g-cat m ads = μ*KC/(1+KC) mg	mg/g-cat
0	0.00	0.00	0.00	0	0.00	0.00	0.00	--	--	0.00	0.00
3	0.12	3.34	0.39	306554.333	0.25	1.16	0.31	3.98	0.86	1.29	0.35
6	0.24	6.68	0.77	598198.533	0.49	2.43	0.65	2.04	0.41	2.44	0.65
9	0.36	10.02	1.16	900841.2	0.74	3.62	0.97	1.35	0.28	3.56	0.95
12	0.48	13.35	1.54	1225758.67	1.01	4.65	1.24	0.99	0.21	4.68	1.25
15	0.60	16.69	1.93	1550894.33	1.27	5.68	1.52	0.79	0.18	5.73	1.53

Anatase => Intercept = 1/ μa = 0.0269 1/mg => μa = **37.175 mg**
= **9.940 mg/g cat**
=> Slope = 1/(Ka μa) = 0.1879 mg/g cat => Ka = **0.143 L/mmol**
= **0.005112902 m3/g**

Adsorption Study of Ethylene on Aerogel CEH6

Whole Reactor System with Anatase Reactor Cell
(no GC by-pass, with spiral)
Date: 4/21/97

m cat =	1.08 g		
Volume =	313.21 ml		
Patm =	28.75 inHg =	0.96 atm	
T =	22.20 °C =	295.35 K	
Mw =	28.00 mg/mmol		

Ethylene calibration
C, mmol/L = 8.0651E-07x GC Area
R2 = 0.9938
n, mmol = P,K*Vfeed,ml/(R T,K)
Co, mmol/L = n feed/Vsys, ml * 1000
R = 0.082057 atm ml/(K mmol)

V feed ml	n feed mmol	m feed mg	no adsorpt. C theor, mmol/l	actual GC-Area	w/ adsorpt C actual, mmol/l	m ads. mg	m ads. mg/g-cat	1/ C actua	1/m ads	Langmuir Model m ads = μ*KC/(1+KC) mg	mg/g-cat
0	0.00	0.00	0.00	0	0.00	0.00	0.00	--	--	0.00	0.00
3	0.12	3.33	0.38	259104	0.21	1.49	1.38	4.70	0.67	1.48	1.37
6	0.24	6.66	0.77	553377	0.45	2.73	2.53	2.20	0.37	2.84	2.63
9	0.36	9.99	1.15	850253	0.70	3.95	3.67	1.43	0.25	3.95	3.67
12	0.48	13.32	1.54	1159450	0.95	5.09	4.72	1.05	0.20	4.91	4.56
15	0.59	16.65	1.92	1515291	1.24	5.89	5.47	0.80	0.17	5.82	5.40

Aerogel => Intercept = 1/ μa = 0.0679 => μa = **14.728 mg**
= **13.662 mg/g cat**
=> Slope = 1/(Ka μa) = 0.1291 => Ka = **0.526 L/mmol**
= **0.018783888 m3/g**

Table 7-7 Data for ethylene adsorption on anatase and aerogels CEH6

Adsorption Study of Ethylene on *T36_raw*

Whole Reactor System with T36_raw Reactor Cell with GC by-pass, with spiral

Date:	10/15/98		
m cat =	0.75 g		
Volume =	308.7 ml		
Patm =	28.91 inHg =	0.97 atm	
T =	23.90 °C =	297.05 K	
Mw =	28.00 mg/mmol		

Ethylene calibration:
C, mmol/L = 5.63E-07 * GC Area
R = 0.082057 atm ml/(K mmol)
n, mmol = P,atm*Vfeed,ml/(R T,K)
Co, mmol/l = n/Vsys, ml * 1000

V feed ml	n feed mmol	m feed mg	no adsorpt. C theor, mmol/l	actual GC-Area	w/ adsorpt C actual, mmol/l	m ads. mg	m ads. mg/g-cat	1/ C actual	1/m ads	Langmuir Fit per g-cat m ads = μ*KC/(1+KC) mg	mg/g-cat
0	0.00	0.00	0.00	0	0.00	0.00	0.00	–	–	0.00	0.00
3	0.12	3.33	0.39	455296.667	0.26	1.11	1.49	3.90	0.90	1.20	1.60
6	0.24	6.66	0.77	1010969.33	0.57	1.74	2.32	1.76	0.57	2.05	2.74
9	0.36	9.99	1.16	1597371.67	0.90	2.22	2.96	1.11	0.45	2.62	3.49
12	0.48	13.32	1.54	2212495.67	1.25	2.55	3.40	0.80	0.39	3.01	4.01
15	0.59	16.65	1.93	2822677.67	1.59	2.91	3.88	0.63	0.34	3.29	4.38

=> Intercept = 1/ μs = 0.2023 l/mg
=> μs = 4.94 mg
= 6.59 mg/g cat
=> Slope = 1/(Ka μs) = 0.1619 mg/g cat
=> Ke = 1.25 m^3/mol
0.04463 m^3/g

Table 7-8 Data for ethylene adsorption on aerogel T36

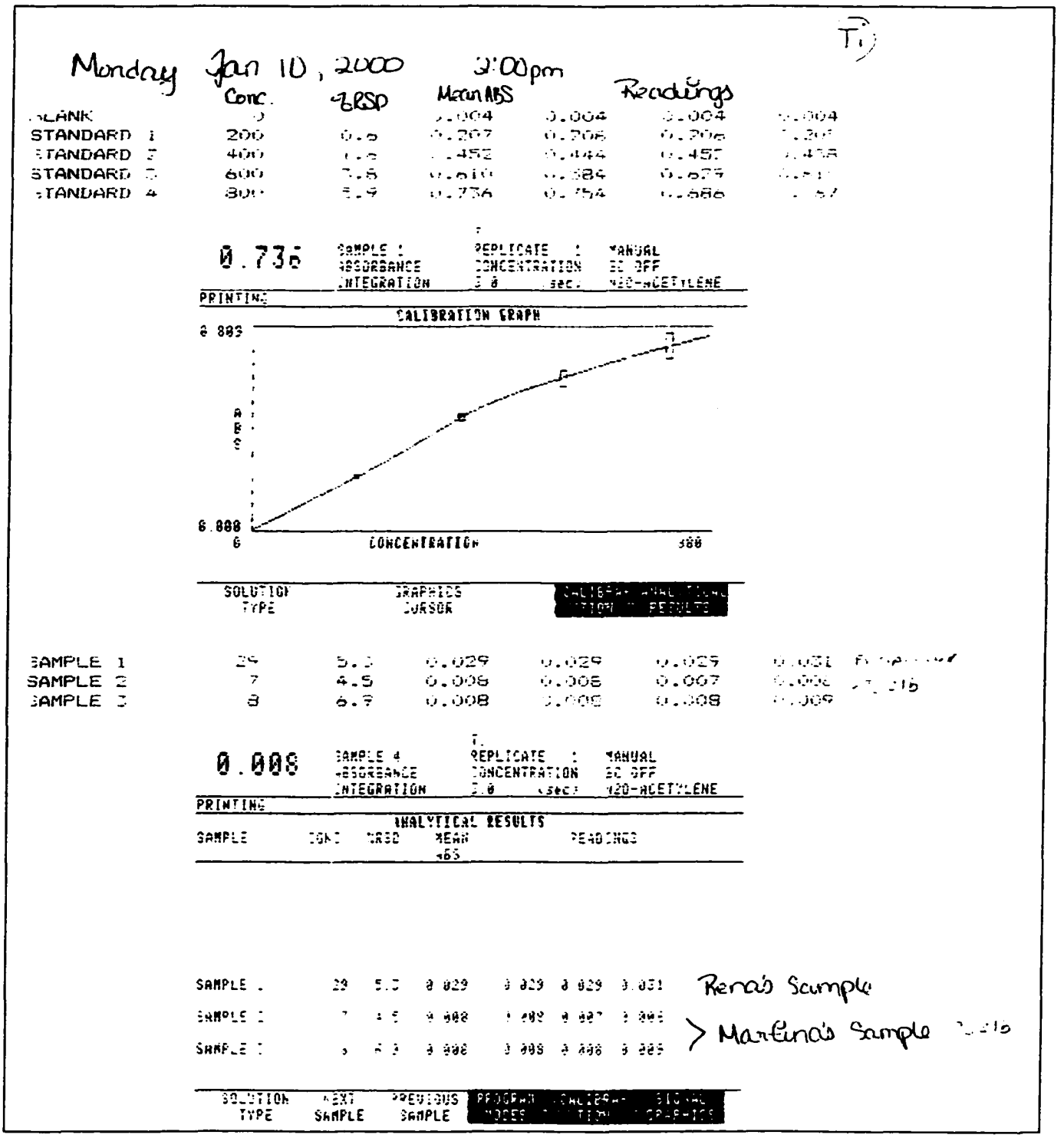

Figure 7-1 AA printout to determine concentration of Ti in binary aerogel TS31b

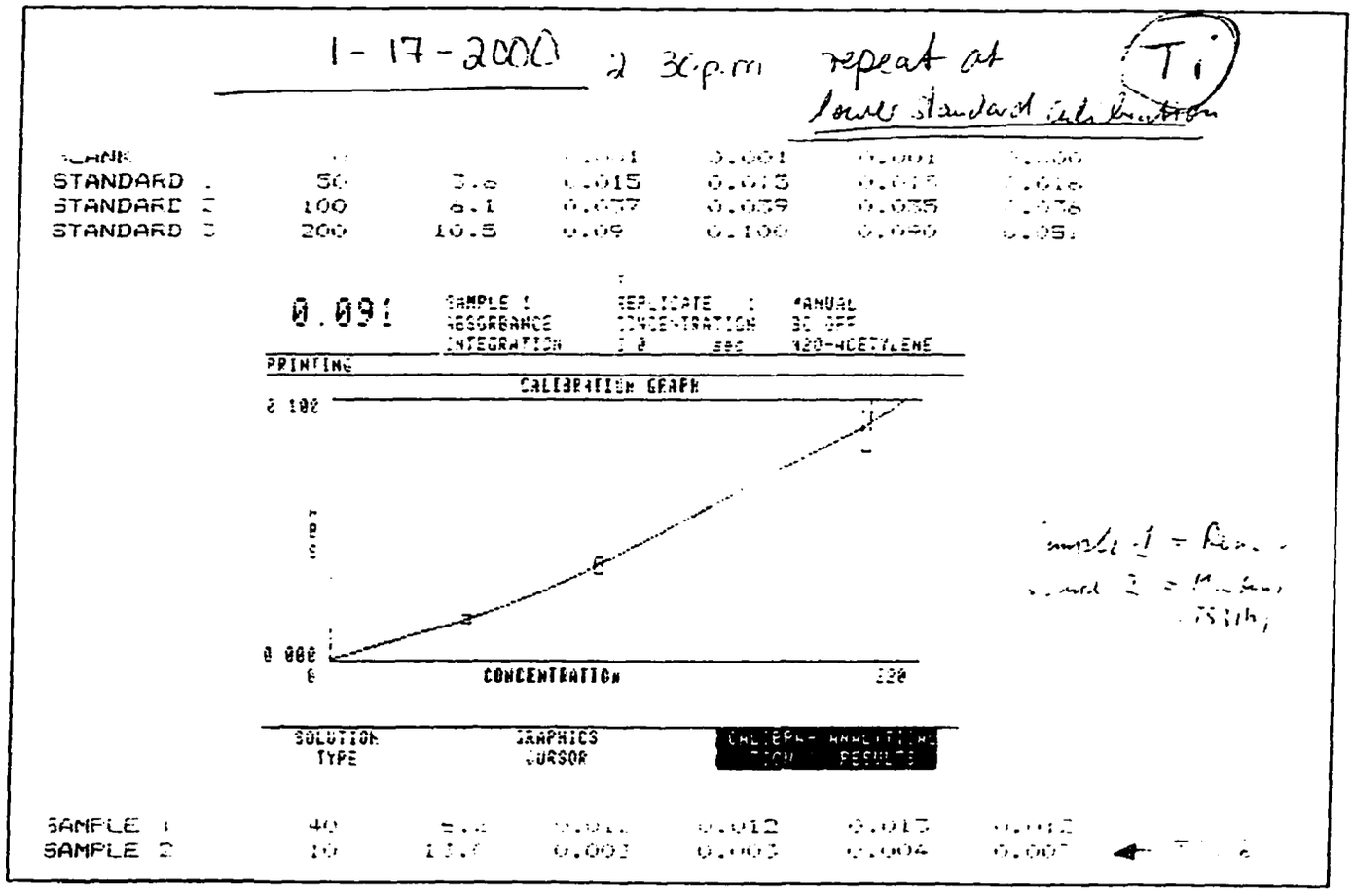

Figure 7-2 AA printout to determine concentration of Ti in binary aerogel TS31, continued

1. Preparation of sample solution for AA:
   1. Dissolve 0.012 g of TS31b in 1 ml of HF (48%)
   2. slowly add DI water to a total volume of 60 ml
   3. use this solution to perform AA measurements

2. AA Results

The measurements were performed twice. The reading indicated 10, 7, and 8 ppm Ti in the prepared solution.

Determination of weight-% Ti in TS31b

m TS31b =	0.012	g
solution volume =	60	ml
AA reading =	10	ppm
	7	ppm
	8	ppm
average AA reading =	**8.3**	**ppm**

$$8.3\ ppm = 8.3\ g / 10^6\ g$$
$$\text{or } 8.3\ ppm = 8.3\ g / 1000000ml\ H_2O$$

mass Ti in 60 ml solution = 8.3 g / 1000000ml * 60 ml
mass Ti in 60 ml solution = 0.0005 g

wt-% Ti in TS31b = 0.0005 g / 0.012 g *100

wt-% Ti in TS31b = 4.2

Table 7-9 Calculation of weight-% Ti in TS31b

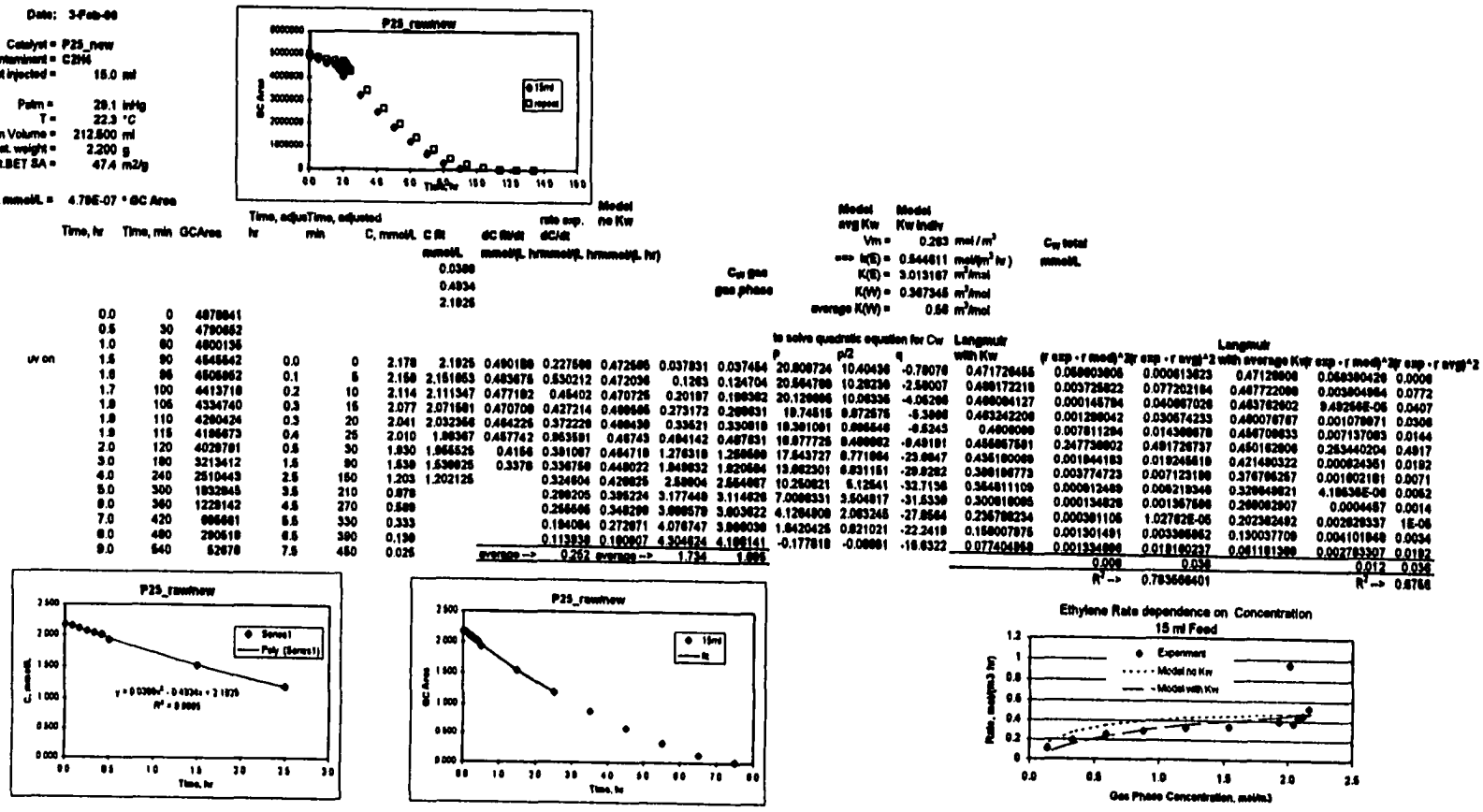

Table 7-10 Example spread sheet of an individual photo oxidation test over Degussa P25 at 15 ml ethylene feed

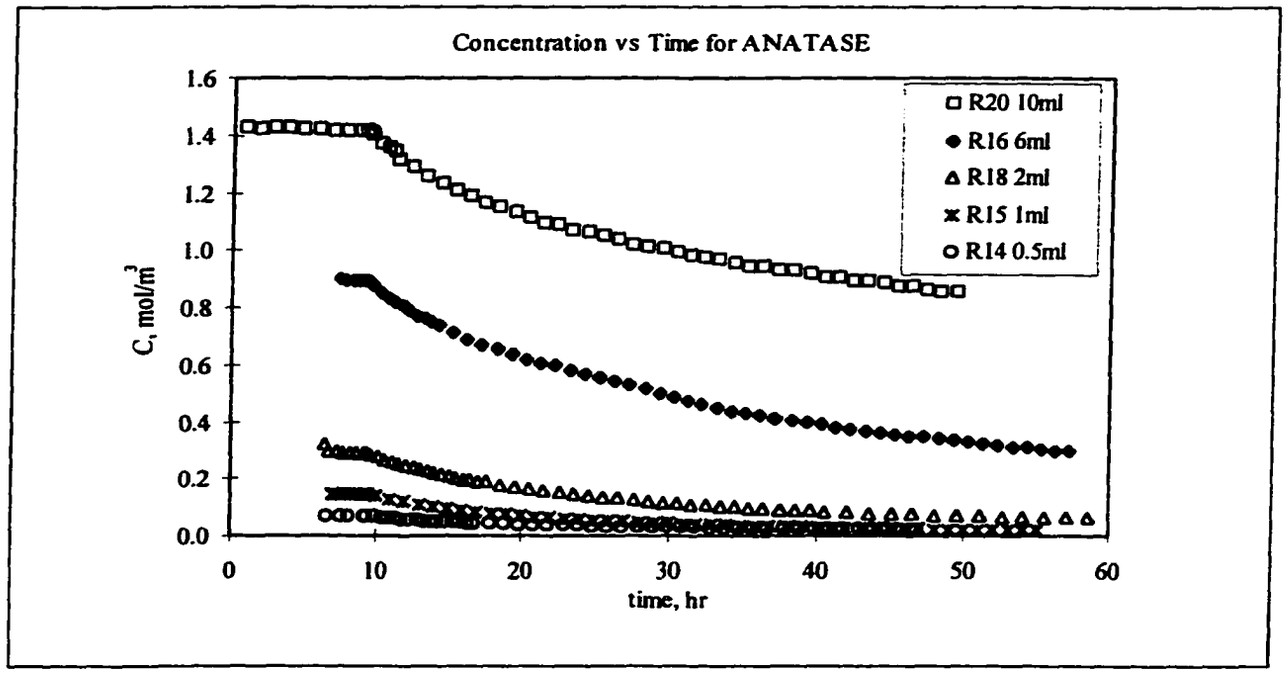

Figure 7-3 Methane Oxidation over Anatase (Aldrich) at different feed concentrations

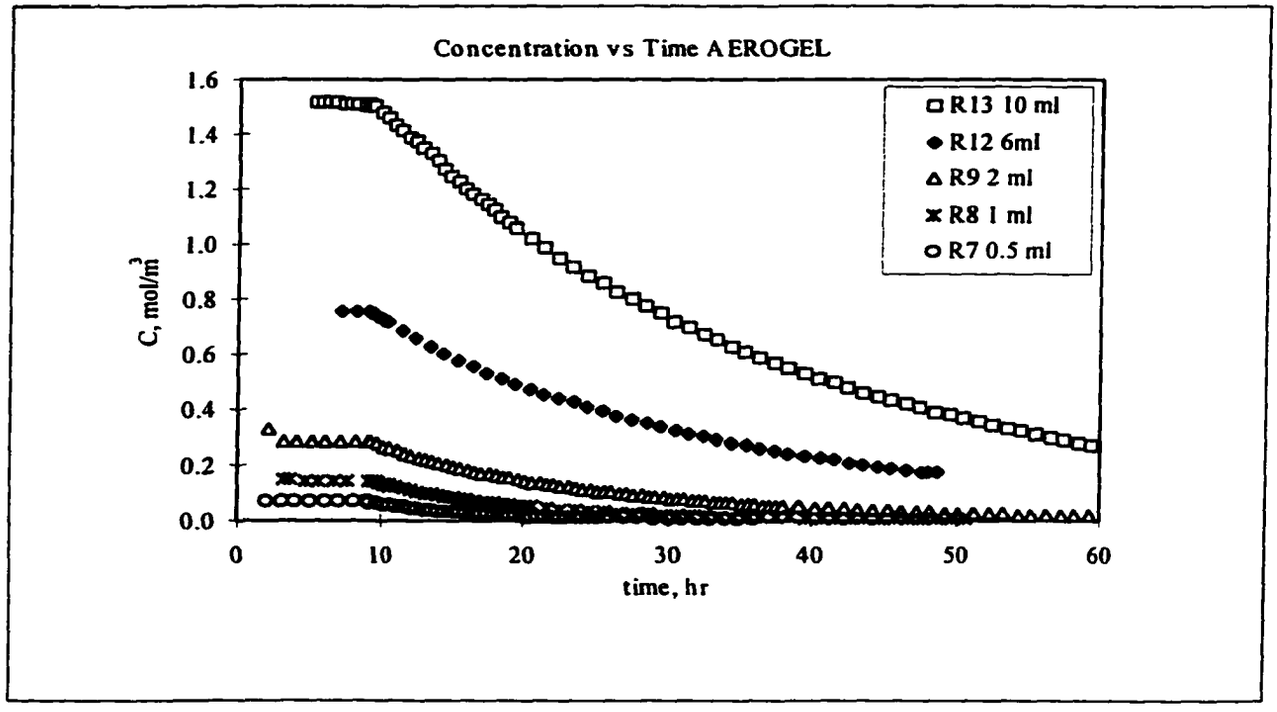

Figure 7-4 Methane Oxidation over Aerogel CEH6 at different CH_4 feed concentrations in a 312 ml photo-reactor

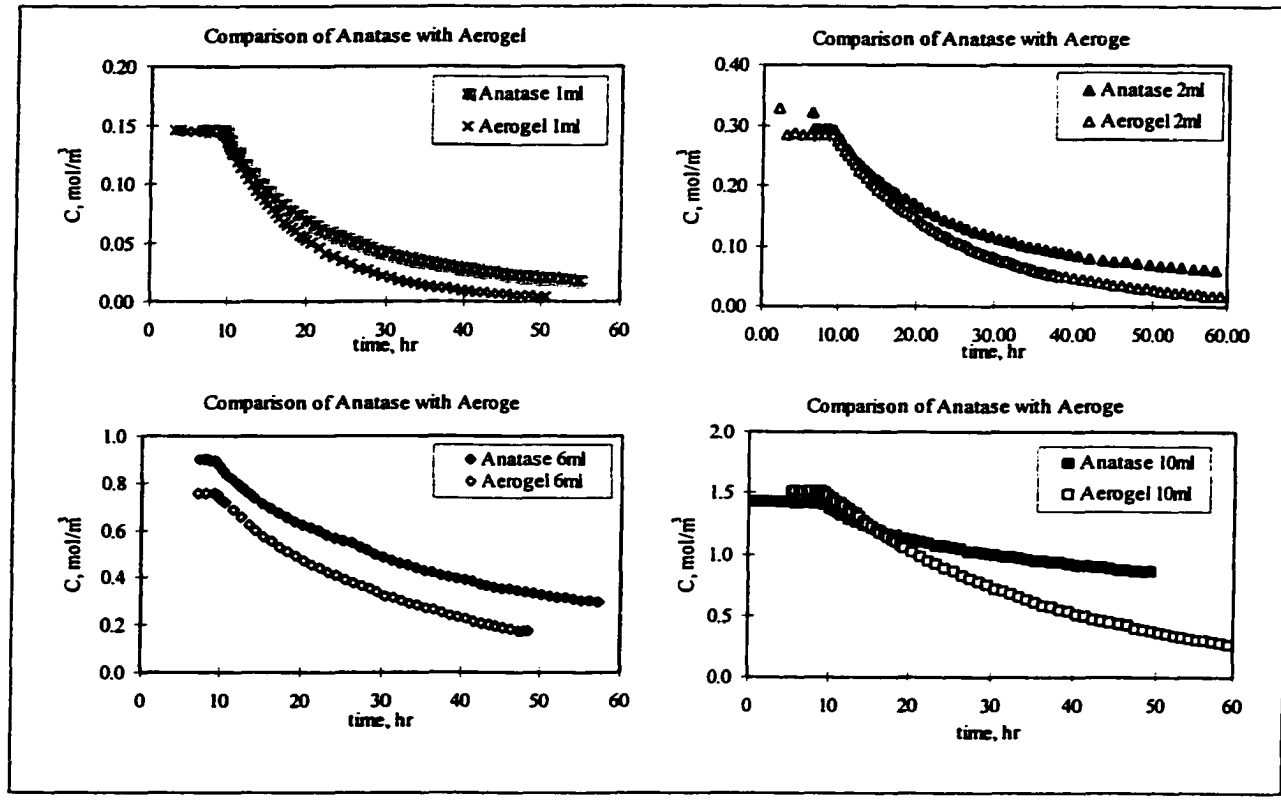

Figure 7-5 Comparison of photocatalytic oxidation over anatase and aerogel at different initial methane feeds (1, 2, 6, 10 ml at STP) in a 298 ml photo-reactor

Vsystem = 289.36 ml

ANATASE		CH_4 Feed ml	avgCo mmol/L	-ro= dC/Dt mmol/(L hr)	-ro mass (mmol)/L (hr g-cat)	o ill Cell windo (mmol)/L (hr cm^2)	-ro ill.cat-SA (mmol)/L (hr cm^2-ill.)	-ro ill.cat-V (mmol)/L (hr cm^3-cat)
m cat, g =	3.7							
ill. cell window area, cm^2=	48.5	0.5	0.070	0.0050	0.0013	0.00010	0.0048	0.2240
Vcat, cm^3 =	3.8	1.0	0.146	0.0118	0.0032	0.00024	0.0115	0.5326
BET SA, m2/g =	47.8	2.0	0.291	0.0180	0.0048	0.00037	0.0174	0.8085
porosity =	0.0	6.0	0.896	0.0426	0.0114	0.00088	0.0413	1.9201
d pore, um =	8.2	10.0	1.407	0.0332	0.0089	0.00068	0.0322	1.4953
ill. cat SA, cm^2=	1.03							
d penet, um =	4.8							
penet. Vol, cm^3=	0.022							

AEROGEL		CH_4 Feed ml	avgCo mmol/L	-ro= dC/Dt mmol/(L hr)	-ro mass (mmol)/L (hr g-cat)	o ill Cell windo (mmol)/L (hr cm^2)	-ro ill.cat-SA (mmol)/L (hr cm^2-ill.)	-ro ill.cat-V (mmol)/L (hr cm^3-cat)
m cat, g =	1.3							
ill. cell window area, cm^2=	26.6							
Vcat, cm^3 =	2.1	0.5	0.066	0.0086	0.0065	0.00033	0.0003	0.0701
BET SA, m2/g =	423.0	1.0	0.144	0.0144	0.0108	0.00054	0.0004	0.1170
porosity =	0.90	2.0	0.284	0.0185	0.0139	0.00069	0.0006	0.1498
d pore, um =	23.0	6.0	0.754	0.0311	0.0234	0.00117	0.0009	0.2520
ill. cat SA, cm^2=	32.9	10.0	1.510	0.0430	0.0323	0.00162	0.0013	0.3488
d penet, um =	46.4							
penet. Vol, cm^3=	0.123							

Table 7-11 Initial rates of methane oxidation of anatase and aerogel CEH6 based on mass in catalytic cell, illuminated cell window area, actual illuminated surface area, and illuminated catalyst volume in catalyst bed

Note: The illuminated catalyst volume was determined according to (7-1), while the actual total illuminated surface area of the catalyst was determined using equation (7-2).

(7-1) $$V_{UV\,ill} = illum.CellWindow * UV\_PentrationDepth$$

(7-2) $$SA_{UV\,ill} = BET\_SA * m_{catalyst} * \frac{UV\_PenetrationDepth}{CatalystBedThickness}$$

where BET_SA = BET catalyst surface area, $m_{catalyst}$ = mass of catalyst in catalytic cell, and catalyst bed thickness = 1/32 inch.

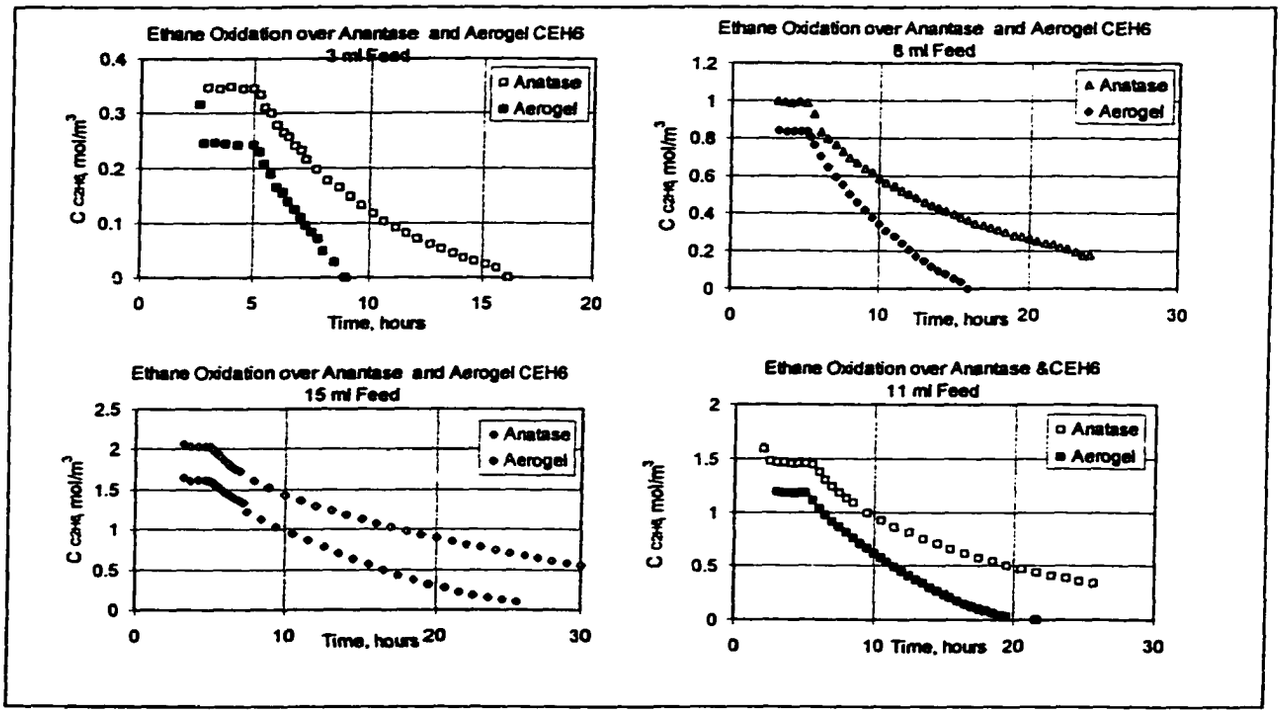

Figure 7-6 Comparison of photocatalytic ethane oxidation over anatase and aerogel at different initial feed concentrations

Vsys = 308.98 ml

Anatase		C_2H_6 Feed ml	avgCe mmol/L	-re= dC/Dt mmol/(L hr)	-ro mass (mmol)/L (hr g-cat)	ill Cell wind (mmol)/L (hr cm^2)	-ro ill.cat-SA (mmol)/L (hr cm^2-ill.)	-ro ill.cat-V (mmol)/L (hr cm^3-cat)
m cat, g =	3.7							
ill. cell window area, cm^2=	48.5							
Vcat, cm^3 =	3.8	3	0.3458	0.0659	0.0176	0.0014	0.0639	2.9659
BET SA, m2/g =	47.8	5	0.7007	0.1399	0.0374	0.0029	0.1356	6.2989
porosity =	0.0	5	0.6737	0.1207	0.0323	0.0025	0.1171	5.4363
d pore, um =	8.2	8	0.9742	0.1198	0.0320	0.0025	0.1162	5.3958
ill. cat SA, m^2=	1.0	11	1.4368	0.1445	0.0386	0.0030	0.1401	6.5083
d penet, um =	4.6	15	2.0435	0.1755	0.0469	0.0036	0.1702	7.9023
penet. Vol, cm^3=	0.022							

Vsys = 313.21ml

AEROGEL		C_2H_6 Feed ml	avgCe mmol/L	-re= dC/Dt mmol/(L hr)	-ro mass (mmol)/L (hr g-cat)	o ill Cell wind (mmol)/L (hr cm^2)	-ro ill.cat-SA (mmol)/L (hr cm^2-ill.)	-ro ill.cat-V (mmol)/L (hr cm^3-cat)
m cat, g =	1.3							
ill. cell window area, cm^2=	26.6							
Vcat, cm^3 =	2.1	3	0.2462	0.0810	0.0609	0.0030	0.0025	0.6572
BET SA, m2/g =	423.0	5	0.5950	0.1325	0.0996	0.0050	0.0040	1.0741
porosity =	0.90	5	0.4792	0.1246	0.0936	0.0047	0.0038	1.0101
d pore, um =	23.0	8	0.8316	0.1305	0.0981	0.0049	0.0040	1.0583
ill. cat SA, m^2=	32.9	11	1.1627	0.1456	0.1094	0.0055	0.0044	1.1804
d penet, um =	46.4	15	1.5475	0.1403	0.1055	0.0053	0.0043	1.1378
penet. Vol, cm^3=	0.123							

Table 7-12 Initial rates of ethane oxidation over anatase and aerogel CEH6 based on mass in catalytic cell, illuminated cell window area, illuminated surface area, and illuminated catalyst volume in catalyst bed

ANATASE μa = 16.29 mg (max adsorbed Acetone for 3.7g cat.)
Ka = 0.42 L/mmol
V sys = 306.96 ml

Anatase		Acetone Feed ml	avgCo mg/L	ro = d(Psi)/dt mg/min	-ro mass mg / (min g-cat)	ill Cell wind mg / (min cm2)	-ro ill.cat-SA mg / (min cm2-ill.)	-ro ill.cat-V mg / (min cm3-cat)
m cat, g =	3.7							
ill. cell window area, cm^2=	48.5							
Vcat, cm^3 =	3.8	0.015	16.217	0.0262	0.0070	0.00054	0.0270	1.1810
BET SA, m^2/g =	45.0	0.025	34.266	0.0311	0.0083	0.00064	0.0320	1.4010
porosity =	0.0	0.050	89.297	0.0453	0.0121	0.00093	0.0466	2.0386
d pore, um =	8.2	0.075	124.081	0.0448	0.0120	0.00092	0.0461	2.0173
ill. cat SA, m^2=	0.97							
d penet, um =	4.6							
penet. Vol, cm^3=	0.022							

DEGUSSA P25 μa = 4.5 mg (max adsorbed Acetone for 2.2 g cat.)
Ka = 0.00021 L/mmol
V sys = 308.98 ml

Degussa P25		Acetone Feed ml	avgCo mg/L	-ro = -d(Psi)/dt mg/min	-ro mass mg / (min g-cat)	ill Cell wind mg / (min cm2)	-ro ill.cat-SA mg / (min cm2-ill.)	-ro ill.cat-V mg / (min cm3-cat)
m cat, g =	2.2							
ill. cell window area, cm^2=	32.9							
Vcat, cm^3 =	2.6	0.025	53.48	0.0472	0.0215	0.0014	0.0792	3.1893
BET SA, m^2/g =	47.8	0.040	64.97	0.0652	0.0296	0.0020	0.1093	4.4010
porosity =	0.00	0.050	110.30	0.0720	0.0327	0.0022	0.1208	4.8627
d pore, um =	0.0	0.750	165.03	0.0769	0.0349	0.0023	0.1290	5.1929
ill. cat SA, m^2=	0.60							
d penet, um =	4.5							
penet. Vol, cm^3=	0.015							

AEROGEL CEH6 μa = 138.890 mg (max adsorbed Acetone for 1.3 g)
Ka = 1.2 L/mmol
V sys = 306.96 ml

AEROGEL		Acetone Feed ml	avgCo mg/L	-ro = -d(Psi)/dt mg/min	-ro mass mg / (min g-cat)	ill Cell wind mg / (min cm2)	-ro ill.cat-SA mg / (min cm2-ill.)	-ro ill.cat-V mg / (min cm3-cat)
m cat, g =	1.3							
ill. cell window area, cm^2=	26.6	0.025	1.04	0.0114	0.0086	0.0004	0.0008	0.1482
Vcat, cm^3 =	2.1	0.050	6.04	0.0325	0.0244	0.0012	0.0022	0.4226
BET SA, m^2/g =	303.73	0.075	11.89	0.0372	0.0280	0.0014	0.0025	0.4841
porosity =	0.84	0.025	1.96	0.0255	0.0192	0.0010	0.0017	0.3314
d pore, um =	185.7	0.075	9.51	0.0264	0.0199	0.0010	0.0018	0.3436
ill. cat SA, m^2=	14.72	0.200	108.97	0.0339	0.0255	0.0013	0.0023	0.4413
d penet, um =	28.9	0.300	178.13	0.0357	0.0268	0.0013	0.0024	0.4641
penet. Vol, cm^3=	0.077							

Table 7-13 Initial rates of acetone oxidation at high initial concentrations over 100% anatase, Degussa P25, and aerogel CEH6 based on mass in catalytic cell, illuminated cell window area, illuminated surface area, and illuminated catalyst volume in catalyst bed

V sys = 236.6 ml

Degussa P25		Acetone Feed ml	avgCo mg/L	-ro = -d(Psi)/dt mg/min	-ro mass mg / (min g-cat)	o ill Cell wind mg / (min cm^2)	-ro ill.cat-SA mg / (min cm^2-ill.)	-ro ill.cat-V mg / (min cm^3-cat)
m cat, g =	2.2							
ill. cell window area, cm^2=	37.2							
Vcat, cm^3 =	3.0	0.005	0.61	0.0044	0.0020	0.0001	0.0074	0.2635
BET SA, m2/g =	47.8	0.010	1.47	0.0089	0.0040	0.0002	0.0149	0.5300
porosity =	0.00	0.015	2.94	0.0146	0.0067	0.0004	0.0246	0.8746
d pore, um =	0.0	0.020	4.35	0.0159	0.0072	0.0004	0.0266	0.9470
ill. cat SA, m^2=	0.60	0.025	7.62	0.0208	0.0095	0.0006	0.0350	1.2452
d penet, um =	4.5							
penet. Vol, cm^3=	0.017							

V sys = 236.6 ml

AEROGEL CEH6		Acetone Feed ml	avgCo mg/L	-ro = -d(Psi)/dt mg/min	-ro mass mg / (min g-cat)	o ill Cell wind mg / (min cm^2)	-ro ill.cat-SA mg / (min cm^2-ill.)	-ro ill.cat-V mg / (min cm^3-cat)
m cat, g =	1.01							
ill. cell window area, cm^2=	22.5							
Vcat, cm^3 =	1.8	0.005	0.09	0.0028	0.0027	0.0001	0.0002	0.0425
BET SA, m2/g =	303.7328	0.010	2.10	0.0349	0.0346	0.0016	0.0031	0.5362
porosity =	0.84	0.015	2.95	0.0408	0.0404	0.0018	0.0037	0.6272
d pore, um =	185.7	0.020	8.01	0.0637	0.0631	0.0028	0.0057	0.9794
ill. cat SA, m^2=	11.18	0.025	8.84	0.0639	0.0632	0.0028	0.0057	0.9812
d penet, um =	28.9							
penet. Vol, cm^3=	0.065							

V sys = 236.6 ml

AEROGEL T38		Acetone Feed ml	avgCo mg/L	-ro = -d(Psi)/dt mg/min	-ro mass mg / (min g-cat)	o ill Cell wind mg / (min cm^2)	-ro ill.cat-SA mg / (min cm^2-ill.)	-ro ill.cat-V mg / (min cm^3-cat)
m cat, g =	0.75							
ill. cell window area, cm^2=	35.9							
Vcat, cm^3 =	2.8	0.005	0.46	0.0179	0.0239	0.0005	0.0030	0.2681
BET SA, m2/g =	336.976	0.010	1.39	0.0322	0.0429	0.0009	0.0054	0.4815
porosity =	0.76	0.015	1.72	0.0371	0.0494	0.0010	0.0063	0.5550
d pore, um =	96.7	0.020	2.91	0.0408	0.0544	0.0011	0.0069	0.6107
ill. cat SA, m^2=	5.93	0.025	4.62	0.0514	0.0686	0.0014	0.0087	0.7699
d penet, um =	18.6							
penet. Vol, cm^3=	0.067							

Table 7-14 Initial rates of acetone oxidation at low initial concentrations over 100% anatase, Degussa P25, and aerogel CEH6 based on mass in catalytic cell, illuminated cell window area, illuminated surface area, and illuminated catalyst volume in catalyst bed

V sys = 216.48 ml

Degussa P25		Ethylene Feed ml	avgCo mol/m³	ro = dC/dt mol/(m³ hr)	-ro mass mol / (m³ hr g-cat)	ll Cell win mol / (m³ hr cm²)	o ill.cat-S mol / (m³ hr cm²-ill.)	ro ill.cat-V mol / (m³ r cm³-cat
m cat, g =	2.2							
ill. cell window area, cm²=	37.2	3	0.226	0.2383	0.1083	0.00641	0.3997	14.2354
Vcat, cm³ =	3.0	5	0.516	0.3270	0.1486	0.00879	0.5485	19.5345
BET SA, m2/g =	47.8	7	0.770	0.3776	0.1717	0.01015	0.6334	22.5587
porosity =	0.00	10	1.272	0.4550	0.2068	0.01223	0.7632	27.1809
d pore, um =	0.0	12	1.630	0.4405	0.2002	0.01184	0.7389	26.3152
ill. cat SA, m²=	0.60	15	2.172	0.4902	0.2228	0.01318	0.8222	29.2807
d penet, um =	4.5	15	2.214	0.4517	0.2053	0.01214	0.7577	26.9858
penet. Vol, cm³=	0.017							

V sys = 313.2 ml

AEROGEL CEH6		Ethylene Feed ml	avgCo mol/m³	ro = dC/dt mol/(m³ hr)	-ro mass mol / (m³ hr g-cat)	ill Cell wind mol / (m³ hr cm²)	-ro ill.cat-SA mol / (m³ hr cm²-ill.)	-ro ill.cat-V mol / (m³ hr cm³-cat)
m cat, g =	1.3	3	0.242823611	0.305716667	0.2299	0.01150	0.0208	3.9762
ill. cell window area, cm²=	26.6	5	0.568	0.2494	0.1875	0.00938	0.0169	3.2438
Vcat, cm³ =	2.1	7	0.613	0.2329	0.1751	0.00876	0.0158	3.0291
BET SA, m2/g =	303.7328	7	0.811	0.2984	0.2244	0.01123	0.0203	3.8809
porosity =	0.84	10	1.100	0.3043	0.2288	0.01145	0.0207	3.9571
d pore, um =	185.7	12	1.307	0.3591	0.2700	0.01351	0.0244	4.6705
ill. cat SA, m²=	14.72	12	0.917	0.2542	0.1911	0.00956	0.0173	3.3055
d penet, um =	28.9	15	1.374	0.3129	0.2352	0.01177	0.0213	4.0692
penet. Vol, cm³=	0.077							

V sys = 314.27 ml

AEROGEL T36		Ethylene Feed ml	avgCo mol/m³	ro = dC/dt mol/(m³ hr)	-ro mass mol / (m³ hr g-cat)	ro ill Cell windo mol / (m³ hr cm²)	-ro ill.cat-SA mol / (m³ hr cm²-ill.)	-ro ill.cat-V mol / (m³ hr cm³-cat)
m cat, g =	0.75							
ill. cell window area, cm²=	40.2							
Vcat, cm³ =	3.2	3	0.218	0.2732	0.3643	0.00680	0.0461	3.6521
BET SA, m²/g =	337.0	5	0.411	0.3427	0.4569	0.00852	0.0578	4.5802
porosity =	0.76	7	0.611	0.3559	0.4745	0.00885	0.0601	4.7569
d pore, um =	96.7	10	0.939	0.3656	0.4874	0.00909	0.0617	4.8865
ill. cat SA, m²=	5.93	12	1.170	0.3917	0.5223	0.00974	0.0661	5.2359
d penet, um =	18.6	15	1.440	0.4390	0.5853	0.01092	0.0741	5.8679
penet. Vol, cm³=	0.075							

System Volume = 295.10 ml

AEROGEL T36_450		Ethylene Feed ml	avgCo mol/m³	ro = dC/dt mol/(m³ hr)	-ro mass mol / (m³ hr g-cat)	ill Cell wind mol / (m³ hr cm²)	-ro ill.cat-SA mol / (m³ hr cm²-ill.)	-ro ill.cat-V mol / (m³ hr cm³-cat)
m cat, g =	1.30							
ill. cell window area, cm²=	40.2							
Vcat, cm³ =	3.2	3	0.179	0.3115	0.2396	0.00775	0.0775	2.9752
BET SA, m²/g =	94.2	5	0.342	0.3687	0.2836	0.00917	0.0918	3.5221
porosity =	0.61	7	0.605	0.4664	0.3588	0.01160	0.1161	4.4554
d pore, um =	96.7	10	0.939	0.5093	0.3918	0.01267	0.1268	4.8654
ill. cat SA, m²=	4.02	12	1.189	0.5054	0.3888	0.01257	0.1258	4.8282
d penet, um =	26.0	15	1.642	0.6262	0.4817	0.01558	0.1558	5.9818
penet. Vol, cm³=	0.105							

Table 7-15 Initial rates of ethylene oxidation at initial high concentrations over Degussa P25, the aerogel CEH6, and the aerogel T36 and heat-treated T36_450 based on mass in catalytic cell, illuminated cell window area, illuminated surface area, and illuminated catalyst volume in catalyst bed

V sys = 216.48 ml

Degussa P25		Ethylene Feed ml	avgCo mol/m^3	ro = dC/dt mol/(m^3 hr)	-ro mass mol / (m^3 hr g-cat)	ll Cell win mol / (m^3 hr cm^2)	o ill.cat-S mol / (m^3 hr cm^2-ill.)	ro ill.cat-mol / (m^3 r cm^3-cat
m cat, g =	2.2							
ill. cell window area, cm^2=	37.2							
Vcat, cm^3 =	3.0	0.1	0.008	0.0382	0.0174	0.00103	0.0641	2.2820
BET SA, m2/g =	47.8	0.3	0.025	0.0646	0.0293	0.00174	0.1083	3.8560
porosity =	0.00	0.5	0.044	0.0877	0.0399	0.00236	0.1471	5.2404
d pore, um =	0.0	0.5	0.043	0.0904	0.0411	0.00243	0.1516	5.4007
ill. cat SA, m^2=	0.60	0.7	0.068	0.1416	0.0644	0.00381	0.2376	8.4608
d penet, um =	4.5	1.0	0.107	0.1273	0.0578	0.00342	0.2135	7.6021
penet. Vol, cm^3=	0.017							

V sys = 216.48 ml

AEROGEL T36		Ethylene Feed ml	avgCo mol/m^3	ro = dC/dt mol/(m^3 hr)	-ro mass mol / (m^3 hr g-cat)	ll Cell win mol / (m^3 hr cm^2)	o ill.cat-S mol / (m^3 hr cm^2-ill.)	ro ill.cat-mol / (m^3 r cm^3-cat
m cat, g =	0.75							
ill. cell window area, cm^2=	35.9	0.1	0.008	0.0434	0.0579	0.00121	0.0070	0.6220
Vcat, cm^3 =	2.8	0.2	0.016	0.0676	0.0902	0.00188	0.0109	0.9695
BET SA, m^2/g =	336.976	0.3	0.025	0.0909	0.1212	0.00253	0.0147	1.3031
porosity =	0.77	0.5	0.039	0.0936	0.1248	0.00261	0.0151	1.3421
d pore, um =	96.7	0.7	0.060	0.1403	0.1871	0.00391	0.0227	2.0113
ill. cat SA, m^2=	6.19	1.0	0.103	0.1892	0.2523	0.00527	0.0306	2.7124
d penet, um =	19.4							
penet. Vol, cm^3=	0.070							

Table 7-16 Initial rates of ethylene oxidation at initial low concentrations over Degussa P25 and the aerogel T36 based on mass in catalytic cell, illuminated cell window area, illuminated surface area, and illuminated catalyst volume in catalyst bed

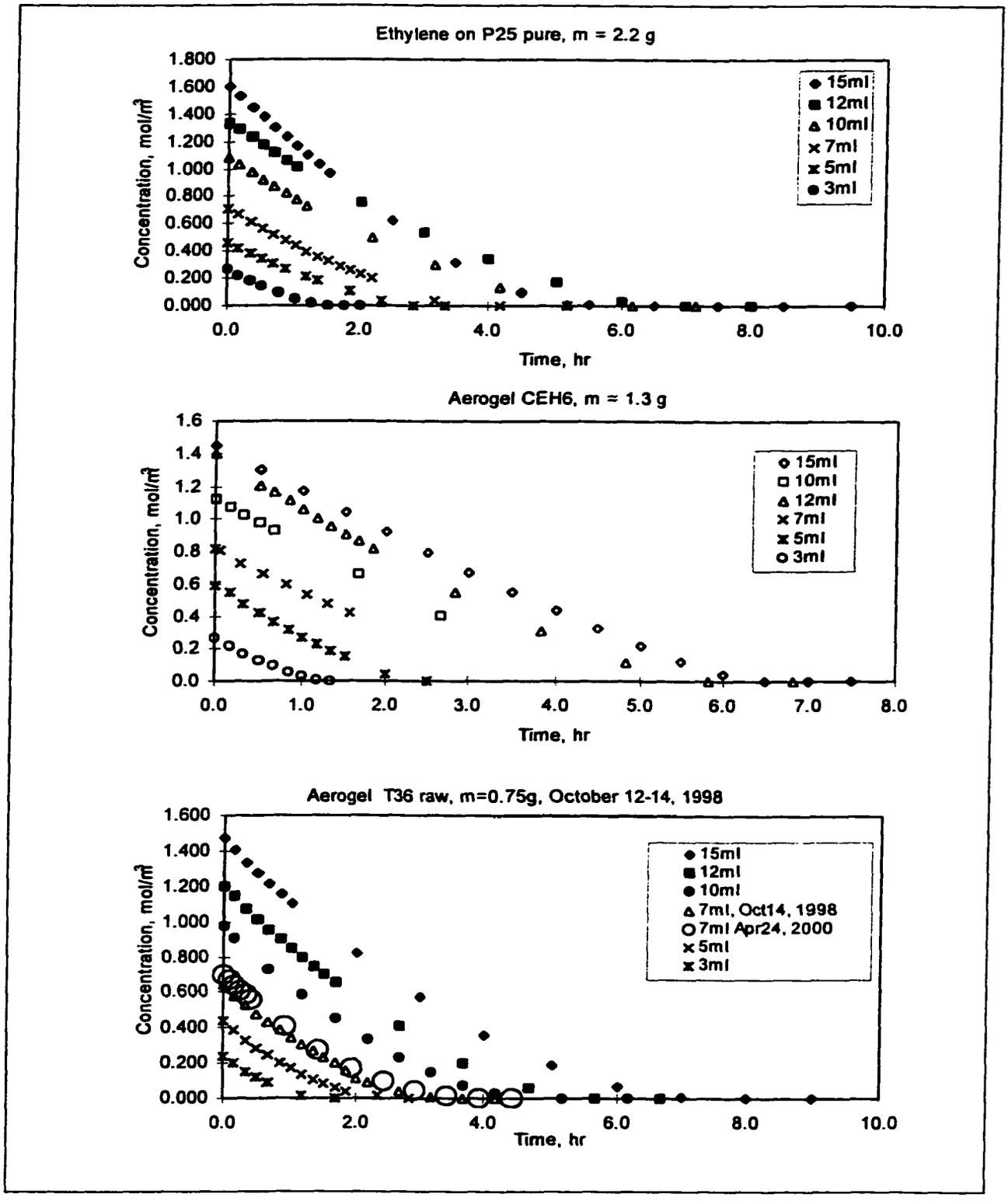

Figure 7-7 Ethylene oxidation over Degussa P25, and the aerogels CEH6 and T36 at different initial ethylene concentrations

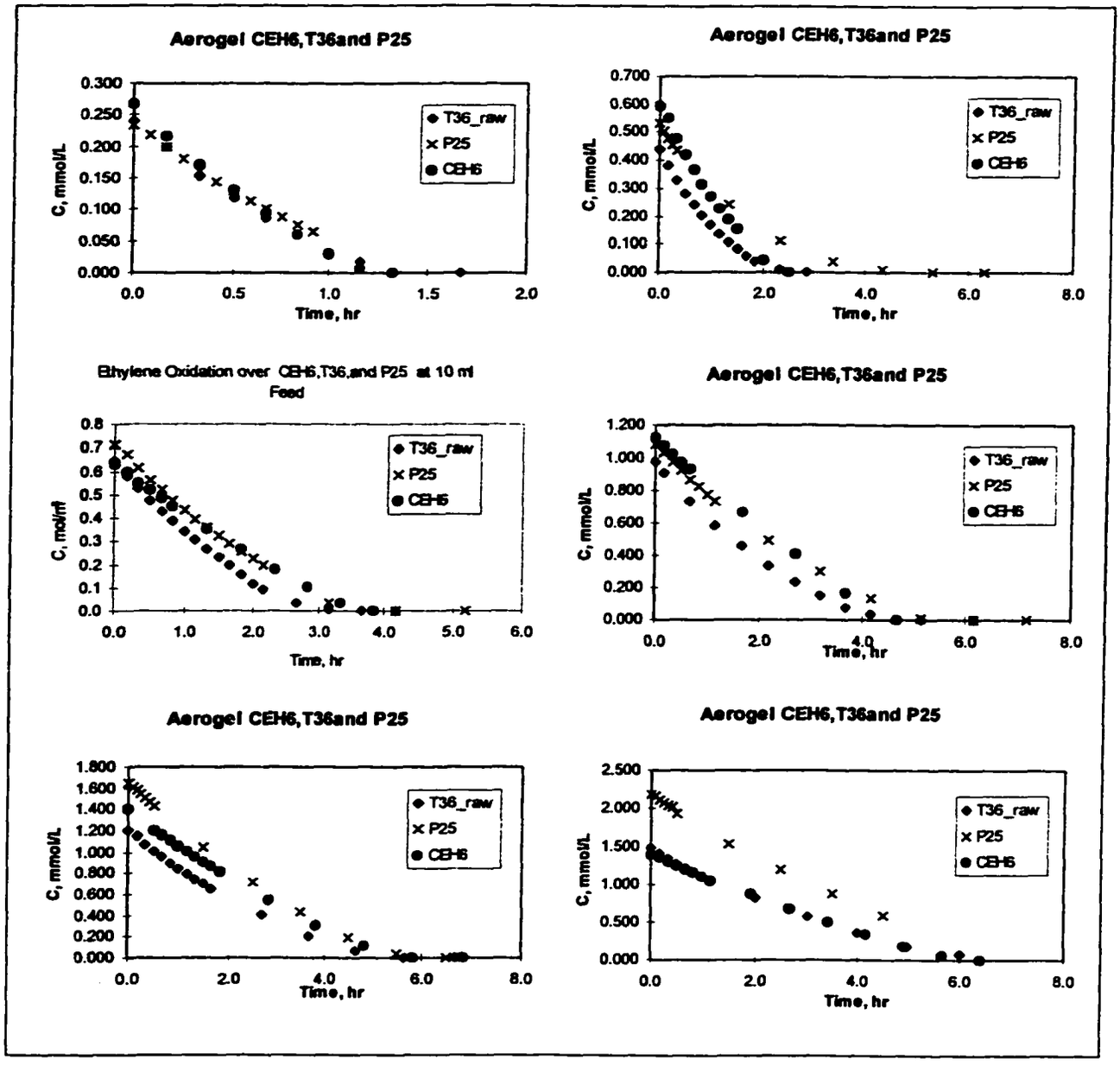

Figure 7-8 Comparison of ethylene oxidation over aerogels T36, CEH6 and the Degussa P25 at different initial ethylene concentrations

Degussa P25		Ethylene Feed ml	avgCo mol/m³	ro = dC/dt mol/(m³ hr)	-ro mass mol / (m³ hr g-cat)	o ill Cell windo mol / (m³ hr cm²)	-ro ill.cat-SA mol / (m³ hr cm²-ill.)	-ro ill.cat-V mol / (m³ hr cm³-cat)
m cat, g =	2.20							
ill. cell window area, cm²=	32.9							
Vcat, cm³ =	2.6	3	0.244	0.2762	0.1255	0.00839	0.4632	18.6525
BET SA, m²/g =	47.8	5	0.441	0.2400	0.1091	0.00729	0.4025	16.2096
porosity =	0.0	7	0.690	0.3071	0.1396	0.00933	0.5151	20.7407
d pore, um =	0.0	10	1.059	0.3396	0.1544	0.01032	0.5697	22.9404
total UV ill. cat-SA, m²=	0.596	12	1.312	0.3470	0.1578	0.01055	0.5821	23.4414
d penet, um =	4.5	15	1.566	0.4668	0.2122	0.01419	0.7830	31.5321
penet. Vol, cm³=	0.015							

Table 7-17 Initial rate data for ethylene oxidation over Degussa P25

V sys = 313.2 ml

AEROGEL CEH6		Ethylene Feed ml	avgCo mol/m³	ro = dC/dt mol/(m³ hr)	-ro mass mol / (m³ hr g-cat)	ill Cell wind mol / (m³ hr cm²)	-ro ill.cat-SA mol / (m³ hr cm²-ill.)	-ro ill.cat-V mol / (m³ hr cm³-cat)
m cat, g =	1.3	3	0.242823611	0.305716667	0.2299	0.01150	0.0208	3.9762
ill. cell window area, cm²=	26.6	5	0.568	0.2494	0.1875	0.00938	0.0169	3.2438
Vcat, cm³ =	2.1	7	0.613	0.2329	0.1751	0.00876	0.0158	3.0291
BET SA, m2/g =	303.7328	7	0.811	0.2984	0.2244	0.01123	0.0203	3.8809
porosity =	0.84	10	1.100	0.3043	0.2288	0.01145	0.0207	3.9571
d pore, um =	185.7	12	1.307	0.3591	0.2700	0.01351	0.0244	4.6705
ill. cat SA, m²=	14.72	12	0.917	0.2542	0.1911	0.00956	0.0173	3.3055
d penet, um =	28.9	15	1.374	0.3129	0.2352	0.01177	0.0213	4.0692
penet. Vol, cm³=	0.077							

Table 7-18 Initial rate data for ethylene oxidation over the aerogel CEH6

V sys = 314.27 ml

AEROGEL T36		Ethylene Feed ml	avgCo mol/m³	ro = dC/dt mol/(m³ hr)	-ro mass mol / (m³ hr g-cat)	ro ill Cell windo mol / (m³ hr cm²)	-ro ill.cat-SA mol / (m³ hr cm²-ill.)	-ro ill.cat-V mol / (m³ hr cm³-cat)
m cat, g =	0.75							
ill. cell window area, cm²=	40.2							
Vcat, cm³ =	3.2	3	0.218	0.2732	0.3643	0.00680	0.0461	3.6521
BET SA, m²/g =	337.0	5	0.411	0.3427	0.4569	0.00852	0.0576	4.5802
porosity =	0.76	7	0.611	0.3559	0.4745	0.00885	0.0601	4.7569
d pore, um =	96.7	10	0.939	0.3656	0.4874	0.00909	0.0617	4.8865
ill. cat SA, m²=	5.93	12	1.170	0.3917	0.5223	0.00974	0.0661	5.2359
d penet, um =	18.6	15	1.440	0.4390	0.5853	0.01092	0.0741	5.8679
penet. Vol, cm³=	0.075							

Table 7-19 Initial rate data for ethylene oxidation over the aerogel T36

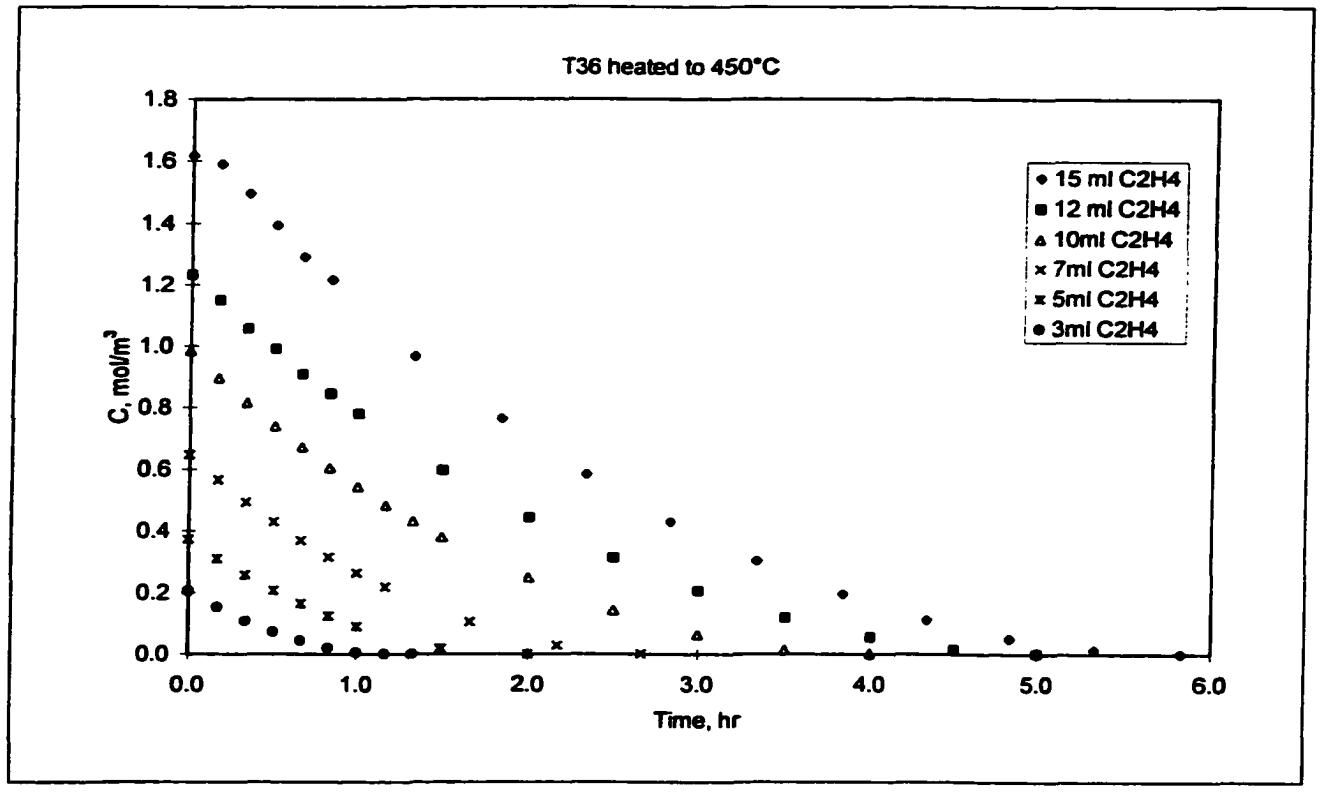

Figure 7-9 Ethylene oxidation over heat-treated aerogel T36_450 at different initial concentrations

System Volume = 295.10 ml

AEROGEL T36_450		Ethylene Feed ml	avgCe mol/m³	ra = dC/dt mol/(m³ hr)	-ro mass mol / (m³ hr g-cat)	ill Cell wind mol / (m³ hr cm²)	-ro ill.cat-SA mol / (m³ hr cm²-ill.)	-ro ill.cat-V mol / (m³ hr cm³-cat)
m cat, g =	1.30							
ill. cell window area, cm²=	40.2							
Vcat, cm³ =	3.2	3	0.179	0.3115	0.2396	0.00775	0.0775	2.9752
BET SA, m²/g =	94.2	5	0.342	0.3687	0.2836	0.00917	0.0918	3.5221
porosity =	0.61	7	0.605	0.4664	0.3588	0.01160	0.1161	4.4554
d pore, um =	96.7	10	0.939	0.5093	0.3918	0.01267	0.1268	4.8654
ill. cat SA, m²=	4.02	12	1.189	0.5054	0.3888	0.01257	0.1258	4.8282
d penet, um =	26.0	15	1.642	0.6262	0.4817	0.01558	0.1558	5.9818
penet. Vol, cm³=	0.105							

Table 7-20 Initial rate data for ethylene oxidation over the heat-treated aerogel T36_450

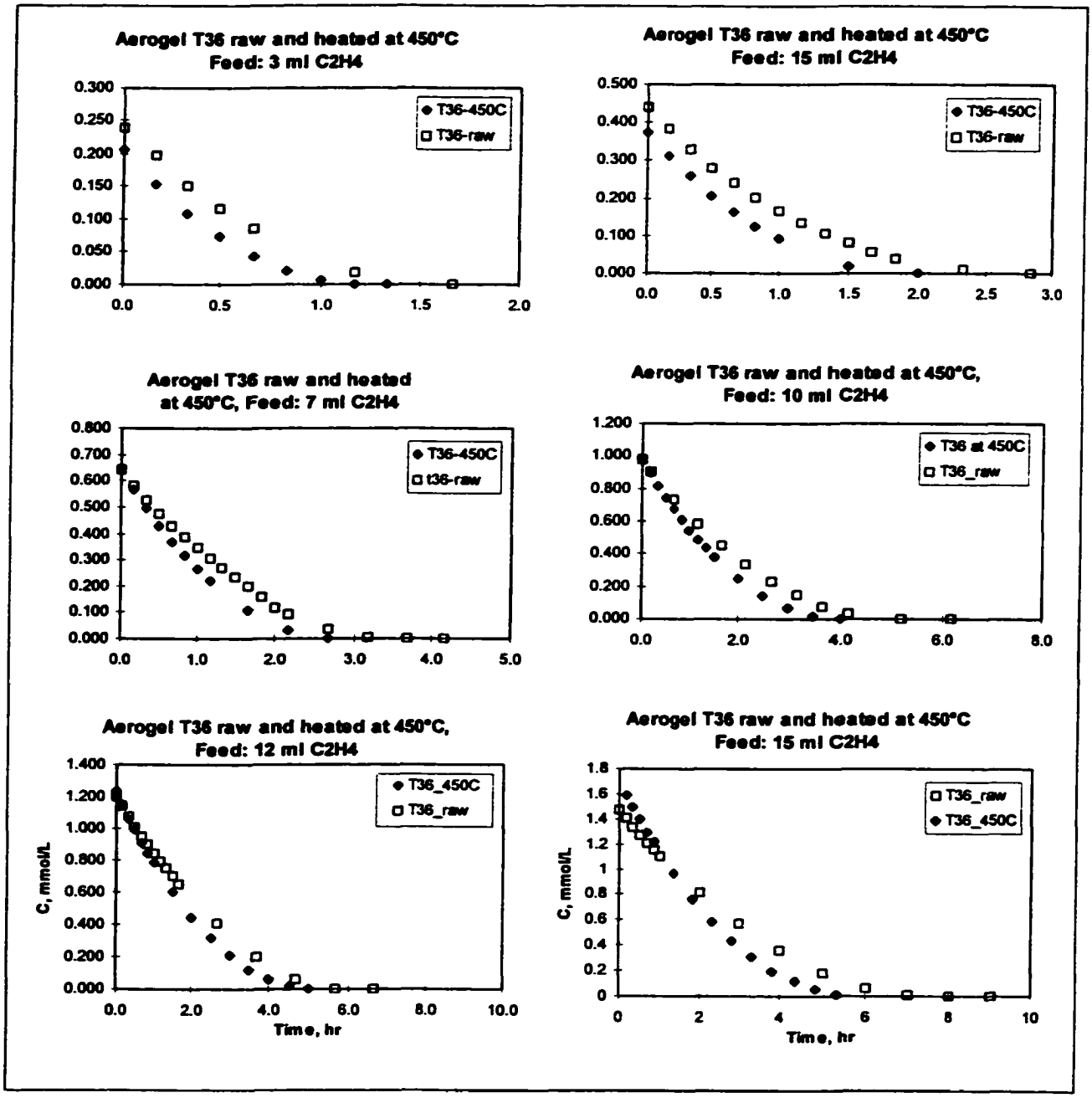

Figure 7-10 Ethylene oxidation over T36_450 compared to the untreated T36 at different initial ethylene concentrations

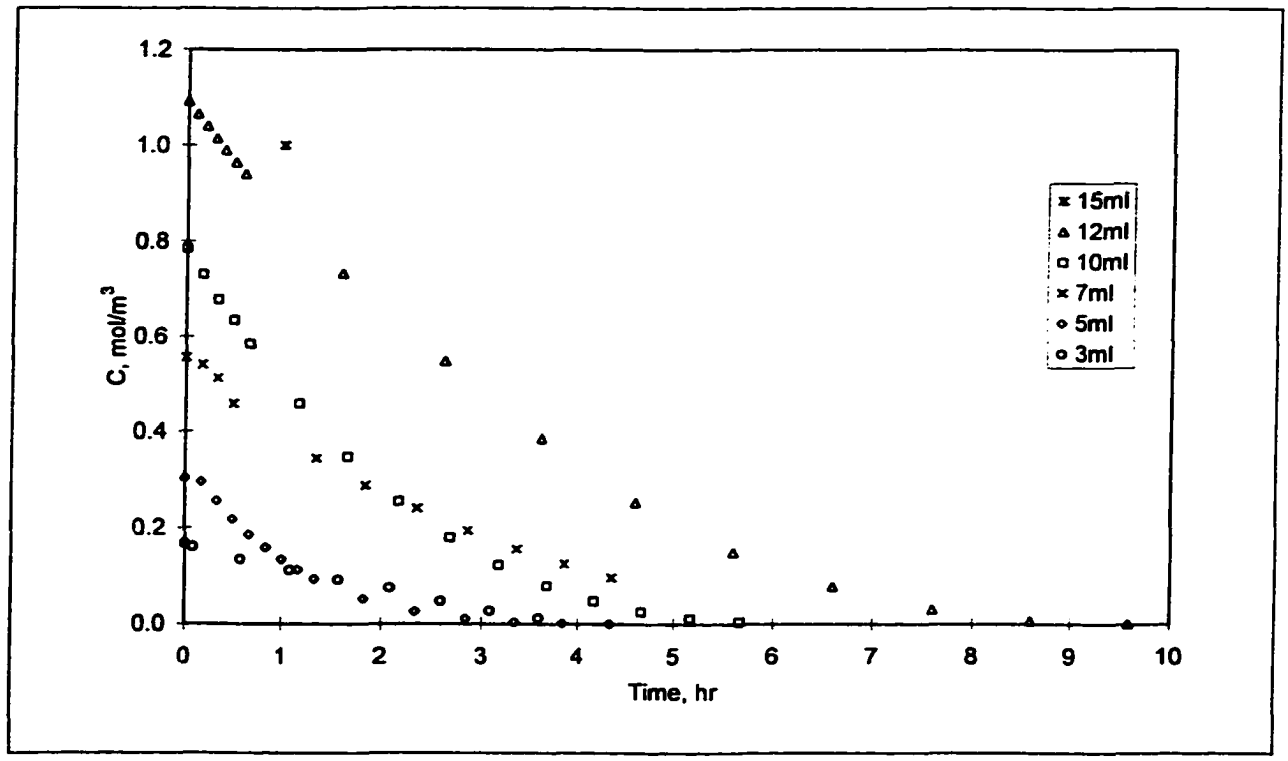

Figure 7-11 Ethylene oxidation over Degussa P25 under humid conditions

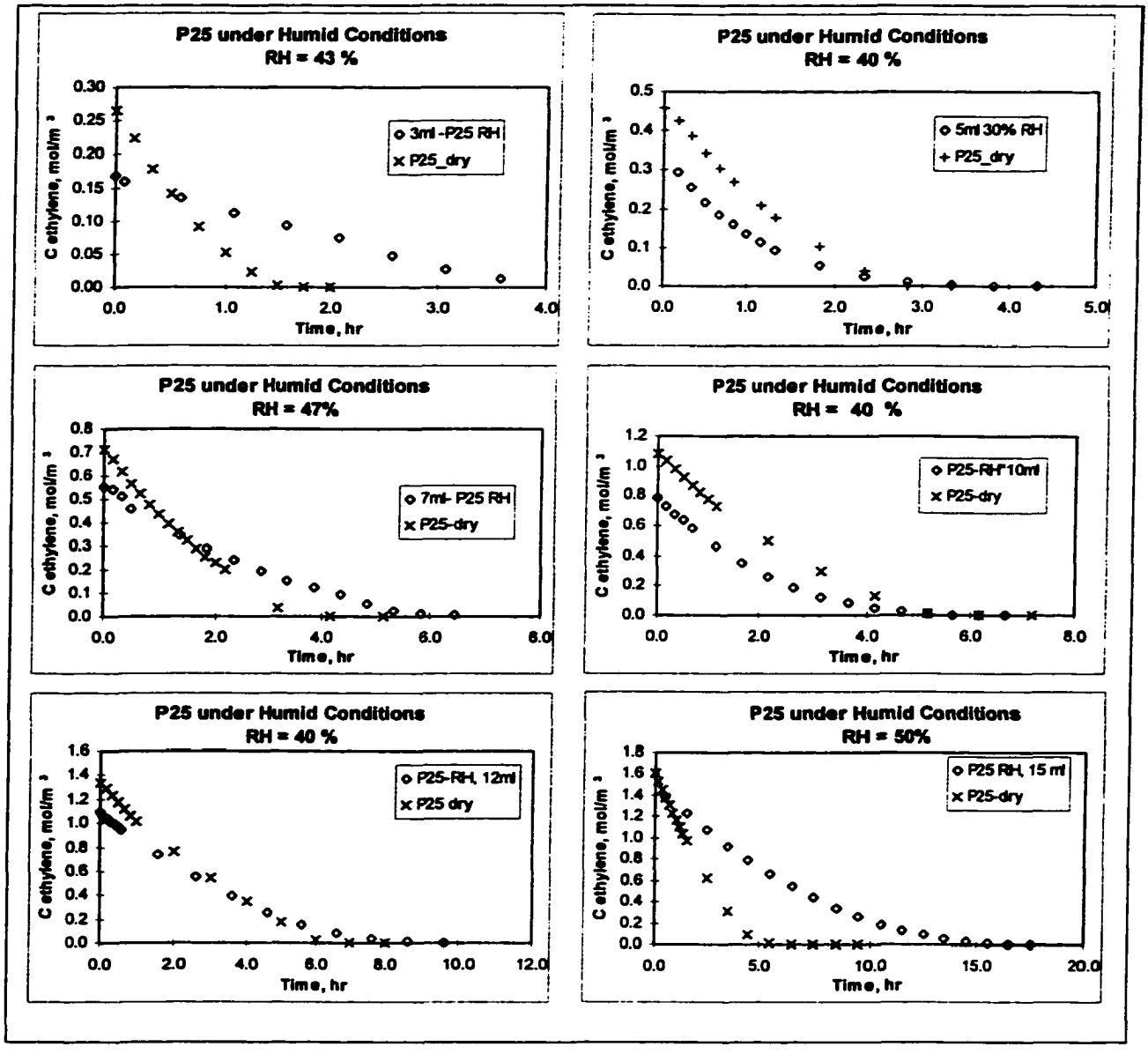

Figure 7-12 Ethylene photo-oxidation over Degussa P25 under humid conditions compared to the oxidation under initial dry conditions at different ethylene feeds.

Vsystem = 295.1 ml

Degussa P25, RH Humid Conditions Apr-98		C_2H_4 Feed ml	avgCo mmol/L	-ro= dC/Dt mmol/(L hr)	-ro mass (mmol)/L (hr g-cat)	ill Cell win (mmol)/L (hr cm^2)	-ro ill.cat-SA (mmol)/L (hr cm^2-ill.)	-ro ill.cat-V (mmol)/L (hr cm^3-cat)
m cat, g =	2.2							
ill. cell window area, cm^2=	36.0	3	0.164	0.0967	0.0439	0.00269	0.2868	5.8666
Vcat, cm^3 =	2.9	5	0.299	0.2465	0.1120	0.00685	0.7312	14.9574
BET SA, m2/g =	47.8	7	0.548	0.1716	0.0780	0.00477	0.5088	10.4095
porosity =	0.0	10	0.758	0.3239	0.1472	0.00900	0.9607	19.6539
d pore, um =	8.3	12	1.078	0.2639	0.1200	0.00733	0.7829	16.0156
ill. cat SA, cm^2=	0.337	15	1.385	0.2803	0 1274	0.00779	0.8314	17.0073
d penet, um =	4.6							
penet. Vol, cm^3=	0.016							

Table 7-21 Initial rate data for ethylene oxidation under humid conditions over the Degussa P25

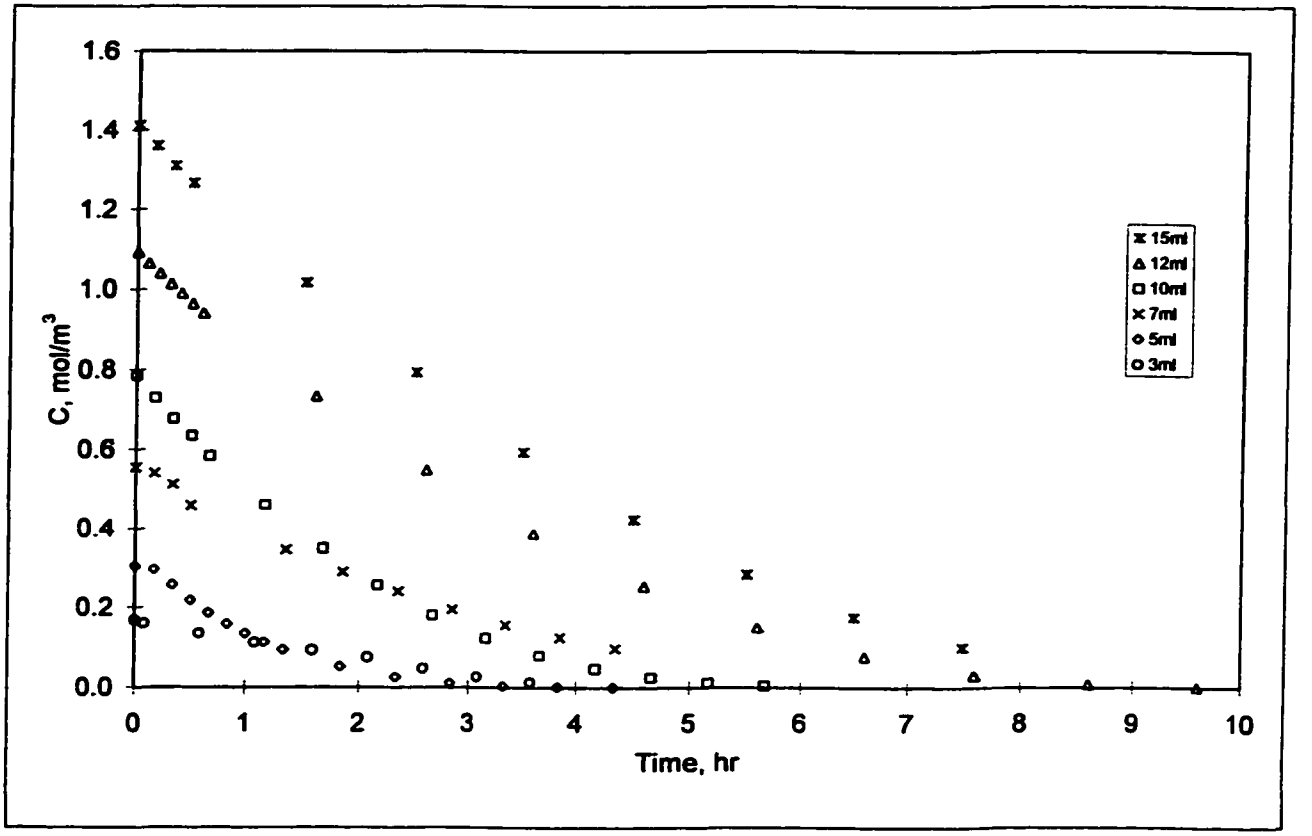

Figure 7-13 Ethylene oxidation under humid conditions (average RH = 43%) over Degussa P25

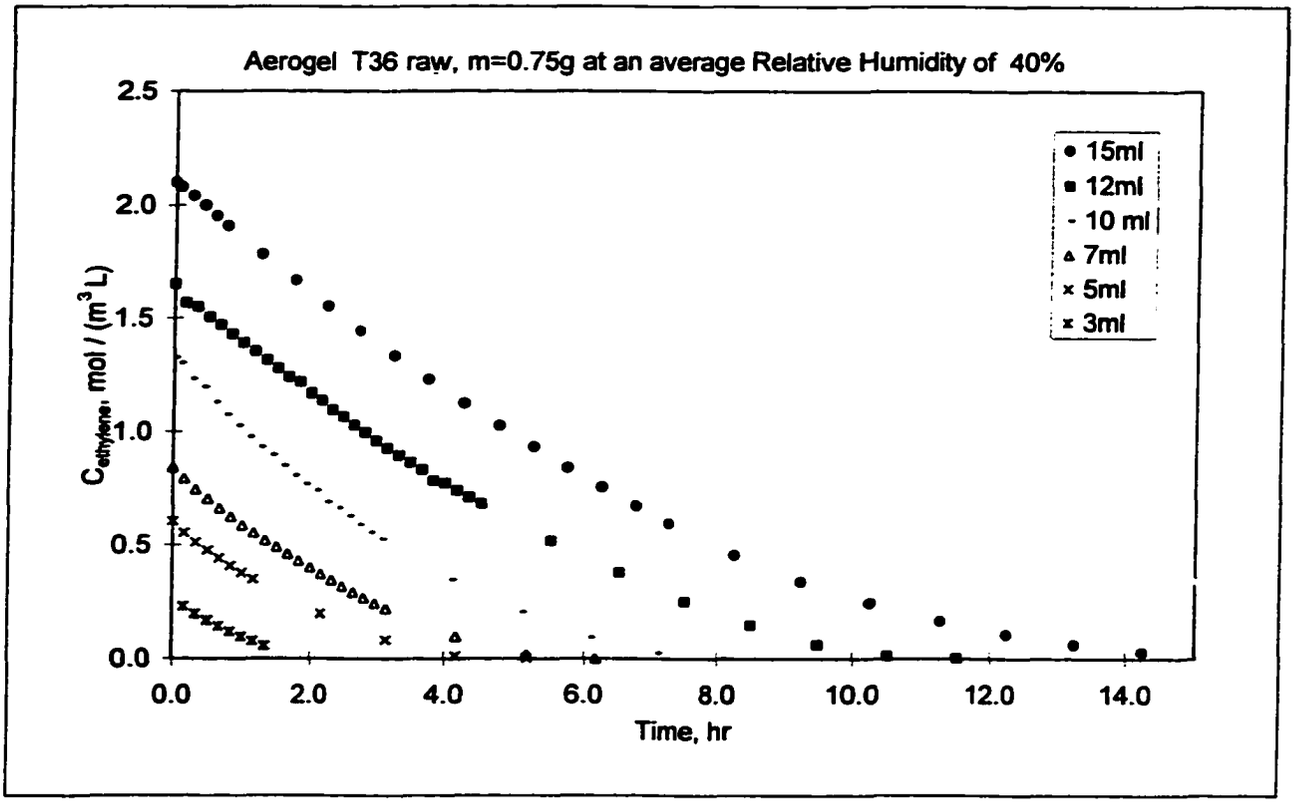

Figure 7-14 Ethylene oxidation under humid conditions (average RH = 40%) over Aerogel T36

V sys = 314.27 ml

AEROGEL T36 Humid Conditions		Ethylene Feed ml	avgCe mol/m^3	re = dC/dt mol/(m^3 hr)	-ro mass mol / (m^3 hr g-cat)	ill Cell win mol / (m^3 hr cm^2)	o ill.cat-S mol / (m^3 hr cm^2-ill.)	-ro ill.cat-V mol / (m^3 hr cm^3-cat
m cat, g =	0.75							
ill. cell window area, cm^2=	40.2							
Vcat, cm^3 =	3.2	3	0.248	0.2245	0.2993	0.00558	0.0379	3.0002
BET SA, m^2/g =	336.976	5	0.579	0.2711	0.3615	0.00674	0.0458	3.6243
porosity =	0.76	7	0.817	0.2898	0.3864	0.00721	0.0489	3.8733
d pore, um =	96.7	10	1.314	0.3603	0.4804	0.00896	0.0608	4.8161
ill. cat SA, m^2=	5.93	12	1.613	0.2561	0.3414	0.00637	0.0432	3.4229
d penet, um =	18.6	15	2.093	0.2607	0.3476	0.00648	0.0440	3.4845
penet. Vol, cm^3=	0.075							

Table 7-22 Initial rate data for ethylene oxidation under humid conditions over the aerogel T36

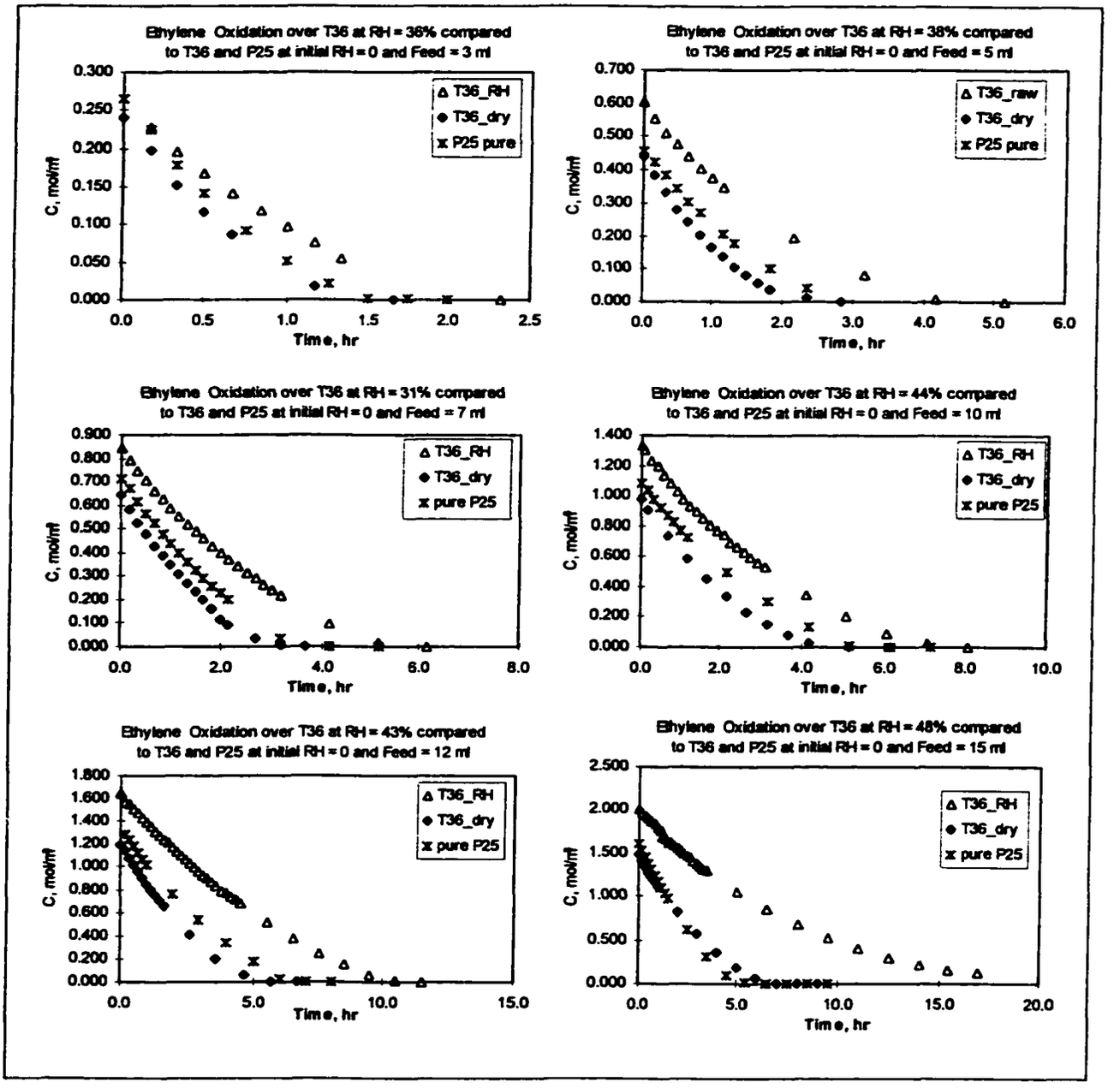

Figure 7-15 Ethylene photo-oxidation over the aerogel T36 under humid conditions compared to the oxidation results under initial dry conditions at different ethylene feeds.

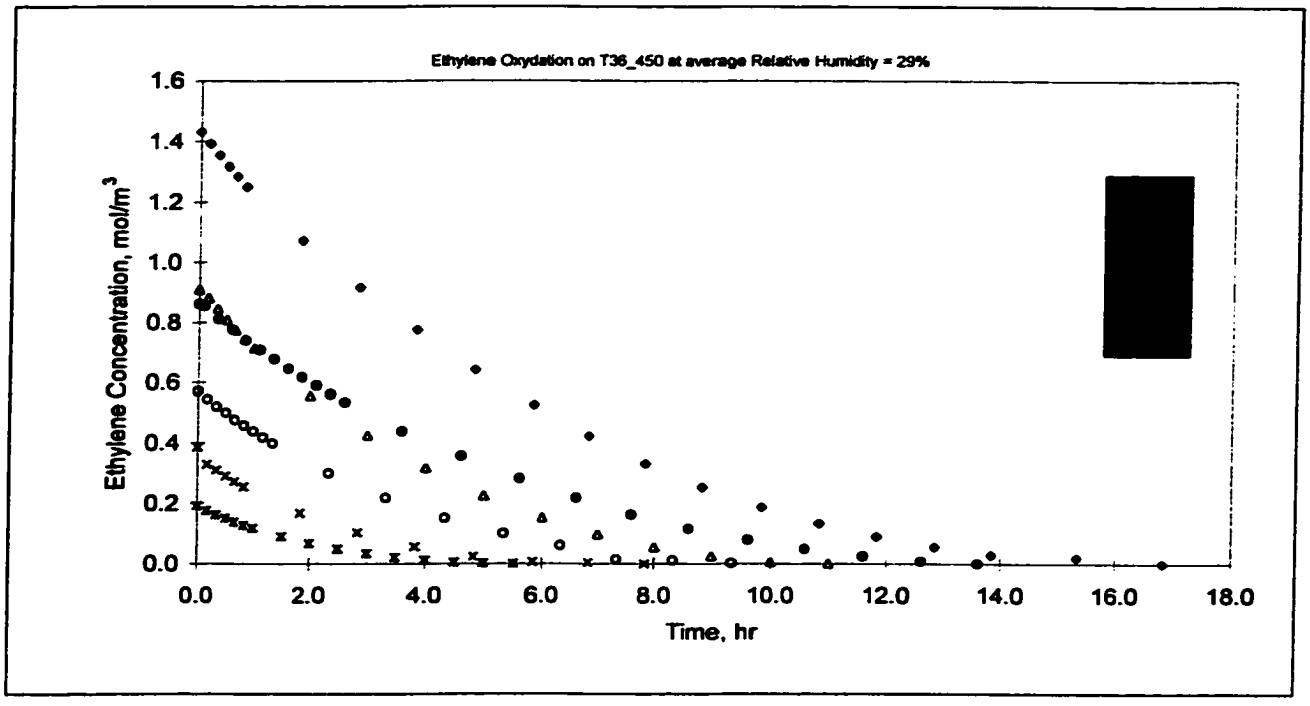

Figure 7-16 Ethylene oxidation under humid conditions (average RH = 30%) over heat-treated aerogel T36_450

System Volume = 295.10 ml

AEROGEL T36_450 under humid conditions		Ethylene Feed ml	avgCo mol/m³	ro = dC/dt mol/(m³ hr)	-ro mass mol / (m³ hr g-cat)	o ill Cell windo mol / (m³ hr cm²)	-ro ill.cat-SA mol / (m³ hr cm²-ill.)	-ro ill.cat-V mol / (m³ hr cm³-cat)
m cat, g =	1.30	3	0.191	0.0901	0.0693	0.00224	0.0322	1.2048
ill. cell window area, cm²=	40.2	5	0.367	0.1507	0.1159	0.00375	0.0539	2.0149
Vcat, cm³ =	3.2	5	0.393	0.1193	0.0918	0.00297	0.0426	1.5947
BET SA, m²/g =	91.8	7	0.571	0.1459	0.1122	0.00363	0.0521	1.9500
porosity =	0.76	10	0.912	0.2135	0.1642	0.00531	0.0763	2.8534
d pore, um =	96.7	10	0.861	0.1981	0.1524	0.00493	0.0708	2.6476
ill. cat SA, m²=	2.80	10	0.928	0.2068	0.1591	0.00514	0.0739	2.7643
d penet, um =	18.6	10	0.718	0.1355	0.1042	0.00337	0.0484	1.8108
penet. Vol, cm³=	0.075	12	0.865	0.1529	0.1176	0.00380	0.0546	2.0436
		15	1.428	0.2218	0.1706	0.00552	0.0793	2.9646

Table 7-23 Initial rate data for ethylene oxidation under humid conditions over the heat-treated aerogel T36_450

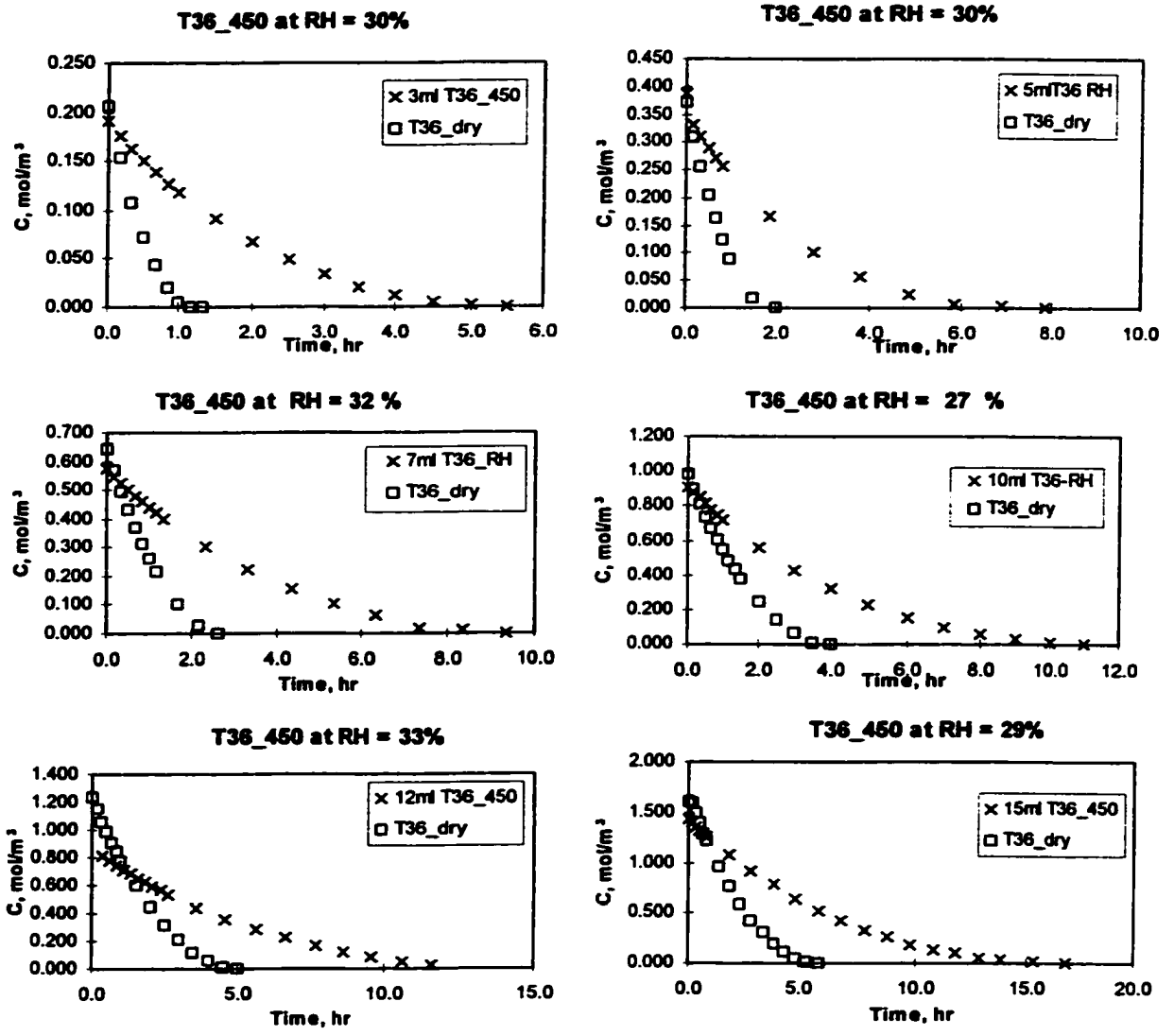

Figure 7-17 Ethylene photo-oxidation over the heat-treated aerogel T36_450 under humid conditions compared to the oxidation results under initial dry conditions at different ethylene feeds.

V sys = 304.6 ml

P25 with 0.1 wt% Pt and 0.1wt%Ru		Ethylene Feed ml	avgCo mol/m3	ro = dC/dt ol/(m3 hr	-ro mass mol / (m3 hr g-cat)	o ill Cell windo mol / (m3 hr cm2)	-ro ill.cat-SA mol / (m3 hr cm2-ill.)	-ro ill.cat-V mol / (m3 hr cm3-cat)
m cat, g =	2.20							
ill. cell window area, cm2=	25.7	3	0.256	0.1378	0.0626	0.00537	0.2311	11.9370
Vcat, cm3 =	2.0	5	0.485	0.1766	0.0803	0.00688	0.2962	15.2985
BET SA, m2/g =	47.8	7	0.746	0.2263	0.1028	0.00882	0.3795	19.6015
porosity =	0.0	10	1.089	0.2229	0.1013	0.00869	0.3739	19.3141
d pore, um =	0.0	12	1.365	0.2544	0.1156	0.00992	0.4267	22.0417
ill. cat SA, m2=	0.596	15	1.687	0.2377	0.1081	0.00927	0.3987	20.5949
d penet, um =	4.5							
penet. Vol, cm3=	0.012							

V sys = 311.99 ml

P25 with 0.1wt%Ru		Ethylene Feed ml	avgCo mol/m3	ro = dC/dt ol/(m3 hr	-ro mass mol / (m3 hr g-cat)	o ill Cell windo mol / (m3 hr cm2)	-ro ill.cat-SA mol / (m3 hr cm2-ill.)	-ro ill.cat-V mol / (m3 hr cm3-cat)
m cat, g =	2.20							
ill. cell window area, cm2=	25.7	3	0.279	0.1068	0.0485	0.00416	0.1791	9.2484
Vcat, cm3 =	2.0	5	0.433	0.1806	0.0821	0.00704	0.3030	15.6494
BET SA, m2/g =	47.8	7	0.658	0.1725	0.0784	0.00673	0.2894	14.9462
porosity =	0.0	10	0.949	0.1651	0.0751	0.00644	0.2770	14.3065
d pore, um =	0.0	12	1.281	0.2476	0.1125	0.00965	0.4153	21.4497
ill. cat SA, m2=	0.596	15	1.454	0.2656	0.1207	0.01035	0.4454	23.0077
d penet, um =	4.5							
penet. Vol, cm3=	0.012							

V sys = 311.9 ml

P25 with 3wt%Ru		Ethylene Feed ml	avgCo mol/m3	ro = dC/dt ol/(m3 hr	-ro mass mol / (m3 hr g-cat)	o ill Cell windo mol / (m3 hr cm2)	-ro ill.cat-SA mol / (m3 hr cm2-ill.)	-ro ill.cat-V mol / (m3 hr cm3-cat)
m cat, g =	2.20							
ill. cell window area, cm2=	23.6	3	0.299	0.1225	0.0557	0.00518	0.2054	11.5171
Vcat, cm3 =	1.9	5	0.524	0.0603	0.0274	0.00255	0.1012	5.6723
BET SA, m2/g =	47.8	7	0.660	0.1117	0.0508	0.00472	0.1873	10.4998
porosity =	0.0	10	0.986	0.1063	0.0483	0.00450	0.1782	9.9936
d pore, um =	0.0	12	1.513	0.1637	0.0744	0.00693	0.2745	15.3916
ill. cat SA, m2=	0.596	15	1.658	0.2123	0.0965	0.00898	0.3561	19.9636
d penet, um =	4.5							
penet. Vol, cm3=	0.011							

Table 7-24 Initial rate data of ethylene oxidation over Degussa P25 with ruthenium deposited using impregnation (photo co-deposition)

V sys = 316.5ml

Degussa P25 with 0.1 wt% Pt		Ethylene Feed ml	avgCo mol/m3	ro = dC/dt ol/(m3 hr	-ro mass mol / (m3 hr g-cat)	ro ill Cell windo mol / (m3 hr cm2)	-ro ill.cat-SA mol / (m3 hr cm2-ill.)	-ro ill.cat-V mol / (m3 hr cm3-cat)
m cat, g =	2.20							
ill. cell window area, cm2=	24.3	3	0.261	0.1416	0.0643	0.00583	0.2374	12.9447
Vcat, cm3 =	1.9	5	0.475	0.1678	0.0762	0.00690	0.2811	15.3269
BET SA, m2/g =	47.8	7	0.709	0.2155	0.0979	0.00887	0.3614	19.7058
porosity =	0.0	10	0.900	0.2078	0.0945	0.00855	0.3486	19.0062
d pore, um =	0.0	12	1.270	0.2044	0.0929	0.00841	0.3428	18.6907
ill. cat SA, m2=	0.596	15	1.469	0.2878	0.1308	0.01184	0.4828	26.3207
d penet, um =	4.5							
penet. Vol, cm3=	0.011							

V sys = 316.5 ml

Degussa P25 with 0.5 wt% Pt		Ethylene Feed ml	avgCo mol/m3	ro = dC/dt ol/(m3 hr	-ro mass mol / (m3 hr g-cat)	ro ill Cell windo mol / (m3 hr cm2)	-ro ill.cat-SA mol / (m3 hr cm2-ill.)	-ro ill.cat-V mol / (m3 hr cm3-cat)
m cat, g =	2.20							
ill. cell window area, cm2=	23.1	3	0.182	0.1392	0.0633	0.00602	0.2335	13.3827
Vcat, cm3 =	1.8	5	0.415	0.1649	0.0749	0.00713	0.2765	15.8449
BET SA, m2/g =	47.8	7	0.604	0.1623	0.0738	0.00702	0.2722	15.5998
porosity =	0.0	10	0.998	0.2323	0.1056	0.01005	0.3897	22.3296
d pore, um =	0.0	12	1.310	0.1877	0.0853	0.00812	0.3148	18.0411
ill. cat SA, m2=	0.596	15	1.523	0.2620	0.1191	0.01133	0.4395	25.1826
d penet, um =	4.5							
penet. Vol, cm3=	0.010							

V sys = 316.5 ml

Degussa P25 with 3 wt% Pt		Ethylene Feed ml	avgCo mol/m3	ro = dC/dt ol/(m3 hr	-ro mass mol / (m3 hr g-cat)	ro ill Cell windo mol / (m3 hr cm2)	-ro ill.cat-SA mol / (m3 hr cm2-ill.)	-ro ill.cat-V mol / (m3 hr cm3-cat)
m cat, g =	2.20							
ill. cell window area, cm2=	23.1	3	0.231	0.0482	0.0219	0.00209	0.0808	4.6469
Vcat, cm3 =	1.8	5	0.501	0.0579	0.0263	0.00251	0.0972	5.5869
BET SA, m2/g =	47.8	7	0.810	0.0769	0.0350	0.00334	0.1291	7.4177
porosity =	0.0	10	1.230	0.0995	0.0452	0.00432	0.1669	9.5911
d pore, um =	0.0	12	1.249	0.0365	0.0166	0.00158	0.0612	3.5189
ill. cat SA, m2=	0.596	15	1.932	0.0394	0.0179	0.00171	0.0661	3.8001
d penet, um =	4.5							
penet. Vol, cm3=	0.010							

Table 7-25 Initial rate data of ethylene oxidation over Degussa P25 with platinum deposited using impregnation (photo co-deposition)

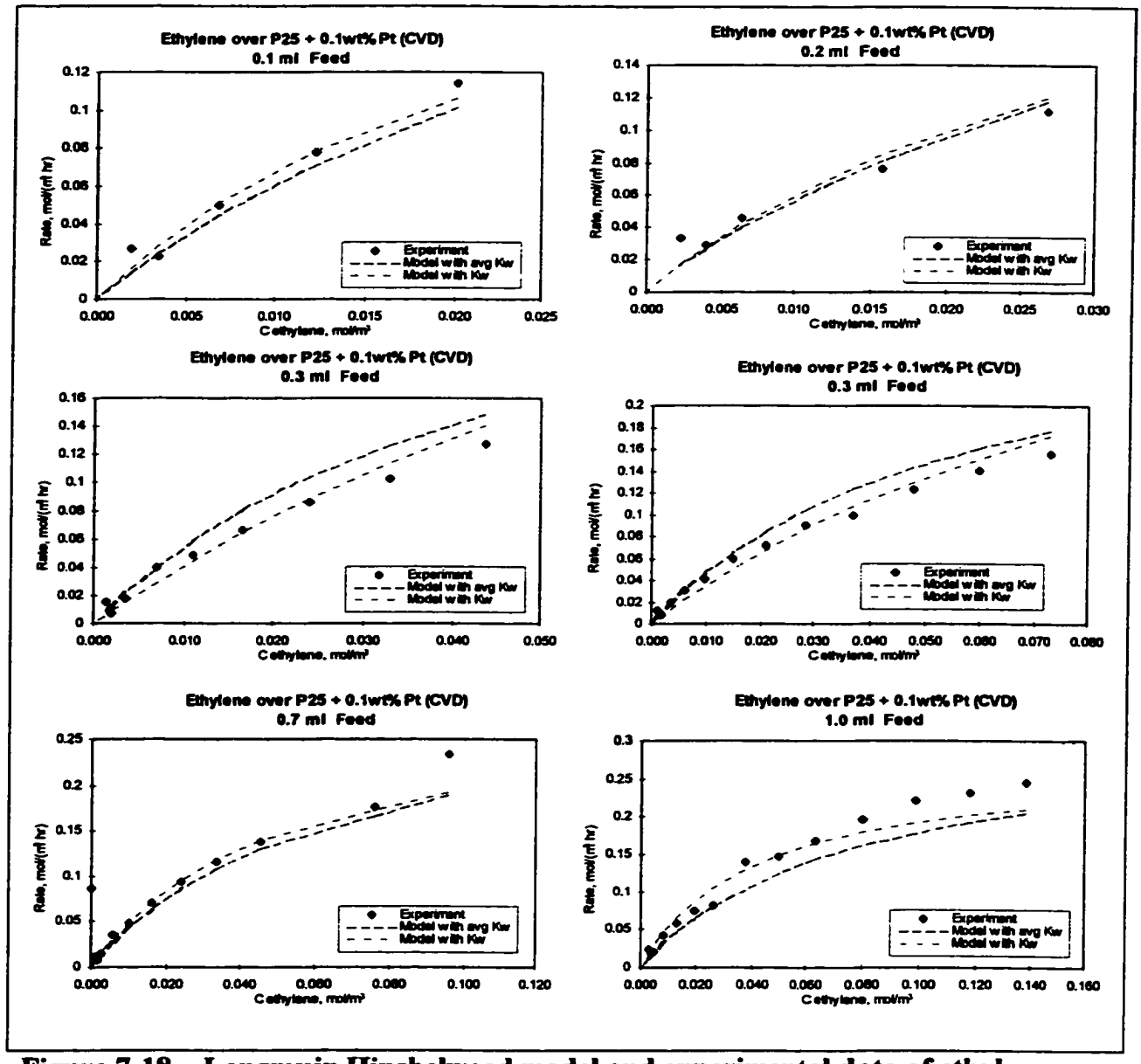

Figure 7-18 Langmuir-Hinshelwood model and experimental data of ethylene oxidation under humid conditions over aerogel P25_0.1wt% Pt (CVD) at different initial ethylene concentrations.

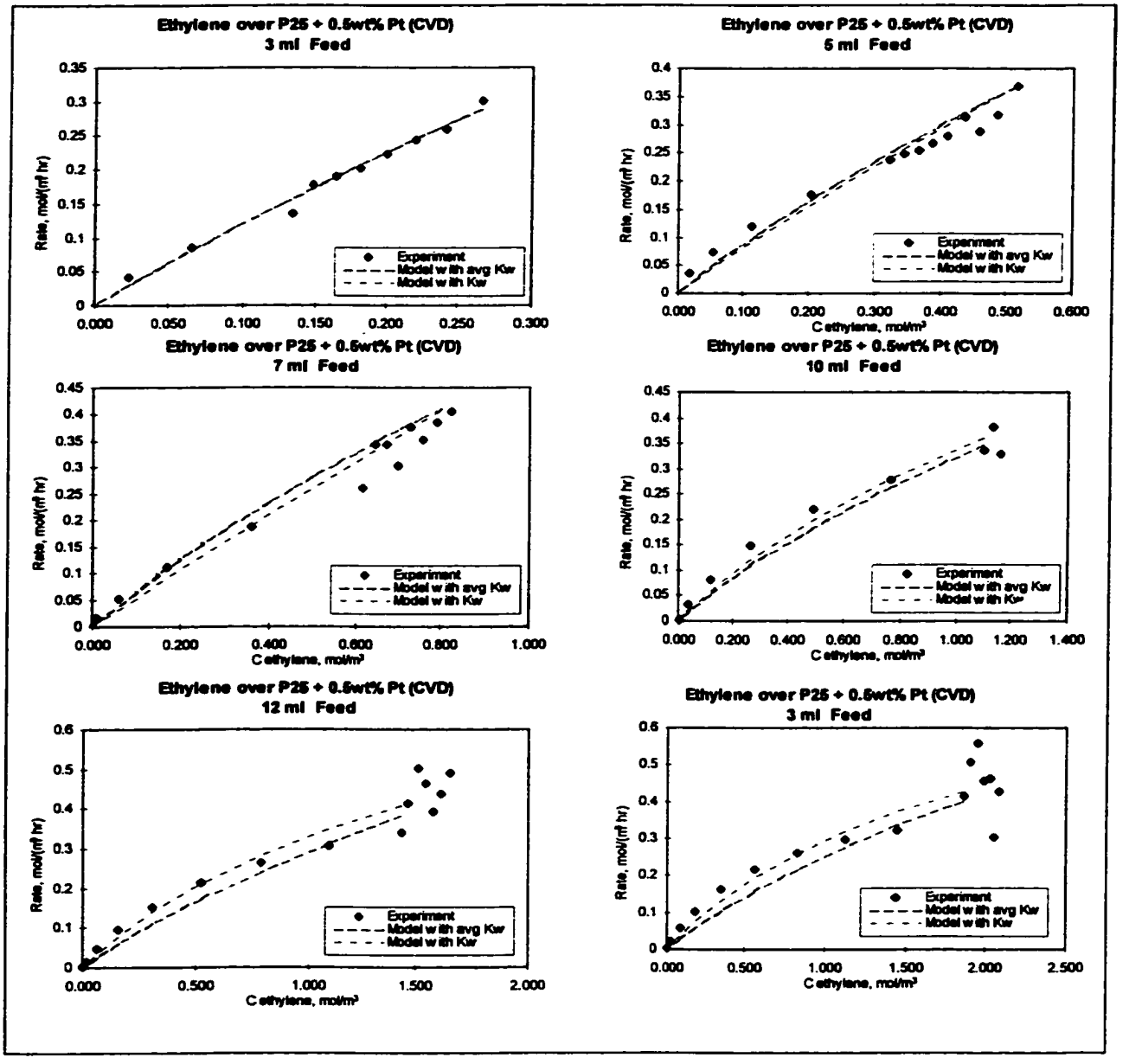

Figure 7-19 Langmuir-Hinshelwood model and experimental data of ethylene oxidation under humid conditions over aerogel P25_0.5wt% Pt (CVD) at different initial ethylene concentrations.

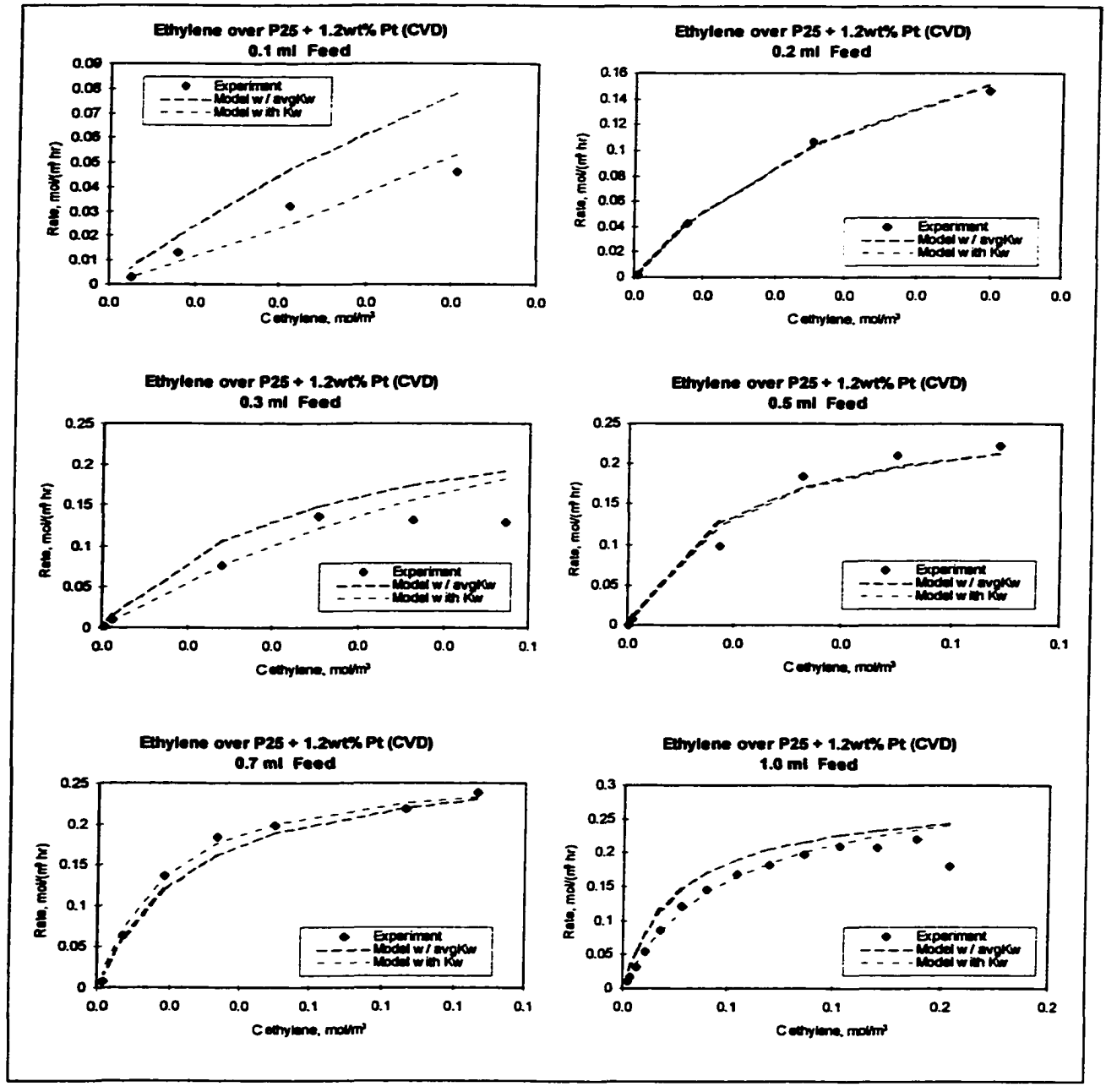

Figure 7-20 Langmuir-Hinshelwood model and experimental data of ethylene oxidation under humid conditions over aerogel P25_1.2wt% Pt (CVD) at different initial ethylene concentrations.

V sys = 216.5ml

Degussa P25 with 0.1 wt% Pt (CVD)		Ethylene Feed ml	avgCo mol/m3	ro = dC/dt ol/(m3 hr	-ro mass mol / (m3 hr g-cat)	o ill Cell windo mol / (m3 hr cm2)	-ro ill.cat-SA mol / (m3 hr cm2-ill.)	-ro ill.cat-V mol / (m3 hr cm3-cat)
m cat, g =	2.20							
ill. cell window area, cm2=	45.1	0.1	0.016	0.1123	0.0510	0.00249	0.1883	5.5320
Vcat, cm3 =	3.6	0.2	0.021	0.1115	0.0507	0.00247	0.1871	5.4960
BET SA, m2/g =	47.8	0.3	0.038	0.1220	0.0554	0.00270	0.2046	6.0106
porosity =	0.0	0.5	0.066	0.1563	0.0710	0.00347	0.2622	7.7015
d pore, um =	0.0	0.7	0.086	0.2183	0.0992	0.00484	0.3661	10.7549
ill. cat SA, m2=	0.596	1	0.128	0.2541	0.1155	0.00563	0.4262	12.5195
d penet, um =	4.5							
penet. Vol, cm3=	0.020							

V sys = 216.5 ml

Degussa P25 with 0.5 wt% Pt CVD		Ethylene Feed ml	avgCo mol/m3	ro = dC/dt ol/(m3 hr	-ro mass mol / (m3 hr g-cat)	o ill Cell windo mol / (m3 hr cm2)	-ro ill.cat-SA mol / (m3 hr cm2-ill.)	-ro ill.cat-V mol / (m3 hr cm3-cat)
m cat, g =	2.20							
ill. cell window area, cm2=	44.1	0.1	0.009	0.0504	0.0229	0.00114	0.0845	2.5393
Vcat, cm3 =	3.5	0.2	0.027	0.1229	0.0559	0.00279	0.2062	6.1948
BET SA, m2/g =	47.8	0.3	0.034	0.1574	0.0716	0.00357	0.2641	7.9333
porosity =	0.0	0.5	0.073	0.1672	0.0760	0.00379	0.2805	8.4255
d pore, um =	0.0	0.7	0.086	0.1783	0.0810	0.00404	0.2991	8.9843
ill. cat SA, m2=	0.596	1	0.101	0.2114	0.0961	0.00479	0.3547	10.6545
d penet, um =	4.5							
penet. Vol, cm3=	0.020							

V sys = 216.5 ml

Degussa P25 with 1.2 wt% Pt		Ethylene Feed ml	avgCo mol/m3	ro = dC/dt ol/(m3 hr	-ro mass mol / (m3 hr g-cat)	o ill Cell windo mol / (m3 hr cm2)	-ro ill.cat-SA mol / (m3 hr cm2-ill.)	-ro ill.cat-V mol / (m3 hr cm3-cat)
m cat, g =	2.20							
ill. cell window area, cm2=	44.9	0.1	0.006	0.0462	0.0210	0.00103	0.0774	2.2848
Vcat, cm3 =	3.6	0.2	0.019	0.1510	0.0686	0.00336	0.2533	7.4738
BET SA, m2/g =	47.8	0.3	0.042	0.1465	0.0666	0.00326	0.2457	7.2490
porosity =	0.0	0.5	0.059	0.2424	0.1102	0.00540	0.4065	11.9954
d pore, um =	0.0	0.7	0.096	0.2386	0.1085	0.00531	0.4002	11.8090
ill. cat SA, m2=	0.596	1	0.129	0.2144	0.0975	0.00478	0.3596	10.6116
d penet, um =	4.5							
penet. Vol, cm3=	0.020							

Table 7-26 Initial Rate data for all P25 with platinum loading by CVD

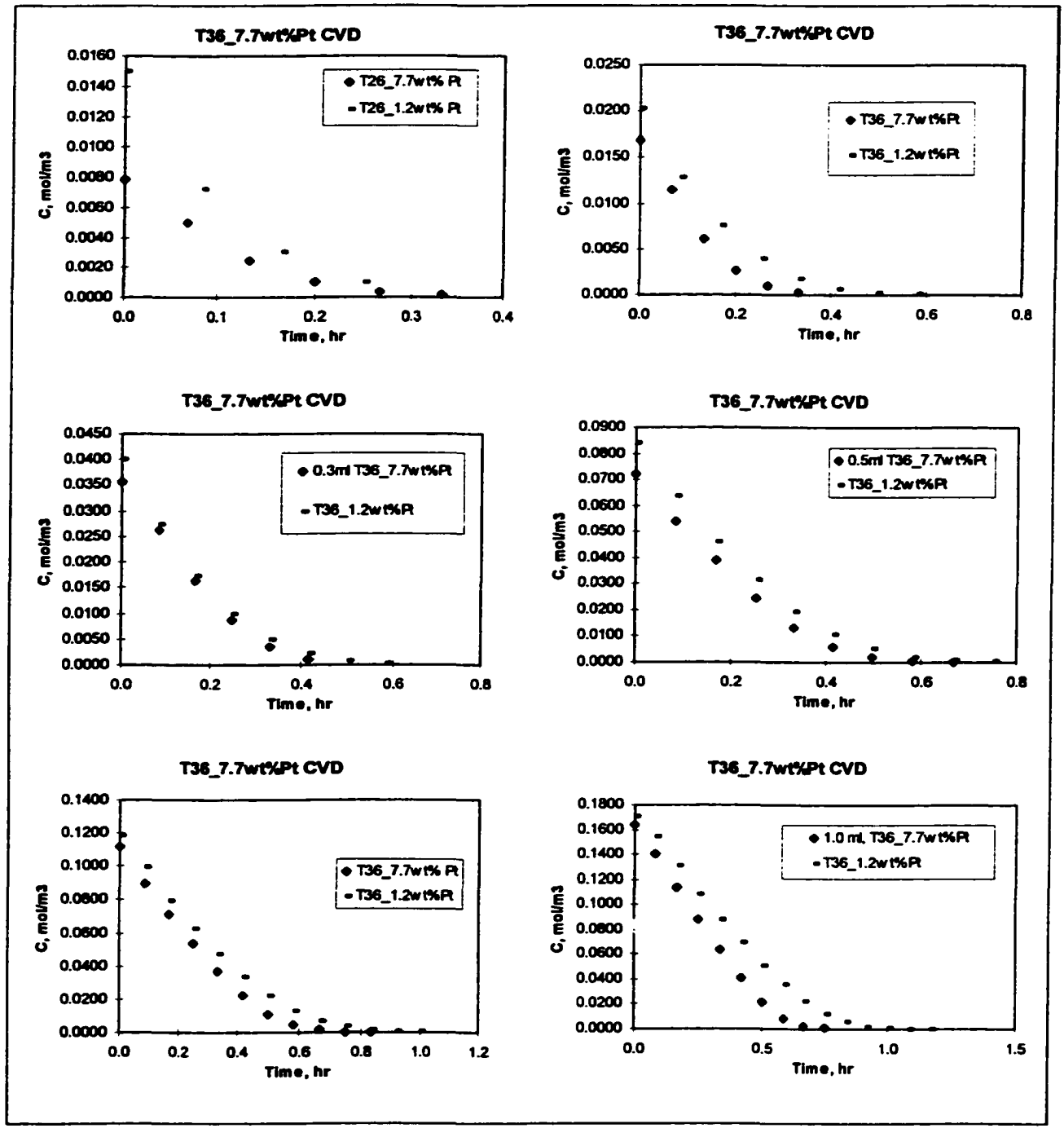

Figure 7-21 Ethylene photo-oxidation over the T36_7.7wt% Pt compared to the oxidation results over the T36_1.2wt% Pt at different ethylene feeds.

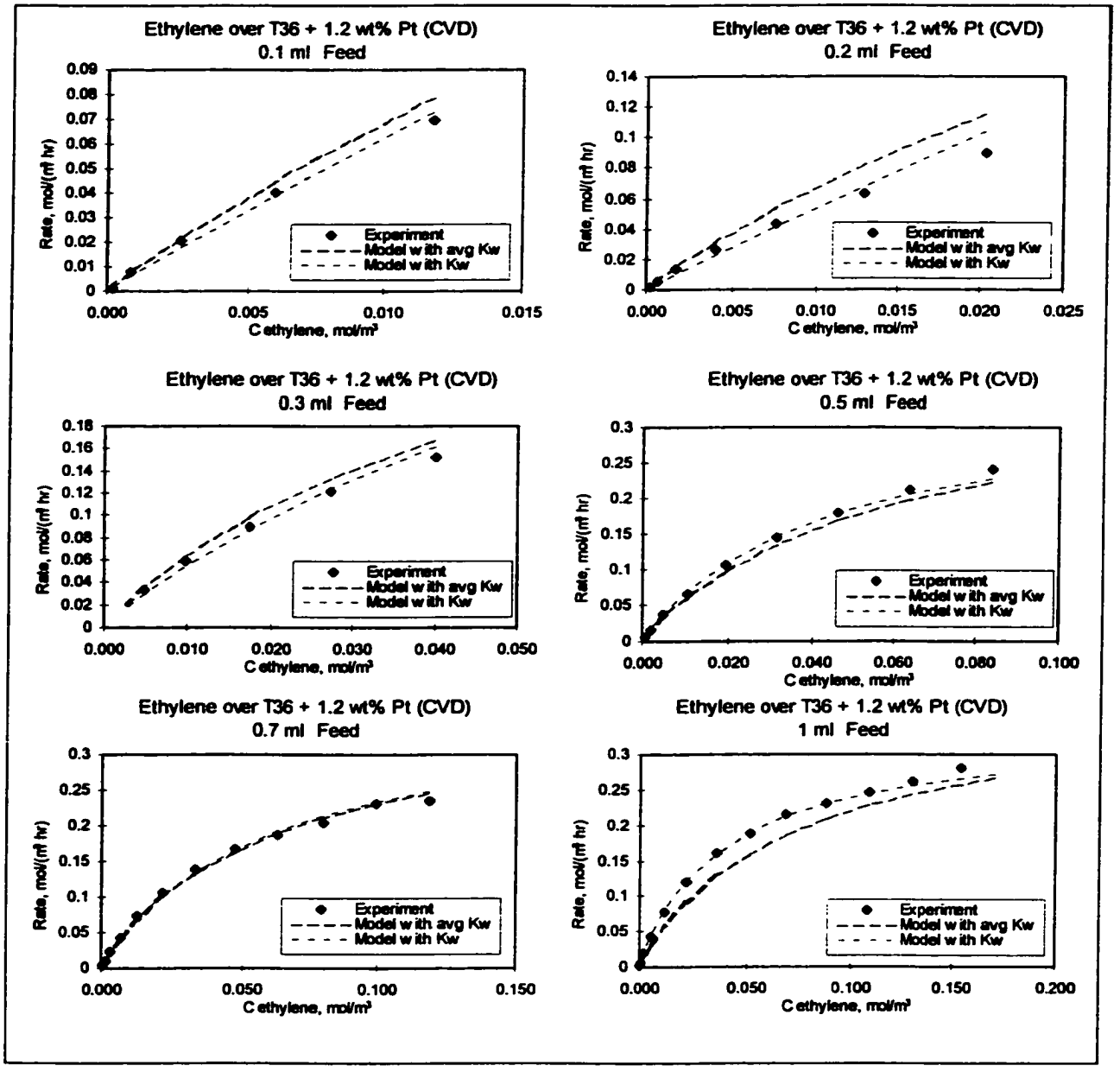

Figure 7-22 Langmuir-Hinshelwood model and experimental data of ethylene oxidation under humid conditions over aerogel T36_1.2wt% Pt (CVD) at different initial ethylene concentrations.

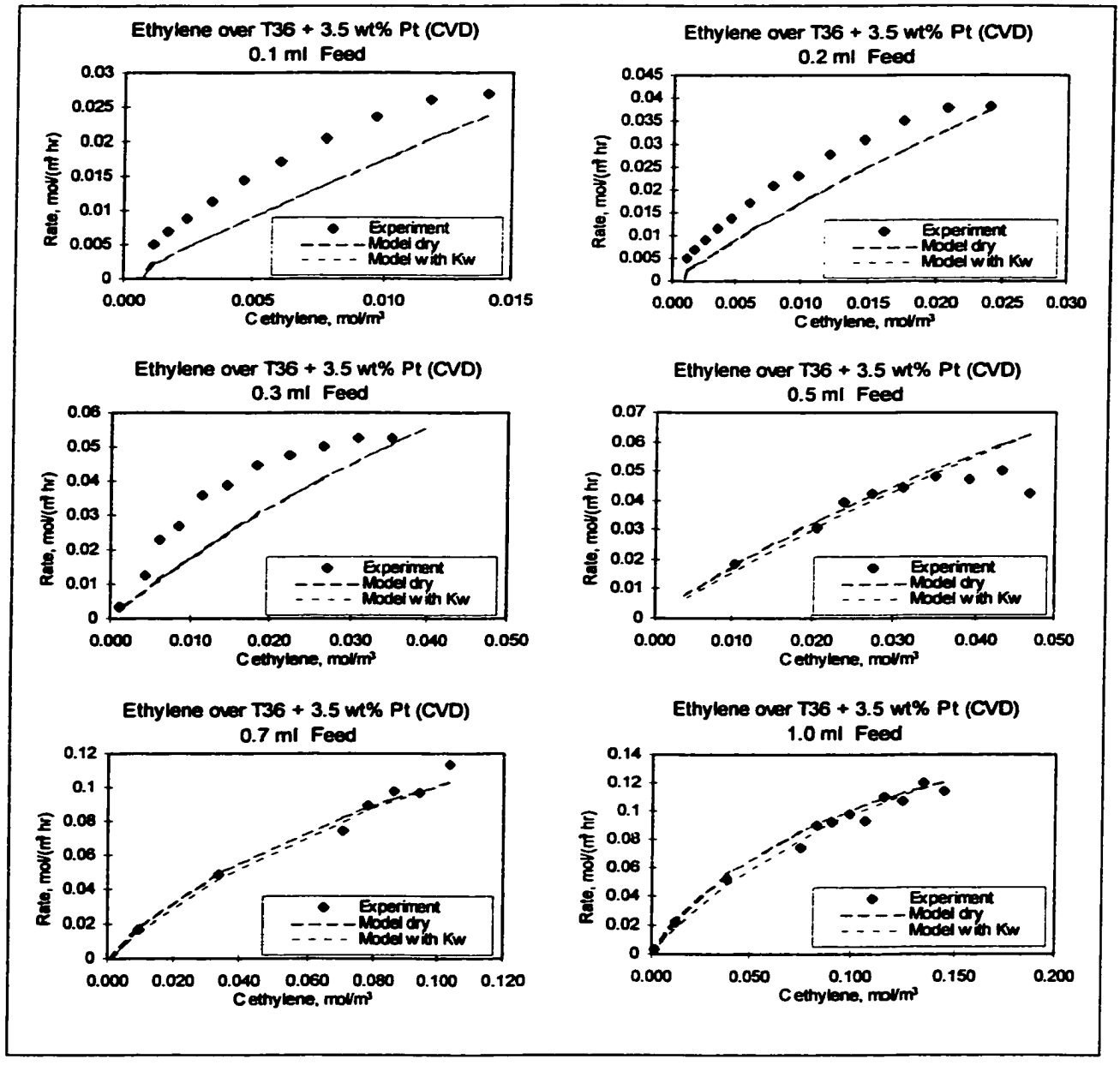

Figure 7-23 Langmuir-Hinshelwood model and experimental data of ethylene oxidation under humid conditions over aerogel T36_3.5wt% Pt (CVD) at different initial ethylene concentrations.

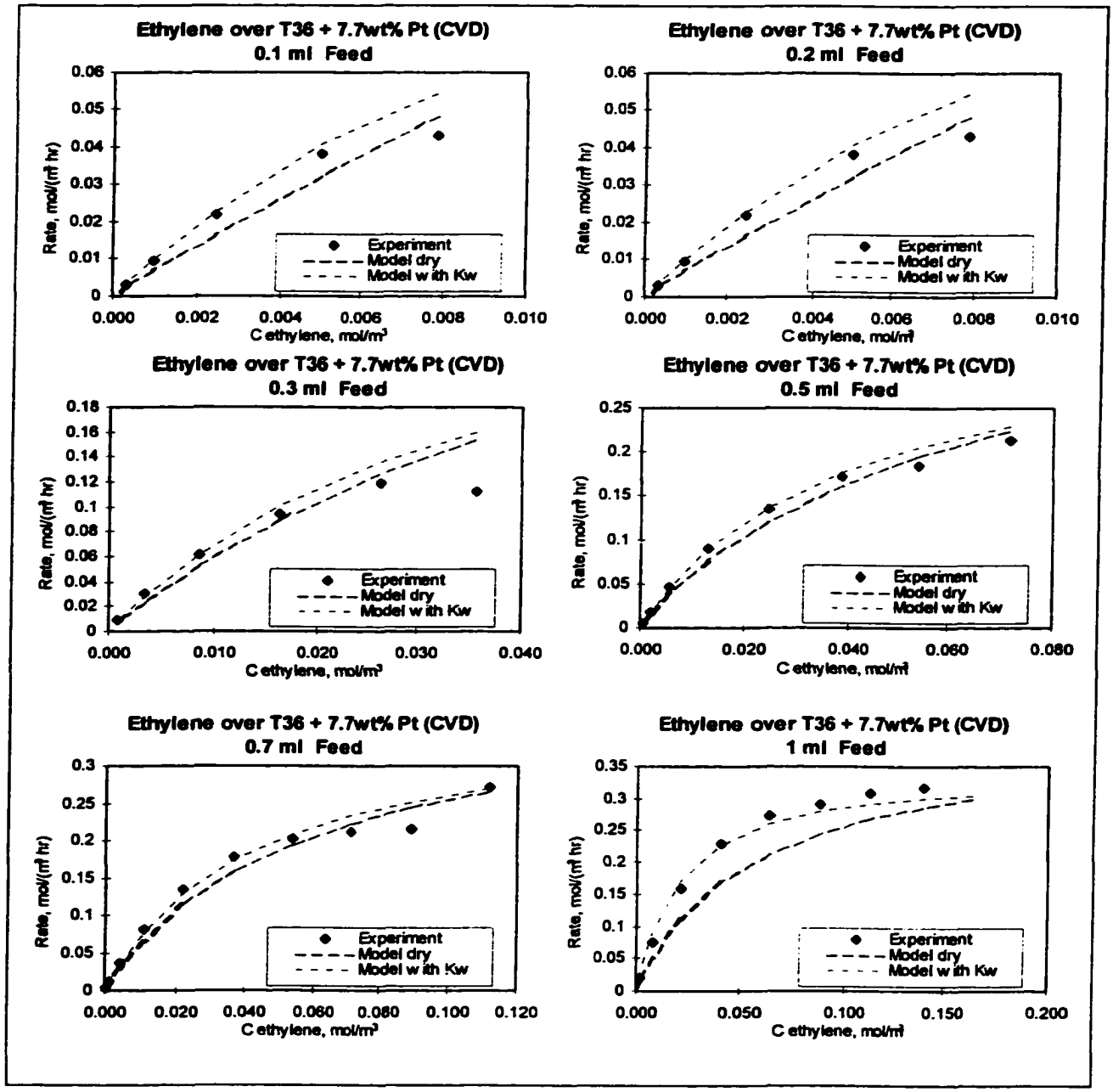

Figure 7-24 Langmuir-Hinshelwood model and experimental data of ethylene oxidation under humid conditions over aerogel T36_7.7wt% Pt (CVD) at different initial ethylene concentrations.

V sys = 216.5ml

T36 with 1.2 wt% Pt (CVD)		Ethylene Feed ml	avgCo mol/m3	ro = dC/dt ol/(m3 hr	-ro mass mol / (m3 hr g-cat)	o ill Cell windo mol / (m3 hr cm2)	-ro ill.cat-SA mol / (m3 hr cm2-ill.)	-ro ill.cat-V mol / (m3 hr cm3-cat)
m cat, g =	0.75							
ill. cell window area, cm2=	30.8	0.1	0.009	0.0676	0.0901	0.00219	0.0105	0.9428
Vcat, cm3 =	2.4	0.2	0.017	0.0883	0.1177	0.00287	0.0138	1.2322
BET SA, m2/g =	291.5	0.3	0.034	0.1523	0.2031	0.00495	0.0238	2.1250
porosity =	0.81	0.5	0.074	0.2440	0.3253	0.00793	0.0380	3.4042
d pore, um =	132.9	0.7	0.109	0.2414	0.3219	0.00784	0.0376	3.3683
ill. cat SA, m2=	6.41	1	0.163	0.2825	0.3766	0.00918	0.0441	3.9414
d penet, um =	23.3							
penet. Vol, cm3=	0.072							

V sys = 216.5ml

T36 with 3.5 wt% Pt (CVD)		Ethylene Feed ml	avgCo mol/m3	ro = dC/dt ol/(m3 hr	-ro mass mol / (m3 hr g-cat)	o ill Cell windo mol / (m3 hr cm2)	-ro ill.cat-SA mol / (m3 hr cm2-ill.)	-ro ill.cat-V mol / (m3 hr cm3-cat)
m cat, g =	0.75							
ill. cell window area, cm2=	23.8	0.1	0.013	0.0281	0.0375	0.00118	0.0100	0.6586
Vcat, cm3 =	1.9	0.2	0.022	0.0399	0.0532	0.00168	0.0142	0.9342
BET SA, m2/g =	166	0.3	0.045	0.0491	0.0655	0.00207	0.0174	1.1500
porosity =	0.75	0.5	0.037	0.0547	0.0729	0.00230	0.0194	1.2808
d pore, um =	167.4	0.7	0.099	0.1064	0.1419	0.00448	0.0377	2.4919
ill. cat SA, m2=	2.82	1x	0.145	0.119	0.1587	0.00501	0.0422	2.7878
d penet, um =	18.0							
penet. Vol, cm3=	0.043							

V sys = 216.5ml

T36 with 7.7 wt% Pt (CVD)		Ethylene Feed ml	avgCo mol/m3	ro = dC/dt ol/(m3 hr	-ro mass mol / (m3 hr g-cat)	o ill Cell windo mol / (m3 hr cm2)	-ro ill.cat-SA mol / (m3 hr cm2-ill.)	-ro ill.cat-V mol / (m3 hr cm3-cat)
m cat, g =	0.69							
ill. cell window area, cm2=	13.9	0.1	0.006	0.0455	0.0660	0.00329	0.0256	2.1904
Vcat, cm3 =	1.1	0.2	0.014	0.0872	0.1263	0.00629	0.0490	4.1925
BET SA, m2/g =	136.42	0.3	0.031	0.1260	0.1826	0.00909	0.0709	8.0625
porosity =	0.70	0.5	0.063	0.2192	0.3177	0.01582	0.1232	10.5447
d pore, um =	167.4	0.7	0.101	0.2549	0.3694	0.01839	0.1433	12.2604
ill. cat SA, m2=	1.78	1	0.152	0.3211	0.4653	0.02317	0.1805	15.4458
d penet, um =	15.0							
penet. Vol, cm3=	0.021							

Table 7-27 Initial rate data for all aerogel T36 with platinum loading by CVD

Literature cited

[1] Serpone, N.; Borgarello, E.; Pelizzetti, E; Photocatalysis and Environment - Trends and Applications; NATO ASI Series, Schiavello (ed.), pp. 499-526; Kluwer Academic Publishers, Dordrecht 1988

[2] Cooper, C.; D., F.C. Alley, Air Pollution Control, Waveland Press, Inc., Illinois, 1994

[3] Pelizzetti, E., C. Minero, and M. Vincenti, Technology for Environmental Cleanup: Toxic and Hazardous Waste Management, 101-138, A. Avogadro and R. C. Ragaini (eds.), 1994

[4] McInnes, Robert G., Explore New Options For Hazardous Air Pollutant Control; Chemical Engineering Progress **91** (11), pp. 36-48, November 1995,

[5] Fox, M. A., Chemtech, 680-685 (November 1992)

[6] Pelizzetti, E.; Pramauro, E.; Minero, C.; Serpone, N.; Photocatalysis and Environment - Trends and Applications; NATO ASI Series, Schiavello (ed.), pp. 469-497; Kluwer Academic Publishers, Dordrecht 1988

[7] Peral, J.; Domènech, X. and Ollis, D.F.; Heterogeneous photocatalysis for purification, decontamination and deodorization of air; Journal of Chemical Technology and Biotechnology **70**, pp. 117-140, 1997

[8] Ibusiki, T. and Takeuchi, K.; Toluene oxidation on U.V.-irradiated titanium dioxide with and without O_2, NO_2 or H_2O at ambient temperature; Atmospheric Environment; Vol. **20**, No. 9; pp. 1711-1715; 1986

[9] Fox, M., A.; CHEMTECH, pp. 690-685; November 1992

[10] Kesselman, M.; Shreve, G. A.; Hoffmann, M. R.; Lewis, N. S.; Journal of Physical Chemistry **98**; 13385-13395; 1994

[11] Tanguay, J. F.; Suib, S. L.; and Coughlin, R. W.; Journal of Catalysis **117**; pp. 335-347; 1989

[12] Reeves, P.; Ohlhausen, R., Sloan, D.; Pamplin, K.; Scoggins, T.; Solar Energy Vol. **48**, No. 6, pp. 413-420, 1992

[13] Pramauro, E.; Vincenti, M.; Augugliaro, V. and Palmisano, L.; Environmental Science Technology **27**, pp.1790-1795, 1993

[14] Sclafani, A., Palmisano, L., Davi, E., New Journal of Chemistry **14**, pp. 265-268, 1990

[15] Brickley, R. I.; Stone, F. S.; Photoadsorption and photocatalysis at rutile surfaces, I Photoadsorptpn of oxygen; Journal of Catalysis 31, 389-397; 1972

[16] Chhabra, V.; Pillai, V.; Mishra, B. K.; Morrone, A.; Shah, D. O.; Synthesis, characterization, and properties of microemulsion-mediated nanophase TiO_2 particles; Langmuir **11**; pp. 3307-3311; 1995

[17] Goswami, D. Y.; Journal of Solar Energy Engineering, Vol. **119**; pp. 101-107; 1997

[18] Anheden, M.; Goswami, D. Y.; Svedberg, G.; Transaction of ASME, Vol. **118**; pp. 2-8, 1996

[19] Lindner, M.; Bahnemann, D. W.; Hirthe, B.; Griebler, W.-D.; Transaction of ASME Vol. **119**; pp. 120-125; 1997

[20] Peral, J.; Domènech, X.; Ollis, D. F.; Heterogeneous photocatalysis for purification, decontamination and deodorization of air; Journal of Chem. Technology and Biotechnology **70**; pp. 117-140; 1997

[21] Gravelle, P.C; Juillet, F; Meriaudeau, P.; and Teichner, S. J.; Surface reactivity of reduced titanium dioxide; Discussion of the Faraday Society **No. 52**; pp. 140-148; 1971

[22] Formenti, M.; Juillet, F; Meriaudeau, P.; and Teichner, S. J.; Heterogeneous photocatalysis for partial oxidation of paraffins; Chem Tech; pp. 680-686; November 1971

[23] Courbon, H.; Formenti, M.; Juillet, Lisachenko, A. A.; Martin, J.; P.; and Teichner, S. J.; Photoactivity of nonporous titanium dioxide (anatase); Kinetic Catalysis **14**; pp. 84-89; 1973

[24] Munuera, G.; Rves-Arnau, V.; Saucedo, A.; Journal of Chemical Society, Faraday Trans. 1, 75

[25] Herrmann, J.M.; Disdier, J.; Mozzanega, M.-N; Pichat, P.; heterogeneous photocatalysis: In Siu photoconductivity study of TiO2 during oxidation of isobutene into acetone; Journal of Catalysis **60**; pp. 369-377; 1979

[26] Djeghri, N.; Teichner, S. J.; Journal of Catalysis **62**; pp. 99-106; 1979

[27] Sabate, J.; Anderson, M. A.; Kikkawa, H.; Edwards, M.; Hill, Jr. C. G.; A kinetic study of the photocatalytic degradation of 3-chlorosalicylic acid over TiO_2 membranes supported on glass; Journal of Catalysis **127**; pp.167-177; 1991

[28] Ollis, D., F.; Peral, J.; Heterogeneous photocatalytic oxidation of atmospheric trace contaminants; First annual semiannual progress report for National Aeronautics and Space Administration, AMES Research Center; Report No. 1, 11 Jan. 1990 – 30. April 199, May 1991

[29] Peral, J.; Ollis, D. F.; Heterogeneous photocatalytic oxidation of gas-phase organics for air purification: Acetone, 1-Butanol, Butyraldehyde, Formaldehyde, and m-xylene oxidation; Journal of Catalysis **136**; pp. 554-565; 1992

[30] Dibble, L. and Roupp, B.; Fluidized bed photocatalytic oxidation of trichloroethylene in contaminated airstreams; Environmental Science and Technology **Vol. 26**, No. 3; pp. 492-495, 1992

[31] Luo, Y.; Ollis, D. F.; Heterogeneous photocatalytic oxidation of trichloroethylene and toluene mixtures in air: Kinetic promotion and inhibition, time-dependent catalyst activity; Journal of Catalysis 163; pp. 1-11; 1996

[32] Augugliaro, V.; Coluccia, S.; Loddo, V.; Marchese, L.; Matra, G.; Palmisano, L.; Schiavello, M.; Photocatalytic oxidation of gaseous toluene on anatase TiO_2 catalyst: mechanistic aspects and FT-IR investigation; Applied Catalysis B; Environmental **20**, pp. 15-27; 1998

[33] Obee, T. N. and Brown, R.; TiO_2 Photocatalysis for indoor air applications: Effect of humidity and trace contaminant levels on the oxidation of formaldehyde, toluene, and 1,3-butadiene; Environmental Science and Technology **Vol. 29**, No. 5; pp.1223-1231; 1995

[34] Obee, T. N.,Photooxidation of sub-parts-per million toluene and formaldehyde levels on titania using a glass plate reactor; Environmental Science & Technology **Vol. 30**, pp. 3578-3584 (1996)

[35] Anderson, M., A.; Zeltner, W. A.; Fu, X.; Tompkins, D. T.; Reindl, D. T.; Photocatalytic degradation of formaldehyde and other VOCs in indoor air; CIAR Currents, pp. 2-4, December 1996

[36] Nimlos, M. R.; Jacoby, W. A.; Blake, D. M.; Milne, T. A.; Direct Mass Spectrometric Studies of the destruction of hazardous wastes. 2. Gas-phase photocatalytic oxidation of trichloroethylene over TiO_2: Products and mechanisms; Environmental Science and Technology **Vol. 27**, No. 4; pp.732-740; 1993

[37] Hennezel, O.; Ollis, D. F.; Trichloroethylene-promoted photocatalytic oxidation of air contaminants; Journal of Catalysis **167**; pp. 118-126; 1997

[38] Block, S. S.; Seng, V. P.; and Goswami, D. W.; Chemically enhanced sunlight for killing bacteria; Journal of Solar Energy Engineering, Vol. **119**; pp. 85-91;February 1997

[39] Goswami, D. Y.; Trivedi, D. M.; Block, S. S.; Photocatalytic disinfection of indoor air; Transactions of ASME, **Vol. 119**, pp. 92-96; 1997

[40] Sauer, M. L., and D. F. Ollis; Acetone oxidation in a photocatalytic monolith reactor; Journal of Catalysis **149**, pp. 81-89; 1994

[41] Nimlos, M. R.; Wolfrum,E. J.; Brewer, M. L.; Fennhell, J. A.; Bintner, G.; Gas-phase heterogeneous photocatalytic oxidation of ethanol: Pathways and kinetic modeling; Environmental Science & Technology **30**; pp. 3102-3110; 1996

[42] Cao, L.; Huang, A.; Spiess, F.-J.; Suib, S. L.; Gas-Phase Oxidation of 1-butene using nanoscale TiO_2 Photocatalysts; Journal of catalysis **188**; pp. 48-57; 1999

[43] Kormann, C. Bahnemann D. W.; Preparation and characterization of quantum-size titanium dioxide; Journal of Physical Chemistry **92**; pp. 5196-5201; 1988

[44] Ahmed, S.; Attia, Y. A.; Aerogel materials for photocatalytic detoxification of cyanide wastes in water; Journal of Non-Crystalline Solids **186**, pp. 402-407; 1995

[45] Anderson, C. and Bard, A. J.; An improved photocatalyst of TiO_2/SiO_2 prepared by a sol-gel synthesis; Journal of Physical Chemistry **99**; pp. 9882-9885; 1995

[46] Takeda, N.; Torimoto, T.; Sampath., S.; Kuwabata, S; and Yoneyama, H; Effect of inert supports for titanium dioxide loading on enhancement of photodecomposition rate of gaseous propionaldehyde; Journal of Physical Chemistry **99**; pp. 9986-9991; 1995

[47] Torimoto, T.; Ito, S.; Kuwabata, S.; Yoneyama, H; Effects of adsorbants used as supports for titanium dioxide loading on photocatalytic degradation of propyzamide; Environmental Science and Technology **30**, pp.1275-1281, 1996

[48] Grätzel, M. and Howe, R. F.; Electron paramagnetic resonance studies of doped TiO_2 colloids; Journal of Physical Chemistry **94**; pp. 2566-2572; 1990

[49] Soria, J., Conesa, J. C.; Dinitrogen photoreaction to ammonia over titanium dioxide powders doped with ferric ions; Journal of Physical Chemistry **95**; pp. 274-282; 1991

[50] Moser, J.; Punchihewa, S.; Infelta, P. P.; and Grätzel, M.; Surface complexation of colloidal semiconductors strongly enhances interfacial electron-transfer rates; Langmuir **7**, pp. 3012-3-18; 1991

[51] Hennig, H., R. Billing, H. Knoll; Photocatalysis: Definitions and Classifications, Photosensitization and Photocatalysis Using Inorganic and Organometallic Compounds; K. Kalyanasundaram, M. Grätzel (eds.), Kluwer Academic Publishers, Dordrecht (Netherlands), pp. 51-69; 1993

[52] Chanon, M.; Schiavello; Introduction to Photocatalysis; pp. 1-14; Chanon, M. (ed.); Homogeneous Photocatalysis; John Wiley & Sons, Chichester, 1997

[53] Kotz, J. C. and Purcell, K. F.; Chemistry and Chemical Reactivity; Saunders College Publishing, Philadelphia, 1987

[54] Fox, M. A.; Photocatalytic oxidation of organic substrates; Schiavello, M.(ed.); Photocatalysis and Environment; pp. 445-467; Kluwer Academic Publishers; Dordrecht, 1988

[55] Voïnov, M. and Augustynski, J.; Introduction to the physics of semiconductor photocatalysis; Schiavello, M (ed.).; Heterogeneous Photocatalysis; John Wiley & Sons, Chichester; 1997

[56] Linsebigler, A.L.; Guangquan Lu; and J. T. Yates, Jr.; Photocatalysis on TiO_2 surfaces: Principles, mechanisms, and selected results; Chemical Reviews **95**; pp. 735-758, 1995

[57] Ibusuku, T. and K. Takeuchi, Atmospheric Environment 20, No. 9, pp. 1711-1715 (1986)

[58] Nogueira, R. F. P and Jardim, W. F.; Photodegradation of methylene blue; Journal of Chemical Education **70**, No. 10; pp. 861-682, October 1993

[59] Mills, G. and Hoffmann, M.R.; Photocatalytic Degreadation of pentachlorophenol on TiO_2 particles: Identification of intermediates and mechanism of reaction; Environmental Science and Technology 27, pp. 1681-1689, 1993
[60] Navio, J. A.; Cerrillos, C.; Marchena F. J.; Pablos, F.; and Pradera, M. A.; Photoassisted degradation of n-butyltin chlorides in air-equilibrated aqueous TiO_2 suspensions; Langmuir 12; pp. 2007-2014; 1996
[61] Cermenati, L; Pichat, P.; Guillard, C.; and Albini, A.; Probing the TiO_2 photocatalytic mechanisms in water purification by use of quinoline, phot-fenton generated OH* radicals and superoxide dismutase; Journal of Physical Chemistry B, 101; pp. 2650-2658; 1997
[62] Sjogren, J. C. and Sierka, R. A.; Inactivation of phage MS2 by iron-aided titanium dioxide photocatalysis; Applied Environmental Microbiology Vol. 60, No. 1; pp. 344-347; 1993
[63] Prairie, M. R.; Evans, L. R.; Stange, B. M.; and Martinez, S. L.; An investigation of TiO_2 photocatalysis for the treatment of water contaminated with metals and organic chemicals; Environmental Science and Technology 27, pp. 1776-1782, 1993
[64] Vinodgopal, K, Wynkoop, D. E.; and Kamat, P. V.; Environmental photochemistry on semiconductor surfaces: Photosensitized degradation of a textile Azo dye, acid orange 7, on TiO_2 particles using visible light; Environmental Science and Technolgy Vol. 30, No. 5, pp. 1660-1666, 1996
[65] Disdier J.; Herrmann, J.-M.; and Pichat, P.; Platinum/Titanium dioxide catalysts; Journal of Chemical Society, Faraday Transcripts 1 79, pp. 651-660; 1983
[66] Viswanathan, B.; Viswanath, R. B.; and Mary, F. D.; Photocatalytic activity of metallised titania systems; Indian Journal of Chemistry 34A; pp. 5-10, 1995
[67] Bahnemann, D. W.; Mönig, J.; and Chapmen, R.; Efficient photocatalysis of the irreversible one-electron and two-electron reduction of Halyhane on platinized colloidal titanium dioxide in aqueous suspension; Journal of Physical Chemistry 91; pp. 3782-3788; 1987
[68] Viswanathan, B.and Lakshmi, T.; Strong metal support interaction (SMSI) state in titania supported iron catalysts – EHMO model cluster calculations; Indian Journal of Chemistry 32A; pp. 937-941, 1993
[69] Choi, W.; Termin, A.; and Offmann, M. R.; The role of metal ion dopants in quantum sized TiO_2: Correlation between photoactivity and charge carrier recombination dynamics; Journal of Physical Chemistry 98; pp. 13669-13679; 1994
[70] Bhakta, D.; Shukla, S.S.; Chandrasekharalah, M. S.; Margrave, J. L.; Environmental Science and Technology 26, pp. 625-626, 1992
[71] Fernandez, A.; Lassaletta, G.; Justo, A.; Gonzales-Elipe, A. R.; Herrmann, J.-M.; Tahiri, H.; Ait-Ichou, Y.; Preparation and characterization of TiO2 photocatalysts supported on various rigid supports (glass, quartz and stainless steel). Comparative studies of photocatalytic activity in water purification; Applied Catalysis B:Envirinmental 7; pp. 49-63; 1995
[72] Palmisano, L.; and Sclafani, A.; Thermodynamics and kinetics for heterogeneous photocatalytic processes; Schiavello, M. (ed.); Heterogeneous Photocatalysis; John Wiley & Son Ltd., pp. 109-132; Chichester, 1997
[73] Bischoff, B. L., and Anderson, M. A.; Peptizatio process in the sol-gel preparation of porous anatase (TiO_2); Chemical Materials 7; pp 1772-1778; 1995
[74] Reeves, P.; Ohlhausen, R.; Sloan, D.; Pamplin, K.; Scoggins, T.; Photocatalytic destruction of organic dyes in aqueous TiO2 suspensions using concentrated simulated and natural solar energy; Solar Energy Vol. 48, No. 6, pp. 413-420, 1992
[75] Product specifications provided by Degussa Corporation
[76] Tewari, P.H; Hunt, A. J.; Lieber, J. G.; and Lofftus, K.; Microstructural properties of transparent aerogels; Proceedings of the First International Symposium, Fricke, J. (ed); pp.2-21; Springer Verlag, Berlin, 1986
[77] Dreyer, M., G.K. Newman, J. H. Harwell, Gas Storage on Silica Aerogels and Metal-Modified Silica Aerogels, Thesis, University of Oklahoma, 1995
[78] Brinker, C. J. and Scherer, G. W.; Relationships between the sol-to-sol gel and gel-to-glas conversion; in Ultrastructure of Processing Ceramics, Glasses, and Composites; Hench, L. L. and Ulrich, D. R. (ed_, John Wiley & Sons, New York; pp. 43-59; 1984
[79] Fricke, J.; Aerogels – A fascinating class of high-performance porous solids; Proceedings of the First International Symposium, Fricke, J. (ed); pp.2-21; Springer Verlag, Berlin, 1986
[80] Dagan, G. and Tomkiewicz, M.; TiO_2 Aerogels for photocatalytic decontamination of aquatic environments"; The Journal of Physical Chemistry 97, No. 49; pp. 12651-12655; 1993
[81] Zang, L.; Lange, C.; Abraham, I.; Storck, S.; Maier, W. F.; and Kisch, H.; Amorphous microporous titania modified with platinum (IV)chloride - A new type of hybride photocatalyst for visible light detoxification; Journal of Physical Chemistry B1 102; pp. 10765-10771; 1998
[82] Chen, J.; Ollis, D. F.; Rilkens, W. H.; and Bruning, H.; Kinetic processes of photocatalytic mineralization of alchohls on metallized titanium dioxide; Water Research Vol. 33, No. 5; pp. 1173-1180; 1999

[83] Sadeghi, M.; Liu, W.; Zhang, T.-G.; Stavropoulos, P.; and Levy, B.; Role of photoinduced charge carrier separation distance in heterogeneous photocatalysis: Oxidative degradation of cH3OH vapor in contact with Pt/TiO_2 and cofumed TiO_2-Fe_2O_3; Journal of Physical Chemistry **100**; pp. 19466-19474; 1996

[84] Zhang, Z.; Wang, C.-C.; Zakaria, R.; and Ying, J., Y.; Role of particle size in nanocrystalline TiO_2-based photocatalysts; Journal of Physical Chemistry B **102**; pp. 10871-10878; 1998

[85] Yoldas, B. E.; Hydrolysis of titanium alkoxide and effects of hydrolytic polycondensation parameters; Journal of Material Science 21; pp. 1087-1092; 1986

[86] Scolan, E.; Sanchez, C.; Synthesis and characterization of surface-protected nanocrystalline titania particles; Chem. Materials **10**; pp. 3217-3223; 1998

[87] Selle, M. H.; Sl0blom, J.; and Lindberg, R.; Preparation of spherical, mixed SiO_2/TiO_2 particles by the sol technique; Colloid Polymer Science **273**; pp. 951-958; 1995

[88] Newman, J. K.; Gas Adsorption on Novel Adsorbents; Dissertation at University of Oklahoma, 1995

[89] Herrman, J.-M.; Disdier, J.; Pichat, P.; Fernandez, A.; Gonzales-Elipe, A.; Munuera, G.; and Leclercq, C.; Titania-supported bimetallic catalyst synthesis by photocatalytic codeposition at ambient temperature: Preparation and characterization of Pt-Rh, Ag-Rh, and Pt-Pd couples; Journal of Catalysis **132**, pp. 490-497; 1991

[90]Herrman, J.-M.; Disdier, J.; Pichat, P.; Photoassisted platinum deposition on TiO_2 powder using various platinum complexes; Journal of Physical Chemistry 90; pp. 6028-6034; 1986

[91] Chen, Y.; Kaesz, H. D.; Thridandam, H.; Hicks, R. F.; Low-temperature organometallic chemical vapor deposition of platinum; Applied Physics Letters **53**, No. 17; pp. 1591-1592; 1988

[92] Dryden, N. H.; Kumar, R.; Ou, E.; Rashidi, M.; Roy, S.; Norton, P. R.; and Puddephatt, R. J.; and Scott, J. D.; Chemical vapor deposition of platinum: New precursors and their properties; Chemical Materials **3**; pp. 677-685; 1991

[93] Dossi, C.; Psaro, R.; Sordelli, L.; Bellatreccia, M.; and Zanoni, R.; Chemical vapor deposition of platinum hexafluoroacetlyacetonate inside HL zeolites: Role of metal-proton interactions; Journal of Catalysis **159**, pp. 435-440; 1996

[94] Dossi, C.; Psaro., R.; Bartsch, A.; Fusi, A.; Sordelli, L.; Ugo, R.; Bellatreccia, M.; Zanoni, R.; and Vlaic, G.; Chemical vapor deposition of platinum hexafluoroacetlyacetonate inside KL zeolites: A new route to nonacidic platinum-in-zeolites catalysts; Journal of Catalysis **145**, pp. 377-383; 1994

[95] Jacobs, G.; Novel Pt/KL Catalysts for the Aromatization of n-Hexane; Dissertation at University of Oklahoma, 2000

[96] Schmaderer, F.; Wahl, G.; Jahnke, B.; Organometallic chemical vapor deposition of superconducting $YBA_2CU_3O_{7-\square}$; Sov. Journal of Low Temperature Physics **16** (5); pp. 362-364; 1990

[97] Alexander, L. and Klug, H. P.; Basic aspects of X-ray absorption in quantitative diffraction analysis of powder mixtures; Powder Diffraction **4**; No. 2; pp. 66-69; 1989

[98] Klug, H. and Alexander, L.; X-Ray Diffraction Procedures For Polycrystalline and Amorphous Materials; Analysis of crystalline powders pp. 531-565; 2nd Edition, John Wiley & Sons, New York, 1974

[99] http://www-biol.paisley.ac.uk/courses/stfunmac/glossary/agarose.html

[100] Kenkel, J.; Analytical Chemistry for Technicians, 2nd Edition; pp., 217-23; Lewis Publishers Boca Raton, 1994

[101] ANSI/ASHREAE 41.6; p.6; 1994

[102] Campbvell, L. K.; Na, B. K.; and Ko, E. I.; Synthesis and characterization of titania aerogels; Chem. Materials; pp. 1329-1333; 1992

[103] Vorontsov, A. V.; Stoyoanova, I. V.; Kozlov, D., V.; Simagina, V., I.; and Savinov, E., E.; Kinetics of the photocatalytic oxidation of gaseous acetone over platinized titanium dioxide; Journal of Catalysis **189**, pp. 360-369; 2000

[104] Campostrini, R., Carturan, G., Palmisano, L., Schiavello, M., Sclafani, A.; Sol-gel derived anatase TiO_2: morphology and photoactivity; Materials Chemistry and Physics **38**, pp. 277-283, 1994

[105] Piaggio, P.; Bottino, A.; Capannelli, and Carosini, E.; Characterization of SiO2 thin film obtained by the sol-gel route from TEOS and Triton X45; Langmuir **11**; pp. 3970-3974; 1995

[106] Chen, H., Ruckenstein, E.; Surfactant-modified hydrous titanium oxide gels; Journal of Colloid and Interface Science, Vol. 145, No. 2, September 1991, pp. 581-590

[107] Martra, G.; Coluccia, S.; Marchese, L.; Augugliaro, V.; Loddo, V.; Palmisano, L.; Schiavello, M.; The role of H_2O in th ephotocatalytic oxidation of toluene in vapour phase on anatase TiO2 catalyst – A FTIR study; Catalysis Today 53, pp. 695-702; 1999

[108] Munuera, G.; Rives-Arnau, V.; and Saucedo, A.; Photo-adsorption abd photo-desorption of oxygen on highly hydroxylated TiO_2 surfaces; Journal of Chemical Society, Faraday Trans. 1 Vol. 75; pp. 736-747; 1979

[109] Primet, M.; Pichat, P.; Mathieu, M.-V.; Infrared study of the surface of titanium dioxides; The Journal of Physical Chemistry, Vol. 75, No. 9; pp. 1221-1226; 1971

[110] Augugliaro, V. Coluccia, S.; Loddo V.; Marchese, L.; Martra, G.; Palmisano, L.; Schiavello, M.;Photocatalytic oxidation of gaseous toluene on anatase TiO2 catalyst: mechanistic aspects and FT-IR investigation; Applied Catalysis B: Environmental 20, pp. 15-27; 1999
[111] Lin-Vien, D.; Colthup, N. B.; Fately, W. G.; Grasselli, J. G.; The Handbook of Infrared and Raman Characteristic Frequencies of Organic Molecules; Academic Press, San Diego, 1998
[112] Aizawa, M.; FT-IR liquid attenuated total reflection study of TiO2-SiO2 sol-gel reaction; Journal of Non-Crystalline Solids 128; pp. 77-85; 1991
[113] Hutter, R.; Dutoit, D. C. M.; Mallat, T.; Schneider, M.; and Baiker, A.; Novel mesoporous titania-silica aerogels highly active for the selective epoxidation of cyclic olefins; Journal of Chemical Society, Chemical Communications Vol. ??; pp. 163-164; 1995
[114] Lin-Vien, D., Colthup, N.B., Fateley, W.G., Grasselli, J.G., Handbook of Infrared and Raman Characteristic Frequencies of Organic Molecules, Academic Press, San Diego, 19??, p.259
[115] Aizawa, M.; FT-IR liquid attenuated total reflection study of TiO2-SiO2 sol-gel reaction; Journal of Non-Crystalline Solids; **Vol. 128**, pp. 77-85, 1991
[116] Nyquist, R. A.; and Kagel, R.; Infrared Spectra of Inorganic Compounds (3800-45 cm^{-1}); p. 211; Academic Press, New York; 1971
[117] Hill, C. G., Jr.; An Introduction to Chemical Engineering Kinetics and Reactor Design; John Wiley & Sons, New York 1977
[118] Perry, R. H.; Green, D. W.; Maloney, J., O.; Perry's Chemical Engineers' Handbook, 6th Edition; McGraw Hill, New York; 1984
[119] Platzer, W.J.; Bergkvist, M., Bulk and surface light scattering from transparent silica aerogel; Solar Energy Materials and Solar Cells, Vol. 31 (1993), pp. 243-251
[120] Vincent, W. F.; Rae, R.; Laurion, I.; Williams, C. H.; and Priscu, J. C.; Transparency of Antarctic ice-covered lakes to solar UV radiation; Limnology and Oceanography **43**, No. 4; pp.618-624; 1998
[121] Armstrong, R.; Encapsulation of TiO2 as a photocatalyst for the decontamination of indoor air; Thesis at the University of Oklahoma, 2001
[122] http://www.toxicology.mc.vanderbilt.edu/Outreach%20web/Poison/NATGAS.html
[123] http://encarta.msn.com/find/Concise.asp?ti=03CCE000
[124] http://www.comptons.com/encyclopedia/ARTICLES/0050/00721664_A.html
[125] http://www.ldeq.org/
[126] http://www-bcf.usc.edu/~bfilter/f376.html
[127] http://www.atsdr.cdc.gov/tfacts21.html
[128] http://www.bulb.com/spring/ethylene.asp
[129] http://www.ethylenecontrol.com/about.html
[130] Felder, R., M. and Rousseau, R. W.; Elementary Principles of Chemical Processes; John Wiley & Sons, Inc.; New York, 1986
[131] Ollis, D. F.; Peral, J.; Heterogeneous photocatalytic oxidation of atmospheric trace contaminants; Semiannual progress Report No.1, North Carolina State University, 1991
[132] Fenoglio, R. J.; Alvarez, W.; Nunez, G. M.; Resasco, D. E.; Interactions of the impregnating solution with the support during the preparation of Rh/TiO2 catalysts; Poncelet, G.; Jacobs, P. A.; Grange, P.; and Delmon, B. (editors) Preparation of Catalysts V, Elsevier Science Publishers B.V., Amsterdam, 1991
[133] Signoretto, M.; Pinna, F.; Strukul, G.; Chies, P.; Cerrato, G.; Ciero, S. D.i; and Morterra, C.; Platinum-promoted and unpromoted sulfated zirconia catalysts prepared by a one-step aerogel procedure; Journal of Catalysis 167, pp. 522-532; 1997